In Israel, fears for the future of science pp. 715 & 723

What is next for cell atlases? p. 733

The progenitor star of a magnetar p. 761

Science

$15
18 AUGUST 2023
science.org

AAAS

BURNED OUT

California tar pits record how fire drove Pleistocene megafauna decline pp. 724 & 746

CONTENTS

18 AUGUST 2023 • VOLUME 381 • ISSUE 6659

The still-bubbling tar at the La Brea Tar Pits and Museum yields clues to a great extinction.

PHOTO: NATALIJA KENT/COURTESY OF NHMLAC

NEWS

IN BRIEF

716 News at a glance

IN DEPTH

718 Maui's deadly blazes reveal a fire-prone Hawaii
Flammable, invasive grasses have changed the island landscape, say its shaken scientists *By M. Rains*

719 NIH project probes the human body's multitude of genomes
Agency launches major effort to explore importance of accumulating mutations in somatic cells *By M. Leslie*

720 After string of failures, Japan aims to launch x-ray telescope
Groundbreaking XRISM will capture spectra, revealing the motion and composition of million-degree gases *By D. Clery*

722 Myth of Alaskan city's immunity to tsunamis dispelled
Lucky low tide helped Anchorage dodge catastrophic 1964 tsunami, first analysis of location's risk finds *By C. Elliott*

723 Israeli scientists speak out against 'destructive' policies
Many fear erosion of academic freedom and loss of talent *By M. Chabin*
EDITORIAL p. 715

FEATURES

724 Death by fire
Wildfires, intensified by climate change and perhaps human activity, may have doomed Southern California's big mammals 13,000 years ago *By M. Price*
RESEARCH ARTICLE p. 746; PODCAST

INSIGHTS

PERSPECTIVES

728 Bacteria stretch and bend oil to feed their appetite
Microbes reshape oil droplets to speed biodegradation *By T. J. McGenity and P. P. Laissue*
RESEARCH ARTICLE p. 748

729 Targeting cancer with molecular glues
Molecular glues suppress the active form of the oncogenic protein KRAS *By J. O. Liu*
RESEARCH ARTICLE p. 794

731 Extracting resources from abandoned mines
Recovering minerals and metals from abandoned mines could aid decarbonization *By Z. Bao* et al.

733 What is a cell type?
A next step for cell atlases should be to chart perturbations in human model systems *By J. S. Fleck* et al.

POLICY FORUM

735 Create a culture of experiments in environmental programs
Organizations need a better "learning by doing" approach *By P. J. Ferraro* et al.

BOOKS *ET AL.*

738 Public health versus personalized medicine
Environmental health research is being undermined by genomic medicine, argues a philosopher *By H. T. Greely*

739 Battling information bias
Do not wait for society to reject scientific disinformation, tout the truth now *By J. Wai*

LETTERS

740 The global impact of EU forest protection policies
By G. Cerullo et al.

740 Solar energy projects put food security at risk
By Z. B. Li et al.

741 Save China's gaurs
By T. Xiang

RESEARCH

IN BRIEF

743 From *Science* and other journals

RESEARCH ARTICLES

746 Paleontology
Pre–Younger Dryas megafaunal extirpation at Rancho La Brea linked to fire-driven state shift *F. R. O'Keefe* et al.
RESEARCH ARTICLE SUMMARY; FOR FULL TEXT: DOI.ORG/10.1126/SCIENCE.ABO3594
NEWS STORY p. 724

747 Human development
Yolk sac cell atlas reveals multiorgan functions during human early development *I. Goh* et al.
RESEARCH ARTICLE SUMMARY; FOR FULL TEXT: DOI.ORG/10.1126/SCIENCE.ADD7564

748 Biophysics
Alcanivorax borkumensis biofilms enhance oil degradation by interfacial tubulation *M. Prasad* et al.
PERSPECTIVE p. 728

754 Protein design
Design of stimulus-responsive two-state hinge proteins *F. Praetorius* et al.

761 Stellar astrophysics
A massive helium star with a sufficiently strong magnetic field to form a magnetar *T. Shenar* et al.

766 Optics
Overcoming losses in superlenses with synthetic waves of complex frequency *F. Guan* et al.

771 Molecular biology
Human POT1 protects the telomeric ds-ss DNA junction by capping the 5′ end of the chromosome *V. M. Tesmer* et al.

778 Physics
Ergodicity breaking in rapidly rotating C_{60} fullerenes *L. R. Liu* et al.

784 Nanomaterials
Ligand-protected metal nanoclusters as low-loss, highly polarized emitters for optical waveguides *X. Wang* et al.

790 Physics
Universal theory of strange metals from spatially random interactions *A. A. Patel* et al.

794 Cancer
Chemical remodeling of a cellular chaperone to target the active state of mutant KRAS *C. J. Schulze* et al.
PERSPECTIVE p. 729

799 Biophysics
MyoD-family inhibitor proteins act as auxiliary subunits of Piezo channels *Z. Zhou* et al.

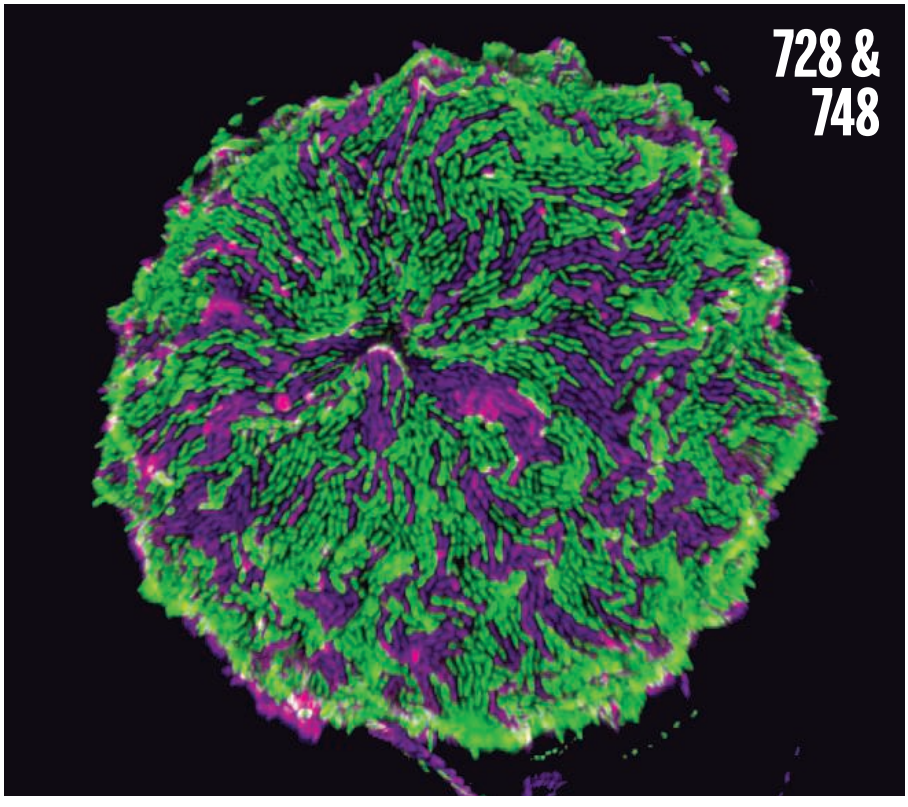

Confocal image of bacteria on the interface after buckling

PHOTO: PRASAD *ET AL.*

DEPARTMENTS

715 Editorial
No democracy, no academia
By E. Albin et al.
NEWS STORY p. 723

806 Working Life
Teaching workplace skills
By T. Głowacki

ON THE COVER

This image shows the youngest dated specimens of (clockwise from top left) Harlan's ground sloth (*Paramylodon harlani*), western camel (*Camelops hesternus*), western horse (*Equus occidentalis*), dire wolf (*Aenocyon dirus*), antique bison (*Bison antiquus*), and saber-toothed tiger (*Smilodon fatalis*). These fossils were excavated at Rancho La Brea in Los Angeles, California, and are the last known surviving members of their species. See pages 724 and 746. *Photo: S. Abramowicz, NHMLAC*

Science Staff 714
Science Careers 805

SCIENCE (ISSN 0036-8075) is published weekly on Friday, except last week in December, by the American Association for the Advancement of Science, 1200 New York Avenue, NW, Washington, DC 20005. Periodicals mail postage (publication No. 484460) paid at Washington, DC, and additional mailing offices. Copyright © 2023 by the American Association for the Advancement of Science. The title SCIENCE is a registered trademark of the AAAS. Domestic individual membership, including subscription (12 months): $165 ($74 allocated to subscription). Domestic institutional subscription (51 issues): $2411; Foreign postage extra: Air assist delivery: $107. First class, airmail, student, and emeritus rates on request. Canadian rates with GST available upon request, GST #125488122. Publications Mail Agreement Number 1069624. **Printed in the U.S.A.**
Change of address: Allow 4 weeks, giving old and new addresses and 8-digit account number. **Postmaster:** Send change of address to AAAS, P.O. Box 96178, Washington, DC 20090–6178. **Single-copy sales:** $15 each plus shipping and handling available from backissues.science.org; bulk rate on request. **Authorization to reproduce** material for internal or personal use under circumstances not falling within the fair use provisions of the Copyright Act can be obtained through the Copyright Clearance Center (CCC), www.copyright.com. The identification code for *Science* is 0036-8075. *Science* is indexed in the *Reader's Guide to Periodical Literature* and in several specialized indexes.

ScienceCareers online @sciencecareers.org

PHARMACY
UNIVERSITY OF MICHIGAN

CHAIR, PHARMACEUTICAL SCIENCES DEPARTMENT
UNIVERSITY OF MICHIGAN, COLLEGE OF PHARMACY

The University of Michigan College of Pharmacy invites applications for the position of **Chair in the Department of Pharmaceutical Sciences**, in association with an endowed faculty position at the rank of **professor**, with tenure.

This is a unique opportunity to provide vision and leadership to faculty at a major research-intensive university who are nationally and internationally recognized for innovative research and teaching in the field of pharmaceutical sciences and its many disciplines.

The Chair is expected to maintain and promote an enabling environment in the department to foster the continued advancement of progressive and innovative research, teaching, and service. In addition to their regular responsibilities as a faculty member, the department chair will maintain overall administrative responsibility for the Department, participate in the overall guidance and administration of the College, and act as a representative of the College of Pharmacy. Applicants are invited to view the College of Pharmacy's web page for more information about our programs (**https://pharmacy.umich.edu**).

Candidates for this position must have a Ph.D., and a distinguished record in research and education, including a well-funded research program and ability to develop programmatic collaborative research and funding across the pharmaceutical, biomedical, chemical, and engineering sciences. We are especially interested in applicants working in biopharmaceutics, pharmacokinetics, delivery of complex and large molecules, the gut microbiome, and other emerging strategies to improve drug formulation and delivery, including machine learning and artificial intelligence methods, but all qualified applicants are encouraged to apply.

We seek applicants who will provide inspiration and leadership in research and teaching by: demonstrating a strong record of leadership in research and professional activities; demonstrating a strong commitment to the educational objectives of the graduate, professional, and undergraduate degree programs at the College; embracing and expanding our commitment to DEI and the College's interdisciplinary, collaborative nature at the University of Michigan; and articulating how they will support the College's mission and values: **https://pharmacy.umich.edu/academic-research-about/about-college/**. Ideal candidates will have a record of successful mentorship of others which speaks to their ability to mentor faculty and trainees at all levels. A record of demonstrated leadership and administrative abilities is desirable.

HOW TO APPLY:
Interested applicants should submit a curriculum vitae electronically to: **apply.interfolio.com/128817**.

Review of applications will begin immediately and continue until the position is filled.

U-M EEO/AA Statement: *The Department of Pharmaceutical Sciences the College of Pharmacy, and the University of Michigan seek to recruit and retain a diverse workforce as a reflection of our commitment to serve our diverse constituents, and to maintain the excellence of the Department, College, and University. The University of Michigan, NSF ADVANCE Institutional Transformation grant awardee, is supportive of the needs of dual career couples, and is an Equal Opportunity/Affirmative Action institution. It is committed to fostering and maintaining a diverse work culture that respects the rights and dignity of each individual, without regard to race, color, national origin, ancestry, religious creed, sex, gender identity, sexual orientation, gender expression, height, weight, marital status, disability, medical condition, age, or veteran status.*
U-M COVID-19 Vaccination Policy: *COVID-19 vaccinations are required for College of Pharmacy students, faculty and staff, if they are working in the following areas: Michigan Medicine including the Medical School, Dental School, University Health System or the Mary A. Rackham Institute. This includes those working remotely and temporary workers. More information on this policy is available on the U-M Health Response.*

PHARMACY
UNIVERSITY OF MICHIGAN

CHAIR, DEPARTMENT OF MEDICINAL CHEMISTRY
UNIVERSITY OF MICHIGAN, COLLEGE OF PHARMACY

The University of Michigan College of Pharmacy invites applications for the position of **Chair in the Department of Medicinal Chemistry**, in association with an endowed faculty position at the rank of **professor**, with tenure.

This is a unique opportunity to provide vision and leadership to faculty at a major research-intensive university who are nationally and internationally recognized for innovative research and teaching in the field of medicinal chemistry and its many disciplines.

The Chair is expected to maintain and promote an enabling environment in the department to foster the continued advancement of innovative research, teaching, and service. In addition to their regular responsibilities as a faculty member, the department chair will maintain overall administrative responsibility for the Department, participate in the overall guidance and administration of the College, and act as a representative of the College of Pharmacy. Applicants are invited to view the College of Pharmacy's web page for more information about our programs (**https://pharmacy.umich.edu**).

Candidates for this position must have a Ph.D. in chemistry, medicinal chemistry, computer science, or a related field. Applicants must also have a distinguished record in research and education, including a well-supported research program and ability to develop programmatic collaborative research and external funding. All qualified applicants are encouraged to apply.

We seek applicants who will provide inspiration and leadership in research and teaching by: demonstrating a strong record of leadership in research and professional activities; demonstrating a strong commitment to the educational objectives of the graduate, professional, and undergraduate degree programs at the College; embracing and expanding our commitment to DEI and the College's interdisciplinary, collaborative nature at the University of Michigan; and articulating how they will support the College's mission and values: **https://pharmacy.umich.edu/academic-research-about/about-college/**. Ideal candidates will have a record of successful mentorship of others, which speaks to their ability to mentor faculty and trainees at all levels. A record of demonstrated leadership experience and administrative abilities is desirable.

HOW TO APPLY:
Interested applicants should submit a curriculum vitae electronically to: **http://apply.interfolio.com/129542**. Review of applications will begin immediately and continue until the position is filled.

U-M EEO/AA Statement: *The Medicinal Chemistry Department at the College of Pharmacy, and the University of Michigan seek to recruit and retain a diverse workforce as a reflection of our commitment to serve our diverse constituents, and to maintain the excellence of the Department, College, and University. The University of Michigan, NSF ADVANCE Institutional Transformation grant awardee, is supportive of the needs of dual career couples, and is an Equal Opportunity/Affirmative Action institution. It is committed to fostering and maintaining a diverse work culture that respects the rights and dignity of each individual, without regard to race, color, national origin, ancestry, religious creed, sex, gender identity, sexual orientation, gender expression, height, weight, marital status, disability, medical condition, age, or veteran status.*
U-M COVID-19 Vaccination Policy: *COVID-19 vaccinations are required for College of Pharmacy students, faculty and staff, if they are working in the following areas: Michigan Medicine including the Medical School, Dental School, University Health System or the Mary A. Rackham Institute. This includes those working remotely and temporary workers. More information on this policy is available on the U-M Health Response.*

Science AAAS

Editor-in-Chief Holden Thorp, hthorp@aaas.org

Executive Editor Valda Vinson

Editor, Research Jake S. Yeston **Editor, Insights** Lisa D. Chong **Managing Editor** Lauren Kmec

DEPUTY EDITORS Gemma Alderton (UK),Stella M. Hurtley (UK), Phillip D. Szuromi, Sacha Vignieri **SR. EDITORS** Caroline Ash (UK), Elisa Collado Fregoso (UK), Michael A. Funk, Brent Grocholski, Di Jiang, Priscilla N. Kelly, Marc S. Lavine (Canada), Sarah Lempriere (UK), Mattia Maroso, Yevgeniya Nusinovich, Ian S. Osborne (UK), L. Bryan Ray, Seth Thomas Scanlon (UK), H. Jesse Smith, Keith T. Smith (UK), Jelena Stajic, Peter Stern (UK), Valerie B. Thompson, Brad Wible **ASSOCIATE EDITORS** Bianca Lopez, Madeleine Seale (UK), Corinne Simonti, Yury V. Suleymanov, Ekeoma Uzogara **LETTERS EDITOR** Jennifer Sills **NEWSLETTER EDITOR** Christie Wilcox **RESEARCH & DATA ANALYST** Jessica L. Slater **LEAD CONTENT PRODUCTION EDITORS** Chris Filiatreau, Harry Jach **SR. CONTENT PRODUCTION EDITOR** Amelia Beyna **CONTENT PRODUCTION EDITORS** Anne Abraham, Robert French, Julia Haber-Katris, Nida Masiulis, Abigail Shashikanth, Suzanne M. White **SR. EDITORIAL MANAGERS** Carolyn Kyle, Beverly Shields **SR. PROGRAM ASSOCIATE** Maryrose Madrid **EDITORIAL ASSOCIATE** Joi S. Granger **SR. EDITORIAL COORDINATORS** Aneera Dobbins, Jeffrey Hearn, Lisa Johnson, Ronmel Navas, Jerry Richardson, Alice Whaley (UK), Anita Wynn **EDITORIAL COORDINATORS** Maura Byrne, Clair Goodhead (UK), Alexander Kief, Isabel Schnaidt, Qiyam Stewart, Brian White **ADMINISTRATIVE COORDINATOR** Karalee P. Rogers **ASI DIRECTOR, OPERATIONS** Janet Clements (UK) **ASI OFFICE MANAGER** Victoria Smith **ASI SR. OFFICE ADMINISTRATORS** Dawn Titheridge (UK), Jessica Waldock (UK) **SCIENCE PRESS PACKAGE EXECUTIVE DIRECTOR** Meagan Phelan **DEPUTY DIRECTOR** Matthew Wright **SENIOR WRITER** Walter Beckwith **WRITERS** Joseph Cariz, Abigail Eisenstadt, Nyla Hussain **SENIOR COMMUNICATIONS ASSOCIATE** Zachary Graber **COMMUNICATIONS ASSOCIATES** Kiara Brooks, Haley Riley, Mackenzie Williams, Sarah Woods

News Editor Tim Appenzeller

NEWS MANAGING EDITOR John Travis **INTERNATIONAL EDITOR** David Malakoff **DEPUTY NEWS EDITORS** Rachel Bernstein, Shraddha Chakradhar, Elizabeth Culotta, Martin Enserink, David Grimm, Eric Hand (Europe) Kelly Servick **SR. CORRESPONDENTS** Daniel Clery (UK), Jon Cohen, Jeffrey Mervis, Elizabeth Pennisi **ASSOCIATE EDITORS** Jeffrey Brainard, Michael Price **NEWS REPORTERS** Adrian Cho, Jennifer Couzin-Frankel, Jocelyn Kaiser, Rodrigo Pérez Ortega (Mexico City), Robert F. Service, Erik Stokstad, Paul Voosen, Meredith Wadman **CONTRIBUTING CORRESPONDENTS** Warren Cornwall, Andrew Curry (Berlin), Ann Gibbons, Sam Kean, Kai Kupferschmidt (Berlin), Andrew Lawler, Mitch Leslie, Virginia Morell, Dennis Normile (Tokyo), Elisabeth Pain (Careers), Charles Piller, Gabriel Popkin, Joshua Sokol, Richard Stone, Emily Underwood, Gretchen Vogel (Berlin), Lizzie Wade (Mexico City) **CAREERS** Katie Langin (Associate Editor) **INTERNS** Tanvi Dutta Gupta, Celina Zhao **COPY EDITORS** Julia Cole (Senior Copy Editor), Cyra Master (Copy Chief) **ADMINISTRATIVE SUPPORT** Meagan Weiland

Creative Director Beth Rakouskas

DESIGN MANAGING EDITOR Chrystal Smith **GRAPHICS MANAGING EDITOR** Chris Bickel **PHOTOGRAPHY MANAGING EDITOR** Emily Petersen **MULTIMEDIA MANAGING PRODUCER** Kevin McLean **WEB CONTENT STRATEGY MANAGER** Kara Estelle-Powers **DESIGN EDITOR** Marcy Atarod **DESIGNER** Noelle Jessup **SENIOR SCIENTIFIC ILLUSTRATOR** Noelle Burgess **SCIENTIFIC ILLUSTRATORS** Austin Fisher, Kellie Holoski, Ashley Mastin **SENIOR GRAPHICS EDITOR** Monica Hersher **GRAPHICS EDITOR** Drew An-Pham **SENIOR GRAPHICS SPECIALISTS** Holly Bishop, Nathalie Cary **SENIOR PHOTO EDITOR** Charles Borst **PHOTO EDITOR** Elizabeth Billman **SENIOR PODCAST PRODUCER** Sarah Crespi **SENIOR VIDEO PRODUCER** Meagan Cantwell **SOCIAL MEDIA STRATEGIST** Jessica Hubbard **SOCIAL MEDIA PRODUCER** Sabrina Jenkins **WEB DESIGNER** Jennie Pajerowski

Chief Executive Officer and Executive Publisher Sudip Parikh

Publisher, Science Family of Journals Bill Moran

DIRECTOR, BUSINESS SYSTEMS AND FINANCIAL ANALYSIS Randy Yi **DIRECTOR, BUSINESS OPERATIONS & ANALYSIS** Eric Knott **MANAGER, BUSINESS OPERATIONS** Jessica Tierney **MANAGER, BUSINESS ANALYSIS** Cory Lipman **MANAGER, WEB ANALYTICS** Samantha Cressman **BUSINESS ANALYSTS** Kurt Ennis, Maggie Clark **FINANCIAL ANALYST** Isacco Fusi **BUSINESS OPERATIONS ADMINISTRATOR** Taylor Fisher **SENIOR PRODUCTION MANAGER** Jason Hillman **SENIOR MANAGER, PUBLISHING AND CONTENT SYSTEMS** Marcus Spiegler **CONTENT OPERATIONS MANAGER** Rebecca Doshi **SENIOR CONTENT & PUBLISHING SYSTEMS SPECIALIST** Jacob Hedrick **SENIOR PRODUCTION SPECIALIST** Kristin Wowk **PRODUCTION SPECIALISTS** Kelsey Cartelli, Audrey Diggs **DIGITAL PRODUCTION MANAGER** Lisa Stanford **SENIOR DIGITAL ADVERTISING SPECIALIST** Kimberley Oster **ADVERTISING PRODUCTION OPERATIONS MANAGER** Deborah Tompkins **DESIGNER, CUSTOM PUBLISHING** Jeremy Huntsinger **SR. TRAFFIC ASSOCIATE** Christine Hall **SPECIAL PROJECTS ASSOCIATE** Shantel Agnew

ASSOCIATE DIRECTOR, BUSINESS DEVELOPMENT Justin Sawyers **GLOBAL MARKETING MANAGER** Allison Pritchard **DIGITAL MARKETING MANAGER** Aimee Aponte **JOURNALS MARKETING MANAGER** Shawana Arnold **MARKETING ASSOCIATES** Ashley Hylton, Mike Romano, Lorena Chirinos Rodriguez, Jenna Voris **SENIOR DESIGNER** Kim Huynh

DIRECTOR AND SENIOR EDITOR, CUSTOM PUBLISHING Erika Gebel Berg **ASSISTANT EDITOR, CUSTOM PUBLISHING** Jackie Oberst **PROJECT MANAGER** Melissa Collins

DIRECTOR, PRODUCT & PUBLISHING DEVELOPMENT Chris Reid **DIRECTOR, BUSINESS STRATEGY AND PORTFOLIO MANAGEMENT** Sarah Whalen **DIRECTOR, PRODUCT MANAGEMENT** Kris Bishop **PRODUCT DEVELOPMENT MANAGER** Scott Chernoff **PUBLISHING PLATFORM MANAGER** Jessica Loayza **SR. PRODUCT ASSOCIATE** Robert Koepke **PRODUCT ASSOCIATES** Caroline Breul, Anne Mason

ASSOCIATE DIRECTOR, INSTITUTIONAL LICENSING MARKETING Kess Knight **BUSINESS DEVELOPMENT MANAGER** Rasmus Andersen **ASSOCIATE DIRECTOR, INSTITUTIONAL LICENSING SALES** Ryan Rexroth **INSTITUTIONAL LICENSING MANAGER** Marco Castellan, Claudia Paulsen-Young **SENIOR MANAGER, INSTITUTIONAL LICENSING OPERATIONS** Judy Lillibridge **SENIOR OPERATIONS ANALYST** Lana Guz **SYSTEMS & OPERATIONS ANALYST** Ben Teincuff **FULFILLMENT ANALYST** Aminta Reyes

ASSOCIATE DIRECTOR, US ADVERTISING Stephanie O'Connor **US MID WEST, MID ATLANTIC AND SOUTH EAST SALES** Chris Hoag **US WEST COAST SALES** Lynne Stickrod **ASSOCIATE DIRECTOR, ROW** Roger Goncalves **SALES REP, ROW** Sarah Lelarge **SALES ADMIN ASSISTANT, ROW** Victoria Glasbey **DIRECTOR OF GLOBAL COLLABORATION AND ACADEMIC PUBLISHING RELATIONS, ASIA** Xiaoying Chu **ASSOCIATE DIRECTOR, INTERNATIONAL COLLABORATION** Grace Yao **SALES MANAGER** Danny Zhao **MARKETING MANAGER** Kilo Lan **ASCA CORPORATION, JAPAN** Rie Rambelli (Tokyo), Miyuki Tani (Osaka)

DIRECTOR, COPYRIGHT, LICENSING AND SPECIAL PROJECTS Emilie David **RIGHTS AND PERMISSIONS ASSOCIATE** Elizabeth Sandler **LICENSING ASSOCIATE** Virginia Warren **RIGHTS AND LICENSING COORDINATOR** Dana James **CONTRACT SUPPORT SPECIALIST** Michael Wheeler

EDITORIAL
science_editors@aaas.org

NEWS
science_news@aaas.org

INFORMATION FOR AUTHORS
science.org/authors/science-information-authors

REPRINTS AND PERMISSIONS
science.org/help/reprints-and-permissions

MULTIMEDIA CONTACTS
SciencePodcast@aaas.org
ScienceVideo@aaas.org

MEDIA CONTACTS
scipak@aaas.org

PRODUCT ADVERTISING & CUSTOM PUBLISHING
advertising.science.org/products-services
science_advertising@aaas.org

CLASSIFIED ADVERTISING
advertising.science.org/science-careers
advertise@sciencecareers.org

JOB POSTING CUSTOMER SERVICE
employers.sciencecareers.org
support@sciencecareers.org

MEMBERSHIP AND INDIVIDUAL SUBSCRIPTIONS
science.org/subscriptions

MEMBER BENEFITS
aaas.org/membership/benefits

INSTITUTIONAL SALES AND SITE LICENSES
science.org/librarian

AAAS BOARD OF DIRECTORS

CHAIR Gilda A. Barabino

PRESIDENT Keith R. Yamamoto

PRESIDENT-ELECT Willie E. May

TREASURER Carolyn N. Ainslie

CHIEF EXECUTIVE OFFICER
Sudip Parikh

BOARD Cynthia M. Beall, Janine Austin Clayton, Kaye Husbands Fealing, Kathleen Hall Jamieson, Jane Maienschein, Robert B. Millard, Babak Parviz, William D. Provine, Juan S. Ramírez Lugo, Susan M. Rosenberg, Vassiliki Betty Smocovitis

BOARD OF REVIEWING EDITORS (Statistics board members indicated with **(S)**)

Erin Adams, *U. of Chicago*
Takuzo Aida, *U. of Tokyo*
Leslie Aiello, *Wenner-Gren Fdn.*
Deji Akinwande, *UT Austin*
Judith Allen, *U. of Manchester*
Marcella Alsan, *Harvard U.*
James Analytis, *UC Berkeley*
Paola Arlotta, *Harvard U.*
Delia Baldassarri, *NYU*
Nenad Ban, *ETH Zürich*
Christopher Barratt, *U. of Dundee*
Franz Bauer, *Pontificia U. Católica de Chile*
Ray H. Baughman, *UT Dallas*
Carlo Beenakker, *Leiden U.*
Yasmine Belkaid, *NIAID, NIH*
Philip Benfey, *Duke U.*
Kiros T. Berhane, *Columbia U.*
Joseph J. Berry, *NREL*
Alessandra Biffi, *Harvard Med.*
Chris Bowler, *École Normale Supérieure*
Ian Boyd, *U. of St. Andrews*
Malcolm Brenner, *Baylor Coll. of Med.*
Emily Brodsky, *UC Santa Cruz*
Ron Brookmeyer, *UCLA* **(S)**
Christian Büchel, *UKE Hamburg*
Johannes Buchner, *TUM*
Dennis Burton, *Scripps Res.*
Carter Tribley Butts, *UC Irvine*
György Buzsáki, *NYU School of Med.*
Mariana Byndloss, *Vanderbilt U. Med. Ctr.*
Annmarie Carlton, *UC Irvine*
Simon Cauchemez, *Inst. Pasteur*
Ling-Ling Chen, *SIBCB, CAS*
Wendy Cho, *UIUC*
Ib Chorkendorff, *Denmark TU*
Chunaram Choudhary, *Københavns U.*
Karlene Cimprich, *Stanford U.*
Laura Colgin, *UT Austin*
James J. Collins, *MIT*
Robert Cook-Deegan, *Arizona State U.*
Virginia Cornish, *Columbia U.*
Carolyn Coyne, *Duke U.*
Roberta Croce, *VU Amsterdam*
Molly Crocket, *Princeton U.*
Christina Curtis, *Stanford U.*
Ismaila Dabo, *Penn State U.*
Jeff L. Dangl, *UNC*
Nicolas Dauphas, *U. of Chicago*
Frans de Waal, *Emory U.*
Claude Desplan, *NYU*
Sandra Díaz, *U. Nacional de Córdoba*
Samuel Díaz-Muñoz, *UC Davis*
Ulrike Diebold, *TU Wien*
Stefanie Dimmeler, *Goethe-U. Frankfurt*
Hong Ding, *Inst. of Physics, CAS*
Dennis Discher, *UPenn*
Jennifer A. Doudna, *UC Berkeley*
Ruth Drdla-Schutting, *Med. U. Vienna*
Raissa M. D'Souza, *UC Davis*
Bruce Dunn, *UCLA*
William Dunphy, *Caltech*
Scott Edwards, *Harvard U.*
Todd Ehlers, *U. of Tübingen*
Nader Engheta, *UPenn*
Tobias Erb, *MPI Terrestrial Microbiology*
Karen Ersche, *U. of Cambridge*
Beate Escher, *UFZ & U. of Tübingen*
Barry Everitt, *U. of Cambridge*
Vanessa Ezenwa, *U. of Georgia*
Toren Finkel, *U. of Pitt. Med. Ctr.*
Natascha Förster Schreiber, *MPI Extraterrestrial Phys.*
Peter Fratzl, *MPI Potsdam*
Elaine Fuchs, *Rockefeller U.*
Caixia Gao, *Inst. of Genetics and Developmental Bio., CAS*
Daniel Geschwind, *UCLA*
Lindsey Gillson, *U. of Cape Town*
Gillian Griffiths, *U. of Cambridge*
Nicolas Gruber, *ETH Zürich*
Hua Guo, *U. of New Mexico*
Taekjip Ha, *Johns Hopkins U.*
Daniel Haber, *Mass. General Hos.*
Sharon Hammes-Schiffer, *Yale U.*
Wolf-Dietrich Hardt, *ETH Zürich*
Louise Harra, *UCL*
Kelley Harris, *U. of Wash*
Carl-Philipp Heisenberg, *IST Austria*
Janet G. Hering, *Eawag*
Christoph Hess, *U. of Basel & U. of Cambridge*
Heather Hickman, *NIAID, NIH*
Hans Hilgenkamp, *U. of Twente*
Janneke Hille Ris Lambers, *ETH Zürich*
Kai-Uwe Hinrichs, *U. of Bremen*
Deirdre Hollingsworth, *U. of Oxford*
Christina Hulbe, *U. of Otago, New Zealand*
Randall Hulet, *Rice U.*
Auke Ijspeert, *EPFL*
Gwyneth Ingram, *ENS Lyon*
Darrell Irvine, *MIT*
Akiko Iwasaki, *Yale U.*
Erich Jarvis, *Rockefeller U.*
Peter Jonas, *IST Austria*
Johanna Joyce, *U. de Lausanne*
Matt Kaeberlein, *U. of Wash.*
Daniel Kammen, *UC Berkeley*
Kisuk Kang, *Seoul Nat. U.*
V. Narry Kim, *Seoul Nat. U.*
Nancy Knowlton, *Smithsonian*
Etienne Koechlin, *École Normale Supérieure*
Alex L. Kolodkin, *Johns Hopkins U.*
LaShanda Korley, *U. of Delaware*
Paul Kubes, *U. of Calgary*
Chris Kuzawa, *Northwestern U.*
Laura Lackner, *Northwestern U.*
Gabriel Lander, *Scripps Res.* **(S)**
Mitchell A. Lazar, *UPenn*
Hedwig Lee, *Duke U.*
Fei Li, *Xi'an Jiaotong U.*
Ryan Lively, *Georgia Tech*
Luis Liz-Marzán, *CIC biomaGUNE*
Omar Lizardo, *UCLA*
Jonathan Losos, *WUSTL*
Ke Lu, *Inst. of Metal Res., CAS*
Christian Lüscher, *U. of Geneva*
Jean Lynch-Stieglitz, *Georgia Tech*
David Lyons, *U. of Edinburgh*
Fabienne Mackay, *QIMR Berghofer*
Zeynep Madak-Erdogan, *UIUC*
Vidya Madhavan, *UIUC*
Anne Magurran, *U. of St. Andrews*
Ari Pekka Mähönen, *U. of Helsinki*
Asifa Majid, *U. of Oxford*
Oscar Marín, *King's Coll. London*
Charles Marshall, *UC Berkeley*
Christopher Marx, *U. of Idaho*
David Masopust, *U. of Minnesota*
Geraldine Masson, *CNRS*
Jennifer McElwain, *Trinity College Dublin*
Rodrigo Medellín, *U. Nacional Autónoma de México*
C. Jessica Metcalf, *Princeton U.*
Tom Misteli, *NCI, NIH*
Jeffery Molkentin, *Cincinnati Children's Hospital Medical Center*
Alison Motsinger-Reif, *NIEHS, NIH* **(S)**
Danielle Navarro, *U. of New South Wales*
Daniel Neumark, *UC Berkeley*
Thi Hoang Duong Nguyen, *MRC LMB*
Beatriz Noheda, *U. of Groningen*
Helga Nowotny, *Vienna Sci. & Tech. Fund*
Pilar Ossorio, *U. of Wisconsin*
Andrew Oswald, *U. of Warwick*
Isabella Pagano, *Istituto Nazionale di Astrofisica*
Giovanni Parmigiani, *Dana-Farber* **(S)**
Sergiu Pasca, *Standford U.*
Daniel Pauly, *U. of British Columbia*
Ana Pêgo, *U. do Porto*
Julie Pfeiffer, *UT Southwestern Med. Ctr.*
Philip Phillips, *UIUC*
Matthieu Piel, *Inst. Curie*
Kathrin Plath, *UCLA*
Martin Plenio, *Ulm U.*
Katherine Pollard, *UCSF*
Elvira Poloczanska, *Alfred-Wegener-Inst.*
Julia Pongratz, *Ludwig Maximilians U.*
Philippe Poulin, *CNRS*
Lei Stanley Qi, *Stanford U.*
Simona Radutoiu, *Aarhus U.*
Trevor Robbins, *U. of Cambridge*
Joeri Rogelj, *Imperial Coll. London*
John Rubenstein, *SickKids*
Mike Ryan, *UT Austin*
Miquel Salmeron, *Lawrence Berkeley Nat. Lab*
Nitin Samarth, *Penn State U.*
Erica Ollmann Saphire, *La Jolla Inst.*
Joachim Saur, *U. zu Köln*
Alexander Schier, *Harvard U.*
Wolfram Schlenker, *Columbia U.*
Susannah Scott, *UC Santa Barbara*
Anuj Shah, *U. of Chicago*
Vladimir Shalaev, *Purdue U.*
Jie Shan, *Cornell U.*
Beth Shapiro, *UC Santa Cruz*
Jay Shendure, *U. of Wash.*
Steve Sherwood, *U. of New South Wales*
Brian Shoichet, *UCSF*
Robert Siliciano, *JHU School of Med.*
Lucia Sivilotti, *UCL*
Emma Slack, *ETH Zürich & U. of Oxford*
Richard Smith, *UNC* **(S)**
John Speakman, *U. of Aberdeen*
Allan C. Spradling, *Carnegie Institution for Sci.*
V. S. Subrahmanian, *Northwestern U.*
Naomi Tague, *UC Santa Barbara*
Eriko Takano, *U. of Manchester*
A. Alec Talin, *Sandia Natl. Labs*
Patrick Tan, *Duke-NUS Med. School*
Sarah Teichmann, *Wellcome Sanger Inst.*
Rocio Titiunik, *Princeton U.*
Shubha Tole, *Tata Inst. of Fundamental Res.*
Maria-Elena Torres Padilla, *Helmholtz Zentrum München*
Kimani Toussaint, *Brown U.*
Barbara Treutlein, *ETH Zürich*
Li-Huei Tsai, *MIT*
Jason Tylianakis, *U. of Canterbury*
Matthew Vander Heiden, *MIT*
Wim van der Putten, *Netherlands Inst. of Ecology*
Ivo Vankelecom, *KU Leuven*
Judith Varner, *UC San Diego*
Henrique Veiga-Fernandes, *Champalimaud Fdn.*
Reinhilde Veugelers, *KU Leuven*
Bert Vogelstein, *Johns Hopkins U.*
Julia Von Blume, *Yale School of Med.*
David Wallach, *Weizmann Inst.*
Jane-Ling Wang, *UC Davis* **(S)**
Jessica Ware, *Amer. Mus. of Natural Hist.*
David Waxman, *Fudan U.*
Alex Webb, *U. of Cambridge*
Chris Wikle, *U. of Missouri* **(S)**
Terrie Williams, *UC Santa Cruz*
Ian A. Wilson, *Scripps Res.* **(S)**
Hao Wu, *Harvard U.*
Li Wu, *Tsinghua U.*
Amir Yacoby, *Harvard U.*
Benjamin Youngblood, *St. Jude*
Yu Xie, *Princeton U.*
Jan Zaanen, *Leiden U.*
Kenneth Zaret, *UPenn School of Med.*
Lidong Zhao, *Beihang U.*
Bing Zhu, *Inst. of Biophysics, CAS*
Xiaowei Zhuang, *Harvard U.*
Maria Zuber, *MIT*

Science serves as a forum for discussion of important issues related to the advancement of science by publishing material on which a consensus has been reached as well as including the presentation of minority or conflicting points of view. Accordingly, all articles published in *Science*—including editorials, news and comment, and book reviews—are signed and reflect the individual views of the authors and not official points of view adopted by AAAS or the institutions with which the authors are affiliated.

EDITORIAL

No democracy, no academia

Over the past 30 weeks, Israel has been undergoing an upheaval marked by unprecedented attacks by the government on the independence of its judiciary, attorney general, government legal advisers, police, military, public broadcasting, and religious freedom. This assault on democratic institutions and principles is an imminent threat to Israeli academia, which relies on a solid democratic foundation. In response, universities, academics, and students have emerged as key proponents of ongoing protests under the banner, "No democracy, no academia."

The relationship between academia and democracy is bidirectional. Most highly ranked academic institutions predominantly operate within liberal democracies. Countries experiencing democratic backsliding, such as Turkey, Poland, and Hungary, witness a decline in academic achievements. In parallel, a robust democracy depends on a free academia that introduces new, liberal, free, and critical thinking into society. Erosion of this two-way association is at the heart of concerns in Israel.

> "This assault on democratic institutions...is an imminent threat to Israeli academia..."

Academia can maintain its excellence only if it operates without undue interference by nonexperts. Academic studies are dynamic and are cross-fertilized through interactions within the international community. Control or limitation of this dynamic by government and politics is bound to reduce excellence. In particular, because of Israel's geographic and geopolitical isolation, its scientists must continue full integration within the global scientific community if they are to maintain the excellence they pursue.

Earlier this month, the presidents of most Israeli universities sent an open letter to Israeli government leaders stating their concerns about destructive processes that will hamper Israel's scientific strength, such as reduced international and philanthropic funding to support Israeli research institutions and collaborations with other nations. The letter also stated that many Israeli scientists' perception of danger to academic freedom is stoking their departure from Israel for a better future elsewhere.

Recent moves by the government to stifle academic freedom include attempts in February by the Minister of Education to influence appointments of the governing body and rector of the National Library Public. Public resistance halted these blatant moves to stamp out the autonomy of an academic institution. There have also been government attempts to influence the nomination of the Council for Higher Education's vice chair without proper consultation with academic institutions.

At this point, over 150 proposed bills that will alter the democratic nature of the country are in different stages of legislation. At least eight will directly limit academic freedom, freedom of speech in academic institutions, and minority rights, enforced through sanctions to limit funding. These proposed laws, if passed, threaten the reputation and status of Israeli scholarship on the global stage. This would degrade the capacity of Israeli institutions to participate in the global community and to recruit leading scientists, and may trigger an exodus of the best and brightest scientists. Outstanding researchers depend on costly state-of-the-art facilities that are funded by competitive international grants. If Israel loses its scientific environment of freedom and excellence, the renewal of its funding agreement with the European Union, for example, will be in jeopardy. This includes its participation in the Horizon Europe program as an associated country, which was renewed in 2021 by the previous government. If cut off from such lucrative and prestigious programs, many Israeli scientists will likely seek a new academic home where they can be supported to conduct robust research as an integral part of the wider scientific community.

In broader terms, increasing the religious orientation of elementary school and high school curricula, as the government is doing, will increase the possibility that science will no longer be at the forefront of primary education. This will have cascading effects, from a decrease in students pursuing scholarly studies to a decline in innovative and entrepreneurial opportunities in science and technology.

Israel now finds itself at the vanguard of countries descending rapidly into a "hollow democracy" with weakened academia. To oppose this demise, the global academic community must unite and work together vigorously to resist attempts in Israel to undermine academic freedom. Petitions from academics around the world, national and global academic and scientific societies, and scientific policy organizations worldwide, and other peaceful means to raise awareness of the situation are needed immediately if scholarship and the pursuit of knowledge are to be safeguarded throughout the world.

–Einat Albin, Shikma Bressler, Asya Rolls, Michal Schwartz, Ehud Shapiro

Einat Albin
is at the Hebrew University of Jerusalem, Jerusalem, Israel. einat.albin@mail.huji.ac.il

Shikma Bressler
is at the Weizmann Institute of Science, Rehovot, Israel. shikma.bressler@weizmann.ac.il

Asya Rolls
is at the Israel Institute of Technology, Haifa, Israel. rolls@technion.ac.il

Michal Schwartz
is at the Weizmann Institute of Science, Rehovot, Israel. michal.schwartz@weizmann.ac.il

Ehud Shapiro
is at the Weizmann Institute of Science, Rehovot, Israel. ehud.shapiro@weizmann.ac.il

10.1126/science.adk3054

Climeworks, which operates this carbon capture and storage plant in Iceland, will help build a similar, larger facility in Louisiana.

PHOTO: ARNALDUR HALLDORSSON/BLOOMBERG/GETTY IMAGES

Edited by **Jeffrey Brainard**

CLIMATE POLICY

United States scales up carbon-removal plants

The U.S. Department of Energy last week announced it will spend $1.2 billion for two pioneering facilities—one in Texas, the other in Louisiana—that will vacuum millions of tons of carbon dioxide (CO_2) annually from the skies using a technology known as direct air capture (DAC). The investment marks the first major governmental backing in the world for the emerging carbon-capture technology. The program aims to create four DAC hubs over the next 10 years, each capable of removing and storing at least 1 million tons of CO_2 annually. Today, 18 DAC plants worldwide collectively remove only about 11,000 tons of CO_2 a year. Critics have slammed DAC as a boondoggle because it requires substantial inputs of energy to capture CO_2 and pump it underground. Currently, DAC typically costs more than $1000 to sequester each ton of CO_2, far more expensive than planting trees or other carbon-removal strategies. But DAC proponents counter that its costs may fall. They add that the limitations of other methods may require countries seeking to limit climate warming to no more than a 1.5°C rise by midcentury to use DAC.

Youths win Montana climate case

LEGAL AFFAIRS | A Montana state judge ruled this week in favor of young people who argued that the state's policies supporting fossil fuels violate their right under its constitution to a "clean and healthful environment." The ruling invalidates a provision of a Montana law that prevented state officials from considering the climate impacts of energy projects. In June, the case, *Held* v. *Montana*, went to trial, the first of its kind in the United States. Plaintiffs ranging in age from 5 to 22 asserted that Montana's policies created environmental damage that harmed them directly, such as wildfire smoke that worsened asthma. Climate scientists called as expert witnesses testified about Montana's worsening natural disasters and high rate of atmospheric warming. The state is expected to appeal. The case was spearheaded by the nonprofit Our Children's Trust, which has related lawsuits pending in four other states. Similar victories have been won in European courts.

Studies halted at N.Y. institute

RESEARCH OVERSIGHT | A U.S. watchdog office in June suspended 124 clinical trials underway at the New York State Psychiatric Institute, a facility affiliated with Columbia University. The unusual move by the Office for Human Research Protections (OHRP), first reported last week by *The New York Times*, came 2 weeks after the institute itself paused all 417 human-subject studies underway there. The actions followed the suicide more than a year ago of a participant in the placebo arm of a study testing a Parkinson's disease drug, levodopa, to treat depression and reduced mobility; that study was suspended in January 2022. Its lead investigator, psychiatrist Bret Rutherford, resigned from the institute on 1 June and is no longer on the Columbia faculty. Two journals have retracted papers related to Rutherford's levodopa research, citing methodological problems. The institute said in a statement it is "working with its federal partners to create a research safety review plan" and is awaiting OHRP's approval to resume the federally funded studies.

China faces mpox surge

INFECTIOUS DISEASES | China last week confirmed 491 cases of mpox in July, a monthly high and nearly five times June's total. Cases of the infectious disease, formerly known as monkeypox, have also increased in other Asian countries after plummeting in the Americas and Europe.

The disease is spread through intimate personal contact and has particularly affected men who have sex with men; more than 96% of the infections in China were among this group, according to a 9 August announcement by the Chinese Center for Disease Control and Prevention. The agency reported no severe cases or deaths. Officials believe China's strict COVID-19 restrictions on international travel, in place until this spring, kept the disease at bay during the 10 months starting in July 2022 when the World Health Organization designated mpox a Public Health Emergency of International Concern. With no vaccine yet available domestically, China is relying on raising public awareness and changes in behavior to limit the outbreak.

Muon magnetism mulled

PARTICLE PHYSICS | Physicists at Fermi National Accelerator Laboratory last week released a new measurement of the magnetism of a particle called the muon, a heavier, unstable cousin of the electron. With an uncertainty of 0.2 parts per billion, the new result confirms with twice the precision the one released 2 years ago. However, it has not elicited as much excitement as the 2021 result, which appeared to slightly exceed the prediction of physicists' prevailing standard model, possibly signaling undiscovered particles lurking in the vacuum around the muon. Theorists now realize the standard model's prediction was less certain than thought, obscuring whether the muon is really extra-magnetic. They hope to make a more reliable prediction before experimenters release their final result in 2025.

NIH reverses course on union

LABOR RELATIONS | After questioning the legal standing of a unionization effort by early-career researchers, the U.S. National Institutes of Health (NIH) now says it won't oppose a vote by potential union members. In a filing with the Federal Labor Relations Authority, NIH officials had contended that many potential members, including postdocs and graduate students, weren't "employees" with a right to unionize. But they reversed that position last week.

India creates research funder

SCIENCE POLICY | India's Parliament last week approved a new research funding agency aimed at boosting the nation's scientific standing. But some analysts are skeptical that the Anusandhan National Research Foundation will have a major impact. (Anusandhan is Hindi for "innovation.") The foundation is rooted in a 2019 proposal to create an agency, modeled after the U.S. National Science Foundation, that would be funded by the government while having an arm's-length relationship with elected officials (*Science*, 14 July, p. 118). But the structure approved by lawmakers gives India's prime minister broad powers to appoint the agency's leaders. Critics say that opens the door to political interference. And some wonder whether the agency can realize its funding plan, which calls for industry to contribute about 70% of an envisioned $6 billion outlay over 5 years.

BY THE NUMBERS

76%

Share of U.S. survey respondents who support requiring all advanced artificial intelligence models to have their safety evaluated by independent experts. (Artificial Intelligence Policy Institute)

China leads in internal citations

PUBLISHING | More than 60% of recent citations of papers from Chinese institutions were made by China-based researchers, according to an analysis by Japan's National Institute of Science and Technology Policy. The unusually high rate raises questions about whether intentional efforts to boost the reputation of Chinese institutions is contributing to China's large share of the most cited papers. The comparable figure for the United States was 29% and for other countries less than 20%, according to the analysis, which averaged data from 2019 to 2021. China produced the biggest share (nearly 30%) of papers among the top 1% most highly cited, the report says, as well as the most scientific publications indexed in Clarivate's Web of Science Core Collection. The United States was second in those categories. The analysis did not explain whether the citations by authors in China are relevant to the studies in which they appear or indicate padding.

Deal aids red wolf conservation

WILDLIFE | The U.S. Fish and Wildlife Service (FWS) has agreed to continue to release captive-bred red wolves (*Canis rufus*) to boost the only wild population of this endangered species, reversing an earlier decision to stop the releases. The new policy resulted from a court settlement, announced last week, with conservation groups that had sued the agency. Although red wolves once lived in most of the southeastern United States, hunting and habitat loss caused a massive fall off that by 1972 drove the species nearly to extinction—unusual among recent declines of large North American mammals. Decades of captive breeding and releases lifted the wild population to only about 120 animals. Car accidents and poaching have taken a toll, and local landowners have objected to the releases. After FWS stopped them in 2015, the wild population fell to about 15 individuals. Now, the agency has made an 8-year pledge to release wolves under a restoration plan more thoroughly informed by research. Some supporters say the population's recovery will require an additional measure—policing poachers.

PHOTO: GERRY BROOME/AP IMAGES

A red wolf and her pup are part of a captive population in North Carolina used to help increase the only wild one.

IN DEPTH

ENVIRONMENT

Maui's deadly blazes reveal a fire-prone Hawaii

Flammable, invasive grasses have changed the island landscape, say its shaken scientists

By **Molly Rains**

Scott Fisher was one of the lucky ones. Last week, early on 8 August, the restoration ecologist and his wife were awoken in their home by cellphone emergency alerts. Outside, on the Hawaiian island of Maui, high winds buffeted their house, shaking eucalyptus and palm trees and scattering debris across the landscape. About 2.5 kilometers away, cutting a path through the darkness, a wildfire was burning through the dry forests of the island's upcountry.

Fisher and his wife escaped to safety, but as *Science* went to press, more than 100 people on Maui had been confirmed killed by multiple wildfires last week—and some officials fear the true death toll is much higher. Maui's tight-knit scientific community has begun to assess the disruptions to island research and conservation efforts, but all that was overshadowed by the loss of so many lives. "We're still wrapping our heads around what this really means, because right now, most of us are still in shock," says Marc Lammers of the Hawaiian Islands Humpback Whale National Marine Sanctuary.

The marine mammal ecologist and other scientists on Maui study whales from ships that are—or were—based in Lahaina, a historic town razed by the fires. Its harbor was "the hub of whaling science here in Hawaii," Lammers says. Now, it is vacant, strewn with charred debris.

Fisher, who grew up on Maui and works for the Hawaii Land Trust, notes that geological evidence suggests major fires were uncommon in Maui's past. But they have become an increasingly recurrent—and worsening—threat in recent decades, especially as nonnative, highly flammable grasses invade the island's large, abandoned plantations and previously burned landscapes. "Every fire it just gets worse," says Fisher, who helped his neighbors evacuate to safer locations.

Their exact origin unknown, last week's fires were driven by a complex host of factors, Fisher says, including a lengthy drought compounded by "exceptional" winds and low humidity. Add in Maui's widespread invasive vegetation and it was a "perfect recipe for disaster," says ecologist Carla D'Antonio of the University of California, Santa Barbara, who has studied the fire potential of Hawaii's nonnative grasses for decades (*Science*, 5 August 2022, p. 568).

She and others call last week's fires unprecedented. "It's never been this bad before," says oceanographer Andrea Kealoha, a lifelong Maui resident and director of an ocean and groundwater laboratory on the island. Previous fires on Maui had been in relatively remote locations, she notes. Now, researchers wonder whether the blazes foreshadow a fiery future for it and other Hawaiian islands. The "big, big question on everybody's mind," Fisher says, is: "What can we do now?"

Spread by fierce winds last week, the westernmost of Maui's major wildfires destroyed the town of Lahaina and killed scores of people.

From a scientific perspective, Kealoha is concerned that postfire soil erosion will release sediment into the island's waterways, and eventually the ocean, creating a murky mess that could profoundly disturb local aquatic ecosystems. The phenomenon "can shift an entire ecosystem away from corals to one dominated by algae," she says.

Future fires could further reshape Maui's distinctive ecology, which conservationists were already struggling to save. The Maui Bird Conservation Center, run by the San Diego Zoo and home to many local species no longer, or rarely, found in the wild, was among the research facilities that barely escaped last week's blazes. "Had the center burned, a good proportion of the ['alalā, an endangered Hawaiian crow] flock could have disappeared," says Christa Seidl, a wildlife ecologist with the Maui Forest Bird Recovery Project. "That would ... potentially threaten that species with literal extinction—not just extinction in the wild."

The fires did not reach the University of Hawaii's (UH's) Olinda Rare Plant Facility, but high winds blew apart growing houses and some buildings, notes biologist Arthur Medeiros of the Auwahi Forest Restoration Project. "A phenomenal collection of propagated native endangered plants was heavily damaged," he says.

PHOTO: RICK BOWMER/AP IMAGES

Shifting ecosystems across Hawaii are making all the islands more vulnerable to wildfires, according to Dan Rubinoff, an invasive species biologist at UH. "It's getting worse, probably due to climate change, in terms of us having longer dry periods," he says. "But it's also exacerbated by differences in land use and habitat."

European colonization of Hawaii 2 centuries ago accelerated introductions of invasive species. Many of the foreign plants, such as fountain grass (*Pennisetum setaceum*) and haole koa (*Leucaena leucocephala*), are fire-tolerant. They grow quickly, serving as fodder for blazes when they ignite and reestablishing rapidly on burned areas, crowding out native species. In particular, various species of African pasture grasses now dominate large areas, D'Antonio says. Droughts can drive their desiccation, creating large amounts of ignitable fuel. "This sort of calamity has been a long time coming," she says.

One reason these foreign grasses have room to expand, researchers say, is that Maui's native plant life is voraciously consumed by the thousands of feral goats and other nonnative hoofed creatures (including deer, hogs, and sheep) that run wild in the island's forests. Invasive species—both plant and animal—also pose a barrier to reestablishing native forests that scientists believe are essential to Maui's environmental health and fire-resilience. Targeting these invasives is just one piece of the puzzle, says Medeiros, who also calls for incorporating more fire-resistant vegetation into the Maui landscape. "There is no magic bullet," he says.

Indeed, Fisher counterintuitively suggests goats and other grazing ungulates could be strategically deployed to keep invasive grasses in check. "I think getting these animals to work in a defined area … might be one" fire prevention strategy, he says.

It won't be easy for Maui to recover from the fires, which Hawaii's governor has called the worst in the state's history. Kealoha anticipates that it will take many years to rebuild, but she retains hope that Maui and its research community can rebound stronger. Already because of the tragedy, she says, "we're working with more groups, building collaborations and relationships with people who have handled these kinds of disasters before."

In the meantime, many of Maui's scientists are in mourning. Even this week, as the fires continued to smolder, many community members remained missing. "Our staff," says UH conservation biologist Shaya Honarvar, "are still in the midst of this tragedy." ■

With reporting by Tanvi Dutta Gupta and Elizabeth Pennisi.

ILLUSTRATION: ELYMAS/SHUTTERSTOCK

BIOLOGY

NIH project probes the human body's multitude of genomes

Agency launches major effort to explore importance of accumulating mutations in somatic cells

By **Mitch Leslie**

Every person starts with just one genome, the unique amalgam of paternal and maternal DNA in the fertilized egg. And researchers long thought that over a lifetime, pretty much all of the body's diverse cells inherit that same genome. But large-scale DNA sequencing over the past decade or so has toppled that view, showing that human DNA starts to accrue mutations early in embryonic development and continues to change throughout life. "The genome you are conceived with is very different from the genome you die with," says cardiovascular biologist Kenneth Walsh of the University of Virginia.

As a result, every person is actually a mosaic of genomes, varying across the body and often within the same organ or tissue. These DNA changes introduce a diversity to the body's somatic, or nonreproductive, cells that may be as important to health as the more pervasive alterations inherited from parents. Now, the National Institutes of Health (NIH) has launched a 5-year, $140 million project to map this universe of genomic diversity—and probe why it matters.

Known as Somatic Mosaicism Across Human Tissues (SMaHT), the program will measure the baseline frequency of these mutations in an assortment of tissues to help researchers better understand how the alterations contribute to health and disease. SMaHT, which in May doled out its first 22 grants, aims to collect samples of 15 tissues from 150 healthy people who donated their bodies for research. It has funded five teams to sequence DNA from these samples—they should begin in the coming months—and is backing others to develop new technologies for analyzing genetic variants and probing their effects.

"The idea is to be able to at least catalog the mutations" so that researchers can delve into links with diseases, says genomicist Harsha Doddapaneni of Baylor College of Medicine, who helps lead one of the SMaHT sequencing groups.

For decades, the conventional wisdom held that a person's somatic cells could pick up mutations but that these genome alterations were rare and not a major cause of health problems. Mutations in the skin, for example, occasionally resulted in unusual pigment patterns such as port-wine stain birthmarks.

But scientists now know that our genomes are riddled with somatic mutations. Even in young children, some cells already carry thousands of these alterations, and one study found that lung cells from a former smoker in her 70s boasted more than 15,000 mutations each. "We used to think about *the* genome. Now, we think about our genomes," says oncologist Dan Landau of Weill Cornell Medicine.

The vast majority of these changes likely have no impact on our health. A portion can trigger cancers, however, and other mutations may drive different illnesses or cause premature deaths. Clonal hematopoiesis, a variety of mosaicism that affects blood-forming cells and becomes more common with age, almost doubles the likelihood of developing cardiovascular disease and boosts the risk of dying from any cause by 40% (*Science*, 10 November 2017, p. 714). As men get older, they become more vulnerable to another type of mosaicism in which the Y chromosome vanishes from some of their cells. Its absence may set them up for ailments such as cardiovascular disease and macular degeneration.

The brain can also incur damage as neurons and other cells accumulate mutations.

Shifting ecosystems across Hawaii are making all the islands more vulnerable to wildfires, according to Dan Rubinoff, an invasive species biologist at UH. "It's getting worse, probably due to climate change, in terms of us having longer dry periods," he says. "But it's also exacerbated by differences in land use and habitat."

European colonization of Hawaii 2 centuries ago accelerated introductions of invasive species. Many of the foreign plants, such as fountain grass (*Pennisetum setaceum*) and haole koa (*Leucaena leucocephala*), are fire-tolerant. They grow quickly, serving as fodder for blazes when they ignite and reestablishing rapidly on burned areas, crowding out native species. In particular, various species of African pasture grasses now dominate large areas, D'Antonio says. Droughts can drive their desiccation, creating large amounts of ignitable fuel. "This sort of calamity has been a long time coming," she says.

One reason these foreign grasses have room to expand, researchers say, is that Maui's native plant life is voraciously consumed by the thousands of feral goats and other nonnative hoofed creatures (including deer, hogs, and sheep) that run wild in the island's forests. Invasive species—both plant and animal—also pose a barrier to reestablishing native forests that scientists believe are essential to Maui's environmental health and fire-resilience. Targeting these invasives is just one piece of the puzzle, says Medeiros, who also calls for incorporating more fire-resistant vegetation into the Maui landscape. "There is no magic bullet," he says.

Indeed, Fisher counterintuitively suggests goats and other grazing ungulates could be strategically deployed to keep invasive grasses in check. "I think getting these animals to work in a defined area … might be one" fire prevention strategy, he says.

It won't be easy for Maui to recover from the fires, which Hawaii's governor has called the worst in the state's history. Kealoha anticipates that it will take many years to rebuild, but she retains hope that Maui and its research community can rebound stronger. Already because of the tragedy, she says, "we're working with more groups, building collaborations and relationships with people who have handled these kinds of disasters before."

In the meantime, many of Maui's scientists are in mourning. Even this week, as the fires continued to smolder, many community members remained missing. "Our staff," says UH conservation biologist Shaya Honarvar, "are still in the midst of this tragedy." ■

With reporting by Tanvi Dutta Gupta and Elizabeth Pennisi.

ILLUSTRATION: ELYMAS/SHUTTERSTOCK

BIOLOGY

NIH project probes the human body's multitude of genomes

Agency launches major effort to explore importance of accumulating mutations in somatic cells

By **Mitch Leslie**

Every person starts with just one genome, the unique amalgam of paternal and maternal DNA in the fertilized egg. And researchers long thought that over a lifetime, pretty much all of the body's diverse cells inherit that same genome. But large-scale DNA sequencing over the past decade or so has toppled that view, showing that human DNA starts to accrue mutations early in embryonic development and continues to change throughout life. "The genome you are conceived with is very different from the genome you die with," says cardiovascular biologist Kenneth Walsh of the University of Virginia.

As a result, every person is actually a mosaic of genomes, varying across the body and often within the same organ or tissue. These DNA changes introduce a diversity to the body's somatic, or nonreproductive, cells that may be as important to health as the more pervasive alterations inherited from parents. Now, the National Institutes of Health (NIH) has launched a 5-year, $140 million project to map this universe of genomic diversity—and probe why it matters.

Known as Somatic Mosaicism Across Human Tissues (SMaHT), the program will measure the baseline frequency of these mutations in an assortment of tissues to help researchers better understand how the alterations contribute to health and disease. SMaHT, which in May doled out its first 22 grants, aims to collect samples of 15 tissues from 150 healthy people who donated their bodies for research. It has funded five teams to sequence DNA from these samples—they should begin in the coming months—and is backing others to develop new technologies for analyzing genetic variants and probing their effects.

"The idea is to be able to at least catalog the mutations" so that researchers can delve into links with diseases, says genomicist Harsha Doddapaneni of Baylor College of Medicine, who helps lead one of the SMaHT sequencing groups.

For decades, the conventional wisdom held that a person's somatic cells could pick up mutations but that these genome alterations were rare and not a major cause of health problems. Mutations in the skin, for example, occasionally resulted in unusual pigment patterns such as port-wine stain birthmarks.

But scientists now know that our genomes are riddled with somatic mutations. Even in young children, some cells already carry thousands of these alterations, and one study found that lung cells from a former smoker in her 70s boasted more than 15,000 mutations each. "We used to think about *the* genome. Now, we think about our genomes," says oncologist Dan Landau of Weill Cornell Medicine.

The vast majority of these changes likely have no impact on our health. A portion can trigger cancers, however, and other mutations may drive different illnesses or cause premature deaths. Clonal hematopoiesis, a variety of mosaicism that affects blood-forming cells and becomes more common with age, almost doubles the likelihood of developing cardiovascular disease and boosts the risk of dying from any cause by 40% (*Science*, 10 November 2017, p. 714). As men get older, they become more vulnerable to another type of mosaicism in which the Y chromosome vanishes from some of their cells. Its absence may set them up for ailments such as cardiovascular disease and macular degeneration.

The brain can also incur damage as neurons and other cells accumulate mutations.

"Somatic mutations are disease-causing in some proportion of patients with epilepsy," says Alissa D'Gama, a clinical fellow at Boston Children's Hospital. In addition, researchers estimate that fetal mutations that may modify brain development account for about 3% to 5% of the risk of developing autism spectrum disorder. Studies have also linked mosaic brain mutations to a variety of other neurological disorders, including schizophrenia and Alzheimer's disease. "Somatic mosaicism is likely playing a role" in these conditions, D'Gama says. "What needs to be teased out is how big a role."

Plenty of other mysteries about somatic mutations remain—for example, whether certain tissues accumulate more mutations than others. "Only a few types of tissues have been investigated," notes developmental scientist Flora Vaccarino of Yale School of Medicine, who has SMaHT funding.

Researchers also want to determine whether some somatic mutations benefit us. Scientists have found that individual cells can gain from certain changes that give them and their descendants, known as a clone, a competitive advantage over other clones. However, what's good for specific cells isn't necessarily good for the tissues they inhabit—cancer is a prime example—and whether any somatic changes improve our overall health is unclear. But some evidence hints they can. For example, scientists have found that clones carrying certain mutations have an advantage in people with fatty liver disease, a condition in which fat accumulates in the organ and can cause it to fail. Those findings raise the possibility that the alterations help the liver cope with disease.

To test that idea, liver biologist Hao Zhu of the University of Texas Southwestern Medical Center and colleagues mimicked gene-disabling somatic mutations in mice with nonalcoholic steatohepatitis (NASH), a type of fatty liver disease that is increasingly common in people. The researchers deleted each of 63 genes linked to NASH from a subset of cells in the livers of the animals. Six months later, the team found, clones missing some of the genes had the upper hand. Because these elite clones grew faster, Zhu and colleagues next asked what would happen if one of them prevailed, expanding so much that it replaced its rivals. To find out, they deleted some of the genes throughout the rodents' livers. For three of the genes, the mice gained protection against fatty liver disease, accumulating less fat and incurring less tissue damage. Liver clones probably grow too slowly in people to reverse fatty liver disease, Zhu says, but the discovery could point to new treatments.

By providing the first bodywide reference for somatic mutations, SMaHT will help scientists investigate their roles. However, finding these mutations is challenging. Researchers and clinical labs are adept at uncovering mutations in tumors, but those alterations are typically found in a large fraction of the abnormal cells. In contrast, some somatic mutations occur in less than 1% of cells in a tissue. Today's DNA-decoding technology can miss such rare mutations because it has a relatively high error rate. Moreover, researchers often sequence DNA from multiple cells simultaneously, which can swamp rare changes. "You are looking for a signal that is hidden among noise," says geneticist Martin Breuss of the University of Colorado School of Medicine.

For SMaHT, five groups of researchers plan to use several techniques to ferret out and verify these hidden signals. Doddapaneni, his Baylor colleague Rui Chen, and their team, for example, will deploy not just conventional whole genome DNA sequencing, but also two types of RNA sequencing, which can help confirm some variants and identify the types of cells carrying them. To weed out errors, they will also use duplex sequencing, a less common technique that decodes both strands of DNA's double helix to reduce mistakes and pinpoint rare mutations.

> **"The genome you are conceived with is very different from the genome you die with."**
>
> **Kenneth Walsh**, University of Virginia

The remaining SMaHT-funded teams will tackle a variety of projects. Geneticist Kathleen Burns of the Dana-Farber Cancer Institute and her colleagues want to better define the role of transposons, lengths of DNA that modify the genome by moving from place to place. The researchers will develop ways to identify restless elements that are primed to relocate and pin down where in the genome they insert. Work by other groups will include probing how somatic mutations affect gene activity and developing new approaches for sequencing the genomes of single cells.

SMaHT won't answer every question about somatic mutations. Walsh notes that although the program will obtain tissues from people of different ages, it won't include samples taken over time from the same person, making it harder to understand the mutations' role in aging, he says. But it is a key next step in what Landau calls "a huge revolution in human genetics." He is eager to see the results. "We are just at the beginning of this incredible adventure." ■

ASTRONOMY

After string of failures, Japan aims to launch x-ray telescope

Groundbreaking XRISM will capture spectra, revealing the motion and composition of million-degree gases

By **Daniel Clery**

The first one failed to reach orbit. The second died soon after getting to space, when its helium coolant was accidentally dumped. The third one lasted for 37 days before its spacecraft broke apart in a fatal spin.

The Japan Aerospace Exploration Agency (JAXA) is hoping the fourth time is the charm for a revolutionary x-ray instrument that will give astronomers unprecedented views of the hot gases around supernovae and black holes and within galaxy clusters. On 26 August, the agency plans to launch the X-Ray Imaging and Spectroscopy Mission (XRISM), a telescope fitted with a NASA-developed device to do something that has long been a challenge for x-ray telescopes: Tease apart the x-rays' wavelengths, the way a prism splits visible light. Detailed x-ray spectroscopy will allow researchers to not only see the hot gases, but also discover what they're made of and how they're moving. "It's a completely new kind of detector," says astrophysicist Poshak Gandhi of the University of Southampton.

Because Earth's atmosphere blocks x-rays, astronomers must go to space to see them. Even there, making x-ray images is a challenge. Because x-rays go straight through conventional mirrors, the photons must be gathered and focused by glancing reflections off nested cylindrical mirrors. X-ray telescopes using that approach can image the hot gases, which make up more than half the visible matter in the universe. But astronomers want more, Gandhi says. "We really need to be able to distinguish the different colors of x-ray light."

Regular spectrometers struggle with x-rays, especially high energy photons from extended sources. But in the 1990s, engineers at NASA's Goddard Space Flight Cen-

"Somatic mutations are disease-causing in some proportion of patients with epilepsy," says Alissa D'Gama, a clinical fellow at Boston Children's Hospital. In addition, researchers estimate that fetal mutations that may modify brain development account for about 3% to 5% of the risk of developing autism spectrum disorder. Studies have also linked mosaic brain mutations to a variety of other neurological disorders, including schizophrenia and Alzheimer's disease. "Somatic mosaicism is likely playing a role" in these conditions, D'Gama says. "What needs to be teased out is how big a role."

Plenty of other mysteries about somatic mutations remain—for example, whether certain tissues accumulate more mutations than others. "Only a few types of tissues have been investigated," notes developmental scientist Flora Vaccarino of Yale School of Medicine, who has SMaHT funding.

Researchers also want to determine whether some somatic mutations benefit us. Scientists have found that individual cells can gain from certain changes that give them and their descendants, known as a clone, a competitive advantage over other clones. However, what's good for specific cells isn't necessarily good for the tissues they inhabit—cancer is a prime example—and whether any somatic changes improve our overall health is unclear. But some evidence hints they can. For example, scientists have found that clones carrying certain mutations have an advantage in people with fatty liver disease, a condition in which fat accumulates in the organ and can cause it to fail. Those findings raise the possibility that the alterations help the liver cope with disease.

To test that idea, liver biologist Hao Zhu of the University of Texas Southwestern Medical Center and colleagues mimicked gene-disabling somatic mutations in mice with nonalcoholic steatohepatitis (NASH), a type of fatty liver disease that is increasingly common in people. The researchers deleted each of 63 genes linked to NASH from a subset of cells in the livers of the animals. Six months later, the team found, clones missing some of the genes had the upper hand. Because these elite clones grew faster, Zhu and colleagues next asked what would happen if one of them prevailed, expanding so much that it replaced its rivals. To find out, they deleted some of the genes throughout the rodents' livers. For three of the genes, the mice gained protection against fatty liver disease, accumulating less fat and incurring less tissue damage. Liver clones probably grow too slowly in people to reverse fatty liver disease, Zhu says, but the discovery could point to new treatments.

By providing the first bodywide reference for somatic mutations, SMaHT will help scientists investigate their roles. However, finding these mutations is challenging. Researchers and clinical labs are adept at uncovering mutations in tumors, but those alterations are typically found in a large fraction of the abnormal cells. In contrast, some somatic mutations occur in less than 1% of cells in a tissue. Today's DNA-decoding technology can miss such rare mutations because it has a relatively high error rate. Moreover, researchers often sequence DNA from multiple cells simultaneously, which can swamp rare changes. "You are looking for a signal that is hidden among noise," says geneticist Martin Breuss of the University of Colorado School of Medicine.

For SMaHT, five groups of researchers plan to use several techniques to ferret out and verify these hidden signals. Doddapaneni, his Baylor colleague Rui Chen, and their team, for example, will deploy not just conventional whole genome DNA sequencing, but also two types of RNA sequencing, which can help confirm some variants and identify the types of cells carrying them. To weed out errors, they will also use duplex sequencing, a less common technique that decodes both strands of DNA's double helix to reduce mistakes and pinpoint rare mutations.

> **"The genome you are conceived with is very different from the genome you die with."**
>
> **Kenneth Walsh**, University of Virginia

The remaining SMaHT-funded teams will tackle a variety of projects. Geneticist Kathleen Burns of the Dana-Farber Cancer Institute and her colleagues want to better define the role of transposons, lengths of DNA that modify the genome by moving from place to place. The researchers will develop ways to identify restless elements that are primed to relocate and pin down where in the genome they insert. Work by other groups will include probing how somatic mutations affect gene activity and developing new approaches for sequencing the genomes of single cells.

SMaHT won't answer every question about somatic mutations. Walsh notes that although the program will obtain tissues from people of different ages, it won't include samples taken over time from the same person, making it harder to understand the mutations' role in aging, he says. But it is a key next step in what Landau calls "a huge revolution in human genetics." He is eager to see the results. "We are just at the beginning of this incredible adventure." ■

ASTRONOMY

After string of failures, Japan aims to launch x-ray telescope

Groundbreaking XRISM will capture spectra, revealing the motion and composition of million-degree gases

By **Daniel Clery**

The first one failed to reach orbit. The second died soon after getting to space, when its helium coolant was accidentally dumped. The third one lasted for 37 days before its spacecraft broke apart in a fatal spin.

The Japan Aerospace Exploration Agency (JAXA) is hoping the fourth time is the charm for a revolutionary x-ray instrument that will give astronomers unprecedented views of the hot gases around supernovae and black holes and within galaxy clusters. On 26 August, the agency plans to launch the X-Ray Imaging and Spectroscopy Mission (XRISM), a telescope fitted with a NASA-developed device to do something that has long been a challenge for x-ray telescopes: Tease apart the x-rays' wavelengths, the way a prism splits visible light. Detailed x-ray spectroscopy will allow researchers to not only see the hot gases, but also discover what they're made of and how they're moving. "It's a completely new kind of detector," says astrophysicist Poshak Gandhi of the University of Southampton.

Because Earth's atmosphere blocks x-rays, astronomers must go to space to see them. Even there, making x-ray images is a challenge. Because x-rays go straight through conventional mirrors, the photons must be gathered and focused by glancing reflections off nested cylindrical mirrors. X-ray telescopes using that approach can image the hot gases, which make up more than half the visible matter in the universe. But astronomers want more, Gandhi says. "We really need to be able to distinguish the different colors of x-ray light."

Regular spectrometers struggle with x-rays, especially high energy photons from extended sources. But in the 1990s, engineers at NASA's Goddard Space Flight Cen-

Japan's X-Ray Imaging and Spectroscopy Mission telescope will open a new eye on the x-ray universe, helped by a long-awaited NASA sensor.

ter developed a chip-based sensor called a microcalorimeter, which can measure the energy—closely related to wavelength—of individual x-ray photons. When an x-ray strikes one of the mercury telluride pixels in the calorimeter, it knocks loose an electron and transfers all its energy to it. The electron bounces around the pixel, raising its temperature by a tiny fraction of a degree and warming an adjacent temperature sensor. To register these tiny quantities of heat, which indicate the energy of the original photon, the whole device must be cooled to 1/20 of a degree above absolute zero.

Astronomers got a taste of a microcalorimeter's capability when one flew aboard the ill-fated Hitomi telescope, JAXA's third try. Before the 2016 mission broke up in the fatal spin, it made groundbreaking observations of the Perseus galaxy cluster and a handful of other objects. "We glimpsed the promised land, but could not go in," says Brian Williams, NASA's project scientist for XRISM. In those few weeks, Hitomi did "transformational science with one single pointing," says Elisa Costantini of the Netherlands Institute for Space Research, principal investigator for the Swiss-Dutch contributions to XRISM. "It proved how necessary it was."

The Perseus cluster is one of the most massive objects in the universe, a conglomeration of thousands of galaxies swimming in a sea of gas heated to 50 million K. With Hitomi's microcalorimeter, researchers were able to see unprecedented details in the gas' x-ray glow. They detected spikes in its spectrum that revealed specific elements, such as iron, indicating what types of supernovae had spewed their heavy elements into space. To their surprise, the chemical recipe was very similar to that of the Sun. It looked "strangely familiar," Costantini says.

Researchers also saw some of the spikes were smeared out by the motions of the gas. But not by much: The cluster's gas was surprisingly quiescent, not the maelstrom theorists had predicted. One of XRISM's first tasks will be to look at other clusters to see whether Perseus is an oddity or the norm. "That's the homework left by Hitomi," says Makoto Tashiro of Saitama University, XRISM's principal investigator.

In addition to galaxy clusters, XRISM will study the hot gases swirling around supernovae remnants and black holes, both the supermassive ones in galactic centers and stellar mass ones that suck material from companion stars. "It's dead easy to find black holes in the universe with an x-ray telescope," Gandhi says.

What isn't so easy is knowing how swirling matter moves and whether some of it is blasted outward into the surrounding galaxy, affecting star formation and the galaxy's evolution. Some of the outflows are known to travel at hundreds of kilometers per second, but there are hints of winds blowing hundreds of times faster, which would have a profound effect on the host galaxy. "There are many things we don't know," Costantini says.

A sector of one of XRISM's mirrors, which focus x-rays by glancing reflection.

JAXA has worked hard to ensure the $190 million XRISM doesn't succumb to the fates of its predecessors. It has a revamped attitude control system, redesigned coolant pipework, and a backup mechanical cooler that could allow it to operate after its helium runs out in 3 years. Although XRISM has fewer other instruments than Hitomi, "spectroscopy is the strongest point, [and] that can extend the science," Tashiro says.

Hopes for XRISM are brightening an otherwise difficult time for x-ray astronomy. The field relies heavily on two flagship missions—NASA's Chandra X-ray Observatory and XMM-Newton from the European Space Agency (ESA)—that are both more than 20 years old, long past their design lifetimes. "Chandra's health is very good overall," says Pat Slane, director of the Chandra X-ray Center. But, he says, deposits on its filters are reducing sensitivity and its shiny thermal shielding is degrading, leading to overheating. As for XMM-Newton, its detectors are aging, says Norbert Schartel, ESA's principal investigator for the mission, but it "can still do science." The ESA team hopes to eke out enough coolant to last until 2030.

If either telescope dies early, "it will be a loss to the field," says Jiachen Jiang of the University of Cambridge. Replacements won't come until the mid-2030s at the earliest.

That raises the stakes for a successful launch even higher. XRISM isn't a general-purpose machine like Chandra and XMM-Newton. But, Williams says, it "will be the predominant x-ray mission of the 2020s." ■

IMAGES: (TOP TO BOTTOM) JAXA; TAYLOR MICKAL/NASA

EARTH SCIENCE

Myth of Alaskan city's immunity to tsunamis dispelled

Lucky low tide helped Anchorage dodge catastrophic 1964 tsunami, first analysis of location's risk finds

By **Christian Elliott**

On a cold March evening in 1964, a colossal earthquake struck off the coast of Alaska. At magnitude 9.2, it was the largest earthquake ever recorded in North America, and it triggered massive tsunamis that killed more than 120 people and leveled communities. But no wave reached Anchorage, the state's biggest city. Many concluded that nearby geography makes the city immune to tsunamis.

A new study published this week by the Alaska Division of Geological and Geophysical Surveys (DGGS), however, finds Anchorage simply got lucky in 1964—and might not the next time an earthquake strikes the seismically active region. In a worst-case scenario—another giant rupture in a worse place at a worse time—a 10-meter wave could flood low-lying areas of the city and its critical port for more than 24 hours, according to the study.

"I think folks in Alaska should take this seriously," said Diego Melgar, a tsunami scientist at the University of Oregon not involved in the study. He says other U.S. coastal communities would benefit from such an analysis. "This is exactly what we need to be doing at a national level."

An entrenched public perception holds that Anchorage is protected from tsunamis by the long, shallow Cook Inlet. False alarms have reinforced the sense of invulnerability: In recent years, residents have dutifully heeded tsunami warnings and evacuated, but no wave has struck. After a 2018 evacuation, an *Anchorage Daily News* story quoted an oceanographer who said, "The science doesn't lend itself to an inundation in Anchorage."

The truth was no one had ever really examined the city's tsunami risk in detail. So Barrett Salisbury, DGGS earthquake and tsunami hazard program manager, and Elena Suleimani, the Alaska Earthquake Center's tsunami modeler, recently took a closer look. They began by simulating the 1964 earthquake, which occurred when the Pacific tectonic plate, which plunges underneath Alaska, ruptured by as much as 20 meters. Their tsunami model traced the resulting wave toward Anchorage through the long Cook Inlet, which has uncommonly large tides. They discovered that when the 3-meter-tall wave reached Anchorage, hours after the earthquake, the city happened to be at low tide, 4 meters below the mean. The low tide simply muffled the tsunami. With a different earthquake timing, the inlet's tides could have just as easily amplified it.

Concerned, the scientists looked to the future, modeling hypothetical earthquakes at different locations and times of day, based on the earthquake zone's behavior in several thousand years of paleoseismic records. In the worst scenario—a magnitude 9.2 rupture striking farther south than the 1964 earthquake and triggering a tsunami that arrives at high tide—a 10-meter-tall wave would swamp Anchorage. "We n… to take it seriously, even though it's a low-probability event," Salisbury says.

Salisbury and Suleimani found most residential areas would be out of harm's way, but the Port of Alaska, which processes most of the state's food, fuel, and consumer goods, would be inundated. "It's kind of shocking how much we depend on the Port of Alaska," Suleimani says. "We don't have a backup." The wave would also flood the critical single highway connecting Anchorage to Canada and the rest of the continental United States.

Jim Jager, Port of Alaska deputy director, remembers hosting tsunami scientists at his docks years ago and being reassured the port was safe. He admits he perpetuated the idea, asking the state for funding to modernize the port's infrastructure because unlike others elsewhere, his couldn't be wiped out by a tsunami. Briefed on the DGGS report, Jager now plans to fortify the docks and install backup batteries above the inundation zone so that supplies could be unloaded even amid a blackout. "If the docks get wiped out, how are we going to get food?" he asks. "If you look at any [emergency] plan for responding to and recovering from an earthquake, as soon as the Port of Alaska is inoperable, the plan collapses."

Hermann Fritz, a tsunami expert at the Georgia Institute of Technology, thinks the study's models are solid. But he says the study doesn't account for another kind of tsunami: secondary ones that arise when earthquakes shake loose landslides that crash into the sea and Alaska's many narrow fjords. For example, he says, a 1958 earthquake in southeastern Alaska triggered the Lituya Bay landslide, which created a 524-meter-tall wave—the largest ever recorded on Earth. With tsunamis, "there are always surprises," Fritz says.

With the report out, the next step is educating the public about the newly recognized hazard. At the front lines will be Anchorage Office of Emergency Management Programs Manager Audrey Gray. She's glad to have a study backing up her gut feeling that the city is not immune to tsunamis. Now, her office is updating emergency operation plans and has launched a joint information system to unify messaging across government agencies. A series of public meetings will begin in September. "The saying is all roads lead to Anchorage up here," she says. "And we've got a road ahead of us, I'll definitely tell you that." ■

Christian Elliott is a freelance science journalist and an audio producer at NASA's Goddard Space Flight Center.

Waves of destruction

Low tides in the Cook Inlet muffled the tsunami from the 1964 Alaskan earthquake. But if another giant rupture occurred at high tide, Anchorage could be swamped with 10 meters of water, according to a new hazard assessment.

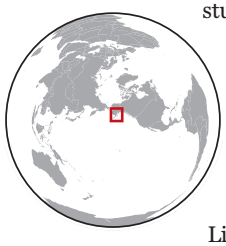

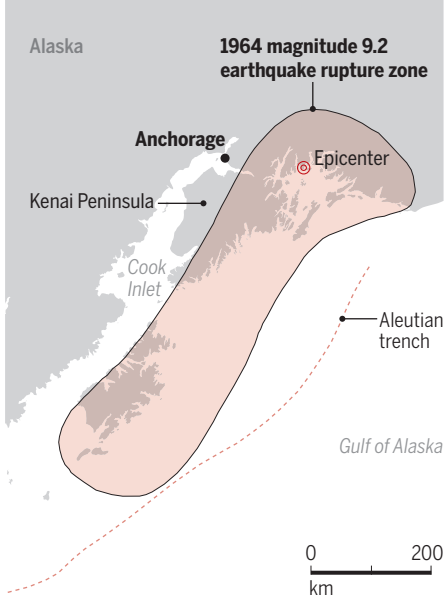

GRAPHIC: M. HERSHER/*SCIENCE*

A protester outside the Ministry of Education in Tel Aviv, Israel, bears a sign reading "Female lab workers are struggling for the future of science."

PHOTO: MIRIAM ALSTER/FLASH90

SCIENCE POLICY

Israeli scientists speak out against 'destructive' policies

Many fear erosion of academic freedom and loss of talent

By **Michele Chabin**, *in Jerusalem*

Until recently, Elena Itskovich, an Israeli stem cell biologist who completed a postdoc at Stanford University 2 years ago, was planning a return to her home nation. But Itskovich says she's now "on the fence." She is uneasy about the policies of the Israeli government elected nearly 8 months ago and largely led by conservative nationalists and ultra-Orthodox parties.

She is not alone in her concerns. Israeli researchers have become increasingly vocal in opposing policies they say threaten academic freedom and Israel's standing as a leader in science and technology (see related Editorial, p. 715). The government's plans, which include downplaying science education and eliminating support for some Arab students, are "destructive" and could do "irreversible" harm to Israel's science and high-tech sectors, the heads of Israel's public research universities and members of a top government science advisory panel warned in a letter earlier this month.

Many Israeli researchers "have feelings of apprehension and danger regarding their future," declared the letter to Prime Minister Benjamin Netanyahu and his science and education ministers. The government's policies have already prompted some donors and investors to pause funding for R&D projects in Israel, and some foreign collaborators have issued "explicit threats" to cancel joint projects with Israeli institutions, members of the Council of University Heads and the National Council for Civilian Research and Development noted. There is also "a significant decrease in the willingness of leading Israeli scientists who are abroad to accept academic positions in Israel," they wrote. They also flagged signs that top researchers in Israel are eyeing moves abroad. "Many [Israeli scientists] are losing confidence and prefer to abandon ship," the authors wrote.

Historically, academic scientists in Israel have been reluctant to air their political views in a highly polarized society, says Uri Sivan, president of the Technion Israel Institute of Technology. "It is indeed unusual for us to step in and speak up."

But the country has been in turmoil since January, when hundreds of thousands of Israelis began taking to the streets to protest what they call "undemocratic" efforts by Netanyahu's government to limit the power of Israel's Supreme Court. Now, many scientists are attending—even leading—street protests around the country. "The motivation is the fact that the future of Israel's academic institutions is being jeopardized," Sivan says.

In May, for example, the government decided to increase funding to ultra-Orthodox boys' schools that offer little or no instruction in science (*Science*, 7 July, p. 17). This month, it announced a plan to reallocate tens of millions of dollars long used to enable Arab high school students from East Jerusalem to gain admission to the Hebrew University of Jerusalem. The money would instead be used for job training, said Finance Minister Bezalel Smotrich, who has claimed that "Islamic radical cells" have organized on Israeli campuses under the guise of academic freedom.

Hebrew University said Smotrich's decision to cancel funding for its program, which has served thousands of Arab students, would damage Israeli society and its economy for decades to come.

Concern that the government could erode academic freedoms "isn't theoretical," says Rivka Carmi, a geneticist and former president of Ben-Gurion University of the Negev. "There has already been political interference."

Carmi and other researchers fear ultraconservative members of the governing coalition will try to replace the scientists, physicians, and educators who have traditionally filled some key posts with less qualified political appointees. They note that right-wing groups have already compiled blacklists of academics they consider politically unacceptable.

Tech sector executives are also worried about the toll the conflict is taking on what some Israeli analysts proudly call "the startup nation." Investment in new Israeli tech firms has dropped 29% since the current government took office in late December 2022, compared with the previous 6 months, according to a report issued this month by Start-Up Nation Central, a nonprofit that promotes innovation. Initial public offerings of stock in new companies, as well as company mergers and acquisitions, have dropped to the lowest rates in years, the organization said.

The drop-off will likely have repercussions for academic researchers, Sivan says. "We are very tightly connected to the high-tech industry. We are an ecosystem. You cannot have cutting-edge engineering schools when the high-tech sector is in trouble."

Still, Sivan is optimistic universities will ride out the current storm. "Israeli academia is very strong," he says. "The roots are deep." Asya Rolls, a psychoneuroimmunologist at Technion, says the willingness of her fellow academics to protest the government's actions leaves her feeling "hopeful, almost optimistic."

In the meantime, Itskovich and her husband are watching and waiting. "We still want to return and hope things will turn around in Israel," she says. "But we have three children and don't want them raised in a country that's so broken apart." ■

Michele Chabin is a journalist in Israel.

PHOTO: NATALJA KENT/NHMLAC

DEATH BY FIRE

Wildfires, intensified by climate change and perhaps human activity, may have doomed Southern California's big mammals 13,000 years ago

By **Michael Price**, *at the La Brea Tar Pits and Museum in Los Angeles*

Crouching beside a shallow pond in a haze of smoke, a saber-toothed cat fixes hungry eyes on a horse sipping a few meters away. Prey has been hard to come by: Wildfires have burnt through the brush, and bison and other grazers have all but disappeared. As the big cat pounces, its quarry bolts forward into a tarry pool. Predator and prey alike sink hopelessly into the muck known today as the La Brea Tar Pits.

Some 13,000 years later, that saber-toothed cat's jawbone sits in a museum drawer alongside those of a western horse, ancient bison, dire wolf, ground sloth, and yesterday's camel. Collectively, the denizens of the "last drawer," as researchers call it, represent the last of their kind in the sticky, fossil-packed asphalt pits surrounded by Los Angeles high rises.

Paleontologists have long tried to understand why once-numerous populations of these and other megafauna vanished across North America toward the end of the last ice age. A study published on p. 746 of this issue of *Science* points to a new catalyst that

Emily Lindsey (left) and Regan Dunn display a fraction of the unlucky saber-toothed cats, dire wolves, sloths, camels, and other mammals entombed in La Brea's tar pits.

ties together the two leading hypotheses: human activity and climate change. Each played a role, but fire was the key mediator, the authors argue. In their scenario, when the climate suddenly became warmer and drier toward the end of the last ice age, human-caused blazes grew out of control, permanently altering the landscape—and spelling the end for the animals.

The new study, which precisely dated more than 170 fossil bones and found a 30-fold increase in wildfire near the pits, is one of the first to focus on fire as a force behind the megafauna's demise. "I really like that this is getting away from the dichotomous arguments we've had forever about megafauna extinction in the Americas, that it's an either-or choice between climate- or human-caused," says Angela Perri, a zooarchaeologist at Texas A&M University who wasn't involved in the study. "The most likely scenario is a combination."

Some others agree. "Quite believable," says Jenny McGuire, a paleoecologist at the Georgia Institute of Technology who wasn't involved with the work. "This is one of those cases where we do see the smoking gun."

However, there's no direct evidence for the human part of this equation, cautions independent consulting archaeologist Joe Watkins, past president of the Society for American Archaeology. "There is no real way to specifically link [early] humans to the increase in fires. … There are alternate possibilities."

But Watkins and others agree that the team's scenario serves as a warning about trends playing out across much of the world today: Landscapes are filling with people, climate is changing, and wildfires are scorching ecosystems. "We're going into a period that's warmer and drier," says Brian Codding, an anthropologist at the University of Utah who wasn't involved in the study. "Some analogs [in the new study] help us understand that what we're going into is very likely another state change in the ecosystem."

FOR MOST OF THE PAST 2.5 million years, Southern California was a far cry from the sun-kissed chaparral made famous by Hollywood. Juniper and oak trees grew thick among its hills and valleys, interspersed with open range. Saber-toothed cats, American lions, and massive dire wolves preyed on mammoths, mastodons, horses, and other herbivores—a menagerie recorded in fossils extracted from the La Brea tar. At some point between 21,000 and 16,000 years ago, humans voyaged into the region, probably traveling along the coast.

For perhaps a few thousand more years, the pollen and fossil records suggest things carried on more or less as usual, with mammals remaining abundant. Then, sometime between 10,000 and 13,000 years ago, something went terribly wrong, says Emily Lindsey, a paleoecologist and excavation leader at the La Brea Tar Pits and Museum. Verdant woods gave way to scrubby brushland and desert; most of the large mammals disappeared. Similar scenes played out across North America as the world transitioned out of the periodic ice ages of the Pleistocene and into the warmer Holocene. Continentwide, about 80% of megafauna went extinct around this time. For decades, scientists have tried to find out why.

Some researchers pin the extinction on the global climate shifts. Starting about 14,000 years ago the Bølling-Allerød warming period, marking the beginning of the end of the last glaciation, sent temperatures spiking and ponds drying for about 1800 years. Then the ice age had one last gasp, a 1000-year cold spell known as the Younger Dryas, before the climate warmed again about 10,000 years ago and settled into conditions similar to today's. By disrupting ecosystems, the whipsawing climate drove large mammals to extinction, some researchers argue.

Others point to the suspicious timing of humans entering North America. Equipped with stone weaponry, the immigrants depleted the large herbivores, dooming their predators as well, the overkill argument goes.

But many have questioned humans' impact. For starters, although archaeologists once thought humans first entered North America about 13,000 years ago, around the time of the extinctions, newer evidence strongly suggests people arrived by at least 16,000 years ago, and possibly thousands of years earlier. So humans had been living and hunting on the continent for thousands of years before the mass extinction began.

F. Robin O'Keefe, a biologist at Marshall University and first author on the new study, says in the past he had been convinced by the overkill hypothesis. "This kind of 20th century masculine 'we're going to hunt them to extinction' kind of thing," he recalls. Then he saw all the data showing people had coexisted with megafauna for thousands of years. "I had to unlearn this idea that it was going to be humans' fault," he says. "It's more nuanced than that."

Settling this thorny debate requires knowing exactly when numerous species disappeared and how the environment changed as they did so. But the available data were spotty and ambiguous.

In the early 2000s, a group of researchers connected to La Brea realized their site could help unlock this mystery. For tens of thousands of years, animals have strayed into the shallow pools covering the site's natural asphalt seeps. If unlucky creatures ventured a few steps in, however, they sank into the sticky mire beneath the surface. Hungry predators—sometimes whole packs—apparently chased after the panicking animals, turning the pits into carnivore traps. Over time, the muck entombed millions of animals.

Today, the museum and urban park is home to the world's largest collection of Pleistocene fossils, containing more than 3.5 million specimens from 60 species of mammals alone. That makes it the perfect place to pin down the dates for many species' disappearances, O'Keefe says. "The attraction is numbers," he says.

In 2018, he and colleagues started on an ambitious plan to radiocarbon date bones from a tar pit first excavated in the 1920s.

The technique relies on the fact that living things absorb tiny amounts of radioactive carbon-14 into their tissue. After death, the carbon-14 slowly decays into other isotopes at a predictable rate, allowing scientists to estimate a sample's age to within a few decades. But the asphalt of a tar pit is rich in very old carbon, which is largely devoid of carbon-14. If carbon from the asphalt makes its way into a sample being dated, the results are useless.

Using a combination of sonic waves, chemical solvents, and molecular filters, Lindsey and colleagues at the University of California (UC), Irvine, developed a new method to painstakingly purge the asphalt from their samples and isolate the collagen within. Radiocarbon dates from La Brea are "always tricky," McGuire notes. "But this paper definitely has the world's experts in doing that."

The team dated 169 specimens from the pit's eight most common species: saber-toothed cats (*Smilodon fatalis*), dire wolves (*Aenocyon dirus*), coyotes (*Canis latrans*), American lions (*Panthera atrox*), ancient bison (*Bison antiquus*), western horses (*Equus occidentalis*), Harlan's ground sloths (*Paramylodon harlani*), and yesterday's camels (*Camelops hesternus*). "They've probably doubled the number of radiocarbon dates for Late Pleistocene megafauna in North America," Perri says. "That alone is a significant contribution."

The results reveal that at La Brea, sloths and camels disappeared first, about 13,600 years ago. Then 13,200 years ago, other mammals began to drop off precipitously, with herbivores vanishing more quickly than carnivores. By 12,900 years ago, all of the megafauna in the study—save coyotes—were gone. This unusually detailed chart of an extinction, with vegetation-dependent herbivores dying off first, set researchers to exploring how plant life changed at the time.

Museum paleobotanist Regan Dunn examined pollen grains from a well-dated core sample taken from the bottom of Lake Elsinore, 100 kilometers southeast of La Brea. The mix of pollen species changed little at 13,600 years ago, but between 13,200 and 12,900 years ago, pollen counts for both oak and juniper plunged, and pines, grasses, and chaparral plants spiked (see timeline, right).

Dunn and colleagues suspected fires were the culprit, because the plants that grew back are fire adapted and thrive in fire-prone areas. But they couldn't prove it.

Then Dunn stumbled across work by Lisa Martinez, a Ph.D. student at UC Los Angeles. Martinez had sorted through the same Lake Elsinore core sample—including at the key time period—for flecks of charcoal that could reveal the region's history of wildfire. "I saw that and just about fell out of my chair," Dunn says. Martinez soon joined the project.

Her results matched the pollen and extinction records perfectly. She found that about 13,200 years ago, charcoal accumulation jumped 30-fold and persisted at heightened levels for the next 400 years. That's the lingering record of rampant wildfires, which likely razed vast tracts of woodlands and encouraged more fire-tolerant plants. Eventually, fire ushered in the current chaparral-dominated habitat.

As with the 2020 Australian bushfires, which killed or displaced an estimated 3 billion animals, these late Pleistocene wildfires probably killed many animals outright. But the sudden loss of habitat and food may have been even more devastating, Lindsey explains. Herbivore numbers dwindled as their food sources burned, and carnivore populations followed suit.

Why so many fires? Paleoclimate records reveal the region had previously gone through similar warm and dry spells without such dramatic ecological consequences. "The difference at the end of the last ice age," Lindsey says, "is humans are here."

THE OLDEST unequivocal evidence of human presence in California comes from a partial skeleton known as the Arlington Springs Man, found on Santa Rosa Island and dated to about 12,900 years ago—after the megafauna were gone. But several other sites including White Sands in New Mexico, Paisley Caves in Oregon, and Monte Verde in Chile all point to humans being in the Americas by between 21,000 and 16,000 years ago.

There's no good reason some wouldn't have settled in coastal Southern California, Lindsey says. "Once humans show up somewhere, we're everywhere," she says.

And where humans go, fire follows. "Fire is a great tool," says Dunn, who studies how fire has shaped human and plant communities. "Humans are very adept at using fire for land management … to create mosaic habitats, to create the right kinds of materials for basketry, for harvesting grasshoppers, for hunting strategies."

In the hands of Indigenous Americans, cultural burning techniques—also known as fire-stick farming—actually prevented the fuel buildup that causes large, out-of-control wildfires, like those that followed the arrival of European settlers, says Watkins, who is a member of the Choctaw Nation of Oklahoma. Europeans suppressed fires and introduced cattle ranching, allowing more fuel to build up and creating larger and larger combustible grasslands. In recent years, Indigenous communities and fire scientists have called for land managers to employ more of the time-tested cultural management techniques to prevent forest fires.

"Fire-stick technology has been documented as a means of controlling fuel loads and contributes to less severe events," Watkins says. "But those technologies have been suppressed as population density has expanded."

Back 13,000 years ago, there are few direct data points about how early Americans used fire, whether as simple campfires or to manage ecosystems. And whatever their fire practices, people in Southern California may have coexisted with the local megafauna for thousands of years. But then something changed. Previously published models of population growth based on archaeological and genetic evidence

Charting California's combustible past

For millions of years, Southern California was covered in woodland, where large mammals such as saber-toothed cats, dire wolves, and camels roamed. New radiocarbon dates from the La Brea Tar Pits suggest these big animals began to disappear about 13,200 years ago, just when charcoal and pollen from a nearby lake suggest rampant wildfires.

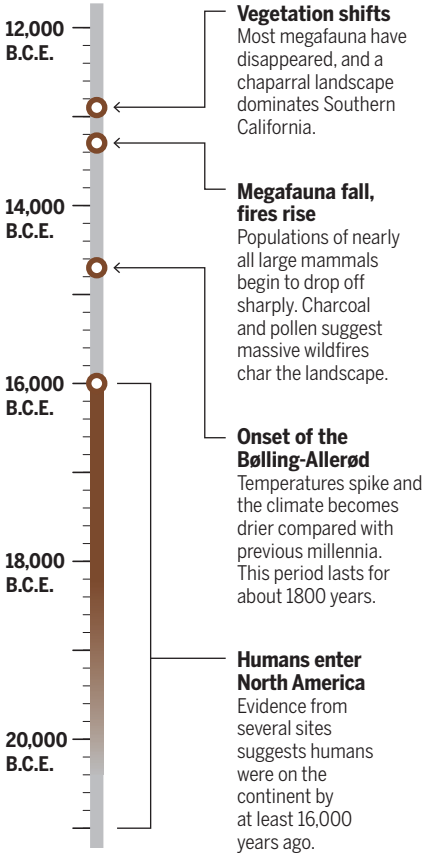
12,000 B.C.E.
14,000 B.C.E.
16,000 B.C.E.
18,000 B.C.E.
20,000 B.C.E.
Vegetation shifts
Most megafauna have disappeared, and a chaparral landscape dominates Southern California.
Megafauna fall, fires rise
Populations of nearly all large mammals begin to drop off sharply. Charcoal and pollen suggest massive wildfires char the landscape.
Onset of the Bølling-Allerød
Temperatures spike and the climate becomes drier compared with previous millennia. This period lasts for about 1800 years.
Humans enter North America
Evidence from several sites suggests humans were on the continent by at least 16,000 years ago.

GRAPHIC: A. FISHER/*SCIENCE*

Liquid asphalt bubbles up from a La Brea tar pit known as No. 61/67, from which most of the animals radiocarbon dated for a new study were excavated.

suggest a demographic explosion in North America between about 15,000 and 13,000 years ago. If that held true for Southern California—a big "if," the researchers admit—it means populations were booming just as the Bølling-Allerød began and the climate turned hotter and drier.

The climate change would have made human-caused fires more likely to burn out of control, the researchers argue. The burning turned the landscape from woodland to chaparral, dooming most of the region's megafauna by 13,000 years ago. Mammoths and mastodons are rare in the La Brea record, but other sites show they hung on for another few thousand years, perhaps because they faced less pressure from human hunters and other predators. And coyotes adapted, as always, probably by switching to smaller prey, Dunn explains.

Loren Davis, an archaeologist at Oregon State University, largely agrees with the team's conclusions. "People in the landscape can't be blamed for all of the fires, but they're probably making some of them," he says. "And they're making them right at this tipping point of environmental change."

Watkins, though, stresses that humans would have been just one source of fire. "The climate is already changing and local areas drying … dry lightning storms could very easily be responsible for the increase in wildfires," he says. He adds that although the authors stress a constellation of factors, he wishes they had more explicitly emphasized that humans living in the region weren't directly responsible for the megafauna extinction, to help head off simplistic interpretations and blame.

Others agree with the combination hypothesis. Huw Groucutt, a prehistoric archaeologist at the Max Planck Institute of Geoanthropology, speculated in a 2021 paper that humans may have indirectly contributed to the extinction of North American megafauna, perhaps by intensive hunting in ecosystems weakened by climate change. "This new study supports [a version of] that perspective," he says. "It suggests humans had an impact on megafauna, but they did so in the context of ecosystems made vulnerable by climate change."

Perri cautions that other regions, such as the Southwest or Florida, may have a different story. "We shouldn't view this extinction as a single event that happened in the same way everywhere." Groucutt agrees, noting that it's difficult to know for sure whether the last appearances of species at La Brea match their disappearances in the greater region. "While it's a great sample of dates, it's still a sample … from one part of one single site."

O'Keefe and Lindsey say more data are on the way. But for them, the existing evidence is enough to spin a cautionary tale for people living in Southern California and other fire-prone regions today. "As we say in the paper, all the preconditions—a warming climate, increasing human population—that caused that state transition back then are reoccurring today," O'Keefe says. "If that state transition happens again, where are we going to end up?" ■

UCLA graduate student Lisa Martinez sorts through sediment from Lake Elsinore, where she found a 30-fold increase in charcoal around the time of extinction.

PHOTOS: (TOP TO BOTTOM) NHMLAC; NATALIA KENT/NHMLAC

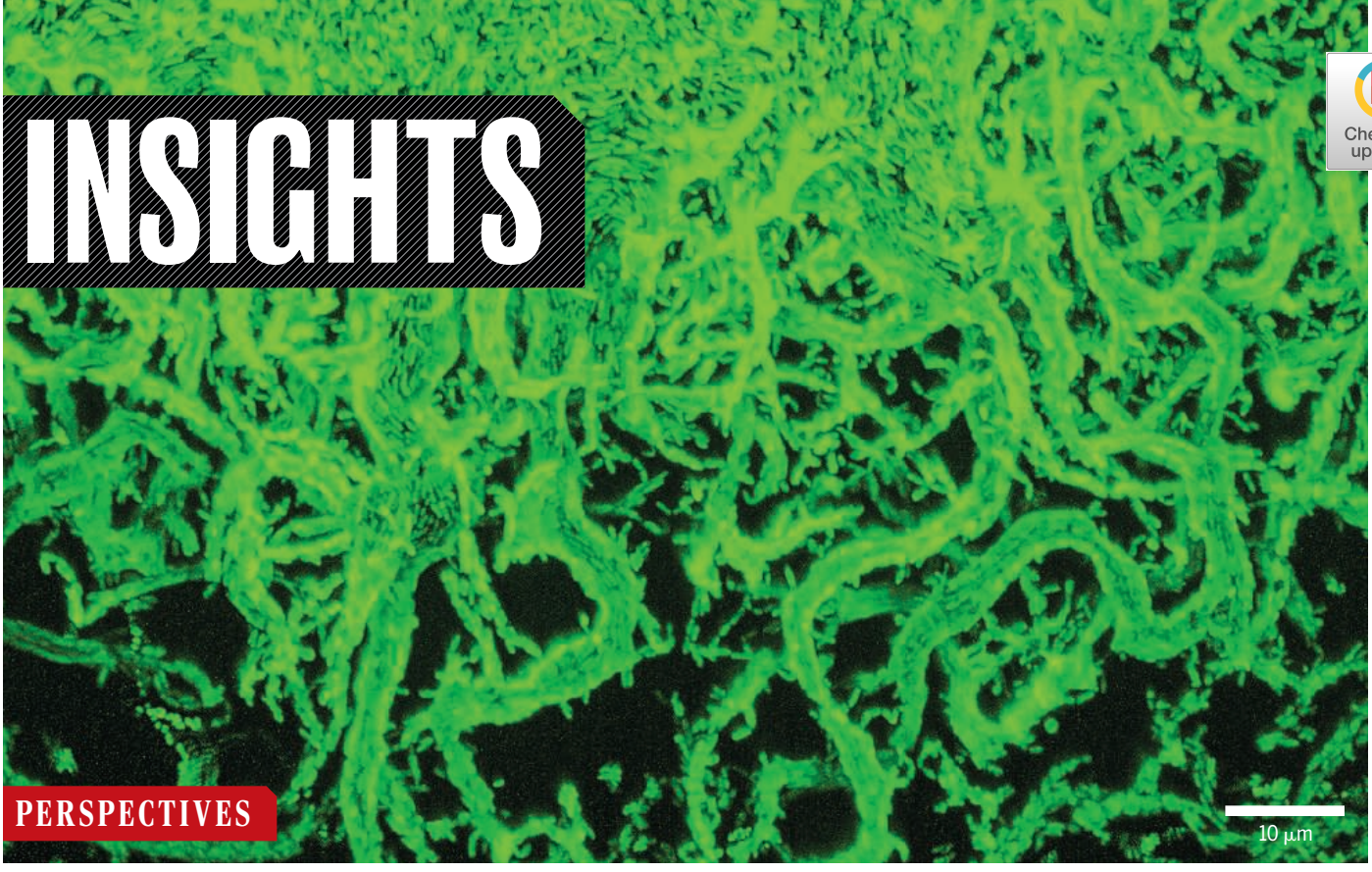

MICROBIOLOGY

Bacteria stretch and bend oil to feed their appetite

Microbes reshape oil droplets to speed biodegradation

By **Terry J. McGenity** *and* **Pierre Philippe Laissue**

It is imperative to understand the fate of crude oil that escapes into the ocean to minimize its environmental, economic, and societal harm. Large amounts of crude oil enter the sea, as occurred this past month on a platform in the Gulf of Mexico. Oil does not easily mix with water, which can restrict oil degradation through microbes, a key pathway to remove hydrocarbons from the environment. However, turbulent seas and response measures, such as dispersant addition, generate smaller oil droplets that are attractive to voracious microbial activity. On page 748 of this issue, Prasad *et al.* (*1*) report that bacteria attach to oil droplets, then grow as a film on the oil surface, sometimes reshaping spherical droplets into finger-like protrusions. This dynamic process increases the oil's surface area and accelerates its biodegradation. The finding should improve predictions of spilled oil transport to ecologically sensitive sites.

Certain marine microbes use hydrocarbons as a carbon and energy source. Collectively, they can metabolize and thereby degrade crude oil. *Alcanivorax borkumensis* (or *Alca*) is a widespread hydrocarbon-degrading marine bacterium that is frequently dominant in seawater contaminated with crude oil (*2*). Alkanes are the simplest family of hydrocarbons in crude oil. Prasad *et al.* used *Alcanivorax* (which translates to "devourer of alkanes") and droplets of *n*-hexadecane—with diameters between 10 and 200 μm—as a model system to examine how *Alca* forms a biofilm on a liquid surface, and how the interfacial oil-water properties affect oil degradation.

Prasad *et al.* microscopically examined living cells of *Alca* on oil droplets in a microfluidic chamber and modeled the dynamic oil-seawater interface. *Alca* forms a biofilm, composed of cells in a polymer matrix, on the surface of oil droplets, which aids with attachment (*2*–*4*). The authors observed that the time in which *Alca* was cultivated on *n*-hexadecane, before being given a new supply of alkane droplets to colonize, determined the shape of the growing biofilm and of these droplets. When transferred after 1 day of culture, *Alca* proliferated and formed thick spherical biofilms on the surface of oil droplets. By contrast, when transferred after 5 days of culture, *Alca* proliferated and frequently formed a biofilm with finger-like (dendritic) protrusions (see the image).

The question addressed by Prasad *et al.* is how *Alca* changes the shape of oil droplets. The authors built on work (*2*–*5*) showing that *Alca's* growth on hydrocarbons for a long time reduces the water-alkane interfacial tension and causes the cells to become more hydrophobic. These biochemical adaptations increase the strength of bacterial adhesion to the alkane, likely through biosurfactants, which are biomolecules with both hydrophobic and hydrophilic moieties. These changes, together with end-to-end cellular alignment and the stress exerted by cell division, buckled and stretched the alkane sphere while stabilizing the resultant alkane-containing protrusions, some of which detached. The biofilm-induced expansion of the alkane's surface area gave *Alca* better access to its carbon and energy source, resulting in a 3.5-fold increase in the rate of oil consumption in dendritic biofilms compared with spherical biofilms.

Prasad *et al.* also demonstrated that *Alca* consumes approximately one cell's volume

School of Life Sciences, University of Essex, Wivenhoe Park, CO4 3SQ, UK. Email: tjmcgen@essex.ac.uk

IMAGE: PRASAD *ET AL.* (*1*)

A film of *Alcanivorax borkumensis* bacteria (green) adheres to oil droplets, creating protrusions filled with oil that boost the rate of microbial consumption.

of alkane per hour, irrespective of the type of biofilm formed. However, the larger calculated rate of oil consumption by dendritic biofilms compared with spherical biofilms is attributed to the presence of more bacteria feeding simultaneously. Notably, the authors developed a mechanistic understanding of the process through live imaging to follow temporal changes in biofilm formation at the spatial resolution of a single bacterial cell—close to 2 μm. The authors further supported the findings by conducting experiments guided by liquid-crystal theories and simulations. For example, they designed experiments that used microfluidics to control and measure deformations of an alkane droplet.

There are several practical implications from the study of Prasad *et al*. Data on the diameter of oil droplets improve estimates of the biodegradation rate by microbes. This can help refine the predictions of the fate and transport of oil at sea (*6*). Whether nonspherical oil-droplet morphologies should be accounted for in oil-spill fate-and-transport models will depend on how frequently and in which environmental conditions dendritic droplets form. A first step to address this will be to count different oil-droplet morphologies after a spill at sea or in realistic experiments. These experiments should take into consideration permutations of assembled and natural microbial communities that are preconditioned in different ways and exposed to mixtures of hydrocarbons and crude oil.

Spherical and dendritic biofilm-coated oil droplets are likely to differ in viscous drag and density, which affects their buoyancy and thus the time spent in the ocean's water column, rather than on the surface, shore, or sea floor (*7*). This is notable because microbes on oil droplets will have greater access to nutrients such as nitrogen, phosphorus, or iron when in the water column. These nutrients can be a limiting factor for biodegradation in the nutrient-depleted ocean but not in experiments that use nutrient-rich media, such as in the study by Prasad *et al*. Bacteria-coated oil droplets rise more slowly than noncoated droplets in a water column, and complex nonspherical morphologies, resembling the detached dendrites with low oil content seen by Prasad *et al*., tend to float or even sink (*8*). The practical implications of these observations depend on whether oil droplets originate from dispersed deep-sea oil spills or from surface spills.

Further examination of the oil-water interfacial properties of spherical and dendritic biofilms could include proteomic and metabolite analyses to identify the amphiphilic biomolecules responsible for the morphological differences in biofilms. Improving temporal resolution with advanced imaging could refine biofilm dynamic processes. For example, light-sheet microscopy enabled the tracing of individual bacterial cells in the *Vibrio cholerae* biofilm over 16 hours, revealing an unexpected fountain-like flow of cells being transported to the growing edge of the biofilm (*9*).

Single-cell spatial transcriptomics (which provides a profile of gene expression) could address why some alkane droplets remained spherical whereas others became dendritic when colonized by *Alca* grown for 5 days. On the fifth day, *Alca* is in stationary phase, a period with no net increase in the number of bacteria and when cells are physiologically different from those in the early stage of growth. At stationary phase, the bacterium *Pseudomonas aeruginosa* has a greater variability in gene expression compared with that in earlier phases when proliferation is rapid (*10*). This variation within the population is presumably a bet-hedging strategy in the face of an unpredictable environment—a tactic that may also be used by *Alca*. The stationary phase also saw increased expression of a gene involved in the synthesis of rhamnolipid, a biosurfactant that may prepare the cell for biofilm formation, highlighting parallels between *P. aeruginosa* (*10*) and *Alca*.

Alca alone cannot degrade the thousands of hydrocarbons in crude oil. This requires a diverse community of microbes (*11*), interacting with each other or sometimes competing (*12*). The findings of Prasad *et al*. lay important groundwork for examining more realistic scenarios. Translating from single-species microscale interactions with surfaces to macroscale multispecies processes will improve understanding of the mechanisms that drive the biodegradation and transport of oil spilled into the oceans. ■

REFERENCES AND NOTES

1. M. Prasad *et al.*, *Science* **381**, 748 (2023).
2. M. M. Yakimov, K. N. Timmis, P. N. Golyshin, *Curr. Opin. Biotechnol.* **18**, 257 (2007).
3. M. P. Godfrin *et al.*, *Langmuir* 2018, **34**, 9047 (2018).
4. M. Omarova *et al.*, *ACS Sustain. Chem. Eng.* **7**, 14490 (2019).
5. J. Cui *et al.*, *Appl. Environ. Microbiol.* **88,** e0112622 (2022).
6. S. A. Socolofsky *et al.*, *Mar. Pollut. Bull.* **143**, 204 (2019).
7. J. C. Conrad, *J. Ind. Microbiol. Biotechnol.* **47**, 725 (2020).
8. V. Hickl, H. H. Pamu, G. Juarez, arXiv:2212.00627 (2022).
9. B. Qin *et al.*, *Science* **369**, 71 (2020).
10. D. Dar, N. Dar, L. Cai, D. K. Newman, *Science* **373**, eabi4882 (2021).
11. B. A. McKew *et al.*, *Environ. Microbiol.* **9,** 165 (2007).
12. T. J. McGenity *et al.*, *Aquat. Biosyst.* **8**, 10 (2012).

ACKNOWLEDGMENTS

The authors thank B. McKew for helpful comments.

10.1126/science.adj4430

CANCER

Targeting cancer with molecular glues

Molecular glues suppress the active form of the oncogenic protein KRAS

By **Jun O. Liu**[1,2,3]

Mutations of KRAS are prevalent in various cancers, but this oncogenic protein (oncoprotein) was considered undruggable owing to its relatively flat surface that has no obvious binding pockets for small molecules. A breakthrough came when the Cys^{12} mutation, $KRAS^{G12C}$, was astutely exploited using a small-molecule drug that covalently reacts with the thiol group of cysteine (*1*). This led to the ensuing development of two US Food and Drug Administration (FDA)–approved $KRAS^{G12C}$ inhibitors, sotorasib and adagrasib, which have brought significant survival benefits to patients with cancers that have the $KRAS^{G12C}$ mutation (*2*, *3*). These inhibitors selectively target the guanosine diphosphate (GDP)–bound inactive form of $KRAS^{G12C}$, which makes them slow acting, but patients can also develop drug resistance. On page 794 of this issue, Schulze *et al*. (*4*) report an approach that targets the active guanosine triphosphate (GTP)–bound $KRAS^{G12C}$ with molecular glues that recruit the cellular chaperone cyclophilin A (CYPA) to block $KRAS^{G12C}$-induced oncogenic signaling.

CYPA was initially discovered as a high-affinity receptor of the immunosuppressive drug cyclosporin A (*5*). Subsequently, CYPA was found to possess peptidyl prolyl cis-trans isomerase activity that is involved in protein folding (*6*). Notably, the CYPA–cyclosporin A complex, but neither CYPA nor cyclosporin A alone, binds to and inhibits the protein phosphatase activity of calcineurin that is required for calcium signaling in helper T cells. This revealed an unprecedented mode of action by a small molecule—working as molecular glue to bring two otherwise noninteract-

[1]Department of Pharmacology, Johns Hopkins School of Medicine, Baltimore, MD, USA. [2]Department of Oncology, Johns Hopkins School of Medicine, Baltimore, MD, USA. [3]The SJ Yan and HJ Mao Laboratory of Chemical Biology, Johns Hopkins School of Medicine, Baltimore, MD, USA. Email: joliu@jhu.edu

A film of *Alcanivorax borkumensis* bacteria (green) adheres to oil droplets, creating protrusions filled with oil that boost the rate of microbial consumption.

of alkane per hour, irrespective of the type of biofilm formed. However, the larger calculated rate of oil consumption by dendritic biofilms compared with spherical biofilms is attributed to the presence of more bacteria feeding simultaneously. Notably, the authors developed a mechanistic understanding of the process through live imaging to follow temporal changes in biofilm formation at the spatial resolution of a single bacterial cell—close to 2 μm. The authors further supported the findings by conducting experiments guided by liquid-crystal theories and simulations. For example, they designed experiments that used microfluidics to control and measure deformations of an alkane droplet.

There are several practical implications from the study of Prasad *et al*. Data on the diameter of oil droplets improve estimates of the biodegradation rate by microbes. This can help refine the predictions of the fate and transport of oil at sea (*6*). Whether nonspherical oil-droplet morphologies should be accounted for in oil-spill fate-and-transport models will depend on how frequently and in which environmental conditions dendritic droplets form. A first step to address this will be to count different oil-droplet morphologies after a spill at sea or in realistic experiments. These experiments should take into consideration permutations of assembled and natural microbial communities that are preconditioned in different ways and exposed to mixtures of hydrocarbons and crude oil.

Spherical and dendritic biofilm-coated oil droplets are likely to differ in viscous drag and density, which affects their buoyancy and thus the time spent in the ocean's water column, rather than on the surface, shore, or sea floor (*7*). This is notable because microbes on oil droplets will have greater access to nutrients such as nitrogen, phosphorus, or iron when in the water column. These nutrients can be a limiting factor for biodegradation in the nutrient-depleted ocean but not in experiments that use nutrient-rich media, such as in the study by Prasad *et al*. Bacteria-coated oil droplets rise more slowly than noncoated droplets in a water column, and complex nonspherical morphologies, resembling the detached dendrites with low oil content seen by Prasad *et al*., tend to float or even sink (*8*). The practical implications of these observations depend on whether oil droplets originate from dispersed deep-sea oil spills or from surface spills.

Further examination of the oil-water interfacial properties of spherical and dendritic biofilms could include proteomic and metabolite analyses to identify the amphiphilic biomolecules responsible for the morphological differences in biofilms. Improving temporal resolution with advanced imaging could refine biofilm dynamic processes. For example, light-sheet microscopy enabled the tracing of individual bacterial cells in the *Vibrio cholerae* biofilm over 16 hours, revealing an unexpected fountain-like flow of cells being transported to the growing edge of the biofilm (*9*).

Single-cell spatial transcriptomics (which provides a profile of gene expression) could address why some alkane droplets remained spherical whereas others became dendritic when colonized by *Alca* grown for 5 days. On the fifth day, *Alca* is in stationary phase, a period with no net increase in the number of bacteria and when cells are physiologically different from those in the early stage of growth. At stationary phase, the bacterium *Pseudomonas aeruginosa* has a greater variability in gene expression compared with that in earlier phases when proliferation is rapid (*10*). This variation within the population is presumably a bet-hedging strategy in the face of an unpredictable environment—a tactic that may also be used by *Alca*. The stationary phase also saw increased expression of a gene involved in the synthesis of rhamnolipid, a biosurfactant that may prepare the cell for biofilm formation, highlighting parallels between *P. aeruginosa* (*10*) and *Alca*.

Alca alone cannot degrade the thousands of hydrocarbons in crude oil. This requires a diverse community of microbes (*11*), interacting with each other or sometimes competing (*12*). The findings of Prasad *et al*. lay important groundwork for examining more realistic scenarios. Translating from single-species microscale interactions with surfaces to macroscale multispecies processes will improve understanding of the mechanisms that drive the biodegradation and transport of oil spilled into the oceans. ■

REFERENCES AND NOTES

1. M. Prasad *et al.*, *Science* **381**, 748 (2023).
2. M. M. Yakimov, K. N. Timmis, P. N. Golyshin, *Curr. Opin. Biotechnol.* **18**, 257 (2007).
3. M. P. Godfrin *et al.*, *Langmuir* 2018, **34**, 9047 (2018).
4. M. Omarova *et al.*, *ACS Sustain. Chem. Eng.* **7**, 14490 (2019).
5. J. Cui *et al.*, *Appl. Environ. Microbiol.* **88,** e0112622 (2022).
6. S. A. Socolofsky *et al.*, *Mar. Pollut. Bull.* **143**, 204 (2019).
7. J. C. Conrad, *J. Ind. Microbiol. Biotechnol.* **47**, 725 (2020).
8. V. Hickl, H. H. Pamu, G. Juarez, arXiv:2212.00627 (2022).
9. B. Qin *et al.*, *Science* **369**, 71 (2020).
10. D. Dar, N. Dar, L. Cai, D. K. Newman, *Science* **373**, eabi4882 (2021).
11. B. A. McKew *et al.*, *Environ. Microbiol.* **9,** 165 (2007).
12. T. J. McGenity *et al.*, *Aquat. Biosyst.* **8**, 10 (2012).

ACKNOWLEDGMENTS

The authors thank B. McKew for helpful comments.

10.1126/science.adj4430

CANCER

Targeting cancer with molecular glues

Molecular glues suppress the active form of the oncogenic protein KRAS

By **Jun O. Liu**[1,2,3]

Mutations of KRAS are prevalent in various cancers, but this oncogenic protein (oncoprotein) was considered undruggable owing to its relatively flat surface that has no obvious binding pockets for small molecules. A breakthrough came when the Cys^{12} mutation, $KRAS^{G12C}$, was astutely exploited using a small-molecule drug that covalently reacts with the thiol group of cysteine (*1*). This led to the ensuing development of two US Food and Drug Administration (FDA)–approved $KRAS^{G12C}$ inhibitors, sotorasib and adagrasib, which have brought significant survival benefits to patients with cancers that have the $KRAS^{G12C}$ mutation (*2*, *3*). These inhibitors selectively target the guanosine diphosphate (GDP)–bound inactive form of $KRAS^{G12C}$, which makes them slow acting, but patients can also develop drug resistance. On page 794 of this issue, Schulze *et al*. (*4*) report an approach that targets the active guanosine triphosphate (GTP)–bound $KRAS^{G12C}$ with molecular glues that recruit the cellular chaperone cyclophilin A (CYPA) to block $KRAS^{G12C}$-induced oncogenic signaling.

CYPA was initially discovered as a high-affinity receptor of the immunosuppressive drug cyclosporin A (*5*). Subsequently, CYPA was found to possess peptidyl prolyl cis-trans isomerase activity that is involved in protein folding (*6*). Notably, the CYPA–cyclosporin A complex, but neither CYPA nor cyclosporin A alone, binds to and inhibits the protein phosphatase activity of calcineurin that is required for calcium signaling in helper T cells. This revealed an unprecedented mode of action by a small molecule—working as molecular glue to bring two otherwise noninteract-

[1]Department of Pharmacology, Johns Hopkins School of Medicine, Baltimore, MD, USA. [2]Department of Oncology, Johns Hopkins School of Medicine, Baltimore, MD, USA. [3]The SJ Yan and HJ Mao Laboratory of Chemical Biology, Johns Hopkins School of Medicine, Baltimore, MD, USA. Email: joliu@jhu.edu

Inhibition of a KRAS mutant with molecular glue

KRAS induces cell proliferation by exchanging GDP (inactive state) with GTP (active state). This leads to its association with and activation of downstream signaling proteins, such as RAF and PI3K. The Gly^{12}-to-Cys^{12} mutation of KRAS impairs its ability to hydrolyze GTP to GDP, causing excessive cell proliferation and cancer. Sotorasib and adagrasib irreversibly inhibit $KRAS^{G12C}$-GDP, whereas the molecular glue RMC-4998 selectively targets $KRAS^{G12C}$-GTP by forming a ternary complex with the prolyl isomerase CYPA.

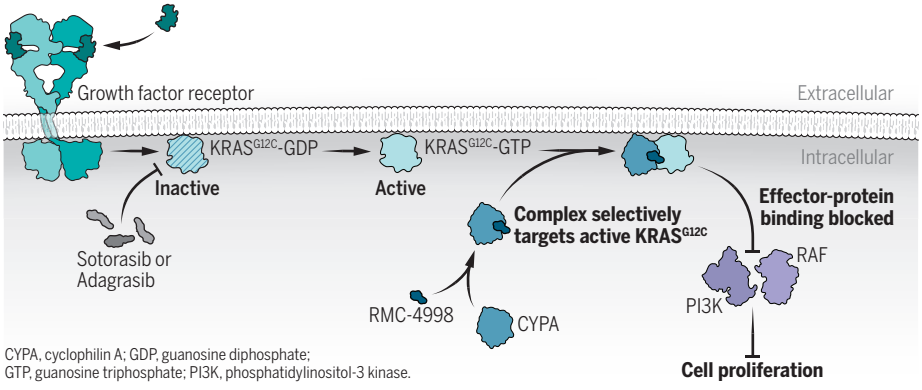

CYPA, cyclophilin A; GDP, guanosine diphosphate; GTP, guanosine triphosphate; PI3K, phosphatidylinositol-3 kinase.

ing proteins together to manifest its activity (*7*). Aside from cyclosporin A, two other macrocyclic immunosuppressive drugs, FK506 and rapamycin, were also found to act as molecular glues (*7*, *8*). A search for cyclosporin A–like natural products led to the discovery of sanglifehrin A, which also binds to CYPA (*9*, *10*). A high-resolution crystal structure of the CYPA–sanglifehrin A complex revealed the presence of a minimal tripeptide motif in sanglifehrin A that mediates its interaction with CYPA (*11*).

Schulze *et al.* began their search for an inhibitor of $KRAS^{G12C}$-GTP by tethering a cysteine-reacting moiety to the tripeptide CYPA-binding motif of sanglifehrin A. The resultant tool compound induced the formation of a ternary complex between CYPA and $KRAS^{G12C}$ bound to a GTP analog (GMPPNP) and covalently modified Cys^{12}. Based on a high-resolution crystal structure of the complex, Schulze *et al.* optimized the tool compound through iterative structure-guided design, syntheses, and evaluation of new analogs, which eventually yielded a lead compound called RMC-4998 that exhibited high potency and selectivity toward $KRAS^{G12C}$-GTP, blocking its signaling activity (see the figure). This paved the way to the subsequent development of a drug candidate, RMC-6291, that is now undergoing testing in a phase I clinical trial of patients with advanced $KRAS^{G12C}$-mutant cancers (NCT05462717).

The ability of RMC-4998 to induce the formation of the ternary complex was attributed in part to the neomorphic surface of CYPA that is induced by RMC-4998 binding and involves at least four residues from CYPA: Asn^{71}, Lys^{151}, Arg^{148}, and Trp^{121}. It is remarkable that CYPA, which does not interact with $KRAS^{G12C}$, is capable of forging such extensive surface interactions with $KRAS^{G12C}$ upon binding to RMC-4998. By comparison, seven CYPA residues directly interact with calcineurin in the CYPA–cyclosporin A–calcineurin ternary complex, of which only Arg^{148} is also used in CYPA–RMC-4998–$KRAS^{G12C}$–GTP (*12*). That CYPA is able to forge direct interactions with different proteins in a ligand-dependent fashion, including with calcineurin (through cyclosporin A), inosine monophosphate dehydrogenase-2 (through sanglifehrin A) (*9*), and now GTP-bound $KRAS^{G12C}$ (through RMC-9448), suggests that the surface of CYPA may have an unusual ability to adapt to a new interacting surface environment.

As a chaperone, CYPA may have a greater intrinsic plasticity and adaptability because, as a prolyl isomerase, it interacts with diverse protein substrates. Similar surface plasticity and adaptability is seen in FK506-binding protein 1A (FKBP1A), another prolyl isomerase that can mediate the formation of ternary complexes with calcineurin (through FK506), mechanistic target of rapamycin (mTOR, through rapamycin), the centrosome-associated protein CEP250 (through WDB002), and equilibrative nucleoside transporter 1 (ENT1, through rapadocin) (*7*, *8*, *13*, *14*). The surface plasticity and adaptability of both CYPA and FKBP1A should bode well for future discovery and design of molecular glues for other targets.

The CYPA-binding molecular glues have several advantages over conventional small-molecule inhibitors of $KRAS^{G12C}$ such as sotorasib and adagrasib. The formation of a more-extensive composite surface of the CYPA–RMC-4998 complex rendered it possible to selectively target $KRAS^{G12C}$-GTP, making RMC-4998 insensitive to growth factor stimulation that increases the concentration of $KRAS^{G12C}$-GTP and desensitizes cells to sotorasib and adagrasib. The presence of CYPA in the ternary complex occluded a space on top of $KRAS^{G12C}$, preventing the binding of known downstream effector proteins, including RAF and phosphatidylinositol-3 kinase (PI3K). Moreover, the multiplicity of interactions of $KRAS^{G12C}$-GTP with both RMC-4998 and surface residues of CYPA makes it more difficult for drug-resistant mutants in KRAS or CYPA to emerge. Indeed, Schulze *et al.* showed that mutation of a CYPA residue involved in the interaction with $KRAS^{G12C}$ incompletely ablated CYPA–RMC-4998–$KRAS^{G12C}$ complex formation. Compared with the existing $KRAS^{G12C}$-GDP inhibitors, it will be interesting to see whether RMC-6291 is superior, with greater efficacy and more-durable responses in patients.

The success of the development of RMC-4998 and RMC-6291 epitomizes the power of combining structural biology, rational design, and medicinal chemistry in molecular-glue discovery. This bottom-up approach is in contrast to the alternative and complementary forward chemical-genetics approach in which a library of structurally diverse, glue-like molecules is generated for both phenotypic and target-based screens (*14*). A combination of both approaches is likely to further accelerate discoveries of new molecular glues (*15*). With the seemingly untouchable active states of $KRAS^{G12C}$ conquered, it will be interesting to explore whether these approaches can be applied to other KRAS mutants, small GTPases, trimeric G proteins, and even other classes of "undruggable" targets. ■

REFERENCES AND NOTES

1. J. M. Ostrem, U. Peters, M. L. Sos, J. A. Wells, K. M. Shokat, *Nature* **503**, 548 (2013).
2. B. A. Lanman *et al.*, *J. Med. Chem.* **63**, 52 (2020).
3. J. B. Fell *et al.*, *J. Med. Chem.* **63**, 6679 (2020).
4. C. J. Schulze *et al.*, *Science* **381**, 794 (2023).
5. R. E. Handschumacher, M. W. Harding, J. Rice, R. J. Drugge, D. W. Speicher, *Science* **226**, 544 (1984).
6. G. Fischer, B. Wittmann-Liebold, K. Lang, T. Kiefhaber, F. X. Schmid, *Nature* **337**, 476 (1989).
7. J. Liu *et al.*, *Cell* **66**, 807 (1991).
8. J. Heitman, N. R. Movva, M. N. Hall, *Science* **253**, 905 (1991).
9. J.-J. Sanglier *et al.*, *J. Antibiot.* **52**, 466 (1999).
10. K. H. Pua, D. T. Stiles, M. E. Sowa, G. L. Verdine, *Cell Rep.* **18**, 432 (2017).
11. J. Kallen, R. Sedrani, G. Zenke, J. Wagner, *J. Biol. Chem.* **280**, 21965 (2005).
12. Q. Huai *et al.*, *Proc. Natl. Acad. Sci. U.S.A.* **99**, 12037 (2002).
13. U. K. Shigdel *et al.*, *Proc. Natl. Acad. Sci. U.S.A.* **117**, 17195 (2020).
14. Z. Guo *et al.*, *Nat. Chem.* **11**, 254 (2019).
15. S. L. Schreiber, *Cell* **184**, 3 (2021).

ACKNOWLEDGMENTS

Intellectual property related to Guo *et al.* (*14*) from the author's laboratory has been licensed by Johns Hopkins University to Rapafusyn Pharmaceuticals, Inc., of which the author is a cofounder and board member. This arrangement has been reviewed and approved by the Johns Hopkins University in accordance with its conflict-of-interest policies.

10.1126/science.adj1001

GRAPHIC: N. BURGESS/*SCIENCE*

GEOLOGY

Extracting resources from abandoned mines

Recovering minerals and metals from abandoned mines could aid decarbonization

By **Zhongwen Bao**, **Carol J. Ptacek**, and **David W. Blowes**

The development of environmentally friendly technologies (e.g., electric vehicles, wind turbines, solar panels, and lithium-ion batteries) to achieve a low-carbon future will require large quantities of critical minerals and metals (*1*). Mining and extraction of these materials are anticipated to generate substantially larger volumes of mine wastes, including waste rock and tailings (*2*). The release of contaminated water from mine wastes can cause long-term environmental damage and land degradation, posing challenges for pollution control and environmental remediation. Resource extraction from contaminated water, mine wastes, and mine workings (e.g., unexploited open pits and underground tunnels) at abandoned mines could potentially address the increased demands of critical minerals and metals for decarbonization. However, careful planning is required to ensure that negative environmental effects are not exacerbated during resource recovery at abandoned mines.

Mining activities can have long-term positive impacts by supplying valuable minerals and metals to advance economic development, energy transition, infrastructure construction, and technological innovation. However, mining has also caused environmental and societal harm. Vast quantities of potentially chemically reactive wastes are accumulated over large land footprints at mine sites. Globally, land that has been affected by mining amounts to 66,000 km^2, including waste-rock piles, tailings impoundments, and open pits as well as mining and processing infrastructure (*3*). Much of this mining-affected land includes abandoned mines, which are neither in operation nor managed. Mines are abandoned for a variety of reasons, including depletion of ores, commodity price fluctuations, and technical challenges associated with mining deeper ores. The global area of land use and contamination level at abandoned mines are unknown. Yet, there is a distinct contrast between the number of active mines and the much larger number of abandoned mines. For example, in Canada, there are ~200 active mines compared with more than 10,000 abandoned mines.

Each abandoned mine has distinct attributes, including the physicochemical and geotechnical characteristics of mine-waste deposits and mine voids. These characteristics strongly influence the impacts to land, water, and ecosystems, including releases of water contaminated with high concentrations of toxic metals and metalloids [e.g., acid mine drainage (AMD)] and releases of carbon dioxide (CO_2). Chronic releases of AMD and catastrophic failures of tailings dams lead to "dead zones" at mine sites, which exhibit biodiversity loss, land deterioration, and degraded surface water and groundwater and can be detrimental to human health (*4*). For instance, in 1999, an extremely low pH of −3.6 was reported in AMD from the Richmond Mine of the Iron Mountain copper deposit, USA, which was mined in the early 1900s (*5*). This AMD resulted in fish death and vegetation denudation. Additionally, release of dissolved contaminants and alteration of groundwater and surface water flow systems can harm aquatic ecosystems, such as effects on salmonids (ray-finned fish) and their habitat in northwestern North America as a result of tailings dam failures, such as that at Mount Polley Mine, Canada, in 2014 (*6*).

Although the stored mass of mine wastes is uncertain, an estimated global mass of tailings totals 223 billion metric tons generated from 1771 to 2019, whereas the total mass of waste rock is estimated to be about 10 times that of the mass of tailings (*7*). Exposure of sulfide-bearing mine wastes to water and oxygen triggers complex microbial-catalyzed biogeochemical reactions that generate acidic, neutral, and saline mine drainage. Mine wastes prone to AMD frequently cause the most severe water quality problems that persist for thousands of years (*5*), and thus AMD has been the focus of intense research and environmental remediation. However, neutral and saline mine drainage also have the potential to cause environmental degradation. Selective mining, segregation and encapsulation, subaqueous disposal, lime or limestone addition, cover construction to limit water infiltration or oxygen ingress, and passive techniques (including constructed wetlands, bioreactors, and permeable reactive barriers) have been widely applied to facilitate AMD mitigation either at the source or along the migration pathway (*8*). Typically, a combination of these techniques is implemented.

These AMD mitigation strategies may demonstrate short-term success; however, their long-term performance remains uncertain under changing climate scenarios. For example, subaqueous disposal of tailings into inland water bodies and oceans limits AMD generation by reducing the oxygen supply. It was found that ocean acidification and the present temperature increase caused by climate change can enhance metal leaching from tailings disposed below a deep-water cover, potentially decreasing water quality and causing negative environmental effects (*9*). Without permanent remediation, the long-term impacts of mine wastes on terrestrial and marine ecosystems will persist.

Supplies from active mines cannot currently meet the increased demands for critical minerals and metals for decarbonization measures. Individual mines are operated to recover targeted commodities, which are determined by the economics of mining, processing, and global availability. Mine wastes at abandoned mines may contain recoverable concentrations of rare earth elements (REEs), platinum group elements, and metals—e.g., cobalt, copper, lithium, and nickel—that are more accessible than the low-grade ores that are currently mined (*10*). Many of these elements are indispensable in technology development to achieve carbon-zero goals. Therefore, AMD, mine wastes, and mine workings at abandoned mines are being evaluated as potential sources for these critical minerals and metals. Integration of resource exploration and recovery with environmental remediation provides a promising opportunity to gain value from mine wastes while tackling the environmental challenges associated with abandoned mines.

Assessing the resource potential of critical minerals and metals in AMD, mine wastes, and mine workings at abandoned mines is the first step. Abandoned mines are often located in remote locations with sensitive environments. Appropriate remediation designs, characterization studies, and monitoring programs are needed to as-

Department of Earth and Environmental Sciences, University of Waterloo, Waterloo, ON, Canada.
Email: z23bao@uwaterloo.ca; blowes@uwaterloo.ca

Resource recovery and environmental remediation at abandoned mines

Minerals and metals that are in high demand could be recovered from abandoned mine wastes (tailings and waste rock) through heap leaching, which could also mitigate environmental contamination. Combining this approach with environmental remediation of any residual mine waste, such as with multilayer vegetated soil covers [including a geosynthetic clay liner (GCL)], could achieve long-term mitigation of the impacts of abandoned mines. However, potential pollution from heap leaching should also be addressed.

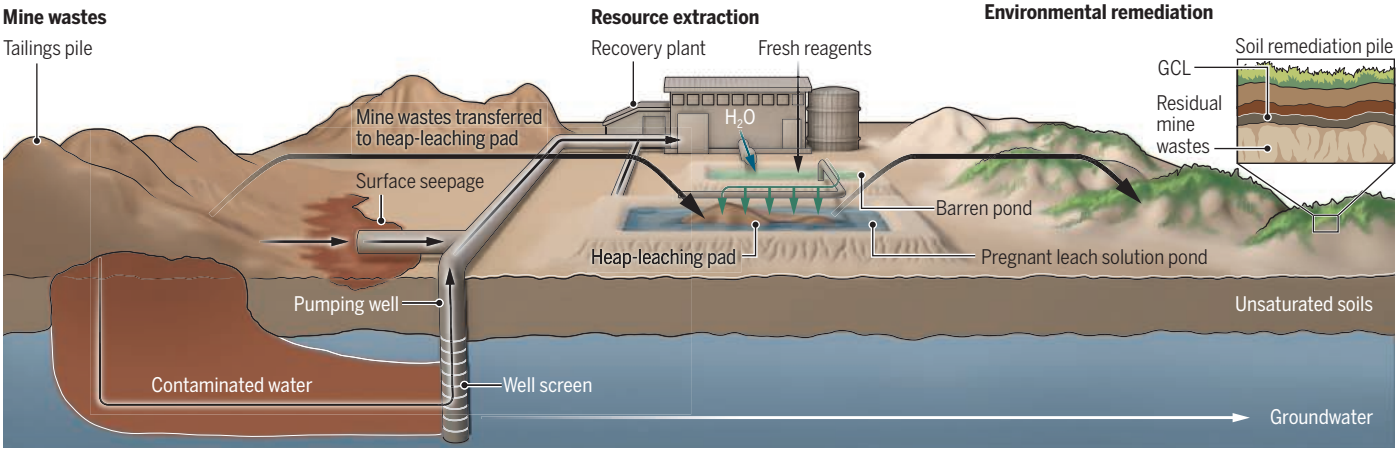

sess the spatial distribution, bioavailability, and migration pathways of contaminants. Many national inventories of abandoned mines with different risk categories and national registries have been established. For example, national mine-waste registries in France, Hungary, Italy, Portugal, Slovenia, Spain, and the UK were created with basic information that can be used for evaluating potential resource recovery (*11*). Resource potentials of other critical minerals and metals (particularly REEs) in mine wastes should be jointly assessed in conjunction with site-specific characterization and monitoring programs to enhance knowledge of the behavior of critical minerals and metals as well as their geochemical interactions. These efforts will complement the knowledge gap in national mine-waste registries and facilitate decision-making to shift abandoned mines from a source of pollution to a resource for mineral recovery.

Advances in exploration and recovery techniques of critical minerals and metals from different waste streams are promising. In Europe, underwater robots, although still at the prototype stage, were successfully demonstrated for exploration of critical minerals and metals at flooded abandoned mines without dewatering costs and groundwater impacts (*12*). Traditional AMD treatment through neutralization using lime or limestone generates large quantities of sludges that are rich in iron oxyhydroxides, REEs, and other valuable minerals. High-grade aluminum, REEs, cobalt, and manganese were recovered from sludges during AMD treatment using neutralization reagents through a three-staged, pH-dependent precipitation and crystallization process (*13*).

Heap leaching is a method for economical recovery from low-grade ores for the extraction of, for example, copper, gold, and uranium (*14*). This method requires the application of leaching solutions (such as sodium cyanide for gold) through ore-bearing heap pads. Leaching solutions dissolve targeted minerals and metals into pregnant leach solution ponds and are subsequently recovered; the barren solutions can then be mixed with fresh reagents and recirculated into the heap-leaching pads. Given that mine wastes might have higher amounts of critical minerals and metals compared with the low-grade ores that are currently mined, heap leaching could function as a feasible technique for resource recovery at abandoned mines (*10*, *15*). A combination of resource recovery through heap leaching with implementation of environmental remediation (e.g., a multilayer vegetated soil cover) may serve as a potentially sustainable solution for mine-waste management and pollution control (see the figure).

Caution is needed to prevent the introduction of new environmental pollution and harm during resource recovery from mine wastes. For instance, a drainage protection layer should be implemented to prevent the infiltration of leach solutions into underlying soils and groundwater to avoid the long-term retention of hazardous materials in the subsurface. Residual solid wastes after heap leaching need further characterization for proper disposal through environmental remediation. Notably, industrial applications of heap leaching are mostly used for the recovery of copper, gold, and uranium from low-grade ores, whereas heap leaching for resource recovery from mine wastes is still under development. Further research is needed to evaluate the potential impacts of the commercialization of these exploration and recovery techniques through thorough monitoring and evaluation programs in laboratory-, pilot-, and industrial-scale applications and to make the extraction of critical minerals and metals from these waste streams environmentally friendly, socially acceptable, and economically feasible. ■

REFERENCES AND NOTES

1. K. Hund *et al.*, *Minerals for Climate Action: The Mineral Intensity of the Clean Energy Transition* (World Bank Group, 2020).
2. R. K. Valenta *et al.*, *Resour. Conserv. Recycl.* **190**, 106859 (2023).
3. L. Tang, T. T. Werner, *Commun. Earth Environ.* **4**, 134 (2023).
4. K. Hudson-Edwards, *Science* **352**, 288 (2016).
5. D. K. Nordstrom, C. N. Alpers, *Proc. Natl. Acad. Sci. U.S.A.* **96**, 3455 (1999).
6. C. J. Sergeant *et al.*, *Sci. Adv.* **8**, eabn0929 (2022).
7. World Mine Tailings Failures—From 1915; https://world-minetailingsfailures.org.
8. The International Network for Acid Prevention, Global Acid Rock Drainage Guide (2009); http://gardguide.com/index.php?title=Main_Page.
9. K. B. Pedersen *et al.*, *Mar. Pollut. Bull.* **184**, 114197 (2022).
10. B. Dold, *J. Geochem. Explor.* **219**, 106638 (2020).
11. G. Žibret *et al.*, *Minerals* **10**, 446 (2020).
12. R. A. Suarez Fernandez *et al.*, *IEEE Access* **7**, 99782 (2019).
13. B. V. Hassas, Y. Shekarian, M. Rezaee, *Resour. Conserv. Recycl.* **188**, 106654 (2023).
14. Y. Ghorbani, J.-P. Franzidis, J. Petersen, *Miner. Process. Extr. Metall. Rev.* **37**, 73 (2016).
15. T. Thenepalli, R. Chilakala, L. Habte, L. Q. Tuan, C. S. Kim, *Sustainability* **11**, 3347 (2019).

ACKNOWLEDGMENTS

This work was supported by the Natural Sciences and Engineering Research Council of Canada TERRE-NET program (NETGP 479708-15) and Crown-Indigenous Relations and Northern Affairs Canada. We thank M. Logsdon, R. Borden, and two reviewers for insightful comments. D.W.B. has participated in consulting activities for Rio Tinto and BHP focused on mine-waste management.

10.1126/science.abn5962

GRAPHIC: A. FISHER/*SCIENCE*

CELL BIOLOGY

What is a cell type?

A next step for cell atlases should be to chart perturbations in human model systems

By **Jonas Simon Fleck[1], J. Gray Camp[1], Barbara Treutlein[2]**

International efforts are underway to provide a comprehensive survey of cells across the human life span (*1*, *2*). These efforts assign cell "types" on the basis of a set of information-rich molecular features (the cell phenotype), which include portions of the transcriptome, epigenome, and proteome, as well as the developmental lineage (*3*, *4*). These features can be quantified in single cells in suspension after tissue dissociation or within intact tissue. The resulting cell atlases provide insight into the organization, ontogeny, and evolution of human tissues. They also help to explore disease susceptibilities, navigate therapy development, and benchmark cell and tissue engineering. However, the atlas data can often identify phenotypic diversity (referred to as different cell states) among cells of the same type, raising the following question: What is a human cell type?

One view is that a cell type or state not only involves the developmental history of the cell and its current set of molecular features but is also linked to how the cell would respond to an environmental change or other perturbation. A perturbation is any input that alters the phenotype of a cell. They can be naturally occurring or experimental and include genetic change; chemical, physical, or electrical stimulus; and pathogen infection. The complexity of perturbation-induced changes can vary substantially: Certain genetic loss-of-function mutations affect a single pathway, and others can alter many cellular processes. Emerging experimental and computational techniques could enable the systematic profiling of perturbation-induced phenotypic changes at large scale, ideally with spatial resolution. This would enable human cell phenoscapes—the landscape of all possible cell phenotypes—to be charted. The totality of phenotypes under all possible perturbations describes a local phenoscape for each individual cell type.

[1]Institute of Human Biology (IHB), Roche Pharma Research and Early Development, Roche Innovation Center, Basel, Switzerland. [2]Department of Biosystems Science and Engineering, ETH Zürich, Basel, Switzerland.
Email: barbara.treutlein@bsse.ethz.ch

Existing cell atlases describe current features, and sometimes the developmental history, of a cell but cannot provide information on the factors that dictate development or predict future cell states. In addition, how to transform cells from one state to another and how to generate a defined cell state in vitro are still not known. Although in silico perturbation methods have been proposed (*5*), they are, at present, difficult to validate systematically because experimental data are scarce. If it became possible to predict the response of a cell from its current state, the existing cell atlases would be a rich resource for in silico screening.

Some perturbations alter a cell's molecular state in a reversible manner: The cell responds to the stimulus by transitioning from a stable state to a new, unstable state and returns once the stimulus is removed. Examples of such perturbations include transient exposure to signaling inhibitors or targeted repression of a gene's expression. By contrast, some perturbations can irreversibly change the type of the cell by inducing a new stable state. Examples include cell states that are engineered through transcription factor conversion of one cell type (e.g., fibroblast or pluripotent stem cell) into another (e.g., neuron) or created through the acquisition of genetic changes that convert from a normal to a cancerous cell type. In such cases, the new cell state is maintained after the original perturbation occurs. Rather than changing the current state of the cell, certain perturbations can alter future cell development. For example, genetic or epigenetic changes can influence cell differentiation paths in later ontogenetic stages and lead to enrichment or depletion in different developmental lineages (*6*, *7*). The effects of this type of perturbation are highly dependent on the developmental stage in which it is induced. These perturbations can be viewed as altering or eroding the developmental landscape such that certain terminal states are excluded, whereas others may become accessible.

Reference atlases of healthy and diseased autopsy or biopsy tissues from individuals with different genetic backgrounds will be vital to elucidate parts of the phenoscape by cataloging naturally occurring base states and perturbations thereof (see the figure). However, the availability and diversity of such tissues is limited, and associations between perturbation and cell phenotype are usually correlative. Furthermore, the number of possible perturbations is vast.

To address these limitations, perturbations need to be induced and cell responses characterized under controlled experimental conditions in high throughput, which requires the use of in vitro model systems. However, studying the effects of perturbations at scale has trade-offs: Single-cell sequencing of massive cell numbers in sufficient detail can be extremely expensive, and delivering many perturbations in parallel can be difficult to achieve. Proposed computational strategies suggest that the full state of a modality (e.g., the transcriptome or the epigenome) can be reconstructed using relatively few measurements (*8*). In addition, industrial engineering and automation solutions are on the horizon to improve throughput and lower costs. There are also genetic (*9*) and chemical toolkits available that make it increasingly feasible to induce and characterize many different perturbations in high-throughput screens. Testing the effects of a large number of perturbations requires sampling many cells to retain statistical power. Such high-throughput sampling might be achieved through combinatorial barcoding of dissociated cells or image-based in situ readouts (*3*, *10*).

At present, high-throughput induction of perturbations can be used to elucidate the effects of drugs on cell phenotypes in relatively simple two-dimensional (2D) monocultures (*11*). However, human physiology is complex, and tissues are composed of many different cell types and states that dynamically interact. Probing the effects of genetic and chemical perturbations on a single cell type in isolation has limited predictive value. Context matters, and perturbation response is dependent on the particular combination of cell states that is present in any multicellular system. Therefore, perturbations to a given cell state should ideally be studied within its tissue microenvironment.

Human 3D cell-culture model systems (such as organoids) can recapitulate some cell states and microenvironmental interactions that are observed in their primary tissue counterparts. Protocols have been developed to generate human stem cell–derived tissues that recapitulate various physiological features of many different organ systems (*12*). For example, brain organoids mirror progenitor and neuronal cell states and show similar cytoarchitecture, enabling the study of neurogenesis

in multiple brain regions (*13*). Intestinal organoids contain stem, absorptive, and secretory cell types (*12*). Because organoids can be grown under controlled and scalable culture conditions, they can be subjected to diverse perturbations and their response can be profiled using high-information content methods. Nevertheless, all human model systems are limited in their capacity to recapitulate the full complexity of human organs and interorgan interactions. In particular, most organoid systems are derived from a single germ layer and therefore often lack important tissue-supporting cell types, such as vasculature or immune compartments. Further optimization of organoid systems is expected to enhance their predictive value.

Another limitation of existing cell atlases is that cell-type annotations mostly rely on single-cell transcriptional or epigenomic profiles. New methods are emerging that provide information on the proteome, metabolome, lipidome, and other molecular features of individual cells from dissociated tissue and in situ. This enhanced characterization, along with computational approaches to integrate the data, will provide more nuanced distinctions of cell types and states. Clarifying what functionally constitutes a cell type might also be aided by the proposed perturbation atlases. Perturbing one set of cellular features (e.g., chromatin organization) and profiling another (e.g., proteome) can help establish causal links between different features and illuminate how their interaction shapes complex emergent phenotypes. Consequently, the perturbation landscape could help distinguish cells based on function rather than observed features, which might ultimately contribute to a more holistic notion of cell type.

Unlike tissue atlases that catalog a finite set of cell states, phenoscape atlases could cover an arguably infinite set of possible single and combinatorial perturbations. It is unclear under what conditions such an atlas can ever be considered "complete," making it crucial to learn to extrapolate from observed perturbations to unseen data. It might be that each cell type has a finite set of adjacent states that are possible to reach or that different perturbations lead to convergent effects across cell types. Such redundancy can be revealed by mapping phenoscapes across cell types and tissues, and it can be leveraged by training machine- and deep-learning models to yield a compressed representation of perturbation effects. A number of models have already been developed to learn links between perturbations and transcriptomic changes from training data and to predict responses of unseen cell states, new combinations of tested perturbations, or even unseen perturbations (*14*). In addition to predictive power, it is also a goal to make models interpretable and to identify which aspects of the inputted data enabled the predictions, with the aim of gaining mechanistic insight or identifying drug targets. However, the accuracy of predictions and the ability of these models to extrapolate to unseen contexts is highly dependent on the quality, quantity, and diversity of training data. As a consequence, development and evaluation of such models will greatly benefit from large, systematically collected datasets on the effects of perturbation in different types of human multicellular model systems.

Ultimately, predictive modeling of perturbations may provide a way to establish when this seemingly boundless phenoscape has been sufficiently charted. With appropriate models, an expanding phenoscape atlas will lead to reduced uncertainty and enhanced accuracy for predictions of the effects of unseen perturbations. Therefore, "completeness," at least within a specific context, would be approached if the effects of unseen perturbations can be accurately predicted and gathering further data results in marginal improvements in prediction accuracy. Model uncertainty can then serve as a valuable compass for informing future study designs, with the aim of systematically mapping unexplored regions of the phenoscape. ■

Charting cell phenoscapes

Single cells in primary-tissue samples can be analyzed using multimodal phenotyping methods to provide information on the effect of perturbations on cell features. Complex three-dimensional human cell-culture models recapitulate aspects of human physiology and are amenable to high-throughput perturbation experiments followed by multimodal phenotyping. The totality of the human-cell phenotypic landscape ("phenoscape") can be simplified and visualized as a topological and spherical map, where the totipotent cells at the core differentiate toward the surface topology.

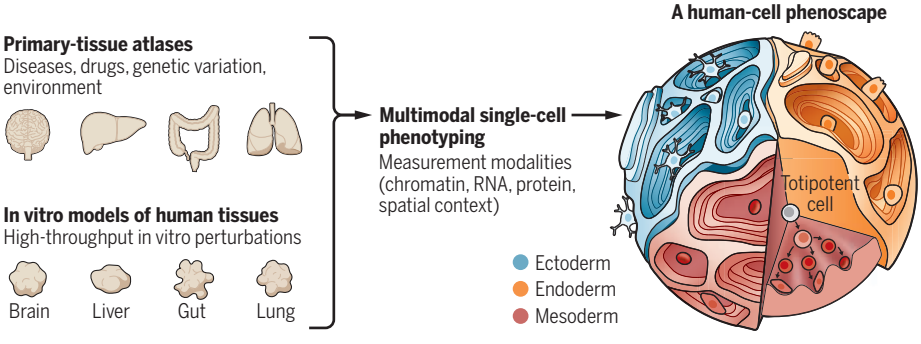

Perturbation types
Differentiated cells in an organoid or tissue are subject to a variety of state transitions if a particular perturbation overcomes a barrier or set of barriers.

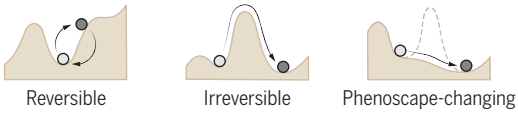

Learning phenoscapes
Predictive modeling of this phenoscape can facilitate extrapolation to unseen perturbation responses and help to propose new cell states, new treatments or treatment combinations, and strategies to engineer specific states.

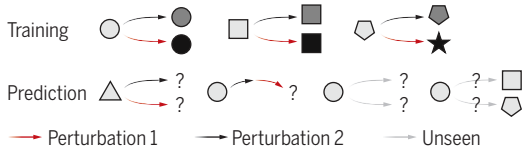

REFERENCES AND NOTES

1. M. Haniffa *et al.*, *Nature* **597**, 196 (2021).
2. A. Regev *et al.*, *eLife* **6**, e27041 (2017).
3. K. Vandereyken *et al.*, *Nat. Rev. Genet.* **24**, 494 (2023).
4. L. Heumos *et al.*, *Nat. Rev. Genet.* **24**, 550 (2023).
5. C. V. Theodoris *et al.*, *Nature* **618**, 616 (2023).
6. J. S. Fleck *et al.*, *Nature* 10.1038/s41586-022-05279-8 (2022).
7. B. Pijuan-Sala *et al.*, *Nature* **566**, 490 (2019).
8. B. Cleary *et al.*, *Cell* **171**, 1424 (2017).
9. J. G. Camp *et al.*, *Science* **365**, 1401 (2019).
10. S. R. Srivatsan *et al.*, *Science* **367**, 45 (2020).
11. J. M. Replogle *et al.*, *Cell* **185**, 2559 (2022).
12. M. Hofer, M. P. Lutolf, *Nat. Rev. Mater.* **6**, 402 (2021).
13. I. Chiaradia, M. A. Lancaster, *Nat. Neurosci.* **23**, 1496 (2020).
14. Y. Ji *et al.*, *Cell Syst.* **12**, 522 (2021).

ACKNOWLEDGMENTS

We thank the Treutlein and Camp laboratories, as well as the laboratory of F. Theis, for helpful discussions and M. Lee for support with the figure. J.G.C. and B.T. are supported by CZF2021-237566 from the Chan Zuckerberg Initiative donor-advised fund (DAF), an advised fund of the Silicon Valley Community Foundation. J.G.C. is supported by the European Research Council (Anthropoid-803441). B.T. is supported by the European Research Council (Organomics-758877), the Swiss National Science Foundation (project grants 310030_192604 and 310030_84795), and the National Center of Competence in Research Molecular Systems Engineering.

10.1126/science.adf6162

GRAPHIC: K. HOLOSKI/*SCIENCE* BASED ON MELANIE LEE

POLICY FORUM

ENVIRONMENTAL POLICY

Create a culture of experiments in environmental programs

Organizations need a better "learning by doing" approach

By **Paul J. Ferraro[1,2], Todd L. Cherry[3], Jason F. Shogren[3], Christian A. Vossler[4], Timothy N. Cason[5], Hilary Byerly Flint[6], Jacob P. Hochard[6], Olof Johansson-Stenman[7], Peter Martinsson[8], James J. Murphy[9], Stephen C. Newbold[3], Linda Thunström[3], Daan van Soest[10], Klaas van 't Veld[3], Astrid Dannenberg[11], George F. Loewenstein[12], Leaf van Boven[13]**

An understanding of cause and effect is central to the design of effective environmental policies and programs. But environmental scientists and practitioners typically rely on field experience, case studies, and retrospective evaluations of programs that were not designed to generate evidence about cause and effect. Using such methods can lead to ineffective or even counterproductive programs. To help strengthen inferences about cause and effect, environmental organizations could rely more on formal experimentation within their programs, which would leverage the power of science while maintaining a "learning by doing" approach. Although formal experimentation is a cornerstone of science and is increasingly embedded in nonenvironmental social programs, it is virtually absent in environmental programs. We highlight key obstacles to such experimentation and suggest opportunities to overcome them.

By "formal experimentation," we mean the deliberate creation of spatial or temporal variation in program implementation with the intent of quantifying impacts and elucidating mechanisms. For example, consider an environmental agency that wants to learn how best to encourage polluters to comply with environmental regulations. Instead of implementing a single change in auditing practices across all polluting facilities, the agency could randomly vary implementation of two auditing practices and contrast how facilities respond (see the figure) [for an analogous real-world example, see (*1*)]. By creating deliberate variation in how programs are implemented, program administrators can more easily learn about the features that make programs effective. Although experimentation in natural resource management has a long history, including in the context of adaptive management, we focus on embedding experiments in the implementation of policies or programs that affect human behavior. For example, in a not-atypical type of environmental policy experiment that tests whether thinning a reforested plot leads to more harvestable timber, human behavior is controlled by the experimentalist, whereas in a much less common type of experiment that tests alternative design features of a program that encourages more reforestation behavior, human behavior is endogenous and uncertain.

Despite the benefits of adding experimental variation to program implementation, as demonstrated in nonenvironmental contexts such as health and education, environmental organizations rarely do so. Consider two US federal agencies with substantial environmental program portfolios: the US Environmental Protection Agency (USEPA) and the US Department of Agriculture (USDA). In the past 30 years, each has embedded formal experimentation in their environmental programs fewer than a half dozen times. In Europe, we know of only a single example of formal experimentation embedded within government-implemented environmental programs (*2*). Formal experimentation is similarly almost nonexistent among nongovernmental and multilateral environmental organizations. Although environmental actors engage in thousands of informal "experiments" every year (such as pilot programs), these are designed to test the implicit hypotheses that justify the implementation of current programs or understand how to make these programs more effective.

Formal experimentation in environmental programs is absent because science typically stops when implementation starts. Over the past five decades, governmental and nongovernmental actors have invested substantial resources to understand the status and trends of myriad environmental indicators. These investments have been motivated by scientific uncertainty about how complex environmental systems function and by a recognition that reducing this uncertainty is critical to designing effective programs.

Yet uncertainty also plagues program efficacy. The coupled natural-human systems in which environmental programs are implemented are complex, and our understanding of how programs influence the trajectory of these systems is incomplete. When new program designs in nonenvironmental contexts are assessed through formal experimentation, proponents often learn that the innovations fail to have the intended effects (*3*). Scientists and practitioners should not expect innovations in environmental programs to be any different.

The absence of experimentation within environmental programs can be explained in part by historical reasons. Compared with other social policy fields such as health, poverty, and education, the environmental policy field is much younger and would be expected to be a late adopter of innovative ways of generating evidence. Moreover, the human benefits from effective environmental programs are less salient than in other social policy fields. The foregone benefits from ineffective programs are also less salient, putting less pressure on program staff to show effectiveness. Last, environmental practice is dominated by lawyers, engineers, and natural and physical scientists who—unlike health, behavioral, and social scientists—do not typically use experimental designs in real-world contexts and may not anticipate complex human responses to what seem like straightforward policy and program decisions. Yet there are no structural barriers to experimentation in the environmental field.

CONCERNS ABOUT EXPERIMENTATION

Four primary concerns about embedding formal experimentation into environmen-

[1]Department of Environmental Health and Engineering, Johns Hopkins University, Baltimore, MD, USA. [2]Carey Business School, Johns Hopkins University, Baltimore, MD, USA. [3]Department of Economics, University of Wyoming, Laramie, WY, USA. [4]Department of Economics, University of Tennessee, Knoxville, TN, USA. [5]Department of Economics, Purdue University, West Lafayette, IN, USA. [6]Haub School of Environment and Natural Resources, University of Wyoming, Laramie, WY, USA. [7]Department of Economics, University of Gothenburg, Gothenburg, Sweden. [8]Department of Technology, Management and Economics, Technical University of Denmark, Kongens Lyngby, Denmark. [9]Department of Economics, University of Alaska-Anchorage, Anchorage, AK, USA. [10]Department of Economics, Tilburg University, Tilburg, Netherlands. [11]Institute of Economics, University of Kassel, Kassel, Germany. [12]Department of Social and Decision Sciences, Carnegie Mellon University, Pittsburgh, PA, USA. [13]Department of Psychology and Neuroscience, University of Colorado, Boulder, CO, USA. Email: pferraro@jhu.edu

tal programs need to be addressed: delayed action, feedback lags, structural barriers, and ethical questions.

First, identifying ways to create experimental variation and measure outcomes can delay scaled-up implementation, letting environmental damages accumulate. Yet for the case of ineffective programs, the accumulated damages could be much larger when program managers rely on retrospective evaluations that use nonexperimental, postimplementation data. The costs of delays from experimentation will depend on how effectively the program meets its objectives and how quickly damages accumulate. In some cases, large-scale action may be required without waiting for experimentation (akin to "emergency authorizations" in medicine). Yet we believe that in many cases, experimentation embedded in program implementation will improve outcomes in the long run, even at the cost of some delay in the short run. Similar arguments have been made in the recent COVID-19 pandemic, in which calls for quick action and for rigorous evidence seemed to be in opposition (*4*).

Second, the full effects of a program may not materialize for many years (for example, long-run climate impacts), and the evidence may no longer be useful by the time it is available. Yet for many environmental problems, the culprit is human behavior, for which the desired changes can be measured on shorter timescales (for example, changes in energy consumption by households or fertilizer use by farmers). Measures of short-term environmental indicators along the hypothesized causal path may also help elucidate whether the intervention is working as intended (for example, measure pollutants that change relatively rapidly rather than health conditions that change more slowly).

Third, structural constraints, such as legal and regulatory rules, may present barriers to experimentation. The degree to which such barriers exist, however, is difficult to ascertain given that there has been so little historical effort allocated to experimentation.

A fourth concern may seem on the surface to be the most problematic: Opponents of experimentation question the ethics of treating some people (or nonhuman organisms or ecological communities) differently than others (*5*). This concern arises from a presumption that those exposed to a program, or a specific version of it, are sure to benefit from it. That assumption, however, is not necessarily true. The effects of many environmental programs are uncertain.

One could argue that environmental organizations have an ethical obligation to better understand the effects of untested programs, or changes in programs, before large groups of humans and other species, particularly vulnerable subgroups, are exposed to them (akin to the principle of "equipoise," a state of genuine uncertainty about the comparative merits of different approaches, which is the ethical basis for justifying randomized treatments in medical trials). Even programs that do not directly harm the environment or people may simply be ineffective. Directing resources to ineffective interventions has substantial ethical implications, especially for environmental problems that are time sensitive, such as the loss of biological diversity and the accumulation of persistent pollutants.

If environmental organizations were guided by an ethical precept that required evidence before changing or scaling up a program, the science and practice of environmental protection would look different and be more successful. Environmental programs would routinely be subjected to experimentation that deliberately manipulates the temporal and spatial variability of implementation. Program managers, perhaps in collaboration with academics, would then evaluate the results to better understand the consequences, intended and unintended, of the variations in implementation. This evidence would provide opportunities to adjust and improve current and future programs (*6*, *7*). This cycle of program innovation, experimentation, learning, and adaptation is a hallmark of evidence-based programs in other fields.

A culture of experimentation within environmental programs

To reduce pollution, regulators can increase on-site inspections, or they can increase opportunities for facilities to do self audits, with some penalty leniency when violations are self reported. Self audits may be less effective at reducing pollution (measured remotely) than on-site inspections because self audits allow facilities to hide their noncompliance. Yet self audits may be more effective because they make facilities more aware about the law and its relationship to their operations and because they transform errors of omission into errors of commission.

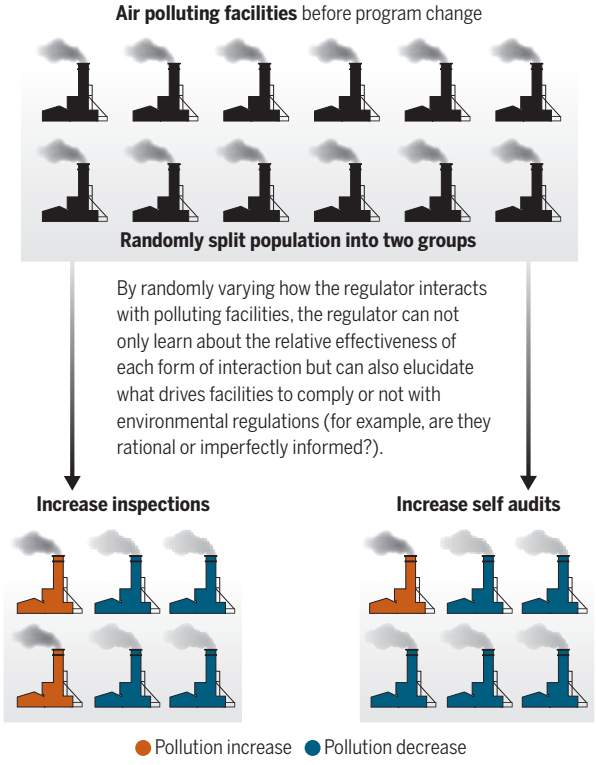
Air polluting facilities before program change
Randomly split population into two groups
By randomly varying how the regulator interacts with polluting facilities, the regulator can not only learn about the relative effectiveness of each form of interaction but can also elucidate what drives facilities to comply or not with environmental regulations (for example, are they rational or imperfectly informed?).
Increase inspections
Increase self audits
Pollution increase
Pollution decrease

ENCOURAGING EXPERIMENTATION

Although the constraints on engaging in experimentation will vary by organization, the opportunities for experimentation have some commonalities. On the basis of experiences in other social policy fields, we offer four recommendations for expanding the opportunities for experimentation in environmental programs [for others, see (*8*, *9*)].

Political and legal simplicity

Running an experiment that contrasts an entire program to a no-program control may require extensive legal and political approvals, as well as expose implementers to reputational risks and coordination costs. Instead, one version of program implementation can be compared with another version by manipulating program attributes for which managers already have the authority to change (often called "A/B testing" in the private sector). For example, program managers could contrast the effects on pollution compliance from on-site inspections (status quo) versus remote inspections. Leveraging already-planned pilot programs can also be a practical way to facilitate learning when the pilot's implementation is varied across space or time in ways unrelated to the program's target outcomes.

Financial simplicity

Given that the additional costs of experimentation largely come from the costs of measuring outcomes, organizations can focus on contexts in which the outcomes are collected as part of program operations (such as pollution discharges) or are publicly available (such as satellite data of land use).

GRAPHIC: N. CARY/*SCIENCE*

Learning focused

To achieve higher returns on investment, organizations should focus on experimentation that yields results that can be generalized across multiple programs. Generalizability is more plausible when the program features being manipulated are found in many programs (such as capacity building and incentives) or motivated by similar theories of change.

Partnership enhanced

A quick, inexpensive way for environmental organizations to acquire the technical capacity to design and analyze experiments, while keeping the operations in-house, is to embed trained experimentalists from outside the organization (for example, through federal Volunteer Service Agreements in the US context).

Strengthening the culture of experimentation in the environmental community will require changes in norms and incentives. Program managers are often not rewarded for evidence about program effectiveness but rather for achieving other objectives (such as moving money to constituents, avoiding litigation by private actors, or pleasing funders). Nevertheless, changes in norms and incentives are occurring. One recent example of change is the creation of "behavioral insights teams" in governmental and multilateral organizations. These teams help program managers to formally experiment with program changes inspired by insights from the behavioral sciences (*10*).

For federal agencies in the United States, changes in norms and incentives are also occurring through the Foundations for Evidence-Based Policymaking Act of 2018 (Evidence Act). The Evidence Act and complementary memoranda from the executive branch encourage a culture of experimentation both directly and indirectly. They encourage experimentation directly by emphasizing the power and political acceptability of randomized implementation designs (*11*–*14*). They encourage experimentation indirectly by requiring agencies to create annual learning agendas and a strategy and budget to meet their agenda objectives. Learning agendas comprise a set of questions that, when answered, are expected to have the biggest impact on an agency's performance. Yet the Evidence Act and its associated guidance do not provide explicit rewards to staff for posing substantive learning questions and using experimentation to generate high-quality answers to these questions. Thus, by itself, the Evidence Act may be insufficient to create a meaningful culture of experimentation within environmental agencies.

One way to further foster a culture of experimentation and embed learning in daily operations among US federal agencies would be through a new executive order (EO) similar in spirit to EO 12291 for Cost-Benefit Analyses. This new EO would be triggered if a new environmental program, or change in a current program, were to exceed a size threshold, which could be measured by program funding or the size of the affected population. The EO would require the implementing agency to first ascertain the equipoise of the proposed program or change in program: Is there strong empirical evidence that the proposed action is the best option? If not, then the agency would be required to embed experimentation into the program with the intent of quantifying environmental and social impacts and understanding the mechanisms through which those impacts arise. The EO would require that agencies insert a step between proposing a programmatic change and scaling that programmatic change up to the entire eligible population. The EO would also encourage environmental agency staff to involve statisticians and behavioral scientists before implementation. Currently, if these experts are called on at all, it is after implementation to assess what may have transpired—a challenging task when implementation was not designed to generate evidence about impacts and mechanisms. In addition to characterizing what type of experimentation is acceptable, the EO would also have a stopping rule, similar in spirit to stopping rules used to decide when to end medical treatment trials. Likewise, the EO would also define when it may be acceptable to forego experimentation.

Four conditions when experimentation pays off

Pre-Change Ambiguity
When theory and experience alone cannot unambiguously predict the expected impacts of changes in program implementation

Post-Change Ambiguity
When estimating counterfactual outcomes in the absence of a change in program implementation is challenging using traditional approaches

High Implementation Cost
When a change in program implementation is unlikely to pass a benefit-cost test, or cost-effectiveness assessment, without medium or large impacts

Generalizability of Results
When the lessons learned from experimentation are generalizable beyond the context in which the program change was implemented

Scientists and practitioners can legitimately argue about the benefits and opportunity costs of allocating scarce time and financial resources to formal experimentation in the environmental sector. Should half of environmental programs include experimentation? Is 10% the right amount? Although the optimal share is debatable, we believe that the current allocation of roughly 0% is suboptimal. How much experimentation is embedded in programs should depend on contextual attributes that make experimentation most valuable (see the box).

We recognize that experimentation is not the only way that a scientific lens can be applied to improve our understanding of program implementation. Experimentation is best viewed as part of a mixed-methods approach to generating evidence rather than as a substitute for more traditional ways of gathering evidence. Experimentation should, however, be a regular feature of programs, not a rarity. ■

REFERENCES AND NOTES

1. D. I. Levine, M. W. Toffel, M. S. Johnson, *Science* **336**, 907 (2012).
2. K. Telle, *J. Public Econ.* **99**, 24 (2013).
3. A. Ventures, *Straight Talk on Evidence*, (13 April 2018); https://www.straighttalkonevidence.org/2018/04/13/how-to-solve-u-s-social-problems-when-most-rigorous-program-evaluations-find-disappointing-effects-part-two-a-proposed-solution.
4. A. J. London, J. Kimmelman, *Science* **368**, 476 (2020).
5. E. L. Pynegar, J. M. Gibbons, N. M. Asquith, J. P. G. Jones, *Oryx* **55**, 235 (2019).
6. Moving to Opportunity (MTO) for Fair Housing Demonstration Program, https://www2.nber.org/mtopublic/.
7. R. H. Brook *et al.*, "The Health Insurance Experiment: A classic RAND study speaks to the current health care reform debate" (RAND Corporation, 2006).
8. J. Fox, *Evidence Matters*, 29 May 2019; https://www.3ieimpact.org/blogs/how-can-rethink-lessons-field-experiments-inform-future-research-transparency-participation.
9. E. Duflo, *Am. Econ. Rev.* **107**, 1 (2017).
10. S. Wendel, *Behavioral Scientist*, (5 October 2020); https://behavioralscientist.org/who-is-doing-applied-behavioral-science-results-from-a-global-survey-of-behavioral-teams.
11. https://www.whitehouse.gov/omb/information-for-agencies/evidence-and-evaluation/.
12. https://www.whitehouse.gov/briefing-room/presidential-actions/2021/01/27/memorandum-on-restoring-trust-in-government-through-scientific-integrity-and-evidence-based-policymaking.
13. https://www.whitehouse.gov/wp-content/uploads/2021/06/M-21-27.pdf.
14. Appendix A of OMB M-19-23 describes four broad types of evidence that agencies should use as they implement the Evidence Act: foundational fact finding, policy analysis, program evaluation, and performance measurement. This guidance goes a step further to specify the broad range of methodological approaches that agencies should consider. These approaches include, but are not limited to, "pilot projects, randomized controlled trials, quantitative survey research and statistical analysis, qualitative research, ethnography, research based on data linkages in which records from two or more datasets that refer to the same entity are joined, well-established processes for community engagement and inclusion in research, and other approaches that may be informed by the social and behavioral sciences and data science."

10.1126/science.adf7774

BOOKS *et al.*

In this October 2014 meeting, President Obama expressed support for a proposal to enroll a million Americans in a nationwide genomics research cohort.

PHOTO: PETE SOUZA/THE WHITE HOUSE

MEDICINE

Public health versus personalized medicine

Environmental health research is being undermined by genomic medicine, argues a philosopher

By **Henry T. Greely**

The 20th-century journalist H. L. Mencken wrote "there is always a well-known solution to every human problem—neat, plausible, and wrong." In his new book, *Tyranny of the Gene: Personalized Medicine and Its Threat to Public Health*, philosopher James Tabery points to "personalized medicine" (by which he seems to mean genomic medicine) as an example. "My thesis," he writes, "is that there have been and remain powerful financial, political, technological, and scientific forces that are driving this embrace of personalized medicine and promoting the idea of medicine as something genetic while simultaneously impeding the study of environmental determinants of wellness and disease." Tabery supports this argument with nine chapters of lively history, each interweaving tales of environmental and genomic medicine.

The first chapter opens in 1957 with Rachel Carson and the rise of environmental health concerns. That same year, pioneering medical geneticist Arno Motulsky published a paper about how individuals' drug responses vary according to their genes. Tabery explores the tensions between these approaches to human health and the two projects they engendered: a long-term research program named the National Children's Study (NCS), which sought to determine the effects of environmental factors on child health and development, and a plan for a massive genomic database to focus on genomic health determinants.

How the George W. Bush administration treated these efforts—discouraging the first, encouraging the second, but implementing neither—dominates the book's middle chapters. Interspersed are fascinating asides on the sequencing giant Illumina's history (it began as an effort to make an artificial nose); about low-tech successes in combating sudden infant death syndrome; and about the imperialistic forays of genomics into archaeology and educational policy.

The book also brings to life two crucial players: Duane Alexander, director of the National Institute of Child Health and Human Development from 1986 to 2009, and Francis Collins, director of the National Center for Human Genome Research (renamed the National Human Genome Research Institute) from 1993 to 2008 and of the entire National Institutes of Health (NIH) from 2009 to 2021. Alexander was the main NIH supporter of the NCS, whereas Collins was the force behind the genomic database. Tabery's presentation of Collins—who could have been the book's villain—is nuanced, if not altogether admiring.

The book then moves to the Obama administration, which ended the debate by canceling the NCS and funding the genomic database. That database, now named "All of Us," is nearly halfway to its goal of collecting health and genomic data on 1 million Americans.

After a chapter on racial and ethnic disparities in genomic medicine, the book ends with a chapter decrying what Tabery calls "the Gleevec scenario." Gleevec, introduced in 2001, is an effective drug against chronic myelogenous leukemia. Some heralded it as a harbinger of a precision medicine future. But Tabery says "it ushered in a new era of drugs that don't work for most patients and are so exorbitantly priced that they risk bankrupting some of those who are biologically eligible."

Tabery is clearly right that genomic medicine has overpromised and that environmental medicine has been underpursued. His analysis of the systemic reasons for the disparity—from commercial interests, to cheap genomic tools, to media and public excitement about genes—seems likely right. So does his disgust at narrowly targeted, overpriced treatments protected by patent games.

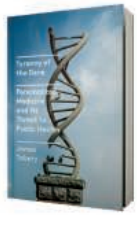

Tyranny of the Gene
James Tabery
Knopf, 2023. 336 pp.

And yet is personalized genomic medicine a threat to public health, as the book's subtitle proclaims? It has helped some people, if only a tiny fraction of those in need. Its progress continues, albeit slowly, now even in sickle cell anemia—a prime example of racial disparities in personalized medicine. And while environmental public health efforts deserve more support, they have their own problems. As Tabery shows, the feasibility of the NCS was unclear when it was killed in 2014. Growing distrust of science will not have made it easier. Finally, although steep drug prices are a huge problem, they afflict many, but not all, interventions, both personalized and not.

Genomic personalized medicine has its merits, but it has not been the panacea its advocates projected. It probably never will be. Tabery's excellent book argues powerfully for a more balanced approach to human health research. ■

The reviewer is at the Center for Law and the Biosciences, Stanford University, Stanford, CA 94305, USA.
Email: hgreely@stanford.edu

10.1126/science.adj0281

Check for updates

SCIENCE AND SOCIETY

Battling information bias

Do not wait for society to reject scientific disinformation, tout the truth now

By **Jonathan Wai**

On Disinformation: How to Fight for Truth and Protect Democracy
Lee McIntyre
MIT Press, 2023. 184 pp.

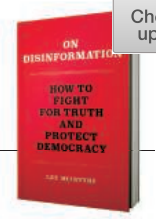

Most scientists have an enduring belief that even if scientific truth is not embraced in the short term, it will be eventually. Lee McIntyre's new manifesto, *On Disinformation*, packaged—like Mao's—in a little red book, urges those who care about scientific truth and democracy to make a stand now rather than wait for society to come around.

McIntyre begins by arguing that "seventy years of lies about tobacco, evolution, global warming, and vaccines" have brought us to the present moment of heightened disinformation because, throughout history, "autocratic leaders and their wannabes have understood that the quickest way to control a population is to control their information sources." He summarizes the history of strategic denialism, describing, for example, how tobacco companies specifically sought "to get the public to question the truth about something that scientists didn't really question" (the health dangers posed by tobacco), and drawing parallels to strategies used by Donald Trump and those engaged in the "Make America Great Again" (MAGA) movement.

Researchers must engage audiences they hope to persuade with respect, as scientist Katharine Hayhoe does when speaking about climate change.

PHOTO: CHICAGO TRIBUNE/GETTY IMAGES

Strategic denialism can only be successful if disinformation is created, amplified, and believed, writes McIntyre. He explains that modern disinformation warfare is commonly practiced in Russian intelligence agencies, a phenomenon described in greater detail in legal philosopher Scott Shapiro's 2023 book, *Fancy Bear Goes Phishing* (*1*).

In the second part of the book, McIntyre introduces "the amplifiers" of disinformation—social media companies with business models that incentivize engagement over getting the facts right. The mainstream media, he argues, has contributed to spreading disinformation as well. When an audience comes away from a story less informed than when they started owing to information bias, this can be even more dangerous than when they are exposed to a politically biased message, he maintains. Undoing the algorithms of disinformation should therefore be a priority.

In the book's third section, McIntyre describes "the believers"—people who do not understand how science works and are therefore most vulnerable to scientific disinformation. Here he emphasizes that beliefs, even those based on empirical evidence, are inextricable from values and identities.

Face-to-face conversation is the best way to counter this phenomenon and change an individual's mind, argues McIntyre. "It always happened in the exact same way," he writes, "through personal engagement with someone they already trusted or had grown to trust." It is worth noting here that, although he spends a great deal of time interrogating the MAGA mindset, McIntyre spends less time exploring how an individual's beliefs may arise not only from having been exposed to incorrect information but also as a consequence of political resentment that is the result of a fundamental difference in worldview.

Real change, McIntyre argues, likely will not come from better education or from efforts to improve critical thinking. Personal engagement seems to be crucial, but changing one mind at a time is difficult to scale. Larger, structural solutions are likely needed, but McIntyre's treatment does not dive deeply into what these solutions might be nor how they might be implemented. Media scholar Victor Pickard's 2019 book *Democracy Without Journalism?* offers interested readers greater context for the larger structural issues at play and potential policy solutions (*2*).

We must "confront the liars" and "heed history," McIntyre advises, bearing in mind the potential unintended consequences of our actions and reaching out to those who disagree with us. Yet he does not fully explore or explain how the actions we might take today would be different from any we have taken in the past. Pseudoscience has, after all, been with us throughout history (*3*). Treatments from cognitive scientists, such as the recently published *Nobody's Fool* (*4*), might provide additional strategies for individual inoculation against disinformation.

McIntyre concludes with ideas on "how to win the war on truth." "We need to increase the number of messengers for truth," he argues. "We simply need more of them." Scientists can help by building relationships with those they seek to persuade and teaching them with respect and dignity. ■

The reviewer is at the Department of Education Reform and Department of Psychology, University of Arkansas, Fayetteville, AR 72701, USA. Email: jwai@uark.edu

REFERENCES AND NOTES

1. S. J. Shapiro, *Fancy Bear Goes Phishing: The Dark History of the Information Age, in Five Extraordinary Hacks* (Farrar, Straus and Giroux, 2023).
2. V. Pickard, *Democracy Without Journalism? Confronting the Misinformation Society* (Oxford Univ. Press, 2019).
3. M. D. Gordin, *Pseudoscience: A Very Short Introduction* (Oxford Univ. Press, 2023).
4. D. Simons, C. Chabris, *Nobody's Fool: Why We Get Taken In and What We Can Do About It* (Basic Books, 2023).

10.1126/science.adj2202

EU policies have unintended consequences for tropical rainforests such as the Amazon.

Edited by **Jennifer Sills**

The global impact of EU forest protection policies

The European Union's Biodiversity and Forest Strategies for 2030 mandate protecting all remaining old-growth forests across the EU, increasing the area of habitat patches set aside within forests harvested for timber, and limiting clear-felling in timber-producing landscapes (*1*). Although saving old-growth forests is critical, standalone policies can produce unintended consequences (*2*). Without simultaneously reducing demand for forest products or increasing supply from plantations and secondary forests, such measures can lead to increased harvesting elsewhere, often in tropical countries, to accommodate demand. Shifting logging activities to countries with weaker legal protections aggravates biodiversity and carbon losses and exacerbates existing inequities in environmental burdens (*3*). Isolated policies displacing production will also undermine the EU's recent Deforestation Regulation to halt imports of deforestation-linked tropical products (*4*).

EU policies have global effects. In 2022, the share of tropical wood and furniture imports into EU27 countries reached a 15-year high of US$4.4 billion (*5*). The risk that EU harvesting restrictions will further shift harvesting pressures to the tropics is considerable. By 2050, logging limits under the EU Biodiversity Strategy could cut European roundwood production by 42%, increasing Brazilian and Malaysian non-coniferous roundwood extraction by 19% and 8%, respectively (*6*). China's analogous ban on natural forest harvesting led to a 15% increase in solid-wood imports (*7*), driving extraction into carbon-dense, endemic-rich frontiers in the Congo Basin (*8*). Meanwhile, recent European trade sanctions on Russia and Belarus have eliminated US$4.95 billion of timber imports to EU27 countries, driving a scramble for additional timber centered on the hyperdiverse tropics (*5*). Tropical harvests in old-growth forest cause disproportionate damage compared with temperate harvests as a result of higher diversity and sensitivity of tropical biota (*9*) and weaker governance in tropical harvesting regions (*10*).

To avoid worsening its global footprint, the EU must urgently integrate better mapping and conservation of old-growth forests (*11*) with additional policies. EU countries should improve timber product longevity and develop resilient, higher-yielding plantations on existing degraded lands alongside ecological approaches that restore native forest while generating timber (*12*). Better quantification of the socio-environmental consequences of homegrown and imported timber (*3*) and robust harvesting safeguards in all timber exporting nations are also needed. Crucially, EU countries must carefully consider the global consequences of domestic forestry changes and logging moratoria. Protecting European forests is laudable, but trading conservation in Europe for far greater impacts in tropical rainforests is unacceptable.

Gianluca Cerullo[1]*, Jos Barlow[2], Matthew Betts[3], David Edwards[4], Alison Eyres[1], Filipe França[5], Rachael Garrett[6], Thomas Swinfield[1], Eleanor Tew[1], Thomas White[7,8], Andrew Balmford[1]

[1]Department of Zoology and Conservation Research Institute, University of Cambridge, Cambridge CB2 3EJ, UK. [2]Lancaster Environment Centre, Lancaster University, Lancaster LA1 4YW, UK. [3]Department of Forest Ecosystems & Society, Oregon State University, Corvallis, OR, USA. [4]Department of Ecology and Evolutionary Biology, School of Biosciences University of Sheffield, Sheffield S10 2TN, UK. [5]School of Biological Sciences, University of Bristol, Bristol BS8 1QU, UK. [6]Department of Geography and Conservation Research Institute, University of Cambridge, Cambridge CB2 3EJ, UK. [7]Department of Biology, Interdisciplinary Centre for Conservation Science, University of Oxford, Oxford OX1 2JD, UK. [8]The Biodiversity Consultancy, Cambridge CB2 1SJ, UK. *Corresponding author. Email: grc38@cam.ac.uk

REFERENCES AND NOTES

1. European Commission, "Communication from the Commission to the European Parliament, the Council, the European Economic and Social Committee and the Committee of the Regions: New EU Forest Strategy for 2030" (2021).
2. M. G. Betts *et al.*, *Biol. Rev.* **96**, 4 (2021).
3. S. Kan, *One Earth* **6**, 55 (2023).
4. European Commission, "Green Deal: EU agrees law to fight global deforestation and forest degradation driven by EU production and consumption" (2022); https://ec.europa.eu/commission/presscorner/detail/en/IP_22_7444.
5. Tropical Timber Market Report (ITTO, 2023), vol. 27, issue 6.
6. M. Dieter *et al.*, "Assessment of possible leakage effects of implementing EU COM proposals for the EU Biodiversity Strategy on forestry and forests in non-EU countries" (Thünen Institute of International Forestry and Forest Economics, 2020).
7. Y. Zhang, S. Chen, *For. Pol. Econ.* **122**, 102339 (2021).
8. T. L. Fuller *et al.*, *Area* **51**, 340 (2019).
9. M. G. Betts *et al.*, *Science* **366**, 1236 (2019).
10. J. Barlow *et al.*, *Nature* **559**, 517 (2018).
11. M. Mikolaš *et al.*, *Science* **380**, 466 (2023).
12. S. H. Harris, M. G. Betts, *J. Appl. Ecol.* **60**, 737 (2023).

COMPETING INTERESTS

E.T. is employed by Forestry England but has contributed to this Letter on an independent basis. T.W. receives income from commercial consultancy services related to biodiversity mitigation in the private sector.

10.1126/science.adj0728

Solar energy projects put food security at risk

Solar photovoltaic deployment is essential to promote renewable energy transition, phase down coal-fired power plants, and achieve the Paris Agreement temperature goals (*1*). However, large-scale solar photovoltaic deployment requires a vast amount of land, and a substantial number of solar photovoltaic projects have been

PHOTO: PAULO BRANDO

built on farmland, threatening food security (*2*, *3*). Given the ambitious climate pledges of signatory countries to the Paris Agreement, the area of land required to deploy global solar photovoltaics in the coming decades is expected to rise (*4*). Governments must act now to mitigate the fierce competition for land between solar energy and crops.

Solar energy projects have encroached on farmland across the Northern Hemisphere (*3*). In 2017 alone, China deployed photovoltaic panels on about 100 km^2 of farmlands in the North China Plain (*3*), one of China's most important agricultural regions. Solar photovoltaic panels have also been deployed over deserts, abandoned mines (*5*), artificial canals (*6*), reservoirs (*7*), and rooftops (*8*), but these options are less attractive to developers because they are more scarce, more unstable, or more expensive than farmlands.

To ensure national food security, some countries have released strict farmland protection regulations [e.g., China's Basic Farmland Protection Regulations in 1994, Germany's Federal Regional Planning Act in 1997, and South Korea's Farmland Act in 1994 (*9*)]. However, solar energy investors and developers continue to occupy farmland illegally (*10*). Local authorities provide inadequate enforcement, allowing development to proceed at the expense of agriculture.

Mitigating solar energy's land competition will require technological innovation and more sustainable deployment strategies. For example, agrivoltaic systems have been proposed that would allow crops to grow under solar panels (*11*). However, the solar panels hinder mechanized farming and harvesting, and the solar photovoltaics need to be deployed at a position much higher than crops, making the project more expensive. Scientists have also developed foldable solar cells that can be integrated into buildings (*12*).

Until these technologies are cost-effective and scalable, governments should preferentially use unproductive lands for large-scale photovoltaic deployment, prevent installations on finite arable land, and provide stricter enforcement of farmland protection policies. Satellite remote sensing technologies should be used to closely monitor solar photovoltaic panels' illegal farmland encroachment and quantify their impacts on food production. Illegally deployed solar photovoltaics should be demolished so that farmland can be restored. Governments, corporations, and nonprofit organizations should also provide funding to scientists to research and develop cost-effective, eco-friendly, energy-efficient solar cells, including agrivoltaic technology. Scientists should also work to better understand the adverse and unintended consequences of large-scale solar photovoltaic deployment to ensure that the technology provides net benefits in the future.

Zhongbin B. Li, Yongjun Zhang*, Mengqiu Wang*
School of Remote Sensing and Information Engineering, Wuhan University, Wuhan, China.
*Corresponding author. Email: zhangyj@whu.edu.cn; mengqiu@whu.edu.cn

REFERENCES AND NOTES

1. F. Creutzig *et al.*, *Nat. Energ.* **2**, 1 (2017).
2. A. Scheidel, A. H. Sorman, *Glob. Environ. Change* **22**, 588 (2012).
3. L. Kruitwagen *et al.*, *Nature* **598**, 604 (2021).
4. S. Battersby, *Proc. Natl. Acad. Sci. U.S.A.* **120**, e2301355120 (2023).
5. G. Lin, Y. Zhao, J. Fu, D. Jiang, *Science* **380**, 699 (2023).
6. B. McKuin *et al.*, *Nat. Sustain.* **4**, 609 (2021).
7. Y. Jin *et al.*, *Nat. Sustain.* **6**, 865 (2023).
8. S. Joshi *et al.*, *Nat. Commun.* **12**, 5738 (2021).
9. X. Liu, C. Zhao, W. Song, *Land Use Pol.* **67**, 660 (2017).
10. Z. Hu, *Energ. Res. Soc. Sci.* **98**, 102988 (2023).
11. G. A. Barron-Gafford *et al.*, *Nat. Sustain.* **2**, 848 (2019).
12. W. Liu *et al.*, *Nature* **617**, 717 (2023).

10.1126/science.adj1614

Save China's gaurs

The gaur (*Bos gaurus*), the largest living bovine species, primarily inhabits tropical and subtropical broadleaf forests, bamboo forests, and sparsely tree-covered grasslands (*1*). In China, the species is mainly found in Xishuangbanna Prefecture in Yunnan Province (*1*, *2*). Anthropogenic changes have brought this population to the brink of extinction. China must take action to save this vulnerable megafauna.

Since the 1950s, crop cultivation has expanded in Yunnan, resulting in the replacement of natural forests (*3*, *4*). In some cases, these cultivated lands have even encroached into natural reserves (*3*, *5*). As a result, the gaur has lost a large area of habitat, likely forcing the population to relocate to steeper natural forest areas (*4*, *6*).

In addition to habitat loss and fragmentation, indiscriminate hunting and illegal trade have contributed to the substantial decline of the gaur population (*1*). Between 1979 and 1985, a staggering total of 83 individuals were killed by hunters in Xishuangbanna (*1*). The total gaur population in Xishuangbanna has declined from between 605 and 712 individuals in 1984 to an estimated 152 and 167 individuals in recent decades (*1*, *6*). In Menglun, Xishuangbanna, gaurs are functionally extinct (*7*).

The gaur is included on the National Class I key protected wildlife list (*2*) and classified as Critically Endangered on the Red List of China's Vertebrates (*8*). To protect the remaining gaurs, China has designated the species as a conservation priority in multiple natural reserves (*9*) and used technologies such as infrared cameras to monitor them in real time and assess their population dynamics and behaviors (*10*). However, these efforts are insufficient.

The fragmented habitats within natural reserves should be restored immediately to natural forests. In areas outside natural reserves where the gaur frequently roams (*11*), poaching should be prevented by means of increased penalties and enforcement. The Chinese government should offer subsidies and tree-planting training programs to incentivize farmers to engage in converting farmland to forests, with rewards based on their farmland area and the number of trees planted. Establishing an ecological compensation mechanism could enable farmers to participate in animal conservation efforts and receive corresponding allowances. Lastly, given that the gaur has a wide range of activity and migratory habits that allow individuals and populations to move based on the weather conditions and the availability of food and water (*4*, *11*, *12*), assisted migration may be feasible. When gaurs are trapped in unsuitable locations, unable to migrate due to barriers like villages and highways, translocating some individuals to sparsely populated and environmentally suitable areas could be successful. Without substantial additional conservation strategies, the gaur could soon go extinct in China.

Tao Xiang
Laboratoire Evolution et Diversité Biologique, UMR5174, Université Toulouse III–Paul Sabatier, Centre National de la Recherche Scientifique, Institute of Research for Development, Toulouse, France. Email: tx.xiang@outlook.com

REFERENCES AND NOTES

1. Z. Y. Zhang, H. P. Yang, Q. Y. Luo, L. Zhang, *For. Inventory Plan.* **43**, 117 (2018) [in Chinese].
2. National Forestry and Grassland Administration of China, "Official release of the updated list of wild animals under Special State Protection in China" (2021); www.forestry.gov.cn/main/586/20210208/095403793167571.html [in Chinese].
3. J. Q. Zhang, R. T. Corlett, D. L. Zhai, *Reg. Environ. Change* **19**, 1713 (2019).
4. S. R. Wen *et al.*, *J. Shandong For. Sci. Technol.* **52**, 27 (2022) [in Chinese].
5. H. F. Chen *et al.*, *PLOS ONE* **11**, e0150062 (2016).
6. Z. Y. Zhang, H. P. Yang, A. D. Luo, *For. Inventory Plan.* **41**, 115 (2016) [in Chinese].
7. G. Huang *et al.*, *Anim. Conserv.* **23**, 689 (2020).
8. Z. G. Jiang *et al.*, *Biodivers. Sci.* **24**, 500 (2016) [in Chinese].
9. X. Chen *et al.*, *Biodivers. Sci.* **29**, 668 (2021) [in Chinese].
10. National Forestry and Grassland Administration of China, "The Naban River Management Bureau completed the infrared camera deployment work for the special monitoring of the gaurs" (2023); http://www.forestry.gov.cn/main/3095/20230323/105828156812230.html [in Chinese].
11. C. C. Ding, Y. M. Hu, C. W. Li, Z. G. Jiang, *Biodivers. Sci.* **26**, 951 (2018) [in Chinese].
12. M. Ashokkumar, S. Swaminathan, R. Nagarajan, A. A. Desai, in *Animal Diversity, Natural History, and Conservation*, V. K. Gupta, A. K. Verma, Eds. (Daya Publishing House, 2011), pp. 77–94.

10.1126/science.adj4691

EU policies have unintended consequences for tropical rainforests such as the Amazon.

Edited by **Jennifer Sills**

The global impact of EU forest protection policies

The European Union's Biodiversity and Forest Strategies for 2030 mandate protecting all remaining old-growth forests across the EU, increasing the area of habitat patches set aside within forests harvested for timber, and limiting clear-felling in timber-producing landscapes (*1*). Although saving old-growth forests is critical, standalone policies can produce unintended consequences (*2*). Without simultaneously reducing demand for forest products or increasing supply from plantations and secondary forests, such measures can lead to increased harvesting elsewhere, often in tropical countries, to accommodate demand. Shifting logging activities to countries with weaker legal protections aggravates biodiversity and carbon losses and exacerbates existing inequities in environmental burdens (*3*). Isolated policies displacing production will also undermine the EU's recent Deforestation Regulation to halt imports of deforestation-linked tropical products (*4*).

EU policies have global effects. In 2022, the share of tropical wood and furniture imports into EU27 countries reached a 15-year high of US$4.4 billion (*5*). The risk that EU harvesting restrictions will further shift harvesting pressures to the tropics is considerable. By 2050, logging limits under the EU Biodiversity Strategy could cut European roundwood production by 42%, increasing Brazilian and Malaysian non-coniferous roundwood extraction by 19% and 8%, respectively (*6*). China's analogous ban on natural forest harvesting led to a 15% increase in solid-wood imports (*7*), driving extraction into carbon-dense, endemic-rich frontiers in the Congo Basin (*8*). Meanwhile, recent European trade sanctions on Russia and Belarus have eliminated US$4.95 billion of timber imports to EU27 countries, driving a scramble for additional timber centered on the hyperdiverse tropics (*5*). Tropical harvests in old-growth forest cause disproportionate damage compared with temperate harvests as a result of higher diversity and sensitivity of tropical biota (*9*) and weaker governance in tropical harvesting regions (*10*).

To avoid worsening its global footprint, the EU must urgently integrate better mapping and conservation of old-growth forests (*11*) with additional policies. EU countries should improve timber product longevity and develop resilient, higher-yielding plantations on existing degraded lands alongside ecological approaches that restore native forest while generating timber (*12*). Better quantification of the socio-environmental consequences of homegrown and imported timber (*3*) and robust harvesting safeguards in all timber exporting nations are also needed. Crucially, EU countries must carefully consider the global consequences of domestic forestry changes and logging moratoria. Protecting European forests is laudable, but trading conservation in Europe for far greater impacts in tropical rainforests is unacceptable.

Gianluca Cerullo[1]*, Jos Barlow[2], Matthew Betts[3], David Edwards[4], Alison Eyres[1], Filipe França[5], Rachael Garrett[6], Thomas Swinfield[1], Eleanor Tew[1], Thomas White[7,8], Andrew Balmford[1]

[1]Department of Zoology and Conservation Research Institute, University of Cambridge, Cambridge CB2 3EJ, UK. [2]Lancaster Environment Centre, Lancaster University, Lancaster LA1 4YW, UK. [3]Department of Forest Ecosystems & Society, Oregon State University, Corvallis, OR, USA. [4]Department of Ecology and Evolutionary Biology, School of Biosciences University of Sheffield, Sheffield S10 2TN, UK. [5]School of Biological Sciences, University of Bristol, Bristol BS8 1QU, UK. [6]Department of Geography and Conservation Research Institute, University of Cambridge, Cambridge CB2 3EJ, UK. [7]Department of Biology, Interdisciplinary Centre for Conservation Science, University of Oxford, Oxford OX1 2JD, UK. [8]The Biodiversity Consultancy, Cambridge CB2 1SJ, UK. *Corresponding author. Email: grc38@cam.ac.uk

REFERENCES AND NOTES

1. European Commission, "Communication from the Commission to the European Parliament, the Council, the European Economic and Social Committee and the Committee of the Regions: New EU Forest Strategy for 2030" (2021).
2. M. G. Betts *et al.*, *Biol. Rev.* **96**, 4 (2021).
3. S. Kan, *One Earth* **6**, 55 (2023).
4. European Commission, "Green Deal: EU agrees law to fight global deforestation and forest degradation driven by EU production and consumption" (2022); https://ec.europa.eu/commission/presscorner/detail/en/IP_22_7444.
5. Tropical Timber Market Report (ITTO, 2023), vol. 27, issue 6.
6. M. Dieter *et al.*, "Assessment of possible leakage effects of implementing EU COM proposals for the EU Biodiversity Strategy on forestry and forests in non-EU countries" (Thünen Institute of International Forestry and Forest Economics, 2020).
7. Y. Zhang, S. Chen, *For. Pol. Econ.* **122**, 102339 (2021).
8. T. L. Fuller *et al.*, *Area* **51**, 340 (2019).
9. M. G. Betts *et al.*, *Science* **366**, 1236 (2019).
10. J. Barlow *et al.*, *Nature* **559**, 517 (2018).
11. M. Mikolaš *et al.*, *Science* **380**, 466 (2023).
12. S. H. Harris, M. G. Betts, *J. Appl. Ecol.* **60**, 737 (2023).

COMPETING INTERESTS

E.T. is employed by Forestry England but has contributed to this Letter on an independent basis. T.W. receives income from commercial consultancy services related to biodiversity mitigation in the private sector.

10.1126/science.adj0728

Solar energy projects put food security at risk

Solar photovoltaic deployment is essential to promote renewable energy transition, phase down coal-fired power plants, and achieve the Paris Agreement temperature goals (*1*). However, large-scale solar photovoltaic deployment requires a vast amount of land, and a substantial number of solar photovoltaic projects have been

PHOTO: PAULO BRANDO

built on farmland, threatening food security (*2*, *3*). Given the ambitious climate pledges of signatory countries to the Paris Agreement, the area of land required to deploy global solar photovoltaics in the coming decades is expected to rise (*4*). Governments must act now to mitigate the fierce competition for land between solar energy and crops.

Solar energy projects have encroached on farmland across the Northern Hemisphere (*3*). In 2017 alone, China deployed photovoltaic panels on about 100 km^2 of farmlands in the North China Plain (*3*), one of China's most important agricultural regions. Solar photovoltaic panels have also been deployed over deserts, abandoned mines (*5*), artificial canals (*6*), reservoirs (*7*), and rooftops (*8*), but these options are less attractive to developers because they are more scarce, more unstable, or more expensive than farmlands.

To ensure national food security, some countries have released strict farmland protection regulations [e.g., China's Basic Farmland Protection Regulations in 1994, Germany's Federal Regional Planning Act in 1997, and South Korea's Farmland Act in 1994 (*9*)]. However, solar energy investors and developers continue to occupy farmland illegally (*10*). Local authorities provide inadequate enforcement, allowing development to proceed at the expense of agriculture.

Mitigating solar energy's land competition will require technological innovation and more sustainable deployment strategies. For example, agrivoltaic systems have been proposed that would allow crops to grow under solar panels (*11*). However, the solar panels hinder mechanized farming and harvesting, and the solar photovoltaics need to be deployed at a position much higher than crops, making the project more expensive. Scientists have also developed foldable solar cells that can be integrated into buildings (*12*).

Until these technologies are cost-effective and scalable, governments should preferentially use unproductive lands for large-scale photovoltaic deployment, prevent installations on finite arable land, and provide stricter enforcement of farmland protection policies. Satellite remote sensing technologies should be used to closely monitor solar photovoltaic panels' illegal farmland encroachment and quantify their impacts on food production. Illegally deployed solar photovoltaics should be demolished so that farmland can be restored. Governments, corporations, and nonprofit organizations should also provide funding to scientists to research and develop cost-effective, eco-friendly, energy-efficient solar cells, including agrivoltaic technology. Scientists should also work to better understand the adverse and unintended consequences of large-scale solar photovoltaic deployment to ensure that the technology provides net benefits in the future.

Zhongbin B. Li, Yongjun Zhang*, Mengqiu Wang*
School of Remote Sensing and Information Engineering, Wuhan University, Wuhan, China.
*Corresponding author. Email: zhangyj@whu.edu.cn; mengqiu@whu.edu.cn

REFERENCES AND NOTES

1. F. Creutzig *et al.*, *Nat. Energ.* **2**, 1 (2017).
2. A. Scheidel, A. H. Sorman, *Glob. Environ. Change* **22**, 588 (2012).
3. L. Kruitwagen *et al.*, *Nature* **598**, 604 (2021).
4. S. Battersby, *Proc. Natl. Acad. Sci. U.S.A.* **120**, e2301355120 (2023).
5. G. Lin, Y. Zhao, J. Fu, D. Jiang, *Science* **380**, 699 (2023).
6. B. McKuin *et al.*, *Nat. Sustain.* **4**, 609 (2021).
7. Y. Jin *et al.*, *Nat. Sustain.* **6**, 865 (2023).
8. S. Joshi *et al.*, *Nat. Commun.* **12**, 5738 (2021).
9. X. Liu, C. Zhao, W. Song, *Land Use Pol.* **67**, 660 (2017).
10. Z. Hu, *Energ. Res. Soc. Sci.* **98**, 102988 (2023).
11. G. A. Barron-Gafford *et al.*, *Nat. Sustain.* **2**, 848 (2019).
12. W. Liu *et al.*, *Nature* **617**, 717 (2023).

10.1126/science.adj1614

Save China's gaurs

The gaur (*Bos gaurus*), the largest living bovine species, primarily inhabits tropical and subtropical broadleaf forests, bamboo forests, and sparsely tree-covered grasslands (*1*). In China, the species is mainly found in Xishuangbanna Prefecture in Yunnan Province (*1*, *2*). Anthropogenic changes have brought this population to the brink of extinction. China must take action to save this vulnerable megafauna.

Since the 1950s, crop cultivation has expanded in Yunnan, resulting in the replacement of natural forests (*3*, *4*). In some cases, these cultivated lands have even encroached into natural reserves (*3*, *5*). As a result, the gaur has lost a large area of habitat, likely forcing the population to relocate to steeper natural forest areas (*4*, *6*).

In addition to habitat loss and fragmentation, indiscriminate hunting and illegal trade have contributed to the substantial decline of the gaur population (*1*). Between 1979 and 1985, a staggering total of 83 individuals were killed by hunters in Xishuangbanna (*1*). The total gaur population in Xishuangbanna has declined from between 605 and 712 individuals in 1984 to an estimated 152 and 167 individuals in recent decades (*1*, *6*). In Menglun, Xishuangbanna, gaurs are functionally extinct (*7*).

The gaur is included on the National Class I key protected wildlife list (*2*) and classified as Critically Endangered on the Red List of China's Vertebrates (*8*). To protect the remaining gaurs, China has designated the species as a conservation priority in multiple natural reserves (*9*) and used technologies such as infrared cameras to monitor them in real time and assess their population dynamics and behaviors (*10*). However, these efforts are insufficient.

The fragmented habitats within natural reserves should be restored immediately to natural forests. In areas outside natural reserves where the gaur frequently roams (*11*), poaching should be prevented by means of increased penalties and enforcement. The Chinese government should offer subsidies and tree-planting training programs to incentivize farmers to engage in converting farmland to forests, with rewards based on their farmland area and the number of trees planted. Establishing an ecological compensation mechanism could enable farmers to participate in animal conservation efforts and receive corresponding allowances. Lastly, given that the gaur has a wide range of activity and migratory habits that allow individuals and populations to move based on the weather conditions and the availability of food and water (*4*, *11*, *12*), assisted migration may be feasible. When gaurs are trapped in unsuitable locations, unable to migrate due to barriers like villages and highways, translocating some individuals to sparsely populated and environmentally suitable areas could be successful. Without substantial additional conservation strategies, the gaur could soon go extinct in China.

Tao Xiang
Laboratoire Evolution et Diversité Biologique, UMR5174, Université Toulouse III—Paul Sabatier, Centre National de la Recherche Scientifique, Institute of Research for Development, Toulouse, France. Email: tx.xiang@outlook.com

REFERENCES AND NOTES

1. Z. Y. Zhang, H. P. Yang, Q. Y. Luo, L. Zhang, *For. Inventory Plan.* **43**, 117 (2018) [in Chinese].
2. National Forestry and Grassland Administration of China, "Official release of the updated list of wild animals under Special State Protection in China" (2021); www.forestry.gov.cn/main/586/20210208/095403793167571.html [in Chinese].
3. J. Q. Zhang, R. T. Corlett, D. L. Zhai, *Reg. Environ. Change* **19**, 1713 (2019).
4. S. R. Wen *et al.*, *J. Shandong For. Sci. Technol.* **52**, 27 (2022) [in Chinese].
5. H. F. Chen *et al.*, *PLOS ONE* **11**, e0150062 (2016).
6. Z. Y. Zhang, H. P. Yang, A. D. Luo, *For. Inventory Plan.* **41**, 115 (2016) [in Chinese].
7. G. Huang *et al.*, *Anim. Conserv.* **23**, 689 (2020).
8. Z. G. Jiang *et al.*, *Biodivers. Sci.* **24**, 500 (2016) [in Chinese].
9. X. Chen *et al.*, *Biodivers. Sci.* **29**, 668 (2021) [in Chinese].
10. National Forestry and Grassland Administration of China, "The Naban River Management Bureau completed the infrared camera deployment work for the special monitoring of the gaurs" (2023); http://www.forestry.gov.cn/main/3095/20230323/105828156812230.html [in Chinese].
11. C. C. Ding, Y. M. Hu, C. W. Li, Z. G. Jiang, *Biodivers. Sci.* **26**, 951 (2018) [in Chinese].
12. M. Ashokkumar, S. Swaminathan, R. Nagarajan, A. A. Desai, in *Animal Diversity, Natural History, and Conservation*, V. K. Gupta, A. K. Verma, Eds. (Daya Publishing House, 2011), pp. 77–94.

10.1126/science.adj4691

EU policies have unintended consequences for tropical rainforests such as the Amazon.

Edited by **Jennifer Sills**

The global impact of EU forest protection policies

The European Union's Biodiversity and Forest Strategies for 2030 mandate protecting all remaining old-growth forests across the EU, increasing the area of habitat patches set aside within forests harvested for timber, and limiting clear-felling in timber-producing landscapes (*1*). Although saving old-growth forests is critical, standalone policies can produce unintended consequences (*2*). Without simultaneously reducing demand for forest products or increasing supply from plantations and secondary forests, such measures can lead to increased harvesting elsewhere, often in tropical countries, to accommodate demand. Shifting logging activities to countries with weaker legal protections aggravates biodiversity and carbon losses and exacerbates existing inequities in environmental burdens (*3*). Isolated policies displacing production will also undermine the EU's recent Deforestation Regulation to halt imports of deforestation-linked tropical products (*4*).

EU policies have global effects. In 2022, the share of tropical wood and furniture imports into EU27 countries reached a 15-year high of US$4.4 billion (*5*). The risk that EU harvesting restrictions will further shift harvesting pressures to the tropics is considerable. By 2050, logging limits under the EU Biodiversity Strategy could cut European roundwood production by 42%, increasing Brazilian and Malaysian non-coniferous roundwood extraction by 19% and 8%, respectively (*6*). China's analogous ban on natural forest harvesting led to a 15% increase in solid-wood imports (*7*), driving extraction into carbon-dense, endemic-rich frontiers in the Congo Basin (*8*). Meanwhile, recent European trade sanctions on Russia and Belarus have eliminated US$4.95 billion of timber imports to EU27 countries, driving a scramble for additional timber centered on the hyperdiverse tropics (*5*). Tropical harvests in old-growth forest cause disproportionate damage compared with temperate harvests as a result of higher diversity and sensitivity of tropical biota (*9*) and weaker governance in tropical harvesting regions (*10*).

To avoid worsening its global footprint, the EU must urgently integrate better mapping and conservation of old-growth forests (*11*) with additional policies. EU countries should improve timber product longevity and develop resilient, higher-yielding plantations on existing degraded lands alongside ecological approaches that restore native forest while generating timber (*12*). Better quantification of the socio-environmental consequences of homegrown and imported timber (*3*) and robust harvesting safeguards in all timber exporting nations are also needed. Crucially, EU countries must carefully consider the global consequences of domestic forestry changes and logging moratoria. Protecting European forests is laudable, but trading conservation in Europe for far greater impacts in tropical rainforests is unacceptable.

Gianluca Cerullo[1]*, Jos Barlow[2], Matthew Betts[3], David Edwards[4], Alison Eyres[1], Filipe França[5], Rachael Garrett[6], Thomas Swinfield[1], Eleanor Tew[1], Thomas White[7,8], Andrew Balmford[1]

[1]Department of Zoology and Conservation Research Institute, University of Cambridge, Cambridge CB2 3EJ, UK. [2]Lancaster Environment Centre, Lancaster University, Lancaster LA1 4YW, UK. [3]Department of Forest Ecosystems & Society, Oregon State University, Corvallis, OR, USA. [4]Department of Ecology and Evolutionary Biology, School of Biosciences University of Sheffield, Sheffield S10 2TN, UK. [5]School of Biological Sciences, University of Bristol, Bristol BS8 1QU, UK. [6]Department of Geography and Conservation Research Institute, University of Cambridge, Cambridge CB2 3EJ, UK. [7]Department of Biology, Interdisciplinary Centre for Conservation Science, University of Oxford, Oxford OX1 2JD, UK. [8]The Biodiversity Consultancy, Cambridge CB2 1SJ, UK. *Corresponding author. Email: grc38@cam.ac.uk

REFERENCES AND NOTES

1. European Commission, "Communication from the Commission to the European Parliament, the Council, the European Economic and Social Committee and the Committee of the Regions: New EU Forest Strategy for 2030" (2021).
2. M. G. Betts *et al.*, *Biol. Rev.* **96**, 4 (2021).
3. S. Kan, *One Earth* **6**, 55 (2023).
4. European Commission, "Green Deal: EU agrees law to fight global deforestation and forest degradation driven by EU production and consumption" (2022); https://ec.europa.eu/commission/presscorner/detail/en/IP_22_7444.
5. Tropical Timber Market Report (ITTO, 2023), vol. 27, issue 6.
6. M. Dieter *et al.*, "Assessment of possible leakage effects of implementing EU COM proposals for the EU Biodiversity Strategy on forestry and forests in non-EU countries" (Thünen Institute of International Forestry and Forest Economics, 2020).
7. Y. Zhang, S. Chen, *For. Pol. Econ.* **122**, 102339 (2021).
8. T. L. Fuller *et al.*, *Area* **51**, 340 (2019).
9. M. G. Betts *et al.*, *Science* **366**, 1236 (2019).
10. J. Barlow *et al.*, *Nature* **559**, 517 (2018).
11. M. Mikolaš *et al.*, *Science* **380**, 466 (2023).
12. S. H. Harris, M. G. Betts, *J. Appl. Ecol.* **60**, 737 (2023).

COMPETING INTERESTS

E.T. is employed by Forestry England but has contributed to this Letter on an independent basis. T.W. receives income from commercial consultancy services related to biodiversity mitigation in the private sector.

10.1126/science.adj0728

Solar energy projects put food security at risk

Solar photovoltaic deployment is essential to promote renewable energy transition, phase down coal-fired power plants, and achieve the Paris Agreement temperature goals (*1*). However, large-scale solar photovoltaic deployment requires a vast amount of land, and a substantial number of solar photovoltaic projects have been

PHOTO: PAULO BRANDO

built on farmland, threatening food security (*2*, *3*). Given the ambitious climate pledges of signatory countries to the Paris Agreement, the area of land required to deploy global solar photovoltaics in the coming decades is expected to rise (*4*). Governments must act now to mitigate the fierce competition for land between solar energy and crops.

Solar energy projects have encroached on farmland across the Northern Hemisphere (*3*). In 2017 alone, China deployed photovoltaic panels on about 100 km^2 of farmlands in the North China Plain (*3*), one of China's most important agricultural regions. Solar photovoltaic panels have also been deployed over deserts, abandoned mines (*5*), artificial canals (*6*), reservoirs (*7*), and rooftops (*8*), but these options are less attractive to developers because they are more scarce, more unstable, or more expensive than farmlands.

To ensure national food security, some countries have released strict farmland protection regulations [e.g., China's Basic Farmland Protection Regulations in 1994, Germany's Federal Regional Planning Act in 1997, and South Korea's Farmland Act in 1994 (*9*)]. However, solar energy investors and developers continue to occupy farmland illegally (*10*). Local authorities provide inadequate enforcement, allowing development to proceed at the expense of agriculture.

Mitigating solar energy's land competition will require technological innovation and more sustainable deployment strategies. For example, agrivoltaic systems have been proposed that would allow crops to grow under solar panels (*11*). However, the solar panels hinder mechanized farming and harvesting, and the solar photovoltaics need to be deployed at a position much higher than crops, making the project more expensive. Scientists have also developed foldable solar cells that can be integrated into buildings (*12*).

Until these technologies are cost-effective and scalable, governments should preferentially use unproductive lands for large-scale photovoltaic deployment, prevent installations on finite arable land, and provide stricter enforcement of farmland protection policies. Satellite remote sensing technologies should be used to closely monitor solar photovoltaic panels' illegal farmland encroachment and quantify their impacts on food production. Illegally deployed solar photovoltaics should be demolished so that farmland can be restored. Governments, corporations, and nonprofit organizations should also provide funding to scientists to research and develop cost-effective, eco-friendly, energy-efficient solar cells, including agrivoltaic technology. Scientists should also work to better understand the adverse and unintended consequences of large-scale solar photovoltaic deployment to ensure that the technology provides net benefits in the future.

Zhongbin B. Li, Yongjun Zhang*, Mengqiu Wang*
School of Remote Sensing and Information Engineering, Wuhan University, Wuhan, China.
*Corresponding author. Email: zhangyj@whu.edu.cn; mengqiu@whu.edu.cn

REFERENCES AND NOTES

1. F. Creutzig *et al.*, *Nat. Energ.* **2**, 1 (2017).
2. A. Scheidel, A. H. Sorman, *Glob. Environ. Change* **22**, 588 (2012).
3. L. Kruitwagen *et al.*, *Nature* **598**, 604 (2021).
4. S. Battersby, *Proc. Natl. Acad. Sci. U.S.A.* **120**, e2301355120 (2023).
5. G. Lin, Y. Zhao, J. Fu, D. Jiang, *Science* **380**, 699 (2023).
6. B. McKuin *et al.*, *Nat. Sustain.* **4**, 609 (2021).
7. Y. Jin *et al.*, *Nat. Sustain.* **6**, 865 (2023).
8. S. Joshi *et al.*, *Nat. Commun.* **12**, 5738 (2021).
9. X. Liu, C. Zhao, W. Song, *Land Use Pol.* **67**, 660 (2017).
10. Z. Hu, *Energ. Res. Soc. Sci.* **98**, 102988 (2023).
11. G. A. Barron-Gafford *et al.*, *Nat. Sustain.* **2**, 848 (2019).
12. W. Liu *et al.*, *Nature* **617**, 717 (2023).

10.1126/science.adj1614

Save China's gaurs

The gaur (*Bos gaurus*), the largest living bovine species, primarily inhabits tropical and subtropical broadleaf forests, bamboo forests, and sparsely tree-covered grasslands (*1*). In China, the species is mainly found in Xishuangbanna Prefecture in Yunnan Province (*1*, *2*). Anthropogenic changes have brought this population to the brink of extinction. China must take action to save this vulnerable megafauna.

Since the 1950s, crop cultivation has expanded in Yunnan, resulting in the replacement of natural forests (*3*, *4*). In some cases, these cultivated lands have even encroached into natural reserves (*3*, *5*). As a result, the gaur has lost a large area of habitat, likely forcing the population to relocate to steeper natural forest areas (*4*, *6*).

In addition to habitat loss and fragmentation, indiscriminate hunting and illegal trade have contributed to the substantial decline of the gaur population (*1*). Between 1979 and 1985, a staggering total of 83 individuals were killed by hunters in Xishuangbanna (*1*). The total gaur population in Xishuangbanna has declined from between 605 and 712 individuals in 1984 to an estimated 152 and 167 individuals in recent decades (*1*, *6*). In Menglun, Xishuangbanna, gaurs are functionally extinct (*7*).

The gaur is included on the National Class I key protected wildlife list (*2*) and classified as Critically Endangered on the Red List of China's Vertebrates (*8*). To protect the remaining gaurs, China has designated the species as a conservation priority in multiple natural reserves (*9*) and used technologies such as infrared cameras to monitor them in real time and assess their population dynamics and behaviors (*10*). However, these efforts are insufficient.

The fragmented habitats within natural reserves should be restored immediately to natural forests. In areas outside natural reserves where the gaur frequently roams (*11*), poaching should be prevented by means of increased penalties and enforcement. The Chinese government should offer subsidies and tree-planting training programs to incentivize farmers to engage in converting farmland to forests, with rewards based on their farmland area and the number of trees planted. Establishing an ecological compensation mechanism could enable farmers to participate in animal conservation efforts and receive corresponding allowances. Lastly, given that the gaur has a wide range of activity and migratory habits that allow individuals and populations to move based on the weather conditions and the availability of food and water (*4*, *11*, *12*), assisted migration may be feasible. When gaurs are trapped in unsuitable locations, unable to migrate due to barriers like villages and highways, translocating some individuals to sparsely populated and environmentally suitable areas could be successful. Without substantial additional conservation strategies, the gaur could soon go extinct in China.

Tao Xiang
Laboratoire Evolution et Diversité Biologique, UMR5174, Université Toulouse III–Paul Sabatier, Centre National de la Recherche Scientifique, Institute of Research for Development, Toulouse, France. Email: tx.xiang@outlook.com

REFERENCES AND NOTES

1. Z. Y. Zhang, H. P. Yang, Q. Y. Luo, L. Zhang, *For. Inventory Plan.* **43**, 117 (2018) [in Chinese].
2. National Forestry and Grassland Administration of China, "Official release of the updated list of wild animals under Special State Protection in China" (2021); www.forestry.gov.cn/main/586/20210208/095403793167571.html [in Chinese].
3. J. Q. Zhang, R. T. Corlett, D. L. Zhai, *Reg. Environ. Change* **19**, 1713 (2019).
4. S. R. Wen *et al.*, *J. Shandong For. Sci. Technol.* **52**, 27 (2022) [in Chinese].
5. H. F. Chen *et al.*, *PLOS ONE* **11**, e0150062 (2016).
6. Z. Y. Zhang, H. P. Yang, A. D. Luo, *For. Inventory Plan.* **41**, 115 (2016) [in Chinese].
7. G. Huang *et al.*, *Anim. Conserv.* **23**, 689 (2020).
8. Z. G. Jiang *et al.*, *Biodivers. Sci.* **24**, 500 (2016) [in Chinese].
9. X. Chen *et al.*, *Biodivers. Sci.* **29**, 668 (2021) [in Chinese].
10. National Forestry and Grassland Administration of China, "The Naban River Management Bureau completed the infrared camera deployment work for the special monitoring of the gaurs" (2023); http://www.forestry.gov.cn/main/3095/20230323/105828156812230.html [in Chinese].
11. C. C. Ding, Y. M. Hu, C. W. Li, Z. G. Jiang, *Biodivers. Sci.* **26**, 951 (2018) [in Chinese].
12. M. Ashokkumar, S. Swaminathan, R. Nagarajan, A. A. Desai, in *Animal Diversity, Natural History, and Conservation*, V. K. Gupta, A. K. Verma, Eds. (Daya Publishing House, 2011), pp. 77–94.

10.1126/science.adj4691

RESEARCH

IN *SCIENCE* JOURNALS

Edited by **Michael Funk**

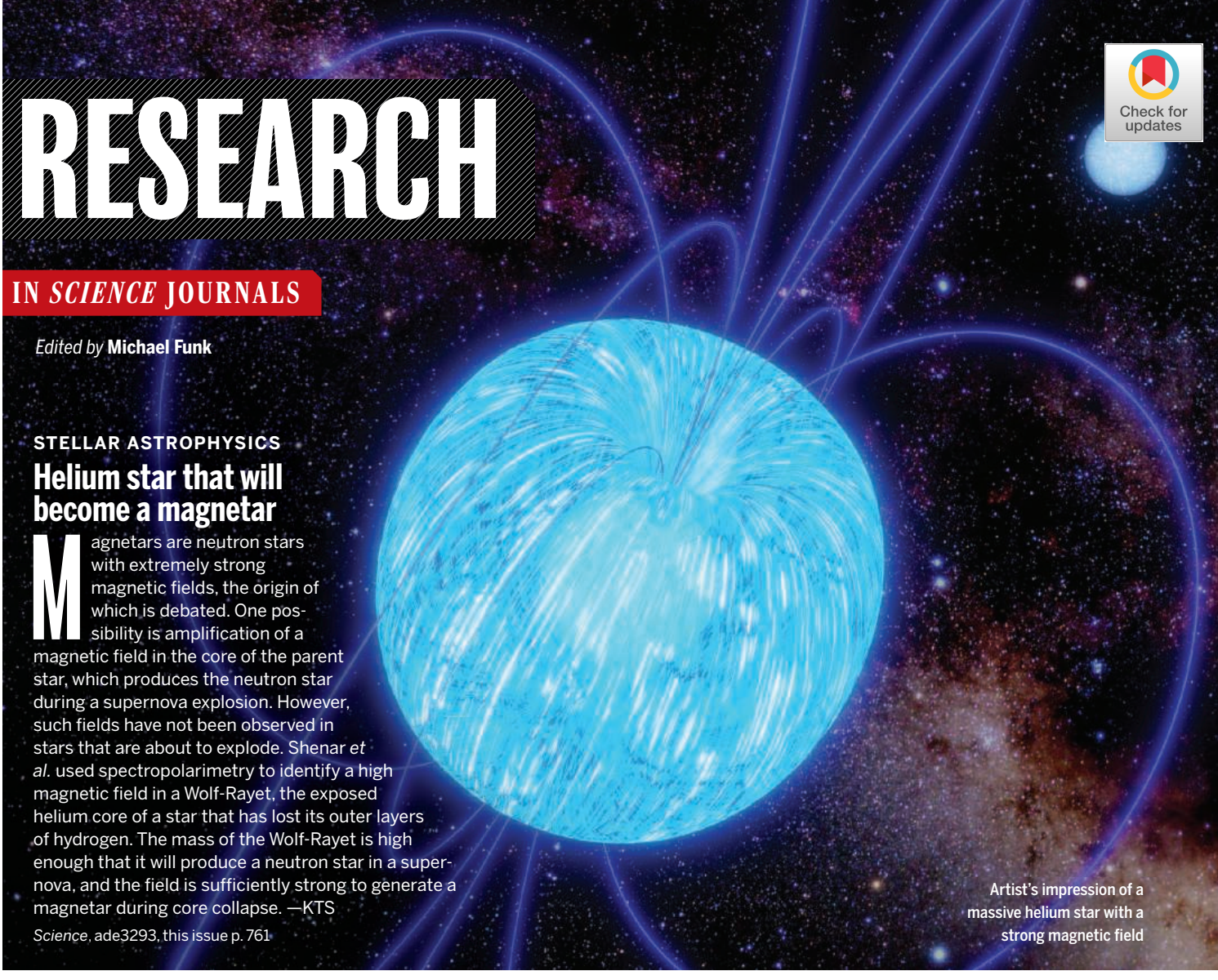

Artist's impression of a massive helium star with a strong magnetic field

ILLUSTRATION: FABIAN BODENSTEINER

STELLAR ASTROPHYSICS

Helium star that will become a magnetar

Magnetars are neutron stars with extremely strong magnetic fields, the origin of which is debated. One possibility is amplification of a magnetic field in the core of the parent star, which produces the neutron star during a supernova explosion. However, such fields have not been observed in stars that are about to explode. Shenar *et al.* used spectropolarimetry to identify a high magnetic field in a Wolf-Rayet, the exposed helium core of a star that has lost its outer layers of hydrogen. The mass of the Wolf-Rayet is high enough that it will produce a neutron star in a supernova, and the field is sufficiently strong to generate a magnetar during core collapse. —KTS

Science, ade3293, this issue p. 761

PHYSICS

Peculiar rotations in fullerenes

Ergodicity breaking, the inability of a system to thermalize, is of fundamental interest in statistical mechanics and physics and has been vigorously studied in many systems. Using high-sensitivity infrared spectroscopy, Liu *et al*. collected compelling experimental signatures of previously unobserved rotational ergodicity breaking in a buckminsterfullerene molecule (C_{60}) that arose from rotation-vibration coupling and were distinctly different from what was found in all prior studies. Because of its symmetry, size, and rigidity, C_{60} can switch back and forth between ergodic and non-ergodic rotational regimes as it rotates faster and faster. The present work reports peculiar rotational dynamics in C_{60} and demonstrates how such a familiar but relatively unexplored molecule can be used to observe new phenomena. —YS

Science, adi6354, this issue p. 778

NANOMATERIALS

Metal clusters as active waveguides

Optical waveguides are often passive devices that rely on changes in the refractive index of materials to confine and guide light, but they can also function through optical active materials that absorb and remit light. Wang *et al*. show that crystals of small metal clusters such as $PtAg_{18}$ protected by ligand shells can exhibit high optical waveguide performance with low optical loss coefficients and high polarization of the re-emitted light. These effects are amplified by favorable crystal packing and molecular orientation effects.—PDS

Science, adh2365, this issue p. 784

PHYSICS

Disorder to the rescue

Many correlated electron systems, such as cuprates and heavy fermion materials, host an unusual type of metallic state called strange metal. Strange metals have transport and thermodynamic properties with temperature dependences that differ from those of ordinary metals. Devising a theory that describes all of these properties correctly remains challenging. Patel *et al*. achieved this goal by introducing disorder in the coupling constants of a model of strongly interacting systems. —JS

Science, abq6011, this issue p. 790

BIOPHYSICS

The search for Piezo channel partners

Piezo ion channels act as sensors that convert mechanical energy into cellular signals, but the mechanistic details of their modulation remains to be fully elucidated. Zhou *et al*. used two molecular strategies in combination with CRISPR/Cas9 editing to identify previously unrecognized Piezo channel–binding partners. Using a blend of electrophysiology and cryo–electron microscopy, the authors provide

molecular details of how MyoD family inhibitor proteins interact with Piezo channels and regulate their gating. They identified an interacting interface that likely represents a scaffold that might be leveraged to generate Piezo-targeted therapeutics. —MMa

Science, adh8190, this issue p. 799

CORONAVIRUS

Protective parasites

Parasitic helminths generate a type 2 immune response that can persist even after clearance of an infection. Using a mouse model of roundworm infection, Oyesola *et al.* found that prior exposure to lung-migrating helminths protects transgenic K18-hACE2 mice against SARS-CoV-2 infection. Pulmonary macrophages from roundworm-infected mice adopted a type 2 transcriptional and epigenetic signature that persisted after parasite clearance and at least 45 days after infection. SARS-CoV-2–specific $CD8^+$ T cell responses were driven by alveolar macrophages and were required for helminth-mediated protection. These results demonstrate that lung-migrating helminths reprogram lung immune homeostasis, leading to enhanced protection against subsequent SARS-CoV-2 infection. —CO

Sci. Immunol. (2023) 10.1126/sciimmunol.adf8161

AGING

Targeting senescence with CAR T cells

Cellular senescence contributes to aging and to aging-associated diseases, and depletion of senescent cells has shown potential for treating such diseases. Yang *et al.* developed chimeric antigen receptor (CAR) T cells targeting Natural Killer Group 2 Member D (NKG2D) ligands, which are highly expressed on senescent cells. The CAR, which is composed of the extracellular domain of NKG2D and the intracellular signaling domains of two receptors, was able to efficiently drive killing of senescent cells in vitro and in vivo in both aged mice and aged nonhuman primates. Aged mice treated with NKG2D-CAR T cells exhibited improved physical performance after treatment. These data support the further development of NKG2D-CAR T cells for aging-associated pathologies. —CM

Sci. Transl. Med. (2023) 10.1126/scitranslmed.add1951

PROTEIN DESIGN

Two-state two-step

Natural proteins often adopt multiple conformational states, thereby changing their activity or binding partners in response to another protein, small molecule, or other stimulus. It has been difficult to engineer such conformational switching between two folded states in human-designed proteins. Praetorius *et al*. developed a hinge-like protein by simultaneously considering both desired states in the design process. The successful designs exhibited a large shift in conformation upon binding to a target peptide helix, which could be tailored for specificity. The authors characterized the protein structures, binding kinetics, and conformational equilibrium of the designs. This work provides the groundwork for generating protein switches that respond to biological triggers and can produce conformational changes that modulate protein assemblies. —MAF

Science, adg7731, this issue p. 754

Illustration of a designed protein that can switch between two different conformational states

IN OTHER JOURNALS

Edited by **Caroline Ash** *and* **Jesse Smith**

ENERGY

Another route to refrigeration

Space cooling accounts for 20% of the world's total energy consumption but relies on refrigerants with large global-warming potential. Zhou *et al.* now demonstrate an alternative to refrigerant-based cooling that uses a compression-based regenerative elastocaloric device that performs phase transformations during which latent heat is absorbed. This tubular nickel–titanium device achieves a temperature difference between the hot and cold sides of 50 kelvin and a cooling power of more than 200 watts. —ECF

Joule (2023) 10.1016/j.joule.2023.07.004

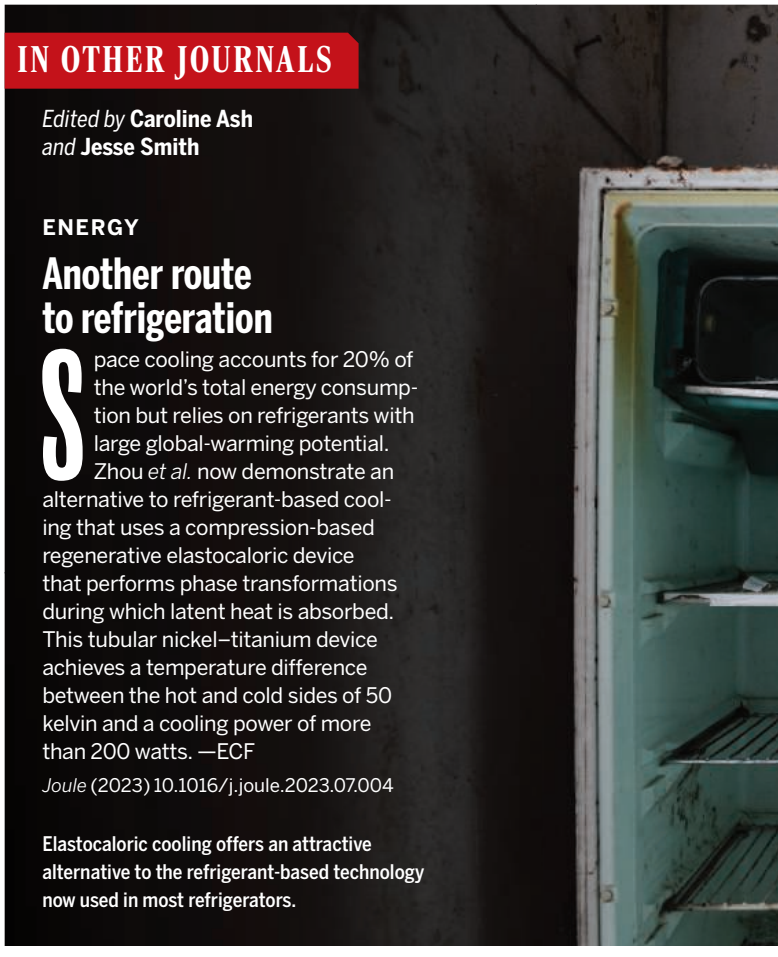

Elastocaloric cooling offers an attractive alternative to the refrigerant-based technology now used in most refrigerators.

CELL BIOLOGY

Spartin mediates lipophagy

Lipid droplets are important for energy storage and lipid homeostasis. Selective autophagy of lipid droplets, called lipophagy, is required for their catabolism, but how lipid droplets are targeted for lipophagy remains unclear. Working in cultured human cells, Chung *et al.* elucidated a role for spartin, a protein that localizes on lipid droplets and endosomal compartments, in lipophagy. Spartin functions as a receptor on lipid droplets that interacts with the core autophagy machinery. Thus, spartin is required to deliver lipid droplets to lysosomes for triglyceride mobilization. Mutations in the gene encoding spartin lead to Troyer syndrome, a form of hereditary spastic paraplegia. Indeed, blocking spartin function caused lipid droplet and triglyceride accumulation in mouse and cultured human neurons. —SMH

Nat. Cell Biol. (2023) https://doi.org/10.1038/s41556-023-01178-w

IMMUNOLOGY

A MASTerful compilation

Mast cells (MCs) are a class of granulocytes that release inflammatory mediators in response to an array of stimuli. MCs are currently organized into mucosal MCs (MMCs), found in the gut and lung, and connective tissue–type MCs (CTMCs), located primarily in the skin and peritoneal cavity. To gain a picture of the heterogeneity and ontogeny of MC subsets, Tauber *et al.* integrated several single-cell datasets of mouse and human MC populations across a variety of tissues. The authors found in mice that *Mrgprb2*$^+$ and

CREDITS: (LEFT TO RIGHT) IAN C. HAYDON/UW INSTITUTE FOR PROTEIN DESIGN; DE ROSA/ALAMY STOCK PHOTO

ALSO IN *SCIENCE* JOURNALS

Edited by **Michael Funk**

PALEONTOLOGY

A fiery demise

It is well known that many large vertebrate species went extinct during the late Pleistocene in most regions of the world. What caused these extinctions remains debated, although both climate change and human impacts have been implicated. O'Keefe *et al*. used the extensive fossil record created by the entrapment of animals in the La Brea tar pits in conjunction with nearby core samples and found a clear relationship between an increase in fire—and fire-related ecosystems—and large mammal extinction. The authors argue that this increase in fire may have resulted from climate change–induced warming and drying in conjunction with increasing impacts of humans in the system. —SNV

Science, abo3594, this issue p. 746

HUMAN DEVELOPMENT

A yolk masterstroke

The yolk sac (YS) is a membranous structure attached to the developing embryo that acts to support hematopoiesis, metabolism, and coagulation. Our current understanding of its role in human development has been limited by a reliance on nonhuman model systems. Goh *et al*. used single-cell RNA sequencing, light-sheet microscopy, and RNAscope-based in situ hybridization to generate a human YS atlas derived from 10 samples spanning 4 to 8 postconception weeks or Carnegie stages 10 to 23. The authors found that endoderm in human YS, but not in murine YS, provides hematopoietic growth factors. Furthermore, in humans, the YS is the dominant source of early erythropoiesis, unlike in mice, in which the liver also plays a role. Finally, the authors report that human YS can fuel the accelerated production of macrophages from hematopoietic stem and progenitor cells independently of monocytes. —STS

Science, add7564, this issue p. 747

CANCER

Using a chaperone to fight cancer

KRAS is one of the most common oncogenes, but unfortunately it is also commonly thought of as "undruggable" because it lacks a suitable binding pocket for small-molecule drug candidates. To get around this limitation, Schulze *et al*. built on observations from natural product–derived drugs to go after oncogenic KRAS indirectly (see the Perspective by Liu). The authors identified a naturally occurring compound that binds cyclophilin A, a type of cellular chaperone, and then modified this compound to also bind oncogenic mutant KRAS in a three-way complex. The authors used this approach to design multiple small molecules that effectively bound mutant KRAS in complex with cyclophilin A. These molecules were very effective at inhibiting the downstream pathways involved in cell proliferation and at suppressing tumor growth in multiple models. —YN

Science, adg9652, this issue p. 794; see also adj1001, p. 729

OPTICS

Making superlenses super

In most imaging techniques, the smallest feature sizes that can be resolved are on the order of the wavelength of light used for illumination. Several techniques have been developed that can resolve subwavelength features. Of these, superlenses fabricated from plasmonic materials and metamaterials suffer optical losses that limit their performance. Guan *et al*. show that illumination with synthetic frequency waves, waveforms that that are temporally attenuated, can retrieve subwavelength features, thus making their superlenses truly super. This work demonstrates a practical approach to overcoming intrinsic losses in plasmonic systems and shows that there is potential for substantial improvements in imaging and sensing capabilities. —ISO

Science, adi1267 this issue p. 766

MOLECULAR BIOLOGY

How POT1 protects human telomeres

Mammalian chromosomes are capped with telomeric DNA that is mostly double-stranded but terminates in a single-stranded overhang. A multiprotein complex called shelterin coats telomeric DNA to protect chromosome ends from being recognized as DNA breaks. Tesmer *et al*. have revealed that the human shelterin protein POT1 protects the telomeric double-stranded–single-stranded DNA junction. Only one of the two mouse POT1 proteins binds this junction, which explains its sufficiency for end protection. Disrupting junction binding of human POT1 alters the 5′ terminus sequence and marks chromosome ends as sites of DNA damage, demonstrating the importance of this interaction for chromosome end protection. —DJ

Science, adi2436, this issue p. 771

BIOPHYSICS

Bacterial degradation of hydrocarbons

Certain marine bacteria can degrade small-molecule hydrocarbons, but there is still limited understanding on how this process works in biofilms. Prasad *et al*. show that one such bacterium, *Alcanivorax borkumensis*, initially forms a spherical biofilm around a droplet of hexadecane, which subsequently grows and buckles (see the Perspective by McGenity and Laissue). This transition is caused by an initial limited interaction with the oil by only some of the cells, followed by rapid cell growth and division that distorts the shape of the biofilm, leading to an increase in the surface area and acceleration in the rate of consumption. Adhesion of aligned rod-shaped bacterial cells to the oil stabilizes the tube-like protrusions. The addition of surfactants commonly used to disperse marine oil spills disrupts the biofilms, and the cells return to their spherical morphology. —MSL

Science, adf3345, this issue p. 748; see also adj4430, p. 728

CORONAVIRUS

Coopting virus-neutralizing antibodies

The emergence of severe acute respiratory syndrome coronavirus 2 (SARS-CoV-2) stimulated interest in repurposing neutralizing antibodies against related viruses such as SARS-CoV-1, which caused a smaller outbreak in 2002–2004. Zhao *et al*. sought to engineer mutations in a SARS-CoV-1–neutralizing monoclonal antibody isolated from a convalescent donor to enable this antibody to neutralize SARS-CoV-2. A candidate engineered antibody blocked SARS-CoV-2 infection of cells in vitro and prophylactically protected hamsters from viral challenge. These results highlight the potential of this approach for refocusing an existing antibody to neutralize a related virus. —JFF

Sci. Signal. (2023) 10.1126/scisignal.abk3516

CELL BIOLOGY

Taking cell atlases a step further

Cell atlases categorize single cells into different types on the basis of molecular features, including the transcriptome and epigenome. However, diversity within the categories in these static atlases have raised questions about how best to define cell types. In a Perspective, Fleck

et al. suggest that cell type is not only defined by the developmental history of the cell and its current set of features, it is also linked to how the cell responds to perturbation. The authors propose that atlasing these perturbation responses, which together are referred to as the phenoscape, in primary tissue and in three-dimensional human cell culture models could provide a more complete understanding of cell types. —SAL

Science, adf6162, this issue p. 733

molecular details of how MyoD family inhibitor proteins interact with Piezo channels and regulate their gating. They identified an interacting interface that likely represents a scaffold that might be leveraged to generate Piezo-targeted therapeutics. —MMa

Science, adh8190, this issue p. 799

CORONAVIRUS

Protective parasites

Parasitic helminths generate a type 2 immune response that can persist even after clearance of an infection. Using a mouse model of roundworm infection, Oyesola *et al.* found that prior exposure to lung-migrating helminths protects transgenic K18-hACE2 mice against SARS-CoV-2 infection. Pulmonary macrophages from roundworm-infected mice adopted a type 2 transcriptional and epigenetic signature that persisted after parasite clearance and at least 45 days after infection. SARS-CoV-2–specific $CD8^+$ T cell responses were driven by alveolar macrophages and were required for helminth-mediated protection. These results demonstrate that lung-migrating helminths reprogram lung immune homeostasis, leading to enhanced protection against subsequent SARS-CoV-2 infection. —CO

Sci. Immunol. (2023) 10.1126/sciimmunol.adf8161

AGING

Targeting senescence with CAR T cells

Cellular senescence contributes to aging and to aging-associated diseases, and depletion of senescent cells has shown potential for treating such diseases. Yang *et al.* developed chimeric antigen receptor (CAR) T cells targeting Natural Killer Group 2 Member D (NKG2D) ligands, which are highly expressed on senescent cells. The CAR, which is composed of the extracellular domain of NKG2D and the intracellular signaling domains of two receptors, was able to efficiently drive killing of senescent cells in vitro and in vivo in both aged mice and aged nonhuman primates. Aged mice treated with NKG2D-CAR T cells exhibited improved physical performance after treatment. These data support the further development of NKG2D-CAR T cells for aging-associated pathologies. —CM

Sci. Transl. Med. (2023) 10.1126/scitranslmed.add1951

PROTEIN DESIGN

Two-state two-step

Natural proteins often adopt multiple conformational states, thereby changing their activity or binding partners in response to another protein, small molecule, or other stimulus. It has been difficult to engineer such conformational switching between two folded states in human-designed proteins. Praetorius *et al*. developed a hinge-like protein by simultaneously considering both desired states in the design process. The successful designs exhibited a large shift in conformation upon binding to a target peptide helix, which could be tailored for specificity. The authors characterized the protein structures, binding kinetics, and conformational equilibrium of the designs. This work provides the groundwork for generating protein switches that respond to biological triggers and can produce conformational changes that modulate protein assemblies. —MAF

Science, adg7731, this issue p. 754

Illustration of a designed protein that can switch between two different conformational states

IN OTHER JOURNALS

Edited by **Caroline Ash** *and* **Jesse Smith**

ENERGY

Another route to refrigeration

Space cooling accounts for 20% of the world's total energy consumption but relies on refrigerants with large global-warming potential. Zhou *et al.* now demonstrate an alternative to refrigerant-based cooling that uses a compression-based regenerative elastocaloric device that performs phase transformations during which latent heat is absorbed. This tubular nickel–titanium device achieves a temperature difference between the hot and cold sides of 50 kelvin and a cooling power of more than 200 watts. —ECF

Joule (2023) 10.1016/j.joule.2023.07.004

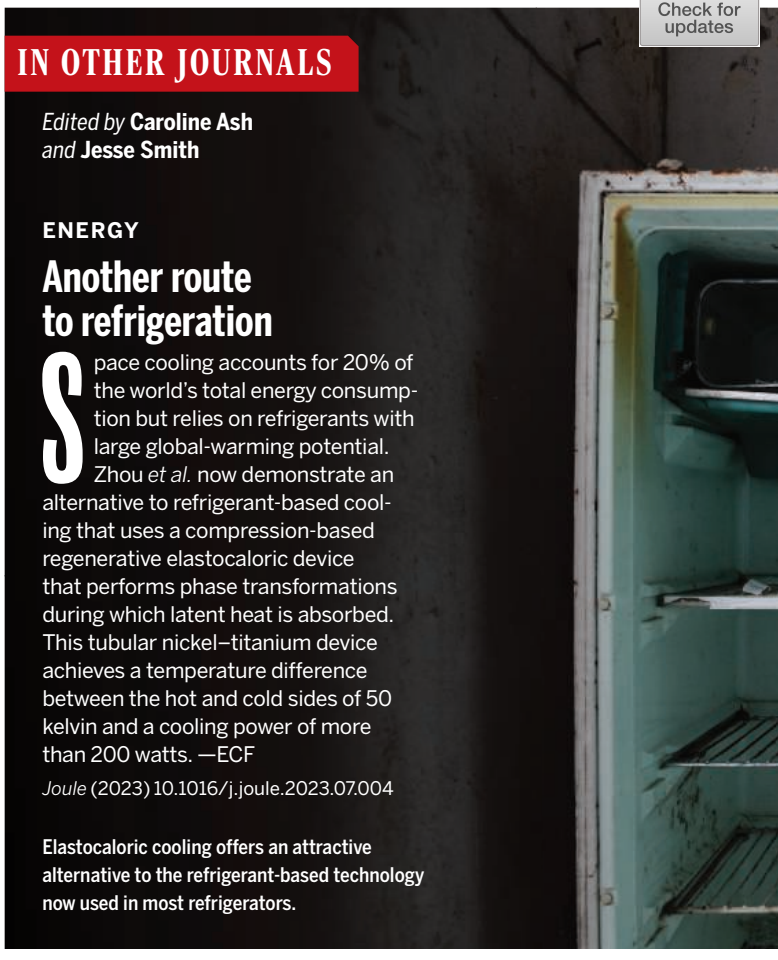

Elastocaloric cooling offers an attractive alternative to the refrigerant-based technology now used in most refrigerators.

CELL BIOLOGY

Spartin mediates lipophagy

Lipid droplets are important for energy storage and lipid homeostasis. Selective autophagy of lipid droplets, called lipophagy, is required for their catabolism, but how lipid droplets are targeted for lipophagy remains unclear. Working in cultured human cells, Chung *et al.* elucidated a role for spartin, a protein that localizes on lipid droplets and endosomal compartments, in lipophagy. Spartin functions as a receptor on lipid droplets that interacts with the core autophagy machinery. Thus, spartin is required to deliver lipid droplets to lysosomes for triglyceride mobilization. Mutations in the gene encoding spartin lead to Troyer syndrome, a form of hereditary spastic paraplegia. Indeed, blocking spartin function caused lipid droplet and triglyceride accumulation in mouse and cultured human neurons. —SMH

Nat. Cell Biol. (2023) https://doi.org/10.1038/s41556-023-01178-w

IMMUNOLOGY

A MASTerful compilation

Mast cells (MCs) are a class of granulocytes that release inflammatory mediators in response to an array of stimuli. MCs are currently organized into mucosal MCs (MMCs), found in the gut and lung, and connective tissue–type MCs (CTMCs), located primarily in the skin and peritoneal cavity. To gain a picture of the heterogeneity and ontogeny of MC subsets, Tauber *et al.* integrated several single-cell datasets of mouse and human MC populations across a variety of tissues. The authors found in mice that *Mrgprb2*$^+$ and

Mrgprb2^{-} MCs are transcriptionally distinct populations that generally recapitulate the CTMC–MMC dichotomy. Seven other distinct MC transcriptomic profiles in humans were also apparent, although whether these are transcriptomic states or genuine MC subsets remains an open question. —STS

J. Exp. Med. (2023) 10.1084/jem.20230570

CONSERVATION

Sequencing a sprinkle of shark dust

Genomics is growing increasingly important for identifying endangered species that have been traded illicitly, but many sequencing methods are expensive or species specific. Prasetyo *et al.* performed meta-barcoded high-throughput sequencing of trace DNA from seven locations in Indonesia engaged in illegal trading of sharks and rays. They were able to assign most of these reads to individual species, but some could only be mapped to family or genus. Although there was good agreement between the species identified using dust and concomitantly collected tissue samples, the authors identified more species using dust. Both methods, however, identified multiple endangered species being processed in these locations, demonstrating the need for better and cheaper genetic tools with which to monitor the illegal wildlife trade. —CNS

Conserv. Lett. (2023) 10.1111/conl.12971

PHOTOCHEMISTRY

Stabilizing excited molybdenum complexes

Complex ligands are usually needed to stabilize long-lived photoexcited states of earth-abundant metals. Kitzmann *et al.* found that a simple tripodal polypyridyl ligand, 1,1,1-tris(pyrid-2-yl)ethane, stabilizes a molybdenum tricarbonyl complex that exhibits intense deep-red phosphorescence with a lifetime of several hundred nanoseconds. The lack of *trans* carbon monoxide ligands appears to limit elongation of the molybdenum–carbon bonds and loss of carbon monoxide in the excited state. This complex was used to upconvert green photons to blue photons and to drive a dehalogenation reaction with green light. —PDS

J. Am. Chem. Soc. (2023) 10.1021/jacs.3c03832

BEHAVIOR

Strong storage

Squirrels are known for their caching behavior. Throughout the northern hemisphere, squirrels are seen digging and burying nuts all summer in preparation for winter. As a widely distributed lineage, however, most squirrels live in warm tropical regions, where burying may result in nut deterioration. Noticing nuts suspended in the crooks of trees and shrubs in Hainan Province, China, Xu *et al*. discovered that at least two species of flying squirrel have come up with a storage solution suitable for wet tropical climates. Video footage revealed that *Hylopetes phayrei electilis* and *Hylopetes alboniger* used their incisors to chisel grooves into nuts that had been primarily harvested from *Cyclobalanopsis* trees. The carved nuts allowed secure storage by acting as a tight mortise-tenon joint at branch nodes. —SNV

eLife (2023) 10.7554/eLife.84967

WATER

Water dissociation at the nanoscale

Despite considerable interest in understanding water behavior at the nanoscale regime, the role of confinement on the chemical reactivity properties of water, such as its self-dissociation, remains poorly understood, and various confusing hypotheses have been made based on indirect experimental evidence and simplified theoretical conceptions. Using rigorous first-principles molecular dynamics simulations, Di Pino *et al.* demonstrated that the initial break of the oxygen–hydrogen covalent bond determines the energetics of bulk water dissociation, which unexpectedly does not translate to small system dimensions of only a dozen molecules or pores of widths below 2 nanometers, in the absence of specific interfacial interactions. This work provides a comprehensive picture of water dissociation at the nanoscale, which should help to eliminate some of the contradictions in previous findings. —YS

Angew. Chem. Int. Ed. (2023) 10.1002/anie.202306526

RESEARCH ARTICLE SUMMARY

PALEONTOLOGY

Pre–Younger Dryas megafaunal extirpation at Rancho La Brea linked to fire-driven state shift

F. Robin O'Keefe*, Regan E. Dunn, Elic M. Weitzel, Michael R. Waters, Lisa N. Martinez, Wendy J. Binder, John R. Southon, Joshua E. Cohen, Julie A. Meachen, Larisa R. G. DeSantis, Matthew E. Kirby, Elena Ghezzo, Joan B. Coltrain, Benjamin T. Fuller, Aisling B. Farrell, Gary T. Takeuchi, Glen MacDonald, Edward B. Davis, Emily L. Lindsey

INTRODUCTION: At the end of the Pleistocene, most of Earth's large mammals (megafauna) became extinct. These extinctions occurred at different times globally, resulting in a drastic reorganization of terrestrial ecosystems. Despite decades of research on extinction causality, the relative importance of late-Quaternary climate changes and spreading human impacts have been difficult to disentangle because poor chronological resolution in the fossil record has precluded alignment of these rapidly occurring, tightly linked phenomena.

RATIONALE: The Rancho La Brea (RLB) locality in Southern California provides a unique opportunity to investigate decadal-scale changes in megafaunal populations and community composition across the latest Pleistocene. At this site, naturally occurring asphalt seeps entrapped and preserved the bones of hundreds, and in some cases thousands, of individuals from numerous megafaunal species across the last 50,000 years of the Pleistocene. Nearly all of these osteological specimens preserve original collagen, which permits precise radiocarbon dating analysis.

RESULTS: We obtained radiocarbon dates on 172 specimens from seven extinct and one extant species: *Smilodon fatalis*, *Aenocyon dirus*, *Panthera atrox*, *Bison antiquus*, *Equus occidentalis*, *Paramylodon harlani*, *Camelops hesternus*, and *Canis latrans*, spanning 15.6 to 10.0 thousand calendar years before present (ka). We used the resulting high-resolution chronology of entrapment at RLB to analyze population dynamics across this time interval and the timing of local disappearance for different taxa. To investigate the potential roles of late-Quaternary environmental change and human activities in driving the observed patterns, we compared our analyses of population structure and megafaunal extirpation against well-resolved regional and continental paleoclimatic proxies, vegetation records, and modeled human demographic growth. We used time-series modeling to investigate the dynamics of ecosystem change and evaluate causal relationships among these different phenomena.

Modeling of extinction timing using several methods established that all taxa except coyotes were extirpated from RLB by 12.9 ka, before the onset of the Younger Dryas and well be[fore] the continental extinction of North Amer[ican] megafauna. The disappearance of all taxa was synchronous except for camels and sloths, which disappeared a few hundred years earlier in concert with aridification and tree loss during the Bølling–Allerød. The simultaneous disappearance of *Smilodon*, *Aenocyon*, *Panthera*, *Equus*, and *Bison antiquus* coincided with a regional ecological state shift characterized by floral community reorganization and unprecedented fire activity. Time-series modeling strongly implicates humans as the primary cause of the state shift and resulting extinctions.

CONCLUSION: Our data document a transition from a postglacial megafaunal woodland to a human-mediated chaparral ecosystem in Southern California before the onset of the Younger Dryas. This transition began with gradual opening and drying of the landscape over two millennia, and terminated in an abrupt (300-year) regime shift characterized by the complete extirpation of megafauna and unprecedented fire activity. This state shift appears to have been triggered by human-ignited fires in an ecosystem stressed by rapid warming, a megadrought, and a millennial-scale trend toward the loss of large herbivores from the landscape. This event parallels processes occurring in Mediterranean ecosystems today. ■

The list of author affiliations is available in the full article online.
*Corresponding author. Email: okeefef@marshall.edu
Cite this article as F. R. O'Keefe *et al.*, *Science* **381**, eabo3594 (2023). DOI: 10.1126/science.abo3594

READ THE FULL ARTICLE AT
https://doi.org/10.1126/science.abo3594

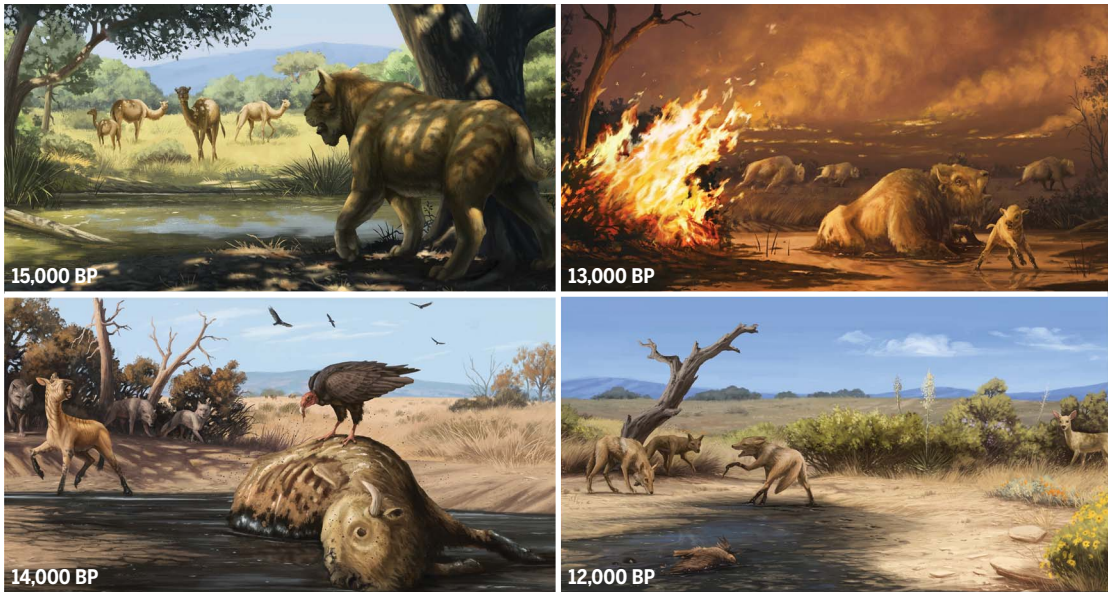

Sequence of ecological events as recorded at Rancho La Brea, California. Top left: conditions around the tar pits were moist and cool, with abundant trees and megafaunal mammals. Bottom left: the onset of postglacial warming and drying begins as human pressure on herbivores increases. Top right: the synergy between climatic and human impacts enables a sudden ecological state transition characterized by unprecedented fire activity. Bottom right: a chapparal ecosystem is established; megafauna are extinct, and only coyote entrapment continues at the tar pits.

ILLUSTRATIONS BY C. TOWNSEND, COURTESY OF THE NATURAL HISTORY MUSEUMS OF LOS ANGELES COUNTY

RESEARCH ARTICLE

PALEONTOLOGY

Pre–Younger Dryas megafaunal extirpation at Rancho La Brea linked to fire-driven state shift

F. Robin O'Keefe[1,2]*, Regan E. Dunn[2,3], Elic M. Weitzel[4], Michael R. Waters[5], Lisa N. Martinez[6], Wendy J. Binder[2,7], John R. Southon[8], Joshua E. Cohen[2,7,9], Julie A. Meachen[2,10] Larisa R. G. DeSantis[2,11,12], Matthew E. Kirby[13], Elena Ghezzo[14,15], Joan B. Coltrain[16], Benjamin T. Fuller[17], Aisling B. Farrell[2], Gary T. Takeuchi[2], Glen MacDonald[6], Edward B. Davis[14,15], Emily L. Lindsey[2,3,18]

The cause, or causes, of the Pleistocene megafaunal extinctions have been difficult to establish, in part because poor spatiotemporal resolution in the fossil record hinders alignment of species disappearances with archeological and environmental data. We obtained 172 new radiocarbon dates on megafauna from Rancho La Brea in California spanning 15.6 to 10.0 thousand calendar years before present (ka). Seven species of extinct megafauna disappeared by 12.9 ka, before the onset of the Younger Dryas. Comparison with high-resolution regional datasets revealed that these disappearances coincided with an ecological state shift that followed aridification and vegetation changes during the Bølling-Allerød (14.69 to 12.89 ka). Time-series modeling implicates large-scale fires as the primary cause of the extirpations, and the catalyst of this state shift may have been mounting human impacts in a drying, warming, and increasingly fire-prone ecosystem.

The disappearance of two-thirds of Earth's large mammals outside of Africa at the end of the last Ice Age had profound impacts on global ecosystems (*1*, *2*), was the largest extinction event of the Cenozoic (*3*), and represents the initial pulse in the ongoing global extinction crisis that will likely result in Earth's sixth mass extinction (*4*). Across different continents, disappearances of megafauna (animals weighing >45 kg) coincided with both late-Quaternary climate changes and human colonization and growth (*5*–*7*). However, the causes, dynamics, and consequences of the end-Pleistocene extinctions remain poorly understood despite their obvious relevance for modern global change research. These lines of inquiry have been hobbled by the lack of reliably dated megafaunal fossils and the resulting lack of chronological precision of extinction timing relative to environmental and human demographic changes (*8*, *9*).

We radiocarbon dated fossils from the Rancho La Brea lagerstätte in Southern California to investigate the timing and dynamics of Pleistocene megafaunal disappearance in this region. The asphaltic deposits at La Brea preserve a nearly continuous record of megafaunal occupation of the Los Angeles Basin from >55 thousand calendar years before present (ka) through the Holocene (*10*), but a lack of stratigraphic control has limited inferences about megafaunal population structure, their history, and their ultimate demise. We developed a high-resolution radiocarbon chronology for the eight most common mammal species at La Brea [sabertoothed cat (*Smilodon fatalis*), dire wolf (*Aenocyon dirus*), coyote (*Canis latrans*), American lion (*Panthera atrox*), ancient bison (*Bison antiquus*), western horse (*Equus occidentalis*), Harlan's ground sloth (*Paramylodon harlani*), and yesterday's camel (*Camelops hesternus*)] from 15.6 to 10.0 ka (*11*) (Table 1). We estimated the timing of species disappearances based on last appearance dates and statistical modeling of extinction timing (*11*, *12*). We also inferred changes in entrapment rates over time using summed probability distributions (SPDs). Sampling effort in our analysis was approximately equal among species (rather than proportional to species occurrence); therefore, SPDs reflect changes in intraspecific entrapment rates and relative population sizes over time, but not absolute population sizes (*11*).

To investigate how large mammals were affected by late-Quaternary environmental and anthropogenic changes, we aligned the La Brea record of faunal change with well-resolved

[1]Department of Biological Sciences, Marshall University, Huntington, WV, USA. [2]La Brea Tar Pits and Museum, Natural History Museums of Los Angeles County, Los Angeles, CA, USA. [3]Department of Earth Sciences, University of Southern California, Los Angeles, CA, USA. [4]Department of Anthropology, University of Connecticut, Storrs, CT, USA. [5]Center for the Study of the First Americans, Department of Anthropology, Texas A&M University, College Station, TX, USA. [6]Department of Geography, University of California, Los Angeles, Los Angeles, CA, USA. [7]Department of Biology, Loyola Marymount University, Los Angeles, CA, USA. [8]Department of Earth System Science, University California, Irvine, Irvine, CA, USA. [9]Department of Biology, Pace University, New York, NY, USA. [10]Department of Anatomy, Des Moines University, Des Moines, IA, USA. [11]Department of Biological Sciences, Vanderbilt University, Nashville, TN, USA. [12]Department of Earth and Environmental Science, Vanderbilt University, Nashville, TN, USA. [13]Department of Geological Sciences, California State University, Fullerton, Fullerton, CA, USA. [14]Department of Environmental Sciences, Informatics, and Statistics, Università Ca' Foscari Venezia, Venice, Italy. [15]Department of Earth Sciences, University Oregon, Eugene, OR, USA. [16]Department of Anthropology, University of Utah, Salt Lake City, UT, USA. [17]Géosciences Environnement Toulouse, UMR 5563, CNRS, Observatoire Midi-Pyrénées, Toulouse, France. [18]Institute of the Environment and Sustainability, University of California, Los Angeles, Los Angeles, CA, USA.
*Corresponding author. Email: okeefef@marshall.edu

Table 1. Last occurrences and modeled extirpation times for five extinct taxa at RLB. Dates are last occurrence in radiocarbon years (RC), calibrated last occurrence in years before 1950, and statistical GRIWM estimates of extirpation time [see section 1 of the supplementary materials (*11*)]. Most densely sampled taxa share a statistically identical extirpation time except for *Camelops*, which predeceases the others (**$P < 0.0001$, Welch's T). *Panthera* and *Paramylodon* have insufficient sample sizes to permit meaningful numerical comparison, but *Paramylodon* may disappear relatively early.

Taxon	No. dated	Last occurrence, RC, ±30	Last occurrence, ka 1-sigma	GRIMW extirpation estimate, ka 1-sigma
Aenocyon dirus	29	11,135	13,082; 12,965–13,117	12,908; 12,763–12,996
Bison antiquus	27	11,260	13,144; 13,097–13,183	12,932; 12,836–13,004
Camelops hesternus	17	11,820	13,683; 13,595–13,770	13,512**; 13,335–13,609
Equus occidentalis	27	11,100	13,029; 12,926–13,097	12,856; 12,737–12,929
Smilodon fatalis	30	11,090	13,021; 12,923–13,094	12,910; 12,821–12,998
Panthera atrox	8	11,160	13,097; 13,116–13,078	12,890; 12,744–13,008
Paramylodon harlani	8	11,940	13,806; 13,995–13,763	13,707; 13,580–13,804
All extinct				**12,957; 12,894–13,066**

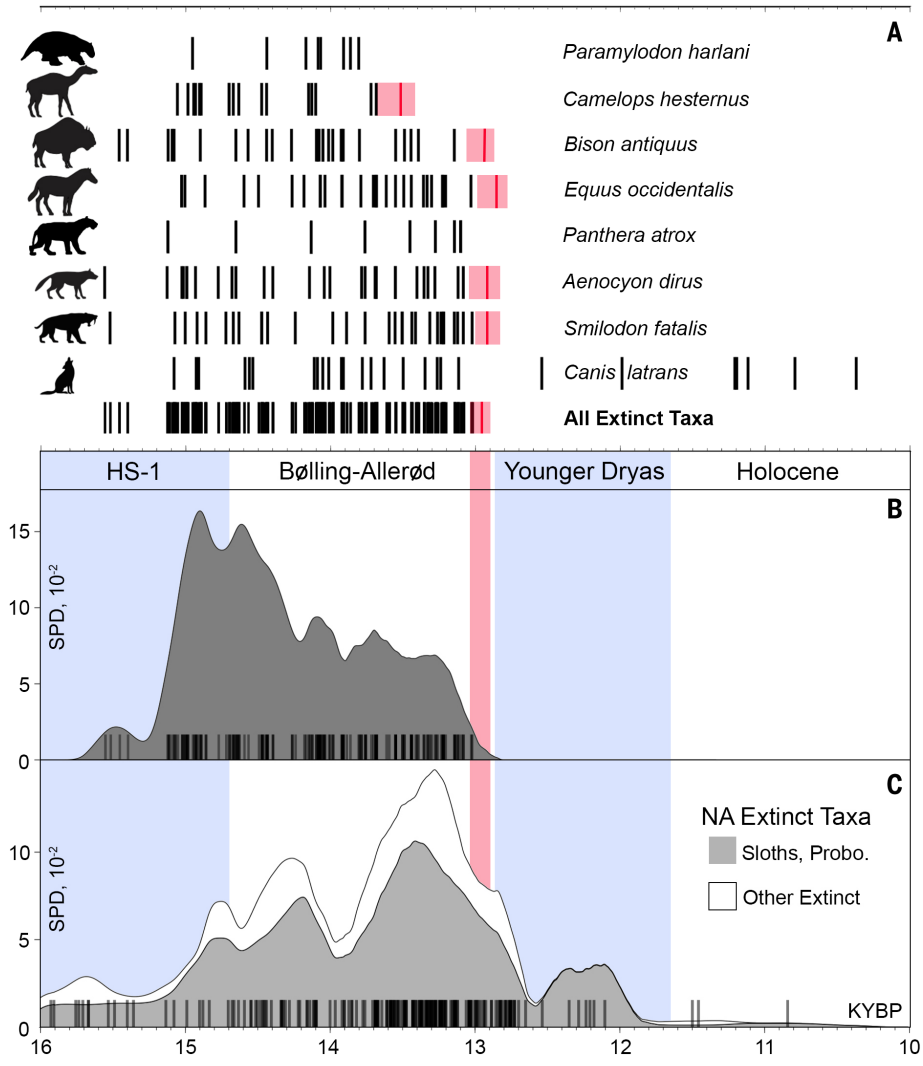

Fig. 1. Record of relative megafaunal occurrence and extirpation at La Brea compared with the North American Record. (**A**) Median calibrated dates for *Camelops* (*n* = 17), *Bison* (*n* = 27), *Equus* (*n* = 27), *Paramylodon* (*n* = 8), *Panthera* (*n* = 8), *Aenocyon* (*n* = 29), *Smilodon* (*n* = 30), *Canis latrans* (*n* = 27), and all extinct taxa pooled (*n* = 144) at La Brea. Hash marks are single, calibrated median carbon dates. The period HS-1 refers to Heinrich Stadial 1. Red lines and confidence intervals are extinction date estimates generated using the GRIWM method [see the supplementary materials section 2 (*11*)]. Last occurences and modeled extirpation times are reported in Table 1. (**B**) SPDs for all extinct taxa at La Brea. The overall trend is long-term decline followed by a precipitous fall to 0 starting at ~13.3 ka (**C**) Stacked SPDs for all extinct North American megafauna south of the Laurentide Ice Sheet, excluding La Brea. Dates drawn from (*9*) and (*14*) and a literature review were subjected to strict quality control and divided into proboscideans and sloths (light gray) and all other extinct species (dark gray). The regional extirpation precedes the continental extinction but coincides with continental decline.

regional paleoclimate, charcoal, and vegetation records and with continental-scale analyses of megafaunal extinction and human demographic growth in North America. Taken together, these data allow the first robust statistical modeling of extinction causality in Southern California.

Extinction timing and dynamics

We obtained accelerator mass spectrometry radiocarbon dates on 172 megafaunal individuals from La Brea (Fig. 1, A and B, and data S1) using a customized protocol for dating bone collagen from asphaltic contexts (*11*, *13*). These dates were then compared with a vetted compilation of published radiocarbon dates on North American megafauna south of Beringia [data S2; (*11*)]. The new dates presented here nearly double the number of reliable megafaunal dates for non-Beringian North America, and establish a precise chronology of Pleistocene megafaunal extirpation in Southern California. All extinct mammals dated in this study have last occurrence dates older than 13.00 ka, with a modeled extirpation time estimate across all taxa of 13.07 to 12.89 ka [using the Gaussian-Resampled Inverse-Weighted McInerney (GRIMW) extinction estimator; Table 1], placing the all-taxon extirpation almost certainly before the onset of the Younger Dryas (12.87 ± 0.03 ka) (*14*). Camels and ground sloths disappeared earlier, with last occurrences of 13.68 and 13.81 ka, respectively, whereas the disappearances of horses (13.03 ka), bison (13.14 ka), saber-toothed cats (13.02 ka), American lions (13.10 ka), and dire wolves (13.08 ka) are statistically contemporaneous (Table 1).

The disappearance of megafaunal species at La Brea precedes the North American megafaunal extinction by at least 1000 years (Fig. 1) but coincides with a precipitous decline in summed probability for North American megafauna at ~13.3 ka (Fig. 1C). Only 25 reliable, direct dates on North American megafauna fall within the Younger Dryas; more than half of these are on proboscideans, which were not dated in this study. Just six dates fall in the Holocene (after 11.7 ka), and all of these were obtained decades ago and should be redated (*11*). Of the seven extinct taxa examined in this study, only one (*Camelops*) has younger dates from elsewhere in North America. For *Smilodon*, *Panthera*, *Aenocyon*, *Equus*, and *Paramylodon*, the new dates reported here are the youngest reliably dated occurrences for North America. Although our database does not include any chronologically younger specimens diagnosed as *B. antiquus*, some authors have argued that this species survived into the mid-Holocene. *Bison bison*, the presumed chronospecies of *B. antiquus*, survives in inland areas of the continent today (*15*).

Occurrence rates of extinct taxa at La Brea decline gradually across the Bølling-Allerød, before beginning a precipitous drop ~13.25 ka. Herbivore and carnivore histories differ across this interval; herbivore summed probability declines steadily from 14.1 ka to the extinction (Fig. 2), whereas carnivore summed probability fluctuates across the interval. These differences in entrapment distributions are statistically significant, as determined by a mark permutation test [see Fig. 2 and section 2 of the supplementary materials (*11*)]. The numbers of extinct carnivores and herbivores dated are approximately equal, and the relative sizes of SPDs normalized, so the null expectation is that the entrapment rates should be equivalent. The observed bias toward carnivore entrapment just before the extinction may reflect increased predator reliance on asphalt-entrapped prey as large herbivores become scarce on the landscape. Coyotes do not mirror this late increase in entrapment frequency, possibly reflecting their ability to switch to smaller prey as large prey disappear and the competition with larger carnivores increases (*16*). Further scrutiny of the herbivore summed probabilities

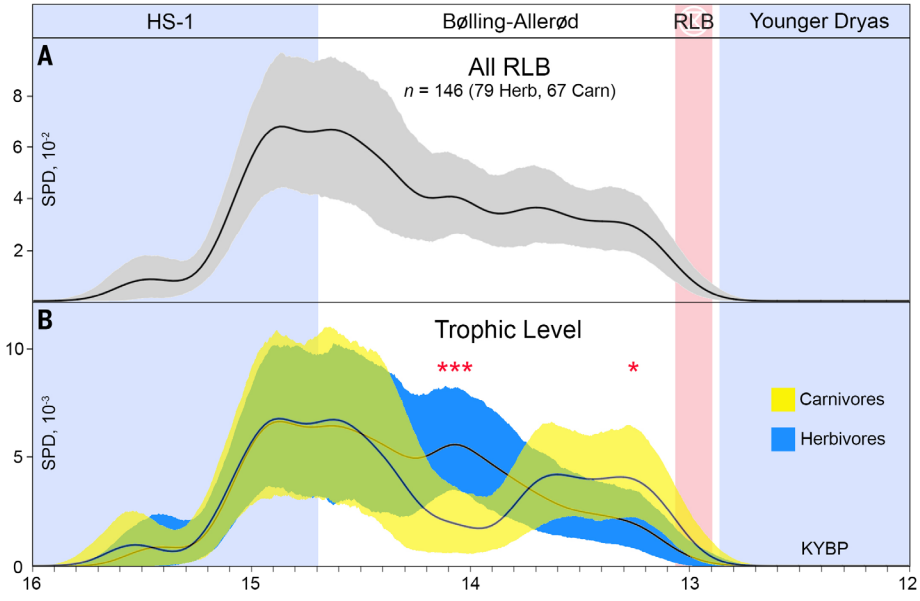

Fig. 2. Resampled summed probability distributions for the La Brea radiocarbon record. Lines are the SPDs for all taxa or indicated groups; envelopes are 95% confidence intervals based on 1000 bootstrap replicates. (**A**) All La Brea dates during the extinction interval; note that the terminal decline begins at ~13.2 ka. (**B**) Taxa split out by trophic level, with distributions for all extinct carnivores (*N* = 67, yellow) and all extinct herbivores (*N* = 79, blue). Red stars indicate areas where the curves differ significantly, as determined by a mark permutation test (*11*).

indicates a transition from a browser-dominated to a grazer-dominated herbivore community (*11*) (Fig. 3). Although the relative proportion of bison remains stable throughout the Bølling-Allerød, camels become less common and horses more common over time (Fig. 3). This changing assemblage likely reflects changing vegetation that favored grazers over browsers (*17*, *18*).

Coyotes (*Canis latrans*) are one of the few large mammal species to survive the extinction, so they serve as a "taphonomic control taxon" (*19*). Coyote occurrence rates drop coincident with those of La Brea megafauna, but occurrences resume at 12.54 ka (Fig. 1) and this continues into the Holocene. The continued deposition of postextinction coyotes is prima facie evidence that the potential for large mammal entrapment remained at La Brea. The absence of megafaunal deposition reflects their extirpation from the region rather than a taphonomic artifact. Neither taphonomic effects nor other sampling biases can explain the differences in herbivore and carnivore demographics noted above. However, these demographic shifts and subsequent extirpations coincided with profound ecological transitions in Southern California.

Climate and vegetation history

Climate warming from Heinrich Stadial 1 through the Bølling-Allerød in the Northern Hemisphere is well documented (*20*), but late-Pleistocene climate dynamics vary regionally. In Southern California, temperature and precipitation proxies indicate that the megafaunal disappearance at La Brea follows a period of significant regional warming and drying, particularly winter drying (*11*, *21*, *22*) (Fig. 3). Marine cores from the Santa Barbara Basin show warming of surface waters of 7 to 8°C from 17 to 15 ka (*23*). Mean annual air temperature proxy records from inland Lake Elsinore, ~100 km southeast of La Brea, show a later warming of 5.6°C between 14.0 and 13.0 ka and an additional 4.4°C warming from 13.0 to 11.8 ka (*24*) (Fig. 3C). Deglacial changes in hydroclimate toward drying at the onset of the Bølling-Allerød (14.7 ka) are evidenced at Lake Elsinore by decreased sand input from runoff, a proxy for precipitation (Fig. 3D), and leaf wax hydrogen isotopic records (*21*, *24*, *25*). Additionally, a steep rise in salinity caused by increased evaporation relative to freshwater input into Lake Elsinore is indicated between 13.7 and 13.2 ka (Fig. 3D) (*24*).

Pollen records from Lake Elsinore track the floral response to this warming and drying trend. Juniper (*Juniperus* spp.), a coniferous shrub or tree, declines with postglacial warming and drying starting ~16 ka (Fig. 4) after being dominant throughout the Last Glacial Maximum. This decline has been documented in most California pollen records (*22*, *26*–*28*). Oak (*Quercus* spp.) increases sharply at the beginning of the Bølling-Allerød, peaking in abundance at 13.6 ka. Then, between 13.2 and 12.9 ka, both oak and juniper decline, with almost complete extirpation of juniper by 12.87 ka. These taxa are then replaced by species with high fire resistance, including fire-tolerant pines (*29*) and grass and chaparral taxa (*30*). Although juniper is generally drought tolerant, it is vulnerable to soil water depletion from dry winters followed by hot, dry summers (*31*) and has low fire resistance (*32*). Today, severe juniper mortality is occurring at low-elevation sites in the Southwestern United States due to warming and drought (*31*).

To quantify floristic change during the extinction interval, we performed a nonmetric multidimensional scaling (NMDS) (Fig. 3E) (*11*) analysis on published Lake Elsinore pollen counts (*29*). NMDS axis 1 (NMDS1) scores reflect proportional changes of woodland tree (*Juniperus*, *Pinus*, and *Quercus*) versus chaparral taxa (Asteraceae, Rhamnaceae/Rosaceae, Amaranthaceae, *Eriogonum*, Cyperaceae, and Poaceae). Lower NMDS1 values indicate more short-statured, open, and xeric vegetation. The primary trend in pollen NMDS1 scores is a decline from 16.0 to 12.0 ka, indicating a drying and opening of habitats that correlates with the pattern of declining herbivore abundance (Fig. 3). The proportional replacement of camels and sloths by horses in the herbivore community (Fig. 3B) is consistent with this transition to a more open and herbaceous vegetational regime. Breakpoint analysis of the NMDS1 time series detects two periods of directional change in vegetation occurring at 13.88 and 13.21 ka (Fig. 3E). These breakpoints separate three stable trends in the vegetation: (i) the gradual opening and drying of habitats from 16.0 to 13.88 ka; (ii) a brief stabilization of this trend between 13.88 and 13.21 ka; and (iii) a rapid and punctuated decline in tree cover 13.21 to 12.90 ka, which is followed by continued opening of landscapes. Given the severity and rapidity of this last interval, we interpret this NMDS shift as a period of drought, probably driven primarily by evaporative water loss in response to rapidly rising temperatures (Fig. 3C). The modest decline in the sand-based proxy for runoff indicates that decreased precipitation may be contributing to increased aridity. A sharp increase in salinity concurrent with the substantial drop in NMDS values supports the inference of aridity during this time (Fig. 3D). Impacts to vegetation during this event include: (i) a tripling in the amount of grass pollen from 5 to 15%; (ii) a substantial decline in juniper and oak; (iii) an increase in herbaceous Asteraceae and Cyperaceae; and (iv) a slight increase in fire-adapted pine and chaparral shrubs (Rhamnaceae and Rosaceae). All of this coincides with the terminal decline and extirpation of the La Brea megafauna.

Fire activity

We analyzed charcoal accumulation rates from the Lake Elsinore sediment core (LEDC10-1),

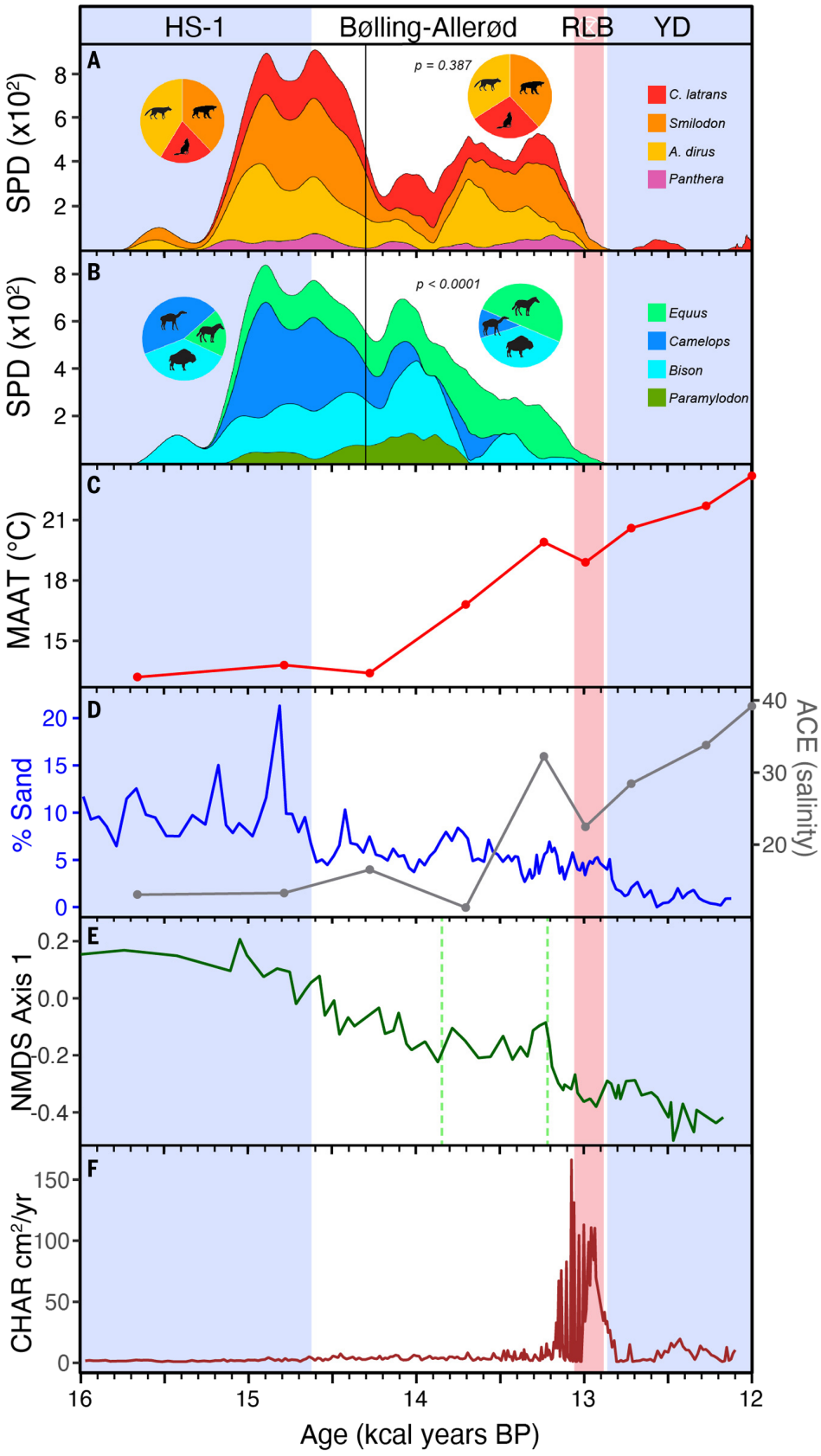

Fig. 3. Summed probability distributions for subsets of the La Brea radiocarbon record and end-Pleistocene records of biotic and abiotic change in Southern California. (**A** and **B**) SPDs for La Brea carnivores (*N* = 67) (A) and herbivores (*N* = 79) (B). The line at 14.3 ka marks the bins for the pie chart and chi-square tests (*11*). Proxy climate data from the Lake Elsinore core (LEDC10-1) including: mean annual air temperature (MAAT; red) derived from (*24*) (C) and sand fraction (blue), a proxy for precipitation (*25*) and salinity (gray) (*24*) (D). The marked rise in salinity reflects increasingly arid conditions driven more by rising temperatures rather than precipitation decrease. (**E**) NMDS1 scores depicting change in pollen composition from Lake Elsinore [see the materials and methods (*11*); data are from (*29*)]. Green vertical lines indicate shifts between regression regimes recovered from a subsidiary breakpoints analysis on pollen NMDS [see section 4 of the supplementary materials and methods (*11*)]. A steady decline in NMDS is followed by a brief stable period, then an abrupt floral transition toward a more open chaparral habitat containing more drought-tolerant and fire-adapted species starting at ~13.3 ka. (**F**) Charcoal particles per square centimeter per year from the Lake Elsinore core. The age model for the Lake Elsinore core, and associated error, can be found in fig. S1 and table S2.

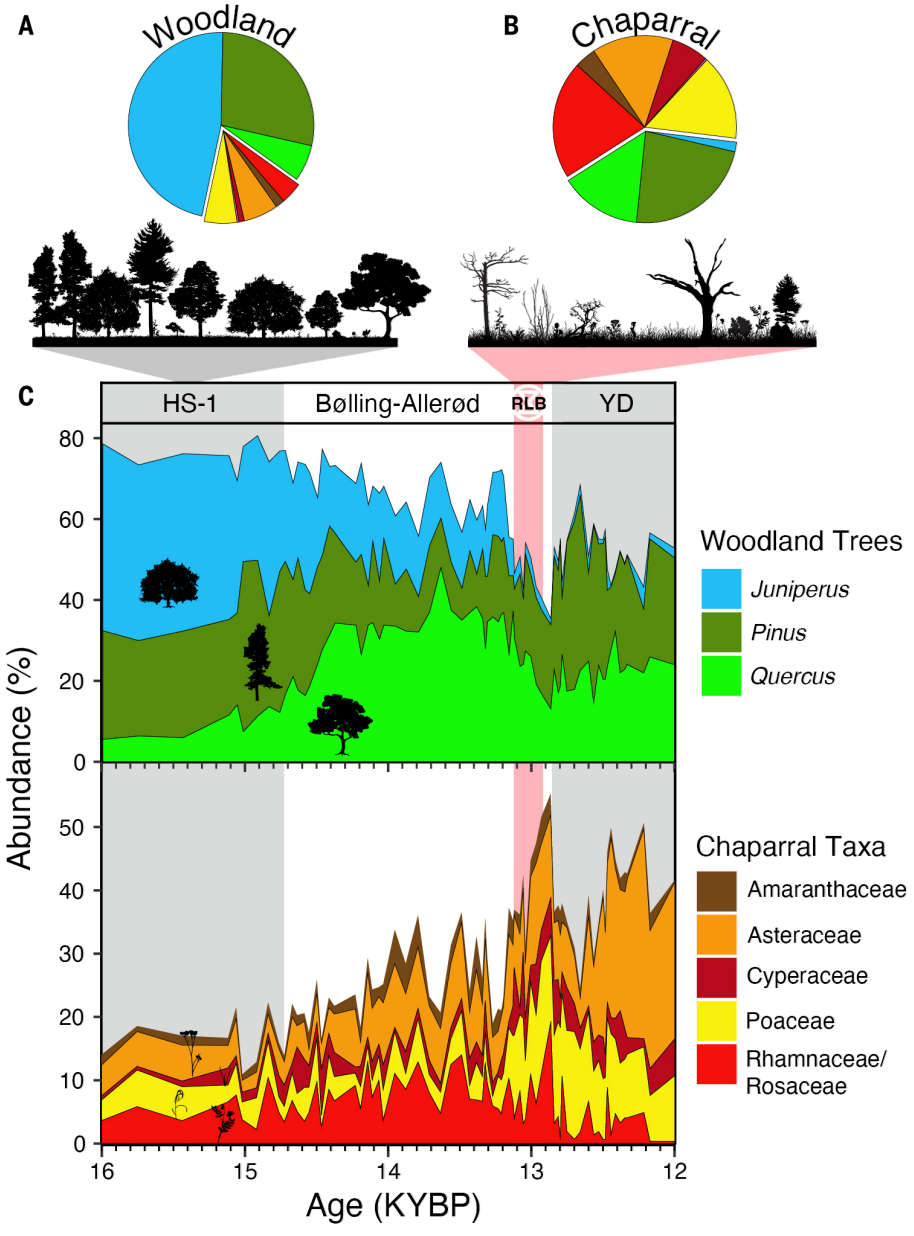

Fig. 4. Record of floral change from 16 to 12 ka based on pollen counts from Lake Elsinore. (**A** and **B**) Pie graphs showing vegetation abundance at 15.4 ka (A) and 13.0 ka (B) from Lake Elsinore (*27*). (**C**) Light gray bars denote the HS-1 and Younger Dryas cooler periods; red bar shows the GRIWM estimate for the La Brea megafaunal extirpation (Fig. 1). A shift from woodland tree dominance to xeric and fire-adapted, grassy and chaparral taxa occurs concurrently with the La Brea regional extinction. Percentages are of taxa representative of chaparral or woodland plant communities only; not all taxa present are shown.

measured as particles per square centimeter per year, from sediment spanning 16.0 to 12.0 ka (*11*) (Fig. 3F). Charcoal accumulation rates are low before the appearance of humans in the archeological record [including during times of previous drought (*29*, *33*)] and increase modestly as humans arrive and the climate warms and dries beginning ~13.5 ka. However, ~13.2 ka, charcoal accumulation rates suddenly increase 30-fold. This interval of significantly heightened charcoal input lasts for ~300 years and is attested in other regional charcoal records (*34*), the Santa Barbara Basin at 13.0 ka (*35*), and continent wide between 13.2 and 13.0 ka (*36*). This interval appears to be a tipping point for fire regimes in Southern California and across North America; after the initial spike, charcoal accumulation rates remain elevated relative to earlier Pleistocene levels during the Younger Dryas and then increase again in the Holocene (*36*). Although the increase in charcoal input observed in the Southern California record is consistent with observed changes in climate and vegetation, as well as with the disappearance of megaherbivores (*37*), its magnitude is unprecedented in the 33,000-year record (*33*). Its ignition source is open to question, but increased human impact on the ecosystem should be considered as a potential causal factor in the intense burning event ~13.2 ka.

Human record

Genetic and archeological data support a human presence south of the North American ice sheets by 16 ka (*38*, *39*) and possibly earlier. The megafauna-specialized Clovis technology is often invoked as the likely driver of North American megafaunal extinctions (*40*). However, the emergence and geographic expansion of the Clovis complex (~13.05 to 12.75 ka) (*41*) postdates the crash in megafaunal occurrences at La Brea at 13.25 ka, as well as the last occurrences of all dated taxa except *Smilodon* and *Equus*. Clovis also emerges after the North American megafauna begin to decline, but coincides with the final megafaunal decline across the continent (Figs. 1 and 5) (*41*). The modeled extirpation time for La Brea megafauna (13.07 to 12.89 ka) suggests an overlap with early Clovis, but Clovis continues for at least 140 years after the extirpation is complete.

The oldest unequivocal evidence of human presence in California is a partial skeleton from Arlington Springs on Santa Rosa Island ~12.89 ka (*42*) (Fig. 5A). No other archeological evidence of late-Pleistocene human presence or association between humans and megafauna has been documented in California. However, such sites would be rare and difficult to find because most deposits of this age are deeply buried or underwater (*43*). To better understand the potential impacts of humans on megafauna in Southern California, we constructed an SPD for human occupation sites in North America (between southern Canada and northern Mexico) to serve as a proxy for human population in the region (*11*). Data from the Canadian Archeological Radiocarbon Database (CARD) were subjected to strict data hygiene (*11*), and the probability distribution was binned to control for variation in sampling intensity (Fig. 5A). Our model indicates that North American human population density is low until ~13.2 ka, when it begins a sharp increase that continues into the Younger Dryas.

State shift

Together, these records of climate and vegetation change, megafaunal extirpation, human demographic growth, and biomass burning document a profound shift in ecosystem structure in Southern California near the end of the Bølling-Allerød. We analyzed the correlations among these time series using principal components analysis and applied a Bayesian structural

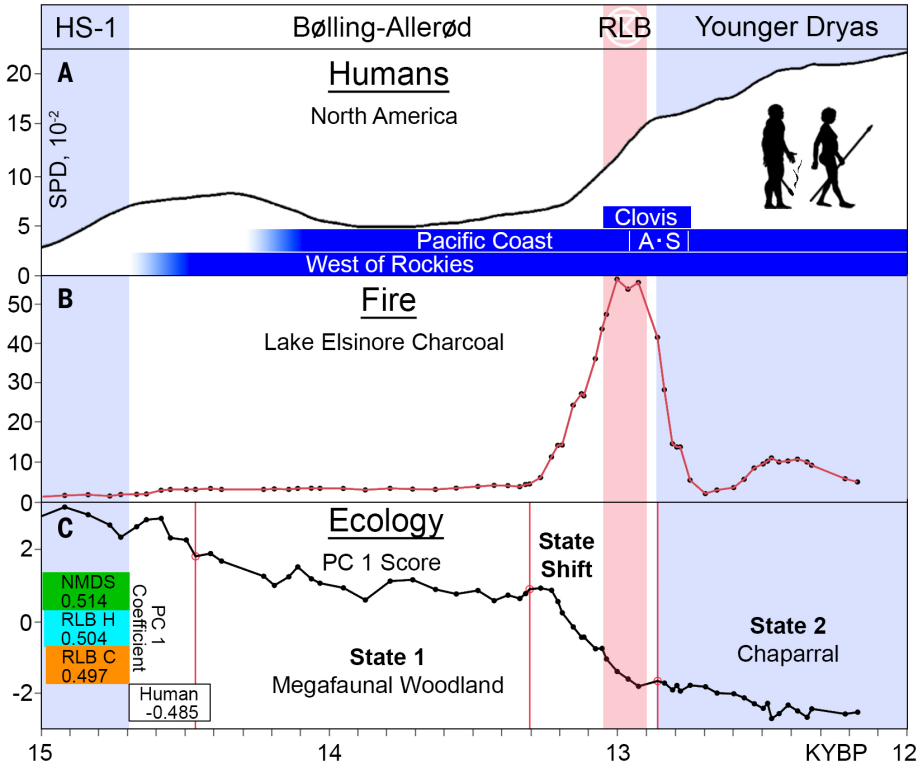

Fig. 5. Correlation among Southern California ecosystem variables. (**A**) Summed probability distribution of human occupation in North America derived from the CARD database (black line). Blue bars present archaeological data including age range for Clovis, earliest evidence of human occupation along the Pacific Coast, "AS" is the date of Arlington Springs Man, and earliest evidence of human occupation west of the Rocky Mountains [see materials and methods (*11*)]. (**B**) The fire record at Lake Elsinore as recorded by particles of charcoal per square centimeter per year; series is a 200-year running mean. (**C**) PC1 scores for ecosystem variables through time. Red regression lines are four regimes identified by breakpoint analysis [see section 4 of the supplemenary materials (*11*)]: the drying transition out of the HS-1 and initial human arrival; relative stability for much of the Bølling-Allerød while humans were scarce ("Megafaunal Woodland"); an abrupt state shift from 13.3 to 13.0 ka ("State Shift"); and the establishment of a new regime ("Chaparral").

change analysis to identify significant shifts in principal component 1 (PC1) scores (*11*) (Fig. 5). These analyses identify four distinct periods of stable regression across the Bølling-Allerød, most notably an ecosystem state shift from 13.3 to 12.9 ka (Fig. 5). This state shift coincides with a 30-fold regional increase in charcoal accumulation rates and a shift in the floral community toward fire-adapted species. During this interval, tree abundance plummets and megafaunal occurrence rates fall to zero. At the end of the state shift, Southern California enters a new ecological regime characterized by chaparral vegetation, intensified fire activity, and complete absence of Pleistocene megafauna. Many large mammals that are associated with fire-adapted ecosystems today (e.g., elk, moose, and grizzly bear) likely do not arrive in non-Beringian North America until the early Holocene (*44*–*46*). Others, such as deer and pumas, are present but rare at La Brea.

Across this time interval, the coefficient for human population size is strongly negatively correlated with those for megafaunal populations and glacial floral communities (Fig. 5C). The trend over the Bølling-Allerød is toward an increasingly fire-prone ecosystem. The unprecedented biomass burning observed during the state shift could have resulted from the confluence of extreme warming and drying, fuel accumulation resulting from reduction of grazing herbivores (*37*), and new, anthropogenic ignition sources. Climate change thus may have facilitated the extinction by pushing the ecosystem toward a state where anthropogenic activities could trigger widespread fires. In Southern California, the Pleistocene megafauna are already gone, and the transition toward a Holocene chaparral is well advanced, before the Younger Dryas begins.

Causality

Numerous studies have found correlations between the timing of megafaunal disappearances and changes in climate (*9*), vegetation (*2*), human populations (*5*), and fire activity (*37*). We leveraged our highly resolved datasets to quantify causality using variable autoregression modeling with exogenous variables (VARX) (*11*) (Fig. 6). Vector autoregressive models use time-series data to identify whether, and to what degree, past values of one variable predict present values of others (*47*, *11*). Our time series included two exogenous variables: local precipitation inferred from percent sand from Lake Elsinore and NMDS1 scores from Lake Elsinore pollen. The NMDS1 scores are highly correlated with the MAAT estimates from Lake Elsinore (R^2 = 0.67; P = 1.18×10^{-12}) (*11*), making pollen our most densely sampled proxy for terrestrial air temperature. Endogenous variables included charcoal accumulation rates from Lake Elsinore, the megafaunal probability distributions from La Brea, and the North American human probability distribution. The average time step was 43 years, and there were 57 steps across a 2382-year span. We limited interpretation of the model to the first two time lags (~85 years), or two parameters per time series. We ran the VARX model both including and excluding our human SPDs for North America. The VARX model fit is much better with the human distribution included [Akaike information criterion (AIC) of −19.71 versus −9.76 with and without humans, respectively; $P < 0.001$]. Given that an AIC difference of 2 is generally considered meaningful, this decrease of 10 is robust evidence that humans are a strong forcing factor in the model.

The VARX model (Fig. 6) identified several significant time-lagged causal relationships. These include: (i) climate warming and aridification predict an increase in charcoal input; (ii) declines in pollen NMDS1 also forecast an increase in charcoal input; and (iii) human population growth predicts a decrease in herbivore populations and, most strongly, an increase in charcoal input. Decrease in herbivore numbers at one lag predicts an increase in carnivore entrapment bias at La Brea. Some effects, such as the impact of vegetation change and fire activity on herbivore populations, likely occurred too rapidly to be captured by the 43-year time lag. The model supports inference of a potential positive feedback loop in which rising human populations cause enhanced fire activity both indirectly by depressing herbivore numbers (resulting in increased fuel loads) and by increasing ignition.

Small populations of humans can have disproportionate impacts on landscapes through the use of fire (*48*); significant increases in regional fire activity after the arrival of humans have also been noted in Australia (*49*), New Zealand (*50*), Panama (*51*), and many other regions worldwide (*52*). Today, changing fire regimes resulting from climate change and human activities are again driving some ecosystems toward tipping points (*53*). Not only can fire cause direct mortality of wildlife, but it can also alter the structure and function of

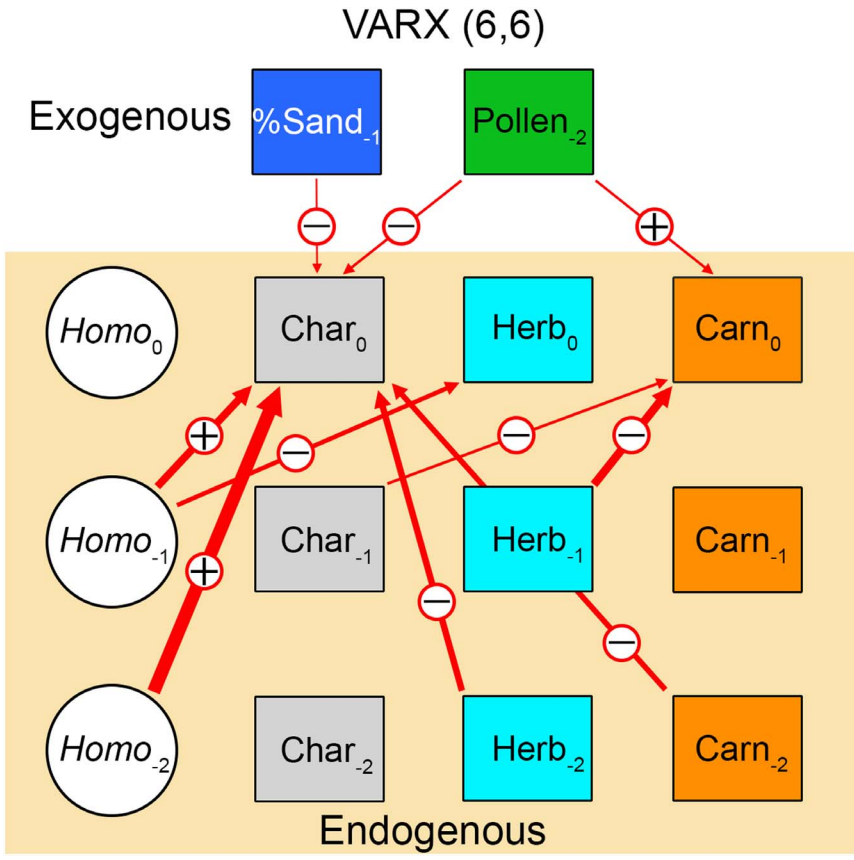

Fig. 6. Summary time-series VARX model of ecosystem variables expressed as a structural equation model. VARX 6,6 model incorporating probability distributions from La Brea herbivores ("Herb") and carnivores ("Carn"), charcoal from Lake Elsinore ("Char"), and our SPD for the North American human population ("*Homo*"). Exogenous variables include Lake Elsinore %Sand, a proxy for precipitation, and NMDS of Lake Elsinore pollen ("Pollen"), a proxy for onshore air temperature. Predictive relationships with effect size >0.4 are shown by red arrows with width scaled to coefficient magnitude. For exogenous variables, all effects are shown. See section 5 of the supplementary materials for values (*11*). Self-prediction is highly significant in most cases but is omitted because the probability distributions are smoothed to 200 years and the average step length is 43 years. For a further discussion of methods, see the supplementary materials (*11*).

vegetation, which affects the availability of key floral resources for animals, alters migration patterns, increases energetic costs of movement, and can put animals at higher risk of predation (*53*). Humans arriving in Southern California in the latest Pleistocene encountered a warming and increasingly arid climate coupled with ample flammable fuels. Anthropogenic hunting and burning could have precipitated a state shift toward today's chaparral ecosystem (Fig. 5).

The debate over the cause of the Pleistocene megafaunal extinctions has raged for decades (*5*). This study demonstrates the necessity of moving beyond dichotomous statements about single extinction drivers and instead moving toward a more nuanced view of past extinctions, one that considers the interplay among biotic and abiotic causal factors. Our results also highlight the importance of considering extinction dynamics on ecologically relevant spatial, temporal, and taxonomic scales. Studies from the northeastern United States (*2*), the Pacific Northwest (*52*), and Alaska (*54*) have also found pre–Younger Dryas disappearances of megafauna coinciding with climate-driven environmental changes, and radiocarbon dates from the Southwestern United States indicate that megafauna may have persisted there well into the Younger Dryas (Fig. 1 and data S2). The results of our study also suggest that individual taxa at La Brea responded differently to climate-driven vegetation shifts (Fig. 3)

A climate-human synergy such as the one we implicate in California's megafaunal extinctions may portend future ecological state shifts (*55*). Data from the National Oceanic and Atmospheric Administration (NOAA) show that Southern California has warmed >2°C over the past century, an order of magnitude faster than warming during the Bølling-Allerød. Anthropogenic climate warming is increasing the risk of prolonged droughts and wildfire activity in highly biodiverse Mediterranean regions worldwide (*56*). These events are predicted to worsen in coming decades, affecting wildlife already experiencing population declines caused by other factors (*57*). As critical thresholds are reached in Mediterranean ecosystems, state shifts are likely to occur, as they did at the end of the Pleistocene. Some such transitions have already begun: in the western United States, wildfire-burned area has increased fourfold in two decades (*58*). Moreover, postfire ecosystems are not recovering to preburned states, suggesting that critical thresholds for re-establishment have already been crossed (*59*). The conditions that led to the end-Pleistocene state shift in Southern California are recurring today across the western United States and in numerous other ecosystems worldwide. Understanding the interplay of climatic and anthropogenic forcings in driving the La Brea extinction event may be helpful in mitigating future biodiversity loss in the face of similar pressures.

REFERENCES AND NOTES

1. A. B. Tóth *et al.*, Reorganization of surviving mammal communities after the end-Pleistocene megafaunal extinction. *Science* **365**, 1305–1308 (2019). doi: 10.1126/science.aaw1605; pmid: 31604240
2. J. L. Gill, J. W. Williams, S. T. Jackson, K. B. Lininger, G. S. Robinson, Pleistocene megafaunal collapse, novel plant communities, and enhanced fire regimes in North America. *Science* **326**, 1100–1103 (2009). doi: 10.1126/science.1179504; pmid: 19965426
3. F. A. Smith, R. E. Elliott Smith, S. K. Lyons, J. L. Payne, Body size downgrading of mammals over the late Quaternary. *Science* **360**, 310–313 (2018). doi: 10.1126/science.aao5987; pmid: 29674591
4. A. D. Barnosky *et al.*, Has the Earth's sixth mass extinction already arrived? *Nature* **471**, 51–57 (2011). doi: 10.1038/nature09678; pmid: 21368823
5. P. L. Koch, A. D. Barnosky, Late Quaternary extinctions: State of the debate. *Annu. Rev. Ecol. Evol. Syst.* **37**, 215–250 (2006). doi: 10.1146/annurev.ecolsys.34.011802.132415
6. A. D. Barnosky, E. L. Lindsey, Timing of Quaternary megafaunal extinction in South America in relation to human arrival and climate change. *Quat. Int.* **217**, 10–29 (2010). doi: 10.1016/j.quaint.2009.11.017
7. J. M. Broughton, E. M. Weitzel, Population reconstructions for humans and megafauna suggest mixed causes for North American Pleistocene extinctions. *Nat. Commun.* **9**, 5441 (2018). doi: 10.1038/s41467-018-07897-1; pmid: 30575758
8. D. J. Meltzer, Overkill, glacial history, and the extinction of North America's Ice Age megafauna. *Proc. Natl. Acad. Sci. U. S. A.* **117**, 28555–28563 (2020). doi: 10.1073/pnas.2015032117; pmid: 33168739
9. M. Stewart, W. C. Carleton, H. S. Groucutt, Climate change, not human population growth, correlates with Late Quaternary megafauna declines in North America. *Nat. Commun.* **12**, 965 (2021). doi: 10.1038/s41467-021-21201-8; pmid: 33594059

10. C. Stock, J. M. Harris, Rancho La Brea: A record of Pleistocene life in California. *LACM Sci. Ser.* **37** (1992).
11. Materials and methods are available as supplementary materials.
12. C. J. A. Bradshaw, A. Cooper, C. S. M. Turney, B. W. Brook, Robust estimates of extinction time in the geological record. *Quat. Sci. Rev.* **33**, 14–19 (2012). doi: 10.1016/j.quascirev.2011.11.021
13. B. T. Fuller *et al*., Ultrafiltration for asphalt removal from bone collagen for radiocarbon dating and isotopic analysis of Pleistocene fauna at the tar pits of Rancho La Brea, Los Angeles, California. *Quat. Geochronol.* **22**, 85–98 (2014). doi: 10.1016/j.quageo.2014.03.002
14. H. Cheng *et al*., Timing and structure of the Younger Dryas event and its underlying climate dynamics. *Proc. Natl. Acad. Sci. U. S. A.* **117**, 23408–23417 (2020). doi: 10.1073/pnas.2007869117; pmid: 32900942
15. J. M. Martin, J. I. Mead, P. S. Barboza, Bison body size and climate change. *Ecol. Evol.* **8**, 4564–4574 (2018). doi: 10.1002/ece3.4019; pmid: 29760897
16. J. A. Meachen, A. C. Janowicz, J. E. Avery, R. W. Sadleir, Ecological changes in Coyotes (*Canis latrans*) in response to the ice age megafaunal extinctions. *PLOS ONE* **9**, e116041 (2014). doi: 10.1371/journal.pone.0116041; pmid: 25551387
17. D. B. Jones, L. R. DeSantis, Dietary ecology of ungulates from the La Brea tar pits in southern California: A multi-proxy approach. *Palaeogeogr. Palaeoclimatol. Palaeoecol.* **466**, 110–127 (2017). doi: 10.1016/j.palaeo.2016.11.019
18. J. E. Cohen *et al*., Dietary stability inferred from dental mesowear analysis in large ungulates from Rancho La Brea and opportunistic feeding during the late Pleistocene. *Palaeogeogr. Palaeoclimatol. Palaeoecol.* **570**, 110360 (2021). doi: 10.1016/j.palaeo.2021.110360
19. S. M. Kidwell, S. M. Holland, The quality of the fossil record: Implications for evolutionary analyses. *Annu. Rev. Ecol. Syst.* **33**, 561–588 (2002). doi: 10.1146/annurev.ecolsys.33.030602.152151
20. K. K. Andersen *et al*., High-resolution record of Northern Hemisphere climate extending into the last interglacial period. *Nature* **431**, 147–151 (2004). doi: 10.1038/nature02805; pmid: 15356621
21. M. E. Kirby, S. J. Feakins, N. Bonuso, J. M. Fantozzi, C. A. Hiner, Latest Pleistocene to Holocene hydroclimates from Lake Elsinore, California. *Quat. Sci. Rev.* **76**, 1–15 (2013). doi: 10.1016/j.quascirev.2013.05.023
22. K. C. Glover *et al*., Evidence for orbital and North Atlantic climate forcing in alpine Southern California between 125 and 10 ka from multi-proxy analyses of Baldwin Lake. *Quat. Sci. Rev.* **167**, 47–62 (2017). doi: 10.1016/j.quascirev.2017.04.028
23. I. L. Hendy, The paleoclimatic response of the Southern Californian Margin to the rapid climate change of the last 60 ka: A regional overview. *Quat. Int.* **215**, 62–73 (2010). doi: 10.1016/j.quaint.2009.06.009
24. S. J. Feakins, M. S. Wu, C. Ponton, J. E. Tierney, Biomarkers reveal abrupt switches in hydroclimate during the last glacial in southern California. *Earth Planet. Sci. Lett.* **515**, 164–172 (2019). doi: 10.1016/j.epsl.2019.03.024
25. M. E. Kirby *et al*., A late Wisconsin (32-10k cal a BP) history of pluvials, droughts and vegetation in the Pacific south-west United States (Lake Elsinore, CA). *J. Quaternary Sci.* **33**, 238–254 (2018). doi: 10.1002/jqs.3018
26. L. Heusser, Direct correlation of millennial-scale changes in western North American vegetation and climate with changes in the California Current system over the past ~60 kyr. *Paleoceanography* **13**, 252–262 (1998). doi: 10.1029/98PA00670
27. O. K. Davis, Pollen analysis of a late-glacial and Holocene sediment core from Mono Lake, Mono County, California. *Quat. Res.* **52**, 243–249 (1999). doi: 10.1006/qres.1999.2063
28. S. A. Mensing, Late-glacial and early Holocene vegetation and climate change near Owens Lake, eastern California. *Quat. Res.* **55**, 57–65 (2001). doi: 10.1006/qres.2000.2196
29. L. E. Heusser, M. E. Kirby, J. E. Nichols, Pollen-based evidence of extreme drought during the last glacial (32.6–9.0 ka) in coastal southern California. *Quat. Sci. Rev.* **126**, 242–253 (2015). doi: 10.1016/j.quascirev.2015.08.029
30. J. E. Keeley, Native American impacts on fire regimes of the California coastal ranges. *J. Biogeogr.* **29**, 303–320 (2002). doi: 10.1046/j.1365-2699.2002.00676.x
31. S. A. Kannenberg, A. W. Driscoll, D. Malesky, W. R. Anderegg, Rapid and surprising dieback of Utah juniper in the southwestern USA due to acute drought stress. *For. Ecol. Manage.* **480**, 118639 (2021). doi: 10.1016/j.foreco.2020.118639
32. J. T. Stevens, M. M. Kling, D. W. Schwilk, J. M. Varner, J. M. Kane, Biogeography of fire regimes in western US conifer forests: A trait-based approach. *Glob. Ecol. Biogeogr.* **29**, 944–955 (2020). doi: 10.1111/geb.13079
33. L. N. Martinez, "Climate, fire, and environmental dynamics at Lake Elsinore, California, from Late Marine Isotope Stage 3 through the Holocene," thesis, University of California, Los Angeles (2020).
34. M. Hardiman *et al*., Fire history on the California Channel Islands spanning human arrival in the Americas. *Philos. Trans. R. Soc. Lond. B Biol. Sci.* **371**, 20150167 (2016). doi: 10.1098/rstb.2015.0167; pmid: 27216524
35. L. E. Heusser, F. Sirocko, Millennial pulsing of environmental change in southern California from the past 24 ky: A record of Indo-Pacific ENSO events? *Geology* **25**, 243–246 (1997). doi: 10.1130/0091-7613(1997)025<0243:MPOECI>2.3.CO;2
36. J. R. Marlon *et al*., Wildfire responses to abrupt climate change in North America. *Proc. Natl. Acad. Sci. U. S. A.* **106**, 2519–2524 (2009). doi: 10.1073/pnas.0808212106; pmid: 19190185
37. A. T. Karp, J. T. Faith, J. R. Marlon, A. C. Staver, Global response of fire activity to late Quaternary grazer extinctions. *Science* **374**, 1145–1148 (2021). doi: 10.1126/science.abj1580; pmid: 34822271
38. E. Willerslev, D. J. Meltzer, Peopling of the Americas as inferred from ancient genomics. *Nature* **594**, 356–364 (2021). doi: 10.1038/s41586-021-03499-y; pmid: 34135521
39. M. R. Waters, Late Pleistocene exploration and settlement of the Americas by modern humans. *Science* **365**, eaat5447 (2019). doi: 10.1126/science.aat5447; pmid: 31296740
40. J. E. Mosimann, P. S. Martin, Simulating overkill by Paleoindians: Did man hunt the giant mammals of the New World to extinction? Mathematical models show that the hypothesis is feasible. *Am. Sci.* **63**, 304–313 (1975).
41. M. R. Waters, T. W. StaffordJr.., D. L. Carlson, The age of Clovis-13,050 to 12,750 cal yr B.P. *Sci. Adv.* **6**, eaaz0455 (2020). doi: 10.1126/sciadv.aaz0455; pmid: 33087355
42. J. R. Johnson, T. W. Stafford Jr, H. O. Ajie, D. P. Morris, "Arlington Springs revisited," in *Proceedings of the Fifth California Islands Symposium* (Santa Barbara Museum of Natural History, 2002), vol. 5, pp. 541–545.
43. M. R. Waters, B. F. Byrd, S. N. Reddy, Geoarchaeological investigations of San Mateo and Las Flores creeks, California: Implications for coastal settlement models. *Geoarchaeology* **14**, 289–306 (1999). doi: 10.1002/(SICI)1520-6548(199903)14:3<289::AID-GEA4>3.0.CO;2-R
44. P. S. Alagona, A. M. Mychajliw, Southern California's three-bear shuffle: Survival, extinction and recovery in an urban biodiversity hotspot. *Environ. Hist.* **27**, 308–313 (2022). doi: 10.1086/719611
45. M. Meiri *et al*., Subspecies dynamics in space and time: A study of the red deer complex using ancient and modern DNA and morphology. *J. Biogeogr.* **45**, 367–380 (2018). doi: 10.1111/jbi.13124
46. M. Meiri, A. Lister, P. Kosintsev, G. Zazula, I. Barnes, Population dynamics and range shifts of moose (*Alces alces*) during the Late Quaternary. *J. Biogeogr.* **47**, 2223–2234 (2020). doi: 10.1111/jbi.13935
47. J. Gan, Causality among wildfire, ENSO, timber harvest, and urban sprawl: The vector autoregression approach. *Ecol. Modell.* **191**, 304–314 (2006). doi: 10.1016/j.ecolmodel.2005.05.013
48. N. Pinter, S. Fiedel, J. E. Keeley, Fire and vegetation shifts in the Americas at the vanguard of Paleoindian migration. *Quat. Sci. Rev.* **30**, 269–272 (2011). doi: 10.1016/j.quascirev.2010.12.010
49. S. Rule *et al*., The aftermath of megafaunal extinction: Ecosystem transformation in Pleistocene Australia. *Science* **335**, 1483–1486 (2012). doi: 10.1126/science.1214261; pmid: 22442481
50. D. B. McWethy *et al*., Rapid landscape transformation in South Island, New Zealand, following initial Polynesian settlement. *Proc. Natl. Acad. Sci. U. S. A.* **107**, 21343–21348 (2010). doi: 10.1073/pnas.1011801107; pmid: 21149690
51. D. R. Piperno, J. G. Jones, Paleoecological and archaeological implications of a Late Pleistocene/Early Holocene record of vegetation and climate from the Pacific coastal plain of Panama. *Quat. Res.* **59**, 79–87 (2003). doi: 10.1016/S0033-5894(02)00021-2
52. D. M. Gilmour *et al*., Chronology and ecology of late Pleistocene megafauna in the northern Willamette Valley, Oregon. *Quat. Res.* **83**, 127–136 (2015). doi: 10.1016/j.yqres.2014.09.003
53. L. T. Kelly *et al*., Fire and biodiversity in the Anthropocene. *Science* **370**, eabb0355 (2020). doi: 10.1126/science.abb0355; pmid: 33214246
54. R. D. Guthrie, New carbon dates link climatic change with human colonization and Pleistocene extinctions. *Nature* **441**, 207–209 (2006). doi: 10.1038/nature04604; pmid: 16688174
55. A. D. Barnosky *et al*., Approaching a state shift in Earth's biosphere. *Nature* **486**, 52–58 (2012). doi: 10.1038/nature11018; pmid: 22678279
56. N. S. Diffenbaugh, D. L. Swain, D. Touma, Anthropogenic warming has increased drought risk in California. *Proc. Natl. Acad. Sci. U. S. A.* **112**, 3931–3936 (2015). doi: 10.1073/pnas.1422385112; pmid: 25733875
57. M. Goss *et al*., Climate change is increasing the likelihood of extreme autumn wildfire conditions across California. *Environ. Res. Lett.* **15**, 094016 (2020). doi: 10.1088/1748-9326/ab83a7
58. V. Iglesias, J. K. Balch, W. R. Travis, U.S. fires became larger, more frequent, and more widespread in the 2000s. *Sci. Adv.* **8**, eabc0020 (2022). doi: 10.1126/sciadv.abc0020; pmid: 35294238
59. A. D. Syphard, T. J. Brennan, J. E. Keeley, Extent and drivers of vegetation type conversion in Southern California chaparral. *Ecosphere* **10**, e02796 (2019). doi: 10.1002/ecs2.2796

ACKNOWLEDGMENTS

Special thanks are due to B. Van Valkenburgh, M. Foote, S. Kidwell, P. Wagner, F. Saltré, C. Howard, K. Palmquist, and A. Axel for help at different stages of this research. Human and some mammal silhouettes used in this paper are from PhyloPic (https://www.phylopic.org/). La Brea mammal silhouettes are by J. Olsson. We thank S. Abramowicz for photography, and C. Townsend for life reconstructions. We also thank S. Vignieri and a host of anonymous reviewers; the review process was unusually beneficial and contributed greatly to the finished work. **Funding:** This work was supported by the National Science Foundation Division of Earth Sciences, Collaborative Research: RUI: Chronology and Ecology of Late Pleistocene Megafauna at Rancho La Brea (NSF EAR grants 1758117, 1757545, 1758116, 1758108, 1757236, and 1758110 to W.B., L.R.G.D., E.L.L., J.A.M., F.R.O., and J.R.S., respectively); NSF Department of Behavioral and Cognitive Sciences (BCS (FAIN): 1759756 to G.M. and L.M.); a UCLA John Muir Endowment to G.M. and L.M.; REFIND grant H2020-MSCA-GF-785821 to E.G.; a Drinko Distinguished Research Fellowship from John Deever Drinko Academy, Marshall University to F.R.O.; and the North Star Archaeological Research Program, Center for the Study of the First Americans, Texas A&M University (M.R.W.). **Author contributions:** Conceptualization: F.R.O., E.L.L., R.E.D., E.M.W., J.R.S., J.E.C., J.A.M., W.J.B., L.R.G.D.; Funding acquisition: W.J.B., F.R.O., J.A.M., E.L.L., L.R.G.D., J.R.S.; Methodology: F.R.O., E.M.W., E.L.L., R.E.D., B.T.F., J.R.S., J.A.M., J.E.C., W.J.B., L.R.G.D.; Investigation: all authors; Visualization: F.R.O., R.E.D., E.M.W., E.L.L., M.R.W.; Project administration: E.L.L., F.R.O., W.J.B., J.E.C., G.T.T., A.B.F.; Supervision: W.J.B.; Writing – original draft: F.R.O., E.L.L., R.E.D., M.R.W.; Writing – review and editing: all authors **Competing interests:** The authors declare no competing interests. **Data and materials availability:** All data are available in the main text or the supplementary materials. Data series taken from the literature are available in cited references. All dated megafaunal specimens are curated in the La Brea Tar Pits Museum collections. **Provenance:** All but two mammal fossils carbon dated for this paper reside in the historically collected Hancock Collection at the Tar Pit Museum, Los Angeles, CA. Specimen numbers and reference numbers for each carbon date may be found in data S1. Fossils were bulk collected from each pit deposit and soaked in gasoline to remove asphalt, then labeled in white paint with pit of origin, a coarse grid reference, and a specimen number. The Hancock Collection is under one accession number, A.239. The two Pit 91 specimens are under accession number A.11177.89-1. **License information:** Copyright © 2023 the authors, some rights reserved; exclusive licensee American Association for the Advancement of Science. No claim to original US government works. https://www.science.org/about/science-licenses-journal-article-reuse

SUPPLEMENTARY MATERIALS

science.org/doi/10.1126/science.abo3594
Materials and Methods
Fig. S1
Tables S1 to S4
R Code Documents 1 to 5
References (*60*–*89*)
Materials Design Analysis Reporting Checklist
Data S1 to S3

Submitted 28 January 2022; resubmitted 30 January 2023
Accepted 12 July 2023
10.1126/science.abo3594

RESEARCH ARTICLE SUMMARY

HUMAN DEVELOPMENT

Yolk sac cell atlas reveals multiorgan functions during human early development

Issac Goh† and Rachel A. Botting† *et al.*

INTRODUCTION: The yolk sac (YS) generates the first blood and immune cells and provides nutritional and metabolic support to the developing embryo. Our current understanding of its functions derives from pivotal studies in model systems, and insights from human studies are limited. Single-cell genomics technologies have facilitated the interrogation of human developmental tissues at unprecedented resolution. Atlases of blood and immune cells from multiple organs have been greatly enhanced by focused, time-resolved analyses of specific tissues.

RATIONALE: To characterize the functions of the human YS, we performed single-cell RNA sequencing (scRNA-seq) and cellular indexing of transcriptomes and epitopes by sequencing (CITE-seq) on the YS and paired embryonic liver. After integration with external datasets, our reference comprised 169,798 cells from 10 samples spanning 4 to 8 postconception weeks (PCW) or Carnegie stages (CS) 10 to 23. A repertoire of two-dimensional (2D) and 3D imaging techniques provided spatial context and validation. We compared the products of two hematopoietic inducible pluripotent stem cell (iPSC) culture protocols against our reference.

RESULTS: We determined that YS metabolic and nutritional support originates in the endoderm and that the endoderm produces coagulation proteins and hematopoietic growth factors [erythropoietin (EPO) and thrombopoietin (THPO)]. Although metabolic and coagulation protein production was conserved among humans, mice, and rabbits, EPO and THPO production was observed in humans and rabbits only.

We reconstructed trajectories from the YS hemogenic endothelium to early hematopoietic stem and progenitor cells (HSPCs). Using transcriptomic signatures of early and definitive hematopoiesis, we parsed YS HSPCs into myeloid-biased early HSPCs and lymphoid- and megakaryocyte-biased definitive HSPCs. Human embryonic liver remained macroscopically pale before CS14, when hematopoietic cells first emerge from the aorta-gonad-mesonephros (AGM) region. Tracking hemoglobin (Hb) subtypes led us to conclude that initial erythropoiesis is YS restricted. By contrast, in mice, Hb subtypes suggested two waves of pre-AGM erythropoiesis, including maturation in the macroscopically red embryonic liver.

Before CS14, monocytes were absent and macrophages originated from HPSCs via a pre-macrophage cell state. After CS14, monocytes emerged and a second, monocyte-dependent differentiation trajectory was reconstructed. A rare subset of *TREM2*$^{+}$ macrophages, with a microglia-like transcriptomic signature, was present after CS14. The iPSC system optimized for macrophage production recapitulated the two routes to macrophage differentiation but did not generate the diversity of macrophages (including *TREM2*$^{+}$ macrophages) observed in developing tissues.

CONCLUSION: Our study illuminates a previously obscure phase of human development, where vital functions are delivered by the YS acting as a transient extraembryonic organ. Our comprehensive single-cell atlas represents a valuable resource for studying the cellular differentiation pathways specific to early life and leveraging these for tissue engineering and cellular therapy. ■

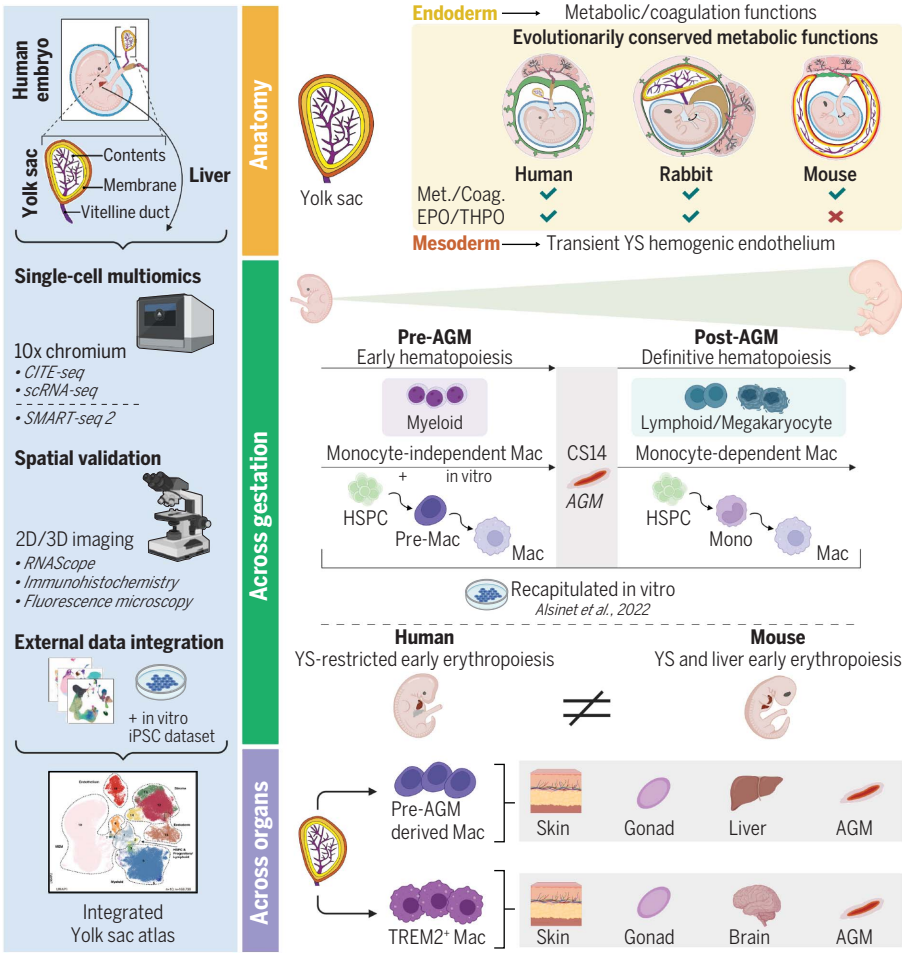

Multiorgan functions of the human YS. We characterized functions of the developing human YS, combining scRNA-seq and CITE-seq with 2D and 3D imaging techniques. Our findings revealed YS contributions to metabolic and nutritional support and to early hematopoiesis. We characterized myeloid bias in early hematopoiesis, distinct myeloid differentiation trajectories, evolutionary divergence in initial erythropoiesis, and YS contributions to developing tissue macrophages. Met., metabolic; Coag., coagulation; Mac, macrophage. [Figure created with Biorender]

The full author list and the list of author affiliations are available in the full article online.
*Corresponding authors: Laura Jardine (laura.jardine@ncl.ac.uk); Berthold Göttgens (bg200@cam.ac.uk); Sarah A. Teichmann (st9@sanger.ac.uk); Muzlifah Haniffa (mh32@sanger.ac.uk)
†These authors contributed equally to this work.
Cite this article as I. Goh *et al.*, *Science* **381**, eadd7564 (2023). DOI: 10.1126/science.add7564

READ THE FULL ARTICLE AT
https://doi.org/10.1126/science.add7564

RESEARCH ARTICLE

HUMAN DEVELOPMENT

Yolk sac cell atlas reveals multiorgan functions during human early development

Issac Goh[1,2]†, Rachel A. Botting[1,2]†, Antony Rose[1,2]‡, Simone Webb[1,2]‡, Justin Engelbert[2], Yorick Gitton[3], Emily Stephenson[1,2], Mariana Quiroga Londoño[4], Michael Mather[2], Nicole Mende[4], Ivan Imaz-Rosshandler[4,5], Lu Yang[1], Dave Horsfall[1,2], Daniela Basurto-Lozada[1,2], Nana-Jane Chipampe[1], Victoria Rook[1], Jimmy Tsz Hang Lee[1], Mai-Linh Ton[4], Daniel Keitley[1,6], Pavel Mazin[1], M. S. Vijayabaskar[4], Rebecca Hannah[4], Laure Gambardella[1], Kile Green[7], Stephane Ballereau[1], Megumi Inoue[3], Elizabeth Tuck[1], Valentina Lorenzi[1], Kwasi Kwakwa[1], Clara Alsinet[1,8], Bayanne Olabi[1,2], Mohi Miah[1,2], Chloe Admane[1,2], Dorin-Mirel Popescu[2], Meghan Acres[2], David Dixon[2], Thomas Ness[9], Rowen Coulthard[9], Steven Lisgo[2], Deborah J. Henderson[2], Emma Dann[1], Chenqu Suo[1], Sarah J. Kinston[4], Jong-eun Park[10], Krzysztof Polanski[1], John Marioni[1,11,12], Stijn van Dongen[1], Kerstin B. Meyer[1], Marella de Bruijn[13], James Palis[14], Sam Behjati[1,15], Elisa Laurenti[4], Nicola K. Wilson[4], Roser Vento-Tormo[1], Alain Chédotal[3], Omer Bayraktar[1], Irene Roberts[16], Laura Jardine[1,2]*, Berthold Göttgens[4]*, Sarah A. Teichmann[1,17]*, Muzlifah Haniffa[1,2,18]*

The extraembryonic yolk sac (YS) ensures delivery of nutritional support and oxygen to the developing embryo but remains ill-defined in humans. We therefore assembled a comprehensive multiomic reference of the human YS from 3 to 8 postconception weeks by integrating single-cell protein and gene expression data. Beyond its recognized role as a site of hematopoiesis, we highlight roles in metabolism, coagulation, vascular development, and hematopoietic regulation. We reconstructed the emergence and decline of YS hematopoietic stem and progenitor cells from hemogenic endothelium and revealed a YS-specific accelerated route to macrophage production that seeds developing organs. The multiorgan functions of the YS are superseded as intraembryonic organs develop, effecting a multifaceted relay of vital functions as pregnancy proceeds.

The primary human yolk sac (YS) derives from the hypoblast at the time of embryo implantation [Carnegie stage 4 (CS4); ~1 postconception week (PCW)] (*1*, *2*). The secondary YS supersedes the primary structure at around CS6 (~2.5 PCW) and persists until CS23 (~8 PCW) (*1*, *2*). The secondary YS has three tissue compartments: the mesothelium (an epithelial layer interfacing the amniotic fluid), the mesoderm (including endothelial cells, blood cells, and smooth muscle), and the endoderm (an inner layer interfacing the vitelline fluid–filled YS cavity) (*1*). The functions of the YS in nutrient uptake, transport, and metabolism are phylogenetically conserved (*2*).

Hematopoiesis originates in the YS of mammals, birds, and some ray-finned fishes (*3*). The first wave of mouse YS hematopoiesis yields primitive erythroid cells, macrophages, and megakaryocytes (MKs) from embryonic day 7.5 (E7.5) (*3*, *4*). After circulation begins, a second wave of erythromyeloid and lymphomyeloid progenitors arise in the YS and supply the embryo (*5*). Finally, definitive hematopoietic stem cells arise in the aorta-gonad-mesonephros (AGM) region of the dorsal aorta and seed the fetal liver (*6*). Limited evidence suggests that the YS also provides the first blood cells during human development. Primitive erythroblasts expressing embryonic globin genes, surrounded by endothelium, emerge in the YS at CS6 (~2.5 PCW) (*7*, *8*). Hematopoietic progenitors and macrophages are detectable at CS11 (~4 PCW) (*9*), with MKs, monocytes, mast cells, and innate lymphocytes also reported (*9*, *10*). Long-term multilineage repopulating (definitive) hematopoietic stem and progenitor cells (HSPCs) originate in the AGM at CS14 (~5 PCW) (*11*). Equivalent cells are subsequently found in the YS at CS16 and the liver from CS17 (*11*, *12*).

In this study, we report a time-resolved atlas of the human YS, combining single-cell protein and gene expression with imaging. This provides a comprehensive depiction of the metabolic and hematopoietic functions of the human YS as well as a benchmark for in vitro culture systems aiming to recapitulate human early development.

A single-cell atlas of human YS

We performed droplet-based single-cell RNA sequencing (scRNA-seq) to profile the human YS and integrated with external datasets to yield 169,798 high-quality cells from 10 samples spanning 4 to 8 PCW (CS10 to CS23), which can be interrogated on our interactive web portal [https://developmental.cellatlas.io/yolk-sac (*13*)] (Fig. 1, A to C; fig. S1, A to C; and data S1 to S18). Graph-based Leiden clustering yielded 39 cell types grouped into 15 broad categories, including hematopoietic cells, endoderm, mesoderm, and mesothelium. Key marker genes were validated by plate-based scRNA-seq (Smart-seq2) (Fig. 1, C and D; fig. S1, B to F; and data S3 to S5, S8, S17, and S18). We used the term "HSPC" for cells collectively on the basis of their expression of a core HSPC signature (e.g., *CD34*, *SPINK2*, and *HLF*) without implying long-term repopulating capacity or multilineage potential. With comparison datasets, unless otherwise specified, we adopted published annotations (data S6 and S7). Surface protein expression from cellular indexing of transcriptomes and epitopes by sequencing (CITE-seq) of $n = 2$ YS cell suspensions (fig. S1, G and H) identified combinatorial antigens for cell purification and functional characterization (fig. S2A and data S9, S19, and S20). We generated matched embryonic liver scRNA-seq and CITE-seq data (fig. S2, B to F; fig. S3, A to C; and data S5, S10, S21, and S22), which confirmed the presence of discrete B cell progenitor stages only in the liver (fig. S3C and data S12). Around half of the YS lymphoid cells were innate lymphoid progenitors, which terminated in natural killer (NK) and innate lymphoid cell (ILC) precursor states on force-directed graph (FDG) visualization (fig. S3D). A small population of cells were referred to as "lymphoid B lineage" because of their expression of *CD19*, *CD79B*, and *IGLL1*. These cells did not express the typical B1 markers *CD5*, *CD27*, or *CCR10*, however. Given

[1]Wellcome Sanger Institute, Wellcome Genome Campus, Hinxton, Cambridge CB10 1SA, UK. [2]Biosciences Institute, Newcastle University, Newcastle upon Tyne NE2 4HH, UK. [3]Sorbonne Université, INSERM, CNRS, Institut de la Vision, Paris, France. [4]Department of Haematology, Wellcome-MRC Cambridge Stem Cell Institute, Cambridge CB2 0AW, UK. [5]MRC Laboratory of Molecular Biology, Cambridge Biomedical Campus, Cambridge CD2 0QH, UK. [6]Department of Zoology, University of Cambridge, Cambridge CB2 3EJ, UK. [7]Translational and Clinical Research Institute, Newcastle University, Newcastle upon Tyne NE2 4HH, UK. [8]Centre Nacional d'Analisi Genomica-Centre de Regulacio Genomica (CNAG-CRG), Barcelona Institute of Science and Technology (BIST), Barcelona, Spain. [9]NovoPath, Department of Pathology, Newcastle Hospitals NHS Foundation Trust, Newcastle upon Tyne NE1 4LP, UK. [10]Korea Advanced Institute of Science and Technology, Daejeon, South Korea. [11]EMBL-EBI, Wellcome Genome Campus, Cambridge CB10 1SD, UK. [12]CRUK Cambridge Institute, University of Cambridge, Cambridge CB2 0RE, UK. [13]MRC Molecular Haematology Unit, MRC Weatherall Institute of Molecular Medicine, Radcliffe Department of Medicine, University of Oxford, Oxford OX3 9DS, UK. [14]Department of Pediatrics, University of Rochester Medical Center, Rochester, NY 14642, USA. [15]Department of Paediatrics, University of Cambridge, Cambridge CB2 0QQ, UK. [16]Department of Paediatrics, University of Oxford, Oxford OX3 9DS, UK. [17]Theory of Condensed Matter Group, Department of Physics, Cavendish Laboratory, University of Cambridge, Cambridge CB3 0HE, UK. [18]Department of Dermatology and NIHR Newcastle Biomedical Research Centre, Newcastle Hospitals NHS Foundation Trust, Newcastle upon Tyne NE1 4LP, UK.
***Corresponding author. Email: laura.jardine@ncl.ac.uk (L.J.); bg200@cam.ac.uk (B.G.); st9@sanger.ac.uk (S.A.T.); mh32@sanger.ac.uk (M.H.)**
†These authors contributed equally to this work.
‡These authors contributed equally to this work.

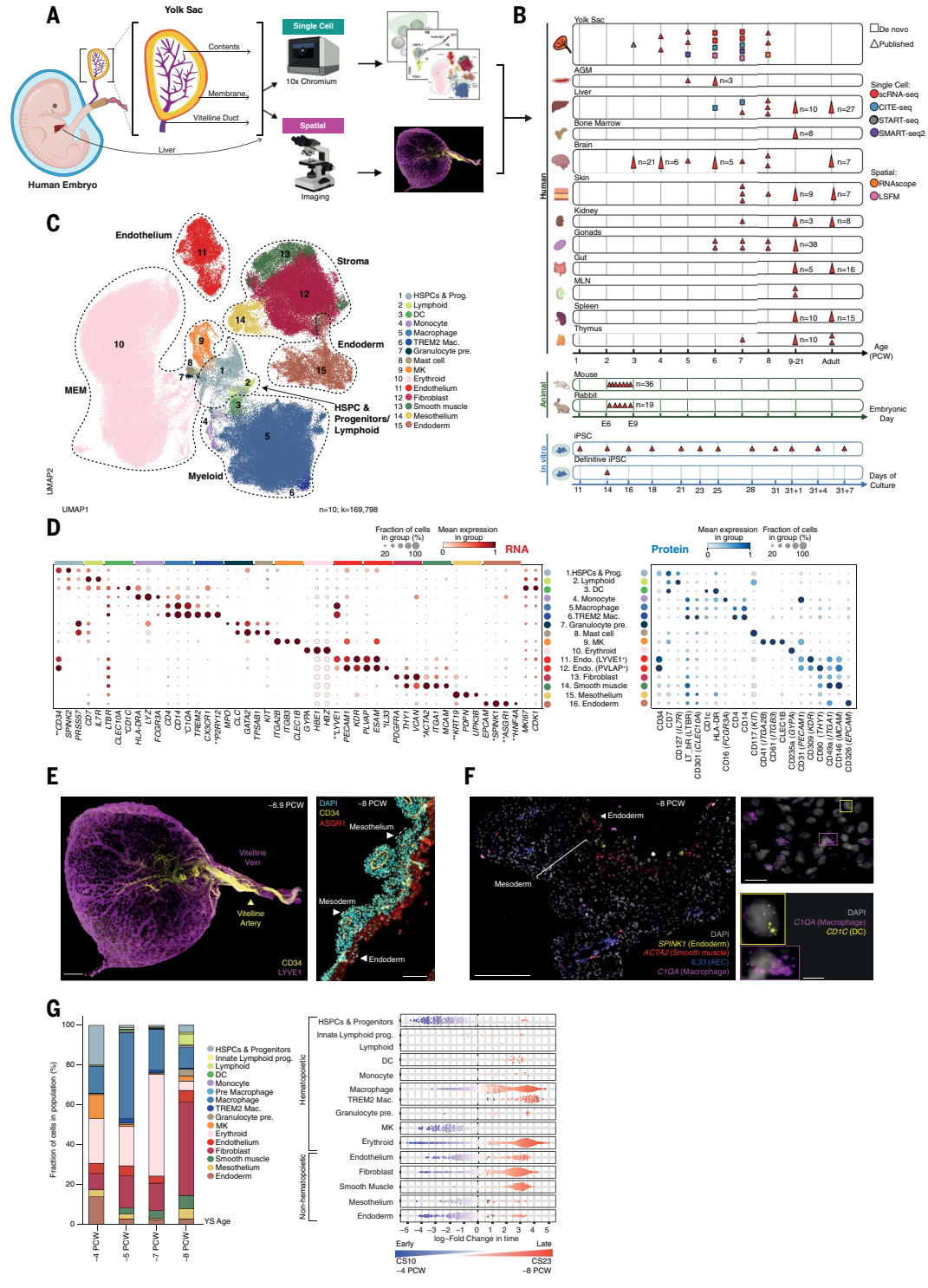

Fig. 1. A single-cell atlas of the human YS. (**A**) Schematic of experimental outline. (**B**) Summary of data included in analyses. Squares represent new data, and triangles represent published data: YS (*10*, *12*, *48*, *63*), AGM (*12*), liver (*10*), fetal BM (*34*), fetal brain (*55*), fetal skin (*48*), fetal kidney (*74*), fetal gonads (*49*), mouse (*75*), and iPSC (*12*, *20*). Color indicates assay used (data S6). (**C**) UMAP visualization of YS scRNA-seq data (n = 10; k = 169,798). Colors represent broad cell states. Mac, macrophage; MEM, megakaryocyte–erythroid–mast cell lineage; pre., precursor; prog., progenitors. (**D**) (Left) Dot plot showing the mean expression (color) and proportion of cells expressing genes (dot size) of broad cell states in YS scRNA-seq data. (Right) Equivalent protein expression (color) and proportion of cells expressing proteins (dot size) from YS CITE-seq data (n = 2; k = 3578). Equivalent gene names are in parentheses. One asterisk indicates genes validated by RNAscope, and two asterisks indicates proteins validated by IHC and/or immunofluorescence (IF) (data S4). Data are variance-scaled and min-max–standardized. (**E**) (Left) Light-sheet fluorescence microscopy of CD34$^+$ and LYVE1$^+$ vascular structures in YS (representative ~6.9 PCW sample). Scale bar, 500 μm (movie S1). (Right) Immunofluorescence of an ~8-PCW YS highlighting endoderm (ASGR1; red) and endothelium (CD34; yellow) costained with DAPI (cyan). Scale bar, 100 μm (data S23). (**F**) RNAscope of YS (representative 8-PCW sample). (Left) Endoderm (*SPINK1*; yellow), smooth muscle (*ACTA2*; red), AEC (*IL33*; blue), and macrophages (*C1QA*; magenta). Scale bar, 200 μm. (Right) DCs (*CD1C*; yellow box) and macrophages (*C1QA*; magenta box). Scale bar, 50 μm. Individual channels are shown in fig. S4A. (**G**) (Left) Bar graph showing the proportion representation of cell states in YS scRNA-seq data by gestational age. (Right) Milo beeswarm plot of YS scRNA-seq neighborhood differential abundance across time. Blue and red neighborhoods are significantly enriched earlier and later in gestation, respectively. Color intensity denotes degree of significance (data S24).

the absence of distinct B cell progenitor stages and their later emergence (>5 PCW), these may constitute migratory B cells of fetal liver origin (fig. S3, D and E).

Three-dimensional visualization of the YS by light-sheet microscopy marked the CD34^{hi}LYVE1^{lo} vitelline artery and CD34^{lo}LYVE1^{hi} vitelline vein contiguous with a branching network of CD34^{lo}LYVE1^{hi} vessels (Fig. 1E, fig. S3F, data S23, and movies S1 and S2). The CD34^{lo}LYVE1^{hi}*IL33*$^+$ vessels were situated within the mesoderm, a distinct layer beneath the ASGR1$^+$*SPINK1*$^+$ endoderm (Fig. 1, E and F; fig. S3, F to I; and fig. S4, A and B). *ACTA2*$^+$ smooth muscle cells formed a sublayer between the mesoderm and endoderm (Fig. 1F and fig. S4, A and B). Macrophages (*C1QA*$^+$*CD1C*$^{+/-}$) and a small number of dendritic cells (DCs) (*C1QA*$^{+/-}$*CD1C*$^+$) were

identified within the mesoderm (Fig. 1F and fig. S4A).

The most prevalent hematopoietic cell types in the early YS (CS10; ~4 PCW) were HSPCs, erythroid cells, macrophages, and MKs. Both HSPCs and MKs proportionately diminished thereafter, whereas erythroid cells and macrophages were sustained. DCs and *TREM2*$^{+}$ macrophages did not emerge until >6 PCW (Fig. 1G and data S4). The ratio of hematopoietic to nonhematopoietic cells was around 3:1 in the early YS (CS10; ~4 PCW), with endoderm relatively abundant (Fig. 1G). The ratio approached 1:3 in the late YS (CS22 to CS23; ~8 PCW) because of the expansion of fibroblasts (Fig. 1G). The transcriptional profile of MKs was consistent across gestation, but both erythroid cells and macrophages had early and late gestation-specific molecular states, suggesting dual waves of production (Fig. 1G, fig. S4C, and data S24).

Multiorgan functions of YS

YS endoderm coexpressing *APOA1/2*, *APOC3*, and *TTR* (similar to embryonic or fetal hepatocytes), was present from gastrulation at ~2 to 3 PCW (*14*) (Fig. 2A and data S3, S7, and S21). The YS endoderm expressed higher levels of serine protease 3 (*PRSS3*), glutathione S-transferase alpha 2 (*GSTA2*), and multifunctional protein galectin 3 (*LGALS3*) compared with embryonic liver hepatocytes, whereas hepatocytes expressed a more extensive repertoire of detoxification enzymes, including alcohol and aldehyde dehydrogenases and cytochrome P450 enzymes (fig. S4D and data S3, S7, and S21). Both cell states shared gene modules implicated in coagulation and lipid and glucose metabolism (Fig. 2B and data S25), which were also conserved in mouse and rabbit extraembryonic endoderm (fig. S4, E and F, and data S25). The expression of transport proteins (alpha-fetoprotein and albumin), a protease inhibitor (alpha-1-antitrypsin), erythropoietin (EPO), and coagulation proteins (thrombin, prothrombin, and fibrin) were validated in human YS endoderm and embryonic liver hepatocytes (Fig. 2C and fig. S4G).

From the earliest time points, the YS endoderm expressed genes for anticoagulant proteins antithrombin III (*SERPINC1*) and protein S (*PROS1*) and components of the tissue factor-activated extrinsic coagulation pathway—thrombin (*F2*), factor VII (*F7*), and factor X (*F10*) (Fig. 2D and data S25), confirmed at the protein level for thrombin (Fig. 2C). Intrinsic pathway factors VIII, IX, XI, and XII (*F8*, *F9*, *F11*, and *F12*) were minimally expressed in the YS but were expressed by embryonic liver hepatocytes (Fig. 2D). Tissue factor, antithrombin III, and fibrinogen subunits were also expressed in mouse extraembryonic endoderm and rabbit YS endoderm (fig. S4E). Embryonic lethality of homozygous-null mice lacking prothrombin, thrombin, and coagulation factor V before liver synthetic function (i.e., at E9 to E12) implies functional relevance of YS expression (Fig. 2D and data S25) (*15*, *16*), whereby coagulant and anticoagulant pathways develop in parallel to balance hemostasis.

YS endoderm cells expressed EPO and thrombopoietin (THPO) that are critical for erythropoiesis and megakaryopoiesis (Fig. 2, C and D; fig. S4H; and data S25 and S26). In mouse development, EPO is produced by the fetal liver and is only essential for definitive and the later stages of primitive erythropoiesis, with *Epo*/*Epor*-knockout mice dying at around E13 (*17*). An EPO source before liver development is therefore likely not needed in mice. Accordingly, EPO has not been found in the mouse YS (*18*) (fig. S4E). In parallel to the human YS, rabbit YS endoderm also produced EPO at gestational stages preceding liver development (fig. S4E). We compiled a 12-organ integrated human fetal atlas spanning 3 to 19 PCW (k = 3.12 million cells, n = 150 donors; fig. S8, G and H, and data S6 and S7) and observed that EPO and THPO production were restricted to the YS and liver (fig. S4H), specifically to YS endoderm and liver hepatocytes (fig. S4I). Differentially expressed genes (DEGs) between the early and late YS endoderm revealed active retinoic acid and lipid metabolic processes until 7 PCW, after which genes associated with cell stress and death were expressed (Fig. 2E and data S26). A decline in the proportion of YS endoderm cells producing EPO was compensated by the onset of EPO production by hepatocytes at 7 PCW (fig. S4J). Thus, the human YS plays a critical role supporting hematopoiesis, metabolism, coagulation, and erythroid cell mass regulation before these functions are taken over by the embryonic or fetal liver and then, ultimately, by the adult liver (metabolism and coagulation), bone marrow (BM) (hematopoiesis), and kidney (erythroid cell mass regulation) (Fig. 2F).

Early versus definitive hematopoiesis in the YS and liver

Human YS hematopoietic progenitors spanned two groups: HSPCs characterized by *SPINK2*, *CYTL1*, and *HOXB9* expression and cycling HSPCs characterized by cell cycle–associated genes, such as *MKI67* and *TOP2A* (fig. S5A and data S17). Using markers recently associated with early (*DDIT4*, *SLC2A3*, *RGS16*, and *LIN28A*) and definitive (*KIT*, *ITGA4*, *CD74*, and *PROCR*) HSPCs (*12*), we identified early and definitive fractions within both HSPCs and cycling HSPCs (Fig. 3, A to C). Early and definitive HSPCs expressed canonical HSPC genes, such as *SPINK2*, *HOPX*, and *HLF* (Fig. 3A and data S17), but diverged in expression of genes involved in multiple processes, such as enzymes (*GAD1*), growth factors (*FGF23*), adhesion molecules (*SELL*), and patterning genes (*HOXA7*) (fig. S5C and data S17). By logistic regression (LR), YS HSPCs had a high median probability of class correspondence to liver hematopoietic stem cells (HSCs), but this probability was higher for definitive than for early HSPCs (fig. S5B). YS cycling HSPCs had a bipartite probability distribution between liver multipotential progenitor (MPP) and common myeloid progenitor (CMP), with the definitive cycling HSPC more MPP-like compared with the early version. Differential protein expression in YS CITE-seq data indicated that CD122, CD194 (CCR4), and CD357 mark early HSPCs, whereas CD44, CD48, CD93, and CD197 (CCR7) mark definitive HSPCs (fig. S5D and data S27), in keeping with the reported use of CD34 and CD44 to segregate early- and definitive-type HSPCs by fluorescence-activated cell sorting (FACS) (*19*). We confirmed that an induced pluripotent stem cell (iPSC)–derived culture system reported to generate definitive HSPCs did express RNA markers characteristic of definitive HSPCs (*12*), but an iPSC-derived culture system optimized for macrophage production (*20*) did not (Fig. 3A).

To assess cross-tissue HSPC heterogeneity, we integrated HSPCs across hematopoietic organs (Fig. 3C, fig. S5E, and data S6 and S7). By kernel density estimation (KDE) score on integrated uniform manifold approximation (UMAP) embeddings, YS definitive HSPCs qualitatively co-localized with definitive HSPCs from age-matched liver (Fig. 3C and fig. S5E). From exclusively early HSPCs at ~3 PCW, we observed rapid accumulation of definitive HSPCs after AGM development CS14 (~5 PCW), likely accounting for the increase in the YS HSPC/progenitor fraction at 8 PCW (Fig. 1G, Fig. 3B, and fig. S5F).

Next, we examined the transition from YS to liver hematopoiesis. Before AGM, the human embryonic liver is macroscopically pale, which suggests that erythropoiesis predominantly occurs in the YS (Fig. 3D). We tracked the proportional representation of hemoglobin (Hb) subtypes over time as a proxy for YS versus embryonic liver contributions. *HBZ* and *HBE1* (genes for Hb Gower 1) were restricted to YS erythroblasts, whereas *HBG1* (which forms fetal Hb/HbF in combination with an alpha chain) was expressed in fetal liver erythroblasts (*21*–*25*) (Fig. 3E and fig. S5H). The sustained *HBZ* production in YS for several days before liver bud formation (4 PCW) was consistent with a scenario where the YS supports initial erythropoiesis. At 7 PCW, the embryonic liver contained both *HBZ* and *HBG1* (Fig. 3E), in keeping with previous studies of Hb switching (*8*). By 8 PCW, embryonic liver erythroblasts expressed *HBZ*-repressors and were *HBG1*-dominant, as we have previously shown (*10*). By contrast, the mouse liver was macroscopically red before AGM maturation (Fig. 3D). Tracking Hb subtype usage in the mouse, we noted two waves of pre-AGM erythropoiesis—an initial wave with *Hbb-y* and *Hba-x* transitioning to *Hba-a1/2*, and a second wave mirrored in both the YS and the torso or liver

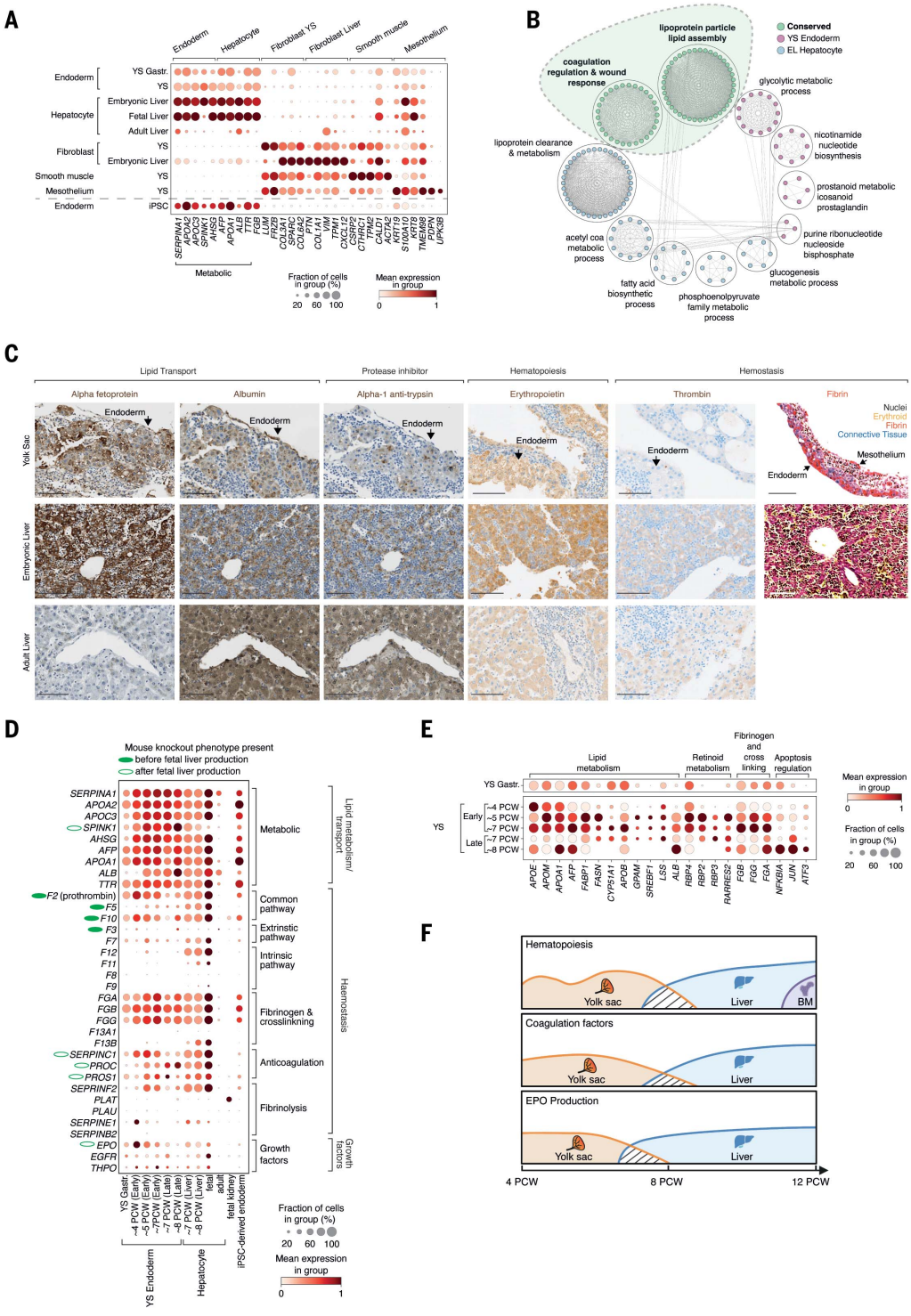

Fig. 2. Multiorgan functions of YS. (**A**) Dot plot showing the mean expression (color) and proportion of YS and liver stromal cells (dot size) expressing stromal DEG markers (data S3, S7, and S21). YS scRNA-seq data include main and gastrulation (gastr.) data. Liver scRNA-seq data include matched embryonic, fetal, and adult liver. (**B**) Flower plot illustrating significantly enriched pathways in YS endoderm (pink) and embryonic liver (EL) hepatocytes (blue). Conserved pathways between tissues are highlighted in green and a dashed outline (data S25). (**C**) (Columns 1 to 3) IHC staining of alpha fetoprotein (*AFP*), albumin (*ALB*), and alpha-1 antitrypsin (*SERPINA1*) in 8-PCW YS (top), EL (middle), and adult liver (bottom). Representative images of n = 5 YS (4 to 8 PCW), n = 3 ELs (7 to 8 PCW), and n = 3 adult liver samples. (Columns 4 and 5) IHC staining of EPO and thrombin (F2) in 7-PCW YS (top), 7-PCW EL (middle), and healthy adult liver (bottom). Representative images from n = 3 samples per tissue: YS (4 to 7 PCW) and EL (7 to 12 PCW). Proteins are brown, and nuclei are blue. (Column 6) Martius scarlet blue (MSB)–stained 8-PCW EL (representative of n = 3) and 4-PCW YS (representative of n = 3). Nuclei are gray, erythroid is yellow, fibrin is red, and connective tissue is blue (data S23). Scale bars, 100 μm. (**D**) Dot plot showing the mean expression (color) and proportion of cells in YS endoderm; embryonic, fetal, and adult liver hepatocytes; and stromal cells from fetal kidneys. Brackets indicate enriched GO annotations. Green ellipses denote genes with prenatal phenotypes in homozygous-null mice. Solid and hollow green outlines denote phenotype onset before and after fetal liver (FL) function, respectively, as per fig. S4E (data S25). (**E**) Dot plot showing the mean expression (color) and proportion of cells expressing Milo-derived DEGs across gestation (dot size) in YS endoderm (data S24). Genes are grouped by function. (**F**) Schematic of the relative contributions of YS (orange), liver (blue), and BM (purple) to hematopoiesis, coagulation factor, and EPO production in the first trimester of human development.

(*Hbb-bt1* and *Hbb-bs*) (fig. S5, G to I). Thus, there is a species-specific difference in YS erythropoiesis and a rapid shift in Hb usage after AGM development in humans.

We examined data from human gastrulation (~2 to 3 PCW) and CS10 to CS11 (~4 PCW)—time points before AGM-HSPC formation—to explore the differentiation potential of early HSPCs. At gastrulation, the YS hematopoietic landscape had a tripartite differentiation structure, with erythroid, MK, and myeloid differentiation (Fig. 3F). This structure was also observed in the mouse YS (fig. S6, A and B, and data S5 and S11). Differential fate–prediction analysis demonstrated that early HSPCs pre-AGM at CS10 to CS11 (~4 PCW) were myeloid-biased, consistent with previous observations (*9*). However, the abundance of differentiating erythroid and MK cells at CS10 to CS11 suggested that an earlier wave of erythroid and MK production had occurred (Fig. 3G and fig. S6C). Post-AGM, the model predicted that remaining early HSPCs were erythroid- and MK-biased, whereas definitive HSPCs were lymphoid- and MK-biased (Fig. 3G). This was in keeping with the first appearance of YS lymphoid cells (ILC progenitors, NK cells, and B lineage cells)

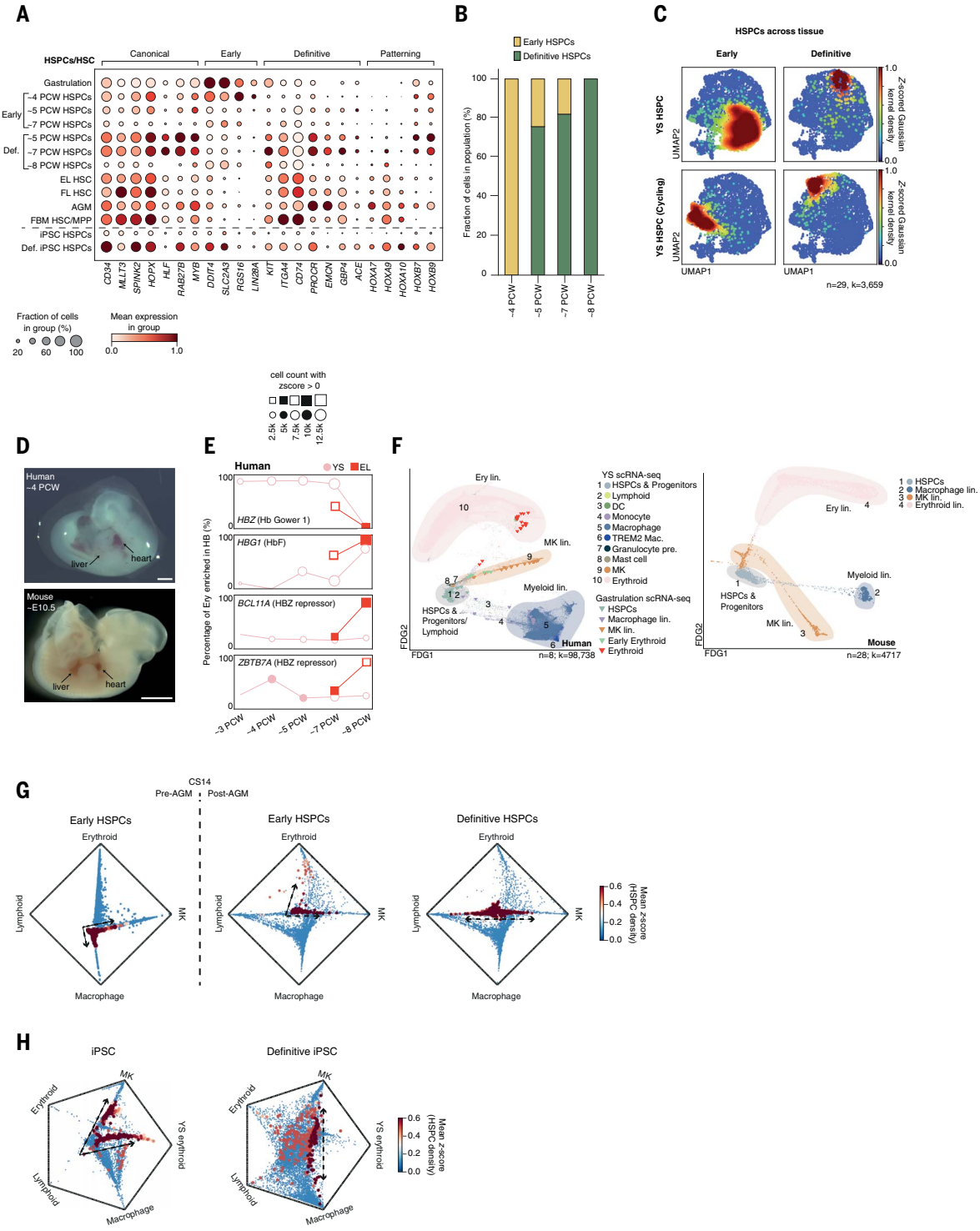

Fig. 3. Early versus definitive hematopoiesis in the YS and liver. (**A**) Dot plot showing mean expression (color) and proportion of cells expressing selected HSPC genes (dot size) in HSPCs from YS [main and gastrulation (*14*)], liver [EL and FL (*10*)], AGM (*76*), BM (*34*), and iPSC cultures [iPSC (*20*) and definitive iPSC (*12*)]. (**B**) Bar chart showing proportion of early (yellow) to definitive HSPCs (green) in the YS scRNA-seq data grouped by gestational age. (**C**) Density plots showing YS HSPC (top) and cycling HSPC (bottom) with early (left) and definitive signatures (right) in an integrated landscape as per (A). Color indicates population *z*-scored KDE (data S5). Tissue contributions are shown in fig. S5E. (**D**) Representative image of whole ~4-PCW or CS12 human (top; *n* = 4) and ~E10.5 or CS12 mouse embryo (bottom). Scale bars, 1 mm. (**E**) Line graphs showing change in erythroid cell proportion (*y* axis) enriched in globin gene expression across gestational age. Colors indicate scRNA-seq dataset: pink, human YS; red, matched EL. Shape size indicates cell count, scale indicates representative counts, and no shape indicates a count <500. Globins are grouped by roles in early or definitive hematopoiesis and repression. (**F**) FDG of hematopoietic cell states in the YS scRNA-seq data (*n* = 8, *k* = 98,738; dots) integrated with human gastrulation (*14*) scRNA-seq data (*n* = 1, *k* = 91; triangles) (left) and equivalent cell states in the mouse gastrulation scRNA-seq dataset (*75*) (*n* = 28, *k* = 4717; dots) (right). Colors represent cell

states, and clouds mark lineages. (**G**) Radial plots showing lineage transition probabilities between pre-AGM (CS10 to CS11; left) and post-AGM (>CS14; right) YS early and definitive HSPCs. Color indicates population *z*-scored KDE. Density position indicates respective lineage priming probability between macrophage, lymphoid (NK and B lineage), erythroid, and MK terminal states. Arrows indicate proposed lineage priming based on KDE. (**H**) Radial plots showing lineage transition probabilities between iPSC-derived HSPCs (left) and definitive iPSC-derived HSPCs (right). Interpretation as in (G), with addition of embryonic erythroid terminal state.

post-CS14 (Fig. 1G). Differential fate–prediction analyses suggested that iPSC-derived HSPCs were embryonic erythroid-, myeloid-, and MK-biased, whereas definitive iPSC-derived HSPCs were lymphoid-, MK-, erythroid-, and myeloid-primed, consistent with the predicted lineage potential of their in vivo early and definitive counterparts (Fig. 3H and fig. S6D).

The life span of YS HSPCs

HSPCs arise from hemogenic endothelium (HE) in the aorta, YS, BM, placenta, and embryonic head in mice (*26*–*30*). In the human AGM, definitive HSPCs emerge from *IL33*$^{+}$*ALDH1A1*$^{+}$ arterial endothelial cells (AECs) via *KCNK17*$^{+}$*ALDH1A1*$^{+}$ HE (*31*). Dissecting YS endothelial cell (EC) states in greater detail, the broad category of PLVAP^{+} ECs included AECs and HE, whereas LYVE1^{+} ECs encompassed sinusoidal, immature, and Von Willebrand factor (VWF)–expressing ECs (Fig. 4A; fig. S7, A and B; and data S4 and S5). HE was a transient feature of early YS (Fig. 4A). Along inferred trajectories, YS HSPCs appeared to arise from AECs via HE as in AGM (*12*), sequentially up-regulating expected genes such as *ALDH1A1* (*32*) (Fig. 4B). The same EC intermediate states and transition points were identified in both iPSC culture systems (Fig. 4B and fig. S7C). In keeping with their more recent endothelial origin, we found that YS HSPCs and AGM HSPCs, but not embryonic liver or fetal BM HSPCs, retained an EC gene signature characterized by the expression of *KDR*, *CDH5*, *ESAM*, and *PLVAP* (Fig. 4C).

Receptor-ligand interactions capable of supporting HSPC expansion and maintenance in YS were predicted using CellPhoneDB (*33*) and compared with predictions in fetal BM (*34*). We identified YS ECs, fibroblasts, smooth muscle cells, and endoderm as likely interacting partners (Fig. 4, D to F, and data S28). YS ECs, like fetal BM ECs, were predicted to maintain and support the HSPC pool (*35*) through the production of stem cell factor (*KITLG*) and *NOTCH1/2*, although the repertoire of NOTCH ligands diverged between tissues (*DLL1* and *JAG1* in YS and *DLK1*, *JAG1/2*, *NOV*, and *DLL4* in BM) (Fig. 4D). The YS endoderm was predicted to support HSC pool expansion (*36*) through *WNT5A* signaling to *FZD3*. *WNT5A* was also expressed by a wide range of BM stromal cell types, but BM HSPCs were predicted to respond via *FZD6* rather than *FZD3*. All YS stromal fractions contributed to the extracellular matrix, which provides a substrate for adhesion but also modifies HSPC function, with *FN1* (from all fractions) potentially expanding the HSPC pool and *VTN* (from the endoderm) contributing to long-term HSC-like quiescence (Fig. 4, D and F) (*37*, *38*). Although BM HSPCs were also predicted to adhere to extracellular matrix proteins, the integrins and matrix constituents differed. The YS endoderm was predicted to form interactions with HSPCs via *EPO*, which may influence the fate of differentiating progenitors (*39*), and *THPO*, which supports HSC quiescence and adhesion in BM (*40*). No BM stromal source of *EPO* or *THPO* was detectable in our data, however (*10*, *34*). Thus, these anatomically different hematopoietic tissues use similar pathways to support HSPCs, albeit with tissue-specific components.

YS HSPC receptor to stromal ligand interactions diminished between CS17 and CS23 (4 to 8 PCW), including the loss of cytokine and growth factor support and the loss of *TFGB1*, *WNT*, and *NOTCH2* signals (Fig. 4E, fig. S7E, and data S29). In many interactions, there was a reduction in HSPC receptor expression as well as stromal ligand expression (Fig. 4E; fig. S7, D and E; and data S29); yet, ligands were still expressed in age-matched liver and AGM stromal cells (fig. S7F and data S29). Adhesive interactions in the YS were also predicted to be significantly modulated (fig. S7, F and G, and data S29). Although aged-matched liver provided opportunities for adhesion with stromal cells, the AGM did not (fig. S7F and data S29). YS interactions gained between CS17 and CS23 included endoderm-derived *IL13* signaling to the *TMEM219*-encoded receptor implicated in the induction of apoptosis (Fig. 4D). Although limited conclusions can be made from studying cells that passed quality control for cell viability, we did observe up-regulation in pro-apoptotic gene scores in late-stage YS HSPCs, both early and definitive (fig. S7H).

Despite a marked change in the stromal environment of the later stage YS, the proportion of HSPC to cycling HSPC remained stable (fig. S5F). Differential lineage priming analysis revealed that very few HSPCs remained in CS22 to CS23 (8 PCW) YS, and most cells were terminally differentiated (fig. S6C). Thus, it is likely that an early burst of early HSPC production arises from transient YS HE, a later influx of definitive HSPCs derives from AGM, and a loss of stromal support between 6 and 8 PCW results in apoptosis and depletion of remaining HSPCs by terminal differentiation.

An accelerated route to macrophage production in YS and iPSC culture

Although YS hematopoietic progenitors are restricted to a short time window in early gestation, mouse models suggest that they contribute to long-lived macrophage populations in some tissues (*41*). By scRNA-seq, transcriptionally similar macrophage populations can be identified in the YS and fetal brain before the emergence of definitive HSPCs (*9*). In our previous work, k = 6682 YS macrophages resolved into two subgroups (*10*). By contrast, our integrated dataset of k = 45,118 YS macrophages in the current study revealed a greater heterogeneity, including premacrophages, *C1QA/B/C*- and *MRC1*-expressing macrophages, and a rare *TREM2*$^{+}$ macrophage subset (fig. S8A). Promonocytes expressing *HMGB2*, *LYZ*, and *LSP1* and monocytes expressing *S100A8*, *S100A9*, and *MNDA* were also detected (fig. S8A). Monocytes were observed only after liver development and AGM-derived hematopoiesis at CS14 (~5 PCW), but premacrophages and macrophages formed as early as CS10 (~4 PCW) (Fig. 5A and fig. S8B). Although the potential of early YS HSPCs to differentiate into monocytes has been demonstrated in vitro (*9*), there were too few promonocytes and monocyte progenitors (MOPs) in our data before CS14 to reliably confirm this potential. We identified two populations of YS monocytes, which diverged in expression of adhesion molecules. YS monocyte 2 expressed adhesion molecules *ICAM3*, *SELL*, and *PLAC8* (Fig. 5B), which were also expressed on fetal liver but not YS HSPCs (fig. S5C). YS monocyte 2 had a high probability of class prediction against fetal liver monocytes (fig. S8C). Thus, monocyte 2 is likely a recirculating fetal liver monocyte, although sequential waves of monocytopoiesis occurring within the YS cannot be excluded. YS CITE-seq data were used to identify discriminatory markers (CD15 and CD43 for monocyte 1; CD9 and CD35 for monocyte 2) and provide protein-level validation for differential expression of *SELL* (CD62L) and CD14 (fig. S8D and data S20).

The YS premacrophage differentially expressed high levels of *PTGS2*, *MSL1*, and *SPIA1* as well as expressing progenitor genes (*SPINK2*, *CD34*, and *SMIM24*), macrophage genes (*C1QA* and *MRC1*), and *CD52*, which is typically associated with monocytes (fig. S8A). This YS premacrophage rapidly declined by 5 PCW (Fig. 5A) and had no equivalent in the embryonic liver (fig. S8C). k-nearest neighbor (KNN) graph–based FDG and partition-based graph abstraction (PAGA) suggested a direct monocyte-independent trajectory to YS macrophages before CS14 (Fig. 5C and data S5). In this pre-AGM trajectory, a transition from HSPC to premacrophages then macrophages (nodes 1, 5, and 6 in Fig. 5C, upper panel) fit with our predictions that pre-AGM HSPCs exhibit myeloid bias (Fig. 3G). After CS14,

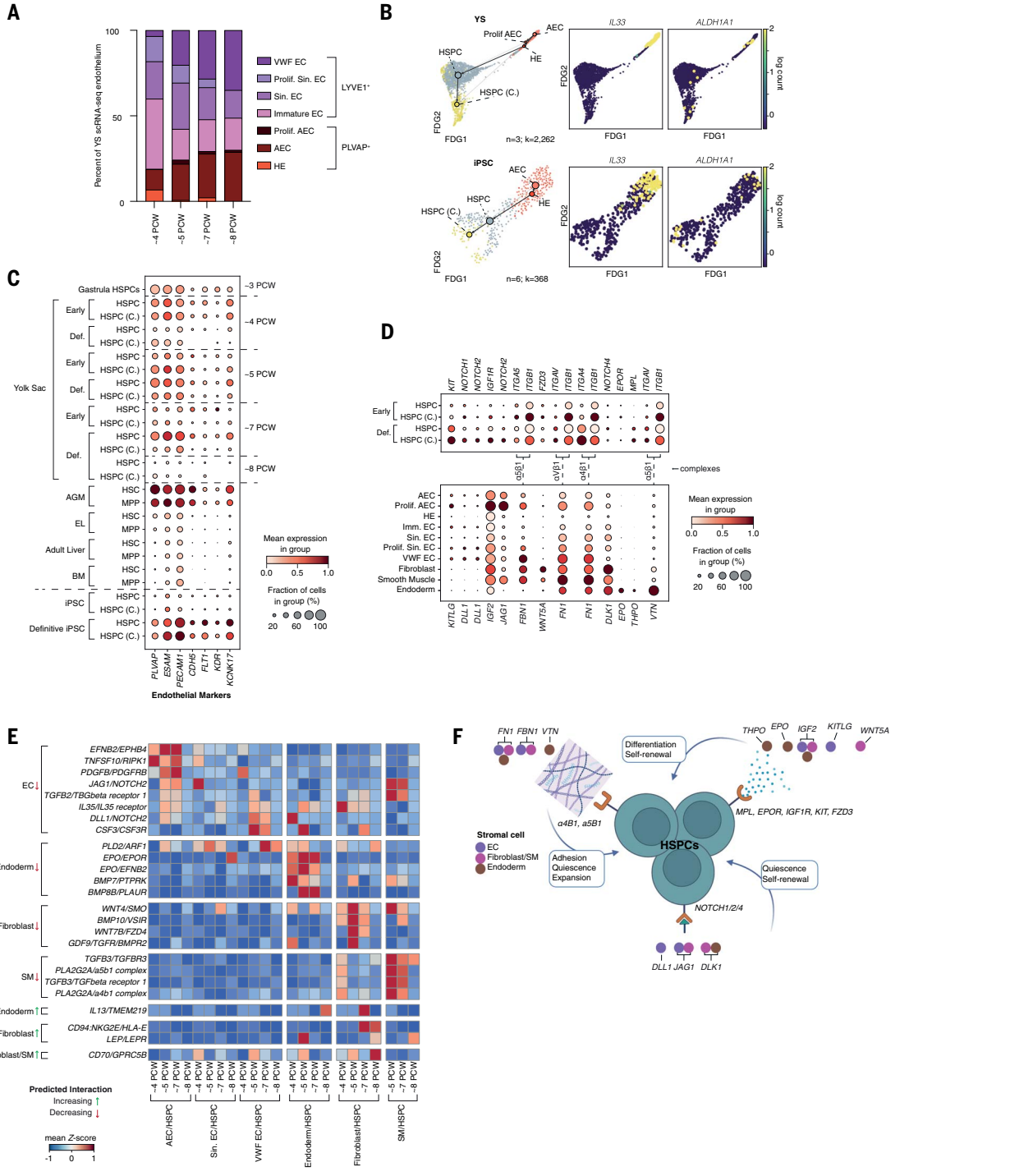

Fig. 4. The life span of YS HSPCs. (**A**) Bar chart showing the relative proportions of YS EC subsets by age (PCW). sin. EC, sinusoidal endothelial cells. (**B**) FDG overlaid with PAGA showing trajectory of HE transition to HSPC in YS scRNA-seq data (n = 3; CS10, CS11, and CS14; k = 2262) (top) and iPSC-derived HSPC scRNA-seq data (n = 7; k = 437) (*20*) (bottom), with feature plots of key genes (*IL33*, *ALDH1A1*) involved in endothelial to hemogenic transition (data S5). (**C**) Dot plot showing the mean expression (color scale) and proportion of cells expressing EC-associated genes (dot size) in HSPCs across gestational age (PCW). HSPCs are derived from YS (including gastrulation), AGM (*12*), matched EL and FL (*10*), fetal BM (*34*), iPSC-derived HSPC (*20*), and definitive iPSC-derived HSPC (*12*) scRNA-seq datasets. (**D**) Dot plot of the mean expression (color scale) and the fraction of cells expressing each gene (dot size) of curated genes predicted by CellphoneDB to form statistically significant (P < 0.05) protein-protein interactions between HSPCs (top) and stromal cells (bottom) across all time gestational points. Brackets indicate which protein counterparts form complexes (data S29). Data are log-normalized, variance-scaled, and min-max–standardized with a distribution of 0 to 1. (**E**) Heatmap showing curated and statistically significant (P < 0.05) CellphoneDB-predicted interactions between YS HSPCs and stromal cells that change across gestation. Color scale indicates relative mean expression z-scores. (**F**) Schematic of selected and statistically significant (P < 0.05) CellphoneDB-predicted interactions between YS HSPCs and endoderm, fibroblasts (Fib), smooth muscle cells (SMCs), or EC derived from scRNA-seq data. Interactions are grouped by predicted receptor to ECM interactions, ligand-receptor interactions, and surface-bound ligand-receptor interactions. Receptors and ligands in italics significantly decrease at CS17 to CS23 (6 to 8 PCW) (data S28 and S29).

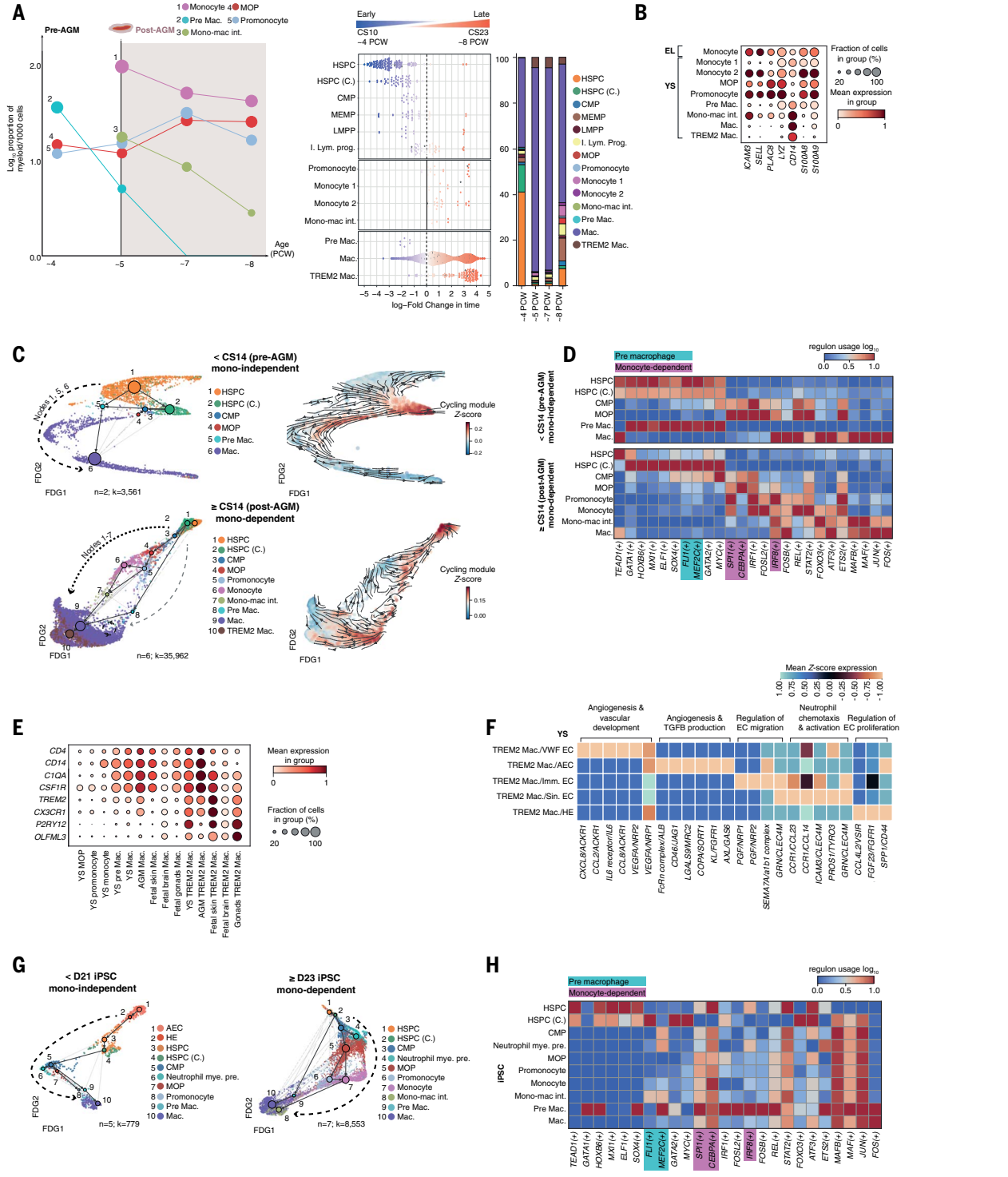

Fig. 5. Accelerated macrophage production in YS and iPSC culture. (**A**) (Left) Line graph of monocyte and macrophage proportions in YS scRNA-seq across time. Dashed line indicates pre- and post-AGM stages. (Middle) Milo beeswarm plot showing differential abundance of YS scRNA-seq myeloid neighborhoods across time. Color shows degree of enrichment (blue, early; red, later) (data S4 and S24). (Right) Bar chart of YS scRNA-seq myeloid cell state proportions across time. Mono-mac int., monocyte macrophage intermediate. (**B**) Dot plot showing the mean expression (color) and proportion of cells expressing monocyte marker genes (dot size) in EL monocytes and YS myeloid cell states. Genes include YS versus EL monocyte DEGs and established monocyte markers (data S17). (**C**) (Left) FDG of macrophage trajectory in YS scRNA-seq, colored by cell state, overlaid with PAGA showing monocyte-independent <CS14 (pre-AGM; n = 2; k = 3561; top) and monocyte-dependent trajectories >CS14 (post-AGM; n = 6; k = 35,962; bottom) (data S5). (Right) FDG overlaid with scVelocity directionality, colored by cell cycle gene enrichment (GO:000704 module). (**D**) Heatmap of regulons associated with trajectories in (C). TFs discussed in the text are highlighted (turquoise, premacrophage; purple, monocyte-dependent). (**E**) Dot plot showing the mean expression (color) and proportion of cells expressing macrophage and microglia marker genes (dot size) in myeloid cell states in YS, AGM (*12*), skin (*48*), gonad (*49*),

and brain (55) fetal scRNA-seq datasets (data S13 and S31). (**F**) Heatmap of significant ($P < 0.05$) CellphoneDB-predicted interactions between YS scRNA-seq *TREM2*$^+$ macrophages and ECs (data S28). Color represents *z*-scored expression of gene pairs, and brackets indicate top curated interactions for cell-state pairs. (**G**) FDG of macrophage trajectory in iPSC scRNA-seq (20) colored by cell state, overlaid with PAGA showing monocyte-independent <D21 ($n = 5$; $k = 779$; left) and monocyte-dependent >D21 ($n = 7$; $k = 8553$; right) transitions (data S7 and S5). (**H**) Heatmap of regulons associated with iPSC macrophage trajectories shown in (G). TFs discussed in the text are highlighted, as in (D).

there was a clear differentiation trajectory from cycling HSPC to monocytes and monocyte-macrophages (nodes 1 to 7 in Fig. 5C, lower panel). After CS14, 15.33% of this macrophage pool was proliferating, and CellRank RNA state transition analysis was in keeping with active self-renewal (fig. S8E and data S5). Using PySCENIC, YS premacrophages were predicted to use a group of transcription factors (TFs), including *FLI1* and *MEF2C*, that have been reported in the differentiation of multiple lineages (42, 43). By contrast, the monocyte-dependent route (CMPs, MOPs, promonocytes, and monocytes) relied on recognized myeloid TFs such as *SPI1*, *CEBPA*, and *IRF8* (Fig. 5D and data S30).

TREM2$^+$ macrophages expressed microglia-associated transcripts *CX3CR1*, *OLFML3*, and *TREM2* and were observed in the YS only after CS14 (Fig. 5, A, C, and E; fig. S8A; and data S13). By PAGA and CellRank state transition analysis, *TREM2*$^+$ macrophages were closely aligned to the self-renewing macrophage population (Fig. 5C and fig. S8E). YS *TREM2*$^+$ macrophages were located adjacent to the mesothelium, in a region enriched by ECs (fig. S8F). CellPhoneDB predicted interactions between *TREM2*$^+$ macrophages and *VWF*$^+$ ECs via *CXCL8* and *NRP1*, both of which are involved in angiogenic pathways (44, 45) (Fig. 5F and data S28). *TREM2*$^+$ macrophages also expressed the purinergic receptor *P2RY12*, which supports trafficking toward adenosine 5′-triphosphate (ATP)– or adenosine 5′-diphosphate (ADP)–expressing ECs, as reported in the mouse central nervous system (46, 47) (Fig. 5E and data S31). To establish whether *TREM2*$^+$ macrophages are present in other fetal tissues, we assembled an integrated 12-organ developmental atlas (fig. S8G). We resolved six macrophage fractions based on harmonized cross-tissue definitions from our recent prenatal immune analysis (by label transfer): premacrophages and *TREM2*$^+$ macrophages (as in our cluster-driven annotations) as well as LYVE1^{hi}, Kupffer-like, iron-recycling, and proliferating macrophages (48) (fig. S8, C and G to J, and data S5 to S7 and S17). *TREM2* is implicated in lipid sensing by anti-inflammatory tissue macrophages in the adult human and mouse (23–25), but we observed the highest expression of *TREM2* in macrophages bearing a microglia-like signature in developing tissues, including YS, skin [as previously reported (48)], gonads [as previously reported (49)], brain, and AGM but not BM, liver, kidney, thymus, mesenteric lymph nodes (MLNs), or gut (fig. S8, I and J, and data S31).

Next, we investigated whether transcriptional features of pre-AGM macrophages could be used to evaluate YS macrophage contribution to developing tissues. In our 12-organ macrophage dataset, pre-AGM macrophages were compared against post-AGM macrophages in an integrated variational-autoencoder (VAE) latent space using a Bayesian differential expression approach. The most predictive pre-AGM macrophage features comprised nine genes, including five genes in common with a TLF$^+$ signature identified from cross-tissue analysis of mouse macrophages (*LYVE1*, *TIMD4*, *FOLR2*, *MRC1*, and *NINJ1*) (50) (fig. S9A and data S17). By KDE, macrophages significantly enriched in our pre-AGM module colocalized with LYVE1^{hi} macrophages from gonads, liver, skin, and AGM and with all macrophage fractions from the YS (fig. S9, B to D; fig. S8H; and data S7 and S32). The proportion of pre-AGM module-enriched macrophages trended downward over time, even in the brain (fig. S9E). By transcriptome alone, it was not possible to separate dilution by influx of non-YS macrophages from transcriptional adaptation to the tissue environment. With this caveat, we assembled a 20-organ, cross-tissue integrated landscape of adult tissue macrophages using publicly available single-cell data from the Human Cell Atlas and Tabula Sapiens (fig. S9, F to H, and data S6, S7, S14, and S17). Fat, vasculature, muscle, brain, and bladder had the highest proportion of macrophages enriched in the pre-AGM signature (fig. S9H and data S7).

We integrated our YS gene expression data with scRNA-seq data from iPSC-derived macrophage differentiation ($n = 19$; $k = 50{,}512$) (20) after refining the annotations of iPSC-derived cell states (fig. S10, A to C, and data S5 and S13). Nonadherent, *CD14*-expressing cells appearing after week 2 of differentiation expressed *C1QA*, *C1QB*, and *APOC1* in keeping with a macrophage identity, whereas *CD14*-, *CD52*-, *FCN1*-, and *S100A8/9*-expressing monocytes only emerged after week 3 (fig. S10, D and E). Before monocyte emergence, a monocyte-independent macrophage differentiation trajectory was observed, consistent with previous observations (20) (Fig. 5G and fig. S10C). TF regulatory profiles of iPSC-derived macrophage differentiation were consistent with both the premacrophage and monocyte-dependent TF profiles inferred from our YS data, including usage of *MEF2C*, *SPI1*, *CEBPA*, and *IRF8* in iPSC-derived premacrophages (Fig. 5H and data S30). However, neither iPSC culture system could recapitulate the heterogeneity of macrophages seen in native tissues (fig. S10E), which suggests that interactions with stromal cells, such as ECs, may be required to acquire specific molecular profiles.

Discussion

Using single-cell multiomic and imaging technologies, we delineate the dynamic composition and functions of human YS in vivo from 3 PCW, when the three embryonic germ layers form, to 8 PCW, when most organ structures are already established (21). Although the scarcity and small sample size necessitated a primarily computational approach, we deliver a comprehensive resource. LR and VAE models provided by our data will facilitate future use of our YS atlas to map scRNA-seq datasets (51, 52), empowering future mechanistic perturbation and lineage-tracing experiments in iPSCs and model systems.

We detail how the YS endoderm shares metabolic, biosynthetic, and erythropoiesis-stimulating functions with the liver. In part, this shared functionality may relate to their common role in creating a hematopoietic niche (53). We identify differences in the handover from YS to liver hematopoiesis between species. In mice, erythroid progenitors in the YS mature before the onset of circulation, but erythromyeloid progenitors can exit the YS and mature in the fetal liver, giving rise to long-lived populations, such as fetal liver monocyte–derived macrophages. We show that in human YS, active differentiation of erythroid and macrophage cells occurs for several weeks before liver handover, and, at least in terms of erythropoiesis, there is a rapid transition from YS erythroid production to embryonic liver erythroid production shortly after AGM-derived HSPCs emerge. In a landmark study on human Hb switching, directly labeled 6-PCW liver and YS erythrocytes contained embryonic Hb subunits (ε and ζ), but colonies derived from liver and YS progenitors at this time produced fetal Hb subunits (α and γ) (8). This is in keeping with YS-derived erythrocytes recirculating throughout the embryo and membranes while a post-AGM progenitor is preparing for liver erythropoiesis. Direct evidence that human liver erythropoiesis is supplied predominantly from AGM-derived HSPCs rather than a YS-derived EMP-like progenitor is still lacking. Future studies are needed to examine the handover of macrophage production from early to definitive sources in humans, which may question the primacy of mouse models of early myelopoiesis. A more expansive species reference, including rabbits with their greater early gestational similarity to humans,

will facilitate selection of appropriate models for genetic manipulation and functional validation (*54*).

The developmental window investigated in this work encompasses hematopoiesis from HSPCs arising both within the YS and within the embryo proper. We reconstructed YS HSPC emergence from a temporally restricted HE, featuring similar transition states and molecular regulation to AGM HSPCs. By gastrulation (CS7; 2 to 3 PCW), YS HSPCs already differentiate into erythroid, MK, and myeloid lineages. Building on a recent compilation of gene scorecards that characterize early and definitive HSPCs (*12*), we were able to parse the two fractions and document the transition to definitive HSPC dominance after CS14 (~5 PCW). This separation also allowed us to identify an early HSPC bias toward myeloid, erythroid, and MK lineages and a definitive HSPC bias toward MK and lymphoid lineages. Both early and definitive YS HSPCs became more quiescent and up-regulated apoptosis-related genes between CS17 and CS23 (~6 to 8 PCW). Stromal cell ligands predicted to support HSPCs were markedly disrupted during this time, which suggests that the barriers to YS HSPC survival may be extrinsic.

Early HSPCs use an accelerated route to macrophage production independent of monocytes. Both accelerated and monocyte-dependent macrophages were recapitulated during in vitro differentiation of iPSCs, but diverse macrophage subtypes, such as *TREM2*$^+$ macrophages, were not. *TREM2*$^+$ macrophages, which are transcriptionally aligned with brain microglia, fetal skin, testes, and AGM *TREM2*$^+$ macrophages, were predicted to interact with ECs, potentially supporting angiogenesis, as has been described in the mouse brain (*55*).

There is a growing appreciation of the potentially life-long consequences of early developmental processes. Our study illuminates a previously obscure phase of human development, where vital organismal functions are delivered by a transient extraembryonic organ using noncanonical cellular differentiation pathways that can be leveraged for tissue engineering and cellular therapy.

Materials and methods

Ethics and sample acquisition

Tissues were obtained from the MRC–Wellcome Trust-funded Human Developmental Biology Resource (HDBR; https://www.hdbr.org) with appropriate written consent and approval from the Newcastle and North Tyneside NHS Health Authority Joint Ethics Committee (18/NE/0290). HDBR is regulated by the UK Human Tissue Authority (HTA; www.hta.gov.uk) and operates in accordance with the relevant HTA Codes of Practice. Tissues used for light-sheet fluorescence microscopy were obtained through INSERM's HuDeCA Biobank and made available in accordance with the French bylaw (Good practice concerning the conservation, transformation and transportation of human tissue to be used therapeutically, published on 29 December 1998). Permission to use human tissues was obtained from the French agency for biomedical research (Agence de la Biomédecine, Saint-Denis La Plaine, France).

Embryos were staged using the Carnegie staging method (*56*). A piece of skin or chorionic villi tissue was collected from each sample to perform quantitative PCR karyotyping of sex chromosomes and autosomal chromosomes 13, 15, 16, 18, 21, and 22 for the most commonly seen chromosomal abnormalities. No abnormalities were detected.

Processing samples for imaging and single-cell sequencing

Tissues were transported in phosphate-buffered saline (PBS) on ice, were dissected within 24 hours, and were processed immediately (<1 hour after dissection). For formalin-fixation and paraffin-embedding, samples were immediately placed in 10% (w/v) formalin. Processing and embedding were performed by NovoPath, Newcastle upon Tyne NHS Trust. For RNAscope, samples were snap-frozen in an isopentane bath in liquid nitrogen before embedding in optimal cutting temperature (OCT) compound. Single-cell suspensions were generated by dicing tissue into segments <1 mm^3, followed by enzymatic digestion for 30 min at 37°C with intermittent shaking. Digestion media was 1.6 mg/ml collagenase type IV (Worthington) in RPMI (Sigma-Aldrich) supplemented with 10% (v/v) heat-inactivated fetal bovine serum (FBS; Gibco), 100 U/ml of penicillin (Sigma-Aldrich), 0.1 mg/ml of streptomycin (Sigma-Aldrich), and 2 mM L-glutamine (Sigma-Aldrich). Digested tissue was passed through a 100-μm filter, and cells were collected by centrifugation (500*g* for 5 min at 4°C). Cells were treated with 1X red blood cell (RBC) lysis buffer (eBioscience) for 5 min at room temperature and washed once with Flow Buffer [PBS containing 5% (v/v) FBS and 2 mM EDTA] before counting. Processing for scRNA-seq was continued promptly on fresh cells, for other uses (including CITE-seq) cells were collected by centrifugation (500*g* for 5 min at 4°C) and resuspended in 10% (v/v) dimethyl sulfoxide (DMSO) in FBS for freezing. For light-sheet fluorescence microscopy, tissues were fixed in 4% paraformaldehyde (PFA) and dissected. Gestational age was then estimated as previously described (*57*).

Processing of single-cell suspensions for scRNA-seq

Immediately after isolation and counting, cells were collected by centrifugation (500*g* for 5 min at 4°C) and resuspended in a residual buffer. Three microliters of CD45 BUV395 (clone: HI30, BD Biosciences) was added to the resuspended cells and incubated on ice in the dark for 30 min, washed with Flow Buffer and resuspended at ~1 × 10^7 cells/ml. Immediately before sorting, cells were passed through a 35-μm filter (Falcon) and 4′,6-diamidino-2-phenylindole (DAPI) (Sigma-Aldrich) was added at a final concentration of 3 μM. Flow sorting was performed on a BD FACSAria Fusion instrument using DIVA v.8, and data were analyzed using FlowJo (v.10.4.1, BD Biosciences). Cells were gated to exclude dead cells and doublets, and then isolated for scRNA-seq analysis (droplet-based 10x Genomics, or plate-based Smart-seq2) using a 100-μm nozzle. For droplet-based scRNA-seq, CD45$^+$ and CD45$^-$ cells were sorted into separate chilled FACS tubes coated with FBS and prefilled with 500 μl of sterile PBS. For plate-based scRNA-seq, CD45$^-$AF$^+$SSC^{++} single cells were index-sorted into 96-well LoBind plates (Eppendorf) containing 10 μl of lysis buffer [TCL (Qiagen) + 1% (v/v) β-mercaptoethanol] per well.

Library preparation and sequencing of scRNA-seq and CITE-seq samples

For the droplet-based scRNA-seq experiments, cell suspensions isolated by FACS were counted and loaded onto the 10X Genomics Chromium Controller to achieve a maximum yield of 10,000 cells per reaction. 5′ V1 kits were used and sequencing libraries were generated according to the manufacturer's protocols. Libraries were sequenced using either an Illumina HiSeq 4000 or NovaSeq 6000 to generate at least 50,000 raw reads per cell.

For the plate-based scRNA-seq experiments, the frozen cell lysates were thawed on ice for 1 min. Purified cDNA was generated and amplified using a modified Smart-seq 2 protocol described in Villani *et al.* (*58*). Sequencing libraries were then generated using Illumina Nextera XT kits with v2 index sets A, B, C, and D. 384 cells were pooled and were sequenced using a HiSeq 4000 to generate at least 1 × 10^6 raw reads per cell.

For the CITE-seq experiments, frozen cells were thawed, counted, and pooled. Fc blocking reagent (Biolegend) was added to the cell pools and left to incubate at room temperature for 10 min. Five hundred nanoliters of CD34 APC/Cy-7 (clone: 581, Biolegend) was then added to the Fc-blocked cells and left to incubate in the dark and on ice for 10 min. During this incubation, the CITE-seq antibody cocktail (Biolegend) (see data S33) was centrifuged at 14,000*g* for 1 min. Flow buffer was then added to reconstitute before incubating for 5 min at room temperature. The resuspended antibody cocktail was then centrifuged at 14,000*g* for a further 10 min before adding to the cells. The cells and CITE-seq antibody cocktail were then left to incubate for 30 min in the dark and on ice. After this time, the cells were washed twice with Flow buffer and resuspended in a final concentration of 50 μg/ml of 7 AAD (Thermo Fisher Scientific) in Flow buffer.

Live, single cells or live, single CD34$^-$ cells and live, single CD34$^+$ cells (for the CITE-seq experiments) were then isolated by FACS into 500 μl of PBS in FACS tubes coated with FBS. Cells were then counted and submitted to the CRUK CI Genomics Core Facility for subsequent processing using 10x Genomics protocols and sequencing. Single-cell gene expression and cell surface protein libraries were generated using single-cell 3′ v3 kits according to the manufacturer's protocol. Libraries were sequenced using a NovaSeq 6000 to achieve a minimum of 20,000 reads per cell for gene expression and 5000 reads per cell for cell-surface protein.

Alignment, quality control, filtering, and preprocessing of scRNA-seq and CITE-seq data

scRNA-seq expression data (including droplet-based and plate-based) were mapped with CellRanger (version 3.0.2) to a human reference genome (see data S1) and low-quality cells expressing <2000 reads, <200 genes, and >20% mitochondrial reads were filtered out of the data. Data on genes expressed in fewer than three cells was removed.

For droplet-based scRNA-seq data, the following additional QC steps were performed. Scrublet (*59*) v0.2.3 was applied to each sequencing lane for doublet detection, and clusters with > [median + (1.48 × MAD)] (where MAD is the median absolute deviation) of the median cluster doublet detection score were removed (data S3). Ambient RNA was removed with Cellbender (v0.2.0) with false discovery rate (FDR) = 0.01 and epochs = 150 (*60*). To determine likelihood of maternal contamination, data were pooled by donor and submitted to Souporcell (v2.4.0) at genotype clusters k = 1 and k = 2 models to represent likelihood of no maternal contamination and possible maternal contamination, respectively. The optimal model was identified via BIC (Bayesian Information Criterion), where we observed a smaller BIC index at k = 2 in one donor (F37, Female, 5 PCW). Cells from the F37 alternate genotype were identified as potential maternal contaminants, composed mainly of monocytes (n = 149), and monocyte–macrophage intermediates (mono–mac int.) (n = 25), and excluded from downstream analysis.

For CITE-seq data, FASTQ alignment was performed for multiplexed RNA lanes with CellRanger (v4.0.0) and GRCh38-2020-A reference genome, and for multiplexed protein lanes with CITE-seq-Count (v1.4.3). Lanes with cells pooled from multiple donors were deconvoluted using Souporcell singularity image at https://github.com/wheaton5/souporcell. Low-quality cells expressing <200 genes and >20% mitochondrial reads were removed, and doublets were removed by applying Scrublet v0.2.3 to each sequencing lane and then removing clusters with >[median + (1.48 × MAD)] of the median cluster doublet detection score. CITE-seq protein data underwent QC and preprocessing as previously described (*34*) (i.e., cells were first filtered to intersect barcodes with counterpart CITE-seq RNA data, then unmapped antibodies were filtered out, and then protein cells were filtered for low quality by cells with <30 proteins and expressing >5000 reads) (data S4, S19, and S22).

scRNA-seq count matrix transformation, normalization, and preprocessing were performed using Scanpy (*61*) (v1.9.0) in python (v3.8.6). We normalized raw gene counts using the *sc.pp.normalize_total* function (*target_sum = 10e4*) and performed *ln(x)+1* transformation. Reported expression values were normalized, log-transformed, and scaled to variance of mean using the *sc.pp.scale* function independently for each analysis.

For CITE-seq data count matrix transformation, we first performed denoised and scaled by background (DSB)–normalization and applied a Gaussian mixture model (GMM) for background nonspecific binding signal regression per sample as previously described (*62*). For the first step, a modified DSB-normalization approach used in our previous study (*34*) was constructed. For each CITE-seq lane, low-quality/empty droplets were identified as droplets under the largest UMI peak which had a value <1.96 × standard deviations (std) of the mean UMI counts value (mu_UMI) per sample. Peak detection was conducted using the *scipy.signal.find_peaks* function. The number of peak detection bins were dynamically estimated as [3.322 × log(X)], where X was the total number of droplets. The model iterated through a series of 20 prominence intervals (0 to 20) with widths (0 to 10) where peaks detected < [mu_UMI-(1.96 × std)] were retained as empty droplet peaks. In cases where no empty droplet peaks were detected, the empty droplet threshold was taken to be <[mu_UMI – (1.96 × std)]. The estimated empty droplets matrix was then taken into downstream DSB normalization in the same way as our previous study (*34*). For the second step of CITE-seq matrix transformation, we trained a GMM to model the variance of protein expression levels in each cell. We used the sckitlearn (v.1.1.3) *sklearn.mixture.GaussianMixture* module to fit 20 models with an increasing number of cell clusters k (between k = 2 and k = 21) to represent expression patterns of each protein by cell. The optimal model was identified using BIC ($BIC_i = 2L_i + k_i \log n$) and AIC (Akaike information criterion) ($AIC_i = 2L_i + 2k_i$) metrics, where k is the number of GMM cell protein expression clusters, n is the number of cells in the sample, and L is the model log likelihood. The models with the best performing BIC and AIC scores were selected. The mean expression values of GMM clusters with lowest expression values from each GMM model were interpreted as mean background expression per protein. Background-signal regression was then carried out using a Gaussian linear model (GLM) per protein, constructed using the *GLM* function from *statsmodels (v0.13.5)* on standardized, per-cell background scores (BG_score). Per-cell background scores were defined by taking the euler number I to the power of each protein background mean (*mu_bg*), divided by *e* to the power of the protein expression in each cell (x), then scaled to a distribution between 0 and 1 by subtracting the minimum score and subsequently dividing by the maximum score. Background scores inversely correlate with the magnitude of background expression per cell. BG_score = [score – $\min(e^{mu\_bg}/e^{x})$]/$\max(e^{mu\_bg}/e^{x})$. The per-cell background signal regressed counts were used for subsequent analyses, interpretation, and visualization. Cells comprising the empty droplet matrix were removed and were not considered for downstream analyses.

Integration and batch correction of scRNA-seq and CITE-seq datasets

For integration of newly generated YS scRNA-seq data with external datasets, CellRanger count was first reapplied for the alignment of CS10/CS11 and CS14 embryonic YS scRNA-seq data previously acquired (*12*, *63*) (data S1). The following steps were then followed for the total integrated YS droplet-based scRNA-seq dataset. Highly variable gene (HVG) selection was performed using the *sc.pp.highly_variable_genes* function (min_mean = 0.001, max_mean = 10) for embedding by dispersion. Dimensionality reduction and batch correction was carried out using the scVI module within *scvi-tools* (v0.19.0) (*52*) as used in scvi-tools (*51*) (HVG = 7500, dropout_rate = 0.2, n_layer = 2) with biological replicate taken as the technical covariate. To ensure model performance was optimal for each independent analysis, scVI was benchmarked against the python implementation of Harmony (*64*) (*Harmonypy* v0.0.5) at various theta values between 1 and 20. kBET (*65*) and Silhouette scores (*sklearn.metric.sil_score*) were computed for each iteration between donor covariates and compared with the scVI integration. For integration of adult scRNA-seq data, publicly available single-cell and single-nuclei RNA-seq data of 20 healthy adult tissues (data S6 and S7) were integrated using scVI (HVG = 1500, layers = 1). Batch correction was conducted on donors, single cells or single nuclei, data source, number of genes, total counts, percentage of mitochondrial genes and ribosomal genes. See data S6 for information regarding external scRNA-seq datasets that have been incorporated and integrated in this study.

For multimodal integration of CITE-seq datasets, we compared the integration of both RNA and protein modalities using the *totalVI* module in *scvi-tools* (v0.19.0) against batch integration

using only the RNA modality the scVI module in scvi-tools. We performed *sc.pp.highly_variable_genes* function on RNA modality (HVG = 4000) accounting for FACs sampling and donor technical covariates. We then generated a multimodal totalVI VAE latent representation following totalVI pipeline (*52*). To benchmark performance between multimodal and single-modality scRNA-seq data integration, global silhouette distances between leiden clusters (res = 3) derived from the multimodal totalVI VAE latent representation were compared against clusters derived from the scVI derived VAE representation as described above (HVG = 4000, dropout_rate = 0.2, n_layer = 2) (fig. S11A). Intersecting cells captured between protein and RNA modalities (by barcode) were considered in the totalVI integration (fig. S11, B to D, and data S4 and S22).

All scVI VAE and ldVAE models trained on the YS and integrated atlases are available on our data portal (see Data and materials availability) and will facilitate transfer learning for future reference mapping of scRNA-seq data with single-cell architectural surgery (scArches) (*18*).

Clustering and annotation of scRNA-seq and CITE-seq data

Clustering of scRNA-seq and CITE-seq datasets was performed using the Leiden algorithm (*66*) (*sc.tl.leiden*) with a resolution parameter of *res* = 1.5 (CITE-seq res = 3) on a KNN graph (k = 30 for scRNA-seq and k = 15 for CITE-seq) unless specified otherwise. To measure the effect of decreasing graph complexity on specific populations (YS scRNA-seq endoderm and IPSC-derived macrophages) and global population specificity and homogeneity in each independent analysis, the neighborhood graph complexity parameter (k) was benchmarked at value intervals between 5 and 50. Benchmarked metrics for population specificity included the adjusted mutual information score (MI) and adjusted Rand index (RAND). Metrics for population homogeneity included the silhouette index (SI) and within-cluster sum of squared errors (WSS) (fig. S12, A and B, and data S3 and S7). In cases where datasets are compared probabilistically, or where new classifications have been made, an implementation of low-dimensional ElasticNet regression (EN) (described in the "Cell state predictions using probabilistic low-dimensional ElasticNet regression" section of the Materials and methods) was used to first classify individual cells where a model-specific decision threshold of 0.9 was used for classification tasks. Cells classified inherited labels from the model trained on YS scRNA-seq data. Clusters were then assigned classes if the majority projected label had a label count distribution of >[mean + (1 × std)] of label counts per cluster. Resultant cell state classifications were further manually checked using DEGs using the *sc.tl.rank_genes_groups* function in Scanpy which performed a two-sided Wilcoxon rank-sum test for genes expressed in >25% of cells, with a log-transformed fold change cutoff of 0.25. All P values were adjusted for multiple testing using the Benjamini–Hochberg method. Annotation of YS and liver CITE-seq data was performed by training an EN model using YS and embryonic liver scRNA-seq datasets as references, respectively. These labels were then distributed by majority voting onto Leiden clusters derived from CITE-seq data (data S9 and S10). The resultant cluster annotations were validated using the same markers identified in matched RNA data and underwent additional manual annotation where required. For differential expression testing of surface proteins in multimodal CITE-seq data, we conducted a one_vs_all DE test using the *vae.differential_expression module* within totalVI (Bayes factor > 3, median LFC > 0.25). Marker proteins and corresponding populations were subsequently subject to hierarchical grouping using the *sc.tl.dendrogram* functionality within Scanpy (fig. S11, B to D, and data S4, S20, and S22). Bayesian differential expression testing between cell states in the integrated 12 fetal organ atlas was carried out using a *scVI* integrated latent VAE representation with a one_vs_all DE test using the *vae.differential_expression module* within scVI (v0.19.0) (Bayes factor > 3, median LFC > 4). Variation of effect-sizes on state-specific normalized counts between latent variables in the integrated latent VAE representation were first modeled. The posterior likelihood of differential expression was attained by repeated one_vs_all sampling of the variational distribution. Significant features were defined with a likelihood of differential expression (Bayes factor) >3 and median LFC >4. Bayesian differential expression testing between myeloid cell states in the integrated 20 organ adult scRNA-seq atlas was carried out as described above (fig. S12C and data S6, S7, and S17).

Dimensionality reduction and marker expression visualization

For visualization, the UMAP algorithm was run using the *sc.tl.umap* function in Scanpy. Dot-plots and violin plots were produced in Scanpy and all gene expression values displayed were normalized, log-transformed, and scaled as described in the preprocessing section unless otherwise stated. Dot plots that display data from multiple datasets used independent log-normalization, variance scaling, and min-max standardization to a distribution of 0 to 1 per dataset unless otherwise stated. FDGs computed with the *sc.tl.draw_graphs* function in Scanpy using the Force Atlas2 parameter were used to infer trajectories. PAGA were computed on the KNN graphs and overlaid onto FDGs where nodes represented the centroid of each cell state cluster and the thickness of edges represented the similarity between cell states (data S5).

Proportion line graphs for specific populations (e.g., erythroid cells) enriched in specific genes (e.g., *HBZ*) using the *sc.tl.enrich* function in Scanpy were produced using Matplotlib (v3.6.2). To ensure temporal changes in population size and background expression were accounted for, we segregated our population of interest by age and computed changes in relative population proportion enriched in each gene, only considering cells expressing >0 log-normalized counts for each gene. Enriched cells were defined with >0 score of each scored gene subtracted with the mean expression of a randomly sampled set of 200 selected reference genes at 50 bins using the aforementioned enrichment function in *Scanpy*. Proportions of enriched cells in each cell type compartment were then plotted as a discrete time series across gestational age to visualize differential enrichment of cells expressing the genes of interest. Data point sizes represented enriched cell counts. To aid interpretation, an ordinal scale of representative cell counts was included as a legend in the plots.

Proportions of specific populations (e.g., macrophages) enriched in specific gene modules (e.g., pre-AGM module) were visualized using violin graphs produced using Matplotlib and *Seaborn* (v0.12.1) python libraries. To ensure background expression profiles were accounted for, we segregated our population of interest and computed changes in relative population proportion enriched in each gene module. Significant module enrichment was defined as described above. Enriched cells from each cell type compartment were then graphed across organs. Enrichment scores were standardized to the median by subtraction of the median and subsequent division by MAD.

Differential abundance testing and FACS correction

We tested for differential cell-state abundance across gestation using the *Milo* framework (*67*), correcting for CD45 positive and negative FACS isolation strategies using a previously published technique (*48*). Where FACs correction was applied, we calculated a FACS isolation correction factor for each sample s sorted with gate i as [fs = $\log(p_i S/S_i)$] where p_i is the true proportion of cells from gate i and S represents the total number of cells from both gates. A KNN graph was then constructed from the remaining cells using the *milopy.core.make_nhoods* function (prop = 0.05). Neighborhood labels were determined by majority voting of cell labels by frequency in each neighborhood (>50%). The YS scRNA-seq data was then split into five age bins (3 PCW, 4 PCW, 5 PCW, 7 PCW, and 8 PCW) and cell counts were modeled as a negative binomial generalized linear model (NB-GLM) with Benjamini–Hochberg weighted correction as previously described (*48*). Significantly differentially abundant neighborhoods

were detected by SpatialFDR– (<0.1, logFC < 0) for early enriched neighborhoods and (<0.1, logFC > 0) for late neighborhoods (data S24).

Beeswarm plots were generated using the *ggplot2* library (v3.4.2). Each node represents an independent neighborhood of cells derived from the KNN graph. The *x*-axis position of each node represents the fold-change (positive or negative) associated with the distribution of age groups present in each neighborhood where larger proportions of older groups in a given neighborhood encourages a positive fold change and vice versa. Colored nodes represent neighborhoods with significant enrichment ($P < 0.05$ spatial FDR) and the intensity represents the degree of significance.

Clustered gene set enrichment analysis

We ranked conserved markers ($P < 0.05$) between the endoderm cell state in YS scRNA-seq data against hepatocytes in embryonic liver scRNA-seq and endoderm in the mouse gastrulation scRNA-seq data using the *FindConservedMarkers* function in Seurat (v3.1) with Bonferroni-corrected FDR-adjusted *P* values. Markers were submitted for gene set enrichment ranking and analysis using the Enrichr tool as implemented in the *GSEApy* (v1.0) package to query the Gene Ontology (GO) Biological Process database (GO_BP_2022) (data S26). Using the enrichrR package (v3.0) in R, enrichment was first computed by Fisher exact test for randomly sampled genes to derive a mean rank and standard deviation to estimate background for each ontological term accessed. A *z*-score for deviation of each term to its background rank was then used to rank output genesets. We derived statistical significance (Fisher exact test < 0.05, ranked by *z*-score) for each gene set enrichment and performed Markov clustering (MCL) using the MCL (v1.0) package in R to derive network neighborhoods based on geneset intersect. Gene set clusters were annotated using the AutoAnnotate function in the RCy3 (v2.16) package and clusters were ranked by the mean *z*-score of all gene sets within each cluster and manually curated based on biological relevance. We used the Cytoscape software (v3.9.1) to visualize clusters.

Cell state predictions using probabilistic low-dimensional ElasticNet regression

Label transfer class assignments and median probability of class correspondence between gene expression matrices in single-cell datasets were carried out using a LR framework, as previously described (*34*), using a similar workflow to the *CellTypist* tool (*68*).

Raw scRNA-seq datasets being compared were first concatenated, normalized, and log-transformed, as described in preprocessing. HVG selection was performed (min_mean = 0.001, max_mean = 10) for embeddings by dispersion. HVG expression matrices were used as training inputs for models unless otherwise stated. For models trained in combined low-dimensional representations, linear VAE latent representations were computed using the *LDVAE* module within *scvi-tools* (hidden layers = 256, dropout-rate = 0.2, reconstruction-loss = negative binomial) with donor, dataset origin, and organ information taken as technical covariates. Where PCs were used as input for training, harmony batch-corrected PCs ($k = 100$ pcs) were used, using Harmonypy (v0.0.9) with technical covariates as described above. Harmony runs were iterated through theta = 1:20 and resultant embeddings benchmarked using kBET and silhouette scores between technical covariates where a low kBET rejection rate and corresponding high silhouette score denoted the optimal theta parameter.

ElasticNet regression (EN) LR models were built using the sklearn.linear_model.LogisticRegression module in the sklearn package (v0.22). The models were trained using either gene expression data or SCVI batch-corrected low-dimensional LDVAE representation of the training data with regularization parameters (L1-ratio and alpha) tuned using the GridSearchCV function in sklearn (v1.1.3). The test grid was designed with five l1_ratio intervals (0, 0.2, 0.4, 0.6, 0.8, 1), five alpha (inverse of regularization strength) intervals (0.2, 0.4, 0.6, 0.8, 1) at five train-test splits and three repeats for cross-validation. The unweighted mean over the weighted mean squared errors (MSEs) of each test fold (the cross-validated MSE) was used to determine the optimal model.

The resultant model was used to predict the probability of correspondence between trained labels and precomputed clusters in the target dataset. To ensure that probabilistic outputs from LR models remained consistent with observed neighborhood graph connectivities, the median LR predicted probability of training label assignment was compared against normalized graph distances between classes computed using the PAGA (tl.paga) module in Scanpy as described in our previous work (*10*) (fig. S13A). Genes predicted to be significantly discriminatory for each LR model were assessed by significance of impact. Features were ranked in descending manner by impact score (e^coefficient per feature for given intercept). Impact significance ($P < 0.05$) of each gene was computed by the survival function (sf) across all gene impact scores (fig. S13B). To further verify the specificity of the TREM2 macrophage gene expression profile, the proportion of DEGs overlapping between the TREM2 macrophage population and other macrophage populations across the 12-organ fetal atlas were computed using a two-sided Wilcoxon rank-sum test as described in the clustering and annotation section (fig. S13, C and D, and data S31).

For dataset comparisons across the 12-organ fetal atlas where predesignated labels already existed in the target dataset, the median probability of training label assignment per predesignated class was computed. The resultant LR probabilistic relationship between labels of the 12-organ atlas were visualized as a heatmap (figs. S14 and S15 and data S8 to S16).

For classification tasks, a model-specific decision threshold of 0.9 was used to determine predicted labels. Clusters were then assigned classes if the majority projected label had a label count distribution of >[mean + (1 × std)] of label counts per cluster. Resultant cell state classifications were further manually checked using DEGs. Further assessment of the predicted cluster labels was carried out by computing the adjusted Rand index and mutual information scores from the modules sklearn.metrics.adjusted_rand_score and sklearn.metrics.mutual_info_score between the original cluster labels and predicted cluster labels in each dataset. This methodology was applied to classify and annotate several external datasets including the scRNA-seq human gastrulation data (*14*), the human AGM data (*12*), the human embryonic liver data and human fetal skin data (*48*), as well as the human YS and liver CITE-seq data (data S6).

An implementation of the EN workflow described above, in conjunction with the SAMap (self-assembling manifold mapping) workflow (v1.0.7) (*69*), was used to classify and probabilistically compare cell states across the human YS scRNA-seq data and the mouse gastrulation YS data. A gene-gene sequence homology graph weighted by human and mouse sequence similarity was first constructed using the SAMAP tool. Reciprocal BLAST mapping using the tblastx tool between the entire mouse and human transcriptomes for significant homology (E value < 10^{-6}) was supplied. The resultant SAM object returned $k = 300$ species-stitched PC components for the top 3000 paired genes. These PC components were used to train the cross-species EN model as a classification task described above (data S11).

LR models and weights trained on the YS and integrated fetal atlases are available via our interactive web portal in ".sav" format (see Data and materials availability) and will facilitate future use of our YS atlas for label transfer and to rapidly annotate scRNA-seq datasets using the Python package CellTypist (v.0.1.9) (*68*).

Differential lineage priming and progenitor cell fate predictions

The CellRank package (v1.5.1) was used to define and rank fate probabilities of terminal state transitions across annotated hematopoietic lineages in the YS and iPSC scRNA-seq datasets. In the YS data, cell clusters broadly annotated to be in the myeloid lineage were first subsetted from the YS data. After refinement, DCs were excluded from this subset. We did not identify any DCs in the <CS14 (pre-AGM) myeloid lineage. Macrophage trajectory inference was then constructed across the myeloid

subset (fig. S8E). Cells were divided by donors aged <CS14 and >CS14 (post-AGM) and trajectory inference recomputed on new embeddings. First-order kinetics matrices were imputed for each dataset using the *pp.moments* function (n_pcs = 20, n_neighbors = 30) in the scVelo package (v0.2.4). A Cytotrace pseudotime for state transitions across each dataset was then computed to direct graph-edges toward estimated neighborhood regions of increasing differentiation using the Cytotrace kernel provided within the CellRank package. The resultant KNN and Cytotrace pseudotime were used to compute a probability transition matrix with the *compute_transition_matrix* command in Cytotrace. Neighborhoods of cells representing terminal states of differentiation were identified using true Schur matrix eigen decomposition of the transition matrix *compute_schur* (n_components = 20, method = brandts), followed by the *compute_macrostates* (n_states = 10) command in Cytotrace. The resultant terminally differentiated cell states were then manually selected if multiple terminal states were identified per lineage. Fate absorption probabilities were then computed across all cells terminating at each prespecified terminal cellstate neighborhood using the *compute_absoprtion_probabilities* command in CellRank. Fate probabilities were then presented as a circular plot using the *pl.circular_projection* with embedding proximity to terminal edges of the graph representing the fate-transition probability of a particular cell toward the prespecified terminally differentiation state. HSPC progenitor population density was then computed by KDE of a precomputed UMAP highlighting relative probabilities of HSPC lineage priming (KDE calculated using the *tl.embedding.density* function in Scanpy).

For HSPC lineage priming analyses which included the respective embryonic erythroid and erythroid terminal states, embryonic erythroid states were defined as any erythroid cell with a HBZ module *z*-score > 0, and erythroid as any erythroid cell with individual module *z*-score of HBA1, HBA2, HBG1, HBG2, HBD > 0.

pySCENIC for regulon analysis

The pySCENIC package (v0.9.19) was used to identify TFs and their target genes in the YS and iPSC scRNA-seq datasets. The ranking database (hg38 refseq-r80 500bp_up_and_100bp_down_tss.mc9nr.feather), motif annotation database (motifs-v9-nr.hgnc-m0.001-o0.0.tbl) and list of TFs (lambert2018.txt) were used. An adjacency matrix of TFs and their targets was generated. TF activity from the AUcell output was modeled along diffusion pseudotime rankings of each trajectory and used to train a nonlinear Generalized Additive Model (nlGAM) using the pyGAM.LinearGAM model to identify TF modules which significantly changed across each lineage pseudotime. A gridsearch of between 50 and 200 splines were calculated. Significantly changing TF regulons across pseudotime were classified with a $P < 0.05$ and reported in Fig. 5, D and H, and data S30). Regulon matrix heatmaps were plotted using the *Seaborn* (v0.12.1) package in Python. Regulon scores were variance-scaled and min-max–standardized with a distribution of 0 to 1.

Cell-cell interaction predictions using CellPhoneDB

To assign putative cell-cell interactions within the YS scRNA-seq dataset, we used CellPhoneDB (v2.1.2). Log-transformed, normalized, and scaled gene expression values for all cell states were exported. CellPhoneDB was run using the statistical method using the receptor-ligand database (v2.0.0) with a significance *P* cutoff of 0.05 (data S28 and S29). Outputs were ranked by log-mean expression for interactions between cell types of interest in each analyses and plotted as a *z*-scored heatmap to show standard deviations from mean for each receptor–ligand pair.

Hiplex RNAscope

Human YS tissue (8 PCW) was frozen in OCT compound (Tissue-Tek). 12-plex smFISH was performed using the RNAscope HiPlex v2 assay (ACD, Bio-Techne) on three cryosections (10 μm) per manufacturer's instructions, using the standard pretreatment for freshly frozen samples and permeabilized with Protease III, for 15 min at room temperature. The imaging cycles, primary probes and label fluorophores were: *Cycle1_KLRB1_AlexaFluor488*, *Cycle1_CD1C_Dylight550*, *Cycle1_IL7R_Dylight650*, *Cycle1_SPINK2_AlexaFluor750*, *Cycle2_P2RY12_AlexaFluor488*, *Cycle2_TNFA_Dylight550*, *Cycle2_LGALS3_Dylight650*, *Cycle2_IL33_AlexaFluor750*, *Cycle3_PLVAP_AlexaFluor488*, *Cycle3_SPINK1_Dylight550*, *Cycle3_C1QA_Dylight650*, *Cycle3_ACTA2_AlexaFluor750*, *Cycle4_P2RY12_Opal570*, and *Cycle4_IBA1_Cy5*. Slides were counterstained with DAPI and coverslipped for imaging.

For protein validation, slides were fixed with 4% (w/v) PFA for 60 min at room temperature and then washed and dehydrated in an ethanol gradient (50 to 100%) for 5 min each. Sections were treated with Protease III (ACD, Bio-Techne) for 15 min at room temperature, then washed with PBS before blocking in 10% (v/v) normal donkey serum containing 1% (w/v) Triton X-100 and 0.2% (w/v) gelatin for 60 min at room temperature. Primary antibodies were incubated at 4°C overnight, then washed three times for 20 min each with a wash buffer [0.1% (w/v) Triton X-100 in PBS]. Slides were blocked with HRP Block (ACD, Bio-Techne) for 60 min at room temperature, and washed with ACD Wash Buffer (ACD, Bio-Techne) before addition of secondary antibody and incubation for 60 min at room temperature. Slides were washed three times for 20 min each [0.1% (w/v) Triton X-100 in PBS]. TSA-Opal570 was added for 10 min at room temperature, then washed three times with ACD Wash Buffer. Slides were counterstained with DAPI and coverslipped for imaging.

Imaging was performed on a custom two-camera spinning disk confocal microscope built around a Crest Optics X-light v3 module by Cairn Research, a scientific equipment manufacturer. The instrument was controlled using the Micro-Manager software (*70*). All imaging was performed in spinning disk confocal mode with a 40X water immersion objective [numerical aperture (NA) 1.15, 180 nm per pixel] and 1.5-μm *z*-step using Prime BSI Express (Teledyne Photometrics) camera.

RNAscope image analysis

Before each imaging experiment, a slide covered in a sparse layer of 0.5-μm Tetraspeck beads was imaged in all channels. The bead images in all channels were then registered against the beads in the DAPI channel, and their respective affine transforms were saved.

After imaging, each individual tile was *z*-projected with a maximum intensity projection, then the channels were transformed using the saved affine transforms. The projected, transformed tiles were saved back to a temporary directory along with a bigstitcher-compatible XML file. The BigStitcher software (*71*) was then used to stitch the transformed tiles together and the final stitched image exported for further analysis.

All imaging cycles for a given tissue section were registered in two steps. First, we used feature registration algorithm implemented in Python via OpenCV-contrib library (version 4.3.0) (*72*) to compute an affine transformation of DAPI channel from cycle r > 1 (moving image) with respect to DAPI channel from the first cycle r = 1 (reference image). Key points were detected using the FAST feature detector, whose surrounding areas were described using the DAISY feature descriptor, and the FLANN-based matcher was used to find correspondences between pairs of key points from reference and moving images and filter out unreliable points. The remaining key points were processed using the RANSAC-based algorithm that aligns them and estimates affine transformation parameters with four degrees of freedom.

For the second registration step, a nonlinear registration algorithm based on Farneback optical-flow available in Python via OpenCV library was used to achieve more accurate registration by warping images locally. Specifically, local warping was computed using the DAPI channel, from cycle r > 1 with respect to the corresponding channel of the first round. The computational pipeline implementing these registration steps was optimized so that it could be performed efficiently on large images. The corresponding code for feature registration is available at https://github.com/BayraktarLab/feature_reg, and the code for optical-flow registration is available at https://github.com/BayraktarLab/opt_flow_reg.

Immunohistochemistry

Formalin-fixed, paraffin-embedded blocks of YS 4 to 8 PCW, embryonic liver 7 to 8 PCW, and healthy adult liver were sectioned at 4-μm thickness onto slides coated with 3-aminopropyltriethoxysilane (APES).

For hematoxylin and eosin staining, slides were dewaxed in xylene and rehydrated through graded ethanol, as previously described (*10*). Rehydrated slides were incubated for 5 min in Mayer's hematoxylin (Dako, Agilent), rinsed in tap water, and then differentiated for 2 s in acid alcohol before washing in tap water followed by Scott's tap water substitute (Leica Biosystems). Sections were counterstained in triple eosin (Dako, Agilent) for 5 min before being rinsed in tap water, dehydrated through graded ethanol (70 to 99%), and then placed in xylene before mounting with DPX (Dako, Agilent).

For immunohistochemistry (IHC), dewaxing, rehydration, and staining was performed using the Discovery Ultra auto Stainer and kits (Ventana, Roche) following the manufacturer's protocols. Primary and secondary antibodies and their concentrations are listed in data S23. Slides were counterstained with one drop of hematoxylin II (Ventana, Roche) for 8 min, rinsed with Reaction Buffer and one drop of Bluing reagent (Dako, Agilent) added for 4 min. The slide was then rinsed with a Reaction buffer, before being dehydrated by hand through graded ethanol (70 to 99%), placed in xylene and mounted with DPX (Dako, Agilent).

Rabbit polyclonal anti-human alpha-1-fetoprotein (AFP; Agilent) staining was performed by NovoPath, Newcastle upon Tyne NHS Trust, using a proprietary method.

For the Martius Scarlet eBlue (MSB) stain, slides were dewaxed in xylene and rehydrated through graded ethanol as previously published (*10*). Rehydrated slides were placed in Bouins' fixative (Atom Scientific) for 1 hour at 60°C, washed in running water, incubated in Weigert's solution (Atom Scientific) for 10 min and washed in water. Slides were differentiated in 0.9% ethanol for 1 to 2 s before rinsing in tap water followed by Scott's tap water substitute (Leica Biosystems), distilled water and finally 95% ethanol. Slides were then incubated stepwise in Martius yellow (3 min) (Atom Scientific), Brilliant crystal scarlet (6 min) (Atom Scientific), and 50% (v/v) Methyl blue (2 min) (Atom Scientific), washing with distilled water between each stain. Slides were washed in tap water, rapidly dehydrated (2 to 3 min) through graded ethanol (70 to 99%), then placed in xylene before mounting with DPX mountant (Dako, Agilent).

All slides were imaged at 20X magnification on a NanoZoomer S360 (Hamamatsu) digital slide scanner. MSB stained images were deconvolved into respective Martius yellow, crystal scarlet and methyl blue channels using the Colour Deconvolution plugin (v1.8) (Masson Trichrome) in FIJI with thresholds set using the Otsu method. Pseudocolors for each deconvolved channel were then assigned as in Fig. 2C.

ASGR1 and CD34 immunofluorescence microscopy

YS sections were baked onto slides for 2 hours at 60°C before being dewaxed in xylene and rehydrated through graded ethanol as previously described (*10*). Slides were washed with distilled water then placed in a pressure cooker with boiling citrate buffer pH 6 [10 mM citric acid (Sigma), 0.05% v/v Tween 20 (Sigma) in deionized (DI) water] for 2 min for antigen retrieval. Slides were then washed for 3 min with distilled water followed by 3 min in PBS (Sigma). Sections were blocked with 20% (v/v) goat serum (R&D Systems) for 45 min at room temperature. Primary antibodies were diluted in blocking solution (data S23), added to the sections and incubated for 1 hour at room temperature. Slides were washed twice for 3 min each in a wash buffer [0.1% (w/v) Triton X (Sigma) in PBS], then twice for 3 min each in PBS. Secondary antibodies (see data S23) were diluted in blocking solution, added to section and incubated for 2 hours at room temperature. The wash step was repeated and then 300 nM DAPI (Sigma) was added. Slides were incubated for 5 min before washing with PBS. Slides were then mounted with ProLong Diamond Antifade (Thermofisher) and imaged on a Zeiss Axioimager with Zeiss ZEN pro software.

SMA and LYVE1/CD34 immunofluorescence microscopy

PFA-fixed YS was cryoprotected with sucrose 10%, embedded in gelatin-sucrose solution [7.5% x/v gelatin (VWR 24350.262), 10% w/v sucrose (VWR27478.296), in 0.12M PBS], frozen at −50°C, then sectioned at 14 μm. Slides were stored at −80°C until use, dried for 30 min, then blocked with PBS Gelatin Triton [0.2% w/v gelatin, 0.25% Triton X-100 (Sigma-Aldrich) in PBS] for 1 hour. Primary antibodies were diluted in blocking solution (data S23), added to the sections, and incubated overnight. Slides washed with PBS three times at 10-min intervals. Secondary antibodies were diluted in blocking solution and added to sections to incubate for 2 hours (data S23). Hoechst 33258 (Sigma-Aldrich) was added to the secondary antibody solution. Sections were washed with PBS three times at 10-min intervals, and coverslips were mounted with Mowiol (Calbiochem). Sections were imaged at 20X magnification on Leica DM6000 widefield microscope with MetaMorph software. Brightness and contrast were adjusted, and a scale bar was added with FIJI (*73*).

Light-sheet fluorescence microscopy

Candidate antibodies were screened by immunofluorescence on cryosections obtained from OCT-embedded specimens as previously described (*10*, *57*). Routine light-sheet immunofluorescence microscopy was then performed on floating whole-mount YSs as previously described, with primary antibody incubation reduced to 10 days and secondary reduced to 2 days, both at 37°C to preserve tissue integrity. Antibody and other reagents including nuclear marker TO-PRO-3 iodide are specified in data S23. YSs were embedded in 1.5% agarose blocks before solvent-based clearing as previously described (*57*). YS retained its spherical shape throughout the procedure. Imaging was performed as previously described in dibenzyl ether with a Miltenyi Biotec Ultramicroscope Blaze (sCMOS camera 5.5MP controlled by Inspector Pro 7.3.2 acquisition software), which generates light sheets at excitation wavelengths of 488, 561, 640, and 785 nm. Objective lenses of 4X magnification (MI Plan 4X, NA 0.35) and 12X magnification (MI Plan, NA 0.53) were used. Imaris (v9.8, BitPlane) was used for image conversion, processing, and video production. Blender 3.0 was used to edit videos and add text. All raw image data are available on request (A.C. and M.H.).

Statistics and reproducibility

The number of cells from each cell type in each de novo single-cell dataset provided in this manuscript are provided in data S4.

REFERENCES AND NOTES

1. C. Ross, T. E. Boroviak, Origin and function of the yolk sac in primate embryogenesis. *Nat. Commun.* **11**, 3760 (2020). doi: 10.1038/s41467-020-17575-w; pmid: 32724077
2. T. Cindrova-Davies *et al.*, RNA-seq reveals conservation of function among the yolk sacs of human, mouse, and chicken. *Proc. Natl. Acad. Sci. U.S.A.* **114**, E4753–E4761 (2017). doi: 10.1073/pnas.1702560114; pmid: 28559354
3. T. Yamane, Mouse Yolk Sac Hematopoiesis. *Front. Cell Dev. Biol.* **6**, 80 (2018). doi: 10.3389/fcell.2018.00080; pmid: 30079337
4. J. Palis, J. Malik, K. E. McGrath, P. D. Kingsley, Primitive erythropoiesis in the mammalian embryo. *Int. J. Dev. Biol.* **54**, 1011–1018 (2010). doi: 10.1387/ijdb.093056jp; pmid: 20711979
5. G. Canu, C. Ruhrberg, First blood: The endothelial origins of hematopoietic progenitors. *Angiogenesis* **24**, 199–211 (2021). doi: 10.1007/s10456-021-09783-9; pmid: 33783643
6. A. L. Medvinsky, N. L. Samoylina, A. M. Müller, E. A. Dzierzak, An early pre-liver intraembryonic source of CFU-S in the developing mouse. *Nature* **364**, 64–67 (1993). doi: 10.1038/364064a0; pmid: 8316298
7. M. Tavian, M. F. Hallais, B. Péault, Emergence of intraembryonic hematopoietic precursors in the pre-liver human embryo. *Development* **126**, 793–803 (1999). doi: 10.1242/dev.126.4.793; pmid: 9895326
8. C. Peschle *et al.*, Embryonic−−Fetal Hb switch in humans: Studies on erythroid bursts generated by embryonic progenitors from yolk sac and liver. *Proc. Natl. Acad. Sci. U.S.A.* **81**, 2416–2420 (1984). doi: 10.1073/pnas.81.8.2416; pmid: 6201856
9. Z. Bian *et al.*, Deciphering human macrophage development at single-cell resolution. *Nature* **582**, 571–576 (2020). doi: 10.1038/s41586-020-2316-7; pmid: 32499656
10. D.-M. Popescu *et al.*, Decoding human fetal liver haematopoiesis. *Nature* **574**, 365–371 (2019). doi: 10.1038/s41586-019-1652-y; pmid: 31597962
11. A. Ivanovs *et al.*, Highly potent human hematopoietic stem cells first emerge in the intraembryonic aorta-gonad-mesonephros region. *J. Exp. Med.* **208**, 2417–2427 (2011). doi: 10.1084/jem.20111688; pmid: 22042975
12. V. Calvanese *et al.*, Mapping human haematopoietic stem cells from haemogenic endothelium to birth. *Nature* **604**, 534–540 (2022). doi: 10.1038/s41586-022-04571-x; pmid: 35418685

13. D. Horsfall, J. McGrath, Adifa software for Single Cell Insights, v0.1.0, *Zenodo* (2022); https://doi.org/10.5281/zenodo.5824896.
14. R. C. V. Tyser *et al*., Single-cell transcriptomic characterization of a gastrulating human embryo. *Nature* **600**, 285–289 (2021). doi: 10.1038/s41586-021-04158-y; pmid: 34789876
15. J. Xue *et al*., Incomplete embryonic lethality and fatal neonatal hemorrhage caused by prothrombin deficiency in mice. *Proc. Natl. Acad. Sci. U.S.A.* **95**, 7603–7607 (1998). doi: 10.1073/pnas.95.13.7603; pmid: 9636196
16. W. Ruf, N. Yokota, F. Schaffner, Tissue factor in cancer progression and angiogenesis. *Thromb. Res.* **125**, S36–S38 (2010). doi: 10.1016/S0049-3848(10)70010-4; pmid: 20434002
17. H. Wu, X. Liu, R. Jaenisch, H. F. Lodish, Generation of committed erythroid BFU-E and CFU-E progenitors does not require erythropoietin or the erythropoietin receptor. *Cell* **83**, 59–67 (1995). doi: 10.1016/0092-8674(95)90234-1; pmid: 7553874
18. I. Hirano, N. Suzuki, The Neural Crest as the First Production Site of the Erythroid Growth Factor Erythropoietin. *Front. Cell Dev. Biol.* **7**, 105 (2019). doi: 10.3389/fcell.2019.00105; pmid: 31245372
19. Y. Zhu *et al*., Characterization and generation of human definitive multipotent hematopoietic stem/progenitor cells. *Cell Discov.* **6**, 89 (2020). doi: 10.1038/s41421-020-00213-6; pmid: 33298886
20. C. Alsinet *et al*., Robust temporal map of human in vitro myelopoiesis using single-cell genomics. *Nat. Commun.* **13**, 2885 (2022). doi: 10.1038/s41467-022-30557-4; pmid: 35610203
21. C. Peschle *et al*., Haemoglobin switching in human embryos: Asynchrony of ζ→α and ε→γ-globin switches in primitive and definite erythropoietic lineage. *Nature* **313**, 235–238 (1985). doi: 10.1038/313235a0; pmid: 2578614
22. J. Palis, Primitive and definitive erythropoiesis in mammals. *Front. Physiol.* **5**, 3 (2014). doi: 10.3389/fphys.2014.00003; pmid: 24478716
23. W. Liu *et al*., *Trem2* promotes anti-inflammatory responses in microglia and is suppressed under pro-inflammatory conditions. *Hum. Mol. Genet.* **29**, 3224–3248 (2020). doi: 10.1093/hmg/ddaa209; pmid: 32959884
24. D. A. Jaitin *et al*., Lipid-Associated Macrophages Control Metabolic Homeostasis in a Trem2-Dependent Manner. *Cell* **178**, 686–698.e14 (2019). doi: 10.1016/j.cell.2019.05.054; pmid: 31257031
25. Y. Wang *et al*., TREM2 lipid sensing sustains the microglial response in an Alzheimer's disease model. *Cell* **160**, 1061–1071 (2015). doi: 10.1016/j.cell.2015.01.049; pmid: 25728668
26. T. Jaffredo, R. Gautier, A. Eichmann, F. Dieterlen-Lièvre, Intraaortic hemopoietic cells are derived from endothelial cells during ontogeny. *Development* **125**, 4575–4583 (1998). doi: 10.1242/dev.125.22.4575; pmid: 9778515
27. L. Yvernogeau *et al*., In vivo generation of haematopoietic stem/progenitor cells from bone marrow-derived haemogenic endothelium. *Nat. Cell Biol.* **21**, 1334–1345 (2019). doi: 10.1038/s41556-019-0410-6; pmid: 31685991
28. Z. Li *et al*., Mouse embryonic head as a site for hematopoietic stem cell development. *Cell Stem Cell* **11**, 663–675 (2012). doi: 10.1016/j.stem.2012.07.004; pmid: 23122290
29. J. M. Frame, K. H. Fegan, S. J. Conway, K. E. McGrath, J. Palis, Definitive Hematopoiesis in the Yolk Sac Emerges from Wnt-Responsive Hemogenic Endothelium Independently of Circulation and Arterial Identity. *Stem Cells* **34**, 431–444 (2016). doi: 10.1002/stem.2213; pmid: 26418893
30. K. E. Rhodes *et al*., The emergence of hematopoietic stem cells is initiated in the placental vasculature in the absence of circulation. *Cell Stem Cell* **2**, 252–263 (2008). doi: 10.1016/j.stem.2008.01.001; pmid: 18371450
31. Y. Zeng *et al*., Tracing the first hematopoietic stem cell generation in human embryo by single-cell RNA sequencing. *Cell Res.* **29**, 881–894 (2019). doi: 10.1038/s41422-019-0228-6; pmid: 31501518
32. R. Thambyrajah *et al*., GFI1 proteins orchestrate the emergence of haematopoietic stem cells through recruitment of LSD1. *Nat. Cell Biol.* **18**, 21–32 (2016). doi: 10.1038/ncb3276; pmid: 26619147
33. M. Efremova, M. Vento-Tormo, S. A. Teichmann, R. Vento-Tormo, CellPhoneDB: inferring cell–cell communication from combined expression of multi-subunit ligand–receptor complexes. *Nat. Protoc.* **15**, 1484–1506 (2020). doi: 10.1038/s41596-020-0292-x; pmid: 32103204
34. L. Jardine *et al*., Blood and immune development in human fetal bone marrow and Down syndrome. *Nature* **598**, 327–331 (2021). doi: 10.1038/s41586-021-03929-x; pmid: 34588693
35. J. Fröbel *et al*., The Hematopoietic Bone Marrow Niche Ecosystem. *Front. Cell Dev. Biol.* **9**, 705410 (2021). doi: 10.3389/fcell.2021.705410; pmid: 34368155
36. B. Murdoch *et al*., Wnt-5A augments repopulating capacity and primitive hematopoietic development of human blood stem cells *in vivo*. *Proc. Natl. Acad. Sci. U.S.A.* **100**, 3422–3427 (2003). doi: 10.1073/pnas.0130233100; pmid: 12626754
37. J. Shen *et al*., Vitronectin-activated αvβ3 and αvβ5 integrin signalling specifies haematopoietic fate in human pluripotent stem cells. *Cell Prolif.* **54**, e13012 (2021). doi: 10.1111/cpr.13012; pmid: 33656760
38. P. Zhang *et al*., The physical microenvironment of hematopoietic stem cells and its emerging roles in engineering applications. *Stem Cell Res. Ther.* **10**, 327 (2019). doi: 10.1186/s13287-019-1422-7; pmid: 31744536
39. A. S. Eisele *et al*., Erythropoietin directly remodels the clonal composition of murine hematopoietic multipotent progenitor cells. *eLife* **11**, e66922 (2022). doi: 10.7554/eLife.66922; pmid: 35166672
40. H. Yoshihara *et al*., Thrombopoietin/MPL signaling regulates hematopoietic stem cell quiescence and interaction with the osteoblastic niche. *Cell Stem Cell* **1**, 685–697 (2007). doi: 10.1016/j.stem.2007.10.020; pmid: 18371409
41. F. Ginhoux, M. Guilliams, Tissue-Resident Macrophage Ontogeny and Homeostasis. *Immunity* **44**, 439–449 (2016). doi: 10.1016/j.immuni.2016.02.024; pmid: 26982352
42. C. Gekas *et al*., Mef2C is a lineage-restricted target of Scl/Tal1 and regulates megakaryopoiesis and B-cell homeostasis. *Blood* **113**, 3461–3471 (2009). doi: 10.1182/blood-2008-07-167577; pmid: 19211936
43. E. Suzuki *et al*., The transcription factor Fli-1 regulates monocyte, macrophage and dendritic cell development in mice. *Immunology* **139**, 318–327 (2013). doi: 10.1111/imm.12070; pmid: 23320737
44. M. L. Petreaca, M. Yao, Y. Liu, K. Defea, M. Martins-Green, Transactivation of vascular endothelial growth factor receptor-2 by interleukin-8 (IL-8/CXCL8) is required for IL-8/CXCL8-induced endothelial permeability. *Mol. Biol. Cell* **18**, 5014–5023 (2007). doi: 10.1091/mbc.e07-01-0004; pmid: 17928406
45. Z. Lyu *et al*., Effects of NRP1 on angiogenesis and vascular maturity in endothelial cells are dependent on the expression of SEMA4D. *Int. J. Mol. Med.* **46**, 1321–1334 (2020). doi: 10.3892/ijmm.2020.4692; pmid: 32945351
46. K. Bisht *et al*., Capillary-associated microglia regulate vascular structure and function through PANX1-P2RY12 coupling in mice. *Nat. Commun.* **12**, 5289 (2021). doi: 10.1038/s41467-021-25590-8; pmid: 34489419
47. F. Ginhoux *et al*., Fate mapping analysis reveals that adult microglia derive from primitive macrophages. *Science* **330**, 841–845 (2010). doi: 10.1126/science.1194637; pmid: 20966214
48. C. Suo *et al*., Mapping the developing human immune system across organs. *Science* **376**, eabo0510 (2022). doi: 10.1126/science.abo0510; pmid: 35549310
49. L. Garcia-Alonso *et al*., Single-cell roadmap of human gonadal development. *Nature* **607**, 540–547 (2022). doi: 10.1038/s41586-022-04918-4; pmid: 35794482
50. S. A. Dick *et al*., Three tissue resident macrophage subsets coexist across organs with conserved origins and life cycles. *Sci. Immunol.* **7**, eabf7777 (2022). doi: 10.1126/sciimmunol.abf7777; pmid: 34995099
51. A. Gayoso *et al*., A Python library for probabilistic analysis of single-cell omics data. *Nat. Biotechnol.* **40**, 163–166 (2022). doi: 10.1038/s41587-021-01206-w; pmid: 35132262
52. R. Lopez, J. Regier, M. B. Cole, M. I. Jordan, N. Yosef, Deep generative modeling for single-cell transcriptomics. *Nat. Methods* **15**, 1053–1058 (2018). doi: 10.1038/s41592-018-0229-2; pmid: 30504886
53. S. Chou, H. F. Lodish, Fetal liver hepatic progenitors are supportive stromal cells for hematopoietic stem cells. *Proc. Natl. Acad. Sci. U.S.A.* **107**, 7799–7804 (2010). doi: 10.1073/pnas.1003586107; pmid: 20385801
54. M.-L. N. Ton *et al*., Rabbit Development as a Model for Single Cell Comparative Genomics. *bioRxiv*2022.10.06.510971 [Preprint] (2022). https://doi.org/10.1101/2022.10.06.510971.
55. U. C. Eze, A. Bhaduri, M. Haeussler, T. J. Nowakowski, A. R. Kriegstein, Single-cell atlas of early human brain development highlights heterogeneity of human neuroepithelial cells and early radial glia. *Nat. Neurosci.* **24**, 584–594 (2021). doi: 10.1038/s41593-020-00794-1; pmid: 33723434
56. T. Strachan, S. Lindsay, D. I. Wilson, *Molecular Genetics of Early Human Development* (Academic Press, 1997).
57. M. Belle *et al*., Tridimensional Visualization and Analysis of Early Human Development. *Cell* **169**, 161–173.e12 (2017). doi: 10.1016/j.cell.2017.03.008; pmid: 28340341
58. A.-C. Villani *et al*., Single-cell RNA-seq reveals new types of human blood dendritic cells, monocytes, and progenitors. *Science* **356**, eaah4573 (2017). doi: 10.1126/science.aah4573; pmid: 28428369
59. S. L. Wolock, R. Lopez, A. M. Klein, Scrublet: Computational Identification of Cell Doublets in Single-Cell Transcriptomic Data. *Cell Syst.* **8**, 281–291.e9 (2019). doi: 10.1016/j.cels.2018.11.005; pmid: 30954476
60. S. J. Fleming *et al*., Unsupervised removal of systematic background noise from droplet-based single-cell experiments using CellBender. *bioRxiv*791699 [Preprint] (2022). https://doi.org/10.1101/791699.
61. F. A. Wolf, P. Angerer, F. J. Theis, SCANPY: Large-scale single-cell gene expression data analysis. *Genome Biol.* **19**, 15 (2018). doi: 10.1186/s13059-017-1382-0; pmid: 29409532
62. M. P. Mulè, A. J. Martins, J. S. Tsang, Normalizing and denoising protein expression data from droplet-based single cell profiling. *Nat. Commun.* **13**, 2099 (2022). doi: 10.1038/s41467-022-29356-8; pmid: 35440536
63. H. Wang *et al*., Decoding Human Megakaryocyte Development. *Cell Stem Cell* **28**, 535–549.e8 (2021). doi: 10.1016/j.stem.2020.11.006; pmid: 33340451
64. I. Korsunsky *et al*., Fast, sensitive and accurate integration of single-cell data with Harmony. *Nat. Methods* **16**, 1289–1296 (2019). doi: 10.1038/s41592-019-0619-0; pmid: 31740819
65. M. Büttner, Z. Miao, F. A. Wolf, S. A. Teichmann, F. J. Theis, A test metric for assessing single-cell RNA-seq batch correction. *Nat. Methods* **16**, 43–49 (2019). doi: 10.1038/s41592-018-0254-1; pmid: 30573817
66. V. A. Traag, L. Waltman, N. J. van Eck, From Louvain to Leiden: Guaranteeing well-connected communities. *Sci. Rep.* **9**, 5233 (2019). doi: 10.1038/s41598-019-41695-z; pmid: 30914743
67. E. Dann, N. C. Henderson, S. A. Teichmann, M. D. Morgan, J. C. Marioni, Differential abundance testing on single-cell data using *k*-nearest neighbor graphs. *Nat. Biotechnol.* **40**, 245–253 (2022). doi: 10.1038/s41587-021-01033-z; pmid: 34594043
68. C. Domínguez Conde *et al*., Cross-tissue immune cell analysis reveals tissue-specific features in humans. *Science* **376**, eabl5197 (2022). doi: 10.1126/science.abl5197; pmid: 35549406
69. A. J. Tarashansky *et al*., Mapping single-cell atlases throughout Metazoa unravels cell type evolution. *eLife* **10**, e66747 (2021). doi: 10.7554/eLife.66747; pmid: 33944782
70. A. Edelstein, N. Amodaj, K. Hoover, R. Vale, N. Stuurman, Computer control of microscopes using μManager. *Curr. Protoc. Mol. Biol.* **92**, 14.20.1–14.20.17 (2010). doi: 10.1002/0471142727.mb1420s92; pmid: 20890901
71. D. Hörl *et al*., BigStitcher: Reconstructing high-resolution image datasets of cleared and expanded samples. *Nat. Methods* **16**, 870–874 (2019). doi: 10.1038/s41592-019-0501-0; pmid: 31384047
72. M. Gataric *et al*., PoSTcode: Probabilistic image-based spatial transcriptomics decoder. *bioRxiv*2021.10.12.464086 [Preprint] (2021). https://doi.org/10.1101/2021.10.12.464086.
73. J. Schindelin *et al*., Fiji: An open-source platform for biological-image analysis. *Nat. Methods* **9**, 676–682 (2012). doi: 10.1038/nmeth.2019; pmid: 22743772
74. B. J. Stewart *et al*., Spatiotemporal immune zonation of the human kidney. *Science* **365**, 1461–1466 (2019). doi: 10.1126/science.aat5031; pmid: 31604275
75. I. Imaz-Rosshandler *et al*., "Tracking Early Mammalian Organogenesis – Prediction and Validation of Differentiation Trajectories at Whole Organism Scale," (2023); https://marionilab.github.io/ExtendedMouseAtlas/.
76. E. I. Crosse *et al*., Multi-layered Spatial Transcriptomics Identify Secretory Factors Promoting Human Hematopoietic Stem Cell Development. *Cell Stem Cell* **27**, 822–839.e8 (2020). doi: 10.1016/j.stem.2020.08.004; pmid: 32946788
77. M. Mather, M. Haniffa, R. Botting, S. Webb, "The role of the yolk sac in human fetal development and identification of a hepatocyte-like cell in the human yolk sac," BioStudies, E-MTAB-10552 (2023); https://www.ebi.ac.uk/biostudies/arrayexpress/studies/E-MTAB-10552.
78. S. Webb, M. Haniffa, E. Stephenson, "Human fetal yolk sac scRNA-seq data (sample ID: F158 for Haniffa Lab; 16099 for HDBR)," BioStudies, E-MTAB-11673 (2022); https://www.ebi.ac.uk/biostudies/arrayexpress/studies/E-MTAB-11673.
79. M. Haniffa, M. Mather, R. Botting, "The role of the yolk sac in human fetal development and identification of a hepatocyte-like cell in the human yolk sac (SS2)," BioStudies, E-MTAB-10888 (2023); https://www.ebi.ac.uk/biostudies/arrayexpress/studies/E-MTAB-10888.
80. M. Haniffa, E. Stephenson, S. Webb, "Human embryonic yolk sac CITE-seq data," BioStudies, E-MTAB-11549 (2022);

https://www.ebi.ac.uk/biostudies/arrayexpress/studies/E-MTAB-11549.
81. S. Webb, E. Stephenson, M. Haniffa, "Human embryonic liver CITE-seq data," BioStudies, E-MTAB-11618 (2022); https://www.ebi.ac.uk/biostudies/arrayexpress/studies/E-MTAB-11618.
82. E. Stephenson, S. Webb, M. Haniffa, "Human fetal liver CITE-seq data," BioStudies, E-MTAB-11613 (2022); https://www.ebi.ac.uk/biostudies/arrayexpress/studies/E-MTAB-11613.
83. I. Goh, FCA_yolkSac, v1.0.0, *Zenodo* (2023); https://doi.org/10.5281/zenodo.7868304.
84. I. Goh, M. Inoue, R. Botting, M. Haniffa, "Yolk sac cell atlas reveals multiorgan functions during early development," BioStudies, S-DHCA0 (2022); https://www.ebi.ac.uk/biostudies/bioimages/studies/S-DHCA0.

ACKNOWLEDGMENTS

We thank T. Dhanaseelan of HDBR for assistance with human fetal tissue processing and cell freezing, N. Elliott for contributions toward CITE-seq panel design, S. Fouquet and Q. Rappeneau for technical support, and J. Haniffa for copyediting support. We also thank the Newcastle University Flow Cytometry Core Facility, Newcastle University Genomics Facility, Sanger Institute Cellular Genetics IT, CRUK CI Genomics Core Facility, and Newcastle upon Tyne NHS Trust NovoPath. We are grateful to the donors and donor families for granting access to the tissue samples. This publication is part of the Human Cell Atlas (www.humancellatlas.org/publications). **Funding:** We acknowledge funding from the Wellcome Human Cell Atlas Strategic Science Support (WT211276/Z/18/Z), an MRC Human Cell Atlas award, the Wellcome Human Developmental Biology Initiative (WT215116/Z/18/Z), and HDBR (MRC/Wellcome MR/R006237/1). M.H. is funded by Wellcome (WT107931/Z/15/Z, WT223092/Z/21/Z, WT206194, and WT220540/Z/20/A), the Lister Institute for Preventive Medicine, and NIHR and Newcastle Biomedical Research Centre. S.A.T. is funded by Wellcome (WT206194) and the ERC Consolidator Grant ThDEFINE. Relevant research in the B.G. group was funded by Wellcome (206328/Z/17/Z) and the MRC (MR/M008975/1 and MR/S036113/1). I.R. is funded by Blood Cancer UK and by the NIHR Oxford Biomedical Centre Research Fund. E.L. is funded by a Sir Henry Dale Fellowship jointly funded by the Wellcome Trust and the Royal Society (107630/Z/15/A). L.J. is funded by a Newcastle Health Innovation Partners Lectureship. M.Ma. is funded by an Action Medical Research Fellowship (GN2779). N.M. was funded by a DFG Research Fellowship (ME 5209/1-1). S.Be. is funded by a Wellcome Senior Research Fellowship (10104/Z/15/Z). C.Al. is funded by the Open Targets consortium (OTAR026 project) and Wellcome Sanger core funding (WT206194). M.I. is supported by Wellcome (215116/Z/18/Z) and thanks the PhD program FIRE and the Graduate School EURIP of Université Paris Cité for their financial support. J.Pal. is funded by NIH NHLBI R01 (HL151777). J.T.H.L. is funded by the Wellcome Trust Grant (108413/A/15/D). A.C. is funded by the Inserm cross-cutting program HuDeCA 2018. M.d.B. is funded by an MRC Molecular Haematology Unit core award MC_UU_00029/5. B.O. is funded by a Wellcome 4Ward North Clinical Training Fellowship. **Author contributions:** Conceptualization: M.H., S.A.T., and B.G. Funding acquisition: M.H., S.A.T., and B.G. Supervision: M.H. and L.J. Data curation: I.G., A.R., S.W., M.Ma., M.Q.L., N.K.W., D.H., and D.B.L. Formal analysis: I.G., A.R., K.G., S.W., I.I.-R., M.Q.L., D.-M.P., K.P., J.Par., S.v.D., J.T.H.L., M.-L.T., D.K., L.Y., and N.K.W. Software: D.H. and D.B.-L. Investigation: R.A.B., S.L., D.J.H., J.E., E.S., I.G., N.K.W., N.-J.C., N.M., R.H., M.S.V., Y.G., M.I., D.D., M.A., R.C., T.N., K.K., E.T., S.J.K., and V.L. Methodology: R.A.B., E.S., O.B., K.K., N.-J.C., V.R., M.I., and Y.G. Resources: C.Al., R.V.-T., S.Ba., P.M., L.G., K.B.M., S.Be., E.L., A.C., I.R., M.d.B., E.D., C.S., and J.M. Writing – original draft: L.J., S.W., I.G., M.H., R.A.B., B.O., M.Mi., and E.S. Writing – review & editing: L.J., I.G., S.W., E.S., M.H., A.R., J.E., R.A.B., B.G., M.Mi., and J.Pal. Visualization: J.E., R.A.B., L.J., C.Ad., I.G., A.R., M.-L.T., and S.W. **Competing interests:** J.M. is an employee of Genentech. The remaining authors declare no competing interests. **Data and materials availability:** All raw sequencing data from this study are made publicly available at ArrayExpress as FASTQs and count matrices as follows: (i) human EL and YS 10X scRNA-seq (*77*), (ii) human embryonic YS 10X scRNA-seq (*78*), (iii) human embryonic YS Smart-seq2 scRNA-seq (*79*), (iv) human embryonic YS CITE-seq (*80*), (v) human EL CITE-seq (*81*), and (vi) human fetal liver CITE-seq (*82*). Accessions for published data reused in this study are detailed comprehensively in data S6. Processed single-cell datasets are available for interactive exploration and download as well as corresponding trained scVI and LR models via our interactive web portal (https://developmental.cellatlas.io/yolk-sac). Note, data on portals are best used for rapid visualization. For formal analysis and all code for reproducibility, including trained scVI VAE, IdVAE, and trained LR models, we recommended following our archived code available on Github (*83*) and our interactive web portal. All raw and processed imaging data are available on the EBI BioImage Archive (*84*). Processed imaging data are available on our interactive web portal. **License information:** Copyright © 2023 the authors, some rights reserved; exclusive licensee American Association for the Advancement of Science. No claim to original US government works. https://www.science.org/about/science-licenses-journal-article-reuse. This research was funded in whole or in part by Wellcome (WT211276/Z/18/Z, MR/R006237/1, WT107931/Z/15/Z, WT223092/Z/21/Z, WT206194, WT220540/Z/20/A, WT206194, 206328/Z/17/Z, 107630/Z/15/A, 10104/Z/15/Z, WT206194, 215116/Z/18/Z, and 108413/A/15/D), a cOAlition S organization. The author will make the Author Accepted Manuscript (AAM) version available under a CC BY public copyright license.

SUPPLEMENTARY MATERIALS

science.org/doi/10.1126/science.add7564
Figs. S1 to S15
References (*85*–*88*)
MDAR Reproducibility Checklist
Movies S1 and S2
Data S1 to S33

Submitted 4 July 2022; resubmitted 6 December 2022
Accepted 3 July 2023
10.1126/science.add7564

PROTEIN DESIGN

Design of stimulus-responsive two-state hinge proteins

Florian Praetorius[1,2]*†, Philip J. Y. Leung[1,2,3]†, Maxx H. Tessmer[4], Adam Broerman[1,2,5], Cullen Demakis[1,2,6], Acacia F. Dishman[1,2,7,8], Arvind Pillai[1,2], Abbas Idris[1,2,9], David Juergens[1,2,3], Justas Dauparas[1,2], Xinting Li[1,2], Paul M. Levine[1,2], Mila Lamb[1,2], Ryanne K. Ballard[1,2], Stacey R. Gerben[1,2], Hannah Nguyen[1,2], Alex Kang[1,2], Banumathi Sankaran[10], Asim K. Bera[1,2], Brian F. Volkman[7], Jeff Nivala[11,12], Stefan Stoll[4], David Baker[1,2,13]*

In nature, proteins that switch between two conformations in response to environmental stimuli structurally transduce biochemical information in a manner analogous to how transistors control information flow in computing devices. Designing proteins with two distinct but fully structured conformations is a challenge for protein design as it requires sculpting an energy landscape with two distinct minima. Here we describe the design of "hinge" proteins that populate one designed state in the absence of ligand and a second designed state in the presence of ligand. X-ray crystallography, electron microscopy, double electron-electron resonance spectroscopy, and binding measurements demonstrate that despite the significant structural differences the two states are designed with atomic level accuracy and that the conformational and binding equilibria are closely coupled.

Although many naturally occurring proteins adopt single folded states, conformational changes between distinct protein states are crucial to the functions of enzymes (*1*, *2*), cell receptors (*3*), and molecular motors (*4*). The extent of these changes ranges from small rearrangements of secondary structure elements (*5*, *6*) to domain rearrangements (*7*) to fold-switching or metamorphic proteins (*8*) that adopt completely different structures. In many cases, these conformational changes are triggered by "input" stimuli such as binding of a target molecule, post translational modification, or change in pH. These changes in conformation can in turn result in "output" actions such as enzyme activation, target binding, or oligomerization (*9*); protein conformational changes can thus couple a specific input to a specific output. The generation of proteins that can switch between two quite different structural states is a difficult challenge for computational protein design, which usually aims to optimize a single, very stable conformation to be the global minimum of the folding energy landscape (*10*, *11*). Design of such proteins requires reframing the design paradigm towards optimizing for more than one minimum on the energy landscape while simultaneously avoiding undesired off-target minima (*12*). Previously, multistate design has been used to design proteins that undergo very subtle conformational changes (*13*, *14*), cyclic peptides that switch conformations based on the presence of metal ions (*15*), and closely related sequences that fold into substantially different conformations (*16*). Stimulus-responsive "LOCKR" (Latching, Orthogonal Cage/Key pRotein) proteins have been designed to undergo conformational changes upon binding to a target peptide or protein (*17*). The "closed" unbound state of these "switch" proteins is a well-defined and fully structured conformation, but the "open" bound state is a broad distribution of conformations. The LOCKR platform has been used to generate biosensors (*18*, *19*), but he lack of a defined second state makes it poorly suited for mechanical coupling in molecular machines or discrete state-based computing systems.

[1]Department of Biochemistry, University of Washington, Seattle, WA, USA. [2]Institute for Protein Design, University of Washington, Seattle, WA, USA. [3]Graduate Program in Molecular Engineering, University of Washington, Seattle, WA, USA. [4]Department of Chemistry, University of Washington, Seattle, WA, USA. [5]Department of Chemical Engineering, University of Washington, Seattle, WA, USA. [6]Graduate Program in Biological Physics, Structure, and Design, University of Washington, Seattle, WA, USA. [7]Department of Biochemistry, Medical College of Wisconsin, Milwaukee, WI, USA. [8]Medical Scientist Training Program, Medical College of Wisconsin, Milwaukee, WI, USA. [9]Department of Bioengineering, University of Washington, Seattle, WA, USA. [10]Molecular Biophysics and Integrated Bioimaging, Lawrence Berkeley National Laboratory, Berkeley, CA, USA. [11]Paul G. Allen School of Computer Science and Engineering, University of Washington, Seattle, WA, USA. [12]Molecular Engineering and Sciences Institute, University of Washington, Seattle, WA, USA. [13]Howard Hughes Medical Institute, University of Washington, Seattle, WA, USA.
***Corresponding author. Email: flop@uw.edu (F.P.); dabaker@uw.edu (D.B.)**
†These authors contributed equally to this work

Hinge Design Method

We set out to design proteins that can switch between two well-defined and fully structured conformations. To facilitate experimental characterization of the conformational change and to ensure compatibility with downstream applications, we imposed several additional requirements. First, the conformational change between the two states should be large, with some inter-residue distances changing by tens of angstroms between the two states. Second, the conformational change should not require global unfolding, which can be very slow. Third, neither of the two states should have substantial exposed patches of hydrophobic residues, which can compromise solubility. Fourth, the conformational change should be readily coupled to a range of inputs and outputs. G[illegible] that proteins are stabilized by hydroph[illegible] cores, collectively achieving all of these properties in one protein system is challenging: protein conformations that differ considerably typically will have different sets of buried hydrophobic residues and require substantial structural rearrangements for interconversion.

We reasoned that these goals could be collectively achieved with a hinge-like design in which two rigid domains move relative to each other while remaining individually folded. The hinge amplifies small local structural and chemical changes to achieve large global changes whereas the chemical environment for most residues remains similar throughout the conformational change, avoiding the need for global unfolding. Provided that the two states of the hinge bury similar sets of hydrophobic residues, the amount of exposed hydrophobic surface area can be kept low in both states. Designing one of the resulting conformations to bind to a target effector couples the conformational equilibrium with target binding (Fig. 1A). This design concept has precedent in nature; for example, bacterial two-component systems use binding proteins that undergo hinging between two discrete conformations in response to ligand binding (*20*).

To implement this two-state hinge design concept, we took advantage of designed helical repeat proteins (DHRs) (*21*) (Fig. 1, B and C, left) and DHR-based junction proteins (*22*). The backbone conformation of the DHR serves as the first conformational state of our hinge protein ("state X"). To generate a second conformation, a copy of the parent protein is rotated around a "pivot helix" (Fig. 1, B and C) and a new backbone conformation is then created by combining the first half of the original protein ("domain 1"), the second half of the copy ("domain 2"), and either the helix following the pivot helix from the original protein or the helix preceding the pivot helix from the rotated copy ("peptide"). Rosetta FastDesign with backbone movement (*23*, *24*) is used to redesign the interface between the three parts, and the two domains are connected into a single chain using fragment-based loop closure (*21*, *25*, *26*). Using a combination of Rosetta two-state design (see methods section for details) and proteinMPNN (*27*) with linked residue identities, a single amino acid sequence is generated that is compatible with the state X hinge as well as with the state Y hinge-peptide complex. AlphaFold2 (AF2) (*28*) with initial guess (*29*) is then used to predict the structure of the hinge with and without the effector peptide, allowing for the selection of designs that are predicted in the correct state X in absence of the peptide and in the correct state Y complex in presence of the peptide. To favor designs that are predominantly in the closed state in absence of the peptide (Fig. 1, A and D), designs are selected only if state X

has lower energy (computed using Rosetta) than state Y in absence of the peptide, and if the state Y complex has lower energy than state X plus spatially separated peptide. Designs are also filtered on standard interface design metrics for the bound conformation (see Methods for details on filtering) (*30*).

Hinges bind effector peptides with sub-nanomolar to low micromolar affinities

We used our hinge design approach to generate hinge-peptide pairs that span a wide structural space (Figs. 1D and 2A and figs. S1 and S2). We experimentally tested multiple rounds of designs, using both DHRs (*21*) and helical junctions (*22*) as input scaffolds, and improving individual steps of the design pipeline between iterations (see Supplementary Note 1 for details on screening and a discussion of success rates and failure modes). We selected hinge and GFP-fused peptide designs that were soluble and interacted with each other as judged by size exclusion chromatography (SEC, figs. S2 and S3) and performed further characterization by fluorescence polarization (FP). Hinge-peptide binding affinities obtained from FP titration experiments with constant peptide concentration and varying hinge concentrations ranged from 1 nM to the low μM range (Fig. 2B, fig. S4, and table S1). To circumvent the bottleneck of finding soluble peptide sequences (see Supplementary Note 1), we also sought to design hinges that bind to a given target peptide. Starting from design cs201, we used a modified version of our design pipeline to redesign the hinge to bind peptides cs074B or cs221B, respectively, which have similar hydrophobic fingerprints as the original target peptide cs201B. This one-sided, two-state design approach yielded hinge designs that bound strongly to their new target peptide with little or no off-target binding (fig. S5).

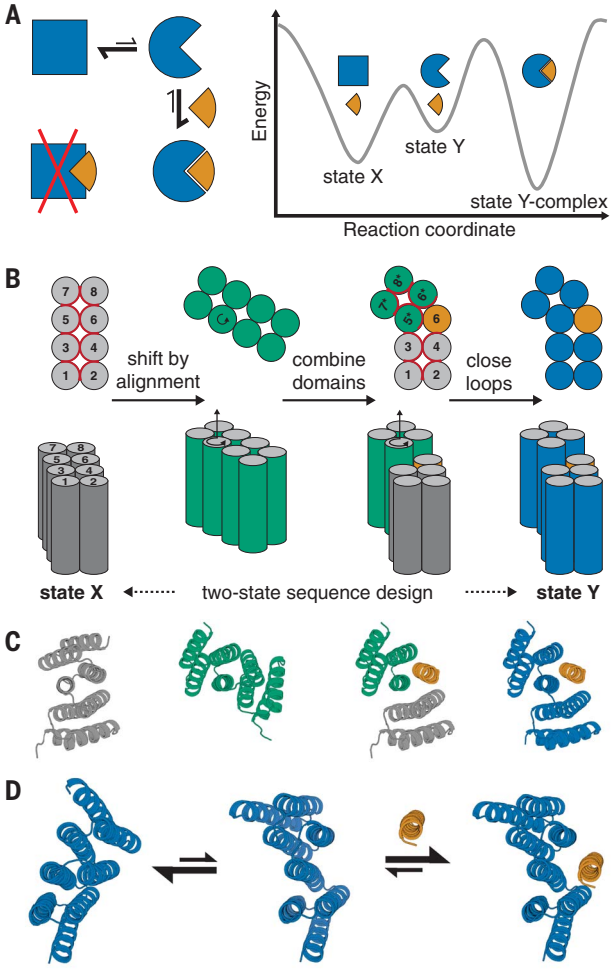

Fig. 1. Strategy for designing proteins that can switch between different conformations. (**A**) (Left) reaction scheme for a protein (blue) that undergoes a conformational change and can bind an effector (orange) in one (circle) but not in the other conformational state (square). (Right) Energy landscape for the system shown on the left. (**B**) Schematic representation of the hinge design approach. Alpha-helices are represented as circles (top view, top) or cylinders (side view, bottom). (From left to right) A previously designed repeat protein (gray) serves as the first conformation of the hinge. To generate the second conformation, a copy of the repeat protein (green) is moved by shifted alignment along a pivot helix, causing a rotation (top and bottom, indicated by the circular arrow) and a translation along the helix axis (bottom). The first 4 helices of the original protein form domain 1 of the hinge, the last 4 helices of the rotated copy form domain 2, and an additional helix is copied over from the original protein to serve as an effector peptide (orange) that can bind to this second conformation of the hinge. The two domains of the hinge are connected into one continuous chain (blue) using fragment-based loop closure, and a single amino acid sequence is designed to be compatible with both conformations. (**C**) Design steps from (B) illustrated using cartoon representations of an exemplary design trajectory. (**D**) Exemplary design models of a designed hinge protein in state X (left), state Y (center), and in state Y bound to an effector peptide (right). Hinge is shown in blue, peptide in orange.

Effector binding modulates the hinge conformational equilibrium

To characterize the conformational equilibrium of the designed hinges, we introduced two surface cysteine residues into the hinge protein and covalently labeled them with the nitroxide spin label MTSL (*31*). We then used double electron-electron resonance spectroscopy (DEER) to determine distance distributions between the two spin labels and compared these with simulated (*32*) distance distributions based on the state X and state Y design models. This experiment was performed on two different labeling site pairs for each design: one pair where the distance is predicted to decrease in the presence of peptide (Fig. 2C and S4, C and D) and the other where it is predicted to increase (Fig. 2D and fig. S4, C and D). In the absence of the peptide, the observed distance distributions closely matched the state X simulations. In all cases the distances between the two pairs of probes shifted upon addition of peptide to better match the state Y simulations, suggesting that addition of effector peptide causes the conformational equilibrium to shift toward state Y as designed. For example, cs074 (site pair 1) showed a clear peak between 40 and 50 Å in absence of the peptide, and a peak between 30 and 40 Å in presence of the peptide, and both peaks agree well with the corresponding simulations (Fig. 2C, top row). In a control experiment using the static parent DHR of design cs074, the distance distributions with and without peptide were identical and matched both the simulation for the parent design model, which closely resembles state X, and the experimental DEER distance distribution for state X of cs074 (fig. S4D).

We solved crystal structures for two designs, cs207 and cs074. For design cs207, crystals were obtained from two separate crystallization screens: one screen for the hinge alone, and one screen for the hinge in complex with the target peptide. In the absence of peptide the experimental structure agrees well with the state X design model (Fig. 3A), and the structure of the hinge-peptide complex agrees well with the state Y design model (Fig. 3B). The crystal structures of hinge cs207 in both designed states demonstrate the accuracy with which two very different conformational states of the same protein can now be designed. For design cs074, the crystal structure of the hinge-peptide complex agrees well with the corresponding state Y design model (Fig. 3C).

One major advantage of de novo designed proteins is their robustness to conditions that typically destabilize native proteins, such as high temperatures, and to structural perturbations, such as mutations, genetic fusion, and incorporation in designed protein assemblies. Circular dichroism (CD) melts show that the hinges remain folded at high temperatures (fig. S6), like the DHRs they were based on

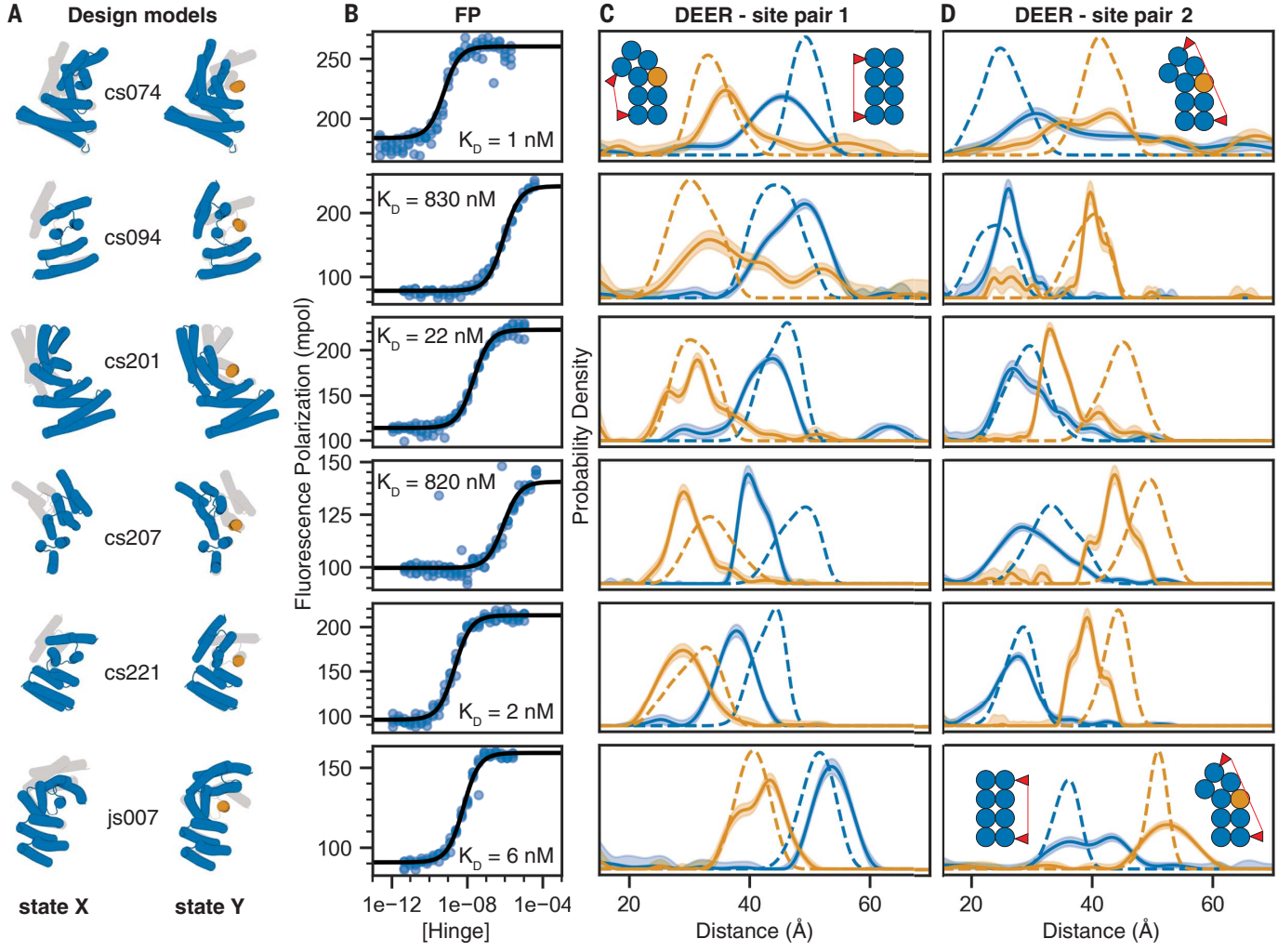

Fig. 2. Experimental validation of peptide-binding hinges. (**A**) Design models of hinges (blue) and peptides (orange) in state X (left model) and state Y bound to the peptide (right model). Gray shades behind models in state X and Y indicate the corresponding states Y and X, respectively. (**B**) Fluorescence polarization (FP) titrations with a constant concentration of TAMRA-labeled peptide (0.1 nM for cs074 and cs221; 0.5 nM for cs201; 1 nM for cs094, cs207, and js007) and varying hinge concentrations. Circles represent data points from four independent measurements; lines are fits of standard binding isotherms to all data points; and dissociation constants (K_D) are obtained from those fits. (**C** and **D**) Distance distributions between spin labels covalently attached to cysteine side chains. Solid lines are obtained from DEER experiments without (blue) or with (orange) an excess of peptide, shaded areas are 95% confidence intervals, and dashed lines are simulated based on the design models for state X (blue) or the state Y complex (orange). For each hinge two different label site pairs were tested, one in which the distance was expected to decrease with peptide binding (C) and one in which the distance was expected to increase upon peptide binding (D). Chemically synthesized peptides were used for all measurements except for cs074 site pair 1, for which sfGFP-peptide fusion was used. For design cs094, the residual state X peak in presence of the peptide likely reflects incomplete binding due to weak binding affinity or insufficient peptide concentration.

(*21*). To test whether our hinges can be incorporated as components of more complex protein assemblies without affecting their ability to undergo conformational changes, we designed a fully structured C3-symmetric protein with three hinge arms (Fig. 3D). We used inpainting (*33*) with RoseTTAFold (*34*) to rigidly connect one end of hinge cs221 to a previously validated homotrimer (*35*, *36*) and the other end of the hinge to a previously validated monomeric protein (*37*). Negative-stain electron microscopy (nsEM) with reference-free class averaging shows straight arms in absence of peptide and bent arms in presence of peptide cs221B, corroborating the designed conformational change (Fig. 3D and fig. S7).

A critical feature of two-state switches in biology and technology is the coupling between the state control mechanism and the populations of the two states. To quantitatively investigate the thermodynamics and kinetics of the effector-induced switching between the two states of our designed hinges, we used Förster resonance energy transfer (FRET). To increase both the absolute distance from N- to C- terminus and the change in termini distance between the two conformational states, we took advantage of the extensibility of repeat proteins and extended hinges cs201, cs221, and cs074 by 1 to 2 helices on their N and C termini, yielding cs201F, cs221F, and cs074F, respectively (Fig. 4A, first column). Single cysteines were introduced in helical regions near the termini of the extended hinges and stochastically labeled with an equal mixture of donor and acceptor dyes. For cs201F, the dye distance is above R_0 in state X and below R_0 in state Y, and hence acceptor emission upon donor excitation decreases upon addition of peptide cs201B (Fig. 4A, second column). For hinges cs074F and cs221F the distance between the label sites is above the R_0 of the dye pair in state X and below R_0 in state

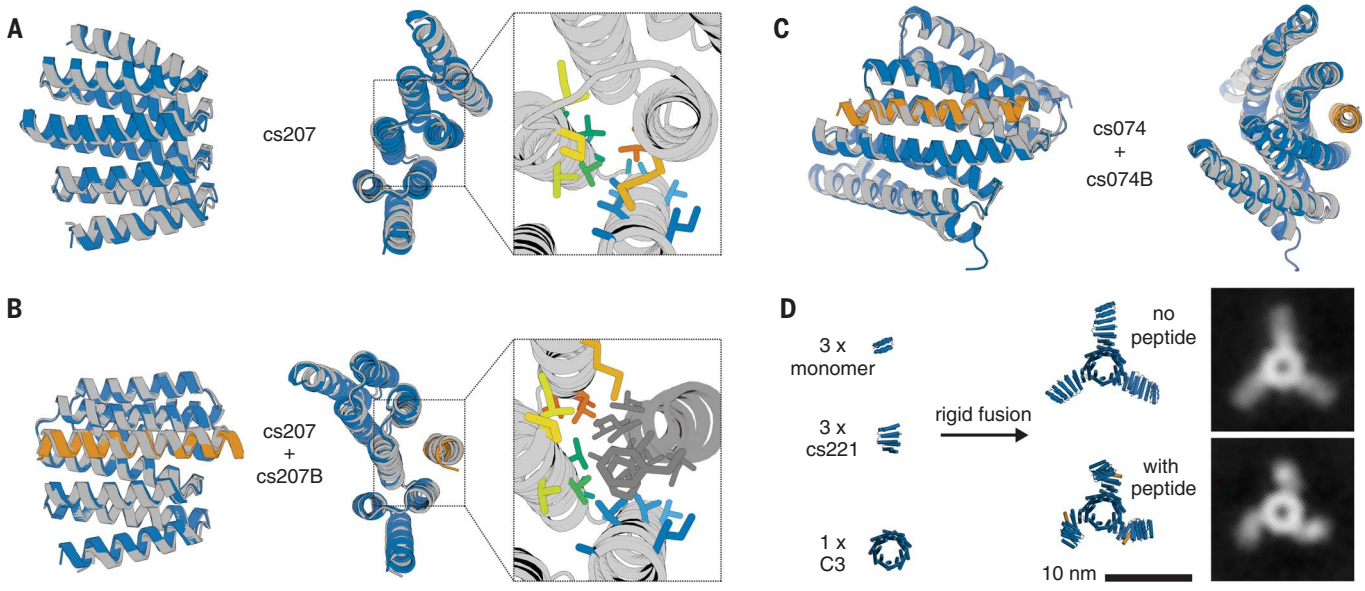

Fig. 3. Close agreement between crystal structures and design models for both designed states. (**A**) Design model (blue) of hinge cs207 in state X overlaid with crystal structure (gray) of hinge cs207 crystallized without peptide. Right panel shows a close-up view of the side chains in the interface between the two hinge domains (side chain colors follow a spectrum from blue to red from N- to C-terminus). (**B**) Design model (hinge in blue, peptide in orange) of the cs207 state Y hinge-peptide complex overlaid with crystal structure (gray) of hinge cs207 co-crystallized with peptide cs207B. Right panel shows a close-up view of the side chains in the interface between hinge and peptide [hinge side chain colors match the corresponding side chains in (A) and peptide side chains are shown in dark gray]. (**C**) Design model (hinge in blue, peptide in orange) of hinge cs074 in state Y overlaid with crystal structure (gray) of hinge cs074 co-crystallized with peptide cs207B. Representative electron densities for all crystal structures are shown in fig. S19. RMSD values between design model and experimental structure are given in table S4. (**D**) (Left) Components for design of a C3-symmetric homotrimer with three cs221 hinge arms. (Center) Design model of the hinge-armed trimer in state X (top) and in state Y (bottom). (Right) nsEM class averages of the trimer in absence (top) and in presence (bottom) of peptide cs221B.

Y and hence acceptor emission upon donor excitation increases upon addition of the corresponding peptides cs074B and cs221B, respectively (Fig. 4A, second column). We used labeled, extended DHR82, the parent protein for cs074F, as a static control, and observed fluorescence spectra comparable to cs074F but observed no change in fluorescence upon addition of the peptide (fig. S8, A and B). To test specificity of our hinge-peptide pairs, we performed pairwise titrations of all three labeled hinges at 2 nM with all three target peptides at varying concentrations. The on-target titrations had sigmoidal transitions that can be fitted with standard binding isotherms (Fig. 4A, third column; S8C), whereas the off-target titrations for cs201F and cs221F show flat lines, indicating no conformational change of these hinges upon addition of off-target peptides at micromolar concentrations. cs074F showed weak off-target binding that was three orders of magnitude weaker for cs201B and two orders of magnitude weaker for cs221B compared with the on-target interaction for cs074B. cs201F and cs221F are thus orthogonal from the nanomolar to the micromolar range, and the set of cs201F, cs221F, and cs074F is orthogonal over two orders of magnitude of effector concentration.

Association kinetics for the on-target interactions measured using constant concentrations of labeled hinge and varying excess concentrations of peptide are well fit by single exponentials (Fig. 4A, fourth column, and fig. S9). The apparent rate constants increase linearly with increasing peptide concentration, exhibiting standard pseudo–first order kinetics for bimolecular reactions (Fig. 4A, fifth column, and fig. S9). We analyzed these data using a model comprising three states (X, Y, Y+peptide) and four rate constants (Fig. 4B). The kinetic measurements using the FRET system follow the decrease in state X over time (d[X]/dt) upon the addition of peptide. The observed pseudo–first order behavior (Fig. 4A, fifth column) indicates that the conformational change happens on a timescale that is faster than that of the observed binding and can be treated as a fast pre-equilibrium (Supplementary Note 2). The slopes of the linear pseudo-first order fits (k_{on}) can thus be interpreted as the product of the microscopic association rate k_2 and the fractional population of state Y in absence of the peptide (F_Y = [Y]/([X]+[Y]), see Supplementary Note 2). FP-based titrations and kinetic characterization using the unlabeled extended hinge cs074F in excess over the TAMRA(Tetramethylrhodamine)-labeled peptide cs074B agree well with the corresponding FRET experiments, further supporting the pre-equilibrium model (Fig. 4C and fig. S9). FP kinetics experiments for other hinge designs also follow pseudo-first order behavior with k_{on} values ranging from 2.5×10^3 $M^{-1}s^{-1}$ to 7.8×10^4 $M^{-1}s^{-1}$ (figs. S4B and S10). To study the reversibility of hinge conformational changes, we started with 30 nM of FRET-labeled hinge cs201F, added 200 nM peptide to drive the conformational change, and then added excess unlabeled hinge cs201 to compete away the peptide (Fig. 4D). The FRET signal decreased upon addition of the peptide, consistent with conformational change from state X to state Y, and then returned to nearly the original level upon addition of unlabeled hinge, indicating that the hinge conformational change is fully reversible.

To explore whether peptide-responsive hinges could be turned into protein-responsive hinges, we used inpainting with RoseTTAFold to add two additional helices to a validated effector peptide, resulting in fully structured 3-helix bundles (3hb). For nine of our validated hinges we designed and experimentally characterized these effector proteins using SEC (Fig 4E and figs. S11A and S12). Hinge-3hb binding was tested qualitatively by SEC and, for hinges which had a corresponding FRET construct, quantitatively with the FRET-labeled variant, and DEER was used in addition to FRET to confirm that 3hb binding caused the same conformational change as effector peptide binding (Fig. 4E,

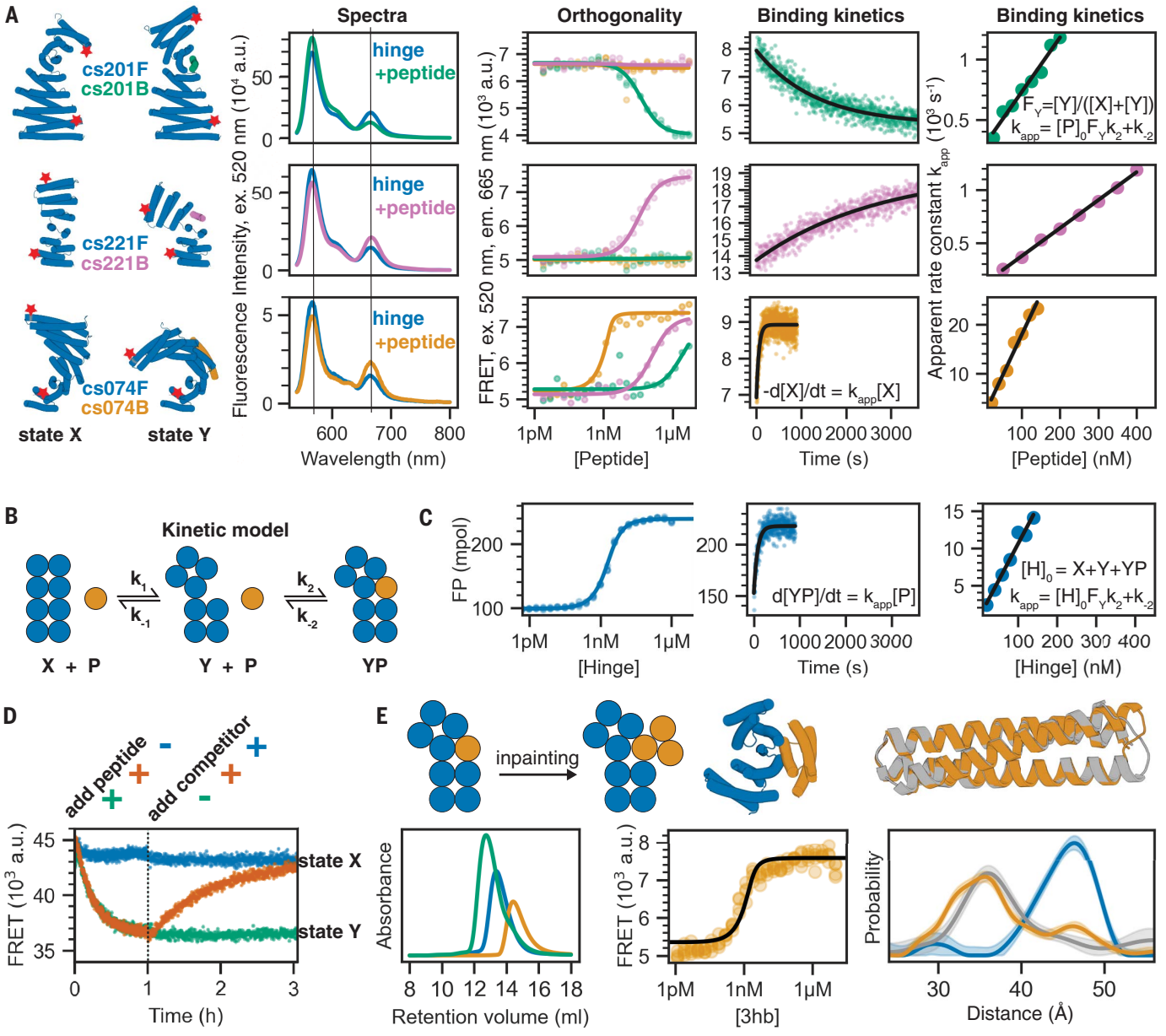

Fig. 4. Quantitative analysis of conformational changes in designed hinge proteins. (**A**) FRET-based characterization of three extended hinges. (From left to right) cylindrical representation of extended hinges (blue) and their corresponding target peptides (green, cs201B; pink, cs221B; orange, cs074B) with red stars indicating attachment sites for fluorescent dyes; fluorescence spectra (excitation at 520 nm) of labeled hinge without (blue) or with (green/pink/orange) target peptide; FRET-based binding titrations (excitation 520 nm, emission 665 nm) at 2 nM labeled hinge and varying peptide concentrations fitted with standard binding isotherms (solid lines); time course after mixing 2 nM (cs201F, cs074F) or 5 nM (cs221F) labeled hinge and 100 nM peptide fitted with a single-exponential equation (black line); and apparent rate constants obtained from single-exponential kinetic fits plotted against absolute peptide concentrations (circles) and fitted with a linear equation (black line). Dotted lines in spectra indicate acceptor and donor emission peaks. (**B**) Kinetic model describing the coupling of the conformational equilibrium to the binding equilibrium. X and Y, hinge in state X and Y, respectively; P, peptide; YP, peptide bound to hinge in state Y. k_1, k_{-1}, k_2, and k_{-2} are the microscopic rate constants. (**C**) FP characterization of unlabeled extended hinge cs074F. (From left to right) binding titration at 0.1 nM TAMRA-labeled peptide and varying hinge concentrations; time course after mixing 2 nM TAMRA-labeled peptide and 100 nM hinge fitted with a single-exponential equation (black line); apparent rate constants obtained from single-exponential kinetic fits plotted against absolute hinge concentrations (circles) and fitted with a linear equation (black line). (**D**) FRET-based reversibility experiment using the labeled extended hinge cs201F introduced in (C). Hinge concentration is 30 nM for all traces; 1 μM peptide is added at t = 0 (green/orange), 3 μM unlabeled competitor hinge is added after 1 h (blue/orange). (**E**) (Top from left to right) schematic representation of the inpainting procedure that adds two helices to the peptide cs074B yielding a three-helix bundle (3hb); cylindrical representation of 3hb_05 (orange) bound to hinge cs074 (blue); overlay of design model (orange) and crystal structure (gray) of 3hb_05. (Bottom from left to right) SEC traces for hinge cs074 (blue), 3hb_05 (orange), and a mixture of both (green); FRET-based titration of 2 nM extended labeled hinge cs074F and varying concentrations of 3hb_05 fitted with a standard binding isotherm (back line); Distance distributions obtained from DEER experiments as described in Fig. 2 (blue, cs074; gray, cs074 + peptide cs074B; orange, cs074 + 3hb_05).

bottom, and fig. S11). The affinity of 3hb05 to cs074F was similar to the affinity observed for the original peptide cs074B (Fig. 4E), whereas 3hb21 bound its target hinge cs221F significantly tighter than the original peptide cs221B (fig. S13). The 3hb approach was able to rescue designs for which the peptide alone or the hinge-peptide complex had shown the tendency to form higher-order oligomers (fig. S12). For two designs, 3hb05 and 3hb12, we obtained crystal structures that agreed well with the design models, indicating that the three-helix bundles are fully structured in isolation (Fig. 4E, top right, and fig. S14).

The conformational pre-equilibrium controls effector binding

To test the effect of the conformational pre-equilibrium on effector binding, we introduced disulfide "staples" that lock the hinge in one conformation. Using FP we analyzed peptide binding to stapled versions of hinge cs221 (Fig. 5, A and B). The variant that forms a disulfide bond in state X ("locked X") showed only weak residual binding, likely due to a small fraction of hinges not forming the disulfide (Fig. 5A). Upon addition of the reducing agent dithiothreitol (DTT) to break the disulfide, peptide binding was fully restored, making this hinge variant a red/ox–dependent peptide binder that binds the effector peptide under reducing—but not oxidizing—conditions. The association rate for the locked Y variant was 200 times higher than that for the original hinge without disulfides (Fig. 5B and fig. S15, A and B; despite this increase the overall binding affinity was weaker, suggesting the disulfide may lock the hinge in a slightly perturbed version of state Y). Using the pre-equilibrium model described above, the observed association rates provide an estimate of the fraction of hinge that is in state Y in absence of the peptide: a 200-fold higher observed on rate for the locked Y variant indicates a 200-fold higher fraction of hinge in state Y compared with the original hinge. Assuming that the locked Y variant is 100% in state Y and assuming that the microscopic rate constant k_2 is identical for the locked Y hinge and state Y of the original hinge, this would indicate that the original hinge is 99.5% in state X and 0.5% in state Y at equilibrium.

Having established the edge cases of locked state X and locked state Y, we sought to tune the pre-equilibrium by introducing single point mutations expected to specifically stabilize one state over the other while not directly affecting the peptide-binding interface. We used proteinMPNN to generate consensus sequences (*38*) for each state and identified non-interface positions with distinct residue preferences that were different between both states (Fig. 5C and fig. S16A). We experimentally tested individual protein variants carrying substitutions expected to stabilize one state over the other without disrupting either conformation, as evaluated by AF2 predictions. Consistent with coupling of the conformational and binding equilibria, substitutions based on state X consensus sequences led to weaker peptide binding, and those based on state Y consensus sequences led to stronger binding (Fig. 5C and fig. S15C). The substitutions that stabilized state Y showed accelerated association kinetics (Fig. 5C and fig. S17), consistent with our kinetic model (Fig. 4B and fig. S16, B and C; Supplementary Note 2): the mutations effectively shift

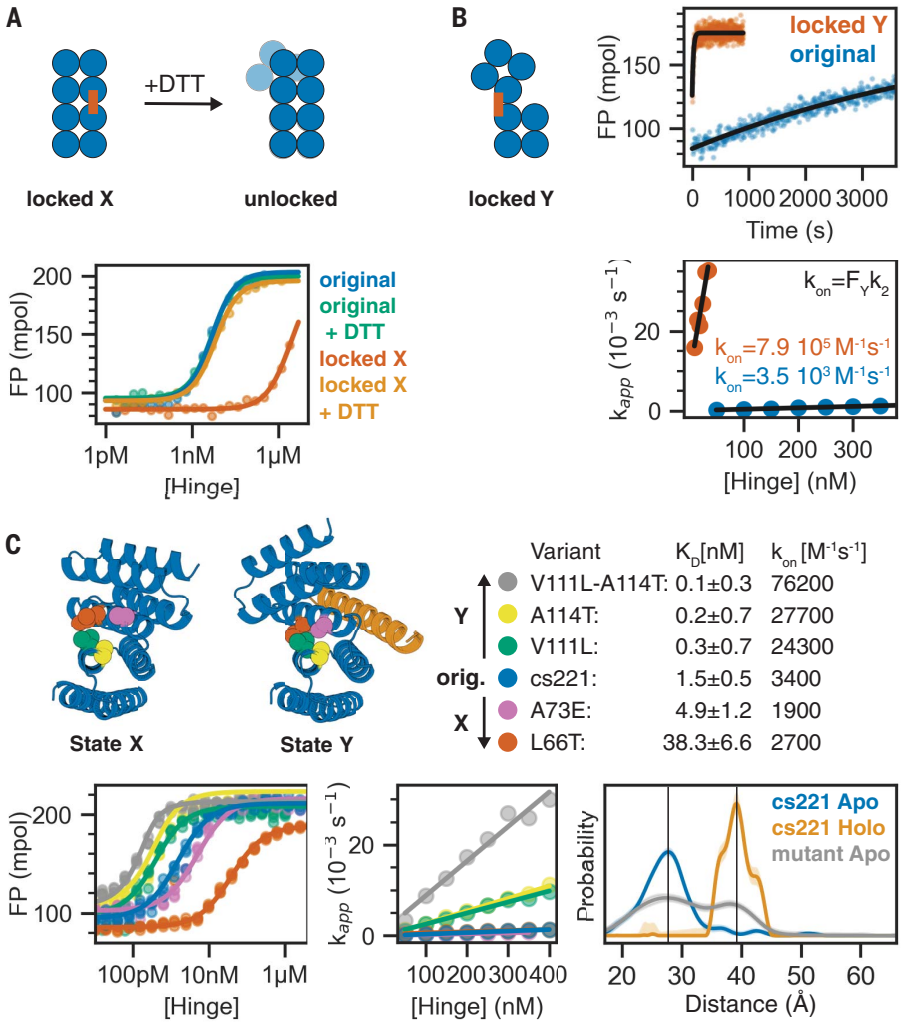

Fig. 5. Controlling the conformational pre-equilibrium affects peptide binding. (**A**) (Left) Schematic representation of a hinge containing two cysteine residues that can form a disulfide bond in state X but not in state Y, effectively locking the hinge in state X under oxidizing conditions. Upon addition of reducing agent DTT the disulfide bond is broken and the conformational equilibrium is restored. (Right) FP-based titration of 1 nM TAMRA-labeled peptide and a hinge with state X disulfide (red, orange) or the parent hinge without cysteines (blue, green) under oxidizing (blue, red) or reducing (green, orange) conditions. (**B**) (Top left) schematic representation of a hinge that is disulfide-locked in state Y; (Top right) time course after mixing 2 nM TAMRA-labeled peptide and 50 nM locked hinge (red) or original hinge without cysteines (blue) fitted with a single-exponential equation (black line); (Bottom) apparent rate constants obtained from single-exponential kinetic fits plotted against absolute hinge concentrations (circles) and fitted with a linear equation (black line). (**C**) Tuning the pre-equilibrium with point mutations. (Top left) Models of hinge cs221 in both states highlighting positions of point mutations. (Top right) Dissociation constants (K_D) and observed binding rate constants (k_{on}). (Bottom left) FP-based titration of 0.1 nM (yellow, green, blue) or 1 nM (pink, red) TAMRA-labeled peptide cs221B and varying concentrations of hinge variants containing one or two point mutations. (Bottom center) Apparent rate constants obtained from single-exponential kinetic fits plotted against absolute hinge concentrations (circles) and fitted with a linear equation (black line). (Bottom right) DEER distance distribution for the double mutant cs221-V111L-A114T in absence of peptide (gray) in comparison to the original cs221 with (orange) and without (blue) peptide. Vertical lines serve as a guide to the eye indicating state X and state Y distances.

the conformational pre-equilibrium toward state Y, increasing the on rates. This close coupling of the conformational equilibrium with association kinetics further supports the model outlined in Fig. 4B, and the fine tunability should be useful in downstream applications.

The state Y–stabilizing double mutant cs221_V111L_A114T has an on rate that is 22 times higher than that of the original cs221, suggesting that the occupancy of state Y in cs221_V111L_A114T is 22 times higher in the absence of peptide. Distance distributions obtained from DEER measurements on site pair 2 of the double mutant cs221_V111L_A114T in absence of the peptide indeed showed an additional peak at a distance closely matching state Y (Fig. 5C and fig. S18). DEER measurements on site pair 1 of the double mutant showed a broader distribution with occupancy in the region corresponding to state Y (Fig. 5C and fig. S18). Measurements in the presence of the peptide were virtually indistinguishable from the original cs221 (fig. S18). The double mutant thus populates two distinct states in the absence of the effector, and collapses to one state upon effector addition (Fig. 5E and fig. S18). The observation of a significant state Y population at equilibrium in the absence of the peptide as predicted based on the kinetic measurements further corroborates that the mutations affect the conformational pre-equilibrium and provides strong support for our quantitative two-state model of the kinetics and thermodynamics of the designed hinge-effector systems.

Conclusion

Our hinge design method generates proteins that populate two well-defined and structured conformational states rather than adopting a heterogeneous mixture of structures and should be broadly applicable to design of functional proteins. Like transistors in electronic circuits, we can couple the switches to external outputs and inputs to create sensing devices and incorporate them into larger protein systems to address a wide range of outstanding design challenges. Hinges containing a disulfide that locks them in state X couple the input "red/ox state" to the output "target binding," where the target can be a peptide or a protein, and our FRET-labeled hinges couple the input "target binding" to the output "FRET signal." Our approach can be readily extended such that state switching is driven by naturally occurring rather than designed peptides: recently designed extended peptide binding proteins (*39*) resemble the state X of our hinges, and recent designs that bind glucagon, secretin, or neuropeptide Y (*40*) resemble the state Y of our hinges. Hinges based on such designs could thus provide new routes to applications in sensing and detection.

Stimulus-responsive protein assemblies that switch between two well-defined shapes or oligomeric states in the presence of an effector can now be built by incorporating the hinges as modular building blocks, which was not possible with the previous LOCKR switches as one of the LOCKR states is disordered. Installing enzymatic sites in hinges such that substrate binding favors one state and product release favors the other state should enable fuel-driven conformational cycling, a crucial step toward the de novo design of molecular motors. More generally, the ability to design two-state systems, and the designed two-state switches presented here, should enable protein design to go beyond static structures to more complex multistate assemblies and machines.

REFERENCES AND NOTES

1. J. B. Stiller *et al*., *Nature* **603**, 528–535 (2022).
2. S. J. Kerns *et al*., *Nat. Struct. Mol. Biol.* **22**, 124–131 (2015).
3. A. Bisello *et al*., *J. Biol. Chem.* **277**, 38524–38530 (2002).
4. T. Movassagh, K. H. Bui, H. Sakakibara, K. Oiwa, T. Ishikawa, *Nat. Struct. Mol. Biol.* **17**, 761–767 (2010).
5. W. A. Catterall, G. Wisedchaisri, N. Zheng, *Nat. Chem. Biol.* **16**, 1314–1320 (2020).
6. E. G. B. Evans, J. L. W. Morgan, F. DiMaio, W. N. Zagotta, S. Stoll, *Proc. Natl. Acad. Sci. U.S.A.* **117**, 10839–10847 (2020).
7. B. Arragain *et al*., *Nat. Commun.* **11**, 3590 (2020).
8. A. K. Kim, L. L. Porter, *Structure* **29**, 6–14 (2021).
9. J.-H. Ha, S. N. Loh, *Chemistry* **18**, 7984–7999 (2012).
10. P.-S. Huang *et al*., *Science* **346**, 481–485 (2014).
11. R. Koga *et al*., *Proc. Natl. Acad. Sci. U.S.A.* **117**, 31149–31156 (2020).
12. A. F. Dishman, B. F. Volkman, *Curr. Opin. Struct. Biol.* **74**, 102380 (2022).
13. N. H. Joh *et al*., *Science* **346**, 1520–1524 (2014).
14. J. A. Davey, A. M. Damry, N. K. Goto, R. A. Chica, *Nat. Chem. Biol.* **13**, 1280–1285 (2017).
15. V. K. Mulligan *et al*., *Protein Sci.* **29**, 2433–2445 (2020).
16. K. Y. Wei *et al*., *Proc. Natl. Acad. Sci. U.S.A.* **117**, 7208–7215 (2020).
17. R. A. Langan *et al*., *Nature* **572**, 205–210 (2019).
18. A. Quijano-Rubio *et al*., *Nature* **591**, 482–487 (2021).
19. J. Z. Zhang *et al*., *Nat. Biotechnol.* **40**, 1336–1340 (2022).
20. M. Wang *et al*., *Proc. Natl. Acad. Sci. U.S.A.* **117**, 30433–30440 (2020).
21. T. J. Brunette *et al*., *Nature* **528**, 580–584 (2015).
22. T. J. Brunette *et al*., *Proc. Natl. Acad. Sci. U.S.A.* **117**, 8870–8875 (2020).
23. F. Khatib *et al*., *Proc. Natl. Acad. Sci. U.S.A.* **108**, 18949–18953 (2011).
24. M. D. Tyka *et al*., *J. Mol. Biol.* **405**, 607–618 (2011).
25. N. Koga *et al*., *Nature* **491**, 222–227 (2012).
26. Y.-R. Lin *et al*., *Proc. Natl. Acad. Sci. U.S.A.* **112**, E5478–E5485 (2015).
27. J. Dauparas *et al*., *Science* **378**, 49–56 (2022).
28. J. Jumper *et al*., *Nature* **596**, 583–589 (2021).
29. N. Bennett *et al*., Improving de novo Protein Binder Design with Deep Learning. bioRxiv 2022.06.15.495993 [Preprint] (2022).
30. L. Cao *et al*., *Nature* **605**, 551–560 (2022).
31. L J. Berliner, J. Grunwal, H. O. Hankovszky, K. Hideg, *Anal. Biochem.* **119**, 450–455 (1982).
32. M. H. Tessmer, S. Stoll, chiLife: An open-source Python package for in silico spin labeling and integrative protein modeling. bioRxiv 2022.12.23.521725 [Preprint] (2022).
33. J. Wang *et al*., *Science* **377**, 387–394 (2022).
34. M. Baek *et al*., *Science* **373**, 871–876 (2021).
35. J. P. Hallinan *et al*., *Commun. Biol.* **4**, 1240 (2021).
36. R. D. Kibler *et al*., Stepwise design of pseudosymmetric protein hetero-oligomers. bioRxiv 2023.04.07.535760 [Preprint] (2023).
37. D. D. Sahtoe *et al*., *Science* **375**, eabj7662 (2022).
38. G. E. Crooks, G. Hon, J.-M. Chandonia, S. E. Brenner, *Genome Res.* **14**, 1188–1190 (2004).
39. K. Wu *et al*., *Nature* **616**, 581–589 (2023).
40. S. V. Torres *et al*., De novo design of high-affinity protein binders to bioactive helical peptides. bioRxiv 2022.12.10.519862 (2022).

ACKNOWLEDGMENTS

We thank B. I. M. Wicky, L. F. Milles, and D. D. Sahtoe for helpful discussions and technical support, A. Courbet for inspiring discussions, A. Philomin and A. Borst for EM support, and K. VanWormer and L. Goldschmidt for technical support. We thank the Advanced Light Source (ALS) beamline 8.2.2/8.2.1 at Lawrence Berkeley National Laboratory for x-ray crystallography data collection. The Berkeley Center for Structural Biology is supported in part by the National Institutes of Health (NIH), National Institute of General Medical Sciences, and the Howard Hughes Medical Institute. The ALS is supported by the Director, Office of Science, Office of Basic Energy Sciences and US Department of Energy (DOE) (DE-AC02-05CH11231). **Author contributions:** F.P. developed the hinge design concept. F.P. and P.J.Y.L. developed the computational hinge design pipeline. F.P. and P.J.Y.L. designed, screened, and characterized most hinges with help from C.D. and A.P. M.H.T. designed, performed and analyzed DEER experiments. S.S. analyzed DEER data and supervised research. C.D. developed the one-sided two-state design protocol and designed and tested hinges with swapped targets. A.B. designed and characterized 3-helix bundles with support from D.C.J. A.I. designed and characterized the hinge-armed trimer with support from A.B. A.I. performed electron microscopy and image processing with support from A.P. J.D. provided conceptual support for two-state sequence design. X.L., P.M.L., M.L., and R.K.B. synthesized and purified peptides. X.L., M.L., and R.K.B. performed LC-MS validation of proteins and peptides. S.R.G. performed additional protein purification. H.N., A.K., B.S., and A.K.B. determined crystal structures. A.F.D. and B.V. contributed conceptual support. D.B. and J.N. supervised research. F.P., P.J.Y.L., and D.B. wrote the manuscript. M.H.T. contributed to the manuscript. All authors read and commented on the manuscript. **Funding:** This work was supported by a Human Frontier Science Program Long Term Fellowship [LT000880/2019 (to F.P.)], the Open Philanthropy Project Improving Protein Design Fund (to P.J.Y.L., C.W.D., H.N., and D.B.), an NSF Graduate Research Fellowship [DGE-2140004 (to P.J.Y.L.)], NERSC award BER-ERCAP0022018 (to P.J.Y.L and D.B.), the Audacious Project at the Institute for Protein Design (to A.B., A.P., A.I., M.L., R.K.B., S.R.G., A.K., and D.B.), a gift from Microsoft (to D.J., J.D., and D.B.), a grant from DARPA supporting the Harnessing Enzymatic Activity for Lifesaving Remedies (HEALR) program [HR001120S0052 contract HR0011-21-2-0012, (to X.L., A.K.B., and D.B.)], the Defense Threat Reduction Agency (DTRA) grant # HDTRA1-19-1-0003 (to P.M.L.), NSF Award #2006864 (to J.N.), and the Howard Hughes Medical Institute (to D.B.). DEER measurements were supported by R01 GM125753 (to S.S.). The spectrometer used was funded by NIH grant S10 OD021557 (to S.S.). **Competing interests:** A provisional patent application will be filed prior to publication, listing F.P., P.J.Y.L., M.H.T., A.B., C.D., A.F.D., A.P., A.I., B.V., S.S., and D.B. as inventors or contributors. B.F.V. has ownership interests in Protein Foundry, LLC and XLock Biosciences, Inc. **Data and materials availability:** All data are available in the main text or as supplementary materials. Design models are available in supplementary file S2 and through Zenodo (*41*). Design scripts are available in supplementary file S3 and through Zenodo (*41*). Raw DEER data are available through Zenodo (*41*). Crystallographic datasets have been deposited in the Protein Data Bank (PDB) (accession codes 8FIH, 8FVT, 8FIT, 8FIN, and 8FIQ).

License information: Copyright © 2023 the authors, some rights reserved; exclusive licensee American Association for the Advancement of Science. No claim to original US government works. https://www.sciencemag.org/about/science-licenses-journal-article-reuse. This article is subject to HHMI's Open Access to Publications policy. HHMI lab heads have previously granted a nonexclusive CC BY 4.0 license to the public and a sublicensable license to HHMI in their research articles. Pursuant to those licenses, the author-accepted manuscript (AAM) of this article can be made freely available under a CC BY 4.0 license immediately upon publication.

SUPPLEMENTARY MATERIALS

science.org/doi/10.1126/science.adg7731
Materials and Methods
Figs. S1 to S22
Tables S1 to S4
Supplementary Notes 1 and 2
Data S1 to S3
References (*41*–*64*)
MDAR Reproducibility Checklist

Submitted 24 January 2023; accepted 11 July 2023
10.1126/science.adg7731

RESEARCH ARTICLE

BIOPHYSICS

Alcanivorax borkumensis biofilms enhance oil degradation by interfacial tubulation

M. Prasad[1]†, N. Obana[2,3], S.-Z. Lin[4], S. Zhao[1], K. Sakai[5,6], C. Blanch-Mercader[7], J. Prost[7,8], N. Nomura[1,3,9], J.-F. Rupprecht[4]*, J. Fattaccioli[5,6]*, A. S. Utada[1,3]*

During the consumption of alkanes, *Alcanivorax borkumensis* will form a biofilm around an oil droplet, but the role this plays during degradation remains unclear. We identified a shift in biofilm morphology that depends on adaptation to oil consumption: Longer exposure leads to the appearance of dendritic biofilms optimized for oil consumption effected through tubulation of the interface. In situ microfluidic tracking enabled us to correlate tubulation to localized defects in the interfacial cell ordering. We demonstrate control over droplet deformation by using confinement to position defects, inducing dimpling in the droplets. We developed a model that elucidates biofilm morphology, linking tubulation to decreased interfacial tension and increased cell hydrophobicity.

Obligately hydrocarbonoclastic bacteria (OHCB) are a group of cosmopolitan marine bacteria with an unusual ecology: They can survive by consuming hydrocarbons as a sole carbon and energy source (*1*). These metabolic specialists are found at very low densities because of the lack of hydrocarbons but are thought to play a global role in metabolizing naturally occurring alkanes (*2*) in the ocean. However, they become the dominant bacteria, out-competing generalists, at the site of oil spills (*1*, *3*, *4*). OHCB are thought to degrade a substantial fraction of spilled oil worldwide (*1*, *5*), which has generated interest for their potential as agents of bioremediation (*5*–*9*).

Alcanivorax borkumensis SK2 is an aerobic and rod-shaped OHCB (*10*) that is often used as a model organism for prevalence (*1*, *2*) and its genetic tractability (*6*, *11*). Like most bacteria, it transitions between planktonic and biofilm lifestyles, which is now recognized as integral to bacterial biology (*12*). Biofilms are often dense three-dimensional communities encased in self-secreted extracellular polymeric substances, which adhere them to surfaces. Biofilms begin with the colonization of a surface. This can lead to high two-dimensional cell densities, which in the case of rod-shaped bacteria, induces nematic liquid crystal order. Bacteria have been shown to escape confinement in dense packings (*13*, *14*) by leveraging regions where the nematic order is undefined, called topological defects (*15*). Unlike most bacteria, because *A. borkumensis* forms biofilms on a liquid, it is not clear how the interfacial fluidity affects cell packing and biofilm morphology formation during oil consumption.

Most knowledge of bacteria-mediated oil degradation comes from chemical, genetic, and metagenomic analysis of ocean samples (*7*, *16*, *17*) and microcosm tests that used crude oil and sea water (*18*–*20*). Recent work has begun to clarify the important initial step of bacterial colonization (*21*) and to characterize biofilm formation (*22*–*25*) on oil drops in the size range commonly found dispersed in the ocean after an oil spill. Biofilms can deform oil drops (*18*, *24*, *25*) and increase their hydrodynamic drag (*23*), potentially mediating the formation of organic-oil aggregates. These aggregates, also known as marine oil snow, have been identified as a mechanism by which large quantities of partially biodegraded oil was transported to the seafloor in the aftermath of the Deepwater Horizon disaster (*4*, *23*, *26*). However, the mechanism of biofilm formation, which depends on the interfacial properties of individual cells, and its relation to oil degradation remains unclear (*18*).

Experimental setup and microfluidic device

To address these questions, we developed a microfluidic device that allows the trapping and real-time imaging of numerous bacteria-covered oil droplets. This platform allows us to capture the full dynamics of biofilm development starting from individual bacteria through the complete consumption of oil droplets.

In the ocean, *A. borkumensis* subsists primarily on naturally occurring organic acids and alkanes (*2*); however, during oil spills, it blooms to exploit the hydrocarbons in the crude oil mélange. To study the biofilm dynamics as *A. borkumensis* adapts (*27*) to using solely alkanes, we initially cultivated using pyruvate and then switched to an artificial seawater medium supplemented with hexadecane (C16) (fig. S1A). We sampled bacteria from liquid cultures cultivated up to 5 days by harvesting the cells and generating cell-laden oil microdroplets with fresh C16, which we incubated in individual microfluidic traps (supplementary text S1). Our device, which is highly permeable to oxygen, facilitates in situ culturing, enabling the longitudinal investigation of biofilm development simultaneously on numerous droplets (Fig. 1A and fig. S2A). Trapped drops initially had approximately 20 to 50 cells attached and reached confluency in ~12 hours, which we define as t_0 (fig. S3A).

Bacteria exhibit two distinct phenotypes and consumption rates

Testing different liquid cultures at 1 and 5 days revealed different phenotypes that manifested vastly different biofilm morphologies and oil consumption rates. When sampled after 1 day, *A. borkumensis* formed a spherical biofilm (SB) that grew outward from the oil, and the oil droplet remained mostly spherical as it was consumed (Fig. 1B, fig. S3B, and movie S1). By contrast, bacteria sampled from 5-day-old culture can develop into thin biofilms with a local nematic ordering of the interfacial cells, which eventually buckle and then tubulate (*24*, *25*) the droplet interface (Fig. 1C), which we call dendritic biofilms (DB) (supplementary text S2). The biofilm buckles the interface to accommodate a population that is continuously increasing in number. The magnitude of the deformations grows as the oil is consumed, which ultimately shreds the droplets into tiny fragments (fig. S3C and movie S2).

To quantify the oil consumption rate for each phenotype, we measured the oil volume (V) over time using confocal microscopy. SBs consumed >90% of their oil droplet volume in ~72 hours, whereas DBs achieved the same level of consumption in ~20 hours. We found that the oil volume of SBs decreases as a polynomial function of time, whereas for DBs, the decay is much faster (Fig. 1, D and E, and fig. S3, D to F). In both cases, the decrease is consistent with a model of oil consumption effected exclusively by bacteria at the interface (supplementary text S3).

The good agreement between our analytical models and data allows us to estimate the single-cell consumption rates of oil by the SB and

[1]Faculty of Life and Environmental Sciences, University of Tsukuba, Tsukuba, Ibaraki 305-8577, Japan. [2]Transborder Medical Research Center, Faculty of Medicine, University of Tsukuba, Tsukuba, Ibaraki 305-8577, Japan. [3]Microbiology Research Center for Sustainability (MiCS), University of Tsukuba, Tsukuba, Ibaraki 305-8577, Japan. [4]Aix Marseille Univ, Université de Toulon, CNRS, CPT (UMR 7332), Turing Centre for Living systems, Marseille, France. [5]PASTEUR, Département de Chimie, École Normale Supérieure, PSL Université, Sorbonne Université, CNRS, 75005 Paris, France. [6]Institut Pierre-Gilles de Gennes pour la Microfluidique, 75005 Paris, France. [7]Laboratoire Physico-Chimie Curie UMR168, Institut Curie, Paris Sciences et Lettres, Centre National de la Recherche Scientifique, Sorbonne Université, 75248 Paris, France. [8]Mechanobiology Institute, National University of Singapore, 117411 Singapore. [9]TARA center, Univeristy of Tsukuba, Tsukuba, Ibaraki 305-8577, Japan.
***Corresponding author. Email: utada.andrew.gm@u.tsukuba.ac.jp (A.S.U.); jacques.fattaccioli@ens.psl.eu (J.F.); jean-francois.rupprecht@univ-amu.fr (J.-F.R.)**
†Present address: School of Biosciences, University of Sheffield, Sheffield, UK.

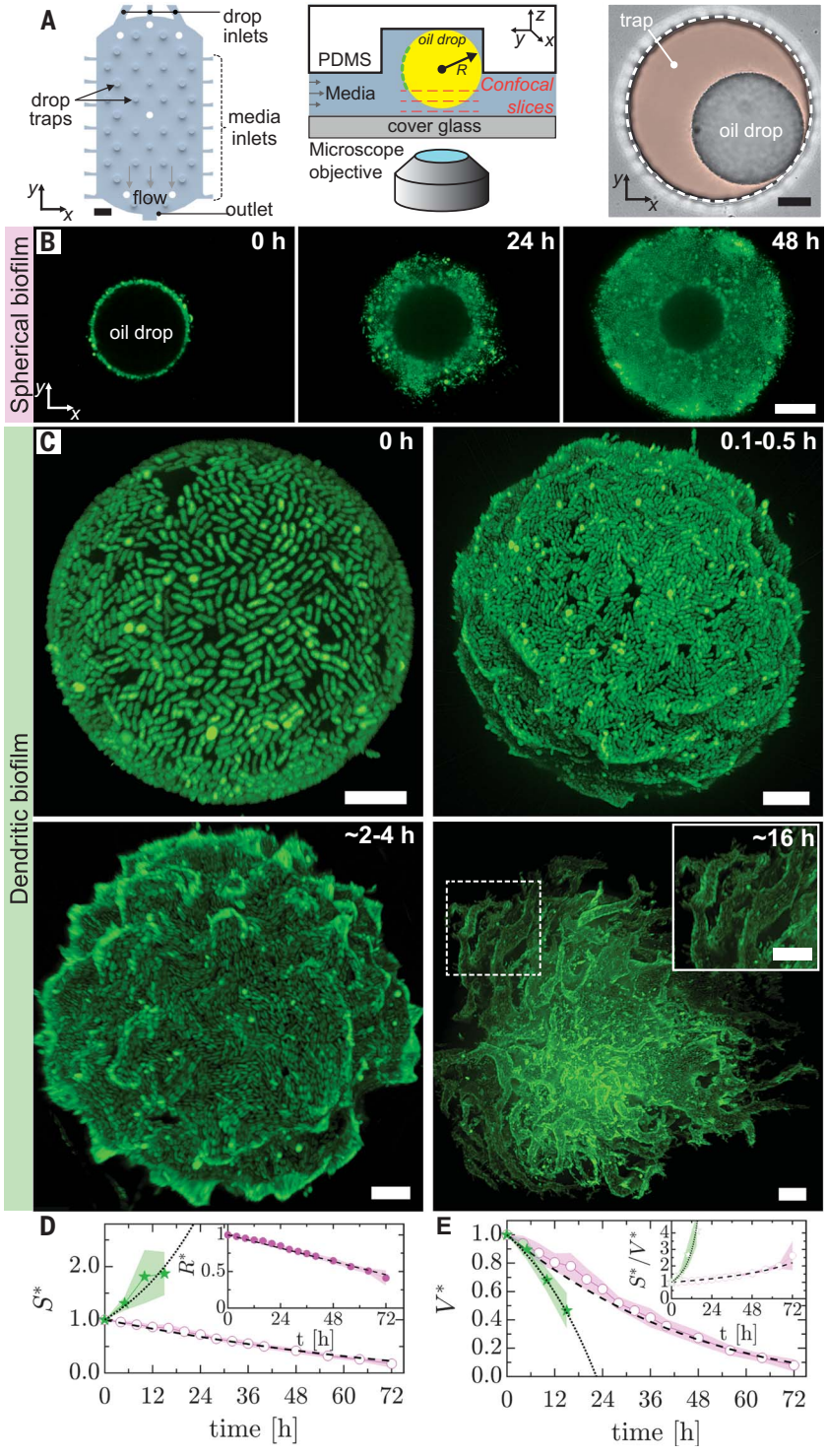

Fig. 1. Spherical and dendritic biofilm phenotypes on oil drops in a microfluidic trap. (**A**) (Left) Schematic of the microfluidic oil-drop trap device, showing media-filled channels. Oil drops are trapped in the raised circular regions. Inlets on either side of the drop chamber connect to reservoirs that provide a gentle flow of media through the trap chamber. The white circles indicate pillars. Scale bar, 200 μm. (Middle) Schematic cross-section of an individual trap. (Right) Bright-field image of a representative drop in a trap. The trap is outlined with a white dashed line, and the pocket is colored orange as a guide for the eye. Scale bar, 20 μm. (**B**) Representative time-lapse sequence of confocal images showing the development of the SB phenotype. As the biofilm (green) grows, the oil droplet (central void) shrinks. Scale bar, 10 μm. (**C**) Maximum intensity projection confocal images showing the development of the DB phenotype on representative drops. Local nematic order is present at confluence (~0 hours), buckling (0.1 to 0.5 hours) and protrusions (2 to 4 hours) appear later, and large-scale remodeling of the interface leading to the formation of tubes occurs much later (16 hours). Scale bar, 10 μm. (**D** and **E**) Normalized surface area (S^*) and volume (V^*) of oil drops as a function of time for (open circles) SBs and (stars) DBs. Solid lines and shaded regions indicate mean ± SD (n_{SB} = 11 drops, and n_{DB} = 12 drops; representative experiment from three or more independent tests) (additional data is provided in fig. S3). Solid symbols indicate measurements, and open symbols indicate values calculated from measured quantities. The dashed and dotted lines are best fits of our analytical models of oil degradation for the phenotypes. [(D), inset] Normalized drop radius (R^*) was used to estimate S^* and V^* for SBs. [(E), inset] S^*/V^* as a function of time. R, S, and V are normalized by their initial values, respectively. We used eqs. S5, S6, S9, and S11 (supplementary text S3) to fit R^*, S^*, and V^* for SB and DBs, respectively.

DB cells as 0.7 and 0.8 fl/hour, respectively. This small difference in consumption rate is consistent with their similar division times (fig. S1D). For comparison, the volume of a single cell is ~1 fl, meaning that these bacteria consume a volume of oil close to their own, every hour. Despite the similarity in consumption rates on a per-cell basis, the normalized surface-to-volume ratio (S^*/V^*) shows that DBs are considerably more efficient: S^*/V^* doubles in 72 hours for SBs, whereas it diverges in less than 24 hours for DBs (Fig. 1E, inset). The S^*/V^* ratio provides a means for comparing the relative efficiencies of the two phenotypes and highlights that these differences arise from the rapid increase in interfacial area caused by DB biofilms. In both cases, the shape of the interface defines the dynamics of volume decrease. For SBs, the interfacial area defined by the spherical droplet determines the number of cells (N) that can pack onto the interface to have access to the oil. Conversely, for DBs, it is the increase of N at the interface due to cell division that determines the interfacial area. Thus, the rate of consumption decreases over time for SBs, whereas it increases continuously for DBs.

Tubulation is facilitated by topological defects

We correlated the onset of the rapid increase in surface area for DBs to the emergence of nematic order of the interfacial cells. Active systems with nematic order have shown the ability to use topological defects to achieve surface deformation, both theoretically (*28*, *29*) and experimentally (supplementary text S4) (*13*, *14*, *30*). Nematic topological defects of charge ±1/2 and ±1 are shown schematically in fig. S4A. At 2 to 4 hours after confluency, we observed the appearance of conical protrusions of cells that originate from the core of aster (+1) topological defects in the nematic director field, which is the average orientation of the bacteria (Fig. 2, A and B; fig. S4B; and supplementary text S3). As the biofilm matures, more protrusions appear, while existing protrusions elongate into branched bacteria-covered tubes (Figs. 1C, 16 hours, and 2C).

Differential labeling of the oil and cells shows that the tubes are not filled with water; instead, they are filled with oil (fig. S5A). This indicates that cell adhesion to the oil stabilizes the tubes against collapse, preventing the deformed oil from regaining a spherical shape. Furthermore, careful inspection of the confocal images of the tubes reveals that the bacteria are well aligned to the tube axis, which becomes clear in the director field of the cells on the tube (Fig. 2D). We characterized cell alignment along the tube with the local average scalar product between the director field and the tube axis, finding values close to 1; this indicates a high degree of alignment between the cells and the tube axis (Fig. 2E and fig. S5, B and C).

Because of this alignment, we hypothesized that the rate of increase of the tube length is proportional to the number of cells on the tube, which should increase exponentially if all cells were to divide. We measured tube elongation on different droplets and found that it increases rapidly and in a manner consistent with exponential elongation, which supports this hypothesis (Fig. 2F and fig. S5D). Furthermore, from the fit to our data, we extracted a tube length–doubling time of ~3.4 hours, which is twofold greater than the cell division time (t_{div}) of 1.65 hours (fig. S1D). This difference likely arises from the imperfect alignment of cells along the tubes and the expulsion of cells from the interface, which is visible around the tubes (Fig. 2C).

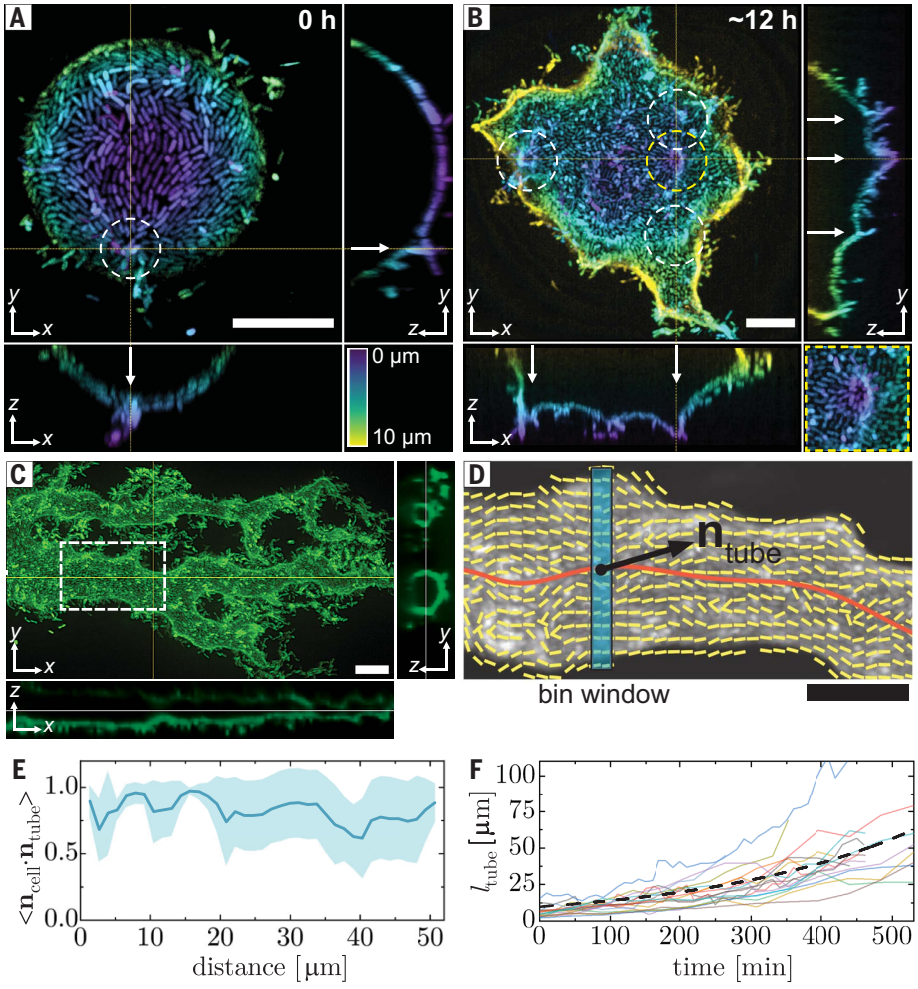

Fig. 2. Dendrites originate from topological defects. (**A** and **B**) Confocal images of representative droplets (A) early (~0 hours) and (B) later (~12 hours) in biofilm development. The images are color coded by depth. The dashed circles enclose +1 topological defects, and the arrows indicate protrusions. [(B), inset] Magnified view of the central defect circled in yellow. (**C**) Confocal image of a bacteria-covered tube connected to a deformed droplet with corresponding orthogonal views (~20 hours). (**D**) Director field of the visible cells in the dashed box in (C). The director field (yellow lines), tube axis (red line), the local tangent unit vector ($\mathbf{n}_{tube}$) along the tube axis, and the bin window (blue) are shown. (**E**) Axial order of the cells along the oil tube shown in (D). For a sliding window of width 1.5 µm along the tube, the local axial order is defined as the average of the individual scalar products between the director-field unit vectors ($\mathbf{n}_{cell}$) and local tangent unit vectors. $\langle \mathbf{n}_{cell} \cdot \mathbf{n}_{tube} \rangle$ = 1 for parallel alignment and 0 for perpendicular alignment. Solid line and shaded region are mean ± SD. (**F**) Oil tube length (l_{tube}) plotted as a function of time (n = 18 tubes; three independent tests). The dashed line is a fit to the average tube length from using an exponential equation [adjusted coefficient of determination (R^2) = 0.96]. Scale bars, 10 µm.

Biofilm phenotypes are associated with a decrease of interfacial tension

The large difference in biofilm morphology between the two phenotypes suggests differences in their interfacial properties. *A. borkumensis* secretes amphiphilic molecules that are thought to aid in the assimilation of oil (*10*, *31*–*33*). Furthermore, autolysis is thought to be important during *A. borkumensis* biofilm formation (*11*), which could liberate membrane-bound biosurfactants into the oil. These molecules can lower the oil-water interfacial tension (γ), making interfacial deformation easier. To measure changes in interfacial properties of the phenotypes, we fractionated SB and DB liquid cultures into three components—cells, conditioned media, and conditioned C16—to independently measure γ for each (fig. S6A). We found that γ for each of the respective fractions was depressed relative to control values; however, the DB-conditioned oil decreased the most. The γ for DB-conditioned oil decreased from 32 to 7 mN/m and was about half the value for SBs (Fig. 3A; fig. S6, B to D; and table S1). Unexpectedly, when we microfluidically tested SB and DB cells using the DB-conditioned C16 instead of fresh C16, we found no change in observed phenotype (fig. S6E). Thus, despite the ~80% lower γ of DB-conditioned oil, the SB cells were unable to deform the oil-water interface, indicating that a lower γ is not sufficient to produce the DB phenotype.

Interfacial behavior is also affected by cell hydrophobicity, which together with γ controls the extent that oil wets the cells (fig. S7A). Cell hydrophobicity is thought to increase the longer that cells consume oil, potentially through accumulation of membrane-bound hydrophobic

biosurfactants (*33*); however, the relationship with phenotype is unclear (*19*, *34*). Although the bacteria appear to lay flat on the surface at t_0, the contact angle is difficult to estimate from confocal images (fig. S7B). Thus, to estimate cell hydrophobicity of both phenotypes, we measured the three-phase contact angle (θ) between a water drop deposited on a bacterial lawn submerged in oil (fig. S7, C to E) (*35*); larger θ values indicate greater hydrophobicity. SB cells, which were isolated after 1 day of culture, had a θ ≈ 80°, whereas DB cells, which were isolated after 5 days, had a θ ≈ 100° (Fig. 3B). This suggests that the midplanes of SB and DB cells were ±10% above and below the interface, respectively (fig. S7A).

The higher hydrophobicity of DB cells also indicates that they have a larger interfacial adhesion strength than that of SB cells, for a constant γ (supplementary text S4). To directly compare the respective adhesion strengths of SB and DB, we forced them to compete for interfacial area on oil microdroplets, noting that both phenotypes have similar division times (fig. S1D). We generated cell-laden droplets using mCherry-expressing SB cells and green fluorescent protein (GFP)–expressing DB cells in a 3:1 ratio and recorded fluorescence intensity as the biofilm developed. In this test, both phenotypes experienced the same γ. We found that although the DB cells were initially in the minority, they dislodged the established SB, becoming dominant in ~5 hours (Fig. 3, C and D). This confirmed our expectation that DB cells, which are more hydrophobic, do indeed have a larger adhesion energy to the interface than that of SB cells.

Rod-shaped gammaproteobacteria such as *Pseudomonas aeruginosa* have been shown to colonize and remodel oil-water interfaces with their biofilms, similar to what we observed in the early stages (<3 hours) of DB formation (*36*, *37*). However, those biofilms lack the large-scale deformations produced by DBs (Fig. 1C, >5 hours). Using our γ, we estimated the biofilm compression modulus to be ~200 Pa (*38*), which is much smaller than the ~1 MPa growth pressure of *P. aeruginosa* (*39*). Assuming a similar growth pressure for *A. borkumensis*, cell division supplies enough stress to easily deform the interface. Thus, DBs generate the biofilm phenotypes we observed only if enough cells remain adhered to the interface to drive the tubulation process. Conversely, the lack of deformations in the SB phenotype is the consequence of insufficient cell hydrophobicity combined with a stiffer interface, leading to cell detachment followed by biofilm formation around the droplet.

Membrane theory predicts the transition from SB to DB phenotype

On the basis of these observations, we developed a coarse-grain membrane model to describe the interfacial dynamics of the growing

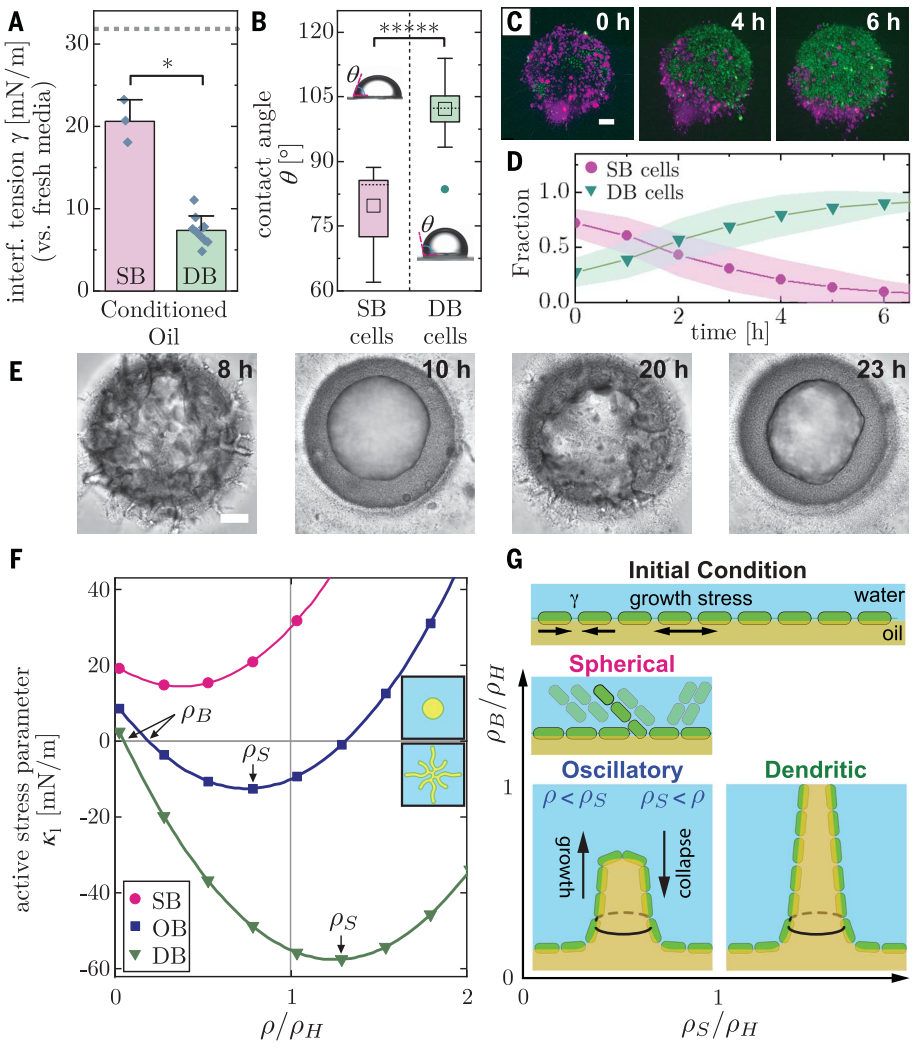

Fig. 3. Theoretical model of tubulation. (**A**) Interfacial tension (γ) between biofilm-conditioned oil and fresh media measured with pendant drop tensiometry for SBs and DBs, respectively. The dashed line indicates γ between fresh oil and fresh medium [mean + SD; n_{SB} = 3, n_{DB} = 10, $n_{control}$ = 5 independent tests; *P < 0.05 (P = 0.012), Welch's t test with Holm-Bonferroni correction]. (**B**) Three-phase contact angle (θ) between a water drop deposited on a bacterial lawn of SB and DB phenotypes, submerged in oil. Open squares indicate mean; horizontal dashed lines indicate medians; and the solid circle indicates an outlier [n_{SB} = 10, n_{DB} = 13 independent tests; *****P < 0.00001 (P = 1.2 × 10^{-6}), Welch's t test]. (Inset) Images of water drops on bacterial lawns, submerged in oil. (**C**) Time-lapse sequence of the competition between SB cells (magenta) and DB cells (green) for interfacial area on a trapped droplet. Droplets are generated in a suspension containing SB and DB cells at a ratio of 3:1 (supplementary text). DB cells displace a monolayer of SB cells over the course of ~6 hours. (**D**) Measurement of the fractional coverage of SB and DB as a function of time from confocal images (solid line and filled regions indicate mean ± SD; n = 10 representative drops). (**E**) Oscillatory biofilm (OB) behavior demonstrated by a culture sampled for an intermediate duration between the SB and DB cultures. (**F**) Model of the tension (κ_1 in the phase-field model) experienced by the tip of a tube as a function of normalized interfacial cell density (ρ/ρ_H) (supplementary text). We normalized cell density by the homeostatic interfacial cell density (ρ_H). Positive and negative values of κ_1 indicate tube retraction and expansion, respectively. The slope at the y intercept is k_1 = 3, 6, and 10 for the SB, OB, and DB models, respectively. The ρ_B is the critical buckling density, where $\kappa_1 < 0$. For SBs, $\rho_B = \infty$. The ρ_S is the optimal cell density, where κ_1 reaches a minimum, and beyond which the effect of spontaneous curvature is reduced. (Insets) Phase-field simulation showing a circular droplet ($\kappa_1 > 0$) and a tubulated droplet ($\kappa_1 < 0$). (**G**) Schematic phase diagram of the biofilm phenotypes in terms of normalized densities: ρ_S/ρ_H and ρ_B/ρ_H. When $\rho_B/\rho_H > 1$, SBs form because the interfacial cell density can never become sufficiently large to induce buckling. For $\rho_B/\rho_H < 1$, cell division drives an increase in cell density beyond ρ_B. When $\rho_S/\rho_H < 1$, oscillations between the spherical and dendritic phenotypes can occur (OB). When, $\rho_S/\rho_H > 1$, stable dendrites (DB) occur.

interfacial biofilm. The model explains the transition between SB and DB phenotypes in terms of a competition between the interfacial tension and the spontaneous curvature of the biofilm, which is its intrinsic tendency to bend in a preferred direction. Interfacial tension resists expansion of the surface by the biofilm, whereas the spontaneous curvature of the biofilm governs the shape of the expanding surface. Tubes are generated when the energetic cost of increasing surface area is lower than the cost of bending; they expand exponentially, according to

$$\eta \frac{1}{L}\frac{dL}{dt} = -\left(\sigma_{t,H} + \sigma_{n,H} - \frac{\kappa_B}{r_0 r_{eq}}\right) \quad (1)$$

where L is the tube length, η is the viscosity of the biofilm layer, $\sigma_{t,H}$ and $\sigma_{n,H}$ are the respective tensions along the circumferential and normal directions of the tube, κ_B is the bending rigidity of the membrane in the circumferential direction of the tube, $1/r_0$ is the spontaneous curvature of the biofilm, and r_{eq} is the tube radius (supplementary text S6 and fig. S14).

Equation 1 encompasses the existence of active extensile nematic stresses driven by bacterial growth, with an effective interfacial tension $\gamma_{eff}(\rho) = \frac{1}{2}(\sigma_{t,H} + \sigma_{n,H})$ that depends on the interfacial cell density (ρ) (supplementary text S6). This implies that tubulation occurs at a critical value of the buckling density (ρ_B), which is consistent with our observation that tubes form after confluency (Fig. 1C). In our model, bacteria populate a circular oil-water interface with a density that increases logistically toward a homeostatic density (ρ_H), at which division and loss are balanced. Depending on the ratio ρ_B/ρ_H, the phenotype changes: When $\rho_B/\rho_H > 1$, tubes are unable to form, resulting in the SB phenotype; when $\rho_B/\rho_H < 1$, the interface buckles and stable tubes form, producing the DB phenotype. Our model implies that physically lowering ρ by removing cells of a DB below the critical value should cause a deformed droplet to recover its unperturbed spherical shape. To test this hypothesis, we infused surfactants into a device containing DBs. We used a formulation similar to that of Corexit 9500, which is used to disperse marine oil spills, and concentrations that ranged from 25 to 100 times the critical micelle concentration (*37*). Our concentrations exceed estimated levels in the top 20 cm of the ocean after the Deepwater Horizon accident (*4*, *37*). After a ~4-hour lag, the biofilm abruptly washed away, and the deformed droplets became spherical; this recovery was the consequence of positive interfacial tension in the absence of bacteria (fig. S8, A and B, and movie S3).

In addition to the SB and DB phenotypes described so far, we observed an intermediate phenotype when we isolated cells at an intermediate culture time (fig. S1A). These biofilms present dynamic oscillatory behavior (OB), alternating between the DBs and SBs, with a period of ~12 hours (Fig. 3E, fig. S9, and movie S4). The relatively short (~30 min) transition from tubulated to spherical is consistent with a sudden loss of tube stability because of a sudden increase in effective surface tension (Eq. 1).

To elucidate the emergence of oscillations between spherical and dendritic phenotypes, we used a phase-field approach following an established literature on simulating interfacial dynamics of multiphasic systems (*40*). In our case, the simulated field is the local fraction of oil [$\varphi(x,y)$] that obeys a Cahn-Hilliard equation with an interfacial term $\kappa_1(\rho)(\nabla\varphi)^2/2$; here, $\kappa_1(\rho)$ is defined by the right side of Eq. 1 and sets the tube elongation rate. $\kappa_1(\rho)$ is thus a proxy for the active stress along the interface (supplementary text S4). In our model, a linear relation of the form $\kappa_1(\rho) = \gamma - k_1\rho$, where k_1 accounts for the force exerted by the biofilm on the oil, is sufficient to understand the SB-to-DB transition. For the SB phenotype, the $\kappa_1(\rho)$ tension is positive for all densities, precluding tube formation. The interface remains spherical until ρ surpasses the critical density, $\rho_B = \gamma/k_1$; here, $\kappa_1(\rho)$ becomes negative, and tubulation occurs as the interface buckles. However, the morphological oscillations emerge only if we consider a second-order expansion of $\kappa_1(\rho)$ in ρ, so that an "optimal" cell density exists where tube elongation and the final tube length are maximal, which we denote ρ_S (Fig. 3F). Oscillations arise for the specific case when $\rho_B < \rho_S < \rho_H$ (supplementary text S5); here, as cell density increases beyond the optimal value ρ_S, tube elongation ceases, and contraction starts. During this contraction, the surface shrinks faster than cells can be ejected from the interface, leading to an abrupt increase in bacterial density. We found that ρ overshoots ρ_H and causes $\kappa_1(\rho)$ to become positive (Fig. 3F, blue). This dynamical overshoot ultimately induces a catastrophic collapse of the tubes and is accompanied by a large reduction in the number of cells at the interface. Consistent with this prediction, in our experiments we observed a large and persistent flow of cells away from the interface soon after tube collapse (movie S4). Our biomechanical model recapitulates the transition from these three phenotypes in terms of a tubulation mechanism that depends on bacterial growth dynamics, with oscillations emerging through a dynamical phase transition mechanism (Fig. 3G and movie S5) (*41*). These oscillations are driven by continuous cell division that pushes density beyond the critical values for tube growth and collapse.

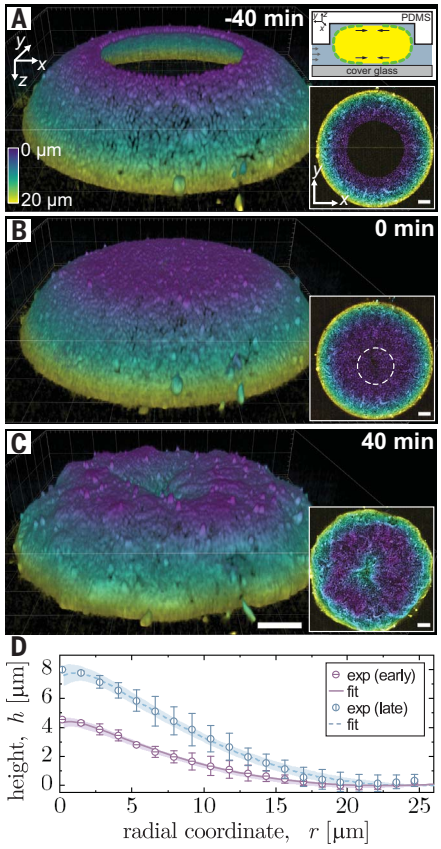

Fig. 4. Defect-mediated buckling of the surface of a confined droplet. (**A** to **C**) Time-lapse confocal image sequence showing the evolution of a dendritic biofilm on a "flattened" drop, color coded by depth. (A) Before confluency (−40 min), interfacial tension excludes cells from the flattened regions at the top and bottom of the droplets. These regions are generated where the nonwetting droplets contact the glass floor and polydimethylsiloxane (PDMS) ceiling. (Top inset) A droplet schematic. (Bottom inset) Top view of the droplet. (B) Confluent monolayer is formed at t_0 = 0 min (fig. S10). (Inset) Top view of droplet, with a circle enclosing the location of the nematic defect. (C) Dimple formation in the droplet at the defect. Scale bars, 10 µm. (**D**) Evolution of the dimple height (h) from xy-line profiles measured across the droplet midplane, at 20 min (early) and 26 ± 3 min (late) after confluency. Dimple height is shown as a function of the radial coordinate (r). The fits to the data are based on eq. S80 (supplementary text). The solid error bars and shaded regions indicate ±SD on the experimental data and fits, respectively (details on the fitting procedure and error estimation are available in the supplementary text). Early-profile data are the average of the x and y profiles (n = 4) at t = 20 min, whereas the late-profile data are the average of the x and y profiles binned at 23, 26, and 29 min (n = 12), respectively. To generate the dimensional values shown, we rescaled the nondimensionalized h values by the dimple heights 4.5 and 8.0 µm, at early and late times, respectively, whereas r was rescaled by 26 µm at all times.

Controlled buckling of confined droplets

We leveraged microfluidics to position the tube-generating topological defects through droplet confinement. By trapping droplets larger than

the chamber height, we can grow biofilms on flattened drops (Fig. 4A, top inset). These flat circular regions allowed us to generate a centered defect, which concentrates growth stress to form a dimple. Interfacial tension, which initially excludes bacteria from the flat region, was eventually overcome by growth pressure (Fig. 4A, fig. S10A,B, and movie S6). As cells invaded, their flow oriented the director field, which formed a single aster defect (or two narrowly separated +1/2 defects) at confluency (Fig. 4B and fig. S10, C and D) (*15*). As cell division continued, dimples formed at the defects at the top and bottom of the drop (Fig. 4C and fig. S10, B, inset, and E). We used the theory of liquid crystal membranes to elucidate the role of the aster defect in generating deformation in the biofilm. The dimple height profile depends on two dimensionless parameters: κ_F/κ_B, where κ_F is the elastic constant of distortions to the director field, and $\kappa_B/\gamma R_{dimple}{}^2$, where R_{dimple} is the radius of the dimple (supplementary text S8). κ_F/κ_B captures the competition between the elastic energy of distortions to the liquid crystalline biofilm and its bending energy, whereas $\kappa_B/\gamma R_{dimple}{}^2$ captures the competition between biofilm bending energy and its surface tension. Buckling at the defect occurs when the energetic cost to deform the membrane exceeds its bending energy, $\kappa_F/\kappa_B > 1$; our fits yield a ratio of ≈2 (fig. S11 and table S2) (*29*, *42*). In agreement with experiments, the profiles in this parameter regime are qualitatively like pseudospheres (Fig. 4D and fig. S12) (*42*).

The ability of marine microorganisms to biodegrade hydrocarbons has been recognized for nearly a century (*1*), with recent improvements to metagenomic and imaging techniques further clarifying the possible mechanisms involved. In this study, we quantified the mechanism by which cultures of *A. borkumensis* preadapted to using an alkane leads to the appearance of a biofilm phenotype primed (*43*) for explosive growth. Leveraging microfluidics, we captured the dynamics of the optimized biofilms, correlating their appearance to measurable changes in the interfacial properties of the bacteria. These biofilms develop liquid crystalline order before buckling the interface at aster topological defects, morphing the spherical droplet into numerous branching dendrites. We developed a theoretical model that recapitulates each phenotype and explains the cause of the spectacular biofilm oscillations we observed. Furthermore, we used microfluidics to control the dimpling of the droplet and used the profiles to confirm the liquid crystalline elastic constant of the biofilm from theory.

Topological defects in layers of both prokaryotic and eukaryotic cells have been shown to be important in defect-driven morphogenesis (*13*, *14*, *29*, *30*, *44*). We found that the optimized *A. borkumensis* cells collectively use defect-driven buckling to escape the confines of the droplet interface and expand the biofilm laterally. Efficiency is achieved not through an increase of individual metabolic throughput but rather by expanding the interface, allowing more cells to simultaneously feed.

Although we found that addition of oil dispersant similar in composition to commercially available mixtures leads to the rapid detachment of the biofilm from the oil drops, numerous factors such as the dispersant concentration; oil composition, temperature, and pressure; and nutrient concentrations likely affect biodegradation. Because our platform is an open system, all inputs can be dynamically controlled; thus, how biofilm formation changes depending on hydrocarbon composition, nutrient profile, as well as the dynamical response of bacteria to dispersant dose may be independently verified. These tests could also serve as a starting point in the investigation of artificially constructed multispecies consortia (*8*), which are more robust and effective than monocultures (*9*).

REFERENCES AND NOTES

1. I. M. Head, D. M. Jones, W. F. M. Röling, *Nat. Rev. Microbiol.* **4**, 173–182 (2006).
2. C. R. Love *et al.*, *Nat. Microbiol.* **6**, 489–498 (2021).
3. Y. Kasai *et al.*, *Environ. Microbiol.* **4**, 141–147 (2002).
4. B. H. Gregson *et al.*, *Front. Mar. Sci.* **8**, 619484 (2021).
5. R. M. Atlas, T. C. Hazen, *Environ. Sci. Technol.* **45**, 6709–6715 (2011).
6. S. Schneiker *et al.*, *Nat. Biotechnol.* **24**, 997–1004 (2006).
7. T. C. Hazen *et al.*, *Science* **330**, 204–208 (2010).
8. F. Mapelli *et al.*, *Trends Biotechnol.* **35**, 860–870 (2017).
9. T. J. McGenity, B. D. Folwell, B. A. McKew, G. O. Sanni, *Aquat. Biosyst.* **8**, 10 (2012).
10. M. M. Yakimov *et al.*, *Int. J. Syst. Bacteriol.* **48**, 339–348 (1998).
11. J. S. Sabirova, T. N. Chernikova, K. N. Timmis, P. N. Golyshin, *FEMS Microbiol. Lett.* **285**, 89–96 (2008).
12. L. Hall-Stoodley, J. W. Costerton, P. Stoodley, *Nat. Rev. Microbiol.* **2**, 95–108 (2004).
13. K. Copenhagen, R. Alert, N. S. Wingreen, J. W. Shaevitz, *Nat. Phys.* **17**, 211–215 (2021).
14. O. J. Meacock, A. Doostmohammadi, K. R. Foster, J. M. Yeomans, W. M. Durham, *Nat. Phys.* **17**, 205–210 (2021).
15. P. G. de Gennes, J. Prost, *The Physics Of Liquid Crystals*, International Series Of Monographs On Physics (Oxford Univ. Press, ed. 2, 1995).
16. R. M. Atlas, R. Bartha, *Biotechnol. Bioeng.* **14**, 309–318 (1972).
17. O. U. Mason *et al.*, *ISME J.* **6**, 1715–1727 (2012).
18. R. Grimaud, in *Handbook of Hydrocarbon and Lipid Microbiology*, K. N. Timmis, Ed. (Springer Berlin Heidelberg, 2010), pp. 1491–1499.
19. M. P. Godfrin, M. Sihlabela, A. Bose, A. Tripathi, *Langmuir* **34**, 9047–9053 (2018).
20. J. Tremblay *et al.*, *ISME J.* **11**, 2793–2808 (2017).
21. N. K. Dewangan, J. C. Conrad, *Langmuir* **34**, 14012–14021 (2018).
22. A. R. White, M. Jalali, J. Sheng, *Sci. Rep.* **9**, 13737 (2019).
23. A. R. White, M. Jalali, J. Sheng, *Front. Mar. Sci.* **7**, 294 (2020).
24. M. Omarova *et al.*, *ACS Sustain. Chem. & Eng.* **7**, 14490–14499 (2019).
25. V. Hickl, G. Juarez, *Soft Matter* **18**, 7217–7228 (2022).
26. U. Passow, *Deep Sea Res. Part II Top. Stud. Oceanogr.* **129**, 232–240 (2016).
27. D. J. Naether *et al.*, *Appl. Environ. Microbiol.* **79**, 4282–4293 (2013).
28. L. Metselaar, J. M. Yeomans, A. Doostmohammadi, *Phys. Rev. Lett.* **123**, 208001 (2019).
29. L. A. Hoffmann, L. N. Carenza, J. Eckert, L. Giomi, *Sci. Adv.* **8**, eabk2712 (2022).
30. P. Guillamat, C. Blanch-Mercader, G. Pernollet, K. Kruse, A. Roux, *Nat. Mater.* **21**, 588–597 (2022).
31. A. Passeri *et al.*, *Appl. Microbiol. Biotechnol.* **37**, 281–286 (1992).
32. M. P. Kem, H. K. Zane, S. D. Springer, J. M. Gauglitz, A. Butler, *Metallomics* **6**, 1150–1155 (2014).
33. J. Cui *et al.*, *Appl. Environ. Microbiol.* **88**, e0112622 (2022).
34. N. L. Olivera *et al.*, *Res. Microbiol.* **160**, 19–26 (2009).
35. L. S. Dorobantu, A. K. C. Yeung, J. M. Foght, M. R. Gray, *Appl. Environ. Microbiol.* **70**, 6333–6336 (2004).
36. L. Vaccari *et al.*, *Soft Matter* **11**, 6062–6074 (2015).
37. R. C. Prince, *Environ. Sci. Technol.* **49**, 6376–6384 (2015).
38. D. Vella, P. Aussillous, L. Mahadevan, *Europhys. Lett.* **68**, 212–218 (2004).
39. H. H. Tuson *et al.*, *Mol. Microbiol.* **84**, 874–891 (2012).
40. J. W. Cahn, *J. Chem. Phys.* **42**, 93–99 (1965).
41. F. Jülicher, A. Ajdari, J. Prost, *Rev. Mod. Phys.* **69**, 1269–1282 (1997).
42. J. R. Frank, M. Kardar, *Phys. Rev. E Stat. Nonlin. Soft Matter Phys.* **77**, 041705 (2008).
43. D. L. Valentine *et al.*, *Proc. Natl. Acad. Sci. U.S.A.* **109**, 20286–20291 (2012).
44. Y. Maroudas-Sacks *et al.*, *Nat. Phys.* **17**, 251–259 (2021).
45. S.-Z. Lin, J.-F. Rupprecht, Phase-field simulation framework; model of Alcanivorax bacteria at an oil/water interface. Zenodo (2023), https://doi.org/10.5281/zenodo.8043717.

ACKNOWLEDGMENTS

We thank Y. Yamashita (University of Tsukuba, Tsukuba, Japan) for use of the contact angle and pendant drop systems, F. Pincet (Ecole Normale Superieure, Paris, France) for assistance with micropipette experiments, D. Quéré (ESPCI, Paris, France) for the fruitful discussion on the O/W/cell contact angle measurements, and F. Brochard-Wyart (Institut Curie, Paris, France) for discussions on tube formation. **Funding:** The research leading to these results was supported by KAKENHI by the Japan Society for the Promotion of Science (JSPS) JSPS–ANR PHC SAKURA 2018 (no. 38559WJ), JSPS BRIDGE (no. BR200204), JST-ERATO (no. JPMJER1502), and by JSPS KAKENHI (no. 21H01720). This work was also supported by the Institut Pierre-Gilles de Gennes–IPGG (Equipement d'Excellence, "Investissements d'avenir" (program ANR-10-EQPX-34) and Laboratoire d'Excellence, "Investissements d'avenir" (program ANR-10-IDEX-0001-02 PSL and ANR-10-LABX-3). J.-F.R. was supported by France 2030 (program ANR-16-CONV-0001), Excellence Initiative of Aix-Marseille University–A*MIDEX (program ANR-20-CE30-0023).
Author contributions: J.F. and A.S.U. designed the project. J.-F.R., J.F., and A.S.U. supervised the project. M.P., N.O., and K.S. performed the key experiments; M.P. and S.Z. performed validation experiments. M.P., N.O., S.Z., N.N., J.F., and A.S.U. analyzed and discussed the data; C.B.-M., J.P., J.-F.R., and S.-Z.L. designed the tubulation theory; S.-Z.L. carried out simulations; C.B.-M. performed the dimple height analysis; M.P., N.O., C.B.-M., J.-F.R., J.F., and A.S.U. wrote the manuscript. All authors discussed the results and implications and commented on the manuscript.
Competing interests: The authors declare that they have no competing interests. **Data and materials availability:** All data are presented in the main text or supplementary materials. The MATLAB code corresponding to the phase-field simulations are available on the following Zenodo repository: https://doi.org/10.1101/2022.08.06.503017 (*45*). **License information:** Copyright © 2023 the authors, some rights reserved; exclusive licensee American Association for the Advancement of Science. No claim to original US government works. https://www.science.org/about/science-licenses-journal-article-reuse

SUPPLEMENTARY MATERIALS

science.org/doi/10.1126/science.adf3345
Materials and Methods
Supplementary Text
Figs. S1 to S17
Tables S1 to S3
References (*46*–*62*)
Movies S1 to S6
MDAR Reproducibility Checklist

Submitted 17 October 2022; accepted 21 June 2023
10.1126/science.adf3345

STELLAR ASTROPHYSICS

A massive helium star with a sufficiently strong magnetic field to form a magnetar

Tomer Shenar[1]*†, Gregg A. Wade[2], Pablo Marchant[3], Stefano Bagnulo[4], Julia Bodensteiner[3,5], Dominic M. Bowman[3], Avishai Gilkis[6], Norbert Langer[7,8], André Nicolas-Chené[9], Lidia Oskinova[10], Timothy Van Reeth[3], Hugues Sana[3], Nicole St-Louis[11], Alexandre Soares de Oliveira[12], Helge Todt[10], Silvia Toonen[1]

Magnetars are highly magnetized neutron stars, the formation mechanism of which is unknown. Hot helium-rich stars with spectra dominated by emission lines are known as Wolf-Rayet stars. We observed the binary system HD 45166 using spectropolarimetry and reanalyzed its orbit using archival data. We found that the system contains a Wolf-Rayet star with a mass of 2 solar masses and a magnetic field of 43 kilogauss. Stellar evolution calculations indicate that this component will explode as a supernova, and that its magnetic field is strong enough for the supernova to leave a magnetar remnant. We propose that the magnetized Wolf-Rayet star formed by the merger of two lower-mass helium stars.

Neutron stars form in supernovae by the collapse of stellar cores that exceed the Chandrasekhar mass limit [mass $M \gtrsim 1.4$ solar masses ($M_\odot$)]. Bare stellar cores can be exposed as hot, evolved helium-rich stars that have shed their outer hydrogen-rich layers. A subset of these massive helium stars is observed as Wolf-Rayet stars, which have spectra dominated by broad emission lines produced by strong stellar winds (*1*, *2*). Massive helium stars (those with $M \gtrsim 1.4 M_\odot$) are thought to be stripped products of more massive stars that lost their hydrogen-rich envelopes through stellar winds, eruptions, or interactions with a binary companion (*3*, *4*). Alternatively, massive helium stars could be produced through the merger of lower-mass objects (*5*).

Approximately 10% of young neutron stars have magnetic fields $>10^{14}$ G (*6*). These are known as magnetars; their origin is debated (*7*, *8*). One formation scenario invokes fossil magnetic fields rooted in the massive core of a progenitor star that collapses during a supernova (*9*). About 7 to 10% of massive main-sequence stars have strong (several kG) large-scale surface magnetic fields (*10*, *11*); such stars could be progenitors of magnetars. However, corresponding magnetic fields have not been detected in evolved massive stars (*12*). Strongly magnetic low-mass helium stars have been observed (*13*–*15*), but not massive magnetic helium stars exceeding the Chandrasekhar limit.

The HD 45166 binary system (also cataloged as ALS 8946) comprises a main sequence star (classified as spectral type B7 V) with a hot stellar companion. The hot companion has a spectrum dominated by the characteristic emission lines of a Wolf-Rayet star (Fig but it is classified as a "quasi–Wolf-Ra (qWR) star owing to its peculiarly narrow emission lines (widths of hundreds of kilometers per second instead of the typical thousands); spectral variability; and the anomalous presence of strong carbon, oxygen, and nitrogen lines in its spectrum. Previous radial velocity (RV) measurements have shown a 1.6-day periodicity in the velocity of the B7 V component, which was interpreted as the orbital period of the system (*16*). This implied a mass of $4.2 \pm 0.7 M_\odot$ for the Wolf-Rayet component and a pole-on orbital configuration (inclination $i = 0.7°$) (*16*). That mass is well below the typical masses of Wolf-Rayet stars in the Milky Way [$M \gtrsim 8 M_\odot$ (*17*)]; no other massive helium stars are known with $M \lesssim 8 M_\odot$ (*18*). Comparison with stellar atmosphere models that do not assume local thermodynamic equilibrium (non-LTE models) has shown that the Wolf-Rayet component is a hot (surface effective temperature $T_* = 70$ kK), helium-rich star with enhanced nitrogen and carbon contents (compared with the composition of the Sun) (*19*). A latitude-dependent wind model can reproduce the spectrum of the Wolf-Rayet component (*19*); however, the implied mass-loss rate is orders of magnitude greater than predictions for helium stars of this mass (*20*–*22*).

The presence of a carbon and nitrogen emission-line complex in the range of 4430 to 4460 Å (known as the Of?p phenomenon) and strong spectral variability are typical indirect signatures of magnetism in hot

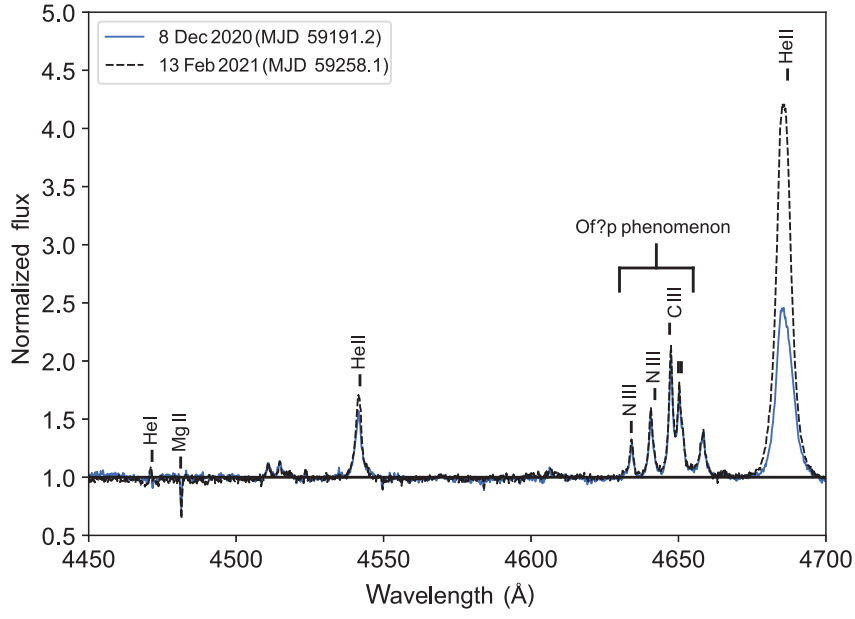

Fig. 1. Indications of possible magnetism in HD 45166. Solid blue and thin dashed black lines indicate two optical HERMES spectra of HD 45166 (*25*) taken ≈70 days apart (see legend). The thick black line indicates the continuum level. Labels indicate the Of?p phenomenon (*23*, *24*) and the He II line at 4686 Å, which is variable (also seen in Fig. 3). These are common features of hot magnetic stars, which indicates that the Wolf-Rayet component might be magnetic. The narrow Mg II ion line at 4481 Å is due to the B7 V component.

[1]Anton Pannekoek Institute for Astronomy, University of Amsterdam, 1098 XH Amsterdam, Netherlands. [2]Department of Physics and Space Science, Royal Military College of Canada, Kingston K7K7B4, Canada. [3]Institute of Astronomy, Katholieke Universiteit Leuven, 3001 Leuven, Belgium. [4]Armagh Observatory and Planetarium, College Hill, Armagh BT61 9DG, UK. [5]European Southern Observatory, 85748 Garching bei München, Germany. [6]The School of Physics and Astronomy, Tel Aviv University, Tel Aviv 6997801, Israel. [7]Argelander-Institut für Astronomie, Universität Bonn, 53121 Bonn, Germany. [8]Max-Planck-Institut für Radioastronomie, 53121 Bonn, Germany. [9]National Optical-Infrared Astronomy Research Laboratory, National Science Foundation, Hilo, Hawai'i 96720, USA. [10]Institut für Physik und Astronomie, Universität Potsdam, D-14476 Potsdam, Germany. [11]Département de physique, Université de Montréal, Montréal H2V 0B3, Canada. [12]Institute of Research and Development, Universidade do Vale do Paraíba, São José dos Campos 12244-000, Brazil.
***Corresponding author. Email: T.Shenar@uva.nl**
†Present address: Centro de Astrobiología (Consejo Superior de Investigaciones Científicas - Instituto Nacional de Técnica Aeroespacial), 28850 Torrejón de Ardoz, Spain.

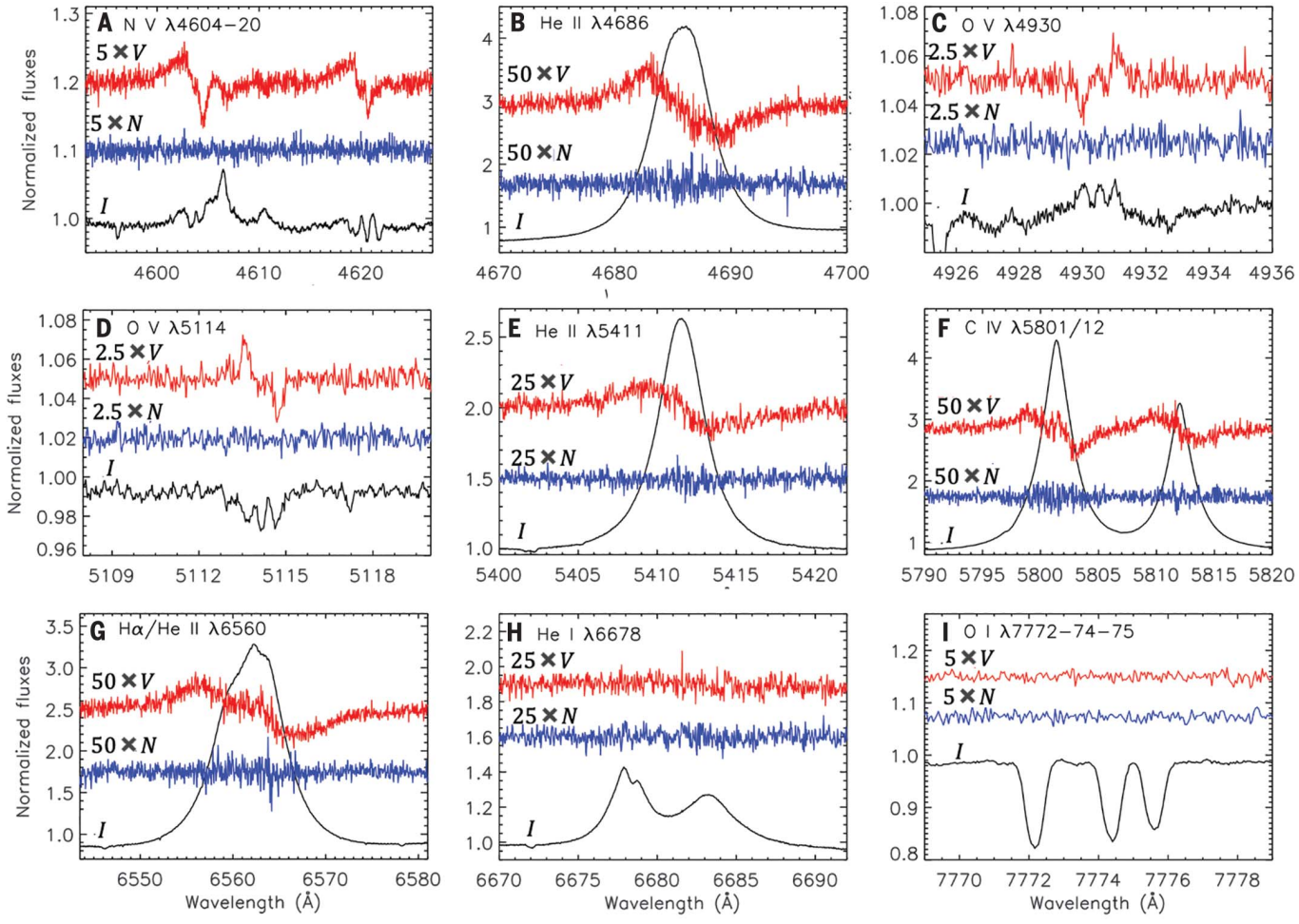

Fig. 2. Spectropolarimetry of HD 45166. (A) to (I) shows the intensity spectrum (Stokes *I*, black lines), diagnostic null spectrum (*N*, blue lines), and Stokes *V* spectrum (red lines) from the co-added ESPaDOnS spectrum. The *N* and *V* spectra have been vertically shifted and scaled for display purposes, by the factors listed in each graph. (**A** to **H**) Diagnostic lines of the Wolf-Rayet component. Zeeman splitting is visible in the O v lines at the λ4930 (C) and λ5114 (D), which are both because of O v. We used these lines to measure the magnetic field strength. (**I**) An O I (neutral oxygen ion) triplet associated with the B7 V star, which has no Stokes *V* signature.

stars (*23*, *24*). We used spectropolarimetry to investigate whether the Wolf-Rayet component in HD 45166 is magnetic.

Observations of HD 45166

We collected eight spectropolarimetric observations of HD 45166 in February 2022 using the Echelle Spectropolarimetric Device for the Observation of Stars (ESPaDOnS) spectropolarimeter on the Canada-France-Hawaii Telescope (CFHT) (*25*). The spectra measure the polarimeteric Stokes parameters *I* and *V* over the wavelength range 3668 to 10,480 Å at a resolving power of 65,000. We used them to measure the magnetic-field strength in the Wolf-Rayet and B7 V components of HD 45166.

We used archival spectra from three other instruments to measure RVs over a longer period (*25*). They were 103 spectra obtained with the Coudé spectrograph at the 1.6 m telescope of Laboratório Nacional de Astrofísica (LNA), mainly covering 4520 to 4960 Å; 36 spectra obtained with the Fiber-fed Extended Range Optical Spectrograph (FEROS) at the 1.52 m telescope of the European Southern Observatory (ESO), covering 3830 to 9215 Å; and 28 spectra acquired with the High-Efficiency and High-Resolution Mercator Echelle Spectrograph (HERMES) on the 1.2 m Mercator telescope, covering 3770 to 9000 Å. We used additional archival ultraviolet spectroscopy and photometric data to analyze the spectral energy distribution (SED) of the system (*25*).

Evidence for magnetism

We detected circular polarization (Stokes *V*) in the ESPaDOnS spectra for the majority of lines associated with the Wolf-Rayet component (Fig. 2). We also detected Zeeman splitting (doubling of spectral lines owing to a magnetic field) in two O v (quadruply ionized oxygen) lines (Fig. 2, C and D) that form in or close to the stellar surface. We measured the magnetic field from the separation of the split Zeeman components of these lines, finding a mean field modulus $\langle B \rangle_{\rm qWR} = 43.0 \pm 2.5$ kG and a mean longitudinal field $\langle B_z \rangle_{\rm qWR} = 13.5 \pm 2.5$ kG (table S1). The ratio between these values (approximately 3:1) is consistent with a dipolar magnetic field viewed near the magnetic pole (*26*).

Such a strong magnetic field in the Wolf-Rayet component implies that its emission-line spectrum is formed in the star's magnetosphere (the region containing plasma confined by the magnetic field loops), not in a radially expanding stellar wind (*25*). If so, one-dimensional (1D) stellar atmosphere models [as used in previous studies (*19*)] are not appropriate for the emission lines, thus affecting the previously derived physical parameters.

Stellar parameters

We reanalyzed the spectra and SED using PoWR, a non-LTE model atmosphere code optimized for Wolf-Rayet stars (*27*, *28*). Because the PoWR code is also 1D, we only used it to

analyze spectral features that originate in the stellar surface of the Wolf-Rayet component, not emission lines from the magnetosphere (*25*). The resulting physical parameters are listed in table S1. We found an effective temperature for the Wolf-Rayet component of $T_* = 56.0 \pm 5.0$ kK, which is ≈15 kK lower than previously determined (*19*). The effective temperature and bolometric luminosity L [we found $\log(L/L_\odot) = 3.830 \pm 0.050$, where $L_\odot$ is the luminosity of the Sun] indicate that the magnetic Wolf-Rayet component is not a main sequence star, but an evolved object.

We applied the same analysis to the B7 V component (*25*) then input the resulting stellar parameters into BONNSAI, a Bayesian tool for comparing observations to stellar models (*29*). That analysis indicates that the mass and age of the B7 V component are $M_B = 3.38 \pm 0.10\ M_\odot$ and 105 ± 35 million years (Myr), respectively (table S1).

The Wolf-Rayet component exhibits changes in line strength, including as the He II (doubly ionized helium) line at 4686 Å. These appear to be periodic (Fig. 3A), with a best-fitting period of 124.8 days (Fig. 3B). Periodic changes in the line strengths of hot magnetic stars are typically interpreted as their rotational periods (*30*, *31*), implying a rotational period $P_{\mathrm{rot,qWR}} = 124.8 \pm 0.2$ days for the Wolf-Rayet component. This period is consistent with the narrow O V lines, which have a projected rotational velocity $v \sin i \lesssim 10$ kms^{-1}.

Binary orbit

The ESPaDOnS spectra indicate that the B7 V component exhibits spectral line profile variations caused by nonradial gravity-mode pulsations (fig. S9). We performed a frequency analysis of an optical light curve obtained with the Transiting Exoplanet Survey Satellite (TESS), which detects several periods, including 1.6 days (*25*). We therefore concluded that the 1.6-day period previously attributed to orbital motion (*16*) is instead caused by pulsations in the B7 V component. We reassessed the binary orbit and the mass of the Wolf-Rayet component M_{qWR} under this interpretation.

To determine the orbit, we analyzed all the RV data, which span 24 years (*25*). We found a long-term antiphase motion of the B7 V and Wolf-Rayet components (Fig. 4). There are multiple RV periodicities associated with both the Wolf-Rayet and B7 V components (*25*). We adopted the best-fitting orbit (table S1), which has an orbital period P = 8200 ± 190 days and a semimajor axis a = 10.5 ± 1.8 astronomical units (au). This indicates that the components are much more widely separated than had previously been determined.

The orbital solution indicates a mass ratio of $q \equiv M_{\mathrm{qWR}}/M_B = 0.60 \pm 0.13$. Combining this with the mass of the B7 V component ($M_B = 3.38 \pm 0.10\ M_\odot$) derived from the BONNSAI analysis implies $M_{\mathrm{qWR}} = 2.03 \pm 0.44\ M_\odot$ (uncertainties are 68% confidence intervals). This is less than the 4.2 $M_\odot$ previously reported, but still above the Chandrasekhar limit.

The derived mass and luminosity of the qWR component are consistent with mass-luminosity relations for helium stars (*32*). The large separation and implied orbital inclination of $i = 49 \pm 11°$ [derived from $M_B \sin^3 i$ and M_B (table S1)] explain the low-amplitude RV motion of both binary components, without invoking a pole-on configuration.

Implications for magnetar formation

With a mass of $2.03 \pm 0.44\ M_\odot$, we expect the Wolf-Rayet component to evolve until it collapses into a neutron star. We calculated evolutionary models of the system, which are consistent with this interpretation, although the final fate of the Wolf-Rayet component is sensitive to uncertainties in the model (*25*). During core collapse, magnetic flux conservation causes an increase in the magnetic field at the surface. With a stellar radius of $R_{*,\mathrm{qWR}} = 0.88 \pm 0.16 R_\odot$ (where $R_\odot$ is the radius of the Sun), calculated with the Stefan-Boltzmann relation, our measured $\langle B \rangle_{\mathrm{qWR}} = 43.0 \pm 2.5$ kG, and assuming a final neutron-star radius of 12 km (*33*), we calculate the expected magnetic field of the neutron star to be $\langle B \rangle_{\mathrm{NS}} = (1.11 \pm 0.42) \times 10^{14}$ G. This is within the range observed for magnetars [$\langle B \rangle \gtrsim 10^{14}$ G (*34*)]. Our observations and stellar-evolution models therefore indicate that the

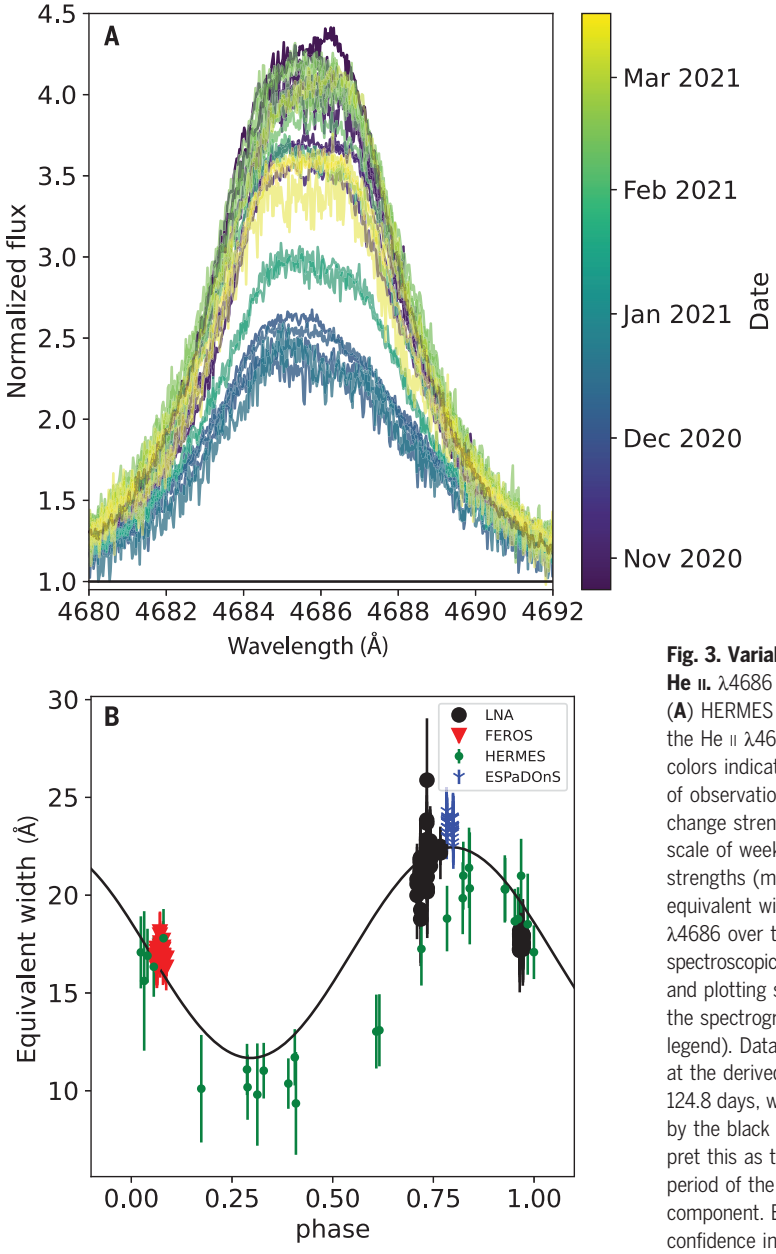

Fig. 3. Variability of the He II. λ4686 emission line. (**A**) HERMES spectra of the He II λ4686 line, with colors indicating the date of observation. The lines change strength on a timescale of weeks. (**B**) Line strengths (measured as equivalent widths) of He II λ4686 over the 24-year spectroscopic dataset. Colors and plotting symbols indicate the spectrograph used (see legend). Data were phased at the derived period of 124.8 days, which is indicated by the black curve. We interpret this as the rotational period of the Wolf-Rayet component. Error bars are confidence intervals of 1σ.

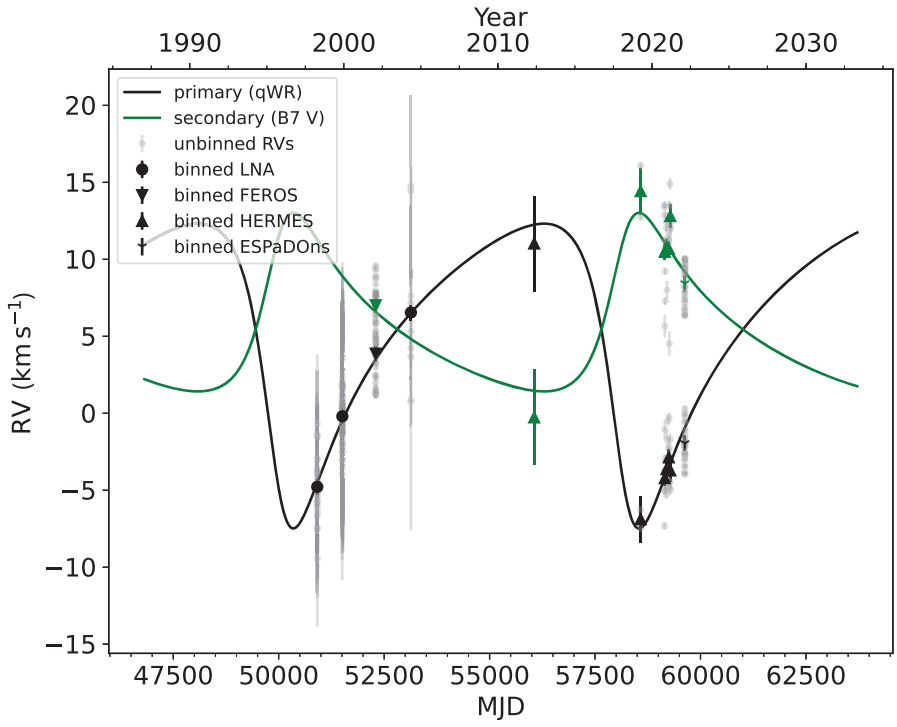

Fig. 4. Two-component orbital solution for HD 45166. RVs of the Wolf-Rayet and B7 V components are plotted in gray, with green and black symbols indicating the same data binned by 30 days for the Wolf-Rayet and B7 V components, respectively. Plotting symbols indicate the instruments used (see legend). Solid lines are the best-fitting RV curves for the Wolf-Rayet (black) and B7 V (green) components. The model fit has a reduced χ^2 of 1.21. Error bars are confidence intervals of 1 σ (*25*).

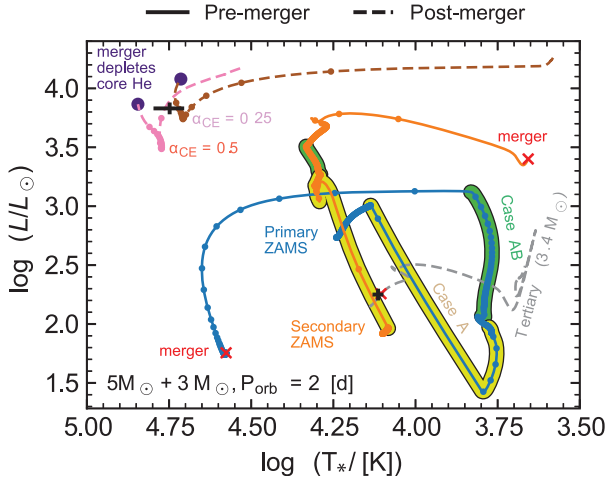

Fig. 5. Models of our proposed evolutionary scenario for HD 45166. MESA models are plotted on a temperature-luminosity diagram for a triple system. The inner binary comprises stars with masses of $5M_\odot$ (primary, blue line) and $3M_\odot$ (secondary, orange line), with an initial orbital period of 2 days. These tracks start from the zero-age main sequence (ZAMS). The outer tertiary star (gray line) has an initial mass of $3.4M_\odot$. Solid lines indicate the evolution of the three components before the inner binary merges; dashed lines show the post-merger evolution. Dots along each track are separated by 0.1 Myr of evolution. The merger is marked with a red cross. Colored regions indicate mass transfer on the main sequence (case A, yellow) and after the main sequence (case AB, green). The upper tracks indicate the evolution of the merger product (representing the Wolf-Rayet component) for assumed common-envelope ejection efficiencies of α_{CE} = 0.25 (brown) and 0.5 (pink) (*25*). The black plus signs indicate the observed properties of the Wolf-Rayet and B7 V components. Purple filled circles mark the core He depletion of the merger, which occurs after 133.2 and 133.7 Myr for α_{CE} = 0.25 and 0.5, respectively.

Wolf-Rayet component could be an immediate progenitor of a magnetar.

All magnetars in the Milky Way are isolated; they do not have a binary companion (*6*). For the Wolf-Rayet component in HD 45166, we expect the mass loss and velocity kick imparted on the magnetar by the supernova explosion to disrupt the system, given the large orbital separation. With an estimated rotation period of 125 d and an estimated radius of ≈0.3 $R_\odot$ for the helium core of the Wolf-Rayet component (*35*), angular-momentum conservation implies that the magnetar immediately after collapse would have a spin period ≲40 ms. This is similar to the spin period of the Crab Pulsar (33 ms), a neutron star that formed about 1000 years ago. Such a spin rate would not provide sufficient energy to power a superluminous supernova or a long-duration gamma-ray burst (*36*, *37*).

Evolutionary model of the system

We next considered how the Wolf-Rayet component itself formed. We excluded the possibly that it is the stripped core of a massive star, because to produce a 2 $M_\odot$ stripped core, the progenitor star would need to have had an initial mass of ≈10 $M_\odot$. Single-star evolution models do not predict that stars of that mass become stripped by mass loss (*22*, *38*), and the B7 V companion is too far away for binary interactions to have done so. In addition, the total lifetime (including post main-sequence evolution) of a 10 $M_\odot$ star would be ≈30 Myr (*39*), which is well below our derived age of the B7 V component (105 ± 35 Myr), so we reject the possibility that they could both be present in the same binary system.

Stellar mergers have been proposed as a potential origin of magnetic stars (*40*–*43*). Strong magnetic fields have been identified in low-mass helium stars (classified as OB-type subdwarfs) that have been suggested to originate from merger events between two white dwarfs (*13*, *14*). However, to produce a ≈2 $M_\odot$ helium star through a merger of white dwarfs, the merger would need to have involved massive CO or ONe white dwarfs, which are rare. Models predict that such a merger product would either immediately explode as a supernova (*44*) or do so after a short life span of approximately 10,000 years (*45*). We argue that observing the stellar product of a white-dwarf merger in the brief time available is unlikely.

We therefore propose that the Wolf-Rayet component in HD 45166 formed from the coalescence of the helium cores of two intermediate-mass stars that were bound in a close binary. We constructed an evolutionary model of this scenario (*25*) (Fig. 5) using the MESA stellar evolution code (*46*). We started the system in a triple configuration, with a tight inner binary and a distant tertiary star (the B7 V component). The model indicates

that the primary (more massive) star of the inner binary expanded and interacted with its companion, losing its outer layers and becoming a stripped star. Meanwhile, the companion (secondary star) accreted material and became rejuvenated with hydrogen. The secondary star later expanded itself, leading to an unstable mass-transfer back to the primary. In the model, this process leads to the formation of a gaseous envelope around the two stars, during which they both lose orbital energy owing to friction with the envelope, causing them to spiral inward (known as common-envelope evolution). Because of the high binding energy of the hydrogen-rich layers, this phase ends with both helium cores merging into a ≈2 $M_{\odot}$ magnetized helium star, while most (but not all) of the hydrogen envelope is ejected.

With a luminosity predicted to be 200 times that of a 2 $M_{\odot}$ main-sequence star (*47*), the merger product has a high luminosity-to-mass ratio. This, combined with its high effective temperature, launches a radiatively driven outflow from its surface. In the absence of a magnetic field, such an outflow would not be easily detectable in a spectrum. However, the trapping of an outflow by a magnetic field is known to increase the density of the circumstellar material and produce spectral emission lines, similar to those we observed in the Wolf-Rayet component (*26*, *48*). The distant tertiary star in our model does not affect the final outcome of the inner binary evolution, except perhaps by catalyzing the merging of its stellar components (*49*). Given its large orbital separation, we do not expect the tertiary star to show any evidence for accreted material from the merger ejecta.

Our proposed evolutionary scenario is quantitatively and qualitatively consistent with the observed properties of the system. The MESA model reproduces the masses of the two components and the estimated system age. The proposed merger provides an explanation for the emergence of a magnetic field in the Wolf-Rayet component, and the magnetic field provides an explanation for the presence of emission lines in the spectrum of a 2-$M_{\odot}$ helium star. The binary nature of HD 45166 enabled us to use the companion as a clock to constrain the evolutionary path of the system, and as a scale to determine the mass of the Wolf-Rayet component, which are conditions that are rarely present in other proposed merger products (*42*, *50*). Given the proximity of HD 45166 to Earth (≈1 kpc), other massive magnetic helium stars have likely already been spectroscopically identified as Wolf-Rayet stars but not recognized as magnetic (supplementary text).

REFERENCES AND NOTES

1. P. A. Crowther, *Annu. Rev. Astron. Astrophys.* **45**, 177–219 (2007).
2. N. Langer, *Annu. Rev. Astron. Astrophys.* **50**, 107–164 (2012).
3. B. Paczyński, *Acta Astron.* **17**, 355 (1967).
4. S. E. Woosley, *Astrophys. J.* **878**, 49 (2019).
5. E. Zapartas *et al.*, *Astron. Astrophys.* **601**, A29 (2017).
6. V. M. Kaspi, A. M. Beloborodov, *Annu. Rev. Astron. Astrophys.* **55**, 261–301 (2017).
7. S. Mereghetti, J. A. Pons, A. Melatos, *Space Sci. Rev.* **191**, 315–338 (2015).
8. L. Ferrario, A. Melatos, J. Zrake, *Space Sci. Rev.* **191**, 77–109 (2015).
9. L. Ferrario, D. Wickramasinghe, *Mon. Not. R. Astron. Soc.* **367**, 1323–1328 (2006).
10. G. A. Wade *et al.*, *Mon. Not. R. Astron. Soc.* **456**, 2–22 (2016).
11. J. H. Grunhut *et al.*, *Mon. Not. R. Astron. Soc.* **465**, 2432–2470 (2017).
12. A. de la Chevrotière, N. St-Louis, A. F. J. Moffat, *Astrophys. J.* **781**, 73 (2014).
13. M. Dorsch *et al.*, *Astron. Astrophys.* **658**, L9 (2022).
14. I. Pelisoli *et al.*, *Mon. Not. R. Astron. Soc.* **515**, 2496–2510 (2022).
15. M. E. Shultz, O. Kochukhov, J. Labadie-Bartz, A. David-Uraz, S. P. Owocki, *Mon. Not. R. Astron. Soc.* **507**, 1283–1295 (2021).
16. J. E. Steiner, A. S. Oliveira, *Astron. Astrophys.* **444**, 895–904 (2005).
17. W. R. Hamann *et al.*, *Astron. Astrophys.* **625**, A57 (2019).
18. Y. Götberg *et al.*, *Astron. Astrophys.* **615**, A78 (2018).
19. J. H. Groh, A. S. Oliveira, J. E. Steiner, *Astron. Astrophys.* **485**, 245–256 (2008).
20. J. S. Vink, *Astron. Astrophys.* **607**, L8 (2017).
21. A. A. C. Sander, J. S. Vink, *Mon. Not. R. Astron. Soc.* **499**, 873–892 (2020).
22. T. Shenar, A. Gilkis, J. S. Vink, H. Sana, A. A. C. Sander, *Astron. Astrophys.* **634**, A79 (2020).
23. N. R. Walborn, *Astron. J.* **77**, 312 (1972).
24. Y. Nazé *et al.*, *Astron. Astrophys.* **520**, A59 (2010).
25. Materials and methods are available as supplementary materials.
26. V. Petit *et al.*, *Mon. Not. R. Astron. Soc.* **429**, 398–422 (2013).
27. W. R. Hamann, G. Gräfener, *Astron. Astrophys.* **410**, 993–1000 (2003).
28. A. Sander *et al.*, *Astron. Astrophys.* **577**, A13 (2015).
29. F. R. N. Schneider *et al.*, *Astron. Astrophys.* **570**, A66 (2014).
30. J. F. Donati *et al.*, *Mon. Not. R. Astron. Soc.* **370**, 629–644 (2006).
31. G. A. Wade *et al.*, *Mon. Not. R. Astron. Soc.* **416**, 3160–3169 (2011).
32. G. Gräfener, J. S. Vink, A. de Koter, N. Langer, *Astron. Astrophys.* **535**, A56 (2011).
33. P. T. H. Pang *et al.*, *Astrophys. J.* **922**, 14 (2021).
34. R. C. Duncan, C. Thompson, *Astrophys. J.* **392**, L9 (1992).
35. N. Langer, Standard models of Wolf-Rayet stars. *Astron. Astrophys.* **210**, 93–113 (1989).
36. S. E. Woosley, *Astrophys. J. Lett.* **719**, L204–L207 (2010).
37. P. K. Blanchard, E. Berger, M. Nicholl, V. A. Villar, *Astrophys. J.* **897**, 114 (2020).
38. A. Maeder, G. Meynet, Stellar evolution with rotation. VI. The Eddington and Omega -limits, the rotational mass loss for OB and LBV stars. *Astron. Astrophys.* **361**, 159–166 (2000).
39. I. Brott *et al.*, *Astron. Astrophys.* **530**, A115 (2011).
40. L. Ferrario, J. E. Pringle, C. A. Tout, D. T. Wickramasinghe, *Mon. Not. R. Astron. Soc.* **400**, L71–L74 (2009).
41. D. T. Wickramasinghe, C. A. Tout, L. Ferrario, *Mon. Not. R. Astron. Soc.* **437**, 675–681 (2014).
42. F. R. N. Schneider *et al.*, *Nature* **574**, 211–214 (2019).
43. S. Bagnulo, J. D. Landstreet, *Astrophys. J. Lett.* **935**, L12 (2022).
44. R. F. Webbink, *Astrophys. J.* **277**, 355 (1984).
45. J. Schwab, E. Quataert, D. Kasen, *Mon. Not. R. Astron. Soc.* **463**, 3461–3475 (2016).
46. B. Paxton *et al.*, *Astrophys. J. Suppl. Ser.* **192** (Supp.), 3 (2011).
47. P. Harmanec, Stellar masses and radii based on modern binary data. *Bull. Astron. Inst. Czechoslov.* **39**, 329–345 (1988).
48. T. Shenar *et al.*, *Astron. Astrophys.* **606**, A91 (2017).
49. S. Toonen, S. Portegies Zwart, A. S. Hamers, D. Bandopadhyay, *Astron. Astrophys.* **640**, A16 (2020).
50. D. R. Gies, K. Shepard, P. Wysocki, R. Klement, *Astron. J.* **163**, 100 (2022).
51. T. Shenar, A massive helium star with a sufficiently strong magnetic field to form a magnetar, version 2, Zenodo (2023); https://doi.org/10.5281/zenodo.8040752.
52. powr-code/PoWR: v20220809, Zenodo (2022); https://doi.org/10.5281/zenodo.7217731.

ACKNOWLEDGMENTS

We thank the three anonymous referees for comments that improved the manuscript. The PoWR code was developed under the guidance of W.-R. Hamann with substantial contributions from L. Koesterke, G. Gräfener, A. Sander, T.S. and other coworkers and students. We thank J. Hessels, N. Przybilla, and H. Henrichs for helpful discussions. The TESS, IUE, and FUSE data were obtained from the Mikulski Archive for Space Telescopes (MAST) at the Space Telescope Science Institute (STScI), which is operated by the Association of Universities for Research in Astronomy under NASA contract NAS5-26555. T.S., P.M., L.O., and H.T. thank the International Space Science Institute (ISSI, Bern) for hosting a discussion meeting. NOIRLab is managed by the Association of Universities for Research in Astronomy (AURA) under a cooperative agreement with the National Science Foundation. This work is partly based on observations made with the Mercator Telescope, operated on the island of La Palma by the Flemish Community at the Spanish Observatorio del Roque los Muchachos of the Instituto de Astrofísica de Canarias. **Funding:** T.S. was supported by the European Union's Horizon 2020 Marie Skłodowska-Curie grant no. 101024605. D.M.B. and T.V.R. were supported by the Fonds Wetenschappelijk Onderzoek (FWO) through senior and junior postdoctoral fellowships under grant agreement nos. 1286521N and 12ZB620N, respectively. H.S. was supported by the European Research Council (ERC) under the European Union's Horizon 2020 research and innovation program (no. 772225: MULTIPLES). A.G. was supported by the Professor Amnon Pazy Research Foundation. N.S.-L. and G.A.W. received financial support from the Natural Sciences and Engineering Research Council (NSERC) of Canada. A.S.d.O. was supported by the FAPESP grant no. 03/12618-7. S.T. was supported by the Netherlands Research Council (NOW) grants VENI 639.041.645 and VIDI 203.061. Support to MAST for TESS, IUE, and FUSE data is provided by the NASA Office of Space Science through grant NAG5-7584 and by other grants and contracts. Funding for the TESS mission is provided by the NASA Explorer Program. T.S. acknowledges support from the Programa Atracción de Talento de la Comunidad de Madrid through grant 2022-T1/TIC-24117. **Author contributions:** T.S. developed the hypothesis, led the ESPaDOnS observations, performed the spectral and orbital analyses, and wrote the manuscript. G.W. performed the spectropolarimetric analysis and contributed to the observations and the manuscript. P.M. conceived the evolutionary scenario and constructed the corresponding MESA model. S.B. contributed to the spectropolarimetric analysis and to the manuscript. J.B. collected the HERMES data. D.M.B. and T.V.R. performed the light curve analysis. A.G. contributed to the evolutionary discussion and performed the population synthesis. N.L., S.T., and L.O. contributed to the discussion. A.N.-C., N.S.-L., and H.S. contributed to the observations, orbital analysis, and the data reduction. L.O. contributed to the discussion of magnetic Wolf-Rayet stars. H.S. contributed to the design of the observational campaign and the orbital analysis. N.S.-L. contributed to the design of the observational campaign. A.S.d.O. collected the LNA and FEROS observations. H.T. contributed to the spectral analysis. **Competing interests:** The authors declare no competing interests. **Data and materials availability:** Reduced and wavelength-calibrated FEROS, ESPaDOnS, LNA and HERMES spectra, the TESS light curve, the input and output files of our stellar evolution models, and the ZEEMAN source code are archived at Zenodo (*51*). The PoWR source code is available on GitHub https://github.com/powr-code/PoWR and archived at Zenodo (*52*). Our measured RVs are provided in data S1. The raw ESPaDOnS spectra are available on the CFHT archive www.cadc-ccda.hia-iha.nrc-cnrc.gc.ca/en/cfht under proposal ID 22BC13. The raw FEROS data are available on the ESO archive http://archive.eso.org/eso/eso_archive_main.html under target name HD 45166; we used the observations taken in 2002. The IUE data are available on MAST at https://archive.stsci.edu/iue/search.php under program IDs WRJSH, JA017, and EI273. The FUSE data are available on MAST at https://archive.stsci.edu/fuse/search.php under program ID P224. The raw TESS data are available on MAST at https://archive.stsci.edu/missions-and-data/tess with the coordinates of HD 45166; we used the data from full-frame images of sectors 6 and 33. **License information:** Copyright © 2023 the authors, some rights reserved; exclusive licensee American Association for the Advancement of Science. No claim to original US government works. https://www.science.org/about/science-licenses-journal-article-reuse

SUPPLEMENTARY MATERIALS

science.org/doi/10.1126/science.ade3293
Materials and Methods
Supplementary Text
Figs. S1 to S11
Tables S1 and S2
References (*53*–*110*)
Data S1

Submitted 10 August 2022; accepted 15 June 2023
10.1126/science.ade3293

OPTICS

Overcoming losses in superlenses with synthetic waves of complex frequency

Fuxin Guan[1]†, Xiangdong Guo[1,2]†, Kebo Zeng[1]†, Shu Zhang[2], Zhaoyu Nie[3], Shaojie Ma[1], Qing Dai[2]*, John Pendry[4]*, Xiang Zhang[1,5,6]*, Shuang Zhang[1,7]*

Superlenses made of plasmonic materials and metamaterials can image features at the subdiffraction scale. However, intrinsic losses impose a serious restriction on imaging resolution, a problem that has hindered widespread applications of superlenses. Optical waves of complex frequency that exhibit a temporally attenuating behavior have been proposed to offset the intrinsic losses in superlenses through the introduction of virtual gain, but experimental realization has been lacking because of the difficulty of imaging measurements with temporal decay. In this work, we present a multifrequency approach to constructing synthetic excitation waves of complex frequency based on measurements at real frequencies. This approach allows us to implement virtual gain experimentally and observe deep-subwavelength images. Our work offers a practical solution to overcome the intrinsic losses of plasmonic systems for imaging and sensing applications.

In conventional optical imaging, Abbe diffraction limits the resolution of feature sizes to larger than half the wavelength. This limit is due to the loss of the subwavelength information carried by evanescent waves. To overcome this limitation, a negative refractive index lens has been proposed to enhance the evanescent waves to recover the deep-subwavelength resolution of imaging (*1*, *2*). Subsequently, superlenses, made of either natural materials with negative permittivities (*3*–*7*) or hyperbolic materials with mixed signs of dielectric constants along different directions (*8*–*13*), have been proposed to attain subdiffractional limited imaging. Nevertheless, losses are non-negligible in materials with negative parameters (*14*–*16*), which reduces the deep-subwavelength information of the superlenses and seriously affects the resolution of imaging (*17*–*19*). To compensate for these losses, it has been proposed that gain materials could be incorporated into metamaterial designs or plasmonics (*20*–*27*), but the setup is extremely complicated and the gain will inevitably introduce instability and noise into the system (*28*–*30*). It has been proposed that complex-frequency waves (CFWs) with temporally growing or attenuating behaviors could provide virtual absorption or virtual gain (*31*–*35*). Some theoretical proposals have been put forward to recover the deep-subwavelength information carried by surface plasmons through the excitation of CFWs with temporal attenuation (*32*–*35*). However, synthesizing CFWs is challenging in optical systems from a practical perspective.

To address this challenge, we synthesized CFW signals using a multifrequency approach. We exploited the fact that a truncated CFW can be expressed as a combination of multiple frequency components with coefficients that follow a Lorentzian spectral lineshape through the Fourier transformation. We performed measurements at multiple real frequencies and numerically synthesized the field distribution under CFW illumination by combining the measured field plots at different frequencies according to the Lorentzian lineshape. As a proof of concept, both a SiC slab operating at optical frequencies and a bulk hyperbolic metamaterial operating at microwave frequencies were used as superlenses. We show that, although the spatial resolution of imaging at real frequencies is poor, caused by the inevitable material loss in these systems, ultrahigh resolution imaging can be obtained with synthesized CFWs that consist of multiple frequency components.

Loss compensation with CFWs

We start with an example of loss compensation for a metallic material described by the Drude model, $\varepsilon(\omega) = 1 - \omega_p/\omega + i\omega\gamma$, where γ is the nonzero ohmic loss term. Below the plasma frequency ω_p, the permittivity becomes negative, making it suitable as a plasmonic material, or for constructing hyperbolic media, to support surface or bulk waves with a very large wave vector for subdiffraction imaging. Owing to the existence of a loss term, the negative permittivity is typically accompanied by an appreciable imaginary part (left panel of Fig. 1A), which seriously limits the imaging performa… Interestingly, from a mathematical perspec… by transforming the frequency into the suitable complex value $\omega \rightarrow \omega - i\gamma/2$, the permittivity is turned into a purely real value $\varepsilon(\omega) = 1 - \omega_p{}^2/(\omega^2 + \gamma^2/4)$.

A CFW with a negative imaginary part corresponds to a wave with temporal attenuation. The mathematical expression of a CFW is expressed as $E(t) \sim e^{-i\tilde{\omega}_0 t}$, where t denotes time, $\tilde{\omega}_0 = \omega_0 - i\tau/2$, and $\tau > 0$ is the temporal attenuation factor. Although an ideal CFW exists mathematically, it is unphysical because it implies that the energy would diverge when t approaches negative infinity. Hence, a truncation at the start of time needs to be implemented to rationalize the CFW, that is, $E_T(t) = E_0 e^{-i\tilde{\omega}_0 t}\theta(t)$, where $\theta(t) = 0$ for $t < 0$ and $\theta(t) = 1$ for $t \geq 0$. Using Fourier transformation, the truncated CFW can be expanded into the integration of the spectral components $E_T(t) = \frac{E_0}{2\pi}\int \frac{1}{i(\tilde{\omega}_0 - \omega)} e^{-i\omega t} d\omega$, where the integration is from $-\infty$ to ∞ and the Fourier coefficient $1/i(\tilde{\omega}_0 - \omega)$ has a Lorentzian lineshape [for details, see supplementary materials (SM) section 6]. Hence, any response of the system at a complex frequency $\tilde{\omega}_0$, including the dielectric constant ε and the transfer function T, can be obtained via the integral of the corresponding real-frequency response, as $F(\tilde{\omega}_0) \approx \int F(\omega) \frac{1}{i(\tilde{\omega}_0 - \omega)} e^{-i\omega t + i\tilde{\omega}_0 t} d\omega/2\pi$ for sufficiently long duration t. In practice, it is sufficient to choose discrete frequency points at a certain frequency interval $\Delta\omega$ to synthesize the signal. Further, based on the compressed sensing theory (*36*–*38*), the CFW can be synthesized based on the information taken from a finite spectrum range. If the spectrum range is broad enough, the noise of the interference between different harmonics is suppressed. The system response under synthesized CFW excitation can be discretized as

$$F(\tilde{\omega}_0) \approx \sum_i F(\omega_i) \frac{1}{i(\tilde{\omega}_0 - \omega_i)} e^{-i\omega_i t + i\tilde{\omega}_0 t} \Delta\omega/2\pi \quad (1)$$

Owing to the frequency being discretized, the signal has an overall $2\pi/\Delta\omega$ temporal periodicity. Feeding the permittivity at a number of frequencies (the black and gray circles in the left panel of Fig. 1A) into Eq. 1, where F represents the permittivity, we can obtain the synthesized permittivity of complex frequency with $\tau = \gamma$, as shown in the right panel of Fig. 1A, which clearly shows that the loss of the Drude model can be largely compensated by virtual gain (for details, see SM section 7).

We use the synthetic CFW to study the imaging performance in a metal-dielectric multilayer lens with a total of 15 layers (Fig. 1B),

[1]New Cornerstone Science Laboratory, Department of Physics, University of Hong Kong, Hong Kong, China. [2]CAS Key Laboratory of Nanophotonic Materials and Devices, CAS Key Laboratory of Standardization and Measurement for Nanotechnology, CAS Center for Excellence in Nanoscience, National Center for Nanoscience and Technology, Beijing, China. [3]Department of Mechanical Engineering, University of California, Berkeley, CA 94720, USA. [4]The Blackett Laboratory, Department of Physics, Imperial College London, SW7 2AZ London, UK. [5]Faculty of Science, University of Hong Kong, Hong Kong, China. [6]Faculty of Engineering, University of Hong Kong, Hong Kong, China. [7]Department of Electrical and Electronic Engineering, University of Hong Kong, Hong Kong, China.
***Corresponding author. Email: daiq@nanoctr.cn (Q.D.); j.pendry@imperial.ac.uk (J.P.); xiangz@hku.hk (X.Z.); shuzhang@hku.hk (Shuang Z.)**
†These authors contributed equally to this work.

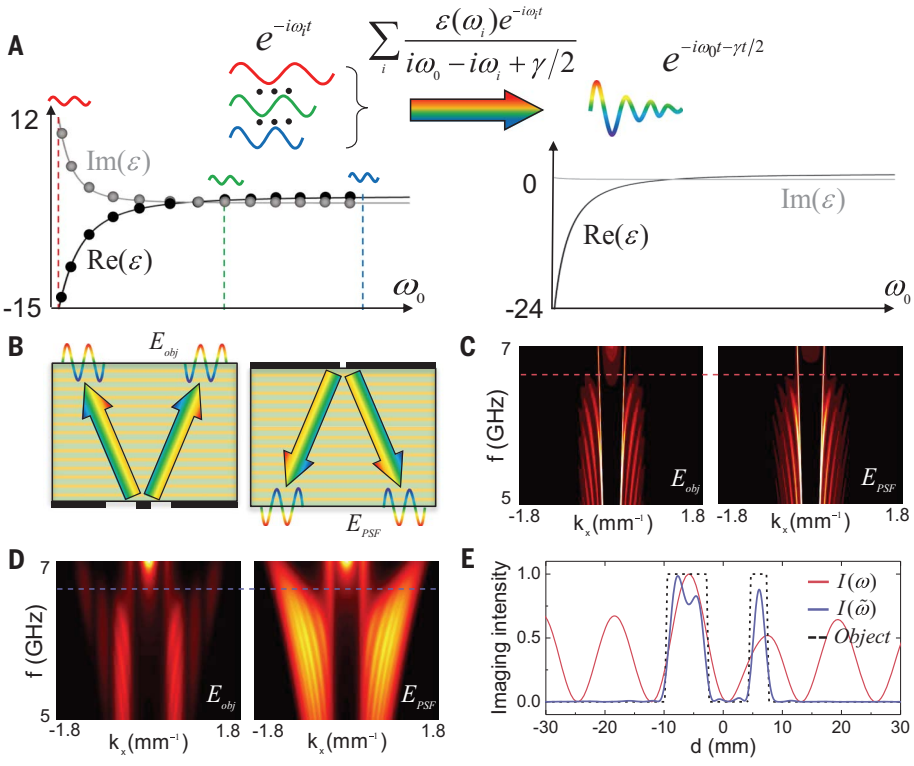

Fig. 1. Illustration of loss compensation of the superimaging lens using synthetic CFWs. (**A**) The permittivities of the Drude model with a finite damping term before (left) and after (right) loss compensation using the CFWs synthesized with permittivities at multiple frequencies. The solid circles indicate that permittivities at discretized frequencies can be used to synthesize the complex-frequency permittivity. Red, green, and blue waves and dashed lines indicate wave components at the three different frequencies and the corresponding real and imaginary parts of the permittivity. (**B**) The left panel shows a schematic of light passing through a metal-dielectric multilayer hyperbolic lens from two closely placed slits at the bottom. The thicknesses for the metal layer and the dielectric layer are d_m = 0.7 mm and d_d = 1.76 mm, respectively. The permittivity of the metal is described by the Drude model, with $\omega_p = 34\pi$ GHz and γ = 0.854 GHz. The permittivity of the dielectric medium is ε_d = 2.2. E_{obj} represents the field distribution at the top surface, whereas the right panel shows schematically the field pattern E_{PSF} generated from a point source. (**C**) The dispersion plots formed by Fourier transformation of E_{obj} and E_{PSF} at different frequencies. (**D**) The complex-frequency dispersion plots with τ = 0.854 GHz derived by synthesizing the dispersions in (C) following Eq. 1. A frequency range from 4 to 8 GHz is used to synthesize the complex-frequency results. (**E**) The corresponding imaging results at a complex frequency of (6.68 − 0.068*i*) GHz and a real frequency of 6.68 GHz, as indicated by the red and blue dashed lines in (C) and (D), respectively. *I*, intensity.

which functions as a type II hyperbolic media with mixed signs of permittivity tensor elements along different directions (*39*). The left panel of Fig. 1B schematically shows the field emitted from two closely spaced slits of different widths from the bottom of a flat hyperbolic material. The waves transmitted to the upper interface form an electric field pattern $E_{obj}(\omega, r)$, where r is the real-space coordinate. The corresponding distribution in the momentum space $E_{obj}(\omega, k)$ can be derived by Fourier transformation, where k is the in-plane wave vector. Inspired by the time-reversal imaging technique that has been demonstrated in acoustics and other wave systems (*40*–*46*), we used a postprocessing procedure to mimick a phase conjugation action to restore the image of the object. We first performed the complex conjugate operation of the momentum space distribution $E_{obj}(\omega, k) \rightarrow E^*_{obj}(\omega, k)$ and then multiplied it by the transfer function to obtain the image in the Fourier space, that is

$$E_{imag}(\omega, k) = E^*_{obj}(\omega, k)T(\omega, k) \qquad (2)$$

In this equation, the transfer function is obtained by Fourier transforming the point spread function $T(\omega, k) = \mathcal{F}[E_{PSF}(\omega, r)]$, where $E_{PSF}(\omega, r)$ is the field emitted from a point source located on one side of the hyperbolic slab to the opposite surface, as shown in the right panel of Fig. 1B. The purpose of multiplying the transfer function is to restore the original image of the object. Finally, the real-space image pattern $E_{imag}(\omega, r)$ can be obtained by the inverse Fourier transformation of Eq. 2.

We used finite element method (FEM) simulation to numerically calculate $E^*_{obj}(\omega, k)$ and $T(\omega, k)$, which are displayed in the left and right panels of Fig. 1C, respectively. The calculated image pattern based on Eq. 2 at frequency f = 6.68 GHz is shown by the red line in Fig. 1E, which deviates from the object (shown as the dashed line). By contrast, by performing phase conjugation in the complex-frequency domain (*47*, *48*), that is, by constructing the $E^*_{obj}(\tilde{\omega}, k)$ and $T(\tilde{\omega}, k)$, respectively, using Eq. 1 with $\tau = \gamma$, the large wave vector components are recovered (Fig. 1D). The complex-frequency image faithfully follows the original pattern, as shown by the blue line in Fig. 1E, verifying the capability of the multifrequency approach to synthesize the CFW for substantially enhancing the imaging resolution compared with that of the real frequency (red line in Fig. 1E).

Experimental results

Microwaves

Equations 1 and 2 require the distribution of both amplitude and phase of field, which can be readily obtained using a microwave characterization setup for a flat hyperbolic metamaterial lens designed to operate at microwave frequencies. The unit cell of the metamaterial consists of a spiral metallic wire–dielectric layer with the dimensions 4 mm by 4 mm by 1.5 mm to form a type II hyperbolic metamaterial with two identical in-plane negative permittivities and one out-plane positive permittivity, as shown in Fig. 2A. The spiral structure can reduce the plasma frequency such that the accessible wave vectors in the Brillouin zone can be much larger than those in the free space. The corresponding equifrequency contours (EFCs) at different frequencies are retrieved using full-wave simulations, as shown in Fig. 2B, where the frequencies of the EFCs increase along the direction of the arrow. At higher frequencies and in the absence of loss, the EFC can reach the horizontal Brillouin edge, providing large in-plane wave vectors for achieving subdiffractional imaging resolution. The corresponding in-plane EFCs are depicted in fig. S3. Figure 2C displays the experimental setup, wherein the bulk metamaterial lens is composed of 80-by-80 in-plane unit cells and 25 layers vertically. A dipole source is placed at the bottom of the sample, and a probe antenna is raster scanned at the top surface to measure the near-field distribution. The details of the experimental setup and samples are depicted in SM sections 1 to 3.

To begin, we scanned a one-dimensional (1D) line above the sample to measure the field distribution, as depicted in Fig. 2D, emitted from a single dipole source across 251 discrete frequency points within the range of 5 to 7.5 GHz. The dispersion is subsequently obtained by Fourier transformation (Fig. 2E). The dispersion plot exhibits two bright lines in the middle, which locate near the light cone in the dielectric material, whereas the other bright lines

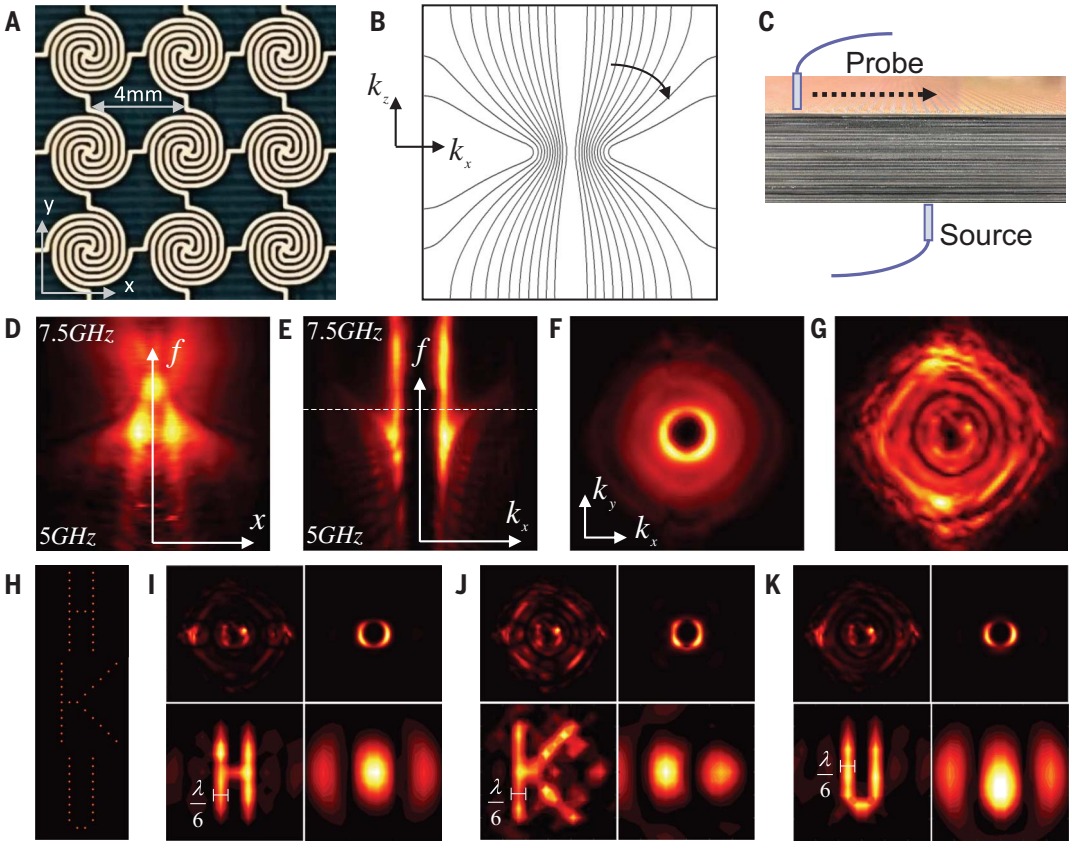

Fig. 2. Experimental demonstration of loss compensation in superimaging using a hyperbolic lens at microwave frequency. (**A** and **B**) Photograph of hyperbolic metamaterial with metallic spiral wires of 0.2-mm width printed on a 1.5-mm-thick Teflon slab (A). The EFCs in the Brillouin zone at different frequencies are depicted in (B), with the frequencies distributed evenly between 0.9 and 6.5 GHz. The Brillouin zone boundaries along the vertical and horizontal directions are π/(4 mm) and π/(1.5 mm), respectively. The arrow implies the direction of increased frequency of the EFCs. (**C**) Schematic of the experimental setup with the two dipole antennas placed near the top and bottom interfaces of the sample, with the bottom and top antennas serving as source and probe, respectively. (**D**) The measured electric field distribution along a line from −150 to +150 mm at the top interface with a frequency step of 0.01 GHz, which locates in the same *y*-*z* plane as the source antenna. (**E**) The dispersion plot obtained by spatial Fourier transformation of the field distribution shown in (D). (**F**) The 2D electric field distribution in the momentum space at a frequency of 6.5 GHz, which serves as the transfer function. (**G**) The 2D electric field distribution in the momentum space for a CFW with a frequency of (6.5 − 0.0065*i*) GHz synthesized by the measurements at multiple frequencies. (**H**) The ground truth of the letters H, K, and U. (**I** to **K**) The imaging results with the dipole sources arranged in the shape of the three letters. The top and bottom subpanels correspond to the Fourier space field distributions and real-space intensity distributions, and the left and right subpanels show the complex-frequency and real-frequency results, respectively.

with larger wave vectors correspond to the hyperbolic modes. Limited by the damping of the system, the measured Fourier components in the momentum space are far from reaching the Brillouin zone edge. Because the frequency marked by the white dashed line (f = 6.5 GHz) exhibits relatively large wave vectors, it is selected as the central frequency for the signal synthesis. The 2D field distribution in the momentum space at the central frequency is shown in Fig. 2F, and the distributions at a number of other frequencies are provided in SM section 8. Using Eq. 1, we synthesized the dispersion of the complex frequency using 251 frequency points, with the temporal snapshot captured at the end of the temporal periodicity (Fig. 2G). Notably, the synthesized results with complex-frequency excitation recover the field components across a large portion of the Brillouin zone, indicating a much better spatial resolution than that of the real frequency. Note that the Fourier space distributions shown in Fig. 2, F and G, correspond to the $T(\omega, k)$ and $T(\tilde{\omega}, k)$ of the real-frequency and complex-frequency cases in Eq. 2, respectively.

We next showcase super-resolution imaging of subwavelength patterns with the synthesized complex frequency. The desired pattern is formed by sequentially placing a single emitting dipole antenna at different locations, and the field distribution at the top surface is measured at each location of the dipole source. The measured field distributions are then linearly superimposed to form the image. Subsequently, Fourier transformation is performed to obtain the Fourier pattern at the real and complex frequencies, $E^*_{\mathrm{obj}}(\omega, k)$ and $E^*_{\mathrm{obj}}(\tilde{\omega}, k)$. The ground truth of three different patterns, letters H, K, and U, are shown in Fig. 2H, and the corresponding imaging results obtained by using Eq. 2 are displayed in Fig. 2, I to K, respectively. The top-left image in each subpanel shows the Fourier pattern with synthesized complex-frequency excitation, which occupies a substantial portion of the Brillouin zone, whereas the corresponding bottom-left image of each subpanel displays the image of the subwavelength letters. By contrast, the imaging results at the real frequency are shown in the right subpanels for all three cases, and, in each case, the original pattern cannot be identified, thereby confirming a substantial improvement in superimaging with the complex-frequency approach, from $\lambda/2$ to $\lambda/6$, where λ is the free-space wavelength at the central frequency (6.5 GHz) of the synthesized CFW.

We next investigated the effect of the number of frequency points used to synthesize the complex-frequency response on the superimaging

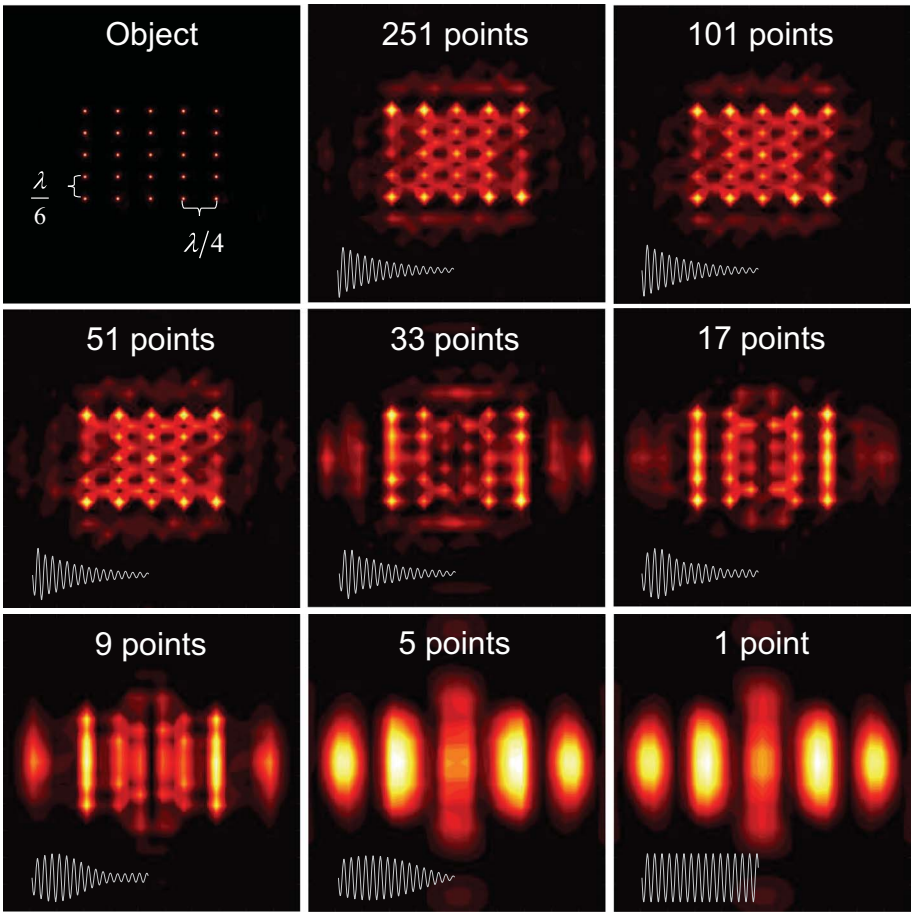

Fig. 3. Investigation of the dependence of the imaging quality over the number of frequency points. The ground truth is shown in the top-left panel, which consists of a five-by-five antenna array, where the lattice constants along the *x* and *y* directions are λ/4 and λ/6, respectively. The other panels show the image intensity distributions that were obtained using different numbers of frequency points, with the central frequency fixed at 6.5 GHz and a fixed frequency step of 0.01 GHz. The corresponding synthetic temporal signal is depicted in the inset of each panel.

performance, with the results shown in Fig. 3. The top-left subpanel of the figure displays the object, which is composed of a five-by-five array of dipole antennas. The horizontal and vertical lattice constants are one-fourth and one-sixth of the central wavelength, respectively. We gradually reduced the number of frequency points from 251 to 1 to construct the synthetic imaging patterns, with a fixed frequency step of 0.01 GHz, and the corresponding synthesized temporal signals are depicted in the insets. Our study shows that reducing the number of frequency points to 51 has a negligible impact on image quality. However, as we continued to reduce the number of frequency points, there was a substantial decrease in imaging resolution, causing the images of the dipoles to merge into vertical lines. When the number of frequency points drops below 17, these lines become wider in the horizontal direction. The corresponding Fourier distributions are shown in fig. S6. This highlights the importance of having a sufficient number of frequency points to maintain good spatial resolution and avoid image degradation.

Infrared

To showcase the versatility of the complex-frequency method, we used a silicon carbide (SiC) superlens operating at mid-infrared (mid-IR) frequency to investigate the loss compensation for superimaging. The design of the superlens is based on a SiC sandwich structure (Fig. 4A), in which the upper and lower surfaces correspond to the image and object planes of the lens, respectively (*6*). The fabrication technique can be found in SM sections 4 and 5. The object is composed of a 1D grating of varying spacings or circular apertures of varying diameters patterned on a metal film [scanning electron microscopy (SEM) image shown in the inset of Fig. 4B]. The optical image is captured by the technique of scattering-type scanning near-field optical microscopy (s-SNOM). With this technique, both the amplitude and phase of the image field can be collected by the probe. The measured field pattern of the 1D grating at the image plane is Fourier analyzed at different frequencies and presented in Fig. 4B. Here, the frequency interval is 2 cm^{-1}, from 900 to 980 cm^{-1}, with a total of 41 points. Figure 4C displays the profiles of the grating captured by the SiC superlens at both the complex and real frequencies, in both real space (left panel) and momentum space (right panel). These profiles demonstrate superior imaging quality at the complex frequency compared with the real frequency.

The SEM image of the array of 2D circular apertures is shown in Fig. 4D. The field distributions in Fig. 4, E to G, correspond to the images captured at the complex frequency and two distinct real frequencies, respectively. The complex-frequency image closely resembles the SEM image, whereas only heavily blurred field patterns are observed at the real frequencies. To investigate the resolution limitations of the SiC superlens with loss compensation, two pairs of holes placed closely together, but with varying displacements, were fabricated; Helium ion microscopy (HIM) images are shown in Fig. 4H. The corresponding s-SNOM images at the complex and real frequencies are shown in Fig. 4, I and J, respectively. Using the complex-frequency method, two pairs of circles with edge-to-edge separations of 40 and 100 nm, respectively, can be clearly resolved, whereas no discernible images are formed at the real frequency. The spatial resolution shown in the measurement of the double-aperture structure using complex frequency is around 400 nm, as shown in Fig. 4I, whereas the distance between two neighboring field maxima at the corresponding central frequency is around 1200 nm, as shown in Fig. 4G.

Concluding remarks

We have presented a method to compensate for the intrinsic loss of hyperbolic metamaterial and for SiC superimaging lenses by synthesizing a complex-frequency excitation through a multifrequency approach, which improves imaging resolution beyond the limit imposed by the damping of the system. Our approach successfully overcomes the challenges of experimentally implementing CFWs in the time domain, which include the need for precise CFW synthesis and time-gated measurements after reaching the quasi–steady state, and holds great potential for high-resolution microscopy. Furthermore, the synthesized complex-frequency approach can be extended to other areas of optics, such as plasmonic sensing applications. By leveraging the enhanced quality factor of plasmonic structures, our approach has the potential to substantially improve sensitivity in sensing applications. In addition, the approach can be tailored to different systems and geometries, providing a flexible and versatile tool for improving optical performance.

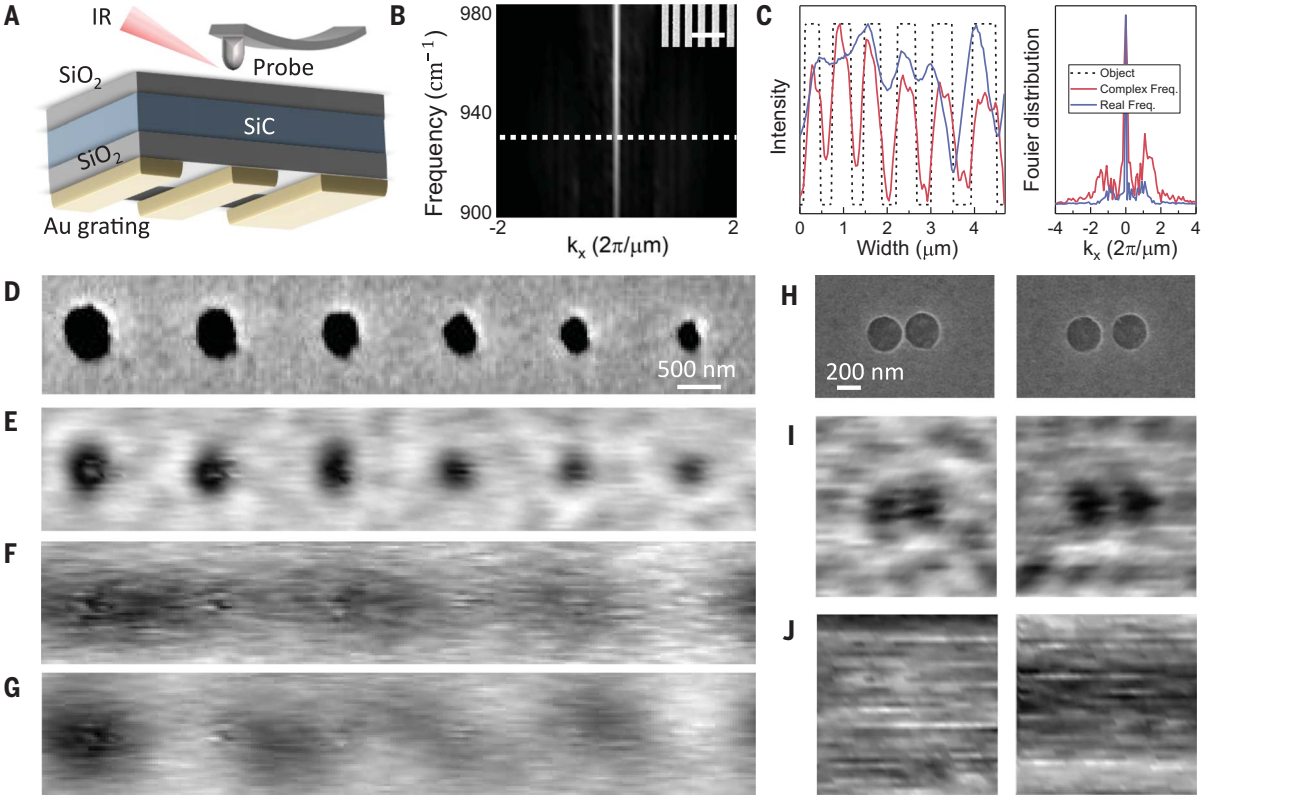

Fig. 4. Experimental observation of loss compensation in mid-IR superimaging using a SiC superlens. (**A**) Schematic of the s-SNOM experimental setup. A ~440-nm-thick SiC layer is sandwiched between two SiO_2 layers of equal thickness (~220 nm). A 60-nm-thick gold grating is placed at the bottom. (**B**) Fourier distribution of a line scan at the imaging plane in the 1D grating structure with varying spacings (SEM image is shown in the inset; scale bar, 2 μm). The dashed line represents the central frequency of 930 cm^{-1}. (**C**) Imaging patterns at both the complex frequency $\tilde{f} = (930 - 12i)\ cm^{-1}$ and real frequency of 930 cm^{-1}, in both the real space (left) and momentum space (right). (**D**) SEM image of a thin gold film with an array of holes of different diameters. (**E**) Image of the electric field at the complex frequency $\tilde{f}$. (**F** and **G**) Real-frequency images at 922 cm^{-1} (F) and 930 cm^{-1} (G). (**H**) HIM images of pairs of circular holes with different spatial separations. (**I** and **J**) Images correspond to electric field distributions of the images at the complex frequency $\tilde{f}$ = (930 − 12*i*) cm^{-1} (I) and real frequency of 930 cm^{-1} (J).

REFERENCES AND NOTES

1. V. G. Veselago, *Sov. Phys. Usp.* **10**, 509–514 (1968).
2. J. B. Pendry, *Phys. Rev. Lett.* **85**, 3966–3969 (2000).
3. N. Fang, H. Lee, C. Sun, X. Zhang, *Science* **308**, 534–537 (2005).
4. D. Melville, R. Blaikie, *Opt. Express* **13**, 2127–2134 (2005).
5. X. Zhang, Z. Liu, *Nat. Mater.* **7**, 435–441 (2008).
6. T. Taubner, D. Korobkin, Y. Urzhumov, G. Shvets, R. Hillenbrand, *Science* **313**, 1595 (2006).
7. T. Li *et al.*, *Photonics Insights* **2**, R01 (2023).
8. Z. Liu, H. Lee, Y. Xiong, C. Sun, X. Zhang, *Science* **315**, 1686 (2007).
9. I. I. Smolyaninov, Y. J. Hung, C. C. Davis, *Science* **315**, 1699–1701 (2007).
10. S. Dai *et al.*, *Nat. Commun.* **6**, 6963 (2015).
11. P. Li *et al.*, *Nat. Commun.* **6**, 7507 (2015).
12. P. A. Belov, C. R. Simovski, P. Ikonen, *Phys. Rev. B* **71**, 193105 (2005).
13. P. A. Belov *et al.*, *Phys. Rev. B* **77**, 193108 (2008).
14. L. D. Landau, E. M. Lifshitz, L.P. Pitaevskii, *Electrodynamics of Continuous Media*, vol. 8 of *Landau and Lifshitz Course of Theoretical Physics* (Pergamon Press, 1984).
15. M. I. Stockman, *Phys. Rev. Lett.* **98**, 177404 (2007).
16. P. Kinsler, M. W. McCall, *Phys. Rev. Lett.* **101**, 167401 (2008).
17. D. R. Smith *et al.*, *Appl. Phys. Lett.* **82**, 1506–1508 (2003).
18. R. Merlin, *Appl. Phys. Lett.* **84**, 1290–1292 (2004).
19. I. A. Larkin, M. I. Stockman, *Nano Lett.* **5**, 339–343 (2005).
20. S. Anantha Ramakrishna, J. B. Pendry, *Phys. Rev. B* **67**, 201101 (2003).
21. A. Fang, T. Koschny, M. Wegener, C. M. Soukoulis, *Phys. Rev. B* **79**, 241104 (2009).
22. S. Xiao *et al.*, *Nature* **466**, 735–738 (2010).
23. A. Fang, T. Koschny, C. M. Soukoulis, *Phys. Rev. B* **82**, 28–31 (2010).
24. J. M. Hamm, S. Wuestner, K. L. Tsakmakidis, O. Hess, *Phys. Rev. Lett.* **107**, 167405 (2011).
25. J. Grgić *et al.*, *Phys. Rev. Lett.* **108**, 183903 (2012).
26. R. S. Savelev *et al.*, *Phys. Rev. B* **87**, 115139 (2013).
27. M. Sadatgol, Ş. K. Özdemir, L. Yang, D. O. Güney, *Phys. Rev. Lett.* **115**, 035502 (2015).
28. M. I. Stockman, *Phys. Rev. Lett.* **106**, 156802 (2011).
29. S. Wuestner, A. Pusch, K. L. Tsakmakidis, J. M. Hamm, O. Hess, *Phys. Rev. Lett.* **107**, 259701 (2011).
30. J. B. Pendry, S. A. Maier, *Phys. Rev. Lett.* **107**, 259703 (2011).
31. H. Li, A. Mekawy, A. Krasnok, A. Alù, *Phys. Rev. Lett.* **124**, 193901 (2020).
32. A. Archambault, M. Besbes, J. J. Greffet, *Phys. Rev. Lett.* **109**, 097405 (2012).
33. K. L. Tsakmakidis, T. W. Pickering, J. M. Hamm, A. F. Page, O. Hess, *Phys. Rev. Lett.* **112**, 167401 (2014).
34. H. S. Tetikol, M. I. Aksun, *Plasmonics* **15**, 2137–2146 (2020).
35. K. L. Tsakmakidis, K. G. Baskourelos, M. S. Wartak, *Metamaterials and Nanophotonics: Principles, Techniques and Applications* (World Scientific, 2022).
36. D. L. Donoho, M. Vetterli, R. A. DeVore, I. Daubechies, *IEEE Trans. Inf. Theory* **44**, 2435–2476 (1998).
37. D. L. Donoho, *IEEE Trans. Inf. Theory* **52**, 1289–1306 (2006).
38. P. Zheng *et al.*, *Adv. Opt. Mater.* **10**, 2200257 (2022).
39. D. R. Smith, J. B. Pendry, *J. Opt. Soc. Am. B* **23**, 391 (2006).
40. D. R. Jackson, D. R. Dowling, *J. Acoust. Soc. Am.* **89**, 171–181 (1991).
41. D. Cassereau, M. Fink, *IEEE Trans. Ultrason. Ferroelectr. Freq. Control* **39**, 579–592 (1992).
42. C. Draeger, M. Fink, *Phys. Rev. Lett.* **79**, 407–410 (1997).
43. J. de Rosny, M. Fink, *Phys. Rev. Lett.* **89**, 124301 (2002).
44. G. Lerosey *et al.*, *Phys. Rev. Lett.* **92**, 193904 (2004).
45. S. Maslovski, S. Tretyakov, *J. Appl. Phys.* **94**, 4241–4243 (2003).
46. J. B. Pendry, *Science* **322**, 71–73 (2008).
47. T. Zhu, *Geophys. J. Int.* **197**, 483–494 (2014).
48. K. Wapenaar, J. Brackenhoff, J. Thorbecke, in vol. 1 of *81st EAGE Conference and Exhibition* (European Association of Geoscientists and Engineers, 2019), pp. 2572–2576.

ACKNOWLEDGMENTS

Funding: This work was supported by the New Cornerstone Science Foundation, the Research Grants Council of Hong Kong (AoE/P-502/20 and 17309021), the National Natural Science Foundation of China (51925203 and 52102160), and the Strategic Priority Research Program of the Chinese Academy of Sciences

(grant no. XDB36000000). **Author contributions:** Shuang Z. and X.Z. conceived the project. Shuang Z. and F.G. proposed using measurements at multiple real frequencies to obtain a complex-frequency measurement. F.G. and K.Z. performed numerical simulations and analytical calculations under the guidance of Shuang Z. F.G. carried out the microwave experiment. X.G., Shu Z., and Q.D. carried out the s-SNOM experiment. F.G., X.G., K.Z., Z.N., S.M., Q.D., J.P., X.Z., and Shuang Z. participated in the analysis of the results. F.G., X.G., and Shuang Z. wrote the manuscript with input from all authors. All authors contributed to the discussion. **Competing interests:** The authors declare no conflicts of interest. **Data and materials availability:** All data are available in the main text or the supplementary materials.
License information: Copyright © 2023 the authors, some rights reserved; exclusive licensee American Association for the Advancement of Science. No claim to original US government works. https://www.science.org/about/science-licenses-journal-article-reuse

SUPPLEMENTARY MATERIALS

science.org/doi/10.1126/science.adi1267
Materials and Methods
Supplementary Text
Figs. S1 to S8
References

Submitted 5 April 2023; accepted 29 June 2023
10.1126/science.adi1267

MOLECULAR BIOLOGY

Human POT1 protects the telomeric ds-ss DNA junction by capping the 5′ end of the chromosome

Valerie M. Tesmer, Kirsten A. Brenner, Jayakrishnan Nandakumar*

Protection of telomeres 1 (POT1) is the 3′ single-stranded overhang-binding telomeric protein that prevents an ataxia telangiectasia and Rad3–related (ATR) DNA damage response (DDR) at chromosome ends. What precludes the DDR machinery from accessing the telomeric double-stranded–single-stranded junction is unknown. We demonstrate that human POT1 binds this junction by recognizing the phosphorylated 5′ end of the chromosome. High-resolution crystallographic structures reveal that the junction is capped by POT1 through a "POT-hole" surface, the mutation of which compromises junction protection in vitro and telomeric 5′-end definition and DDR suppression in human cells. Whereas both mouse POT1 paralogs bind the single-stranded overhang, POT1a, not POT1b, contains a POT-hole and binds the junction, which explains POT1a's sufficiency for end protection. Our study shifts the paradigm for DDR suppression at telomeres by highlighting the importance of protecting the double-stranded–single-stranded junction.

Nucleoprotein complexes called telomeres cap chromosome ends to ensure genome integrity. Human telomeric DNA contains ~10 to 15 kb of tandem 5′-GGTTAG-3′/3′-CCAATC-5′ repeats. Although telomeric DNA is primarily double-stranded (ds), all chromosomes terminate in a 50- to 500-nucleotide (nt) single-stranded (ss) G-rich telomeric overhang (Fig. 1A, bottom) (*1*). The six-protein shelterin complex coats telomeric DNA to protect chromosome ends from being recognized as dsDNA breaks by the ataxia telangiectasia and Rad3–related (ATR) kinase– and ataxia-telangiectasia mutated (ATM) kinase–mediated DNA damage response (DDR) machineries (*2*, *3*). ATR signaling involves multiple protein factors and coordinated recognition of both the ss and the adjacent ds-ss junction of its DNA substrates (*4*). Protection of telomeres 1 (POT1) is a shelterin component that binds the ss G-rich overhang with high affinity and sequence specificity and prevents ATR signaling at telomeres (*2*, *5*, *6*). POT1 recognizes ssDNA through its DNA binding domain (DBD), which consists of two oligonucleotide/oligosaccharide-binding (OB) domains (Fig. 1A). Previous studies have reported a decanucleotide TTAGGGTTAG within two telomeric ss repeats, ^{1}GGTTAGGGTTAG^{12}, to be sufficient for high-affinity binding to human POT1 (hPOT1) (*7*). The first OB domain (OB1) of hPOT1 binds ^{3}TTAGGG^{8} (OB1^{DNA}), whereas its second OB domain (OB2) binds ^{9}TTAG^{12} (OB2^{DNA}) (Fig. 1, A and B) (*7*). Homologs of POT1 are identifiable across eukaryotes (*5*, *8*–*15*), and deleting the POT1 paralog in mice that is involved in chromosome-end protection (POT1a) is embryonic lethal (*14*, *15*).

Department of Molecular, Cellular and Developmental Biology, University of Michigan, Ann Arbor, MI 48109, USA.
*Corresponding author. Email: jknanda@umich.edu

The current model for ATR suppression at telomeres invokes the prevention by POT1 of replication protein A (RPA) loading onto the ss overhang, through POT1's high affinity for telomeric ssDNA and its tethering to the rest of shelterin at telomeric dsDNA (*2*, *6*, *16*). Yet, multiple observations suggest that additional features of POT1 are involved in ATR repression. First, mouse POT1 paralogs POT1a and POT1b display indistinguishable ssDNA-binding activity, but only POT1a is sufficient for chromosome-end protection (*6*, *15*, *17*), whereas POT1b regulates chromosome-end processing and replication activities (*16*, *18*–*21*). Replacing the DBD of POT1b with that of POT1a or hPOT1 enables ATR repression at telomeres (*17*). Second, replacing the DBD of POT1a with that of ssDNA-binding protein RPA70 is not sufficient to fully repress ATR signaling at telomeres in mouse cells that lack *POT1a* (*16*). Moreover, POT1's binding to the G-rich ss overhang does not explain how it dictates the 5′ end of the C-rich strand, which terminates predominantly in ATC-5′ in mammals (*22*, *23*) (Fig. 1A, bottom). These observations are consistent with the DBD of hPOT1 and mouse POT1a carrying out an additional function relevant to ATR suppression.

Results

Human POT1 binds a 5′-phosphorylated telomeric ds-ss DNA junction

We hypothesized that hPOT1 binds to the telomeric ds-ss junction after we reanalyzed its published DNA binding-site preferences. Two classes of POT1 binding sites emerged from previous SELEX (systematic evolution of ligands by exponential enrichment) analysis, one of which was the expected ^{3}TTAGGGTTAG^{12} (OB1^{DNA} and OB2^{DNA}) site (Fig. 1B, Class I) (*24*). A second class contained OB1^{DNA}, an upstream tri-K ("K" indicates a G or T nucleotide), and a seemingly non-telomeric (NT) sequence implicated in binding to OB1 (consensus: CTCCAGCAG*GGG*^{3}TTAG (Fig. 1B, Class II) (*24*). Junction binding suspected on the basis of the observation that the tri-K *GGG* motif corresponds to the telomeric repeat sequence upstream of OB1^{DNA}, and NT sequences in the Class II hits could fold into a hairpin (hp) containing a 2-base-pair (bp) stem $^{-1}$GG^{0}/$^{-6}$CC^{-7} and a variable tetraloop (positions −5 to −2) (Fig. 1B and fig. S1, A and B). In this interpretation, G^{0} and C^{-7} represent the first base pair at the ds-ss junction (with C^{-7} corresponding to the 5′ end of the mammalian chromosome), and the 3′ overhang initiates in the GGTTAG register (Fig. 1, A and B, and fig. S1, A and B). We conducted a quantitative electrophoretic mobility shift assay (EMSA) with purified hPOT1 DBD (hDBD) (fig. S2A) and a 5′-^{32}P–labeled hp oligonucleotide derived from the Class II consensus terminating in a C at the 5′ end and containing a 3′ overhang of sequence ^{1}GGTTAGGG^{8} (hp-ss$^{1-8}$) (Fig. 1C). The absence of OB2^{DNA} from the Class II consensus attenuates the affinity of hDBD for ssDNA (*7*), allowing us to assess DNA affinity of POT1 for the ds-ss junction. hDBD bound strongly to hp-ss$^{1-8}$ [dissociation constant (K_d) = 2.6 ± 0.3 nanomolar (nM)] but not to a similar target (no_hp-ss$^{1-8}$) that lacks the ability to form a hairpin (Fig. 1, C and D). The natural telomeric ds-ss junction ends in a 5′-phosphate (5′-P), which has been previously exploited to determine the 5′-terminal nt of chromosomes by using DNA ligase-mediated methods (*25*). To test the importance of this phosphate in binding hPOT1, we performed a competition experiment mixing 5′-^{32}P-hp-ss$^{1-8}$ with either nonradiolabeled 5′-phosphorylated hp-ss$^{1-8}$ or 5′-OH-hp-ss$^{1-8}$ before binding to hDBD. The 5′-P was required to effectively outcompete POT1 binding to the radiolabeled DNA (Fig. 1E). The absence of a 5′-P at the DNA junction in past in vitro studies may have prevented the detection of this previously unappreciated POT1 DNA-binding activity (*17*, *26*–*29*). POT1 bound to a telomeric ds-ss junction in vivo is poised to engage both OB1^{DNA} and OB2^{DNA}. Extension of the overhang of the hp to include OB2^{DNA} (hp-ss$^{1-12}$) resulted in a higher affinity for hDBD [K_d = 70 picomolar (pM)] (Fig. 1, C and F) compared with either ss$^{1-12}$ (K_d = 190 pM) (Fig. 1C and fig. S2B) or hp-ss$^{1-8}$ (Fig. 1, C and D). We confirmed that a heterodimer of full-length hPOT1 and shelterin partner TINT1-PTOP-PIP1 (TPP1) (by using the TPP1N truncation construct), which approximates the context of hPOT1 coating the ss overhang in vivo (*30*, *31*), exhibited robust binding to 5′-P-hp-ss$^{1-12}$ (Fig. 1G). DBD bound a two-stranded DNA (duplex reinforced with 30 bp of arbitrary, nontelomeric sequence) terminating in 5 bp of native ds telomeric junction sequence and an 8-nt overhang (long_ds-ss$^{1-8}$) with an affinity that was approximately one order of magnitude greater than observed with hp-ss$^{1-8}$, likely

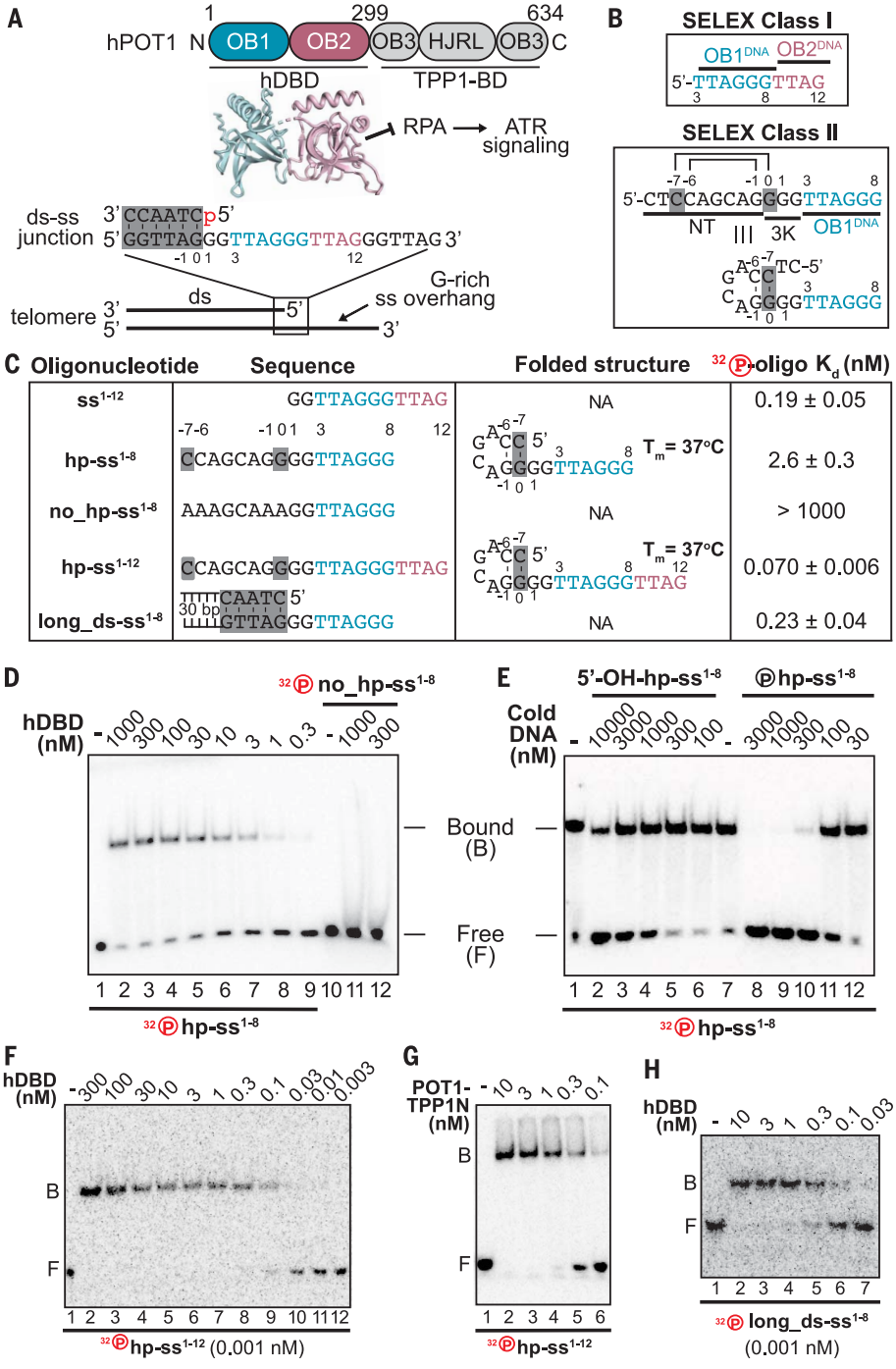

Fig. 1. Human POT1 recognizes the 5′-phosphorylated ds-ss junction of telomeres. (**A**) (Top) Schematic of hPOT1 includes binding domains for ssDNA (hDBD) and TPP1 (TPP1-BD). hDBD (PDB: 1XJV) is composed of OB1 and OB2. The current model suggests that POT1 outcompetes the ssDNA-binding RPA complex to prevent ATR signaling at telomeres. HJRL, Holliday junction resolvase-like. (Bottom) Mammalian chromosomes end in a ds-ss junction containing ATC-5′ (predominantly) and a ss G-rich overhang. Numbering starts with the first overhang nucleotide. (**B**) A previous SELEX study revealed two hPOT1-binding DNA classes (*24*). Class I harbors the known sites for OB1 and OB2, denoted as $OB1^{DNA}$ (cyan) and $OB2^{DNA}$ (pink), respectively. Class II revealed a consensus containing a seemingly nontelomeric (NT) sequence upstream of $OB1^{DNA}$ that can potentially fold into a hp; "K" indicates a G or T nucleotide, and the shaded area indicates the sequence of the first bp at the telomeric ds-ss junction. (**C**) Annotated name, sequence, predicted hp structure [with T_m (where T_m is the temperature at which 50% of dsDNA is denatured) calculated by the UNAFold web server], and mean K_d and SD (of binding to hDBD) of the oligonucleotides used in EMSA analysis. NA indicates not applicable. (**D** to **H**) EMSA of indicated proteins (hDBD or POT1-TPP1N heterodimer) and 5′-^{32}P–labeled DNA oligonucleotides. (D), (F), (G), and (H) indicate direct binding experiments, and (E) indicates a competition experiment. In (D), 0.1 nM 5′-^{32}P-hp-ss$^{1-8}$ was used; the number of experimental replicates n = 5 for hp-ss$^{1-8}$ (full and partial titrations); n = 3 for no_hp-ss$^{1-8}$. In (E), 100 nM hDBD and 0.1 nM 5′-^{32}P–labeled hp-ss$^{1-8}$ were incubated with indicated amounts of unlabeled hp-ss$^{1-8}$ (cold DNA) containing either a 5′-OH or a 5′-P; n = 3. In (F), 0.001 nM 5′-^{32}P-hp-ss$^{1-12}$ was used; n = 3. In (G), 0.01 nM 5′-^{32}P-hp-ss$^{1-12}$ was used; n = 3. (H) 0.001 nM 5′-^{32}P-long_ds-ss$^{1-8}$ was used; n = 3. Circled red "P" indicates radiolabeled; circled black "P" indicates nonradiolabeled. Bound (B) indicates DNA bound to protein; Free (F) indicates free, unbound DNA.

reflecting the greater stability of the more physiologically representative duplex DNA versus that of the hp (Fig. 1, C and H). Our data demonstrate that the telomeric ds-ss junction is a previously unappreciated high-affinity binding site for hPOT1.

High-resolution structures reveal how human POT1 caps the phosphorylated 5′ end of a telomeric junction

To determine the structural basis for hPOT1's telomeric ds-ss junction–binding activity, we formed complexes of hDBD with two substrates that mimic the telomeric ds-ss junction—5′-P-ds-ss$^{1-12}$ (DNA containing a 5-bp arbitrary, nontelomeric tether upstream of GTTAG/CAATC-5′-P native telomeric ds sequence extending into a 12-nt 3′ overhang) (fig. S2, C and D) and 5′-P-hp-ss$^{1-12}$ (Fig. 1C)—and solved their structures using x-ray crystallography (Fig. 2, A and B). The hDBD-bound 5′-P-ds-ss$^{1-12}$ and 5′-P-hp-ss$^{1-12}$ structures were solved to 2.60- and 2.16-Å resolution, respectively (table S1). Both structures are similar to each other (fig. S3D) and recapitulate the previously reported hDBD-ss DNA-binding interface with minor differences (fig. S3, A to C, and E to J) (*7*). These structures reveal how hPOT1 binds the phosphorylated 5′ end of the telomeric ds-ss junction (Fig. 2). An electropositive pocket of four amino acids (Y9, R80, H82, and R83) in the hPOT1 OB1 domain that we name the "POT-hole" caps the 5′-P-cytidine nucleotide by means of a network of stacking and electrostatic interactions (Fig. 2, D to F, and fig. S4A). R83 acts as the linchpin by forming an ionic interaction with the 5′-P,

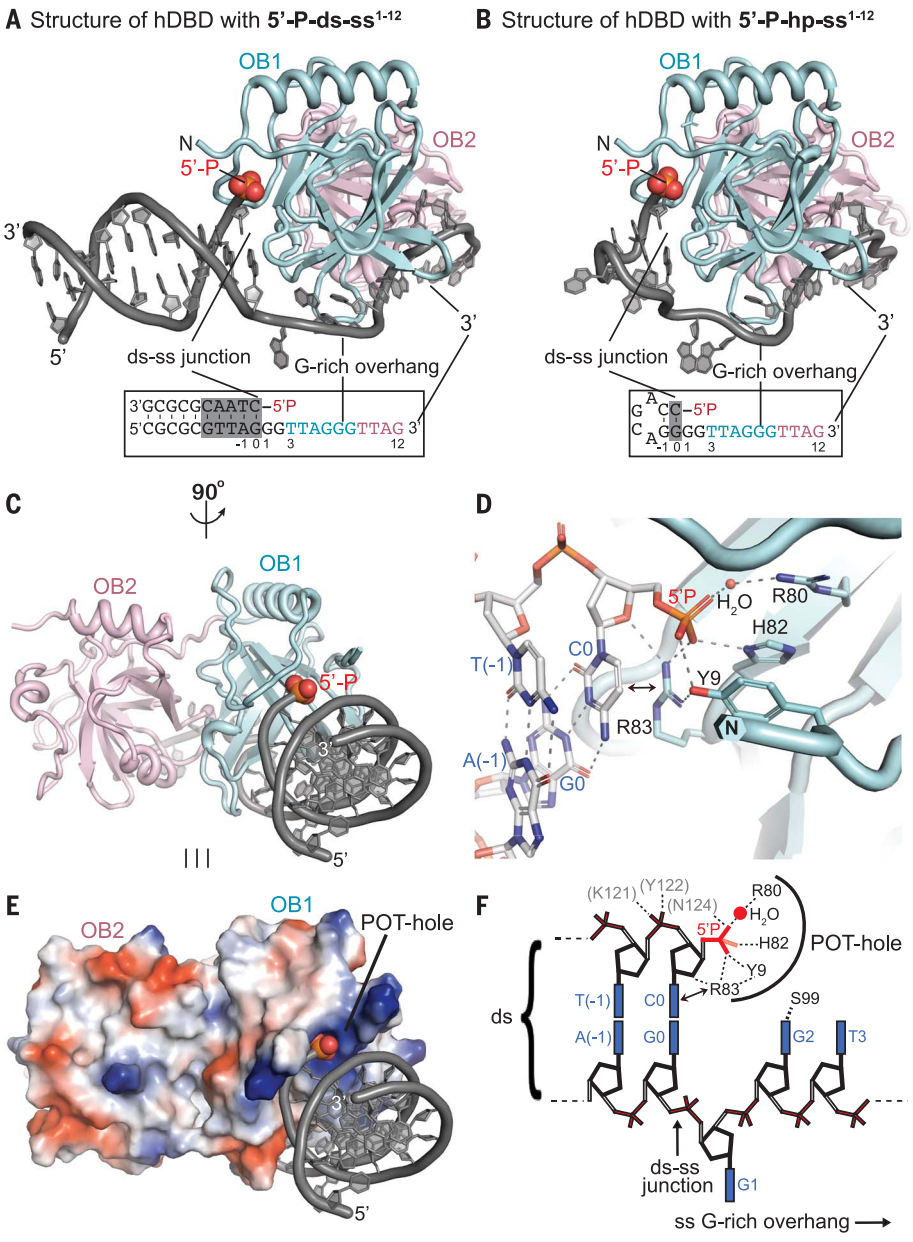

Fig. 2. Structural basis of telomeric junction 5′-end protection by human POT1. (**A** and **B**) Cartoon representation of high-resolution crystal structures of complexes of (A) hDBD with 5′-P-ds-ss$^{1\text{-}12}$ and (B) 5′-P-hp-ss$^{1\text{-}12}$, showing OB1 (cyan) and OB2 (pink) bound to DNA [gray, with the exception of the 5′-P, whose atoms are shown as spheres and in Corey-Pauling-Koltun (CPK) coloring]. A boxed schematic of the DNA is shown below the structure, with the ds sequence found naturally at the telomeric ds-ss junction shaded gray, the 5′-P in red, and residues in the G-rich 3′ overhang colored to indicate binding by OB1 and OB2, respectively. (**C**) Cartoon and (**E**) electrostatic surface (blue is electropositive and red is electronegative) representations of the hDBD-5′-P-ds-ss$^{1\text{-}12}$ structure shown in a view orthogonal to that in (A). The 5′-P occupies a pocket in POT1 that is complementary in shape and charge. Single-letter abbreviations for the amino acid residues are as follows: H, His; R, Arg; and Y, Tyr. (**D**) The POT-hole-DNA interface within the hDBD-5′-P-hp-ss$^{1\text{-}12}$ structure is shown with POT-hole side chains (carbon in cyan) and the nucleotides (carbon in light gray) near the junction shown as sticks. A water molecule bridging hPOT1 R80 to the 5′-P is shown as an orange sphere. The dashed lines indicate H-bonds and ionic interactions, the double-headed arrow indicates stacking of the hPOT1 R83 side chain with the 5′-C at the junction (numbered C0), and N indicates the N terminus of hDBD resolved in the crystal structure. (**F**) Interaction map of hDBD with the ds-ss junction.

stacking against the 5′-cytosine base, and forming hydrogen bonds (H-bonds) with the ribose-ring oxygen of the 5′-cytidine nucleoside (5′-C) (Fig. 2, D and F, and fig. S4A). R83 also forms an H-bond with Y9, which along with H82 interacts with the 5′-P. R80 forms a water-mediated H-bond with the 5′-P. We observed that the POT-hole is not optimally sized to accommodate a bulkier adenine (purine instead of a pyrimidine) or thymine (methyl group on the base) at the 5′ end because of steric clashes (fig. S5, A to C). Furthermore, the fixed distance between the POT-hole and the ssDNA-binding region of hPOT1 dictates the preference for the naturally occurring ATC-5′ versus alternative 5′-C iterations: ATCC-5′ and ATCCC-5′ (fig. S5D).

In addition to interactions involving the POT-hole, junction recognition is fortified by contacts made by the backbone amides of hPOT1 amino acids 121 to 124 with the phosphodiester group penultimate to the 5′-C (Fig. 2F and fig. S4B), as well as S99 with G^2 (Fig. 2F and fig. S3, K and L). These data provide the structural basis for binding of the telomeric ds-ss junction by hPOT1.

The POT-hole dictates telomeric DNA junction binding and inhibits DDR at telomeres

We evaluated the importance of the POT-hole in binding the telomeric ds-ss junction in vitro using purified hDBD variants with alanine mutations at Y9, R80, H82, and R83 (fig. S6A). We also engineered an R83E charge-reversal mutant to test the importance of the ionic R83-5′-P interaction. Alanine substitution of F62, a residue in hPOT1 OB1 that is indispensable for binding telomeric ssDNA (*32*), was included as a control to disrupt binding to both ssDNA and the ds-ss junction. In agreement with the structural data, little to no DNA binding was observed for any POT-hole mutant with the 5′-P-hp-ss$^{1\text{-}8}$, even at concentrations 100-fold greater than the K_d with wild-type (WT) hDBD (Fig. 3A, left). By contrast, POT-hole mutants bound 5′-P-ss$^{1\text{-}12}$ with an affinity similar to that of wild type (Fig. 3A, right, and fig S6, B and C). F62A failed to bind either oligonucleotide, which is consistent with binding to OB1^{DNA}

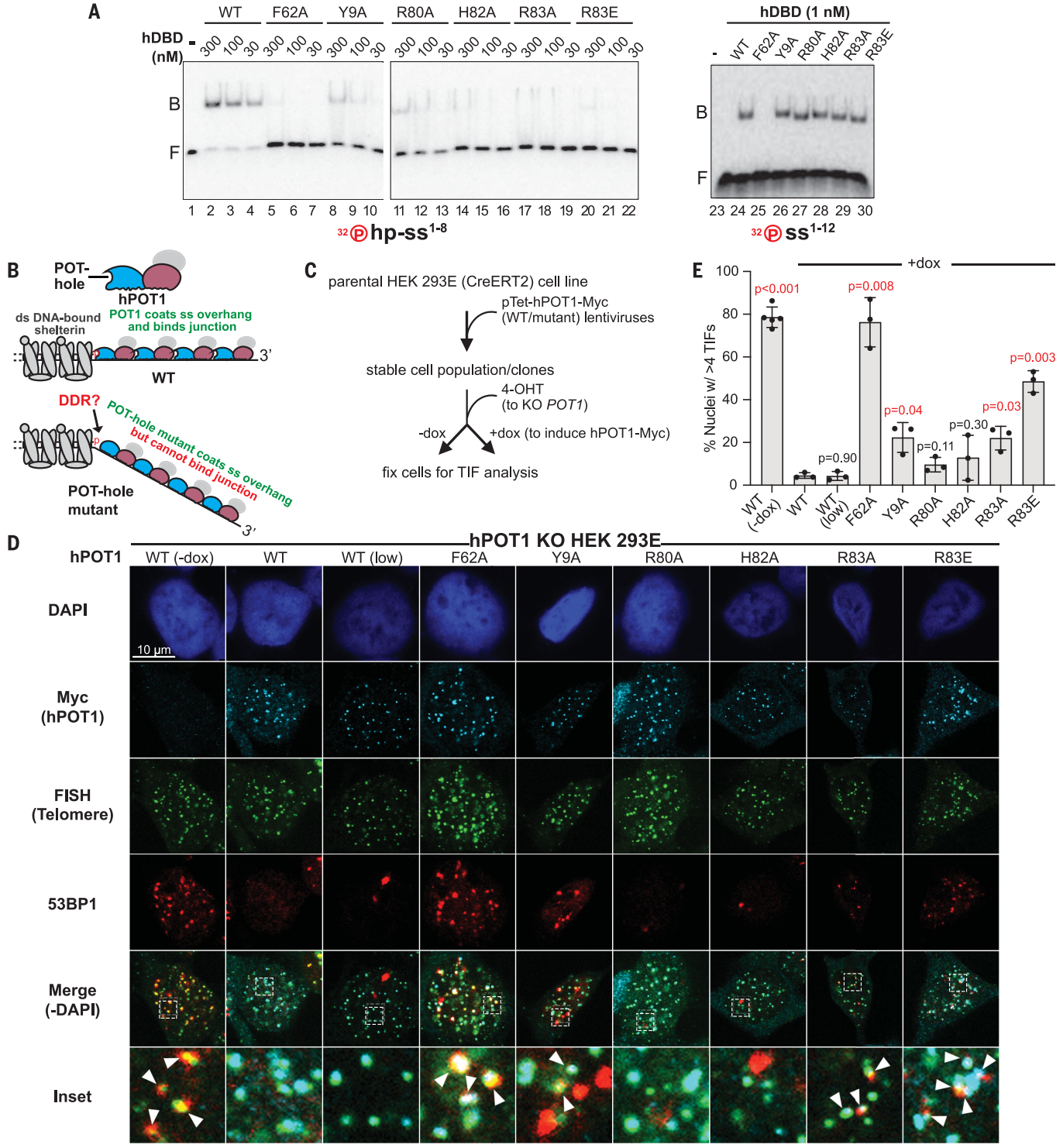

Fig. 3. Separation-of-function POT-hole mutations abrogate ds-ss DNA junction binding in vitro and result in a DDR at human telomeres. (**A**) EMSA to detect direct binding of WT or indicated mutant hDBD constructs with 5′-^{32}P-hp-ss$^{1-8}$ (0.1 nM; lanes 1 to 22) and 5′-^{32}P-ss$^{1-12}$ (0.1 nM; lanes 23 to 30); *n* = 3. (**B**) Schematic conveying how POT-hole mutations would disrupt binding to the ds-ss junction but not coating of the ss overhang by POT1. (**C**) Scheme for deletion of endogenous *POT1* and complementation with lentivirally transduced hPOT1-Myc to assess the ability of mutants to suppress TIF formation in a HEK 293E–based cell line (*34*). (**D**) TIF analysis of cell lines after 4-OHT and dox (1000 ng/ml; 25 ng/ml in "low dox" wild type) treatment as described in (C) performed with peptide nucleic acid fluorescent in situ hybridization (PNA-FISH) for telomeres (green) and immunofluorescence (IF) for Myc (hPOT1; cyan) and 53BP1 (red). 4′,6-diamidino-2-phenylindole (DAPI) was used to stain the nucleus (blue). Overlap of the telomeric and 53BP1 foci (and Myc foci, if applicable) in the "Merge" panel indicates TIFs. (Inset) Magnified view of the boxed area within the image; arrowheads indicate TIFs. (**E**) Quantitation of TIF data of which (D) is representative. Mean and SD (*n* = 3 for all conditions except WT −dox, for which *n* = 5; each +dox set containing >75 nuclei and each −dox set containing >50 nuclei) for TIFs are plotted for the indicated cell lines. *P* values calculated with a two-tailed Student's *t* test for comparisons against WT +dox data are indicated above the bars.

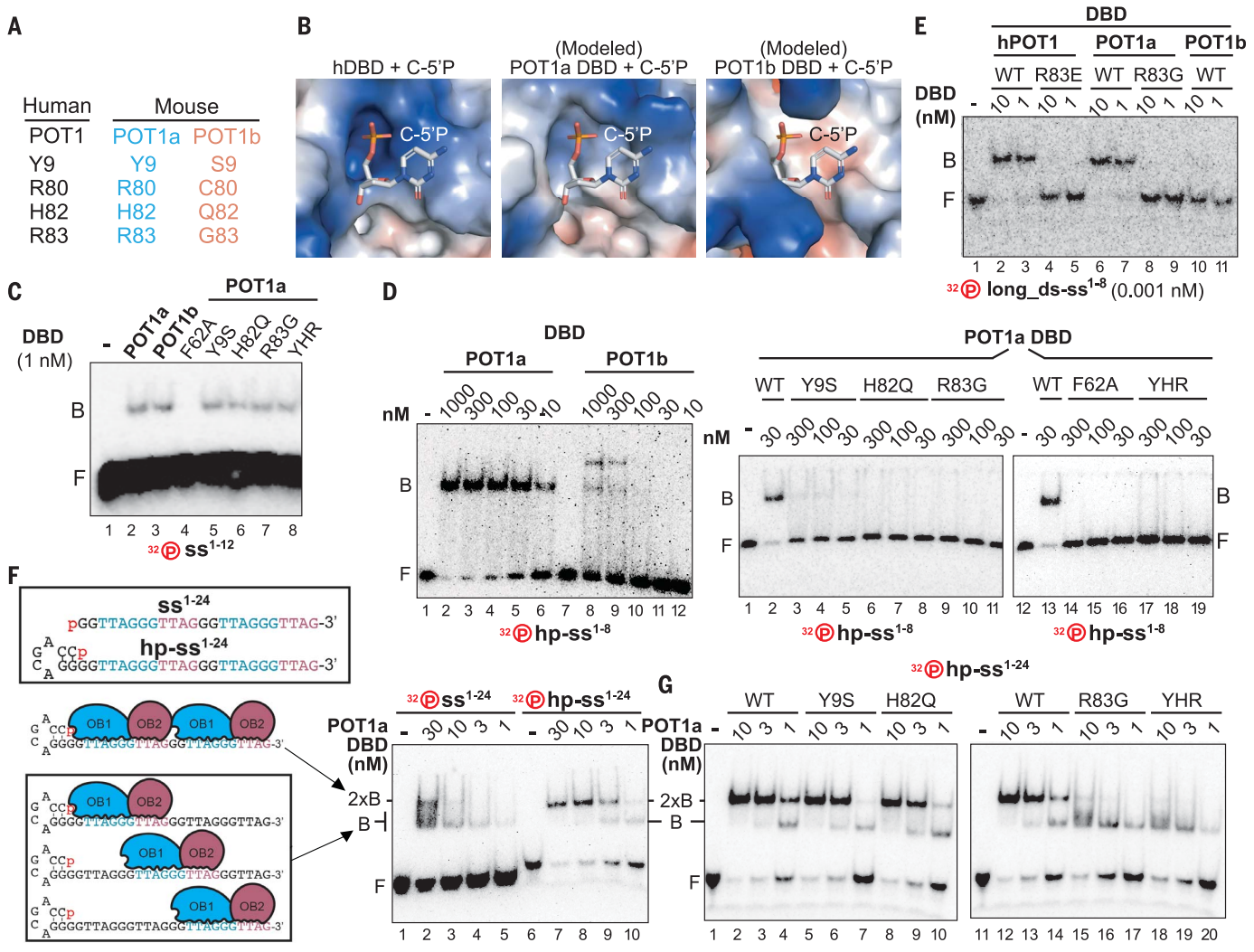

Fig. 4. Presence of the POT-hole dictates POT1 paralog choice for chromosome-end protection in mice. (**A**) Human POT-hole residues are conserved in mouse POT1a but not mouse POT1b. (**B**) Electrostatic surface comparisons of hDBD (from hDBD-5′-P-ds-ss$^{1\text{-}12}$ structure) and POT1a and POT1b DBD (Alphafold models), with the phosphorylated 5′-C of the hDBD-bound structure shown in sticks. (**C** and **D**) EMSA analysis of indicated mouse POT1a and POT1b DBD constructs with the indicated 5′-^{32}P–labeled oligonucleotides [0.1 nM for (C) and (D), right; 0.01 nM for (D), left]; *n* = 3. (**E**) EMSA analysis of indicated human and mouse POT1 DBD constructs with 0.001 nM 5′-^{32}P-long_ds-ss$^{1\text{-}8}$ two-stranded DNA; *n* = 3. (**F**) (Top left) Names and sequences of the two DNA oligonucleotides, hp-ss$^{1\text{-}24}$ and ss$^{1\text{-}24}$, used to evaluate 5′-end–binding preference. Both DNAs were labeled at the 5′ end with ^{32}P for EMSA analysis. (Bottom left) Three possible DNA-binding registers for the first DBD molecule are shown with the center-binding register precluding the binding of a second DBD molecule. (Right) EMSA analysis of POT1a DBD with hp-ss$^{1\text{-}24}$ (discrete slow-migrating band with increasing concentrations of protein; 2×B) and ss$^{1\text{-}24}$ (smeary band; mixture of B and 2×B), DNA at 0.1 nM; *n* = 3. (**G**) EMSA analysis of indicated POT1a DBD constructs with 0.1 nM hp-ss$^{1\text{-}24}$. YHR, triple mutant Y9S-H82Q-R83G; *n* = 3.

being critical for both DNA-binding modes. These data highlight the importance of the POT-hole in 5′-end binding and provide separation-of-function mutants to test the importance of hPOT1's junction-binding activity in cells (Fig. 3B).

Loss of POT1 binding at the 3′ overhang results in telomere dysfunction–induced foci (TIF), which signify the recognition of telomeres by the DDR machinery (*33*). To determine the biological importance of the POT-hole binding to the telomeric junction, we used a previously described cell line in which POT1 can be deleted in an inducible fashion (*POT1* KO) (*34*) to test the ability of transduced WT and mutant hPOT1 Myc-tagged constructs to compensate for the loss of endogenous POT1 (materials and methods). Transduced cells were treated first with 4-OHT to delete *POT1* and then either treated with doxycycline (dox) to induce exogenous hPOT1 expression ("+dox") or left untreated ("−dox") (Fig. 3C). In the absence of dox, 4-OHT treatment resulted in a robust TIF phenotype, characterized by colocalization of the DDR factor 53BP1 at telomeres (fig. S6, E and F). hPOT1 wild type and "low dox" wild type, but not hPOT1 F62A, suppressed TIFs (Fig. 3, D and E). POT-hole mutants Y9A, R83A, and R83E were defective in TIF suppression compared with wild type, with R83E being the most deleterious (Fig. 3, D and E). This trend emphasizes the importance of the ionic interaction between R83 and the 5′-P. Clones isolated from 6X-Myc–tagged hPOT1 WT, F62A, and R83E cell populations also recapitulated the TIF phenotypes (fig. S7, A to D). Furthermore, TIFs were smaller (Fig. 3D, inset) and less frequent (Fig. 3, D and E) in POT-hole mutant cells compared with those in F62A

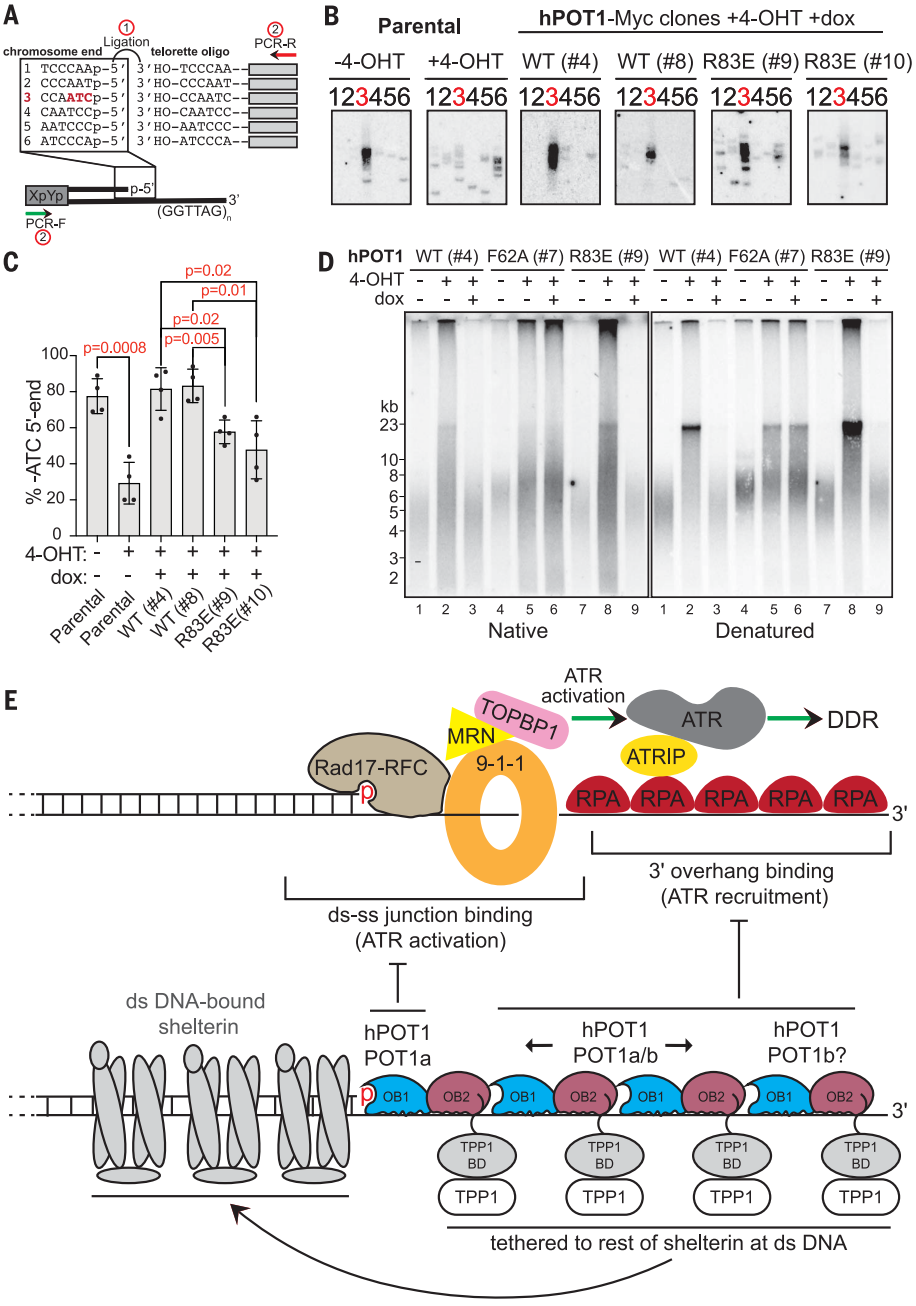

Fig. 5. Maintenance of the ATC-5′ end of chromosomes by the POT-hole. (**A**) Schematic of the modified STELA technique for determining the chromosomal 5′-terminal nucleotide in human cell lines. Step 1: DNA ligation of genomic DNA 5′-P ends with telorettes ending in each of the six possible repeat registers at the 3′-OH ends. Step 2: PCR amplification of the ligation products performed with a forward primer (PCR-F) targeting the subtelomere of chromosome XpYp and a reverse primer (PCR-R) targeting a sequence shared by all telorettes. The products are visualized with Southern blot analysis performed with a 5′-^{32}P–labeled XpYpB2 reverse primer. (**B**) STELA-based determination of the chromosomal 5′-terminal nucleotide in the HEK 293E–based *POT1* KO parental cell line (−4-OHT and +4-OHT) and hPOT1-Myc WT– or R83E-complemented clonal cell lines treated with both 4-OHT and dox. (**C**) Quantitation of ATC-5′ preference calculated as the ratio of the total band intensity in the primer 3 lane over the total intensity over all six lanes. Mean and SD for $n = 4$ replicates of which B is representative are plotted. *P* values were calculated with a two-tailed Student's *t* test for comparisons against parental −4-OHT data (for parental +4-OHT) or hPOT1-Myc WT clones (for hPOT1-Myc R83E clones). (**D**) (Left) TRF analysis of cell lines used in (B) performed first under native conditions with a 5′-^{32}P–labeled telomeric C-probe $(CTAACC)_4$ to detect the ss G-rich overhang. (Right) TRF analysis after denaturing the DNA on the same gel and reprobing it to detect the total telomeric DNA signal; $n = 1$. (**E**) Model for ATR inhibition at telomeres by POT1. The ssDNA-binding of hPOT1 prevents the loading of RPA to curb ATR recruitment to the 3′ overhang. Protection of the ds-ss junction by hPOT1 prevents loading of the 9-1-1/Rad17-RFC clamp and clamp-loader complex and ATR activator TOPBP1. In mice, both POT1 paralogs coat the ss overhang, but only POT1a protects the ds-ss junction. The shelterin proteins protecting the telomeric dsDNA are expected to keep POT1-TPP1 tethered to the ss overhang, facilitated by protein-protein interactions and the conformational flexibility within the proteins (*29*) and the telomeric DNA.

cells. This finding suggests that both junction- and ssDNA-binding activities of hPOT1 must be compromised to trigger a full DDR (see Discussion). Our results demonstrate that junction binding, which should involve a single POT1 molecule per chromosome end (Fig. 3B), is critical for chromosome-end protection.

The POT-hole differentiates mouse POT1 paralogs and enables POT1a to protect the telomeric junction

Despite being strictly conserved in other mammalian POT1 homologs, including mouse POT1a, each of the four POT-hole amino acids is replaced with a structurally disparate residue in mouse POT1b (Fig. 4A and fig. S8A). By contrast, the residues used in ss DNA binding are conserved in all mammalian POT1 homologs, including POT1b (fig. S8A). Aligning Alphafold predictions (*35*) of POT1a and POT1b DBDs with the junction-bound structure of hDBD illustrates that the shape and electropositive nature of the POT-hole are predicted to be lost in POT1b (Fig. 4B and fig. S8, B and C). We hypothesized that POT1a, but not POT1b, protects the 5′ end at the junction. Indeed, POT1a- and POT1b-DBD proteins bound ss[1-12], but only POT1a DBD engaged a telomeric ds-ss junction with high affinity (Fig. 4, C to E, and fig. S8, D and E). POT1a replaced with POT1b residues in the POT-hole (except R80; fig. S8F legend explains rationale) retained affinity toward ss[1-12] (Fig. 4C) but failed to bind the junction (Fig. 4D, right, and E, and fig. S8D).

To measure junction-binding in the presence of multiple ss DNA-binding sites, we developed an EMSA-based "POT1 packing" assay with two DNA targets, each containing four telomeric ss repeats (24 nt) spanning three possible

POT1-binding registers. The 5′ and 3′ registers are compatible with the packing of two POT1 molecules, whereas binding to a central register precludes the loading of a second POT1 (Fig. 4F, left). hp-ss$^{1\text{-}24}$ includes a ds-ss junction upstream of this ss region, whereas ss$^{1\text{-}24}$ does not. A fully packed 2:1 DBD-DNA complex would produce a sharp, slow-migrating band at higher DBD concentrations, whereas a mix of 2:1 and 1:1 complexes (of various binding registers) would generate a smear. POT1a DBD binding resulted in a sharp band for hp-ss$^{1\text{-}24}$ but not ss$^{1\text{-}24}$, suggesting that the protein packs preferentially against a ds-ss junction but that there is no end-binding bias to dissuade it from binding to the central site of ss$^{1\text{-}24}$ (Fig. 4F, right). POT1a POT-hole mutants R83G and triple mutant YHR lost the ability to pack at the junction (Fig. 4G), which is consistent with R83 capping the 5′ terminus (Fig. 2, D and F) and repressing TIFs (Fig. 3, D and E). hDBD and mouse POT1b DBD formed a discrete complex with not only hp-ss$^{1\text{-}24}$ but also ss$^{1\text{-}24}$, which is consistent with a 3′-end–binding preference (fig. S9, A and B) (*7*). Our results demonstrate that the POT-hole allows POT1a to preferentially bind the telomeric junction.

The POT-hole helps maintain the 5′-end identity of human chromosomes

Consistent with the structures we solved, the POT-hole of hDBD and mouse POT1a DBD protect the 5′-P end from 5′ exonucleolytic action in vitro (fig. S10, A to F). We next asked whether the POT-hole helps maintain the 5′-terminal sequence of the chromosomes in cells. We used a modified single telomere length analysis (STELA) approach that uses ligation-mediated polymerase chain reaction (PCR) amplification to determine the abundance of each of the six possible chromosomal 5′-end permutations (Fig. 5A) (*23*). Genomic DNA extracted from the parental human embryonic kidney (HEK) 293E cell line displayed the expected ATC-5′ preference that is lost after *POT1* deletion (Fig. 5, B and C). WT hPOT1, but not R83E hPOT1, was able to restore the ATC-5′ bias to untreated (parental –4-OHT) levels, demonstrating that the POT-hole helps maintain the 5′ end of the human chromosome (Fig. 5, B and C, and fig. S10G). The 5′-end scrambling of hPOT1 R83E was less severe than that of *POT1* KO. This difference may be explained by the unleashing of 5′ exonuclease activity at telomeres completely devoid of POT1 (*36*). Terminal restriction fragment (TRF) analysis reproduced previously characterized phenotypes (*15*, *34*, *37*), including the accumulation of slow-migrating species (denatured and native blots) and an increase in the G-rich ss signal (native blot) upon *POT1* deletion, which were suppressed by expression of hPOT1 wild type but not F62A (Fig. 5D and fig. S10H). R83E recapitulated the WT phenotypes, suggesting that the end-protection function of the POT-hole is separable from hPOT1's role in bulk-telomere or overhang-length maintenance. Thus, the POT-hole helps maintain ATC-5′ ends without acutely influencing telomere length.

Discussion

The major pathway of ATR activation requires RPA binding to exposed ssDNA and recognition of the ds-ss junction by the 9-1-1/Rad17-RFC (RAD9–RAD1–HUS1/Rad17-RFC2–RFC3–RFC4–RFC5) clamp and clamp loader, which with the MRN (MRE11-RAD50-NBS1) complex recruit TOPBP1 (DNA topoisomerase 2-binding protein 1) to activate ATR (Fig. 5E) (*4*, *38*). The structure of human 9-1-1/Rad17-RFC bound to a ds-ss junction revealed a basic pocket in Rad17 that is poised to bind the 5′-phosphorylated end of a junction by using a mechanism similar to that of POT1 (fig. S11, A and B) (*39*). Consistent with a competition between POT1 and 9-1-1/Rad17-RFC in binding the ds-ss junction, subunits of the 9-1-1 and MRN complexes, as well as TOPBP1, are enriched at telomeres in the absence of hPOT1 (*34*). We therefore propose that POT1 not only outcompetes RPA at the telomeric ss overhang but also prevents ATR activation by denying 9-1-1/Rad17-RFC access to the telomeric ds-ss junction (Fig. 5E).

The duplication of POT1 (*40*), the conservation of the POT-hole in POT1a (fig. S12A), the disruption of the POT1-hole in POT1b (fig. S12B), and the retention of CTC1-STN1-TEN1 (CST)–binding motifs in POT1b (*40*) within the Muridae and Cricetidae families of the Rodentia order provide support to the hypothesis that POT1b relinquished junction binding to facilitate processes at the 3′ end. We propose that POT1a wards off 9-1-1/Rad17-RFC at the junction, although both POT1a and POT1b paralogs could counter RPA at the overhang in mouse cells (Fig. 5E).

The POT-hole is conserved in species distant to mammals, such as *Sterkiella nova* and *Caenorhabditis elegans* (fig. S13A). The precisely defined *S. nova* macronuclear telomere contains a 5′-C at the ds-ss junction and a 16-nt overhang that binds one telomere end–binding protein (TEBP)α/β complex (homologous to the POT1-TPP1 complex) (*41*). TEBPα has been crystallized with a sulfate ion bound in a manner indistinguishable from how the 5′-P binds hDBD in our junction-bound structures (fig. S13B) (*42*). Indeed, like hPOT1, TEBPα binds the telomeric ds-ss junction more strongly than it binds telomeric ssDNA (*8*). These observations point to a single TEBPα/β complex simultaneously protecting the 5′ and 3′ ends of the chromosome (*8*, *41*, *42*). *Schizosaccharomyces pombe*, in which a POT-hole is not obvious (fig. S13, A and C) (*5*, *43*), and eukaryotes whose chromosomes do not end in a 5′-C, must have evolved alternative approaches for junction protection.

We updated the model for how telomeres avert detection by the DDR machinery to include a critical role of POT1 in binding the telomeric ds-ss junction. Thus, POT1 protects both DNA strands at human chromosome ends by coating the G-rich ss overhang and recognizing the phosphorylated 5′ end of the C-rich strand.

REFERENCES AND NOTES

1. W. Palm, T. de Lange, *Annu. Rev. Genet.* **42**, 301–334 (2008).
2. E. L. Denchi, T. de Lange, *Nature* **448**, 1068–1071 (2007).
3. T. de Lange, *Annu. Rev. Genet.* **52**, 223–247 (2018).
4. J. C. Saldivar, D. Cortez, K. A. Cimprich, *Nat. Rev. Mol. Cell Biol.* **18**, 622–636 (2017).
5. P. Baumann, T. R. Cech, *Science* **292**, 1171–1175 (2001).
6. Y. Gong, T. de Lange, *Mol. Cell* **40**, 377–387 (2010).
7. M. Lei, E. R. Podell, T. R. Cech, *Nat. Struct. Mol. Biol.* **11**, 1223–1229 (2004).
8. D. E. Gottschling, V. A. Zakian, *Cell* **47**, 195–205 (1986).
9. C. M. Price, T. R. Cech, *Genes Dev.* **1**, 783–793 (1987).
10. M. P. Horvath, V. L. Schweiker, J. M. Bevilacqua, J. A. Ruggles, S. C. Schultz, *Cell* **95**, 963–974 (1998).
11. C. I. Nugent, T. R. Hughes, N. F. Lue, V. Lundblad, *Science* **274**, 249–252 (1996).
12. J. J. Lin, V. A. Zakian, *Proc. Natl. Acad. Sci. U.S.A.* **93**, 13760–13765 (1996).
13. M. Raices *et al*., *Cell* **132**, 745–757 (2008).
14. L. Wu *et al*., *Cell* **126**, 49–62 (2006).
15. D. Hockemeyer, J. P. Daniels, H. Takai, T. de Lange, *Cell* **126**, 63–77 (2006).
16. K. Kratz, T. de Lange, *J. Biol. Chem.* **293**, 14384–14392 (2018).
17. W. Palm, D. Hockemeyer, T. Kibe, T. de Lange, *Mol. Cell. Biol.* **29**, 471–482 (2009).
18. P. Gu *et al*., *Nat. Commun.* **12**, 5514 (2021).
19. L. Y. Chen, S. Redon, J. Lingner, *Nature* **488**, 540–544 (2012).
20. P. Wu, H. Takai, T. de Lange, *Cell* **150**, 39–52 (2012).
21. M. Wan, J. Qin, Z. Songyang, D. Liu, *J. Biol. Chem.* **284**, 26725–26731 (2009).
22. D. Hockemeyer, A. J. Sfeir, J. W. Shay, W. E. Wright, T. de Lange, *EMBO J.* **24**, 2667–2678 (2005).
23. A. J. Sfeir, W. Chai, J. W. Shay, W. E. Wright, *Mol. Cell* **18**, 131–138 (2005).
24. K. H. Choi *et al*., *Biochimie* **115**, 17–27 (2015).
25. D. M. Baird, J. Rowson, D. Wynford-Thomas, D. Kipling, *Nat. Genet.* **33**, 203–207 (2003).
26. C. J. Lim, A. J. Zaug, H. J. Kim, T. R. Cech, *Nat. Commun.* **8**, 1075 (2017).
27. T. Paul, W. Liou, X. Cai, P. L. Opresko, S. Myong, *Nucleic Acids Res.* **49**, 12377–12393 (2021).
28. S. Ray, J. N. Bandaria, M. H. Qureshi, A. Yildiz, H. Balci, *Proc. Natl. Acad. Sci. U.S.A.* **111**, 2990–2995 (2014).
29. J. C. Zinder *et al*., *Proc. Natl. Acad. Sci. U.S.A.* **119**, e2201662119 (2022).
30. F. Wang *et al*., *Nature* **445**, 506–510 (2007).
31. J. Nandakumar *et al*., *Nature* **492**, 285–289 (2012).
32. H. He *et al*., *EMBO J.* **25**, 5180–5190 (2006).
33. H. Takai, A. Smogorzewska, T. de Lange, *Curr. Biol.* **13**, 1549–1556 (2003).
34. G. Glousker, A. S. Briod, M. Quadroni, J. Lingner, *EMBO J.* **39**, e104500 (2020).
35. J. Jumper *et al*., *Nature* **596**, 583–589 (2021).
36. T. Kibe, M. Zimmermann, T. de Lange, *Mol. Cell* **61**, 236–246 (2016).
37. D. Loayza, T. De Lange, *Nature* **423**, 1013–1018 (2003).
38. C. A. MacDougall, T. S. Byun, C. Van, M. C. Yee, K. A. Cimprich, *Genes Dev.* **21**, 898–903 (2007).
39. M. Day, A. W. Oliver, L. H. Pearl, *Nucleic Acids Res.* **50**, 8279–8289 (2022).
40. L. R. Myler *et al*., *Genes Dev.* **35**, 1625–1641 (2021).
41. L. A. Klobutcher, M. T. Swanton, P. Donini, D. M. Prescott, *Proc. Natl. Acad. Sci. U.S.A.* **78**, 3015–3019 (1981).
42. S. Classen, J. A. Ruggles, S. C. Schultz, *J. Mol. Biol.* **314**, 1113–1125 (2001).
43. M. Lei, E. R. Podell, P. Baumann, T. R. Cech, *Nature* **426**, 198–203 (2003).

ACKNOWLEDGMENTS

We thank S. Padmanaban (Nandakumar laboratory) for input on the design of the cell-based experiments; G. Glousker and J. Lingner [Ecole Polytechnique Fédérale de Lausanne (EPFL),

Switzerland] for graciously gifting the *POT1*-inducible KO HEK 293E cell line and the pCW22_TREtight_MCS_UBC_rtTA_IRES_Blast lentiviral vector for dox-inducible expression and for sharing detailed protocols and troubleshooting tips for these resources; J. Schmidt (Michigan State University, USA) for the 53BP1 antibody; the beamline staff at the Life Sciences Collaborative Access Team (LS-CAT) beamline of the Argonne National Laboratory for help with x-ray diffraction data collection [use of the Advanced Photon Source, an Office of Science User Facility operated for the US Department of Energy (DOE) Office of Science by Argonne National Laboratory, was supported by the US DOE under contract no. DE-AC02-06CH11357]; F. C. Lowder and L. Simmons (University of Michigan at Ann Arbor, USA) for helpful suggestions for the exonuclease protection experiment carried out with fluorophore-labeled DNA and for preparation of an RNA ladder; T. de Lange and S. Cai (Rockefeller University, USA), J. Schmidt (Michigan State University, USA), H. Shibuya (University of Gothenburg, Sweden), and J. Williams (Nandakumar laboratory) for helpful comments on the manuscript; and G. Sobocinski for help with microscopy.
Funding: This study was supported by NIH grants R01GM120094, R01HD108809, and R35GM148276 (J.N.) and by American Cancer Society Research Scholar grant RSG-17-037-01-DMC (J.N.).
Author contributions: Conceptualization: V.M.T. and J.N. Methodology: V.M.T., K.A.B., and J.N. Investigation: V.M.T. and K.A.B. Visualization: V.M.T., K.A.B., and J.N. Funding acquisition: J.N. Project administration: V.M.T. and J.N. Supervision: V.M.T. and J.N. Writing – original draft: V.M.T. and J.N. Writing – review and editing: V.M.T., K.A.B., and J.N. **Competing interests:** The authors declare that they have no competing interests. **Data and materials availability:** All data are available in the main and supplementary figures. All material generated in this study, such as plasmids for protein expression and cell lines, are available upon request. Coordinates and structure factors of the crystal structures of hDBD with 5′-P-hp-ss$^{1\text{-}12}$ and 5′-P-ds-ss$^{1\text{-}12}$ are deposited in the Protein Data Bank (PDB) under accession codes 8SH0 and 8SH1, respectively. **License information:** Copyright © 2023 the authors, some rights reserved; exclusive licensee American Association for the Advancement of Science. No claim to original US government works. https://www.science.org/about/science-licenses-journal-article-reuse

SUPPLEMENTARY MATERIALS

science.org/doi/10.1126/science.adi2436
Materials and Methods
Figs. S1 to S13
Tables S1 and S2
References (*44*–*55*)
MDAR Reproducibility Checklist

Submitted 19 April 2023; accepted 19 July 2023
10.1126/science.adi2436

PHYSICS

Ergodicity breaking in rapidly rotating C_{60} fullerenes

Lee R. Liu[1,2]*, Dina Rosenberg[1,2], P. Bryan Changala[1,2]†, Philip J. D. Crowley[3], David J. Nesbitt[1,2,4], Norman Y. Yao[3], Timur V. Tscherbul[5], Jun Ye[1,2]*

Ergodicity, the central tenet of statistical mechanics, requires an isolated system to explore all available phase space constrained by energy and symmetry. Mechanisms for violating ergodicity are of interest for probing nonequilibrium matter and protecting quantum coherence in complex systems. Polyatomic molecules have long served as a platform for probing ergodicity breaking in vibrational energy transport. Here, we report the observation of rotational ergodicity breaking in an unprecedentedly large molecule, $^{12}C_{60}$, determined from its icosahedral rovibrational fine structure. The ergodicity breaking occurs well below the vibrational ergodicity threshold and exhibits multiple transitions between ergodic and nonergodic regimes with increasing angular momentum. These peculiar dynamics result from the molecule's distinctive combination of symmetry, size, and rigidity, highlighting its relevance to emergent phenomena in mesoscopic quantum systems.

Isolated systems that break ergodicity have been explored in a variety of experimental settings, including spin glasses (*1*), ultracold neutral atoms (*2*, *3*) and ions (*4*), and photonic crystals (*5*). These systems exhibit ergodicity breaking of spin configurations and momentum or spatial distributions. By contrast, gas-phase polyatomic molecules provide opportunities to probe the ergodicity breaking of collective (rotational and vibrational) excitations in a finite quantum system. In this context, a topic of major interest has been the transport of energy deposited into molecular vibrations by optical pumping or collisions. Intramolecular vibrational redistribution (IVR) sets in once a critical threshold, defined by the product of vibrational coupling and the local density of vibrational states (which has a power-law scaling with vibrational energy), is exceeded (*6*–*11*). This vibrational ergodicity transition has been studied vigorously in the context of understanding and controlling unimolecular reaction dynamics (*12*).

Among polyatomic molecules, buckminsterfullerene ($^{12}C_{60}$) is notable for its structural rigidity and high degree of symmetry, which suppress IVR and allow for spectroscopic resolution (*13*) and optical pumping (*14*) of individual rovibrational states—an unusual and fortuitous situation for a molecule with 174 vibrational modes. Its small rotational constant and stiff, cage-like structure ensure that hundreds of rotational states are populated even when vibrational excitations are largely frozen out, which can be achieved with modest buffer gas cooling to ~120 K. Thus, a thermal ensemble of $^{12}C_{60}$ can reveal extensive, state-resolved rotational perturbations spanning hundreds of rotational quanta by eliminating vibrational "hot bands."

First observed and understood in atomic nuclei (*15*–*22*), rotational perturbations can arise from spherical symmetry breaking in the frame fixed to a rotating self-bound deformable body (*23*), which lifts the degeneracy of different body-fixed projections of the total angular momentum vector **J**. Such perturbations, also called "tensor interactions" because of their anisotropic nature, manifest in fine-structure splitting of the total angular momentum (J) multiplets in rovibrational spectra and encode rich dynamics such as rotational bifurcations (*18*, *24*), as previously observed in tetrahedral SnH_4, CD_4, CF_4, SiH_4, and SiF_4 and octahedral SF_6 molecules (*25*–*33*). Nevertheless, observing icosahedral tensor interactions, first predicted for $^{12}C_{60}$ over three decades ago (*34*), has remained an elusive goal, because there are far fewer examples of icosahedral molecules, nonspherical interactions occur only at higher orders of interactions, and icosahedral molecules are necessarily larger than lower-symmetry spherical top molecules, implying a smaller rotational constant.

In this work, we observed these icosahedral tensor interaction splittings, revealing rotational ergodicity transitions in $^{12}C_{60}$ at energies well below its IVR threshold (*10*). Specifically, as the molecule "spins up" to higher J, the dynamics of the angular momentum vector J in the molecule-fixed frame switches between ergodic and nonergodic regimes. In the nonergodic regime, distinct vector **J** trajectories exist in the same energy range but remain separated by energy barriers. In the limit of high J, the tunneling between these trajectories is too weak to restore ergodicity, leaving a characteristic signature in the fine-structure level statistics. This phenomenon differs from IVR in three key respects: (i) It involves the "transport" of the molecule frame orientation of vector **J** instead of vibrational energy; (ii) it can occur well below the IVR threshold; and (iii) it switches back and forth multiple times between ergodic (described by a 6th rank tensor interaction) and nonergodic (described by a 10th rank tensor interaction) regimes as the angular momentum is varied. This peculiar dynamical behavior arises from multiple avoided crossings with other vibrational states, which induce nonmonotonic variations in the molecule's anisotropic character as J is varied. The rotational ergodicity transitions bear some similarity to those studied in asymmetric top molecules in a static electric field (*35*, *36*) in that both concern the transport of angular momentum in the molecule frame. However, unlike in (*35*, *36*), the rotational ergodicity transitions in $^{12}C_{60}$ are induced by intramolecular rovibrational coupling in the freely rotating molecule, rather than by an externally applied electric field.

Effective $^{12}C_{60}$ rovibrational Hamiltonian

The rovibrational structure of C_{60} can be described by a field-free molecular Hamiltonian

$$H = H_{\text{scalar}} + H_{\text{tensor}} \quad (1)$$

The scalar Hamiltonian H_{scalar} contains only those combinations of vector **J** and vibrational angular momentum ℓ that preserve their spherical degeneracy (*37*)

$$H_{\text{scalar}} = \nu_0 + B\mathbf{J}^2 + D\mathbf{J}^4 + \cdots - 2B\zeta\mathbf{J}\cdot\ell \quad (2)$$

where ν_0 is the vibrational band origin, B is the rotational constant, D is the scalar centrifugal distortion constant, and ζ is the Coriolis coupling constant.

Rovibrational fine structure is encoded in the tensor Hamiltonian H_{tensor}. For simplicity, we considered a pure rotational tensor Hamiltonian consisting of the two lowest-order "icosahedral invariants." These invariants are linear combinations of spherical tensors of the same rank that transform according to the totally symmetric irreducible representation in the icosahedral point group (I_h) (*38*). They can be expressed (*39*) in the basis of spherical harmonics $Y_q^k(\theta,\phi)$ of degree k and order q, which depend explicitly on the molecular frame's polar θ and azimuthal ϕ angles (Fig. 1A). The first two nontrivial (anisotropic) icosahedral invariants, with ranks 6 and 10, are given by

$$T^{[6]}(\theta,\phi) = \frac{\sqrt{11}}{5}Y_0^6(\theta,\phi) + \frac{\sqrt{7}}{5}\left(Y_5^6(\theta,\phi) - Y_{-5}^6(\theta,\phi)\right) \quad (3)$$

[1]JILA, National Institute of Standards and Technology and University of Colorado, Boulder, CO 80309, USA. [2]Department of Physics, University of Colorado, Boulder, CO 80309, USA. [3]Department of Physics, Harvard University, Cambridge, MA 02135, USA. [4]Department of Chemistry, University of Colorado, Boulder, CO 80309, USA. [5]Department of Physics, University of Nevada, Reno, NV 89557, USA.
*Corresponding author. Email: lee.richard.liu@gmail.com (L.R.L.); ye@jila.colorado.edu (J.Y.)
†Present address: Center for Astrophysics, Harvard and Smithsonian, Cambridge, MA 02138, USA.

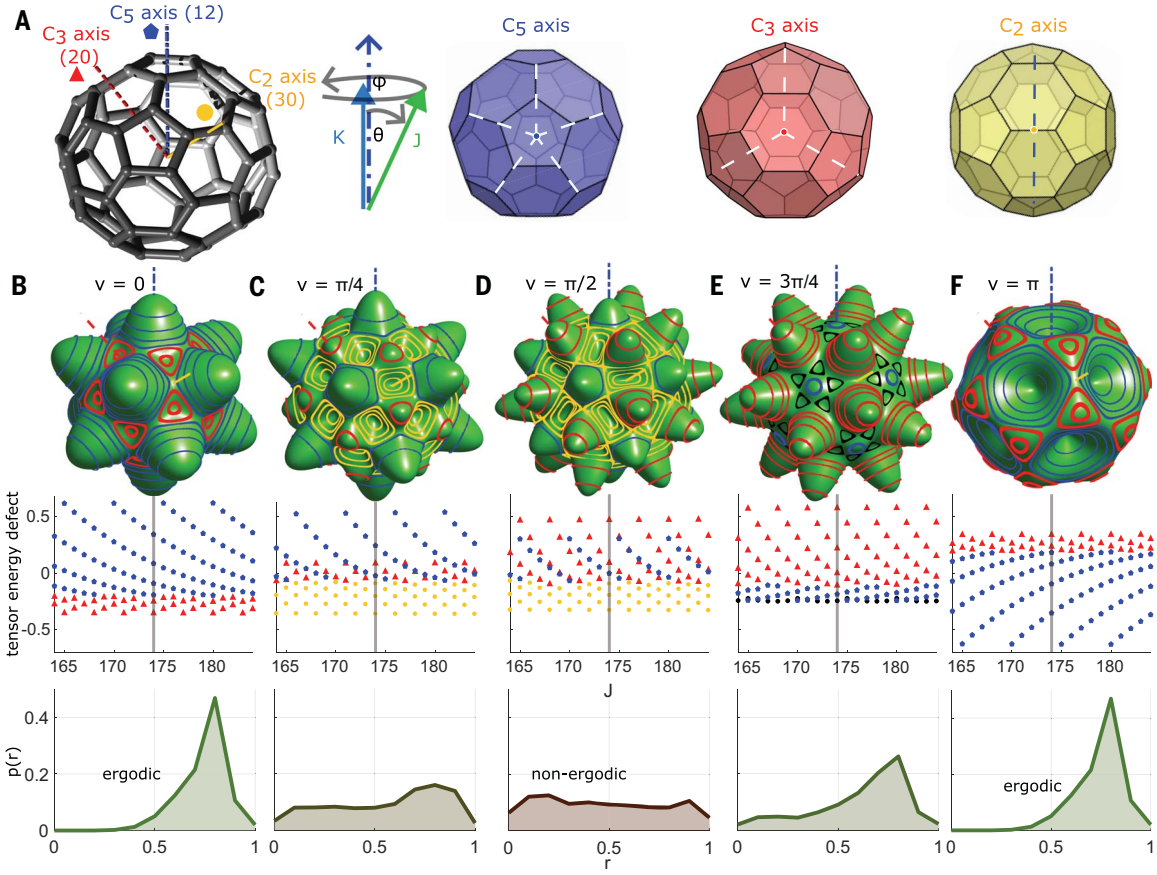

Fig. 1. Rotational energy surfaces and eigenvalues corresponding to icosahedral invariant spherical tensors. (**A**) Symmetries of C_{60}. (Left to right) (1) Ball-and-stick model of C_{60}, with the three different types of rotational symmetry axes that label stationary points on the rotational energy surface (RES). The degeneracies of the stationary points are listed in parentheses. Color and plot marker coding for each type of rotational symmetry axis are shown. (2) Body-fixed coordinates: polar θ and azimuthal ϕ angles. (3–5) View along C_5, C_3, and C_2 rotational symmetry axes. (**B** to **F**) (Top panels) RESs, defined by their radii $r(\theta,\phi) = 1 + H^{(6+10)}_{\text{tensor}}(\nu;\theta,\phi)/2$, for ν ranging from 0 to π. Eigenvalues of $1 + H^{(6+10)}_{\text{tensor}}(\nu)/2$ calculated for the fully symmetrized $J = 174$ subspace are plotted on the surface as radial contours, colored corresponding to their dominant rotational symmetry character. (Center panels) Tensor energy defects [eigenvalues of $H^{(6+10)}_{\text{tensor}}(\nu)$] over a range of J. The gray vertical line highlights $J = 174$. Eigenvalues are plotted using the marker corresponding to their dominant C_5, C_3, or C_2 character (A). Near the separatrices, the assignment is somewhat ambiguous owing to strong mixing. (Bottom panels) Distribution $p(r)$ of energy gap ratios r (see text) calculated from tensor energy defect spectra aggregated over J = 0 to 400. Away from $\nu = 0, \pi$ [(C) to (E)], the finite value of $p(r)$ as $r \to 0$ is a signature of ergodicity breaking.

$$T^{[10]}(\theta,\phi) = \frac{\sqrt{3\cdot 13\cdot 19}}{75}Y^{10}_0(\theta,\phi) - \frac{\sqrt{11\cdot 19}}{25}\left(Y^{10}_5(\theta,\phi) - Y^{10}_{-5}(\theta,\phi)\right) + \frac{\sqrt{3\cdot 11\cdot 17}}{75}\left(Y^{10}_{10}(\theta,\phi) + Y^{10}_{-10}(\theta,\phi)\right) \quad (4)$$

which are combined to construct a truncated tensor Hamiltonian

$$H^{(6+10)}_{\text{tensor}} = \gamma\left(\cos\nu T^{[6]} + \sin\nu T^{[10]}\right) \quad (5)$$

This Hamiltonian is parameterized by an overall scaling factor γ and mixing angle ν such that $\nu = 0$ and $\nu = \pi/2$ correspond to pure $T^{[6]}$ and pure $T^{[10]}$, respectively.

All operators that are incompatible with icosahedral point group symmetry, including any spherical harmonics of rank 1 to 5, 7 to 9, 11, 13, 14,... (*40*), vanish from the Hamiltonian. The use of full rovibrational tensor operators is unlikely to change the picture qualitatively, particularly when J (~100 to 300) is much greater than the vibrational angular momentum quantum number $\ell = 1$ (*38*). These polyhedral invariants are similar to those used to describe the crystal field splitting of electronic orbitals owing to an external lattice environment (*41*) or the ligand field splitting in transition-metal complexes (*42*).

The energetic correction, or tensor energy defect, associated with orienting **J** in different directions in the molecule frame can be visualized by the altitude of a semi-classical "rotational energy surface" (RES), defined at a fixed J. Various possible icosahedral RESs, defined by their radii $r(\theta,\phi) = 1 + H^{(6+10)}_{\text{tensor}}(\nu;\theta,\phi)/2$, corresponding to different mixing angles ν, are plotted for $J = 174$ in the top panels of Fig. 1, B to F. Stationary points always lie on C_2, C_3, or C_5 rotational symmetry axes. However, as ν varies, they change in character between minima, maxima, and saddle points. The RES dictates the dynamics of **J** in the molecule frame (*30*, *43*–*46*), analogous to how an adiabatic potential energy surface steers the relative motions of nuclei (*47*). During free evolution, the trajectory of **J** follows an equipotential contour of the RES.

In a full quantum-mechanical treatment, the perturbation $H^{(6+10)}_{\text{tensor}}$ leads only to discrete tensor energy defects e_i given by the eigenvalues of $H^{(6+10)}_{\text{tensor}}$ in a fully symmetrized fixed-J subspace. These orbits trace out the closed contours on the RES in Fig. 1. The orbits may also be obtained directly from the RES: They are the trajectories that both (i) satisfy a Bohr quantization condition (*44*, *48*) and (ii) transform according to the totally symmetric irreducible representation of the icosahedral point group (*38*). The latter condition accounts for the

quantum indistinguishability of each bosonic nucleus in the $^{12}C_{60}$ isotopolog (*13*, *49*) and is analogous to the selection of odd or even rotational states in ortho- or para-hydrogen molecules, respectively. The tensor energy defects are plotted for a range of J in the center panels of Fig. 1, B to F, and may be expected to appear in the rovibrational fine structure of $^{12}C_{60}$.

Resolving $^{12}C_{60}$ rovibrational fine structure

In the preceding discussions, we have focused solely on the geometric effects of icosahedral symmetry. In general, however, the measured tensor defect spectra may exhibit additional J-dependent scaling and offsets, which depend on intramolecular couplings specific to $^{12}C_{60}$. To resolve rovibrational perturbations in $^{12}C_{60}$, in this work, we explored the P-branch region of the 1185 cm^{-1} T_{1u} (3) band, first identified as a region of potential interest in (*13*). Using cavity-enhanced continuous-wave (cw) spectroscopy with a quantum cascade laser (QCL) source, we achieved a minimum absorption sensitivity $\alpha_{min} = 2.1 \times 10^{-10} cm^{-1}\,Hz^{-1/2}$, or 1000-fold better detection sensitivity per spectral element than in (*13*) ($\alpha_{min} = 2.2 \times 10^{-7}$ $cm^{-1}\,Hz^{-1/2}$ per comb mode). We acquired 600-MHz-wide absorption spectra by simultaneously scanning the QCL frequency and free spectral range of the enhancement cavity across molecular absorption lines, and recording the frequency-dependent absorption. These spectra were stitched together by a combination of direct calibration of the QCL frequency with a Fourier transform spectrometer and comparison to matching spectral features in the broadband, low signal-to-noise (SNR) frequency comb spectrum of (*13*). We obtained an absolute frequency accuracy of ~6 MHz throughout the entire measured frequency range, limited by the resolution of the reference frequency comb spectrum. Finally, to ensure consistency of the absorption signal over multiple days of data collection, we have periodically remeasured the molecular absorption feature at R($J = 181$) at $\nu = 1186.27\,cm^{-1}$ and normalized all data taken around the same time to its line strength and measured cavity finesse.

Assigning $^{12}C_{60}$ rovibrational fine structure

The culmination of these efforts is the infrared spectrum in Fig. 2, spanning the spectral region from 1182.0 to 1184.7 cm^{-1}. At $J \lesssim 70$, there is a regular progression of rotational lines, similar to those in the R-branch (*13*). They rapidly split into intricate patterns before merging at and beyond $J \approx 300$. Zooming into the region labeled B), the rotational line centers could be fit to the scalar part of Eq. 1, as was done in (*13*).

$$\nu^P(J) = \nu_0 + B'(J-1)(J+2\zeta) - B''J(J+1) \quad (6)$$

where J here refers to the ground-state total angular momentum. The scalar centrifugal distortion term was not significant at our spectral precision and range of J. The fit yielded B'' = 0.0028 cm^{-1} for the ground-state rotational constant, $B' = B'' - 2.876 \times 10^{-7}$ cm^{-1} for the excited-state rotational constant, $\zeta = -0.37538$ for the Coriolis coupling constant, and $\nu_0 = 1184.85$ cm^{-1}. Equation 6 yields a progression of rotational lines with a spacing of $\sim 2B(1-\zeta)$, where $B = (B' + B'')/2$. The spectroscopic constants were underdetermined and only served to facilitate J-assignment of the peaks in a manner consistent with the R-branch assignments of (*13*). The extrapolated P-branch spectral line positions based on this scalar fit are plotted as gray vertical lines in Fig. 2, B to F, with every fifth J value labeled in red. The agreement with the measured line positions is excellent in the region $J < 70$, where the spectrum appears unperturbed (Fig. 2B).

To confirm our J assignment, we compared the peak absorption cross sections to the nuclear spin weights of the ground-state rotational levels and found that they match well. Finally, we applied a frequency-dependent scaling factor to the raw absorption spectrum $(2J+1)^{-1} e^{B'J(J+1)/k_B T}$. This scaling removes the effects of lab frame angular momentum degeneracy and the thermal ensemble, emphasizing the dynamics in the molecule-fixed frame.

The peaks were identified manually and circled in blue. Figure 2, C and D, show two representative regions, at $J \sim 90$ and $J \sim 170$, respectively, where peaks could still be individually resolved. The local peak density again matches the predicted nuclear spin weights (in blue), confirming that the rovibrational

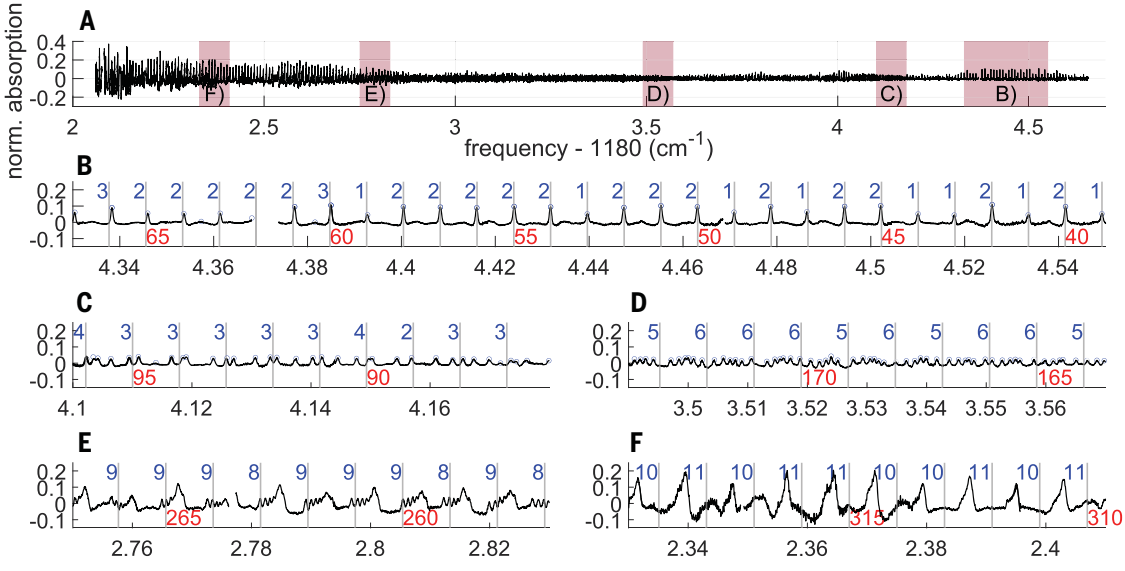

Fig. 2. Direct continuous-wave (cw) absorption spectroscopy of C_{60} P-branch. (**A**) Complete normalized cw spectrum of P-branch to expose the J dependence of the nuclear spin weights. Red highlighted regions are shown in greater detail in subsequent panels. (**B** to **F**) Enlargement of red highlighted regions in (A). (B) Enlargement of low-J region of the P-branch. This relatively unperturbed region of the P-branch is fit to a rigid-rotor Hamiltonian to obtain the rotational spacing $2B(1-\zeta)$. Fitted line positions are indicated by the gray vertical grid lines, with J labeled in red. Blue numbers denote calculated nuclear spin weights, which match the measured peak intensities well. In (C) and (D), peaks are resolvable and marked with blue circles. In (E) and (F), spectral congestion prohibits identification of individual peaks.

fine-structure splitting originates from icosahedral tensor interactions of Eq. 5 that lift K-degeneracy. Figure 2, E and F, show two regions where the peaks have begun to merge, and individual peaks can no longer be easily identified ($J > 247$).

Interpreting the tensor splittings requires assigning each absorption peak to a particular J. We began by assigning each peak to its nearest J value according to the scalar fit of Eq. 6. Subtracting the scalar contribution (Eq. 6) from the central frequency of each peak generated a single "period" of a Loomis-Wood-like defect plot in Fig. 3A. There remains some ambiguity in the defect assignments, as illustrated in the inset of Fig. 3A: Each defect is constrained to the line with slope $2B(1-\zeta)$, which passes through its current position.

By carefully rearranging individual defects according to these discrete allowed "moves," we unwrapped five distinct regions that exhibit continuous-looking patterns (Fig. 3B). Because of the discontinuities at $J \simeq 80$, 110, 160, and 220, there was still some ambiguity in the overall shift of the four perturbed sections labeled (i) to (iv). To remove this ambiguity, we recognized each section's dominant pure-rank tensor character as follows: (i) $-T^{[6]}$; (ii) $T^{[10]}$; (iii) $T^{[6]}$; (iv) $-T^{[6]}$. Eigenvalue spectra in Fig. 1, B, D, and F, show that the extremal eigenvalues associated with C_n rotational symmetry axes occur when J is an integer multiple of n. The J-assignment depicted in Fig. 3B satisfies this condition for all sections simultaneously. This final J-assignment was confirmed by the excellent agreement between J-resolved peak counts and calculated nuclear spin weight far from the discontinuities Fig. 3C.

Rotational ergodicity transitions

The J-dependent tensor energy defects imply rovibrational dynamics of $^{12}C_{60}$. To infer these dynamics, we parameterized each of the four perturbed regions (i) to (iv) in Fig. 3B in terms of a mixed tensor (Eq. 5), J-dependent scaling $b(J)$, and J-dependent scalar offset $a(J)$:

$$a(J) + b(J) \times e(\nu; J, K) \qquad (7)$$

where $e(\nu; J, K)$ are the J-dependent tensor splittings as plotted in the lower panels of Fig. 1, B to F.

First, $a(J)$ was obtained from the observed mean defect of each section. Next, by performing a point-cloud registration (*50*–*52*) to the theoretical eigenvalue spectra and the measured defect plot, we assigned a best-fit mixing angle ν to each section: (i) π; (ii) 0.45π; (iii) 1.9π; and (iv) π (*38*). Finally, $b(J)$ was obtained from a least-squares fit to a polynomial in J (*38*). The resulting reconstructed defect plot for regions (i) to (iv) is shown in Fig. 3D.

The abrupt changes in mixing angles ν are associated with transitions between ergodic and nonergodic rotational dynamics as the molecule "spins up" to higher J. These dynamics

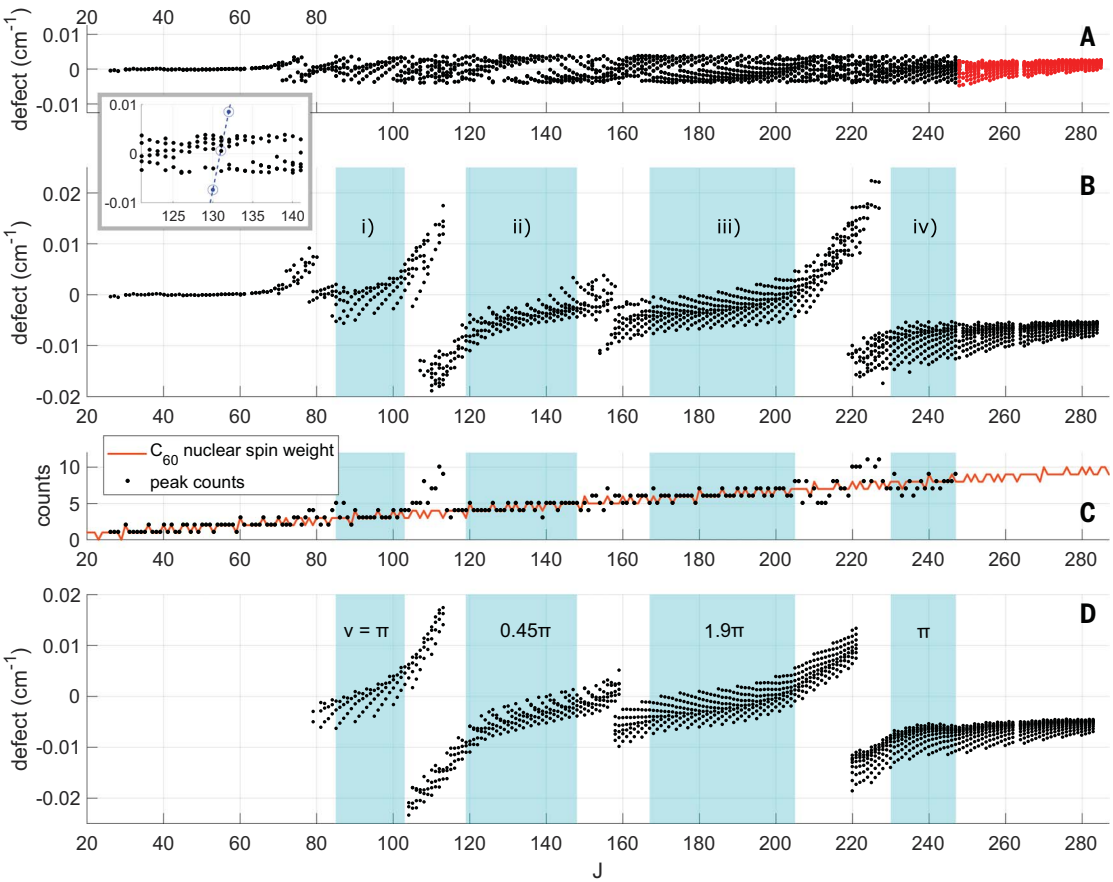

Fig. 3. Obtaining P-branch tensor energy defects versus *J*. (**A**) Plot of experimental energy defects from nearest-neighbor J assignment. Peaks are assigned to nearest J according to rigid rotor model (gray vertical grid lines in Fig. 2, B to F). Red defect points ($J > 247$) correspond to peaks in the absorption spectrum that are no longer individually resolved. Their peak centers are obtained from fitting to a cluster of Voigt lineshapes (*38*). (Inset) Unwrapping procedure follows a series of allowed "moves" that simultaneously translate points in vertical steps of $\pm 2B(1-\zeta)$ and horizontal steps of ±1. (**B**) "Unwrapped" defect plot. Four avoided crossings with varying strengths are seen at J ≃ 80, 110, 160, and 220. Defect patterns resemble eigenvalue spectra of icosahedral invariant tensors. (**C**) Calculated nuclear spin weights overlaid with measured peak counts. Blue highlighted sections show excellent agreement between calculated nuclear spin weights of C_{60} and assigned peak counts. (**D**) Reconstruction of perturbed sections of P-branch spectrum based on eigenvalue spectra of mixed tensor operator $H^{(6+10)}_{\text{tensor}}(\nu)$. Four perturbed portions of (B) are reproduced with four mixing angles ν.

transition from ergodic for region (i), to nonergodic for region (ii), and back again for regions (iii) and (iv).

The origin of this ergodicity breaking can be understood semi-classically using the RESs in Fig. 1, B, D, and F. The dynamics of vector **J** are ergodic when time evolution explores the full space of symmetry-allowed states at the same energy. For region (iii), the dominant tensor character is $T^{[6]}$. Naïvely, the existence of 12 disconnected trajectories encircling the C_5 axes breaks ergodicity. However, these trajectories cannot be distinguished in $^{12}C_{60}$: Owing to the indistinguishability of the ^{12}C nuclei, all 12 semi-classical trajectories correspond to a single quantum state given by their fully symmetric superposition. As such, the vector **J** dynamics do explore the full range of states at a given energy, and hence are ergodic. The same argument applies for regions (i) and (iv), which differ from (iii) only in the sign of tensor energy defects (Fig. 1F).

By contrast, for region (ii), the dominant tensor character is $T^{[10]}$. The C_5 and C_3 axes both correspond to peaks on the RES and to host trajectories over the same range of energies (Fig. 3D). Trajectories encircling the C_5 and C_3 axes are distinguishable, and hence correspond to distinct quantum states. The quantum tunneling between these trajectories is unable to restore the ergodicity: The tunneling integral between C_5 and C_3 is exponentially small in J (*53*, *54*), whereas the level spacing only scales as $1/J$. The scaling of the tunneling integral follows from standard Wentzel–Kramers–Brillouin (WKB) results (*55*), and the scaling of level spacings can be seen by comparing the relatively fixed bandwidth of tensor energy defects (Fig. 3B) with the nuclear spin weight $\sim(2J+1)/60$. Consequently, for our measured J (well within the large-J limit), tunneling corrections are typically only perturbative.

Energy-level statistics provide a simple probe of this ergodicity breaking in molecular spectra (*56*, *57*). Quantum ergodicity is associated with eigenstates extended in phase space that can be strongly coupled by local perturbations, inducing energy-level repulsion. By contrast, ergodicity breaking is associated with the existence of localized eigenstates, which are not strongly coupled by perturbations and whose energies are uncorrelated (*58*). Ergodic and nonergodic dynamics are therefore respectively associated with level repulsion and its absence (*59*). A useful diagnostic tool is the distribution $p(r)$, where r is the ratio of consecutive level spacings e_i (*60*, *61*):

$$r_i = \min\left(\frac{s_i}{s_{i-1}}, \frac{s_{i-1}}{s_i}\right) \tag{8}$$

$$s_i = e_{i+1} - e_i \tag{9}$$

In the limit of $r \to 0$, level repulsion in an ergodic system causes $p(r) \to 0$, and for a nonergodic system $p(r) \to$ constant. Similar energy-level statistics have been used to analyze systems as diverse as nuclear spectra (*59*), ultracold atomic scattering (*62*), and many-body localization (*63*).

Figure 4, A to C, show the energy-gap ratios computed from sections (i) to (iii), respectively, of the experimental defect plot (Fig. 3B). Here, sections (i) and (iii) exhibit persistent level repulsion characteristic of ergodicity, whereas section (ii) does not, indicating nonergodicity. We aggregated the energy-gap ratios over each one of sections (i) to (iii) and their respective distributions in Fig. 4, D to F. These distributions confirm the presence of level repulsion in sections (i) and (iii) and its absence in section (ii).

The physical origin of rovibrational tensor energy defects in $^{12}C_{60}$ can be inferred from Fig. 3B. The defects arise from rovibrational coupling between the bright P-type excited $T_{1u}^{(+)}(3)$ state and a background of perturbing dark states. Specifically, both the discontinuities and excess observed peaks at specific J values are characteristic of avoided crossings with perturbing zero-order dark vibrational combination states. As they cross $T_{1u}^{(+)}(3)$ from below, rovibrational coupling lifts the degeneracy of J multiplets in the $T_{1u}^{(+)}(3)$ state, imparting tensor character that depends on the identity of the perturbing vibrational state. The tensor character of the $T_{1u}^{(+)}(3)$ state (specifically the fitted ν values) is stable in between avoided crossings, suggesting that each of these sections is dominantly affected by just one perturbing state at a time. At the avoided crossings, this assumption breaks down, as made particularly evident by the rapid change in mixing angle just before and after the avoided crossing at $J = 160$ of Fig. 3B. There is no apparent structure to the changes in mixing angle and coupling strength induced by the different avoided crossings, suggesting that the perturbing dark states are distinct and not part of the same Coriolis manifold. Finally, using the observed local density of perturbing states $\rho_{obs} \approx 2/\mathrm{cm}^{-1}$ and average measured vibrational coupling strength (bandwidth of the avoided crossings) of $\beta_{avg} \approx 2\times 10^{-2}\ \mathrm{cm}^{-1}$ (*38*), we arrive at an IVR threshold parameter (*10*) $T(E) = \sqrt{2\pi/3}\rho_{obs}\beta_{avg} \approx 0.06 \ll 1$. Our $^{12}C_{60}$ rotational ergodicity transitions are observed well below the IVR threshold, a conclusion supported by the spectroscopically well-resolved $T_{1u}(3)$ band. This further highlights the fact that, although the rotational ergodicity transition relies on intramolecular vibrational coupling, it is completely distinct from IVR.

Conclusion

We have measured and characterized icosahedral tensor rovibrational coupling in $^{12}C_{60}$. Analysis of the spectrum of rovibrational tensor energy defects revealed that as the molecule is spun up to higher J, there is a series of transitions in the dynamical behavior of **J** in the fixed body frame. Specifically, vector **J** switches between ergodic and nonergodic behavior at particular J values, leaving a characteristic imprint on the defect-level statistics. These ergodicity transitions arise from dark vibrational combination states that cross the $T_{1u}^{(+)}(3)$ state at particular J values, transferring their anisotropic character onto the $T_{1u}^{(+)}(3)$ state through rovibrational coupling.

Our measurements open the door to a rich hierarchy of emergent behavior in C_{60} isotopologs, accessible at ever-higher spectral resolution. The small nuclear spin-rotation interaction—for example, in ^{13}C-substituted isotopologs of C_{60}—can have a magnified effect owing to the small superfine splittings near RES extrema.

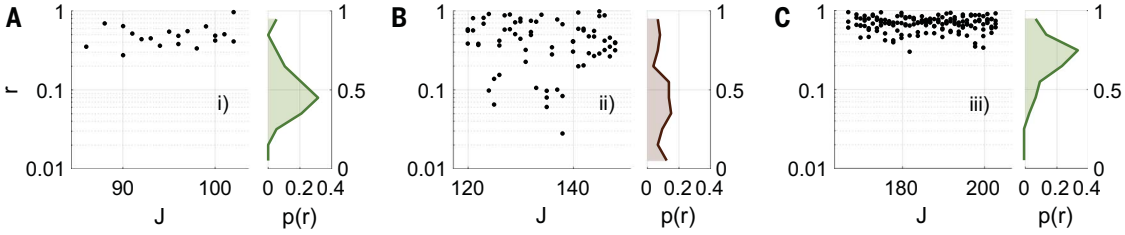

Fig. 4. Energy-level statistics in ergodic and nonergodic regimes. (**A** to **C**) (Left panels) Gap ratio r as a function of J calculated from sections (i) to (iv) of the defect spectrum (Fig. 3B). Gap ratios are only plotted at J values for which the peak counts match the calculated nuclear spin weight (Fig. 3C). (Right panels) Normalized distribution $p(r)$ of gap ratios aggregated over sections (i) to (iii). Note the change from logarithmic to linear r scale between left and right panels. Sections (i) and (iii) exhibit level repulsion, a signature of ergodicity, whereas section (ii) does not, indicating nonergodicity.

Such "hyperfine" coupling can lead to spontaneous symmetry breaking in a finite system (*31*, *64*). These insights could prove useful for exploiting the exotic orientation state space of C_{60} for quantum information processing (*65*) and for investigating the quantum-to-classical transition of information spreading (*66*). Ultimately, spectroscopy of C_{60} isotopologs at ever-higher spectral resolution promises to uncover deeper insights into the emergent dynamics of mesoscopic quantum many-body systems.

REFERENCES AND NOTES

1. K. Binder, A. P. Young, *Rev. Mod. Phys.* **58**, 801–976 (1986).
2. T. Kinoshita, T. Wenger, D. S. Weiss, *Nature* **440**, 900–903 (2006).
3. M. Schreiber *et al*., *Science* **349**, 842–845 (2015).
4. J. Smith *et al*., *Nat. Phys.* **12**, 907–911 (2016).
5. M. Segev, Y. Silberberg, D. N. Christodoulides, *Nat. Photonics* **7**, 197–204 (2013).
6. J. D. McDonald, *Annu. Rev. Phys. Chem.* **30**, 29–50 (1979).
7. G. M. Nathanson, G. M. Mcclelland, *J. Chem. Phys.* **81**, 629–642 (1984).
8. G. M. McClelland, G. M. Nathanson, J. H. Frederick, F. W. Farley, Excited States, E. C. Lim, K. K. Innes, eds. (Academic Press, Inc., 1988), vol. 7, pp. 83–106.
9. K. Sture, J. Nordholm, S. A. Rice, *J. Chem. Phys.* **61**, 203–223 (1974).
10. D. E. Logan, P. G. Wolynes, *J. Chem. Phys.* **93**, 4994–5012 (1990).
11. D. M. Leitner, *Entropy (Basel)* **20**, 673 (2018).
12. D. J. Nesbitt, R. W. Field, *J. Phys. Chem.* **100**, 12735–12756 (1996).
13. P. B. Changala, M. L. Weichman, K. F. Lee, M. E. Fermann, J. Ye, *Science* **363**, 49–54 (2019).
14. L. R. Liu *et al*., *PRX Quantum* **3**, 030332 (2022).
15. I. M. Pavlichenkov, *Sov. Phys. JETP* **55**, 5–12 (1982).
16. I. M. Pavlichenkov, B. I. Zhilinskii, *Ann. Phys.* **184**, 1–32 (1988).
17. Y. R. Shimizu, J. D. Garrett, R. A. Broglia, M. Gallardo, E. Vigezzi, *Rev. Mod. Phys.* **61**, 131–168 (1989).
18. I. M. Pavlichenkov, *Phys. Rep.* **226**, 173–279 (1993).
19. S. Frauendorf, *Rev. Mod. Phys.* **73**, 463–514 (2001).
20. H. Hübel, *Prog. Part. Nucl. Phys.* **54**, 1–69 (2005).
21. J. Kvasil, R. G. Nazmitdinov, *Phys. Rev. C Nucl. Phys.* **73**, 014312 (2006).
22. J. Kvasil, R. G. Nazmitdinov, A. S. Sitdikov, P. Veselý, *Phys. At. Nucl.* **70**, 1386–1391 (2007).
23. K. Fox, H. W. Galbraith, B. J. Krohn, J. D. Louck, *Phys. Rev. A Gen. Phys.* **15**, 1363–1381 (1977).
24. G. Pierre, D. A. Sadovskii, B. I. Zhilinskii, *Europhys. Lett.* **10**, 409–414 (1989).
25. R. S. McDowell *et al*., *J. Mol. Spectrosc.* **83**, 440–450 (1980).
26. C. W. Patterson, A. S. Pine, *J. Mol. Spectrosc.* **96**, 404–421 (1982).
27. J. P. Aldridge *et al*., *J. Mol. Spectrosc.* **58**, 165–168 (1975).
28. K. C. Kim, W. B. Person, D. Seitz, B. J. Krohn, *J. Mol. Spectrosc.* **76**, 322–340 (1979).
29. W. G. Harter, *J. Stat. Phys.* **36**, 749–777 (1984).
30. W. G. Harter, C. W. Patterson, *J. Math. Phys.* **20**, 1453–1459 (1978).
31. W. G. Harter, H. P. Layer, F. R. Petersen, *Opt. Lett.* **4**, 90–92 (1979).
32. R. S. McDowell, H. W. Galbraith, B. J. Krohn, C. D. Cantrell, E. D. Hinkley, *Opt. Commun.* **17**, 178–183 (1976).
33. J. Bordé, C. J. Bordé, *Chem. Phys.* **71**, 417–441 (1982).
34. W. G. Harter, D. E. Weeks, *Chem. Phys. Lett.* **132**, 387–392 (1986).
35. M. Abd El. Rahim, R. Antoine, M. Broyer, D. Rayane, P. Dugourd, *J. Phys. Chem. A* **109**, 8507–8514 (2005).
36. S. M. Pittman, E. J. Heller, *J. Phys. Chem. A* **119**, 10563–10574 (2015).
37. K. T. Hecht, *J. Mol. Spectrosc.* **5**, 355–389 (1961).
38. Materials and methods are available as supplementary materials.
39. Y. Zheng, P. C. Doerschuk, *Acta Crystallogr. A* **52**, 221–235 (1996).
40. P. R. Bunker, P. Jensen, *Mol. Phys.* **97**, 255–264 (1999).
41. K. R. Lea, M. J. Leask, W. P. Wolf, *J. Phys. Chem. Solids* **23**, 1381–1405 (1962).
42. B. J. S. Griffith, L. E. Orgel, *Q. Rev. Chem. Soc.* **11**, 381–393 (1957).
43. W. G. Harter, *Phys. Rev. A Gen. Phys.* **24**, 192–263 (1981).
44. W. G. Harter, C. W. Patterson, *J. Chem. Phys.* **80**, 4241–4261 (1984).
45. W. G. Harter, *Comput. Phys. Rep.* **8**, 319–394 (1988).
46. D. A. Sadovskii, B. I. Zhilinskii, J. P. Champion, G. Pierre, *J. Chem. Phys.* **92**, 1523–1537 (1990).
47. M. Khauss, *Annu. Rev. Phys. Chem.* **21**, 39–46 (1970).
48. W. G. Harter, D. E. Weeks, *J. Chem. Phys.* **90**, 4727–4743 (1989).
49. R. D. Johnson, G. Meijer, D. S. Bethune, *J. Am. Chem. Soc.* **112**, 8983–8984 (1990).
50. Y. Chen, G. Medioni, *Image Vis. Comput.* **10**, 145–155 (1992).
51. P. J. Besl, N. D. Mckay, *IEEE Trans. Pattern Anal. Mach. Intell.* **14**, 239–256 (1992).
52. A. V. Segal, D. Haehnel, S. Thrun, *Robot. Sci. Syst.* **5**, 435 (2010).
53. A. Auerbach, *Interacting electrons and Quantum magnetism* (Springer Science+Business Media, 1994).
54. J. L. van Hemmen, A. Sütö, *Europhys. Lett.* **1**, 481–490 (1986).
55. L. Landau, E. Lifshitz, Quantum Mechanics (Non-Relativistic Theory), vol. 3 (Pergamon Press, 1958).
56. M. V. Berry, M. Tabor, *Proc. R. Soc. London Ser. A* **356**, 375–394 (1977).
57. E. Abramson, R. W. Field, D. Imre, K. K. Innes, J. L. Kinsey, *J. Chem. Phys.* **80**, 2298–2300 (1983).
58. M. V. Berry, *Proc. R. Soc. London Ser. A* **413**, 183–198 (1987).
59. E. P. Wigner, *SIAM Rev.* **9**, 1–23 (1967).
60. V. Oganesyan, D. A. Huse, *Phys. Rev. B Condens. Matter Mater. Phys.* **75**, 155111 (2007).
61. Y. Y. Atas, E. Bogomolny, O. Giraud, G. Roux, *Phys. Rev. Lett.* **110**, 084101 (2013).
62. A. Frisch *et al*., *Nature* **507**, 475–479 (2014).
63. D. A. Abanin, E. Altman, I. Bloch, M. Serbyn, *Rev. Mod. Phys.* **91**, 021001 (2019).
64. J. Bordé *et al*., *Phys. Rev. Lett.* **45**, 14–17 (1980).
65. V. V. Albert, J. P. Covey, J. Preskill, *Phys. Rev. X* **10**, 031050 (2020).
66. C. Zhang, P. G. Wolynes, M. Gruebele, *Phys. Rev. A* **105**, 033322 (2022).
67. L. R. Liu *et al*., Supplementary data for ergodicity breaking in rapidly rotating C60 fullerenes, Harvard Dataverse (2023); https://doi.org/10.7910/DVN/E4KHWX [accessed 13 June 2023].

ACKNOWLEDGMENTS

We gratefully acknowledge comments on the manuscript from A. W. Young and Y.-C. Chan. **Funding:** This research was supported by AFOSR grant no. FA9550-19-1-0148; the National Science Foundation Quantum Leap Challenge Institutes (grant QLCI OMA-2016244); the National Science Foundation (grant Phys-1734006); and the National Institute of Standards and Technology. Support is also acknowledged from the US Department of Energy, Office of Science, National Quantum Information Science Research Centers, Quantum Systems Accelerator. D.R. acknowledges support from the Israeli council for higher education quantum science fellowship and is an awardee of the Weizmann Institute of Science–Israel National Postdoctoral Award Program for Advancing Women in Science. P.J.D.C. and N.Y.Y. acknowledge support from the AFOSR MURI program (FA9550-21-1-0069). D.J.N. acknowledges support from the US DOE (DE-FG02-09ER16021) and NSF (CHE 2053117). T.V.T. acknowledges support from the NSF EPSCoR RII Track-4 Fellowship no. 1929190. **Author contributions:** L.R.L., D.R., and J.Y. designed, discussed, and performed the experiment and analyzed the data. L.R.L., D.R., P.B.C., P.J.D.C., D.J.N., N.Y.Y., T.V.T., and J.Y. participated in theory discussions and calculations and in writing of the paper. **Competing interests:** None declared. **Data and materials availability:** Data for raw absorption spectra and unwrapped tensor energy defect plots are deposited in Harvard Dataverse (*67*). All other data needed to evaluate the conclusions in the paper are present in the paper or the supplementary materials. **License information:** Copyright © 2023 the authors, some rights reserved; exclusive licensee American Association for the Advancement of Science. No claim to original US government works. https://www.sciencemag.org/about/science-licenses-journal-article-reuse

SUPPLEMENTARY MATERIALS

science.org/doi/10.1126/science.adi6354
Supplementary Text
Figs. S1 to S3
Table S1
Reference (*68*)

Submitted 9 May 2023; accepted 23 June 2023
10.1126/science.adi6354

NANOMATERIALS

Ligand-protected metal nanoclusters as low-loss, highly polarized emitters for optical waveguides

Xiaojian Wang[1]†, Bing Yin[1]†, Lirong Jiang[1]†, Cui Yang[2], Ying Liu[1], Gang Zou[2], Shuang Chen[1]*, Manzhou Zhu[1]*

Photoluminescent molecules and nanomaterials have potential applications as active waveguides, but such a use has often been limited by high optical losses and complex fabrication processes. We explored ligand-protected metal nanoclusters (LPMNCs), which can have strong, stable, and tunable emission, as waveguides. Two alloy LPMNCs, Pt_1Ag_{18} and Au_xAg_{19-x} ($7 \le x \le 9$), were synthesized and structurally determined. Crystals of both exhibited excellent optical waveguide performance, with optical loss coefficients of 5.26×10^{-3} and 7.77×10^{-3} decibels per micrometer, respectively, lower than those demonstrated by most inorganic, organic, and hybrid materials. The crystal packing and molecular orientation of the Pt_1Ag_{18} compound led to an extremely high polarization ratio of 0.91. Aggregation enhanced the quantum yields of Pt_1Ag_{18} and Au_xAg_{19-x} LPMNCs by 115- and 1.5-fold, respectively. This photonic cluster with low loss and high polarization provides a generalizable and versatile platform for active waveguides and polarizable materials.

Optical waveguide systems can be made of passive elements based on refractive index changes, as in an optical fiber, or of active elements that create gain or introduce nonlinear optical effects for signal amplification (*1*–*3*). For molecular active optical waveguides, dipole orientations affect the direction of photon transmission. (*4*–*9*) Reported active waveguide materials, such as organic chromophores, hybrid materials, and polymer materials, have had drawbacks such as high loss, complex synthesis, and low yield (*6*, *8*–*15*). Ligand-protected metal nanoclusters (LPMNCs), which are composed of a few to hundreds of metal atoms and surface ligands (*16*–*21*), are suitable for optical waveguide materials (*16*, *22*). They have strong, stable and tunable emission, good photostability, a large Stokes shift, and high quantum yields (QYs) (*23*, *24*) and can be synthesized in high purity and yield. For waveguide applications, aggregation-induced emission enhancement could further enhance the photoluminescence (PL) of LPMNCs (*25*, *26*).

We report the optical waveguide performance of two LPMNCs, $[Pt_1Ag_{18}(S\text{-}Adm)_2(DPPP)_6Cl_6](SbF_6)(AgCl_2)$ (hereafter referred to as Pt_1Ag_{18}, where S-Adm is adamantane mercaptan and DPPP is 1,3-bis-diphenylphosphine propane) and $[Au_xAg_{19-x}(S\text{-}Adm)_2(DPPP)_6Cl_6](ClO_4)_3$ (hereafter referred to as Au_xAg_{19-x}, where $7 \le x \le 9$), both of which had rod-like structures and strong emission properties. The emission spectra of Pt_1Ag_{18} and Au_xAg_{19-x} were orange and red and were centered at 600 and 770 nm, respectively. One-dimensional (1D) microrod crystals of these LPMNCs exhibited excellent optical waveguide performance, with low optical loss coefficients and distinct polarized waveguide performance. The polarization ratios of Pt_1Ag_{18} and Au_xAg_{19-x} were 0.91 and 0.17, respectively, which we attributed to the differences in their crystal structure and packing modes. Both LPMNCs displayed aggregation-induced emission enhancement in that the QYs of Pt_1Ag_{18} and Au_xAg_{19-x} in the solid state were 115 and 1.5 times higher than those in solution, respectively. We propose that Pt_1Ag_{18} and Au_xAg_{19-x}, along with other LPMNCs, could find applications in optoelectronic devices.

Crystal structure of Pt_1Ag_{18}

We prepared Pt_1Ag_{18} ligand-protected nanoclusters (NCs) by reacting Pt_1Ag_{28} NCs (*27*) with $Ag_2(DPPP)Cl_2$ complexes in dichloromethane (see the supplementary materials), and their structure was determined to be $[Pt_1Ag_{18}(S\text{-}Adm)_2(DPPP)_6Cl_6](SbF_6)(AgCl_2)$ by single-crystal x-ray diffraction (SCXRD) (table S1 and Fig. 1). The Pt_1Ag_{18} structure consisted of a kernel composed of a central Pt atom and 12 Ag atoms (Fig. 1A) surrounded by a shell composed of six DPPP ligands (Fig. 1C) and two crown-like $Ag_3Cl_3(S\text{-}Adm)_1$ staple motifs (Fig. 1B). The two $Ag_3Cl_3(S\text{-}Adm)_1$ motifs of the surface shell were distributed on each side of the Pt_1Ag_{12} kernel, and each motif was connected to the Ag atoms in the kernel through three Ag–Cl bonds with a bond length of 2.44 Å, forming a rod-like $Pt_1Ag_{18}Cl_6(DPPP)_6(S\text{-}Adm)_2$ structure. The two P atoms in each of the DPPP ligands bonded to the Ag atoms in the crown-like motif and the Pt_1Ag_{12} kernel in a form parallel to the $Pt_1Ag_{18}Cl_6(S\text{-}Adm)_2$ rod (Fig. 1C), leading to the total structure of $[Pt_1Ag_{18}(S\text{-}Adm)_2(DPPP)_6Cl_6]^{2+}$ (Fig. 1H).

Each crystal cell contained two Pt_1Ag_{18} molecules with the counterions SbF_6^- and $AgCl_2^-$ (Fig. 1M); one was at the apex of the unit cell (**Pt_1Ag_{18}-1**, yellow highlights in Fig. 1M), and the other was in the center (**Pt_1Ag_{18}-2**, pink highlights in Fig. 1M). An important difference between the two Pt_1Ag_{18} clusters in each unit cell was the pattern of their associated DPPP benzene rings (Fig. 1H), which resulted in differing intermolecular and intramolecular noncovalent interactions. In **Pt_1Ag_{18}-1**, π…π interactions within each DPPP ligand and between adjacent DPPP ligands were observed (Fig. 1D), whereas in **Pt_1Ag_{18}-2**, π…π interactions were only observed between two adjacent DPPP ligands (Fig. 1F). The bonding patterns of the three DPPP methylene groups in **Pt_1Ag_{18}-1** (Fig. 1E) and **Pt_1Ag_{18}-2** were also different and led to differences in noncovalent interactions. The C–H bonds of the DPPP methylene groups interacted with the benzene π electrons, forming C–H…π secondary bonds for **Pt_1Ag_{18}-1** and **Pt_1Ag_{18}-2** (Fig. 1, E and G, respectively).

In layered **Pt_1Ag_{18}-1** and **Pt_1Ag_{18}-2**, π…π intermolecular interactions were evident between the top and bottom benzene rings of the DPPP ligands (Fig. 1I), and the C–H bonds of the benzene rings in **Pt_1Ag_{18}-2** interacted with π electrons in **Pt_1Ag_{18}-1** (Fig. 1J), which together induced C–H…π…π intermolecular interactions (Fig. 1K). Such interactions increased the rigidity and stability of Pt_1Ag_{18}, facilitating its crystallization, and were similar to the interactions associated with the self-assembly of organic molecules. From the [001] crystallographic direction, **Pt_1Ag_{18}-1** and **Pt_1Ag_{18}-2** alternated to form an orthohexagonal pattern (Fig. 1L, left). From the [100] crystallographic direction, layered stacking of the **Pt_1Ag_{18}-1** and **Pt_1Ag_{18}-2** orthohexagonal structures can be observed (Fig. 1L). Thus, the differing intermolecular and intramolecular noncovalent interactions of the benzene rings affected the crystallization and self-assembly of the LPMNCs.

Crystal structure of Au_xAg_{19-x}

Au_xAg_{19-x} NCs were prepared in a one-pot synthesis. A mixture of DPPP and HS-Adm was added to a solution of $AgNO_3$ in ethanol, and then an aqueous solution of $HAuCl_4$ was introduced, followed by an aqueous solution of $NaBH_4$ (see the supplementary materials), and their structure was determined to be $[Au_xAg_{19-x}(S\text{-}Adm)_2(DPPP)_6Cl_6](ClO_4)_3$ by single-crystal x-ray crystallography (table S2 and Fig. 2). The Au_xAg_{19-x} structure consisted

[1]Institute of Physical Science and Information Technology, Key Laboratory of Structure and Functional Regulation of Hybrid Materials of Ministry of Education, Center for Atomic Engineering of Advanced Materials, Anhui Province Key Laboratory of Chemistry for Inorganic/Organic Hybrid Functionalized Materials, Anhui University, Hefei, Anhui 230601, P. R. China. [2]CAS Key Laboratory of Soft Matter Chemistry, Collaborative Innovation Center of Chemistry for Energy Materials (iChEM), Department of Polymer Science and Engineering, University of Science and Technology of China, Hefei, Anhui 230601, P. R. China.
*Corresponding author. Email: chenshuang@ahu.edu.cn (S.C.); zmz@ahu.edu.cn (M.Z.)
†These authors contributed equally to this work.

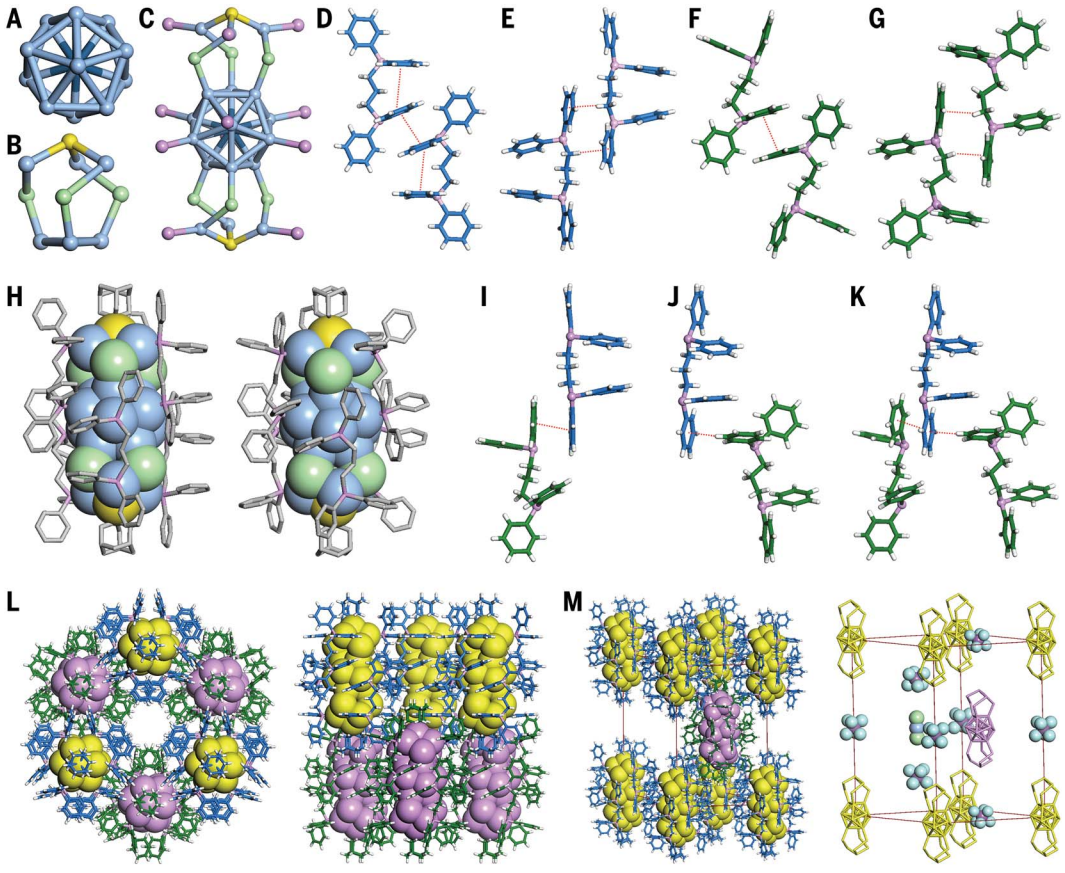

Fig. 1. Crystal structure of Pt_1Ag_{18}. (**A** to **C**) Pt_1Ag_{12} kernel (A), Ag_3Cl_3S motif (B), and structure (C) of the $Pt_1Ag_{18}Cl_6(DPPP)_6(S\text{-}Adm)_2$ rod. (**D**) Intramolecular π...π interaction in **Pt_1Ag_{18}-1**. (**E**) Intramolecular C–H...π interaction in **Pt_1Ag_{18}-1**. (**F**) Intramolecular π...π interaction in **Pt_1Ag_{18}-2**. (**G**) Intramolecular C–H...π interaction in **Pt_1Ag_{18}-2**. (**H**) Overall structure of **Pt_1Ag_{18}-1** [left, yellow highlights in (L) and (M)] and **Pt_1Ag_{18}-2** [right, pink highlights in (L) and (M)]. (**I**) Intermolecular π...π interaction between **Pt_1Ag_{18}-1** and **Pt_1Ag_{18}-2**. (**J**) Intermolecular C–H...π interaction between **Pt_1Ag_{18}-1** and **Pt_1Ag_{18}-2**. (**K**) Interaction between **Pt_1Ag_{18}-1** and **Pt_1Ag_{18}-2**. (**L**) Orthohexagonal packing pattern for **Pt_1Ag_{18}-1** and **Pt_1Ag_{18}-2**. (**M**) A unit cell of Pt_1Ag_{18}. C and H atoms have been omitted for clarity in (A) to (C). H atoms have been omitted for clarity in (H). C, H, and P atoms have been omitted for clarity in the right side of (M). The intramolecular and intermolecular interactions are indicated by red dotted lines in (D) to (G) and (I) to (K).

of an Au_7Ag_6 kernel and an $(AuAg)_6Cl_6(S\text{-}Adm)_2(DPPP)_6$ shell (Fig. 2C). In the Au_7Ag_6 kernel, Ag_3, Au_7, and Ag_3 were stacked sequentially in layers (Fig. 2A). The shell was composed of two crown-like $M_3Cl_3(S\text{-}Adm)_1$ staple motifs (Fig. 2B, where M is a metal, i.e., Au or Ag) and six DPPP ligands (Fig. 2C). The three metal sites in each of the two $M_3Cl_3(S\text{-}Adm)_1$ staple motifs were occupied by either Au or Ag. The two $M_3Cl_3(S\text{-}Adm)_1$ motifs were connected to the Ag atoms on the Au_7Ag_6 kernel through three M–Cl bonds with a bond length of 2.36 Å. Six DPPP ligands bonded to the metal atoms in the staple motifs and the exterior Au atoms of the Au_7Ag_6 kernel through their P atoms. The P–Au–S bond angle was larger than the P–Ag–S bond angle; the average angles were 173.56° and 144.20°, respectively. The resulting total structure of $[Au_xAg_{19-x}(S\text{-}Adm)_2(DPPP)_6Cl_6]^{3+}$ is shown in Fig. 2D.

Each crystal cell contained two Au_xAg_{19-x} molecules with six ClO_4^- counterions (Fig. 2N). Unlike Pt_1Ag_{18}, the patterns of the associated benzene rings of the two Au_xAg_{19-x} molecules in each unit cell were the same (Fig. 2D). However, the orientations of the two Au_xAg_{19-x} NCs were different. In a single molecule of Au_xAg_{19-x}, π...π interactions in a single DPPP ligand and between two DPPP ligands were observed (Fig. 2, E to G). The C–H bonds from the DPPP methylene groups also interacted with the benzene π electrons, forming a C–H...π interaction between two ligands (Fig. 2, H to J). The C–H bonds of the benzene rings in each Au_xAg_{19-x} NCs formed either C–H...π, C–H...π...H–C, or C–H...π...π interactions with the π electrons in the other adjacent Au_xAg_{19-x} NCs (Fig. 2, K and L). Such interactions facilitated crystallization. The different metal atoms and different intermolecular and intramolecular interactions of Pt_1Ag_{18} and Au_xAg_{19-x} led to different packing patterns. Au_xAg_{19-x} formed a zigzag pattern along the [100] crystallographic direction (Fig. 2M).

Characterization of Pt_1Ag_{18} and Au_xAg_{19-x}

The Pt_1Ag_{18} and Au_xAg_{19-x} NCs were further characterized by ultraviolet-visible (UV-vis) spectroscopy, electrospray ionization mass spectrometry (ESI-MS), x-ray photoelectron spectroscopy, and thermogravimetric analysis. The UV-vis absorption spectrum of Pt_1Ag_{18} (fig. S1) includes peaks centered at ~330, 365, and 490 nm (fig. S1A); the energy difference between highest-occupied and lowest-unoccupied molecular orbitals (i.e., the HOMO-LUMO gap) was estimated to be 1.92 eV (fig. S1B). The UV-vis absorption spectrum of Au_xAg_{19-x} had peaks centered at ~353, 427, 483, and 545 nm (fig. S2A), corresponding to a HOMO-LUMO gap of 1.97 eV (fig. S2B). The multiple absorption peaks revealed the quantum size effect of Pt_1Ag_{18} and Au_xAg_{19-x} NCs, which is different from the surface plasmon resonance of nanoparticles.

The ESI-MS spectrum of Pt_1Ag_{18} had a mass-to-charge (m/z) peak centered at 2579.69 (fig. S3), which corresponded to $[Pt_1Ag_{18}(DPPP)_6$

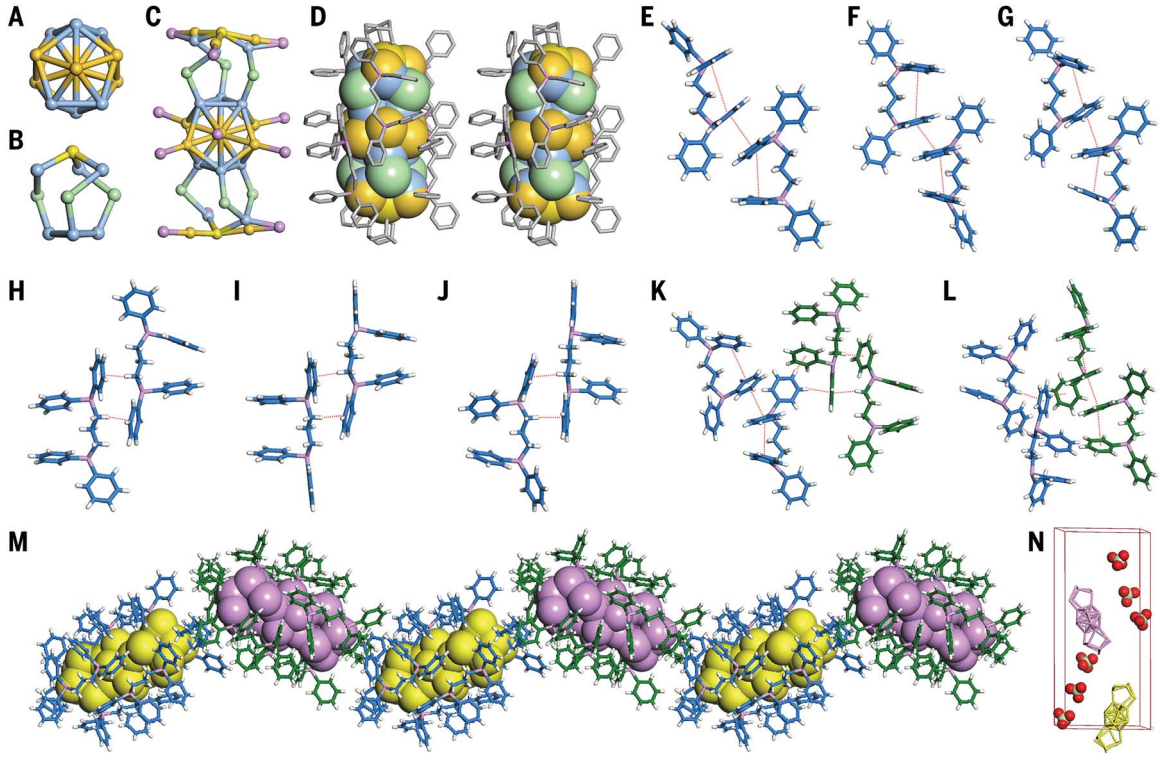

Fig. 2. Crystal structure of Au_xAg_{19-x}. (**A** to **C**) Au_7Ag_6 kernel (A), M_3Cl_3(S-Adm)$_1$ motifs (B), and structure (C) of $Au_xAg_{19-x}Cl_6$(DPPP)$_6$(S-Adm)$_2$. (**D**) Overall structure of Au_xAg_{19-x}. (**E** to **G**) Intramolecular π…π interaction in Au_xAg_{19-x}. (**H** to **J**) Intramolecular C–H…π interaction between two DPPP ligands. (**K** and **L**) Intermolecular C–H…π, C–H…π…H–C, and C–H…π…π interaction in Au_xAg_{19-x}. (**M**) 1D packing pattern for Au_xAg_{19-x}. (**N**) A unit cell of Au_xAg_{19-x}. C and H atoms have been omitted for clarity in (A) to (C). H atoms have been omitted for clarity in (D). C, H, and P atoms have been omitted for clarity in (N). The intramolecular and intermolecular interactions are indicated by red dotted lines in (E) to (L).

(S-Adm)$_2$Cl$_6$]$^{2+}$ (calculated formula weight: 2579.58). The ESI-MS spectrum of Au_xAg_{19-x} showed a series of six peaks corresponding to [Au_xAg_{19-x}(S-Adm)$_2$(DPPP)$_6$Cl$_6$(ClO$_4$)$_1$]$^{2+}$ and [Au_xAg_{19-x}(S-Adm)$_2$(DPPP)$_6$Cl$_6$]$^{3+}$, with $7 \le x \le 9$ (fig. S4). These data were consistent with the results obtained by SCXRD. x-ray photoelectron spectroscopy of Pt_1Ag_{18} (figs. S5 and S6) and Au_xAg_{19-x} (figs. S7 and S8) confirmed the presence of all of the expected elements. Thermogravimetric analysis of Pt_1Ag_{18} showed a total weight loss of 54.7 wt % (fig. S9A), which is consistent with the theoretical loss (53.96 wt %) calculated based on the formula determined from x-ray crystallography. Similarly, the total weight loss of 49.64% is consistent with the theoretical value for [$Au_{10.1}Ag_{8.9}$(S-Adm)$_2$(DPPP)$_6$Cl$_6$](ClO$_4$)$_3$ (fig. S9B).

Pt_1Ag_{18} and Au_xAg_{19-x} microrods as optical waveguides

We investigated the photonic properties of Pt_1Ag_{18} and Au_xAg_{19-x} NCs by optical waveguide. Both Pt_1Ag_{18} and Au_xAg_{19-x} NCs readily formed defect-free single crystals with smooth surfaces (fig. S10) through multiple noncovalent interactions within their structures and their high synthesis purities, thereby ensuring high PL efficiency and minimal light scattering from the domain boundary. Fluorescence microscopy was applied to hexagonal sheets of Pt_1Ag_{18} and Au_xAg_{19-x} to monitor their PL. Under unfocused irradiation, the edges of the Pt_1Ag_{18} and Au_xAg_{19-x} crystals were brighter than the center, indicating their optical waveguide behavior (Fig. 3, B and C).

Next, spatially resolved PL imaging was performed on 1D microrod crystals of Pt_1Ag_{18} and Au_xAg_{19-x} to evaluate the optical waveguide efficiency (Fig. 3A) by moving a focused excitation laser beam (450 nm) to different local positions along the microrod crystal body. Photons propagated predominantly along both directions of the axis of the 1D microrod crystals in two predominant transmission directions (Fig. 3, D and E). The emission intensity at the tip of the microrod decreased with increasing propagation distance, but the spectral intensity and profiles of the excited points were constant.

To quantify the optical loss of the microrod crystals, we calculated the optical loss coefficient (R) by single-exponential fitting: $I_{tip}/I_{body} = A\exp(-RD)$, where I_{tip} and I_{body} are the intensities at the emitted tip and the excited site, respectively, and D is the distance between the excited site and the emitted tip (Fig. 3, D and E). In the Pt_1Ag_{18} microrod, R was calculated to be 5.26×10^{-3} dB μm^{-1}, and in the Au_xAg_{19-x} microrod, it was calculated to be 7.77×10^{-3} dB μm^{-1}. These values exhibited high consistency across different microrods from the same and different batches (figs. S11 to S13), indicating good repeatability. These values are lower than those previously reported for inorganic (*12*), organic (*1*, *6*, *8*, *10*, *11*, *15*), and hybrid materials (*9*, *28*), the R values of which range from ~10 to 60×10^{-3} dB μm^{-1}, and are indicative of high optical waveguide efficiency. Intramolecular interactions of the NCs inhibited nonradiative transitions. Intermolecular interactions, which result in denser crystal packing, high levels of crystallinity, and smooth surfaces, helped to diminish emission losses by scattering.

The optical waveguides of the microrods exhibited stability, with the Au_xAg_{19-x} microrod displaying higher stability than the Pt_1Ag_{18} microrod at a temperature of 50°C in an air environment (figs. S14 to S16). The observed increase in optical loss over time could be attributed to the evaporation of solvent molecules within the crystals under high-temperature and oxygen-rich conditions. Furthermore, the microrods composed of NCs demonstrated excellent stability when subjected to various solvents. As shown in figs. S17 to S19, the Au_xAg_{19-x} microrod displayed a reduced loss coefficient when treated with toluene, p-xylene,

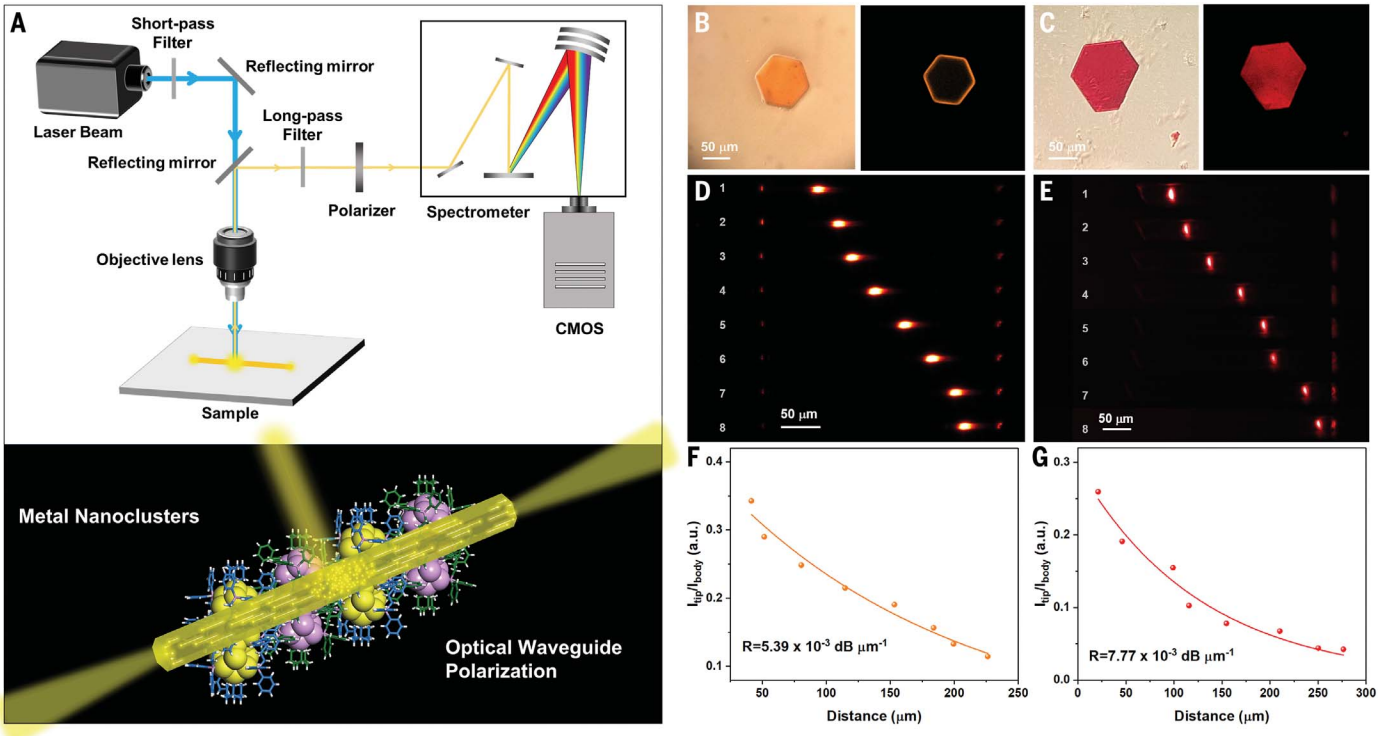

Fig. 3. Optical waveguide of Pt_1Ag_{18} and Au_xAg_{19-x}. (**A**) Experimental setup for the optical waveguide equipment. (**B** and **C**) Photographs of hexagonal sheets of Pt_1Ag_{18} and Au_xAg_{19-x} under visible light (left) and fluorescence microscopy images under unfocused 405 nm irradiation (right). (**D** and **E**) PL images of microrod crystals of Pt_1Ag_{18} and Au_xAg_{19-x} excited with a 450 nm laser focused at different positions. Numbers 1 to 8 correspond to PL images of excitation along the microrod crystal body from left to right. (**F** and **G**) Ratio of the intensities at the tip and body of microrod crystals (I_{tip}/I_{body}) of Pt_1Ag_{18} and Au_xAg_{19-x} versus the distance between the excitation and emission spots on the right side of the images in (D) and (E). The curve was fitted by the exponential decay function $I_{tip}/I_{body} = A\exp(-RD)$.

and c-pentane, whereas the Pt_1Ag_{18} microrod exhibited a slight increase in the loss coefficient when treated with p-xylene, c-pentane, and t-butyl methyl ether. Solvents may affect the weak interactions within the microrods, thereby influencing the optical waveguide performance of NCs.

We observed that NC crystals in bent and branched states exhibited significant optical waveguide effects (figs. S20 and S21). The formation of bent crystals can be attributed to the flexibility of surface organic ligands and the intermolecular interactions of NCs. The waveguides formed by NCs in bent and branched states provide opportunities for photonic propagation within miniaturized complex structures. Additionally, both NC 2D crystal microsheets exhibited optical waveguiding, and we further investigated their waveguide directionality. As shown in figs. S22 and S23, the luminescence intensities of each side of the microsheets were virtually identical when excited in the center. When one side of the crystal was excited, the other sides exhibited similar emission intensities. These results indicate the absence of anisotropy in the optical waveguide behavior. However, optical waveguide behavior was barely observed in the amorphous powder state (fig. S24) and film state (fig. S25) of the NCs, which can be attributed to the limited ability of photons to propagate in the absence of highly ordered structures of NCs.

We studied whether other LPMNCs could exhibit the optical waveguide properties, and found that Au_4Cu_5 (*29*), Au_1Cu_{14} (*30*), and Pt_1Ag_{37} (*31*) also exhibited low R, with $R = 13.21 \times 10^{-3}$ dB μm^{-1} for Au_4Cu_5, 15.88×10^{-3} dB μm^{-1} for Au_1Cu_{14}, and 9.92×10^{-3} dB μm^{-1} for Pt_1Ag_{37} (fig. S26). We further studied the effect of Stokes shifts of all of these LPMNCs on R. The large Stokes shifts of NCs correspond to a narrow overlap in the emission and main absorption spectra and effectively diminished reabsorption of light during propagation along the crystals. However, R did not decrease with the increase of Stokes shifts (fig. S27), which indicated that the Stokes shift was not the only factor affecting the optical loss coefficient of metal NCs. Smooth surfaces and high crystal quality also have important effects on optical waveguide properties (*22*, *32*).

Polarized optical performance of Pt_1Ag_{18} and Au_xAg_{19-x}

The optical properties of emitters are directly affected by the packing of their constituent molecules and the orientation of their optical transition dipoles. In particular, packing and orientation lead to distinct PL polarization, an effect that is important for waveguide design, optical connections, and active optical communication device integration. To elucidate the optical anisotropy caused by the orientation of the molecules in the microrods, polarized optical microscopy was performed. By rotating the polarizer to different polarization angles (θ), the linear polarization of the light signal emitted from the tips of microrods of Pt_1Ag_{18} and Au_xAg_{19-x} could be obtained. We measured θ as the angle between the horizontal direction of the 1D crystal and the polarization direction of the polarizer placed in front of the charge-coupled device detector (Fig. 3A) and recorded the PL intensities of the polarized light signals from the tip at 30° increments (Fig. 4).

The relationship between the maximum luminous intensity and the polarization angle of the microrod crystals was well with a $\sin^2$ curve. The Pt_1Ag_{18} microrod displayed the highest fluorescence intensities at polarized angles of 8° and 188° and the lowest at 98° and 278° (Fig. 4A), leading to an emission dichroic ratio ($R_d = I_{8°}/I_{98°}$) of 21.4 and a polarization ratio [$\rho = (R_d - 1)/(R_d + 1)$] of 0.91, which was beneficial to materials. However, Au_xAg_{19-x} microrods exhibited weak polarization properties,

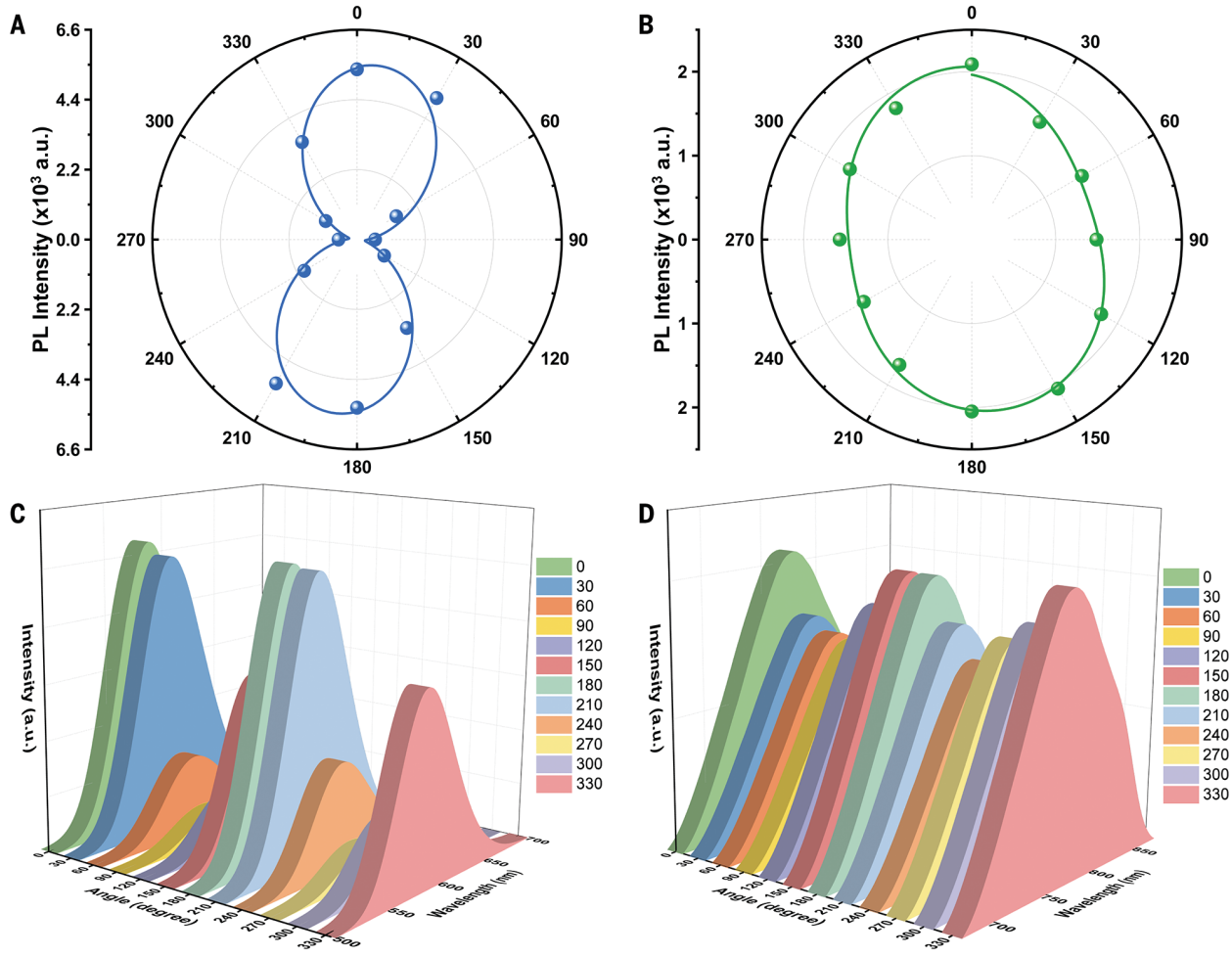

Fig. 4. Polarized optical performance of Pt_1Ag_{18} and Au_xAg_{19-x}. (**A** and **B**) Photoemission intensity of the Pt_1Ag_{18} and Au_xAg_{19-x}, respectively, as a function of the polarizer rotation angle θ. (**C** and **D**) Polarized PL spectra of Pt_1Ag_{18} and Au_xAg_{19-x} microrods, respectively, at various angles (~0 to 360°).

with a ρ of 0.17, as calculated from its highest and lowest PL intensities at 174° and 71°, respectively.

Observation of the molecular orientations of Pt_1Ag_{18} and Au_xAg_{19-x} (Figs. 1M and 2M), the angle between the transition dipole moment of the Pt_1Ag_{18} NCs, and their preferred direction of growth results in high polarization emission. For Au_xAg_{19-x} microrods, however, the weak PL anisotropy detected was attributed to the zigzag pattern in which the two molecules in each unit cell pack together (Fig. 2M). Thus, the differences in the polarization properties of Pt_1Ag_{18} and Au_xAg_{19-x} can be attributed to the partially anisotropic structure of NC entities and their incomplete mirror symmetry packing modes (*33*).

PL properties

We further explored the emissions of Pt_1Ag_{18} and Au_xAg_{19-x} as amorphous solids and in dichloromethane solution by measuring their QY, defined as the ratio of emitted photons to absorbed photons, and their PL lifetime. The solution of Pt_1Ag_{18} was weakly emissive; the maximum emission was centered at 600 nm under an excitation of 366 nm (Fig. 5A) with a QY of 0.25%. By comparison, solid Pt_1Ag_{18} exhibited an intense orange emission (Fig. 5B) with a much higher QY of 28.9%. The average PL lifetime of Pt_1Ag_{18} was also improved in the solid state, with the lifetimes in solution and in the solid state of 0.54 and 1.88 μs, respectively (fig. S28). This trend held, although with smaller increases, for Au_xAg_{19-x}. In solution, Au_xAg_{19-x} displayed a weak red emission at 770 nm with a QY of 4.66% under excitation at 467 nm (Fig. 5, A and B), but a slightly stronger emission was observed in the solid state, with a QY of 6.91%. The average PL lifetimes of Au_xAg_{19-x} similarly had a small increase in the solid state, as the lifetime in solution and in the solid state were 2.68 and 3.17 μs, respectively (fig. S29). The differences in emission between Pt_1Ag_{18} and Au_xAg_{19-x} can be attributed to the alloy effect, which influences the origin of the PL.

This difference in the emissions of Pt_1Ag_{18} and Au_xAg_{19-x} in different states led us to further explore their aggregation-induced emission enhancement (AIEE) performance. We analyzed solutions of each material in mixtures of acetonitrile (MeCN) and H_2O, selected for their ability to dissolve the two NCs readily and poorly, respectively. The PL intensity of Pt_1Ag_{18} was enhanced 30-fold as the proportion of water in the binary solvent mixture increased, reaching a maximum value of PL at a 4:6 volume ratio of MeCN:H_2O (Fig. 5C). Increasing the proportion of water >60% decreased the emissions, but the PL was still much higher than that in pure MeCN. Similar results were observed previously in other AIEE active materials (*34*).

Dynamic light scattering was used to evaluate the aggregation degree and size distribution of Pt_1Ag_{18}, showing that the aggregation of the NCs was highest at 4:6 MeCN:H_2O, with an average aggregate diameter of 342 nm (range 220 to 531 nm) (fig. S30), thus confirming the relationship between increased aggregation and increased PL emission. Similar results were observed in solutions of Au_xAg_{19-x}, with a fivefold enhancement in the PL intensity of strong red emissions at a MeCN:H_2O volume

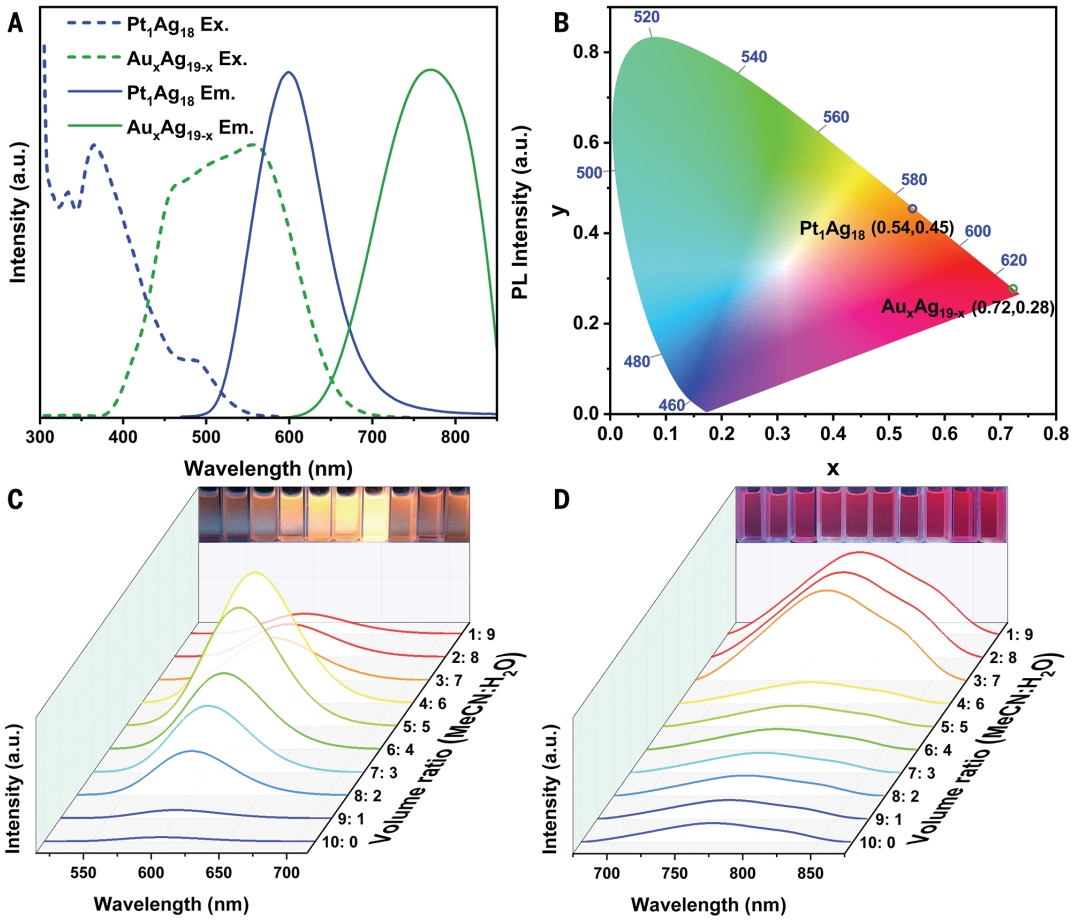

Fig. 5. PL of Pt_1Ag_{18} and Au_xAg_{19-x}. (**A**) Excitation (blue dashed line) and emission (blue solid line) spectra of Pt_1Ag_{18} in solution and the excitation (green dashed line) and emission (green solid line) spectra of Au_xAg_{19-x} in solution. (**B**) Commission Internationale de l'Eclairage (CIE) chromaticity coordinates of the PL of Pt_1Ag_{18} (blue circle) and Au_xAg_{19-x} (green circle). (**C** and **D**) Photoemission spectra of Pt_1Ag_{18} and Au_xAg_{19-x}, respectively, in mixed solvents of MeCN and H_2O with different volume ratios. Insets: digital photos of Pt_1Ag_{18} and Au_xAg_{19-x} in mixed solvents with different volume ratios under 365 nm UV light irradiation.

ratio of 3:7 (Fig. 5D) caused by the maximum degree of aggregation (fig. S31).

To evaluate the effect of aggregation on absorption, UV-vis absorption spectra of Pt_1Ag_{18} and Au_xAg_{19-x} in various mixed solvent systems were collected. As shown in fig. S32A, neither a shift in absorption peak nor a change in relative intensity was observed across 10 different solvent mixtures, suggesting that the aggregation of Pt_1Ag_{18} is not associated with decomposition or structural changes. As shown in fig. S32B, the UV-vis absorption spectra of Au_xAg_{19-x} in 10 mixed solvent systems also showed no absorption peak shift or relative intensity change. Both Pt_1Ag_{18} and Au_xAg_{19-x} NCs exhibited AIEE performance without decomposition or structural changes to the ligand-protected NCs, although the PL enhancement of Pt_1Ag_{18} was more pronounced.

Conclusions

Here, we synthesized and characterized ligand-protected Pt_1Ag_{18} and Au_xAg_{19-x} NCs and studied their optical waveguide properties. Both NCs consist of an icosahedral M_{13} core, two crown-like $M_3Cl_3(SR)_1$ staple motifs, and six DPPP ligands. Crystals of the Pt_1Ag_{18} and Au_xAg_{19-x} NCs exhibited excellent optical waveguide performance, with low optical loss coefficients of 5.26×10^{-3} and 7.77×10^{-3} dB μm^{-1}, respectively, which can be attributed to their inhibition of nonradiative transition, dense crystal packing, and large Stokes shifts. Furthermore, the optical waveguide performance of other NCs was investigated, which revealed the universality among ligand-protected, atomically precise NCs. The different crystal structures and packing modes of Pt_1Ag_{18} and Au_xAg_{19-x} account for their distinct polarized waveguide performance. Pt_1Ag_{18} microrods displayed excellent polarizing properties with a polarization ratio of 0.91, whereas Au_xAg_{19-x} microrods showed weak polarized emission with a polarization ratio of 0.17. Furthermore, Pt_1Ag_{18} and Au_xAg_{19-x} displayed an AIEE effect, and 115- and 1.5-fold enhancements in QY were observed for Pt_1Ag_{18} (28.9% versus 0.25%) and Au_xAg_{19-x} (6.91% versus 4.66%) from the solid state to solution. Collectively, these results suggest that Pt_1Ag_{18} and Au_xAg_{19-x} NCs have potential for use in optical communication and miniaturized optoelectronic devices.

REFERENCES AND NOTES

1. S. Wu, B. Zhou, D. Yan, *Adv. Opt. Mater.* **9**, 2001768 (2021).
2. Y. Yan, C. Zhang, J. Yao, Y. S. Zhao, *Adv. Mater.* **25**, 3627–3638 (2013).
3. B. Zhou, G. Xiao, D. Yan, *Adv. Mater.* **33**, e2007571 (2021).
4. W. Yao *et al.*, *Angew. Chem. Int. Ed.* **52**, 8713–8717 (2013).
5. Y. Liu *et al.*, *Angew. Chem. Int. Ed.* **59**, 4456–4463 (2020).
6. Q. H. Cui, Y. S. Zhao, J. Yao, *Adv. Mater.* **26**, 6852–6870 (2014).
7. S. Li, B. Lu, X. Fang, D. Yan, *Angew. Chem. Int. Ed.* **59**, 22623–22630 (2020).
8. X. Ye *et al.*, *Nat. Commun.* **10**, 761 (2019).
9. J. Zhao *et al.*, *J. Am. Chem. Soc.* **141**, 15755–15760 (2019).
10. H. Luo *et al.*, *Adv. Funct. Mater.* **24**, 4250–4258 (2014).
11. M.-D. Qian *et al.*, *Mater. Horiz.* **7**, 1782–1789 (2020).
12. A. Pan *et al.*, *Small* **1**, 980–983 (2005).
13. Z.-F. Chang *et al.*, *Chemistry* **21**, 8504–8510 (2015).
14. Y. Li *et al.*, *ACS Appl. Mater. Interfaces* **9**, 8910–8918 (2017).
15. W. Hu *et al.*, *Adv. Mater.* **26**, 3136–3141 (2014).
16. R. Jin, C. Zeng, M. Zhou, Y. Chen, *Chem. Rev.* **116**, 10346–10413 (2016).
17. I. Chakraborty, T. Pradeep, *Chem. Rev.* **117**, 8208–8271 (2017).
18. Y. Li *et al.*, *Nature* **594**, 380–384 (2021).

19. P. D. Jadzinsky, G. Calero, C. J. Ackerson, D. A. Bushnell, R. D. Kornberg, *Science* **318**, 430–433 (2007).
20. C. Zeng, Y. Chen, K. Kirschbaum, K. J. Lambright, R. Jin, *Science* **354**, 1580–1584 (2016).
21. M. Zhou *et al*., *Science* **364**, 279–282 (2019).
22. Q. Bao *et al*., *Adv. Mater.* **22**, 3661–3666 (2010).
23. X. Kang, M. Zhu, *Chem. Soc. Rev.* **48**, 2422–2457 (2019).
24. Q. Li *et al*., *Science* **378**, 768–773 (2022).
25. N. Goswami *et al*., *J. Phys. Chem. Lett.* **7**, 962–975 (2016).
26. H. Zhang *et al*., *Adv. Mater.* **32**, e2001457 (2020).
27. X. Kang *et al*., *Chem. Sci.* **8**, 2581–2587 (2017).
28. B. Zhou, Z. Qi, D. Yan, *Angew. Chem. Int. Ed.* **61**, e202208735 (2022).
29. M. Zhou *et al*., *J. Phys. Chem. C* **124**, 7531–7538 (2020).
30. Y. Song *et al*., *Sci. Adv.* **7**, eabd2091 (2021).
31. Y. Zhen *et al*., *Inorg. Chem. Front.* **9**, 3907–3914 (2022).
32. X. Yang, X. Lin, Y. Zhao, Y. S. Zhao, D. Yan, *Angew. Chem. Int. Ed.* **56**, 7853–7857 (2017).
33. H. Li *et al*., *J. Am. Chem. Soc.* **144**, 4845–4852 (2022).
34. M. Shyamal *et al*., *J. Photochem. Photobiol. Chem.* **342**, 1–14 (2017).

ACKNOWLEDGMENTS

We thank J. Ni at University of Science and Technology of China. S.C. acknowledges the support of E. Ye. **Funding:** This work was supported by the National Natural Science Foundation of China (grants 22004001, 21631001, and 21871001), the Ministry of Education, the University Synergy Innovation Program of Anhui Province (grant GXXT-2020-053), and the Anhui Provincial Natural Science Foundation (grant 2008085QB84). **Author contributions:** S.C. and M.Z. conceived the initial idea. S.C. and X.W. designed the research. X.W., B.Y., and L.J. performed NC preparation, structural determination, and characterization. X.W., B.Y., and C.Y. conducted the optical waveguide and polarization test. X.W., B.Y., and L.J. performed PL experiments. S.C., X.W., G.Z., and M.Z. wrote the paper, and all authors commented on it. **Competing interests:** The authors declare no competing interests. **Data and materials availability:** Crystallographic data are provided free of charge by the joint Cambridge Crystallographic Data Centre at www.ccdc.cam.ac.uk/data_request/cif (deposition numbers 2098494 for Pt_1Ag_{18} and 2178943 for Au_xAg_{19-x}). All remaining data are available in the main text or the supplementary materials. **License information:** Copyright © 2023 the authors, some rights reserved; exclusive licensee American Association for the Advancement of Science. No claim to original US government works. https://www.science.org/about/science-licenses-journal-article-reuse

SUPPLEMENTARY MATERIALS

science.org/doi/10.1126/science.adh2365
Materials and Methods
Supplementary Text
Figs. S1 to S32
Tables S1 and S2
References (*35*–*37*)

Submitted 18 February 2023; accepted 10 July 2023
Published online 27 July 2023
10.1126/science.adh2365

PHYSICS

Universal theory of strange metals from spatially random interactions

Aavishkar A. Patel[1,2], Haoyu Guo[3,4,5], Ilya Esterlis[4,6], Subir Sachdev[4,7]*

Strange metals—ubiquitous in correlated quantum materials—transport electrical charge at low temperatures but not by the individual electronic quasiparticle excitations, which carry charge in ordinary metals. In this work, we consider two-dimensional metals of fermions coupled to quantum critical scalars, the latter representing order parameters or fractionalized particles. We show that at low temperatures (T), such metals generically exhibit strange metal behavior with a T-linear resistivity arising from spatially random fluctuations in the fermion-scalar Yukawa couplings about a nonzero spatial average. We also find a $T\ln(1/T)$ specific heat and a rationale for the Planckian bound on the transport scattering time. These results are in agreement with observations and are obtained in the large N expansion of an ensemble of critical metals with N fermion flavors.

A major theme in the study of correlated metals has been their strange metal behavior at low temperatures—i.e., a linear-in-temperature resistivity smaller than the quantum unit of resistivity (h/e^2 in two dimensions), which appears to be controlled by a dissipative Planckian relaxation time of order $\hbar/(k_B T)$ (where h is Planck's constant, $\hbar = h/(2\pi)$, e is the electron charge, k_B is Boltzmann's constant, and T is the absolute temperature) (*1*–*8*). This behavior is in sharp contrast to T^2 dependence of the resistivity and the $1/T^2$ relaxation time, invariably observed in conventional metals described by Fermi liquid theory. Moreover, the anomalous resistivity of strange metals is accompanied by a logarithmic enhancement of the Sommerfeld metallic specific heat to $T\ln(1/T)$ (*1*) from the $\sim T$ behavior of conventional metals.

Starting with the seminal work by Hertz (*9*), there has been extensive research on the properties of electronic Fermi surfaces at quantum phase transitions (*10*). The quantum critical fluctuations are represented by a scalar field, which is usually a symmetry-breaking order parameter but could also be a fractionalized particle at phase transitions without an order parameter (*11*). This scalar field has a Yukawa coupling to the electrons, by which the electrons scatter by emitting or absorbing a scalar field excitation (the Yukawa coupling is similar to the electron-phonon coupling but without a suppression by the gradient of the scalar field). It is now known that such a Fermi surface coupled to a quantum critical scalar leads to a breakdown of the electronic quasiparticle excitations in two spatial dimensions (*10*, *12*). But the Fermi surface survives as a sharp boundary in momentum space, separating particle- and hole-like excitations, which are diffuse in energy space. In the presence of random impurities that scatter the electrons (*13*–*17*), there are cases where the quasiparticles are at the boundary of stability, which leads to marginal Fermi liquid behavior (*18*) in single-particle observables, such as those observed in photoemission experiments.

However, despite these advances, theory has so far found limited success in explaining all of the defining transport properties (such as the linear-in-T resistivity) of strange metals. Conservation of momentum in the low-energy theory of a clean metal implies that the dc and optical conductivities are not affected by the anomalous self-energy of the excitations near the Fermi surface (*15*–*17*, *19*–*22*). In other words, the strong coupling between the Fermi surface and the scalar field places the system in the limit of strong scalar drag, and this clean metal theory cannot describe strange metal behavior. This is in contrast to the electron-phonon system, where the weak electron-phonon coupling makes phonon drag a factor only in ultrapure samples (*23*). Umklapp scattering can lead to nonzero resistance, and its influence in quantum critical metals has been investigated in other works (*16*, *24*). However, umklapp is suppressed at low T, its predictions for transport are not universal and depend upon specific Fermi surface details, and there is no corresponding $T\ln(1/T)$ specific heat.

Given the ubiquity of strange metal transport across numerous correlated electron materials (from the cuprates and the pnictides to recently discovered twisted bilayer graphene), a simple and universal mechanism may h… play. We propose that spatial disorder in … fermion-scalar Yukawa coupling, about a nonzero spatial average, provides just such a universal mechanism. Such disorder is ubiquitous in models of correlated electron materials; for example, in a Hubbard model with on-site repulsion U and an impurity-induced disorder in the electron hopping t_{ij}, the Schrieffer-Wolff transformation generates disorder in the exchange interaction $J_{ij} = 4t_{ij}^2/U$, and this disorder then feeds into the Yukawa coupling after a standard decoupling procedure (*9*) that introduces the scalar field. Moreover, our mechanism applies universally across different classes of quantum critical metals, with scalars that are either fractionalized particles or order parameters at zero or nonzero momentum, which have distinct critical behaviors in the clean limit. In the limit of a large number of fermion flavors, N, we find a universal phenomenology that matches observations, including the T-linear resistivity, the Planckian relaxation time, and the $T\ln(1/T)$ specific heat.

A key observation of our analysis is that although the fermion inelastic self-energy corrections can be dominated by the spatially uniform coupling, the transport is nevertheless dominated by the spatially random coupling, and this leads to our main results. Our work follows other recent works with random Yukawa interactions (*25*–*34*) inspired by the Sachdev-Ye-Kitaev (SYK) model (*35*, *36*) along with studies that found linear-in-T resistivity with random interactions but with vanishing spatial average (*32*, *34*, *37*–*39*).

Spatially uniform quantum critical metal

We begin by recalling the SYK-inspired large N theory of the two-dimensional quantum critical metal (*32*, *34*) for the case where the order parameter has zero momentum. The imaginary time (τ) action for the fermion field ψ_i and scalar field φ_i (with $i = 1 \ldots N$ a flavor label carried by the fermions introduced only to enable a controlled large N limit) is (*34*)

$$\mathcal{S}_g = \int d\tau \sum_{\mathbf{k}} \sum_{i=1}^{N} \psi_{i\mathbf{k}}^{\dagger}(\tau)[\partial_\tau + \varepsilon(\mathbf{k})]\psi_{i\mathbf{k}}(\tau) + \frac{1}{2}\int d\tau \sum_{\mathbf{q}} \sum_{i=1}^{N} \phi_{i\mathbf{q}}(\tau)(-\partial_\tau^2 + K\mathbf{q}^2 + m_b^2)\phi_{i,-\mathbf{q}}(\tau) + \frac{g_{ijl}}{N}\int d\tau d^2 r \sum_{i,j,l=1}^{N} \psi_i^{\dagger}(\mathbf{r},\tau)\psi_j(\mathbf{r},\tau)\phi_l(\mathbf{r},\tau) \quad (1)$$

where $\mathbf{k}$ and $\mathbf{q}$ are spatial momenta, the fermion dispersion $\varepsilon(\mathbf{k})$ determines the Fermi surface, the scalar mass m_b must be tuned to criticality and is needed for infrared regularization but does not appear in final results, and the Yukawa fermion-scalar coupling g_{ijl} is space independent but random in flavor

[1]Center for Computational Quantum Physics, Flatiron Institute, New York, NY 10010, USA. [2]Department of Physics, University of California Berkeley, Berkeley, CA 94720, USA. [3]Laboratory of Atomic and Solid State Physics, Cornell University, Ithaca, NY 14853, USA. [4]Department of Physics, Harvard University, Cambridge, MA 02138, USA. [5]Kavli Institute for Theoretical Physics, University of California Santa Barbara, Santa Barbara, CA 93106, USA. [6]Department of Physics, University of Wisconsin–Madison, Madison, WI 53706, USA. [7]School of Natural Sciences, Institute for Advanced Study, Princeton, NJ 08540, USA.
*Corresponding author. Email: sachdev@g.harvard.edu

space with

$$\overline{g_{ijl}} = 0, \overline{g^*_{ijl} g_{abc}} = g^2 \delta_{ia}\delta_{jb}\delta_{lc} \quad (2)$$

where the overline represents average over flavor space. The hypothesis is that a large domain of flavor couplings all flow to the same universal low-energy theory (as in the SYK model), so we can safely examine the average of an ensemble of theories. Momentum is conserved in each member of the ensemble, and the flavor-space randomness does not lead to any essential difference from nonrandom theories. This is in contrast to position-space randomness, which we consider later and which does relax momentum and modify physical properties.

The disorder average of the partition function of $\mathcal{S}_g$ leads to a so-called G-Σ theory, whose large N saddle point of Eq. 1 has singular fermion (Σ) and boson (Π) self-energies at T = 0 (where ω is frequency) (*34*)

$$\Pi(i\omega, \mathbf{q}) = -c_b \frac{|\omega|}{|\mathbf{q}|}, \Sigma(i\omega, \mathbf{k}) = -ic_f \mathrm{sgn}(\omega)|\omega|^{2/3}$$
$$c_b = \frac{g^2}{2\pi\kappa v_F}, c_f = \frac{g^2}{2\pi v_F \sqrt{3}} \left(\frac{2\pi v_F \kappa}{K^2 g^2}\right)^{1/3} \quad (3)$$

These results are obtained on a circular Fermi surface with curvature $\kappa = 1/m$, where m is the effective mass of the fermions. The result is consistent with the theory of two antipodal patches around $\pm\mathbf{k}_0$ on the Fermi surface to which $\mathbf{q}$ is tangent, with axes chosen so that $\mathbf{q} = (0, q)$ and fermionic dispersion $\epsilon(\pm\mathbf{k}_0 + \mathbf{k}) = \pm v_F k_x + \kappa k_y^2/2$.

The large N computation of the conductivity (*17*, *22*) yields only the clean Drude result $\mathrm{Re}[\sigma(\omega)]/N = \pi\mathcal{N}v_F^2\delta(\omega)/2$, where $\mathcal{N} = m/(2\pi)$ is the fermion density of states at the Fermi level. This is in contrast to the results of previous studies (*12*, *40*), in which it has been found that dc resistivity is $\sim T^{4/3}$ and optical conductivity is $\sim|\omega|^{-2/3}$.

Potential disorder

We now add to the model a spatially random fermion potential

$$\mathcal{S}_v = \frac{1}{\sqrt{N}} \int d^2 r d\tau v_{ij}(\mathbf{r}) \psi_i^\dagger(\mathbf{r}, \tau)\psi_j(\mathbf{r}, \tau)$$
$$v_{ij}(\mathbf{r}) = 0, \overline{v_{ij}^*(\mathbf{r}) v_{lm}(\mathbf{r}')} = v^2 \delta(\mathbf{r} - \mathbf{r}')\delta_{il}\delta_{jm} \quad (4)$$

Here, the overline is an average over both spatial coordinates and flavor space. The large N limit of the G-Σ theory (*17*) yields a saddle point that has statistical translational invariance and is similar to that found in earlier studies (*13*, *15*, *16*). The low-frequency boson propagator now has the diffusive form $\sim(q^2 + c_d|\omega|)^{-1}$ with dynamic critical exponent z = 2, whereas the fermion self-energy has an elastic scattering term along with a marginal Fermi liquid (*18*) inelastic term at low frequencies

$$\Pi(i\omega, \mathbf{q}) = -\frac{\mathcal{N}g^2|\omega|}{\Gamma}, \Gamma = 2\pi v^2 \mathcal{N},$$
$$\Sigma\left(i\omega, \mathbf{k} = k_F\hat{k}\right) = -i\frac{\Gamma}{2}\mathrm{sgn}(\omega)$$
$$-\frac{ig^2\omega}{2\pi^2\Gamma}\ln\left(\frac{e\Gamma^3}{\mathcal{N}g^2 v_F^2|\omega|}\right) \quad (5)$$

at T = 0. However, the marginal Fermi liquid self-energy, although leading to a $T\ln(1/T)$ specific heat, does not (*17*) lead to the claimed (*18*) linear-T term in the dc resistivity because it arises from forward scattering of electrons off the $\mathbf{q} \sim 0$ bosons. These forward-scattering processes are unable to relax either current or momentum because of the small wavevector of the bosons involved and the momentum conservation of the g interactions. As a result, even a perturbative computation of the conductivity at $\mathcal{O}(g^2)$ (Fig. 1) shows a cancellation between the interaction-induced self-energy contributions and the interaction-induced vertex correction, leading to a dc conductivity that is just a constant set by the elastic potential disorder scattering rate Γ. The leading frequency dependence of the optical conductivity at frequencies $\omega \ll \Gamma$ is just a constant, and there is no linear in-frequency correction (*17*). Correspondingly, in the dc limit, there is no linear in-T correction, and a conventional T^2 correction is expected.

Interaction disorder

Our main results are obtained with additional spatially random interactions. In principle, such terms will be generated under a renormalization analysis from $\mathcal{S}_v$. However, such a renormalization is not part of our large N limit, so we account for such interactions by adding an explicit term

$$\mathcal{S}_{g'} = \frac{1}{N}\int d^2 r d\tau g'_{ijl}(\mathbf{r})\psi_i^\dagger(\mathbf{r}, \tau)\psi_j(\mathbf{r}, \tau)\phi_l(\mathbf{r}, \tau)$$
$$\overline{g'_{ijl}(\mathbf{r})} = 0, \overline{g'^*_{ijl}(\mathbf{r}) g'_{abc}(\mathbf{r}')}$$
$$= g'^2 \delta(\mathbf{r} - \mathbf{r}')\delta_{ia}\delta_{jb}\delta_{lc} \quad (6)$$

Note, v, g, and g' are all independent flavor-random variables. Earlier works have considered the limiting case of g = 0, v = 0, and $g' \neq 0$ (*32*, *34*). We will instead describe the more physically relevant regime where spatial disorder is a weaker perturbation to a clean quantum critical system, with g the largest interaction coupling. We therefore now have g, v, and g' all nonzero. The theory of $\mathcal{S}_g + \mathcal{S}_v + \mathcal{S}_{g'}$ is described in the supplementary materials (*41*).

As with $\mathcal{S}_g + \mathcal{S}_v$ above, we find a statistical translational invariance at large N, with a low-frequency boson propagator characterized by z = 2 and the low-frequency fermion self-energy with an elastic scattering term along with a marginal Fermi liquid inelastic term (*42*)

$$\Pi(i\omega, \mathbf{q}) = -\frac{\mathcal{N}g^2|\omega|}{\Gamma} - \frac{\pi}{2}\mathcal{N}^2 g'^2|\omega| \equiv -c_d|\omega|,$$
$$\Sigma\left(i\omega, \mathbf{k} = k_F\hat{k}\right) = -i\frac{\Gamma}{2}\mathrm{sgn}(\omega) - \frac{ig^2\omega}{2\pi^2\Gamma}$$
$$\ln\left(\frac{e\Gamma^2}{v_F^2 c_d|\omega|}\right) - \frac{i\mathcal{N}g'^2\omega}{4\pi}\ln\left(\frac{e\Lambda_d^2}{c_d|\omega|}\right)(T = 0) \quad (7)$$

where $\Lambda_d \sim \Gamma/v_F$. This self-energy leads to a $T\ln(1/T)$ specific heat, as for the large g' case (*34*). However, there is now an important difference with respect to the previous case where g' = 0, which leads to markedly different charge transport properties: The marginal Fermi liquid self-energy now contains a term (last term in Eq. 7) that does not arise solely from the forward scattering of electrons. This term is produced by the disordered part of the interactions in Eq. 6. Thus, this part of the self-energy represents scattering that relaxes both current and momentum carried by the electron fluid, and therefore its imaginary part on the real frequency axis determines the inelastic transport scattering rate.

We can show this as follows by computing the conductivity using the Kubo formula. If we work perturbatively in g and g', then the

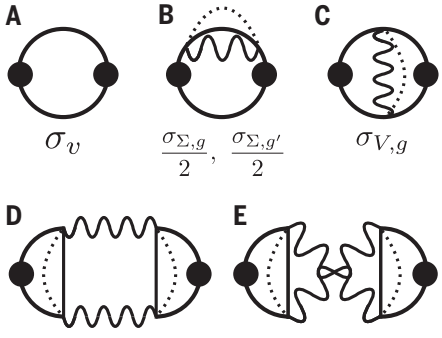

Fig. 1. Interaction corrections to the conductivity in the large *N* limit. (**A** to **E**) The current operators are denoted by solid circles, and the wavy lines denote boson propagators. Dashed lines denote random flavor averaging of the interaction couplings. The fermion Green's functions (solid lines) include the effects of the disordered potential (v), and the quantum critical boson propagators include the effects of damping due to interactions. Vertex corrections [(C) to (E)] contain only g interactions because the contributions from g' interactions vanish as a result of the decoupling of the momentum integrals in the loops containing the external current operators. The sum of the two Aslamazov-Larkin diagrams [(D) and (E)] vanishes exactly in the limit of large Fermi energy, and the perturbative result (Eq. 9) is therefore valid to all orders in the interaction strength (*41*).

conductivity at $\mathcal{O}(g^2)$ and $\mathcal{O}(g'^2)$ in the large N limit is given by the sum of self-energy contributions and vertex corrections (Fig. 1). However, owing to the isotropy of the scattering processes arising from the g' interactions, only the vertex correction caused by the g interactions survives. The conductivity up to the first subleading frequency-dependent correction is then given by (*41*)

$$\frac{1}{N}\mathrm{Re}[\sigma(\omega \gg T)] = \sigma_v + \sigma_{\Sigma,g} + \sigma_{V,g} + \sigma_{\Sigma,g'};$$
$$\sigma_v(\omega) = \frac{\mathcal{N}v_F^2}{2\Gamma}, \sigma_{\Sigma,g}(\omega) = -\frac{\mathcal{N}v_F^2 g^2|\omega|}{8\pi\Gamma^3},$$
$$\sigma_{V,g}(\omega) = \frac{\mathcal{N}v_F^2 g^2|\omega|}{8\pi\Gamma^3}, \sigma_{\Sigma,g'}(\omega) = -\frac{\mathcal{N}^2 v_F^2 g'^2|\omega|}{16\Gamma^2} \tag{8}$$

Note that the g^2 vertex and self-energy terms cancel, and we have

$$N\mathrm{Re}\left[\frac{1}{\sigma(\omega \gg T)}\right] = \frac{1}{\mathcal{N}v_F^2}\left(2\Gamma + \frac{\mathcal{N}g'^2|\omega|}{4}\right) \tag{9}$$

The g'^2 term does not cancel and leads to a linear in-frequency correction to the constant transport scattering rate Γ. In the opposite limit $|\omega| \ll T$, this translates into a T-linear correction to the resistivity in the dc limit; computing the coefficient of the linear-T resistivity requires a self-consistent numerical analysis, which has been carried out in the large g' limit (*32*, *34*). Notably, the slope of this scattering rate with respect to $|\omega|$ (and therefore T) does not depend on Γ and hence on the residual ($\omega = T = 0$) resistivity. We show (*41*) that the perturbative result described here continues to be valid under a full resummation of all diagrams at large N in the Kubo formula because all surviving higher-order contributions are merely repetitions of the interaction insertions in Fig. 1, B and C.

We can also consider the case where $v = 0$ but $g \neq 0$ and $g' \neq 0$. In this case, we have (at $T = 0$) (*41*)

$$\Pi(i\omega, \mathbf{q}) = -c_b\frac{|\omega|}{|\mathbf{q}|} - \frac{\pi}{2}\mathcal{N}^2 g'^2|\omega|,$$
$$\Sigma(i\omega, \mathbf{k}) = -ic_f \mathrm{sgn}(\omega)|\omega|^{2/3} - \frac{i\mathcal{N}g'^2\omega}{6\pi}$$
$$\ln\left(\frac{e\tilde{\Lambda}^3}{c_b|\omega|}\right) \tag{10}$$

where $\tilde{\Lambda} \sim g^2/(g'^2 v_F \mathcal{N})$ is an ultraviolet (UV) momentum cutoff. Notably, the disordered interactions induce a marginal Fermi liquid term in Σ, which manifests as the first higher-order correction to the translationally invariant result in Eq. 3 (*43*)

It is sufficient in this $v = 0$ but $g \neq 0$ and $g' \neq 0$ case to compute the conductivity using the theory of modes in the vicinity of antipodal points on the Fermi surface (*44*) We then find, as before, that $\sigma_{\Sigma,g}$ and $\sigma_{V,g}$ cancel and (*41*)

$$\frac{1}{N}\sigma(i\omega \gg T) = \frac{\mathcal{N}v_F^2}{2\omega} - \frac{\mathcal{N}^2 v_F^2 g'^2}{24\pi\omega}\ln\left(\frac{e^3\tilde{\Lambda}^6}{c_b^2\omega^2}\right)$$
$$\approx \frac{\mathcal{N}v_F^2}{2\omega + \frac{\mathcal{N}g'^2\omega}{6\pi}\ln\left(\frac{e^3\tilde{\Lambda}^6}{c_b^2\omega^2}\right)};$$
$$\frac{1}{N}\frac{\mathrm{Re}[\sigma(\omega \gg T)]}{\mathcal{N}^2 v_F^2 g'^2} =$$
$$\left(6|\omega|\left\{\left[2 + \frac{\mathcal{N}g'^2}{6\pi}\ln\left(\frac{e^3\tilde{\Lambda}^6}{c_b^2\omega^2}\right)\right]^2 + \frac{\mathcal{N}^2 g'^4}{36}\right\}\right)^{-1} \tag{11}$$

The transport scattering rate is therefore still linear in $|\omega|$ (and hence T) up to logarithms, and there is no residual resistivity when $v = 0$, despite the presence of disorder in g'. This also turns out to be valid to all orders in perturbation theory in the large N limit (*41*).

Crossovers

For energy (E) scales larger than $E_{c,1} \sim \Gamma^2/(v_F^2 c_d)$ but smaller than $E_{c,2} \sim g^4/(g'^6 v_F^2 \mathcal{N}^4)$ ($E_{c,1} < E_{c,2}$ because $\mathcal{N}g'^2 < g^2/\Gamma$ as disorder is a correction to the clean system), the leading frequency dependence of the inelastic part of the fermion self-energy induced by g changes from $i\omega\ln(1/|\omega|)$ to $i\mathrm{sgn}(\omega)|\omega|^{2/3}$, as in the theory with $v = 0$ described above (*41*). However, then, as shown above for $v = 0$, the $|\omega|$ or T dependence of the transport scattering rate continues to arise from g' and remains linear (up to logarithms) but with a slope that is ~⅔ of the slope in the $E < E_{c,1}$ theory. For energy scales larger than $E_{c,2}$, there is an additional crossover to the theory with $g = 0$ considered in previous studies (*32*, *34*), which also has a linear $|\omega|$ or T dependence (up to logarithms) of the transport scattering rate, but now with the same slope as in the $E < E_{c,1}$ theory (*41*).

Planckian behavior

Experimental analyses (*6*, *7*) have compared the slope of the linear-T resistivity to the renormalization of the effective mass in a proximate Fermi liquid and have so deduced a scattering time τ_{tr}^* appearing in a Drude formula for the resistivity. In our theory, we obtain

$$\frac{1}{\tau_{\mathrm{tr}}^*} = \alpha\ \frac{k_B T}{\hbar} \tag{12}$$

The dimensionless number α has been computed previously (*32*, *34*) in the limit $g' \gg g$ to be $\alpha \approx (\pi/2) \times$ (ratio of logarithms of T). For smaller g', we find (at $v \neq 0$) (*41*)

$$\alpha \approx \frac{\pi}{2}\frac{g'^2}{g'^2 L_1(T) + \frac{g^2}{\Gamma\mathcal{N}}L_2(T)},\ L_{1,2}(T) \sim -\ln T \tag{13}$$

Therefore, Planckian behavior [$\alpha \sim \mathcal{O}(1)$ and depending only slowly on T and nonuniversal parameters] only occurs in the regime of large g' considered in previous studies (*32*, *34*). Otherwise, $\alpha \ll 1$ when g is the largest interaction coupling. Our theory therefore provides a concrete realization of the often-conjectured Planckian bound of $\alpha \lesssim 1$ on the transport scattering times of quantum critical metals (*1*, *5*, *8*). It is worth noting that quantum critical T-linear resistivity with $\alpha \ll 1$ has been observed recently in experiments on heavy fermion materials (*7*). Finally, for $v = 0$ but $g \neq 0$, $\alpha \ll 1$ and has a power law dependence on T; therefore, there is manifestly no Planckian behavior in this case.

Scalar mass disorder

Finally, we consider spatial disorder in the scalar mass m_b and argue that it does not modify our results over substantial intermediate scales. Such a term is not allowed for emergent gauge fields, but it can appear as a fluctuation in the position of the quantum critical point for the cases where ϕ is a symmetry-breaking order parameter

$$\mathcal{S}_w = \int d\tau \frac{1}{2\sqrt{N}}\int d^2 r \sum_{ij=1}^{N} w_{ij}(\mathbf{r})\phi_i(\mathbf{r},\tau)\phi_j(\mathbf{r},\tau) \tag{14}$$

with

$$\overline{w_{ij}(\mathbf{r})w_{lm}(\mathbf{r}')} = \frac{w^2}{2}\delta(\mathbf{r}-\mathbf{r}')(\delta_{il}\delta_{jm} + \delta_{im}\delta_{jl}) \tag{15}$$

The large N analysis shows that $\mathcal{S}_w$ is strongly relevant, so w may well be a substantial source of spatial disorder in experimental systems. Consequently, it is appropriate to account for $\mathcal{S}_w$ first by transforming to the bases of eigenmodes of ϕ, which are eigenstates of the harmonic terms for ϕ in a given disorder realization. On this basis, we obtain a theory that has the same form as $\mathcal{S}_g + \mathcal{S}_v + \mathcal{S}_{g'}$ with additional spatial disorder in the couplings, including in K. However, it is not difficult to show that spatial disorder in K is unimportant. So, $\mathcal{S}_w$ can be absorbed in a renormalization of the values of v and g', and we can continue to use our results for $\mathcal{S}_g + \mathcal{S}_v + \mathcal{S}_{g'}$. A more thorough analysis of disorder fluctuation effects is required to determine whether this transformation remains valid at the longest scales near the quantum critical point.

Discussion and outlook

A phenomenologically attractive feature of our theory is that the residual resistivity and the slope of the linear-T resistivity are determined by different types of disorder—the potential disorder v (which determines the elastic scattering rate Γ) and the interaction disorder g' (which determines the inelastic self-energy in the last

term of Eq. 7), respectively. We obtain a marginal Fermi liquid electron self-energy (*18*) as is often observed in quantum critical metals (*45*).

Because the coupling g' is spatially random, momentum is not conserved at its Yukawa interaction vertex. The physical properties therefore remain unchanged for order parameters at nonzero momentum and for theories with multiple Fermi surfaces.

Our calculations were done in the large N limit; we argue that computing all diagrams directly at $N = 1$ would have led to the same crucial cancellations. The large N mainly serves to systematically select a consistent set of diagrams to resum from the saddle point of an effective action. Furthermore, the large N or Eliashberg theory agrees well with quantum Monte Carlo (QMC) studies in the clean limit (carried out with the number of fermion or boson flavors of order one) (*46*–*49*) and does not have a potentially destabilizing Schwarzian zero mode (*34*). A comparison with QMC for the disordered case requires substantially more advanced computational techniques and is the subject of ongoing work (*50*). The mechanism in the work of Shi *et al.* (*22*) for the noncommutativity of the large N and small ω limits applies only for order parameters with the same symmetry as the momentum in the spatially uniform case and does not apply for the spatially disordered case, which has no conserved momentum and for which the patches do not decouple.

Our theory of the influence of spatial disorder includes some disorder terms to all orders, and this yields the $z = 2$ diffusive scalar propagator. This is in contrast to the perturbative disorder analysis of earlier memory function treatments (*16*, *20*).

Unlike earlier approaches (*2*) to constructing controlled theories of strongly correlated metals with low-temperature T-linear resistivity, there is no local criticality in our theory. The quantum critical scalar fluctuations live in two—and not zero—spatial dimensions.

When the values of the interaction couplings and T are large enough to make the fermion self-energy Σ comparable to the Fermi energy, we expect the theories described in this work to cross over into a so-called bad metal regime (*51*). It would be interesting to examine the transport properties of such a regime.

REFERENCES AND NOTES

1. S. A. Hartnoll, A. P. Mackenzie, *Rev. Mod. Phys.* **94**, 041002 (2022).
2. D. Chowdhury, A. Georges, O. Parcollet, S. Sachdev, *Rev. Mod. Phys.* **94**, 035004 (2022).
3. S. Sachdev, *Quantum Phase Transitions* (Cambridge Univ. Press, 1999).
4. J. A. N. Bruin, H. Sakai, R. S. Perry, A. P. Mackenzie, *Science* **339**, 804–807 (2013).
5. J. Zaanen, *Nature* **430**, 512–513 (2004).
6. G. Grissonnanche *et al.*, *Nature* **595**, 667–672 (2021).
7. M. Taupin, S. Paschen, *Crystals* **12**, 251 (2022).
8. S. Ahn, S. Das Sarma, *Phys. Rev. B* **106**, 155427 (2022).
9. J. A. Hertz, *Phys. Rev. B* **14**, 1165–1184 (1976).
10. S.-S. Lee, *Annu. Rev. Condens. Matter Phys.* **9**, 227–244 (2018).
11. T. Senthil, M. Vojta, S. Sachdev, *Phys. Rev. B* **69**, 035111 (2004).
12. P. A. Lee, *Phys. Rev. Lett.* **63**, 680–683 (1989).
13. B. I. Halperin, P. A. Lee, N. Read, *Phys. Rev. B* **47**, 7312–7343 (1993).
14. A. Rosch, *Phys. Rev. Lett.* **82**, 4280–4283 (1999).
15. D. L. Maslov, V. I. Yudson, A. V. Chubukov, *Phys. Rev. Lett.* **106**, 106403 (2011).
16. X. Wang, E. Berg, *Phys. Rev. B* **99**, 235136 (2019).
17. H. Guo, A. A. Patel, I. Esterlis, S. Sachdev, *Phys. Rev. B* **106**, 115151 (2022).
18. C. M. Varma, P. B. Littlewood, S. Schmitt-Rink, E. Abrahams, A. E. Ruckenstein, *Phys. Rev. Lett.* **63**, 1996–1999 (1989).
19. S. A. Hartnoll, P. K. Kovtun, M. Muller, S. Sachdev, *Phys. Rev. B* **76**, 144502 (2007).
20. S. A. Hartnoll, R. Mahajan, M. Punk, S. Sachdev, *Phys. Rev. B* **89**, 155130 (2014).
21. A. Eberlein, I. Mandal, S. Sachdev, *Phys. Rev. B* **94**, 045133 (2016).
22. Z. D. Shi, D. V. Else, H. Goldman, T. Senthil, *SciPost Phys.* **14**, 113 (2023).
23. C. W. Hicks *et al.*, *Phys. Rev. Lett.* **109**, 116401 (2012).
24. P. A. Lee, *Phys. Rev. B* **104**, 035140 (2021).
25. W. Fu, D. Gaiotto, J. Maldacena, S. Sachdev, *Phys. Rev. D* **95**, 026009 (2017).
26. J. Murugan, D. Stanford, E. Witten, *J. High Energ. Phys.* **2017**, 146 (2017).
27. A. A. Patel, S. Sachdev, *Phys. Rev. B* **98**, 125134 (2018).
28. E. Marcus, S. Vandoren, *J. High Energ. Phys.* **2019**, 166 (2019).
29. Y. Wang, *Phys. Rev. Lett.* **124**, 017002 (2020).
30. I. Esterlis, J. Schmalian, *Phys. Rev. B* **100**, 115132 (2019).
31. Y. Wang, A. V. Chubukov, *Phys. Rev. Res.* **2**, 033084 (2020).
32. E. E. Aldape, T. Cookmeyer, A. A. Patel, E. Altman, *Phys. Rev. B* **105**, 235111 (2022).
33. W. Wang, A. Davis, G. Pan, Y. Wang, Z. Y. Meng, *Phys. Rev. B* **103**, 195108 (2021).
34. I. Esterlis, H. Guo, A. A. Patel, S. Sachdev, *Phys. Rev. B* **103**, 235129 (2021).
35. S. Sachdev, J. Ye, *Phys. Rev. Lett.* **70**, 3339–3342 (1993).
36. A. Y. Kitaev, "A simple model of quantum holography," in KITP Program: Entanglement in Strongly-Correlated Quantum Matter (University of California, Santa Barbara, Talks at KITP, 2015).
37. A. A. Patel, S. Sachdev, *Phys. Rev. Lett.* **123**, 066601 (2019).
38. H. Guo, Y. Gu, S. Sachdev, *Ann. Phys.* **418**, 168202 (2020).
39. P. T. Dumitrescu, N. Wentzell, A. Georges, O. Parcollet, *Phys. Rev. B* **105**, L180404 (2022).
40. Y. B. Kim, A. Furusaki, X.-G. Wen, P. A. Lee, *Phys. Rev. B* **50**, 17917–17932 (1994).
41. See the supplementary materials.
42. Because g' is a small fluctuation about g, we will consider $\mathcal{N}g'^2 < g^2/\Gamma$, which makes the g' contributions to Π and Σ smaller than the g contributions in Eq. 7.
43. Because the marginal Fermi liquid correction is subleading, the specific heat in this case is $\sim T^{2/3}$ (*34*) and not $\sim T \ln(1/T)$.
44. Corrections to the conductivity that may arise from going beyond this antipodal patch theory are subleading to the effects of the disordered interactions.
45. Y. Nakajima *et al.*, *Commun. Phys.* **3**, 181 (2020).
46. A. Klein, A. V. Chubukov, Y. Schattner, E. Berg, *Phys. Rev. X* **10**, 031053 (2020).
47. X. Y. Xu, A. Klein, K. Sun, A. V. Chubukov, Z. Y. Meng, *npj Quantum Mater.* **5**, 65 (2020).
48. X. Wang, Y. Schattner, E. Berg, R. M. Fernandes, *Phys. Rev. B* **95**, 174520 (2017).
49. A. V. Chubukov, A. Abanov, I. Esterlis, S. A. Kivelson, *Ann. Phys.* **417**, 168190 (2020).
50. A. A. Patel, "Abstract G24.00003: Universal theory of strange metals from spatially random interactions," presented at the APS March Meeting 2023, Las Vegas, NV, 7 March 2023.
51. A. A. Patel, J. McGreevy, D. P. Arovas, S. Sachdev, *Phys. Rev. X* **8**, 021049 (2018).

ACKNOWLEDGMENTS

We thank E. Berg, A. Chubukov, and J. Schmalian for valuable discussions. **Funding:** H.G. and S.S. were supported by the National Science Foundation (NSF) under grant no. DMR-2002850. A.A.P. was supported by the Miller Institute for Basic Research in Science. I.E. was supported by NSF grant DMR-2038011 and AFOSR grant no. FA9550-21-1-0216. This work was also supported by the Simons Collaboration on Ultra-Quantum Matter, which is a grant from the Simons Foundation (651440; to S.S.). H.G. was supported in part by the Heising-Simons Foundation, the Simons Foundation, and NSF grant no. NSF PHY-1748958. The Flatiron Institute is a division of the Simons Foundation. S.S. acknowledges funding from the Moore Foundation's EPiQS Initiative grant no. GBMF4306. **Author contributions:** All authors performed the research. A.A.P. and S.S. wrote the paper. **Competing interests:** The authors declare no competing interests. **Data and materials availability:** All information needed to reach the conclusions of this paper is presented in the main text and the supplementary materials. **License information:** Copyright © 2023 the authors, some rights reserved; exclusive licensee American Association for the Advancement of Science. No claim to original US government works. https://www.science.org/about/science-licenses-journal-article-reuse

SUPPLEMENTARY MATERIALS

science.org/doi/10.1126/science.abq6011
Supplementary Text

Submitted 19 April 2022; accepted 17 July 2023
10.1126/science.abq6011

CANCER

Chemical remodeling of a cellular chaperone to target the active state of mutant KRAS

Christopher J. Schulze[1]†, Kyle J. Seamon[1]†, Yulei Zhao[2]†, Yu C. Yang[1], Jim Cregg[3], Dongsung Kim[2], Aidan Tomlinson[3], Tiffany J. Choy[1], Zhican Wang[4], Ben Sang[2], Yasin Pourfarjam[2], Jessica Lucas[2], Antonio Cuevas-Navarro[2], Carlos Ayala-Santos[2], Alberto Vides[2], Chuanchuan Li[2], Abby Marquez[3], Mengqi Zhong[3], Vidyasiri Vemulapalli[1], Caroline Weller[1], Andrea Gould[1], Daniel M. Whalen[3], Anthony Salvador[3], Anthony Milin[3], Mae Saldajeno-Concar[3], Nuntana Dinglasan[1], Anqi Chen[3], Jim Evans[1], John E. Knox[3], Elena S. Koltun[3], Mallika Singh[1], Robert Nichols[1], David Wildes[1], Adrian L. Gill[3], Jacqueline A. M. Smith[1]*, Piro Lito[2,5,6]*

The discovery of small-molecule inhibitors requires suitable binding pockets on protein surfaces. Proteins that lack this feature are considered undruggable and require innovative strategies for therapeutic targeting. *KRAS* is the most frequently activated oncogene in cancer, and the active state of mutant KRAS is such a recalcitrant target. We designed a natural product–inspired small molecule that remodels the surface of cyclophilin A (CYPA) to create a neomorphic interface with high affinity and selectivity for the active state of $KRAS^{G12C}$ (in which glycine-12 is mutated to cysteine). The resulting CYPA:drug:$KRAS^{G12C}$ tricomplex inactivated oncogenic signaling and led to tumor regressions in multiple human cancer models. This inhibitory strategy can be used to target additional KRAS mutants and other undruggable cancer drivers. Tricomplex inhibitors that selectively target active $KRAS^{G12C}$ or multiple RAS mutants are in clinical trials now (NCT05462717 and NCT05379985).

KRAS is a small guanosine triphosphatase (GTPase) that cycles between an inactive [guanosine diphosphate (GDP)–bound, OFF] state and an active (GTP-bound, ON) state (*1*). Active KRAS binds to and activates several effector proteins to regulate cell growth and proliferation (*2*). KRAS mutations act as oncogenic drivers that stimulate excessive downstream signaling and proliferation (*3*). $KRAS^{G12C}$ (in which glycine-12 is mutated to cysteine) is the most frequent KRAS mutation in non–small-cell lung cancer (NSCLC) (*4*, *5*), and 37 to 43% of patients with NSCLC who harbor this variant respond to treatment with inhibitors that target the inactive state of $KRAS^{G12C}$, such as sotorasib and adagrasib (*6*–*9*). The clinical benefits of these agents represent an important advance in precision oncology. Nevertheless, both are limited with regard to the depth and duration of response. Although the reasons for such limitations are multifactorial, cancer cells appear to bypass inactive state–selective inhibition by increasing the amount of drug-insensitive, GTP-bound $KRAS^{G12C}$ (*10*–*15*).

To date, efforts to target the active state of KRAS by traditional small-molecule drug discovery strategies have been unsuccessful, suggesting that innovative approaches are needed for its inhibition. One such approach is inspired by natural products such as rapamycin and FK506, which engage the immunophilin FKBP12 to inhibit mechanistic target of rapamycin (mTOR) or calcineurin, respectively (*16*–*18*). Although the targets of these natural products are dictated by evolution (*19*), we used structure-based redesign of an immunophilin ligand to direct its paired endogenous immunophilin to target the active state of mutant KRAS.

Results

Remodeling cyclophilin A to generate a neomorphic interface that binds to active KRAS

We began by focusing on the immunophilin cyclophilin A (CYPA) because of its favorable electrostatic surface charge complementarity with residues on the effector binding interface of KRAS, which is not a feature of FKBP12 (fig. S1A). Sanglifehrin A (fig. S1B) is a natural product known to bind CYPA with high affinity (*20*). A tool ligand (compound-1) containing a minimal CYPA-binding motif of sanglifehrin A and a promiscuous cysteine-reactive warhead (Fig. 1, A and B) was synthesized to facilitate covalent tethering and de novo tricomplex formation. The crystal structure of the primitive CYPA:compound-1:$KRAS^{G12C}$ tricomplex (1.40 Å; Fig. 1A and table S1) suggested that macrocyclization of the ligand (fig. S1C) would decrease conformational entropy and increase protein contacts. Macrocyclization through a substituted indole linker introduced specific interactions with KRAS (see next paragra[illegible] and the phenolic hydroxyl was remove[illegible] reduce the number of hydrogen-bond donors and acceptors. The resulting cyclized core was modified with either an acetamide moiety that enables reversible binding (compound-2; Fig. 1B) or an acrylamide warhead to covalently engage the C12 residue (compound-3; Fig. 1B). As expected, compound-2 induced CYPA complexes with guanosine-5′-[(β,γ)-imido]triphosphate (GMPPNP)–bound wild-type KRAS ($KRAS^{WT}$) as well as $KRAS^{G12C}$ [half-maximal inhibitory concentration (IC_{50}): 510 or 180 nM, respectively; Fig. 1C]. By comparison, compound-3 had increased potency for inducing CYPA complexes with active $KRAS^{G12C}$ (IC_{50}: 52 nM) while retaining weak reversible binding to $KRAS^{WT}$ (IC_{50}: 520 nM). Compound-3 was modified to further increase the selectivity for $KRAS^{G12C}$. Replacement of the acrylamide in compound-3 with an ynamide warhead generated compound-4, which had greater potency and selectivity for $KRAS^{G12C}$-CYPA tricomplex formation (IC_{50}: 28 nM, 39-fold more selective; Fig. 1C). Owing to the limit of detection in the tricomplex formation assay (see materials and methods), we elected to further optimize the warhead and linker using a kinetic target engagement assay, which affords higher resolution for potent compounds. The maximal rate of $KRAS^{G12C}$ target engagement for compound-4 was 26-fold higher than that of compound-3 (Fig. 1, B and D, and fig. S1D). Installation of a conformationally optimized linker improved the maximal rate a further 14-fold and resulted in RMC-4998 (Fig. 1, B and D, and fig. S1D). The covalent engagement efficiency of RMC-4998 [the ratio of the rate constant of enzyme inactivation (k_{inact}) to the inhibition constant (K_I): 272,000 M^{-1} s^{-1} (k_{inact}/K_I): 272,000 $M^{-1}s^{-1}$] was greater than that of existing inactive state–selective inhibitors (*21*–*23*), even though RMC-4998 targets the active or guanosine triphosphate (GTP)–bound state of $KRAS^{G12C}$.

We next sought to determine the structural basis for tricomplex formation and KRAS inhibition. RMC-4998 bound to CYPA reversibly to form a low-affinity binary complex [dissociation constant (K_d) = 1.09 μM, dissociation rate constant (k_{off}) = 1.0 s^{-1}; Fig. 1E and fig. S1E]. The crystal structure of the mature CYPA:RMC-4998:$KRAS^{G12C}$-GMPPNP tricomplex (1.53 Å; table S1) revealed that the aforementioned chemical optimizations increased the number of contacts between RMC-4998 and CYPA, compared with those observed in the primitive complex (fig. S2, A and B). RMC-4998 retained the piperazic acid and peptidic linker of compound-1 to maintain interactions with Q63 and the N102 backbone, but the substituted indole in the macrocycle of RMC-4998 introduced an additional cation-π interaction with R55 as well as numerous favorable hydrophobic contacts (fig. S2, A to G). Through these interactions, RMC-4998 remodeled the molecular

[1]Department of Biology, Revolution Medicines, Inc., Redwood City, CA 94063, USA. [2]Human Oncology and Pathogenesis Program, Memorial Sloan Kettering Cancer, New York, NY 10065, USA. [3]Department of Discovery Chemistry, Revolution Medicines, Inc., Redwood City, CA 94063, USA. [4]Department of Non-clinical Development and Clinical Pharmacology, Revolution Medicines, Inc., Redwood City, CA 94063, USA. [5]Department of Medicine, Memorial Sloan Kettering Cancer Center, New York, NY 10065, USA. [6]Department of Medicine, Weill Cornell Medical College, New York, NY 10065, USA.
*Corresponding author. Email: jan@revmed.com (J.A.M.S.); litop@mskcc.org (P.L.)
†These authors contributed equally to this work.

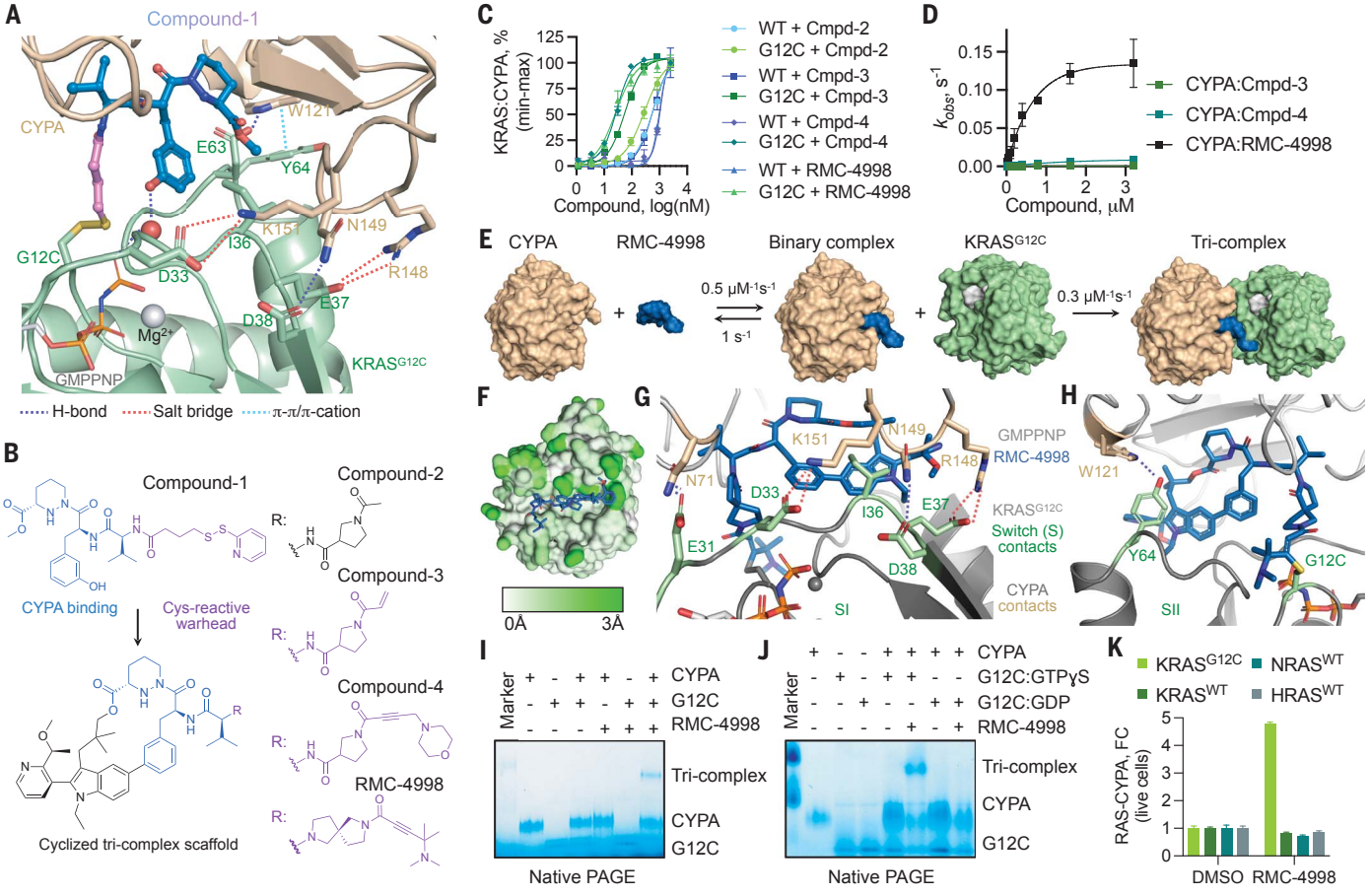

Fig. 1. Development of a tricomplex inhibitor that targets the active state of KRAS^{G12C}. (**A**) Tertiary structure of the primitive CYPA:compound-1: KRAS^{G12C}-GMPPNP complex at 1.40-Å resolution. (**B**) The chemical structure of compound-1 and the macrocyclized scaffold for subsequent compounds, with the sanglifehrin-derived CYPA-binding moiety shown in blue. R denotes divergent chemical moieties comprising noncovalent (black) and covalent (purple) derivatives. (**C**) The interaction between the indicated KRAS proteins (50 nM) and CYPA (20 μM) in the presence of increasing compound concentrations was determined by time-resolved fluorescence resonance energy transfer (TR-FRET) (mean ± SEM, n = 3, N = 2). (**D**) The rate (k_{obs}) of covalent modification of KRAS^{G12C} in the presence of CYPA (25 μM) and the indicated compounds (mean ± SEM, N = 3). (**E**) Schematic of tricomplex formation by RMC-4998 along with rate constants for each reaction. (**F** to **H**) Mapped pairwise atomic distances between structures of apo-CYPA [Protein Data Bank (PDB) ID 3K0N (*30*)] and RMC-4998–bound CYPA showing the structural rearrangements (white-to-green gradient) that gave rise to the high-affinity neomorphic binding interface for KRAS^{G12C} (F). Interactions between RMC-4998, CYPA, and the switch I (G) or switch II (H) regions of KRAS^{G12C} in the crystal structure of the mature tricomplex (1.53 Å). Dashed lines indicate interactions as per the key in (A). (**I**) The interaction between KRAS^{G12C} (2 μM), RMC-4998 (10 μM), and CYPA (2 μM) was determined by native polyacrylamide gel electrophoresis (PAGE). (**J**) As in (I), but KRAS^{G12C} was loaded with nonhydrolysable GTPγS (active state) or GDP (inactive state). A representative of at least two independent experiments is shown in (I) and (J). (**K**) Human embryonic kidney 293 (HEK293) cells coexpressing small-bit luciferase-tagged RAS variants and large-bit luciferase tagged CYPA were treated with RMC-4998 (100 nM) for 2 hours followed by determination of luciferase activity (mean ± SEM, N = 4). FC, fold change. Single-letter abbreviations for amino acid residues are as follows: A, Ala; C, Cys; D, Asp; E, Glu; F, Phe; G, Gly; H, His; I, Ile; K, Lys; L, Leu; M, Met; N, Asn; P, Pro; Q, Gln; R, Arg; S, Ser; T, Thr; V, Val; W, Trp; and Y, Tyr. For all figures, unless otherwise indicated, N and n denote biological and technical replicates, respectively.

surface of CYPA to create a neomorphic interface with affinity for KRAS^{G12C} (Fig. 1F and movie S1).

The covalent engagement of KRAS^{G12C} by CYPA:RMC-4998 led to the formation of a stable tricomplex (Fig. 1E) with a half-life that was longer than 8 hours after compound washout in biophysical assays (fig. S3A) and cellular experiments (fig. S3B). The crystal structure of the tricomplex revealed several key interactions that enable stable binding (Fig. 1, G and H): (i) Noncovalent contacts between RMC-4998 and the switch I and II motifs of KRAS^{G12C}. These were mediated by the indole introduced during macrocyclization and included lipophilic interactions with I36 on the switch I motif (Fig. 1G) and a π-π interaction with Y64 on the switch II motif (Fig. 1H) of KRAS. (ii) Neomorphic contacts between CYPA and KRAS^{G12C}, including hydrogen bonds between N71, K151, and R148 in CYPA and E31, D33, and E37 in the switch I motif of KRAS (Fig. 1G), as well as W121 in CYPA and Y64 in KRAS (Fig. 1H). (iii) Covalent modification of C12 by the ynamide warhead in RMC-4998 (Fig. 1H and fig. S2D).

The remodeled molecular surface of inhibitor-bound CYPA enabled selective and active state–specific binding to KRAS^{G12C}. All three components were required for tricomplex formation (Fig. 1I and fig. S4A); neither RMC-4998 nor CYPA were able to bind to KRAS^{G12C} alone. No complex was detected with GDP-loaded KRAS^{G12C}, suggesting a selectivity for the active (GTP-bound) state of the mutant (Fig. 1J). RMC-4998 induced a tricomplex between KRAS^{G12C} and CYPA in live cells without affecting wild-type KRAS, NRAS, or HRAS (Fig. 1K). RMC-4998 had comparable activity on G12C-mutant

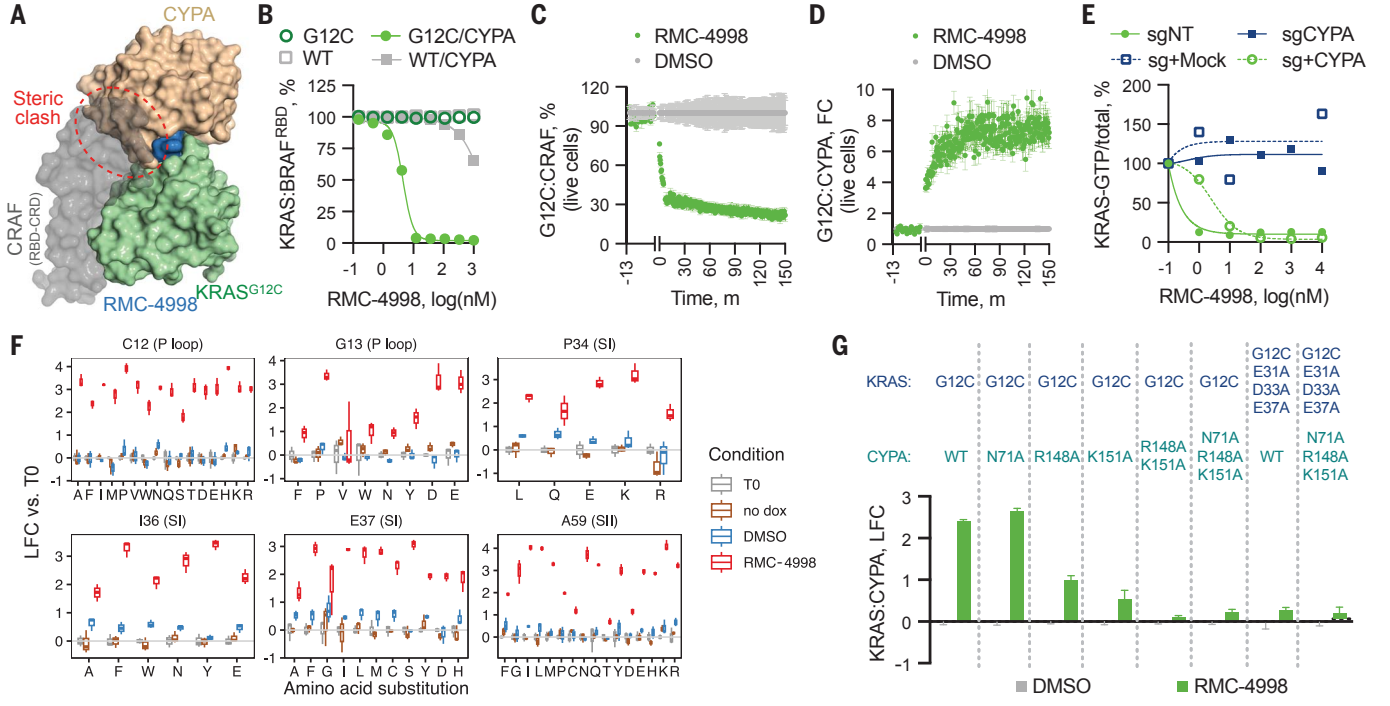

Fig. 2. Structural constraints for tricomplex formation and active state–selective KRAS inhibition. (**A**) Superimposition of the structures of the CYPA:RMC-4998:KRAS^{G12C} tricomplex and the KRAS:CRAF$^{RBD/CRD}$ complex (PDB ID 6XI7) (*31*). (**B**) The effect of RMC-4998 on the interaction between the indicated KRAS proteins (12.5 nM) and BRAF^{RBD} (50 nM) in either the presence or the absence of CYPA was determined by TR-FRET (mean ± SD, *N* = 4). (**C** and **D**) HEK293 cells coexpressing small-bit luciferase-tagged KRAS^{G12C} and large-bit luciferase-tagged CYPA (C) or full-length CRAF (D) were treated with RMC-4998 (100 nM) followed by determination of reconstituted luciferase activity in live cells (mean ± SEM, *N* = 3). (**E**) The indicated parental, CYPA-null, or CYPA-rescued H358 cells were treated as shown and their extracts were analyzed by RBD-pulldown and immunoblotting to determine the effect on KRAS activation. A representative of two independent experiments is shown. sgCYPA, CYPA-targeting single guide RNA; sgNT, nontarget single guide RNA. (**F**) KRAS mutant cells were infected with a dox-inducible saturation mutagenesis library based on a KRAS^{G12C} backbone and treated with either DMSO or RMC-4998 (100 nM) for 2 weeks. Shown is the log(fold change) (logFC) in abundance relative to the start time (mean ± 95% confidence interval, *N* = 3) for variants meeting the threshold for statistical significance (see materials and methods). (**G**) The effect of the indicated CYPA variants on tricomplex formation in live cells was determined as in (C) (mean ± SEM, *N* = 3). LFC, $\log_2$(fold change).

HRAS, NRAS, and KRAS, with little, if any, activity on KRAS^{G13C} (fig. S4, B and C).

Tricomplex formation disrupts effector binding to active KRAS

Structural superpositions suggested that when bound in the tricomplex, CYPA occludes the effector binding interface of KRAS^{G12C}, including that occupied by the RAS-binding and cysteine-rich domains (RBD and CRD, respectively) of CRAF (Fig. 2A), the catalytic subunit (p110) of phosphatidylinositol 3-kinase (PI3K) (fig. S5A), the allosteric site of the catalytic domain of SOS1 (SOS_{cat}; fig. S5B), and the RAS-interacting domain (RID) of RAL guanine nucleotide dissociation stimulator (RALGDS; fig. S5C). Indeed, the formation of the CYPA:RMC-4998:KRAS^{G12C} tricomplex led to a concentration-dependent dissociation of the BRAF RBD and RALGDS RID from mutant KRAS in biochemical assays (Fig. 2B and fig. S5D). In a live-cell kinetic assay, RMC-4998 treatment led to rapid association of KRAS^{G12C} with CYPA, an effect that was paralleled by the dissociation of full-length CRAF from KRAS^{G12C} (Fig. 2, C and D). CYPA was indispensable for inhibition by RMC-4998, as evidenced in biochemical assays (Fig. 2B) as well as in CYPA-null cells and those with rescued expression (Fig. 2E and fig. S6, A and B). By comparison, CYPA loss had no effect on the cellular activity of the inactive state–selective KRAS^{G12C} inhibitor adagrasib (fig. S6, C and D). It is possible that a dependency on CYPA expression could limit the therapeutic utility of tricomplex inhibitors like RMC-4998. This is unlikely to be true, however, when considering that CYPA is highly abundant across various cancer types (fig. S6E), has low interpatient variation in expression (fig. S6F), and has higher expression in tumors compared with normal tissue (fig. S6G).

Functional interrogation of the neomorphic binding interface

The distinct inhibitory mechanism of RMC-4998 prompted an unbiased evaluation of the functional role of the amino acid residues in the neomorphic binding interface between CYPA and KRAS^{G12C}. To this end, KRAS^{G12C} mutant cells were infected with a doxycycline (dox)–inducible cDNA library, encoding all possible amino acid substitutions in KRAS^{G12C}, followed by treatment with either dimethyl sulfoxide (DMSO) or RMC-4998 for 2 weeks in the presence or absence of dox (fig. S7A). The analysis confirmed the importance of the KRAS C12, I36, and E37 residues (Fig. 2F), as predicted by the structural studies described in the previous sections (Fig. 1, G and H). The screen, however, revealed that mutations in additional residues, including those at G13, P34, and A59, attenuated the effect of RMC-4998 (Fig. 2F and fig. S7B). The latter likely disrupt the conformation of the switch regions to prevent CYPA:RMC-4998 from engaging active KRAS^{G12C}. Cells expressing KRAS^{G12C} that contains a P34R (P34→R), I36Q, or A59G secondary mutation confirmed the ability of these variants to activate extracellular signal–regulated kinase (ERK) signaling in the presence of RMC-4998 (fig. S7C). Secondary in-cis mutations on KRAS^{G12C} (for example, R68, H95, and Y96) confer resistance to adagrasib and/or sotorasib (*11*–*13*). RMC-4998 occupies a distinct binding site and does not contact any of these residues, suggesting that it should retain inhibitory activity

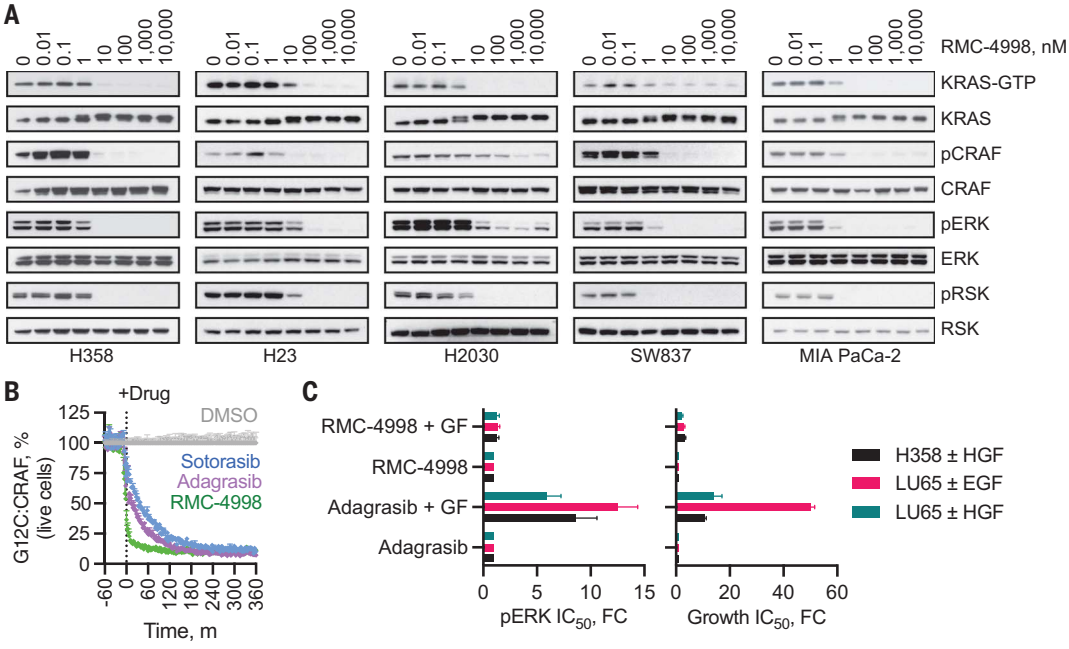

Fig. 3. Cellular effects of active state–selective KRAS^{G12C} inhibition. (**A**) Extracts from the indicated KRAS^{G12C} mutant cell lines were treated with RMC-4998 for 2 hours before lysis and immunoblotting. The levels of active KRAS (KRAS-GTP) were determined by pulldown with the RBD of CRAF. A representative of at least two independent experiments for each cell line is shown. p, phosphorylated. (**B**) The kinetics of target inhibition in live cells treated with an active state–selective (100 nM RMC-4998) or an inactive state–selective (10 μM sotorasib or 1 μM adagrasib) were determined as in Fig. 2C (mean ± SEM, *N* = 3). (**C**) The indicated cell lines were treated as shown in the presence or absence of growth factor (GF) stimulation to determine the effect on ERK phosphorylation (pERK/total, 4 hours) or cell proliferation (120 hours) (mean ± SEM, *N* = 3 or 4). EGF, epidermal growth factor; HGF, hepatocyte growth factor.

against these mutants (Fig. 1G). Indeed, mutations in these residues were not identified in the saturation mutagenesis screen (fig. S7A) and had no effect on displacement of the CRAF RBD by RMC-4998 in a live-cell assay (fig. S7D).

We next used the live-cell biosensor to interrogate residues in CYPA that contribute to the neomorphic interface. Alanine mutations at the N71, K151, and R148 residues of CYPA that form direct contacts with KRAS^{G12C} resulted in a loss of tricomplex formation (Fig. 2G). Mutations in their interacting partners on switch I of KRAS^{G12C} (E31A, D33A, and E37A) also abolished the formation of the tricomplex, highlighting the importance of these residues in binding (Fig. 2G). These mutations had a minimal effect on the enzymatic proline isomerase activity of CYPA (fig. S8).

Selective inhibition of oncogenic signaling and proliferation

Disruption of effector binding by RMC-4998 inhibited downstream ERK signaling in KRAS^{G12C} mutant cancer cell models, with an IC_{50} ranging between 1 and 10 nM (Fig. 3A). RMC-4998 treatment also attenuated AKT-MTOR and RAL signaling (fig. S9, A and B). The latter pathways, however, had residual activity despite the presence of the drug, suggesting that they are only partially activated by mutant KRAS in cancer cells. Targeting the GTP-bound state of KRAS^{G12C} with the tricomplex inhibitor RMC-4998 (0.1 μM) led to a faster disruption of the interaction between KRAS^{G12C} and CRAF compared with inactive state–selective inhibitors adagrasib (1 μM) and sotorasib (10 μM) (Fig. 3B). A similar disruption was observed for the interaction between KRAS^{G12C} and SOS_{cat} (fig. S9C). Complete covalent modification of KRAS^{G12C} in RMC-4998–treated MIA PaCa-2 cells occurred within 5 min, again faster than that observed with adagrasib (fig. S9D). The kinetics of inactive state–selective inhibition are limited by the rate of GTP hydrolysis by KRAS^{G12C} (*24*), which RMC-4998 overcomes by directly targeting the active state.

Another limitation of inactive state–selective inhibitors is their susceptibility to cellular stimuli (*10*) that drive nucleotide exchange to induce GTP loading of KRAS^{G12C}. This is particularly evident after receptor tyrosine kinase (RTK) activation (*25*, *26*). Indeed, exposure to epidermal growth factor (EGF) or hepatocyte growth factor (HGF) led to attenuated target engagement (fig. S9E), ERK inhibition, and antiproliferative effect by the inactive state–selective inhibitor adagrasib (Fig. 3C). By contrast, RTK stimulation had a minimal effect on RMC-4998 activity. In the absence of growth factor stimulation, treatment of KRAS^{G12C}-mutant cell lines with either RMC-4998 or adagrasib produced initial pathway suppression followed by a rebound over the course of the next 72 hours. The readdition of RMC-4998, but not adagrasib, suppressed the reactivated pathway signaling (fig. S9F). Therefore, targeting of the active state KRAS^{G12C} through tricomplex formation has distinct biological properties from existing inactive state–selective clinical-stage inhibitors.

Potent antitumor activity in cell line and patient-derived xenografts

Further optimization of RMC-4998 led to RMC-6291, an active state–selective KRAS^{G12C} inhibitor now undergoing clinical testing. RMC-4998 and RMC-6291 have similar chemical structures and nearly identical kinetic constants for engaging active KRAS^{G12C} (fig. S10A). Both RMC-4998 and RMC-6291 inhibited ERK signaling and induced apoptosis in KRAS^{G12C}-mutant H358 cells (fig. S10B). In a cancer cell line panel (Fig. 4A and table S2), RMC-6291 inhibited the proliferation of KRAS^{G12C} mutant cells with a median IC_{50} of 0.11 nM, or 13,500 times more potently than non-G12C mutant models, indicating its selectivity index. RMC-4998 had a median IC_{50} of 0.28 nM and a selectivity index of 1450. Of note, both the potency and the selectivity index of RMC-4998 and RMC-6291 were greater than those of adagrasib. Selective cellular engagement of KRAS^{G12C} was further evidenced by a proteome-wide cysteine-reactivity assay, wherein RMC-6291 reacted with KRAS^{G12C} to a greater degree than it did with other cellular proteins (fig. S11A and data S1).

Daily oral administration of RMC-6291 in mice bearing NCI-H358 xenografts was well tolerated (fig. S11B) and led to near-complete tumor regression (Fig. 4B). RMC-6291 achieved dose-dependent plasma concentrations and inhibition of downstream signaling output, as assessed by the effect on tumor *DUSP6* mRNA expression (Fig. 4C). A single dose of RMC-6291

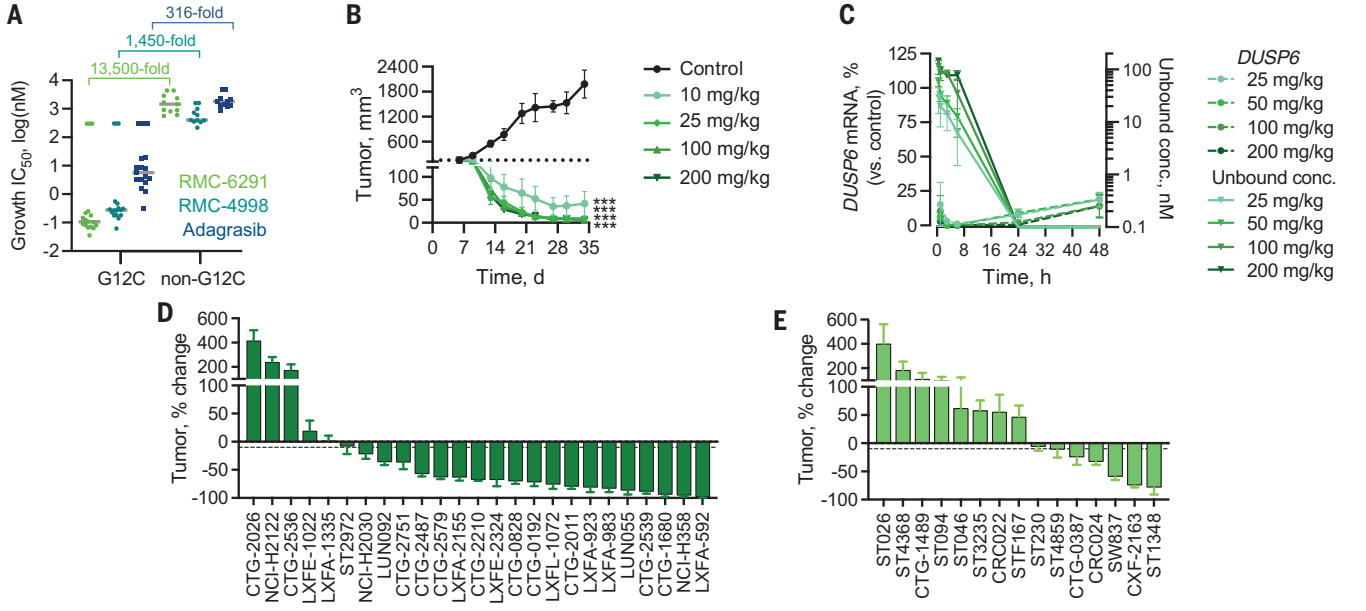

Fig. 4. Potent and selective suppression of KRAS^{G12C}-driven tumor growth by tricomplex inhibitors. (**A**) The indicated cells were treated with increasing concentrations of RMC-6291, RMC-4998, or adagrasib for 120 hours and the effect on cell viability was determined using the 3D CellTiter-Glo assay. Each point represents an individual cell line (n = 17 cell lines for G12C, n = 11 cell lines for non-G12C), and the gray line indicates the median IC_{50} for each group of cell lines. (**B**) Mice bearing H358 CDX tumors were treated with RMC-6291 at the indicated dose, administered orally once daily, and the tumor volume was assessed for 28 days (mean ± SEM). ***Adjusted $p < 0.001$ for RMC-6291 (all dose groups) versus control, using repeated measures two-way analysis of variance (ANOVA) (n = 6 mice per group for control, n = 8 mice per group for RMC-6291); values were adjusted based on multiple comparison via Dunnett's test on the final tumor measurement. (**C**) The unbound plasma concentration of RMC-6921 and the expression of *DUSP6* mRNA in H358 tumors after administration of a single oral dose of RMC-6291 at the indicated doses (mean ± SEM, n = 3 replicate mice). (**D** and **E**) The indicated NSCLC (D) or CRC (E) xenograft model mice were treated with RMC-6291 (200 mg per kg of body weight administered orally once daily) to determine the effect on mean tumor growth or regression after 28 ± 2 days (percent change from baseline, mean ± SEM, n as indicated in table S3). The dashed line indicates a 10% reduction in tumor volume from baseline.

led to sustained engagement of KRAS^{G12C} and inhibition of ERK phosphorylation in tumors for ~24 hours and also induced apoptosis, as evidenced by TUNEL (terminal deoxynucleotidyl transferase–mediated deoxyuridine triphosphate nick end labeling) staining (fig. S12, A to D). These data indicate that the tricomplex inhibitor RMC-6291 is a potent and selective inhibitor of the active conformation of KRAS^{G12C} in vivo. Similar in vivo activity was observed with RMC-4998 (fig. S13, A to C).

Next, we evaluated the antitumor activity of RMC-6291 across a panel of cell line–derived (CDX) and patient-derived (PDX) xenograft models of KRAS^{G12C} mutant NSCLC and colorectal cancer (CRC). Targeted exome DNA sequencing revealed that the PDX panels were representative of the genomic landscape of patients with KRAS^{G12C} mutant lung cancer or CRC (fig. S14, A and B). RMC-6291 treatment resulted in mean tumor regression in 76% (19/25) of NSCLC models and in 40% (6/15) of the CRC models tested after a standard 28-day treatment period (Fig. 4, D and E, and table S3). These results indicate that RMC-6291 can drive deep antitumor responses after daily oral administration in preclinical studies.

Discussion

The discovery of RMC-4998 and RMC-6291 as tricomplex inhibitors of GTP-bound KRAS^{G12C} represents the successful reengineering of an immunophilin-binding natural product to engage a target previously thought to be undruggable. Neither CYPA nor its natural product ligand have been previously reported to interact with KRAS. Their complex formation was the product of purposeful, structure-guided chemical modifications to mold a high-affinity binding interface between CYPA and active KRAS^{G12C}. The target-directed approach described here differs from other pharmacologic or proteomic screens that describe the identification of rapamycin or sangliferin analogs that engage additional targets besides MTOR or CYPA, respectively (*27*, *28*). Selective disruption of effector binding to the active state of KRAS^{G12C} by the recruitment of CYPA is a distinct inhibitory mechanism that promises to overcome some of the limitations of inactive state–selective KRAS^{G12C} inhibitors while maintaining selective target engagement and a potentially wide therapeutic index. A phase 1/1B clinical trial testing RMC-6291 (NCT05462717) is ongoing at present.

The tricomplex inhibitory strategy described here has broad implications for cancer therapy. It can be used to develop inhibitors of additional oncogenic RAS mutants through the introduction of distinct covalent warheads or functional groups that can selectively target other RAS mutants (G13C, G12D, etc.) in an allele-specific manner. Alternatively, further optimization of the reversible drug binding capacity demonstrated by compound-2 would enable the concurrent (nondiscriminatory) inhibition of multiple RAS oncoproteins. A reversible tricomplex inhibitor RMC-6236 (*29*) (RAS^{MULTI}) developed through this approach is also in a phase 1/1B clinical trial (NCT05379985). Although its broader applicability requires further investigation, the reengineering of natural products to create neomorphic binding interfaces on their paired immunophilins may prove effective at targeting additional "undruggable" cancer drivers, even beyond RAS.

REFERENCES AND NOTES

1. D. K. Simanshu, D. V. Nissley, F. McCormick, *Cell* **170**, 17–33 (2017).
2. M. Malumbres, M. Barbacid, *Nat. Rev. Cancer* **3**, 459–465 (2003).
3. Y. Pylayeva-Gupta, E. Grabocka, D. Bar-Sagi, *Nat. Rev. Cancer* **11**, 761–774 (2011).
4. G. J. Riely *et al*., *Clin. Cancer Res.* **14**, 5731–5734 (2008).
5. H. Yang, S. Q. Liang, R. A. Schmid, R. W. Peng, *Front. Oncol.* **9**, 953 (2019).
6. J. M. Ostrem, U. Peters, M. L. Sos, J. A. Wells, K. M. Shokat, *Nature* **503**, 548–551 (2013).
7. P. Lito, M. Solomon, L. S. Li, R. Hansen, N. Rosen, *Science* **351**, 604–608 (2016).
8. F. Skoulidis *et al*., *N. Engl. J. Med.* **384**, 2371–2381 (2021).
9. P. A. Jänne *et al*., *N. Engl. J. Med.* **387**, 120–131 (2022).
10. J. Y. Xue *et al*., *Nature* **577**, 421–425 (2020).
11. M. M. Awad *et al*., *N. Engl. J. Med.* **384**, 2382–2393 (2021).
12. Y. Zhao *et al*., *Nature* **599**, 679–683 (2021).
13. N. Tanaka *et al*., *Cancer Discov.* **11**, 1913–1922 (2021).

14. C. S. L. Ho *et al*., *Eur. J. Cancer* **159**, 16–23 (2021).
15. M. B. Ryan *et al*., *Clin. Cancer Res.* **26**, 1633–1643 (2020).
16. Z. Zhang, K. M. Shokat, *Angew. Chem. Int. Ed.* **58**, 16314–16319 (2019).
17. L. A. Banaszynski, C. W. Liu, T. J. Wandless, *J. Am. Chem. Soc.* **127**, 4715–4721 (2005).
18. J. Liu *et al*., *Cell* **66**, 807–815 (1991).
19. U. K. Shigdel *et al*., *Proc. Natl. Acad. Sci. U.S.A.* **117**, 17195–17203 (2020).
20. J. J. Sanglier *et al*., *J. Antibiot.* **52**, 466–473 (1999).
21. J. Hallin *et al*., *Cancer Discov.* **10**, 54–71 (2020).
22. J. Canon *et al*., *Nature* **575**, 217–223 (2019).
23. A. Weiss *et al*., *Cancer Discov.* **12**, 1500–1517 (2022).
24. C. Li *et al*., *Science* **374**, 197–201 (2021).
25. N. Santana-Codina *et al*., *Cell Rep.* **30**, 4584–4599.e4 (2020).
26. K. Lou *et al*., *Sci. Signal.* **12**, eaaw9450 (2019).
27. K. H. Pua, D. T. Stiles, M. E. Sowa, G. L. Verdine, *Cell Rep.* **18**, 432–442 (2017).
28. Z. Guo *et al*., *Nat. Chem.* **11**, 254–263 (2019).
29. E. S. Koltun *et al*., *Cancer Res.* **82**, 3597 (2022).
30. J. S. Fraser *et al*., *Nature* **462**, 669–673 (2009).
31. T. H. Tran *et al*., *Nat. Commun.* **12**, 1176 (2021).

ACKNOWLEDGMENTS

We thank G. Verdine, A. Borisy, and others at Warp Drive Bio for their contributions to the early sanglifehrin analogs and K. Shokat for helpful discussions. P.L. thanks M. Mroczkowski for discussing this work and the manuscript. **Funding:** This study was funded by Revolution Medicines, Inc. P.L. is supported in part by the National Institutes of Health–National Cancer Institute (1R01CA23074501, 1R01CA23026701A1, and 1R01CA279264-01), The Pew Charitable Trusts, the Damon Runyon Cancer Research Foundation, and the Pershing Square Sohn Cancer Research Alliance. P.L. is also supported by the Josie Robertson Investigator Program and the Support Grant-Core Grant program (P30 CA008748) at Memorial Sloan Kettering Cancer Center (MSKCC).
Author contributions: P.L., J.A.M.S., A.G., D.W., R.N., M.S., E.S.K., and J.E.K. contributed to the conception and design of this work. C.J.S., K.J.S., Y.Z., D.K., T.J.C., B.S., Y.P., J.L., A.C.N., C.A.-S., A.V., C.L., C.W., A.G., N.D., and J.E. contributed to cellular experiments. J.C. synthesized compounds. A.Mar., M.Z., A.S., and A.Mil. contributed to biochemical and biophysical characterization. Y.C.Y. and Z.W. contributed to in vivo characterization. A.T., D.M.W., M.S.-C., and A.C. solved x-ray crystal structures. V.V. performed analysis of CYPA expression levels. C.J.S., K.J.S., Y.Z., D.W., J.A.M.S., and P.L. were the main writers of the manuscript. All other authors reviewed and edited the manuscript. **Competing interests:** P.L. is an inventor on patent US20200009138A1 submitted by MSKCC that covers the treatment of RAF- and RAS-driven tumors. P.L. reports grants to his institution from Amgen, Mirati, Revolution Medicines, Boehringer Ingelheim, and Virtec Pharmaceuticals. P.L. reports consulting fees from Black Diamond Therapeutics, AmMax, OrbiMed, PAQ-Tx, Repare Therapeutics, and Revolution Medicines, as well as membership on the scientific advisory board of Frontier Medicines and Biotheryx (consulting fees and equity in each). C.J.S., K.J.S., Y.C.Y., J.C., A.T., T.J.C., Z.W., A.Mar., M.Z., V.V., C.W., A.G., D.M.W., A.S., A.Mil., M.S.-C., N.D., A.C., J.E., J.E.K., E.S.K., M.S., R.N., D.W., A.L.G., and J.S. are current or former employees of Revolution Medicines, Inc. **Data and materials availability:** Protein Data Bank (PDB) files have been deposited into the Research Collaboratory for Structural Bioinformatics (RCSB) PDB with the accession numbers 8G9Q and 8G9P. All other data are available in the main text or supplementary materials. **License information:** Copyright © 2023 the authors, some rights reserved; exclusive licensee American Association for the Advancement of Science. No claim to original US government works. https://www.science.org/about/science-licenses-journal-article-reuse

SUPPLEMENTARY MATERIALS

science.org/doi/10.1126/science.adg9652
Materials and Methods
Supplementary Text
Figs. S1 to S14
Tables S1 to S3
References (*32*–*46*)
MDAR Reproducibility Checklist
Data S1
Movie S1

Submitted 2 February 2023; accepted 28 June 2023
10.1126/science.adg9652

BIOPHYSICS

MyoD-family inhibitor proteins act as auxiliary subunits of Piezo channels

Zijing Zhou[1,2]†, Xiaonuo Ma[3,4]†, Yiechang Lin[5], Delfine Cheng[1,2], Navid Bavi[6], Genevieve A. Secker[7], Jinyuan Vero Li[1,2], Vaibhao Janbandhu[1,2], Drew L. Sutton[7,8], Hamish S. Scott[7,8,9], Mingxi Yao[10], Richard P. Harvey[1,2,11], Natasha L. Harvey[7,8], Ben Corry[5], Yixiao Zhang[3,4]*, Charles D. Cox[1,12]*

Piezo channels are critical cellular sensors of mechanical forces. Despite their large size, ubiquitous expression, and irreplaceable roles in an ever-growing list of physiological processes, few Piezo channel–binding proteins have emerged. In this work, we found that MyoD (myoblast determination)–family inhibitor proteins (MDFIC and MDFI) are PIEZO1/2 interacting partners. These transcriptional regulators bind to PIEZO1/2 channels, regulating channel inactivation. Using single-particle cryogenic electron microscopy, we mapped the interaction site in MDFIC to a lipidated, C-terminal helix that inserts laterally into the PIEZO1 pore module. These Piezo-interacting proteins fit all the criteria for auxiliary subunits, contribute to explaining the vastly different gating kinetics of endogenous Piezo channels observed in many cell types, and elucidate mechanisms potentially involved in human lymphatic vascular disease.

To decode mechanical cues, cells are endowed with a palette of molecular force sensors. Among these sensors, Piezo ion channels (*1*) have emerged as critical force sensors that participate in determining how cells sense their physical environment.

Piezo channels assemble as trimers that possess all the structural requirements for mechanosensitivity (*2*, *3*). However, native PIEZO1 channels can display nonuniform subcellular localization (*4*–*7*) and exhibit different gating kinetics—principally, slower inactivation (*1*, *8*–*13*)—in many cell types when compared with heterologous expression systems. These observations could be explained by differences in lipid composition (*14*, *15*), curvature-dependent sorting (*5*, *7*), or protein-protein interactions. Many ion channels interact with auxiliary subunits (*16*, *17*) to modify their cellular location and gating properties. Ion-channel auxiliary subunits are commonly defined by four criteria: (i) they are non–pore-forming subunits, (ii) they have a direct and stable interaction with the pore-forming subunit, (iii) they modulate channel properties in heterologous systems, and (iv) they regulate endogenous channel activity in native cells (*17*). Despite substantial effort, to our knowledge, no Piezo channel–binding partners or auxiliary subunits have emerged that fit these criteria.

Identification of Piezo channel–binding proteins

To identify binding partners for Piezo channels we used two complementary affinity-capture mass spectrometry (AC-MS) strategies in conjunction with two CRISPR-Cas9–edited, PIEZO1-expressing, human dermal fibroblast (hDF) lines (Fig. 1, A to F, and fig. S1). The reason we chose fibroblasts lies in the previously reported slower inactivation kinetics of PIEZO1 in this cell type (*10*, *12*, *13*). Our pipeline consisted of three comparator groups: (i) hDF with PIEZO1 ablated with CRISPR/cas9 (that were compared with wild-type cells in which PIEZO1 was enriched through a conventional anti-PIEZO1 antibody strategy), (ii) hDF with a HaloTag added into the endogenous PIEZO1 loci (P1-Halo) where PIEZO1 was enriched with HaloTrap resin, and (iii) primary human cardiac fibroblasts (hCF) in which PIEZO1 was enriched through a conventional anti-PIEZO1 antibody strategy. We then stringently analyzed the resulting MS data to identify PIEZO1-interacting proteins present in all three groups that were not present in any of their respective negative controls. Using these criteria, we only identified two proteins, the first of which was PIEZO1 (Fig. 1E). This provided strong validation for both affinity-capture strategies. The second protein identified was the sparsely studied transcriptional regulator MyoD (myoblast determination) family–inhibitor domain-containing protein (MDFIC) (*18*, *19*). MS provided 39 ± 14% coverage of MDFIC protein aver over the three groups (Fig. 1F).

Using RNA expression data, we identified many cell types in addition to fibroblasts that coexpress Piezo channels and the MyoD-family inhibitor proteins, MDFIC or MDFI (fig. S2, A and B) (*20*). We then validated the protein-protein interaction by expressing N-terminally hemagglutinin (HA)–tagged MDFIC together with PIEZO1 in human embryonic kidney 293 cells with SV40 large-T antigen (HEK293T). Using a coimmunoprecipitation (co-IP) assay, we could reciprocally capture PIEZO1 with MDFIC and found that the complex was present under mechanical (shear stress) or chemical [10 μM Yoda-1 (*21*)] activation of PIEZO1 (fig. S2C), which indicated the stability of the interaction. We also confirmed that PIEZO1 interacted with the closely related MDFI (fig. S2D) (*22*). PIEZO2 has high sequence similarity with PIEZO1, so we next tested whether MDFIC selectively interacted with PIEZO1/2 channels using native gels. We identified MDFIC at the size of the respective PIEZO1/2 trimers but not in oligomeric complexes of other structurally unrelated channels such as TRPM4 (tetramer) or TREK-1 (dimer) (fig. S2E). In doing so, we found that PIEZO1 enhanced the protein amounts of both MDFIC and MDFI by greater than three- to fourfold (fig. S2, C to E). To determine the specificity of this effect, we coexpressed MDFIC with PIEZO1 and PIEZO2 and compared the amount of MDFIC when expressed alongside other unrelated ion channels. Coexpression of MDFIC with green fluorescent protein (GFP), TRPM4, TRPV4, or TREK-1 did not enhance the amount of MDFIC (fig. S3, A and B). To understand the mechanism, we used a cycloheximide chase assay to observe the degradation time course of MDFIC. In cells treated for 4 to 8 hours with the protein synthesis inhibitor cycloheximide, we observed using Western blotting that the protein amount of MDFIC fell much more rapidly in the absence of PIEZO1 (fig. S3, C and D). This suggests that interacting with PIEZO1 decreased MDFIC turnover.

MDFIC binds the PIEZO1 pore module

To provide molecular details of the interaction, we coexpressed mouse PIEZO1 (mPIEZO1) with N-terminally FLAG-tagged mouse MDFIC and purified the complex using FLAG resin. Using single-particle cryogenic electron microscopy (cryo-EM), we determined the structure of the PIEZO1-MDFIC complex at an overall resolution of 3.66 Å (Fig. 2, A and B, and fig. S4). We resolved the C-terminal 21 amino acids of MDFIC (Fig. 2, A to D), whereas the N-terminal portion displayed little or no density, presumably owing to local dynamics. The resolved region of MDFIC (residues 225 to 246) consists of an amphipathic helix that sits parallel to the membrane at the membrane interface (Fig. 2C). This helix inserts laterally into the PIEZO1

[1]Victor Chang Cardiac Research Institute, Sydney, NSW 2010, Australia. [2]School of Clinical Medicine, Faculty of Medicine and Health, University of New South Wales, Sydney, NSW 2052, Australia. [3]Interdisciplinary Research Center on Biology and Chemistry, Shanghai Institute of Organic Chemistry, Chinese Academy of Sciences, Shanghai 200032, China. [4]State Key Laboratory of Chemical Biology, Shanghai Institute of Organic Chemistry, Chinese Academy of Sciences, Shanghai 200032, China. [5]Research School of Biology, Australian National University, Acton, ACT 2601, Australia. [6]Department of Biochemistry and Molecular Biophysics, University of Chicago, Chicago, IL 60637, USA. [7]Centre for Cancer Biology, University of South Australia and SA Pathology, Adelaide, SA 5001, Australia. [8]Adelaide Medical School, University of Adelaide, Adelaide, SA 5005 Australia. [9]Department of Genetics and Molecular Pathology, SA Pathology, Adelaide, SA 5000, Australia. [10]Department of Biomedical Engineering, Southern University of Science and Technology, Shenzhen 518055, China. [11]School of Biotechnology and Biomolecular Science, University of New South Wales Sydney, Kensington, NSW 2052, Australia. [12]School of Biomedical Sciences, Faculty of Medicine and Health, University of New South Wales Sydney, Kensington, NSW 2052, Australia.
*Corresponding authors. Email: c.cox@victorchang.edu.au (C.D.C.); yzhang@mail.sioc.ac.cn (Y.Z.).
†These authors contributed equally to this work.

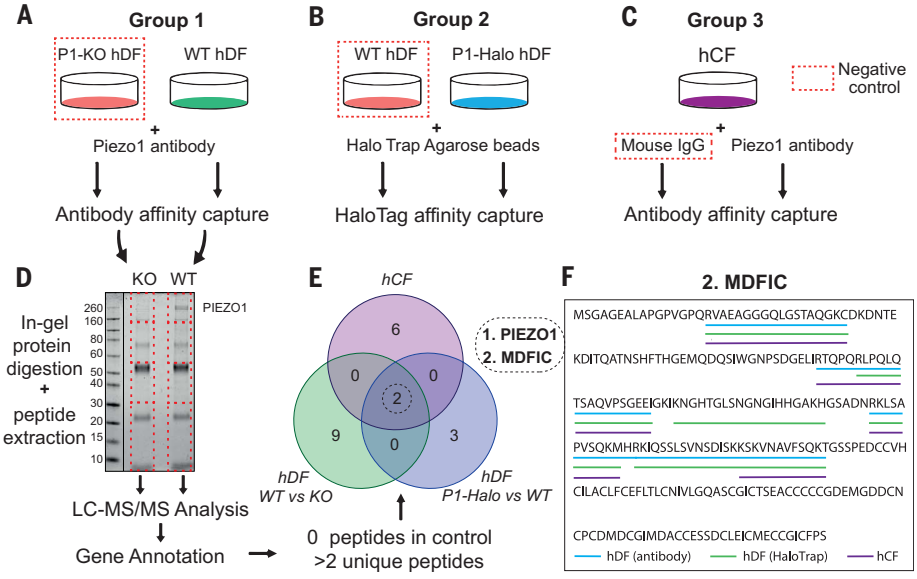

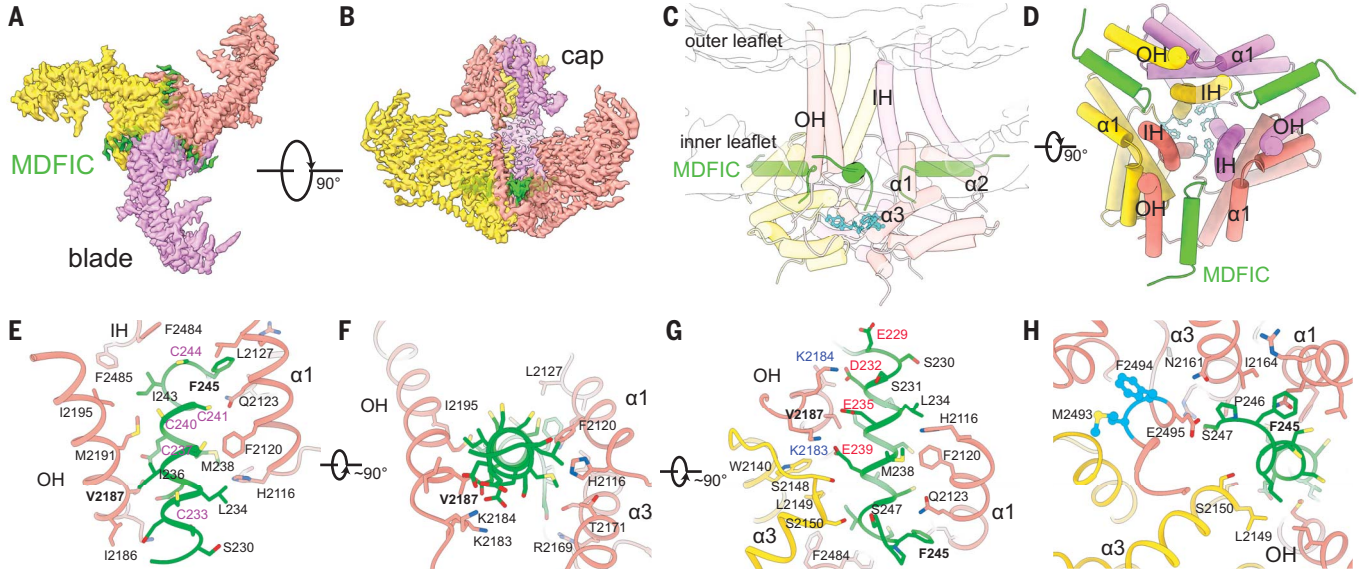

Fig. 1. AC-MS identifies a newly characterized family of Piezo-channel binding partners. Groups for AC-MS consisted of: (**A**) WT and PIEZO1-edited (knockout, KO) human dermal fibroblasts (hDF; n = 2), (**B**) WT and PIEZO1-HaloTag (P1-Halo) hDF (n = 2), and (**C**) primary human cardiac fibroblasts (hCF; n = 2). (**D**) Affinity-captured protein lysates were run on SDS–polyacrylamide gel electrophoresis (SDS-PAGE) gels and sectioned into quadrants (red dashed lines). Each quadrant was subjected to in-gel protein digestion, peptide extraction and liquid chromatography (LC), and MS, in that order. (**E**) Venn diagram illustrating proteins identified in each experimental group that had ≥2 distinct peptides that were absent from negative control replicates. (**F**) Two proteins were identified in all positive control replicates: PIEZO1 and MDFIC. Alignment of distinct MDFIC peptides identified with MS.

Fig. 2. Structural elucidation of the PIEZO1-MDFIC complex. (**A** and **B**) Cryo-EM density maps of the mouse PIEZO1-MDFIC complex at 3.66-Å nominal resolution viewed from the top (A) and side (B), with the resolved MDFIC region colored green. (**C**) The distal C-terminal of MDFIC resides parallel to the bilayer between the anchor domain (α1 to α3) and the outer helix (OH). The cytoplasmic constriction residues Met2493 and Phe2494 are shown in cyan. (**D**) The C-terminal region of MDFIC penetrates deep into the pore module of PIEZO1, approaching the inner helix (IH). (**E** to **H**) The interactions between PIEZO1 and MDFIC from the (E) membrane-facing view, (F) lateral view, and (G and H) cytoplasmic-facing view. Variants linked to lymphatic malformations (mPIEZO1 V2187 and mMDFIC F245) are labeled in bold.

pore module, nestling between the anchor domain and the outer helix of PIEZO1 (Fig. 2, C and D), making contacts with His^{2116}, Phe^{2120}, and Gln^{2123} from the α1 helix of the anchor domain; Val^{2187}, Met^{2191}, and Ile^{2195} from the outer helix; and Phe^{2484} and Phe^{2485} at the base of the inner helix that lines the PIEZO1 pore (Fig. 2E). The amphipathic helix of MDFIC consists of a sequence of five cysteines that point toward the bilayer interior (Fig. 2, E and F) and a sequence of four negatively charged residues that point toward the solvent, forming salt bridges with multiple lysine residues (Fig. 2, F and G). The MDFIC C terminus penetrates far enough to come close to the cytoplasmic constriction formed by Met^{2493} and Phe^{2494} (Fig. 2H) and residues critical for voltage-dependent inactivation, Lys^{2479} and Arg^{2482} (*23*, *24*). Despite its central location, MDFIC binding did not influence the closed structure of the PIEZO1 pore module (fig. S4I).

Because both PIEZO1 and MDFIC are essential for lymphatic development in mice and humans (*19*, *25*, *26*), we investigated using the ClinVar database whether any disease-causing mutations were located within this binding interface. We found mutations in both PIEZO1 (human V2171f; Fig. 2, E and G) and MDFIC (human F244L; Fig. 2, E and H) associated with human lymphatic disease.

MDFIC and MDFI regulate Piezo gating

Given the location of MDFIC binding, we next tested whether human MDFIC and MDFI-modified human PIEZO1 (hPIEZO1) gating in HEK293T cells. MDFIC and MDFI expressed

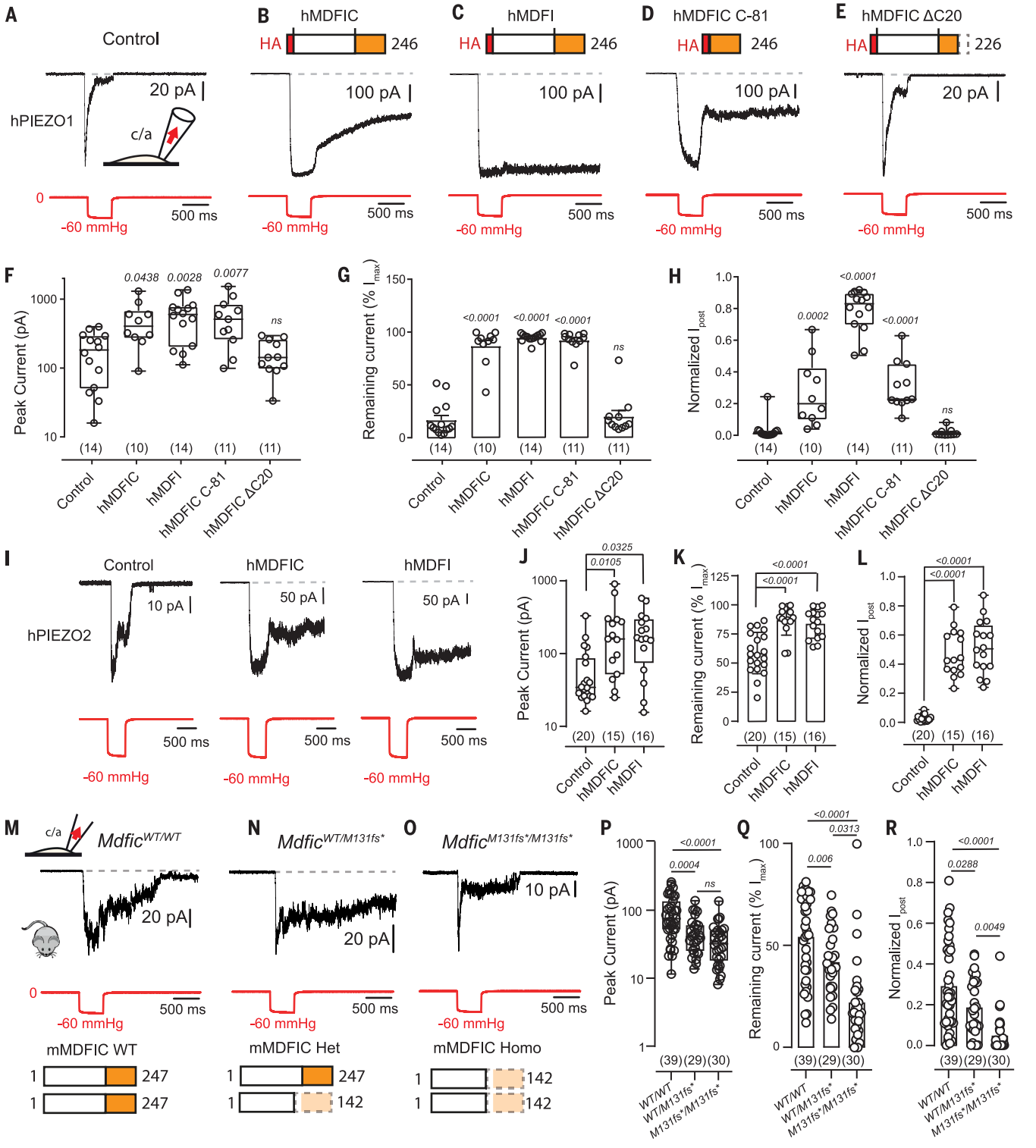

Fig. 3. MyoD-family inhibitor proteins regulate PIEZO1 and PIEZO2 channel gating. (**A** to **E**) Representative cell-attached patch-clamp recordings from hPIEZO1 (A) control and hPIEZO1 in the presence of (B) hMDFIC, (C) hMDFI, (D) the conserved C terminus of MDFIC (hMDFIC C-81), and (E) with MDFIC lacking its C-terminal 20 amino acids (hMDFIC ΔC20) all at a holding potential of −65 mV. (**F** to **H**) Quantification of (F) peak currents per patch, (G) percent current remaining, and (H) normalized current 1 s after pressure release (normalized I_{post}) for replicates of cell-attached recordings shown in (A) to (E). (**I** to **L**) Representative cell-attached recordings from (I) hPIEZO2 control and hPIEZO2 in the presence of hMDFIC and hMDFI, and [(J) to (L)] quantification of replicates. (**M** to **O**) Representative cell-attached patch-clamp recordings from mouse cardiac fibroblasts isolated at E16.5 from (M) WT, (N) heterozygous, and (O) homozygous $Mdfic^{M131fs*}$ mice. (**P** to **R**) Quantification of (P) peak current per patch, (Q) percent current remaining, and (R) normalized I_{post} for replicates of cell-attached recordings shown in [(M) to (O)] All data are displayed as mean ± SEM or as maximum-to-minimum box-and-whiskers plot. *P* values are noted above the plots and were determined with one-way analysis of variant (ANOVA) and either Dunnett's or Tukey's multiple comparison test. ns, not significant.

alone did not generate stretch-activated currents (fig. S5, A to D). Compared with hPIEZO1 alone, coexpression with MDFIC resulted in a mild right shift in the pressure response curve [from 14.5 ± 3.2 mmHg (n = 9 cells) to 23.9 ± 3.9 mmHg (n = 6)] (fig. S5, E to G), a marked increase in the peak stretch-evoked currents, a substantial slowing of channel inactivation, and continued channel gating even after the pressure was released (Fig. 3, A to H, and fig. S5). We quantified the latter of these effects using the current that remained 1 s after application of stretch (I_{post}). Neither MDFIC nor MDFI influenced mRNA TMEM150c, demonstrating that these inactivation effects were independent of TMEM150c (fig. S5N) (*27*). MDFIC did not influence PIEZO1 protein amounts in either HEK293T or LNCaP cells transfected with MDFIC (fig. S6, A to D) but did increase PIEZO1 single-channel conductance from 26 ± 3pS (n = 4) to 48 ± 8 pS (n = 4) (fig. S6, E to G). Thus, the increase in stretch-activated currents in the presence of MDFIC is likely driven by changes in conductance and its strong

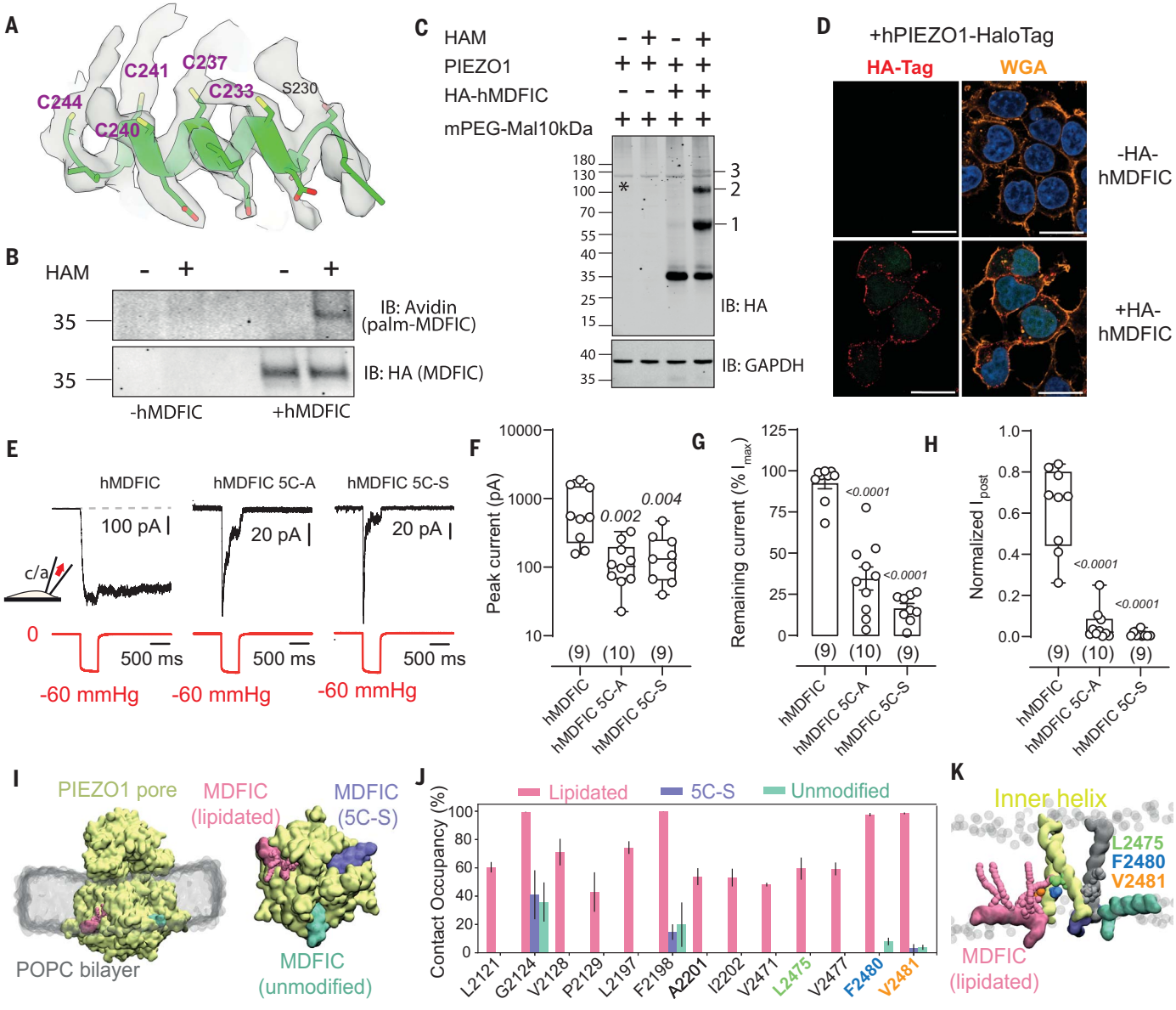

Fig. 4. C-terminal lipidation of MDFIC underlies regulation of PIEZO1 channel gating. (**A**) Cryo-EM density map showing extension of density on cysteine residues within the C terminus of MDFIC. (**B**) Representative immunoblot (IB) with Avidin (top) or anti-HA (bottom) from acyl biotin exchange showing lysate ± hydroxylamine (HAM). Blots show a band at the correct size for HA-tagged MDFIC, but the biotinylated MDFIC can only be seen in the HAM-treated group, which indicates palmitoylated-MDFIC (palm-MDFIC). (**C**) Mass-tagging of MDFIC with methoxy-polyethylene glycol (mPEGylated) maleimide reveals at least three palmitoylation sites labeled 1 to 3 (* represents a nonspecific band in all groups). (**D**) Membrane-localized HA-tagged MDFIC in PIEZO1-HaloTag expressing HEK293T cells and the wheat germ agglutinin (WGA)–delineated membrane. (**E**) Representative cell-attached recordings of hPIEZO1 in the presence of WT MDFIC and mutation of the five C-terminal cysteine residues to either alanine (5C-A) or serine (5C-S), which abolishes the regulatory effects of MDFIC. (**F** to **H**) Quantification of (F) peak currents per patch, (G) percent current remaining, and (H) normalized I_{post} for replicate recordings shown in (E). (**I**) All-atom molecular dynamic simulations of the mPIEZO1 pore module in complex with unmodified (green), 5C-S mutant (purple), and lipidated MDFIC (pink) C-termini. (**J** and **K**) Contact occupancy for MDFIC monomers with PIEZO1 residues from replicate simulations and a snapshot of the location of three inner helix residues important for inactivation that interact with lipidated MDFIC for prolonged periods. P values are noted above the plots and were determined with one-way ANOVA and Dunnett's multiple comparison test. ns, not significant.

effect on inactivation. The slow "closure" after pressure release—identified in single-channel recordings (fig. S6, H to J) and from macrocurrents—was more pronounced at hyperpolarizing voltages (fig. S7, A and B), which suggests an effect on the structural transition–governing voltage-dependent inactivation (*23*, *24*). Consistent with this, the channel could be rapidly closed by flipping the voltage to depolarizing potentials (fig. S7, C and D). We identified slower inactivation in both cell-attached and whole-cell modes (fig. S8). Additionally, MDFIC expression did not influence the function of mechanosensitive TREK-1 channels, ruling out nonspecific effects (fig. S9).

The C termini of MDFIC and MDFI are highly homologous, whereas the N termini bear little resemblance and have no known function (fig. S10A); therefore, we asked whether the MyoD-inhibitor domain of MDFIC (residues 165 to 246, which we name C-81) expressed alone could modify PIEZO1 function. Despite being unstable, this domain reduced channel inactivation (Fig. 3, D and G, and fig. S10B). Moreover, the amount of C-81 protein was dramatically increased when coexpressed with PIEZO1 (fig. S10, C and D). Conversely, truncation of the C-terminal 20 residues (ΔC20) prevented MDFIC from regulating PIEZO1 gating (Fig. 3, E to G). This truncation reduced the interaction with PIEZO1, and MDFIC ΔC20 protein amounts were only marginally affected by PIEZO1 (fig. S10, D and E). Thus, functional regulation of the PIEZO1-MDFIC complex depends on the conserved C terminus of MDFIC.

Given the homology of PIEZO1 and PIEZO2 in the MDFIC-binding region, we additionally showed that the same regulation occurs for both hPIEZO2 and mouse Piezo orthologs (Fig. 3, I to L, and fig. S11). Moreover, the expression of MDFIC and MDFI correlated with the native inactivating phenotype of PIEZO1 in multiple human and mouse cell lines (fig. S12). This included HEK293T, in which fast PIEZO1 inactivation was seen, and prostate cancer cell lines (LNCaP and DU145), in which differential stretch-activated kinetics were previously reported (*9*). HEK293T and LNCaP have almost undetectable amounts of MDFIC and MDFI and display fast inactivation, whereas DU145 has notable amounts of MDFI at the mRNA level and inactivates slowly (fig. S12, A to F). Overexpression of MDFIC in LNCaP cells markedly slowed inactivation of native PIEZO1 channels (fig. S12, B to F). In mouse embryonic fibroblasts and C2C12 myoblasts, we detected MDFIC, and both cell types displayed slow PIEZO1 inactivation indicated by larger current remaining at the end of pressure pulses (fig. S12, G to I). By contrast, in Neuro2A (N2A) cells, PIEZO1 channels exhibited rapid inactivation with undetectable expression of MDFIC and MDFI.

We next asked whether genetic loss of MDFIC could modify the kinetics of native PIEZO1 currents. To investigate this, we used a mouse model of a complex lymphatic anomaly known as central conducting lymphatic anomaly, bearing a truncated variant of MDFIC that lacked the complete conserved C-terminal but retained the N-terminal region (*19*). Our assessment of PIEZO1 activity in embryonic cardiac fibroblasts isolated from embryonic day 16.5 (E16.5) wild-type (WT/WT), heterozygous (WT/M131fs*), and homozygous mice (M131fs*/M131fs*) revealed that fibroblasts harboring C-terminally truncated MDFIC had smaller PIEZO1 currents that inactivated more rapidly (Fig. 3, M to R). This effect on inactivation was phenocopied by silencing MDFIC in fibroblasts with small interfering RNA (siRNA) (fig. S13, D to J).

PIEZO1 regulation requires MDFIC lipidation

Cryo-EM maps of MDFIC revealed extra densities on Cys^{233}, Cys^{237}, Cys^{240}, Cys^{241}, and Cys^{244} (Fig. 4A). Given that this helix is situated at the membrane interface and contains motifs for cysteine lipidation (*28*), we hypothesized that these extra densities resulted from lipidation, which is the covalent addition of acyl chains to amino acids (*29*). A second cryo-EM complex of the MDFIC mutant Cys240Ala (3.68 Å) specifically lacked the extra density at Cys^{240}, which is consistent with posttranslational modification (fig. S14). Acyl biotin exchange confirmed that MDFIC was palmitoylated (Fig. 4B). Mass tagging with polyethylene gycol–modified (PEGylated) maleimide (increases mass per palmitoylated site) showed that there were at least three sites for lipidation on MDFIC (Fig. 4C), that two were in the distal C terminus (fig. S15), and that like most lipidated proteins, MDFIC associated with the plasma membrane (Fig. 4D).

To check whether MDFIC lipidation is functionally relevant, we mutated all five C-terminal cysteines to alanine or serine. MDFIC with $Cys^{233/237/240/241/244}$Ala (5C-A) or $Cys^{233/237/240/241/244}$Ser (5C-S) bound to PIEZO1, but neither mutant influenced PIEZO1 activity, which suggests that the lipidation of the MDFIC C terminus is critical for PIEZO1 regulation (Fig. 4, E to H, and fig. S15C).

To probe the role of lipidation, we used all-atom molecular-dynamics simulations of the PIEZO1 pore module (residues 1956 to 2547) in complex with the MDFIC C terminus (Fig. 4, I to K, and fig. S16). Simulations consisted of three MDFIC monomers: one unmodified, one lipidated at all five cysteine residues in the helix, and one where each cysteine was mutated to serine (5C-S mutants) (Fig. 4I). All variations of the MDFIC C terminus remained stably bound (fig. S16, A and B). An overlay of a snapshot from simulations shows that the acyl chains coincide with the additional MDFIC cryo-EM densities (fig. S16C). We compared all interactions that occurred in either unmodified or lipidated MDFIC monomers with those in the 5C-S mutant, which we know binds to but does not modulate PIEZO1 function (Fig. 4J and fig. S16). Interactions between the unmodified and 5C-S MDFIC were indistinguishable, which supports the critical role of MDFIC lipidation in modulating PIEZO1 function. By contrast, the lipidated MDFIC had multiple distinct interactions with inner-helix residues (Fig. 4, J and K, and fig. S16, D and E). Some of these residues within the inner helix are critical for inactivation, including Leu2475 (*30*), making this the likely pathway for functional modification. Given that MDFIC would need to stay bound throughout the PIEZO1 conformational cycle, we also examined whether MDFIC could bind to the flattened state of PIEZO1 (*31*). When MDFIC was aligned to the same pocket, simulations showed that it interacted with the inner helix and remained stably bound (fig. S16, F to H).

Discussion

Using AC-MS, we have identified a family of Piezo-channel binding partners—the MyoD-family inhibitor proteins, MDFI and MDFIC—that fit all the criteria for Piezo-channel auxiliary subunits. Although our study does not resolve full-length MDFIC or its native membrane topology, it does reveal that MDFIC binds to the PIEZO1 pore module through its conserved C terminus, which regulates channel inactivation. The regulation of Piezo-channel inactivation critically involves palmitoylation of the distal C-terminal of MDFIC. Because palmitoylation is a reversible lipid addition (*29*), this adds the potential for dynamic spatiotemporal regulation of Piezo inactivation by MDFIC. Although we identified few other Piezo-channel binding-partner candidates with our "fibroblast-centric" screen, we speculate that the binding region of MDFIC could form a conserved binding site for alternate membrane-associated Piezo regulators or auxiliary subunits. In support of this hypothesis, the PIEZO1 lysine residues that form salt bridges with MDFIC have been proposed to interact with other proteins (*32*). Despite PIEZO1 channels being able to function as independent mechanosensors in simplified systems (*2*), ample evidence suggests that Piezos, particularly PIEZO2, may receive force through molecular tethers (*33*). Given the location of binding, it seems unlikely that MDFIC could act as a tethering molecule.

It remains to be seen how ubiquitous this regulatory mechanism is; MDFIC and MDFI are absent from many cell types with rapidly inactivating PIEZO1 channels, including LNCaP (*9*) and N2A (*1*), but are expressed in others, including fibroblasts (*10*, *12*, *13*) and endothelial cells that exhibit slower PIEZO1 inactivation (*8*, *11*, *14*). We isolated cardiac fibroblasts from mice that harbored a truncated MDFIC lacking the C terminus (*19*), in which PIEZO1 exhibited faster inactivation than in wild-type

fibroblasts. Thus, MDFIC- or MDFI-mediated regulation of Piezo channels could be widely used. Despite our study not defining a PIEZO1-MDFIC complex in lymphatic endothelial cells, the similar lymphatic phenotypes associated with loss of function of MDFIC (*19*) and PIEZO1 (*25*, *26*) means that this interaction may unearth molecular aspects underlying lymphatic vascular disease. Furthermore, both MDFIC and MDFI bind to transcription factors (*19*, *34*) [including GATA2, a master regulator of lymphatic valve development (*35*)]. Whether PIEZO1/2 channels influence this aspect of their function is unknown but may lay the foundation for the unveiling of a direct mechanosignaling pathway by means of Piezos to transcription through GATA2 or other transcription factors.

Thus, our structural and functional data not only reveal a family of Piezo-channel auxiliary subunits but may also reveal a conserved binding site for other membrane-associated proteins that modulate Piezo-channel function and, in doing so, the basis for an alternate Piezo-dependent mechanosignaling pathway.

REFERENCES AND NOTES

1. B. Coste *et al*., *Science* **330**, 55–60 (2010).
2. R. Syeda *et al*., *Cell Rep.* **17**, 1739–1746 (2016).
3. C. D. Cox *et al*., *Nat. Commun.* **7**, 10366 (2016).
4. M. Yao *et al*., *Sci. Adv.* **8**, eabo1461 (2022).
5. G. Vaisey, P. Banerjee, A. J. North, C. A. Haselwandter, R. MacKinnon, *eLife* **11**, e82621 (2022).
6. J. R. Holt *et al*., *eLife* **10**, e65415 (2021).
7. S. Yang *et al*., *Nat. Commun.* **13**, 7467 (2022).
8. S. Wang *et al*., *Nat. Commun.* **11**, 2303 (2020).
9. R. Maroto, A. Kurosky, O. P. Hamill, *Channels (Austin)* **6**, 290–307 (2012).
10. N. M. Blythe *et al*., *J. Biol. Chem.* **294**, 17395–17408 (2019).
11. J. I. Del Mármol, K. K. Touhara, G. Croft, R. MacKinnon, *eLife* **7**, e33149 (2018).
12. E. Glogowska *et al*., *Cell Rep.* **37**, 110070 (2021).
13. D. Jakob *et al*., *J. Mol. Cell. Cardiol.* **158**, 49–62 (2021).
14. J. Shi *et al*., *Cell Rep.* **33**, 108225 (2020).
15. L. O. Romero *et al*., *Nat. Commun.* **10**, 1200 (2019).
16. A. C. Dolphin, *J. Physiol.* **594**, 5369–5390 (2016).
17. D. Yan, S. Tomita, *J. Physiol.* **590**, 21–31 (2012).
18. S. Thébault, F. Gachon, I. Lemasson, C. Devaux, J. M. Mesnard, *J. Biol. Chem.* **275**, 4848–4857 (2000).
19. A. B. Byrne *et al*., *Sci. Transl. Med.* **14**, eabm4869 (2022).
20. M. Karlsson *et al*., *Sci. Adv.* **7**, eabh2169 (2021).
21. R. Syeda *et al*., *eLife* **4**, e07369 (2015).
22. C. M. Chen, N. Kraut, M. Groudine, H. Weintraub, *Cell* **86**, 731–741 (1996).
23. M. Moroni, M. R. Servin-Vences, R. Fleischer, O. Sánchez-Carranza, G. R. Lewin, *Nat. Commun.* **9**, 1096 (2018).
24. J. Wu *et al*., *Cell Rep.* **21**, 2357–2366 (2017).
25. K. Nonomura *et al*., *Proc. Natl. Acad. Sci. U.S.A.* **115**, 12817–12822 (2018).
26. E. Fotiou *et al*., *Nat. Commun.* **6**, 8085 (2015).
27. E. O. Anderson, E. R. Schneider, J. D. Matson, E. O. Gracheva, S. N. Bagriantsev, *Cell Rep.* **23**, 701–708 (2018).
28. Y. Xie *et al*., *Sci. Rep.* **6**, 28249 (2016).
29. A. Main, W. Fuller, *FEBS J.* **289**, 861–882 (2022).
30. W. Zheng, E. O. Gracheva, S. N. Bagriantsev, *eLife* **8**, e44003 (2019).
31. X. Yang *et al*., *Nature* **604**, 377–383 (2022).
32. J. Wang *et al*., *Cell Rep.* **38**, 110342 (2022).
33. C. Verkest, S. G. Lechner, *Curr. Opin. Physiol.* **31**, 100625 (2023).
34. L. Snider *et al*., *Mol. Cell. Biol.* **21**, 1866–1873 (2001).
35. J. Kazenwadel *et al*., *J. Clin. Invest.* **125**, 2979–2994 (2015).

ACKNOWLEDGMENTS

We thank B. Martinac, E. Perozo, J. Xu, and the Patapoutian Lab for useful scientific input and Y. Zhang and Y. Yuan for mass spec support. We thank the Cryo-EM Center at the Interdisciplinary Research Center on Biology and Chemistry of the Shanghai Institute of Organic Chemistry for help with data collection. **Funding:** This work was supported by Australian Research Council (ARC) Future Fellowship FT220100159 (C.D.C.); STI2030-Major Projects 2022ZD0207400, Shanghai Municipal of Science and Technology Project 20JC1419500, and Shanghai Municipal Science and Technology Major Project 2019SHZDZX02 (Y.Z.); National Health and Medical Research Council Ideas Grant 2021260 and the Lymphatic Malformation Institute (N.L.H.); ARC DP200100860 (B.C.); and Medical Research Future Fund grant GHFM76777 (H.S.S.). Research was undertaken with the assistance of resources and services from the National Computational Infrastructure, supported by the Australian Government. **Author contributions:** Z.Z., M.Y., and D.C. generated cell lines and performed biochemical and imaging experiments. Z.Z., N.B., and C.D.C. performed electrophysiology. G.A.S., D.L.S., H.S.S., V.J., R.P.H., and N.L.H. generated animal models and isolated cells. Z.Z. and J.V.L. generated reagents. X.M. and Y.Z. performed cryo-EM structural studies. B.C. and Y.L. performed molecular dynamics simulations. C.D.C. and Y.Z. conceived of and supervised the project. All authors wrote and approved the manuscript. **Competing interests:** C.D.C. and Z.Z. note an Australian provisional patent application #2023902096 entitled "Piezo channel regulators." **Data availability:** The composite map of the PIEZO1-MDFIC complex has been deposited in the Electron Microscopy Data Bank under the accession code EMD-35577. The composite map may contain artificial features near the boundaries of the masks. The consensus map, masked refined cap map, masked refined TMD map, and the map of PIEZO1-MDFIC (C240) have been deposited under the accession codes EMD-36241, EMD-36242, EMD-36243, and EMD-36244. The atomic coordinates have been deposited in the Protein Data Bank under the accession code 8IMZ. All data are available in the main text or the supplementary materials. **License information:** Copyright © 2023 the authors, some rights reserved; exclusive licensee American Association for the Advancement of Science. No claim to original US government works. https://www.science.org/about/science-licenses-journal-article-reuse

SUPPLEMENTARY MATERIALS

science.org/doi/10.1126/science.adh8190
Materials and Methods
Supplementary Text
Figs. S1 to S16
Tables S1 to S3
References (*36*–*47*)

Submitted 16 March 2023; accepted 19 July 2023
10.1126/science.adh8190

By **Tomasz Głowacki**

Teaching workplace skills

The email got my heart racing. "Thank you for letting me observe your classes. It was an unusual experience," it began. I am an industry scientist, and in my spare time I was teaching a course for computer science students at a local university. By that point in the semester, I hadn't asked the students to solve any technical problems or even open their computers. Instead, I'd focused on practical exercises that taught them teamwork and communication, skills they'd need in industry. My approach caught the attention of the university, so a teaching expert was dispatched. The note made me wonder whether university officials would hail the unique perspective I brought from industry—or remove me from the classroom.

Ever since I was a child, I admired my mother, who was a teacher, and I wanted to follow in her footsteps. During my own studies, I enjoyed serving as a teaching assistant, helping students understand complicated concepts and witnessing their "aha" moments. But upon finishing my Ph.D., I decided against pursuing an academic position after realizing that although my research was well-regarded, it was not making any practical difference. I felt unfulfilled and discontented, and I eventually transitioned into industry.

Over the past 10 years, I have worked a variety of jobs. I used my analytical skills to uncover insurance fraud at a consulting company. I built and managed teams at a technology company. And, in my current job, I oversee a team of people that uses data science to boost company efficiency and enable better decision-making. In all these roles in business, I have tapped into my scientific expertise. But I have also had the opportunity to develop skills I didn't learn in academia.

At the consulting company, for instance, I worked with software developers, insurance experts, and lawyers. This helped me learn how to communicate what I was doing in a nontechnical way so everyone could understand. Later, at the technology company, I learned about the importance of team dynamics and collaboration after recruiting a highly skilled individual, complete with a Ph.D., who seemed the right fit for the job. It quickly became apparent, however, that he had difficulties dealing with others. Some of his colleagues called him a "smart jerk" behind his back. From then on, I didn't just look at someone's technical expertise when hiring; I also wanted to know what soft skills they could bring to the table.

"I decided to use games and challenges to encourage teamwork and creativity."

I thought of these lessons when I started to develop the university class. The part-time role was appealing because I was eager to share my expertise and get back to working with students. But I didn't want to use my old teaching style, which focused on lectures and whiteboard exercises. I wanted to cultivate the same qualities I was looking for in job candidates at my company.

I decided to use games and challenges to encourage teamwork and creativity. In one, students had to work together to decide how to survive a harsh desert environment. In another, they built the tallest structure they could out of spaghetti and marshmallows. The teaching expert sat in on one such class.

I worried they might have been taken aback. But after that unsettling opening, their email was positive: "I understand the important message you're conveying," they wrote. "Today's industry is about people, not just computers. I fully support you. Keep up the good work."

I've now been teaching this course for 4 years, enough time for some of my students to have graduated and taken jobs in industry. At a recent networking event, some of them told me how the skills and knowledge they gained in my class helped them land their jobs. Hearing that my teaching had a positive impact on their career paths was truly rewarding.

In the end, education is not just about imparting knowledge. It's also about helping students develop soft skills that will help them succeed wherever they plan to go, be it academia or industry. ■

Tomasz Głowacki is the head of data science at Żabka, a company in Poland, and an assistant professor at WSB Merito University Poznań.

ILLUSTRATION: ROBERT NEUBECKER